See: NIST SP861, W. L. Grosshandler, et al., Editors

3. FLUID DYNAMICS OF AGENT DISCHARGE

William M. Pitts, Jiann C. Yang, Grzegorz Gmurczyk,
Leonard Y. Cooper, William L. Grosshandler
Building and Fire Research Laboratory

William G. Cleveland, Cary Presser
Chemical Science and Technology Laboratory

3.1 Introduction

The extinguishment of a fire using gaseous agents is a very complicated process which is not completely understood. Current fire-fighting agents such as halon 1301 and halon 1211 are believed to function by a combination of chemical (catalytic removal of hydrogen atoms at the flame front due to the presence of bromine atoms) and physical (cooling and dilution of flame gases) actions. All of the proposed alternative agents are known to be less effective (*i.e.*, considerably higher molar concentrations of the agent are required) than halon 1301. This reduction in effectiveness is attributed to the absence of bromine atoms in these chemicals and thus the absence of a highly effective chemical means of fire extinguishment.

An aspect of fire extinguishment using halons which has not received a great deal of attention is the role that the dispersion and evaporation characteristics of the agent play in fire-fighting effectiveness. The reason for this lack of interest in the past was that these properties have been nearly optimized by the use of halon 1301 for total flooding applications and halon 1211 for spray applications. With regard to total flooding applications, which are of most interest for this study, the low boiling point of halon 1301 has ensured that, for the majority of applications, it can be dispersed and vaporized very rapidly into a space. Design of total flooding systems generally have focused on the use and placement of hardware designed to ensure all areas of an enclosure quickly receive concentrations of the agent sufficient to extinguish the fire.

The fire fighting applications--nacelle and dry bay fires on aircraft--which are the focus of the current investigation have different requirements with respect to these agent characteristics. Due to the nature of dry bay fires, detection and extinguishment is generally required within tens of milliseconds. On the other hand, nacelle fires tend to have burned for longer periods before extinguishment and a premium is placed on the achievement of extinguishing concentrations which can be maintained for a period of time following extinguishment to prevent relight on heated surfaces. Effective dispersion throughout the volume is required, but the dispersion can take place over longer periods of time than for the dry-bay application. Due to the more stringent requirements for dry bay fire extinguishment, much of the work which follows has focused on rapid release and dispersion of agents. It should be kept in mind, however, that the findings also have applications for nacelle fire-fighting.

Even though the physical mixing processes involved are not generally considered in designs of halon fire-fighting systems, they are crucial. The important processes can be characterized into three major categories--release rate, dispersion and mixing, and evaporation. The release rate determines the minimum time required to extinguish a fire. If the release is very slow it is possible that the fire may never be extinguished.

The release rate for an agent also generally, but not always, affects the subsequent dispersion and mixing behavior of the agent. Much of the dispersion and mixing is the result of the momentum imparted to the agent by its release. If sufficiently high, this momentum causes the development of turbulent flows which can effectively transport the released agent throughout a volume.

In order to be fully effective, gaseous agents must interact with the flame as a gas. All of the alternative agents considered here, with the exception of FC-116, are liquids when stored under pressure at room temperature. As will be shown shortly, the room-temperature agents are released from pressurized bottles into ambient atmospheres as superheated liquids, *i.e.*, the liquid has a vapor pressure which is above the ambient pressure. Therefore, the vaporization behavior of these liquids following release becomes an important characteristic for fire fighting effectiveness.

This chapter discusses experimental and modeling studies which were designed to rank the proposed alternative agents with respect to release rate, dispersion and mixing, and evaporation. The following section (Section 3.2) describes the development of a model for predicting the release behavior of pressurized liquids from a containment vessel. This effort provided guidance for the design of an experimental system for investigating the release behavior and subsequent mixing and evaporation of the proposed alternative agents and halon 1301. The vessel design is discussed in Section 3.3. Experimental characterizations of the release rates from the vessel and characterization of vessel interior conditions are summarized in Section 3.4 for all of the agents and halon 1301. Section 3.5 describes the development and use of an experimental system for characterizing the dispersion and evaporation behavior of the alternative agents and halon 1301 following release from the pressurized vessel. During the course of this study initial attempts were made to modify existing computer models for two-phase evaporating flows to allow computation of agent release behaviors. These efforts are discussed in Section 3.6. The final section of the report summarizes the major findings of the chapter and provides recommendations for future work as well as a ranking for the alternative agents based solely on their release rate, dispersion and mixing, and evaporation behaviors.

3.2 Model of Discharging Vessel

3.2.1 The Problem and the Objective. This work formulates a mathematical model to simulate the discharge of halon and halon-alternative fire extinguishment agents from N_2-pressurized vessels. The objective is to develop a mathematical model which simulates agent-discharge experiments.

The model is expected to have three applications. First, it was used to guide the development of the experimental design and procedure (see Section 3.3) which closely simulates discharge of field-deployed vessels while allowing for acquisition of data, including high speed photography, to characterize adequately the discharge process. Second, the model will be used to evaluate the discharge characteristics of a wide range of alternative-agent/pressure-vessel configurations, thereby extending the slow and relatively costly experimental method of making such evaluations. Finally, it will be used to determine the discharge vessel exit-flow conditions for use in the simulation of agent dispersal outside of the vessel. [See Section 3.6.3 and Cooper (1993b).] After presenting the mathematical model, this section will include results of example calculations which addressed the first of these applications. Descriptions of the model have been presented previously elsewhere (Cooper, 1993a).

The analysis is based on the experimental arrangement depicted in Figure 1.

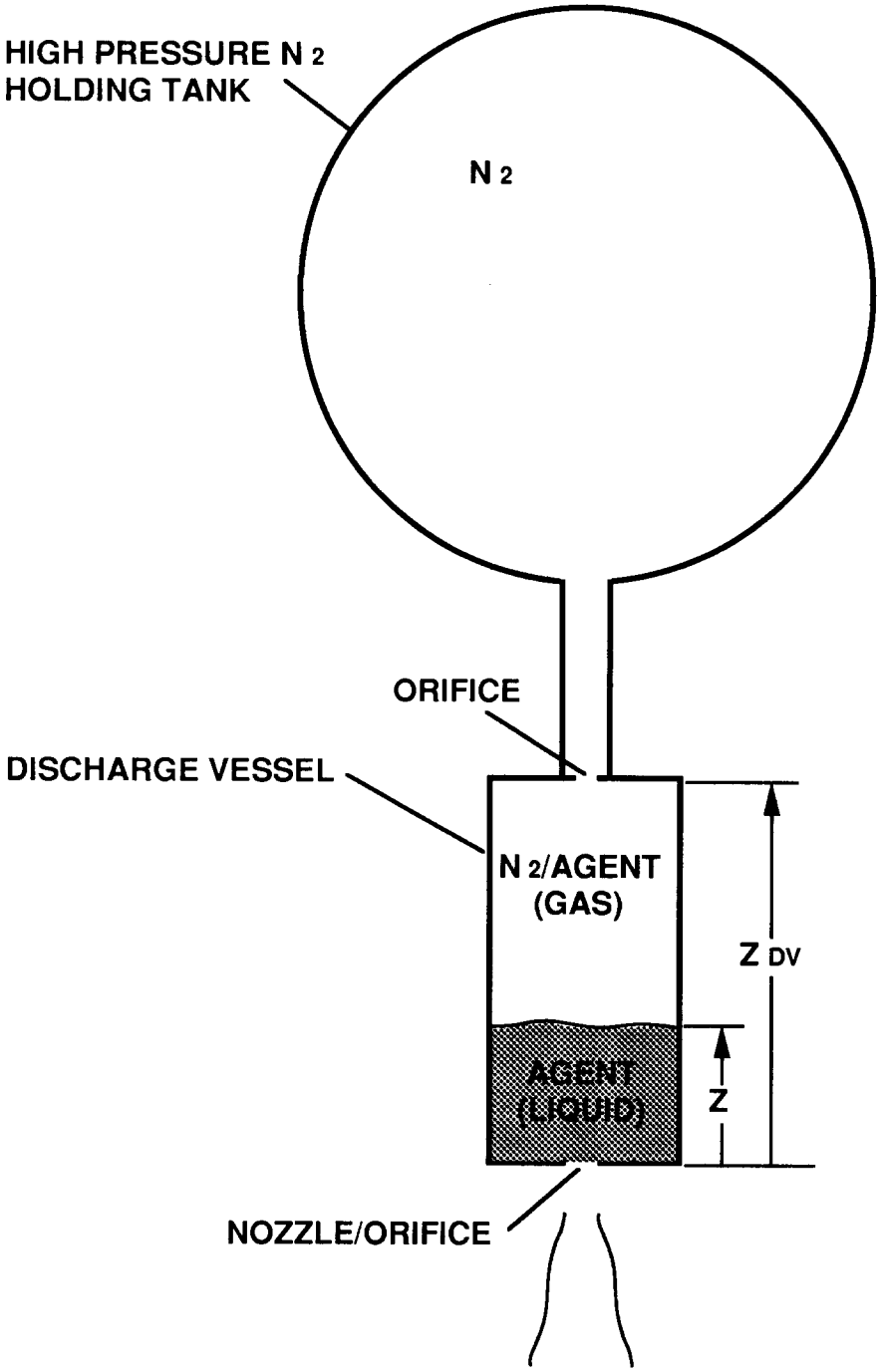

Figure 1. The experimental arrangement.

3.2.2 The Experiment and the Model Assumptions

3.2.2.1 The Experimental Arrangement. Refer to Figure 1. This represents generically the arrangement associated with the downward discharge experiments which were carried out at NIST. The Figure 1 arrangement can also be used to describe the phenomena of discharge from vessels under field conditions.

The experimental arrangement involves a right cylinder discharge vessel at pressure P_{DV}, which contains N_2-pressurized test agent, and a holding tank filled with mass $M_{HT,N2}$ of N_2 at pressure P_{HT}. The discharge vessel is of height Z_{DV} and cross-sectional area A_{DV}. The volume of the holding tank is V_{HT}.

The holding tank is connected *via* an orifice of area A_O to the discharge vessel. It is assumed that the flow path through the orifice can be opened or closed with a relatively fast-acting solenoid valve. If the path is open it is assumed that $P_{HT} \geq P_{DV}$, *i.e.*, the flow is always from the holding tank to the discharge vessel. In the case of a field-deployed system there is no holding tank and A_O is zero.

At the bottom of the vessel is a short-nozzle/orifice-type opening (note that the containment vessel exit will be referred to as the "nozzle/orifice" for the purposes of this section and Section 3.6.3) of area A_N. The agent will be discharged through this to the outside ambient environment which is at pressure $P_{AMB} < P_{DV}$. The discharge flow path is originally closed off by a cap or diaphragm. When the cap is removed, the test agent liquid is driven out of the discharge vessel by virtue of the cross-nozzle/orifice pressure difference.

3.2.2.2 The Procedure Prior to An Experimental Run or a Field-Deployed Discharge. The orifice and nozzle/orifice flow paths are closed and the discharge vessel is evacuated. The vessel is then filled completely with a known mass of test agent. There will be a volume of liquid agent below and a volume of gaseous agent above and the pressure will be P_{SAT}, the saturation pressure at the agent temperature. The vessel is then pressurized with N_2. This flows into the vessel from the holding tank or from some other relatively high-pressure N_2 source. In general, the upper gas volume is now a two-component mixture of N_2 and test agent gas. Although some N_2 may be dissolved in the liquid volume, it is assumed that the amount is always so small that throughout subsequent sequential (additional) pressurization and discharge processes to be studied here the properties of the liquid in the discharge vessel are well approximated by the liquid properties of the pure test agent.

Now consider the system at the time, $t = 0$, when an experimental run or a field-deployed discharge is initiated. The liquid/gas interface is a distance Z_1 above the bottom of the vessel. The mass of liquid in the vessel is $M_{DV,AL}$ (the subscript refers to that portion of Discharge Vessel test Agent in the Liquid state) and, throughout the experimental run or field-deployed discharge, the temperature and density of the liquid that remains in the vessel will be assumed to maintain their respective initial values, T_{AL} and $\rho_{AL} = \rho_{SAT}(T_{AL})$. As indicated, ρ_{AL} is estimated to be the density of saturated test agent liquid at the saturation temperature T_{AL}. The gas mixture is at an assumed uniform initial temperature $T_{DV,1}$ and the initial masses of gaseous test agent and N_2 in the discharge vessel are $M_{DV,AG}$ and $M_{DV,N2,1}$, respectively. Note that the prepressurization process, prior to $t = 0$, may have been so rapid that the liquid and gas are not in thermal equilibrium with each other. For this reason, $T_{DV,1}$ is not necessarily identical to T_{AL}. The discharge vessel and the holding tank are at the uniform pressures $P_{DV,1}$ and $P_{HT,1}$, respectively.

3.2.2.3 During an Experimental Run or Field-Deployed Discharge. During discharge of a Figure 1-type system, the flow path through the orifice is either open or closed at $t = 0^+$. When the orifice is closed the discharge will simulate discharge of a field-deployed system which does not involve a holding tank. When the orifice is open the discharge will simulate discharge of the experimental system where additional N_2 pressurization during the discharge is provided by the holding tank. The flow path through the nozzle/orifice at the exit of the discharge vessel is either opened at $t = 0^+$ (as in the field-deployed system, which uses an explosive cap to initiate discharge from an equilibrium state at the specified $P_{DV,1}$) or else it opens if and when P_{DV} rises to some specified diaphragm rupture/burst pressure, $P_{BURST} < P_{HT,1}$ (as in the experimental system). The time when this latter flow path is opened is designated as t_{BURST}.

3.2.2.4 Further Assumptions. For times and conditions of interest, it is assumed that as long as liquid remains in the vessel $P_{DV} > P_{SAT}(T_{AL})$, and there is no possibility of flashing (*i.e.*, spontaneous change from a thermodynamically unstable liquid state to an equilibrium, two-phase, liquid/gas state) in the liquid volume. Future work will address the problem of removing this latter constraint from the analysis. It is assumed that any N_2 dissolved in the liquid that may come out of solution during the discharge process is negligible.

The purpose of this work is to mathematically model the state of the system at any $t > 0$ up to t_D, where t_D is the smaller of 1) the time when the discharge vessel is emptied of test-agent liquid, and 2) the time when P_{DV} is reduced to $P_{SAT}(T_{AL})$. For experimental systems of interest here, t_{BURST} is expected to be of the order of 10 s and the time interval of the discharge process, $(t_D - t_{BURST})$, of the order of 10^{-2} s. Prior to t_D there is no gas mixture discharge from the vessel. The mass of gaseous agent in the vessel therefore remains constant at its initial value $M_{DV,AG}$.

In view of the relatively short times of interest it is assumed that during an experimental run or field-deployed discharge there is no heat or mass transfer across the liquid/gas interface. It is also assumed that there is no heat or mass transfer across the interface that contains the nitrogen and gaseous test agent in the combined holding-tank/discharge-vessel system, *e.g.*, there is negligible heat transfer to the walls of the vessel and holding tank. This is the basis of the assumption that both $M_{DV,AG}$ and the total mass of N_2 in the combined system, designated as M_{N2}, are constant for all t, $0 < t < t_D$. M_{N2} is determined from the initial conditions.

It is assumed that the gaseous test agent and the N_2 can be modeled as perfect gases with constant specific heats and gas constants, $C_{V,AG}$ $C_{P,AG}$, R_{AG} and $C_{V,N2}$ $C_{P,N2}$, R_{N2}. The values of the specific heats, which depend on temperature, are taken to be those which correspond to $T_{DV,1}$.

3.2.3 The Model Equations. Together with specified parameters, the unknown time-dependent variables of the problem that define the state of system at an arbitrary time are: P_{HT}, P_{DV}, $M_{HT,N2}$, $M_{DV,N2}$, $M_{DV,AL}$, T_{HT}, T_{DV}, and Z. Known/specified parameters would include: the initial values of these variables, $P_{HT,1}$, $P_{DV,1}$, $M_{HT,N2,1}$, $M_{DV,N2,1}$, $M_{DV,AL,1}$, $T_{HT,1}$, $T_{DV,1}$, and Z_1, respectively; the geometric parameters of the system, A_O, A_N, A_{DV}, Z_{DV}, and V_{HT}; material properties of the test agent and of N_2; the constant value $M_{DV,AG}$; and nozzle/orifice discharge coefficients, to be introduced below. The equations governing the variables are:

Equations of State in the Holding Tank and in the Discharge Vessel and the Law of Partial Pressure in the Discharge Vessel:

$$P_{HT} = \left(\frac{M_{HT,N2}}{V_{HT}}\right) R_{N2} T_{HT} \tag{1}$$

and

$$P_{DV} = \frac{(M_{DV,AG} R_{AG} + M_{DV,N2} R_{N2}) T_{DV}}{[(Z_{DV} - Z) A_{DV}]} \tag{2}$$

Conservation of Mass of N_2:

$$M_{DV,N2} + M_{HT,N2} = constant = M_{N2} = M_{DV,N2,1} + M_{HT,N2,1} \tag{3}$$

Relation of Z to $M_{DV,AL}$:

$$\frac{M_{DV,AL}}{\rho_{AL}} = A_{DV} Z \tag{4}$$

Reversible Adiabatic Expansion for N_2 in Holding Tank:

$$\frac{P_{HT}}{(M_{HT,N2})^{\gamma}} = constant = \frac{P_{HT,1}}{(M_{HT,N2,1})^{\gamma}} \; ; \quad \gamma = \frac{C_{P,N2}}{C_{V,N2}} = \frac{R_{N2}}{C_{V,N2}} + 1 \tag{5}$$

First Law of Thermodynamics for Entire Gas System:

$$\frac{d[(M_{DV,AG} C_{V,AG} + M_{DV,N2} C_{V,N2}) T_{DV} + M_{HT,N2} C_{V,N2} T_{HT}]}{dt} = P_{DV} A_{DV} \frac{dZ}{dt} \tag{6}$$

Flow Across the Orifice:

$$\frac{dM_{HT,N2}}{dt} = \begin{cases} -C_{D,O}A_O P_{HT}\left[\left[\frac{\gamma}{R_{N2}T_{HT}}\right]\left[\frac{2}{(\gamma+1)}\right]^{(\gamma+1)/(\gamma-1)}\right]^{1/2} \\ \quad if\ \frac{P_{HT}}{P_{DV}} \geq \left[\frac{(\gamma+1)}{2}\right]^{\gamma/(\gamma-1)}\ (i.e.,\ choked\ flow) \\ -C_{D,O}A_O P_{HT}\left[\frac{P_{DV}}{P_{HT}}\right]^{1/\gamma}\left[\frac{2\gamma\left[1-\left[\frac{P_{DV}}{P_{HT}}\right]^{(\gamma-1)/\gamma}\right]}{[(\gamma-1)R_{N2}T_{HT}]}\right]^{1/2} \\ \quad if\ \frac{P_{HT}}{P_{DV}} < \left[\frac{(\gamma+1)}{2}\right]^{\gamma/(\gamma-1)}\ (i.e.,\ un\text{-}choked\ flow) \end{cases} \tag{7}$$

where $C_{D,O}$ is the (compressible) flow coefficient for the orifice (Shapiro, 1953).

Flow Across the Nozzle/Orifice:

$$\frac{dM_{DV,AL}}{dt} = \begin{cases} -C_{D,N}A_N[2\rho_{AL}(P_{DV}-P_{AMB})]^{1/2} & if\ P_{AMB} \geq P_{SP} \\ -C_{D,N}A_N[2\rho_{AL}(P_{DV}-P_{SP})]^{1/2} & if\ P_{AMB} < P_{SP} \end{cases} \tag{8}$$

where $C_{D,N}$ is the flow coefficient for the nozzle/orifice and P_{SP} is defined below. Assuming that $A_N/A_{DV} << 1$ in discharge vessels of interest here, in Equation (8) the kinetic energy of the liquid upstream of the exit nozzle is neglected compared to the kinetic energy at, and immediately downstream of the nozzle.

3.2.4 Definition of P_{SP} and Comments on Equation (8). In Equation (8) it is assumed that the liquid in the discharge vessel, at state $[T, P] = [T_{AL}, P_{DV} > P_{SAT}(T_{AL})]$, flows into and through the exit nozzle/orifice while moving along state paths of constant entropy. When the pressure of the liquid drops below its saturation pressure, the liquid is assumed to initiate its movement into the "vapor dome" as a metastable superheated liquid.

For the generic pure material, the relevant *P-V* diagram which depicts the metastable states is sketched in Figure 2. This includes the region of metastable superheated liquid states and the corresponding region of metastable subcooled vapor states. For a pure material the metastable liquid or vapor state can only be maintained where $(\partial P/\partial V)|_T < 0$ (Modell and Reid, 1983), *i.e.*, only outside the locus of points, referred to as the spinoidal curve, where $(\partial P/\partial V)|_T = 0$. The spinoidal curve, sketched in Figure 2, passes through the critical state and has the superheated liquid region to its left and the subcooled vapor region to its right.

At any time during the discharge, P_{SP} is defined as the particular pressure along the liquid-leg of the spinoidal curve of the test agent associated with the intersection of the spinoidal curve and the

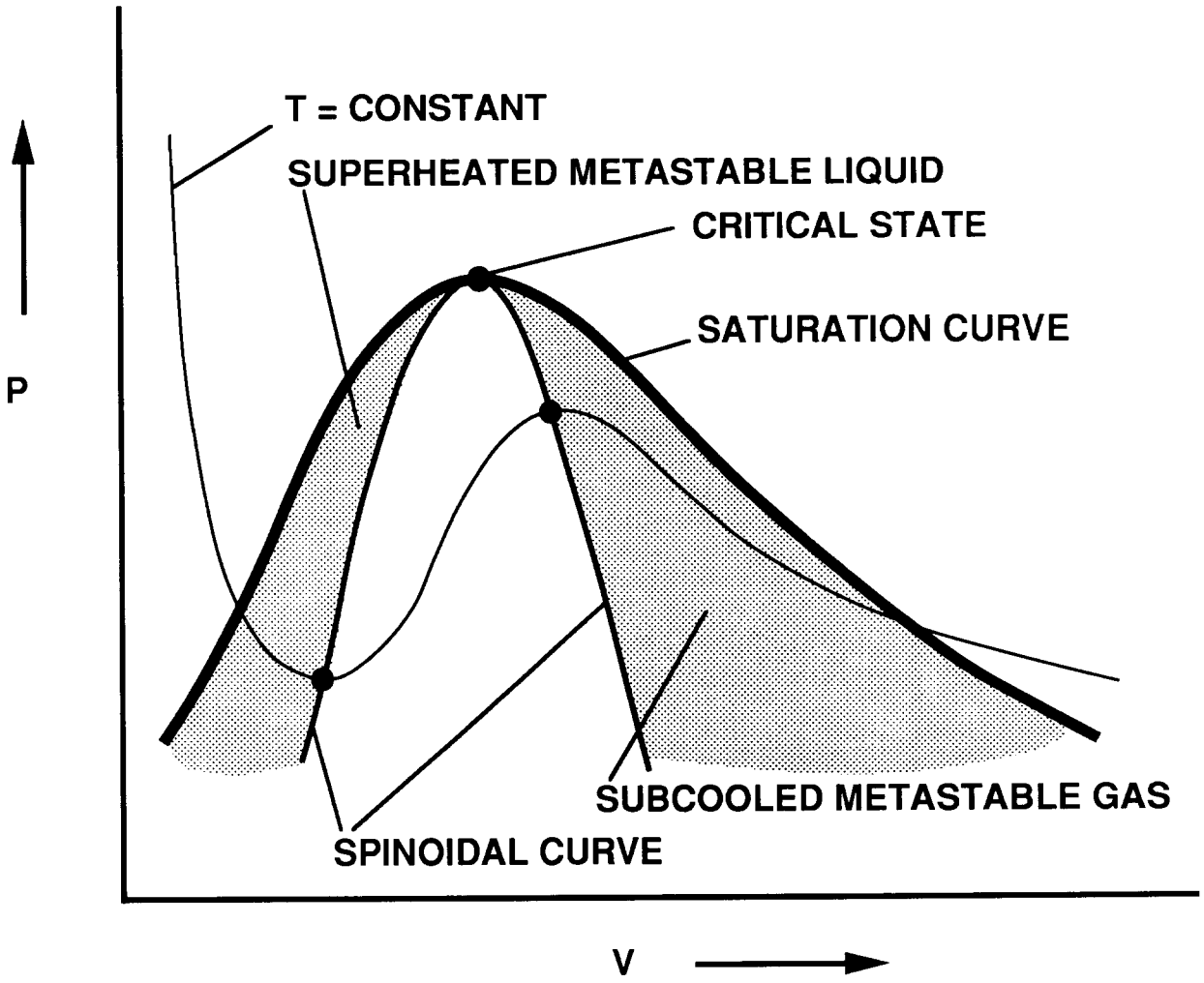

Figure 2. *P-V* diagram for a generic material; the spinoidal curve and regions of metastable liquid and vapor.

above-mentioned, instantaneous, constant-entropy paths. Since states along the spinoidal curve are states of unstable equilibrium where spontaneous nucleation will occur (Modell and Reid, 1983; Kim-E and Reid, 1983), *i.e.*, the constant-entropy metastable-state path of the liquid cannot be sustained at the state defined by the intersection point, it is conjectured that if $P_{SP} > P_{AMB}$ violent flashing of the liquid jet occurs where and when its pressure reaches P_{SP}. This would be upstream of a physically unachievable, *i.e.*, unstable, *vena contracta* at pressure P_{AMB}.

If P_{AMB} is achieved prior to the P_{SP} state then the top portion of Equation (8) is used. For this circumstance the constant-entropy state of the possibly metastable superheated liquid at P_{AMB} is a physically admissible endpoint to the liquid-jet development process. The situation is consistent with the idea that: 1) the endpoint state coincides with the *vena contracta* of the jet; 2) the jet is convected for some distance downstream of this endpoint without substantial changes and at the *vena contracta* diameter; and 3) the jet eventually breaks apart due to fluid-dynamic and/or thermodynamic (flashing) instabilities. Note that the upper Equation (8)-description of the nozzle flow rate of a superheated liquid as an incompressible, nonflashing fluid, is consistent with results reported in the literature, *e.g.*, (Benjamin and Miller, 1941) for flow through sharp-edge orifices and short nozzles.

If P_{SP} is achieved prior to P_{AMB} then flashing of the metastable liquid will be initiated immediately downstream of the position in space where the intercept occurs. In the latter case the incompressible flow calculation methodology is still applicable at and upstream of the spinoidal-curve intercept point. This is indicated by the use of the bottom portion of Equation (8).

The above discussion is illustrated with CO_2. For stable and metastable liquid CO_2, a sketch based on a drawing by Kim-E (1981, see his Figure 4) of constant-entropy paths in a P-T diagram is presented in Figure 3. In preparing his figure, Kim-E used the Peng-Robinson (1976) equation of state to describe the metastable liquid CO_2.

First assume that liquid CO_2 is in a Figure 1-type discharge vessel at $P_{DV} = 70 \times 10^5$ Pa and $T_{AL} = 288$ K. In Figure 3 this initial state is seen to lie on the $s = s2$ constant-entropy line, which has no positive P intercept with the spinoidal curve. As the liquid CO_2 flows toward and then out of the vessel's nozzle/orifice its state is assumed to move downward along the $s2$ curve of Figure 3. As can be seen, the $P = P_{ATM} \approx 1 \times 10^5$ Pa intercept on this curve, corresponding to $T \approx 277$ K, represents an achievable metastable liquid state for the material. This is the metastable liquid state that is predicted by the present model. It would be expected at, and for some distance downstream of, the jet's *vena contracta*.

Now assume that liquid CO_2 in a discharge vessel is at $P = P_{DV} = 60 \times 10^5$ Pa and $T = T_{AL} = 291$ K. In Figure 3 this initial state is seen to lie on the $s = s3$ constant-entropy line, which intersects the spinoidal curve at approximately $P_{SP} = 10 \times 10^5$ Pa $>> P_{AMB}$. In this case, as the liquid CO_2 flows through and out of the vessel nozzle/orifice the model predicts that it will flash explosively when $P = P_{SP}$. This will occur upstream of the position at which a fluid jet *vena contracta* would otherwise occur; well within a distance of one nozzle/orifice diameter downstream of the vessel exit.

This nozzle/orifice flow model is consistent with a discharge process involving a smoothly time-varying P_{DV}, a constant T_{AL}, and an abrupt change in nozzle/orifice exit flow from a simple incompressible-fluid-jet type flow to an explosively flashing two-phase flow. Note that the idea of using the condition of the existence of $P_{SP} > P_{AMB}$ as a criterion for violent flashing of liquids flowing through sharp-edged orifices or very short nozzle-like openings does not seem to have been proposed previously. Nor has it been validated quantitatively.

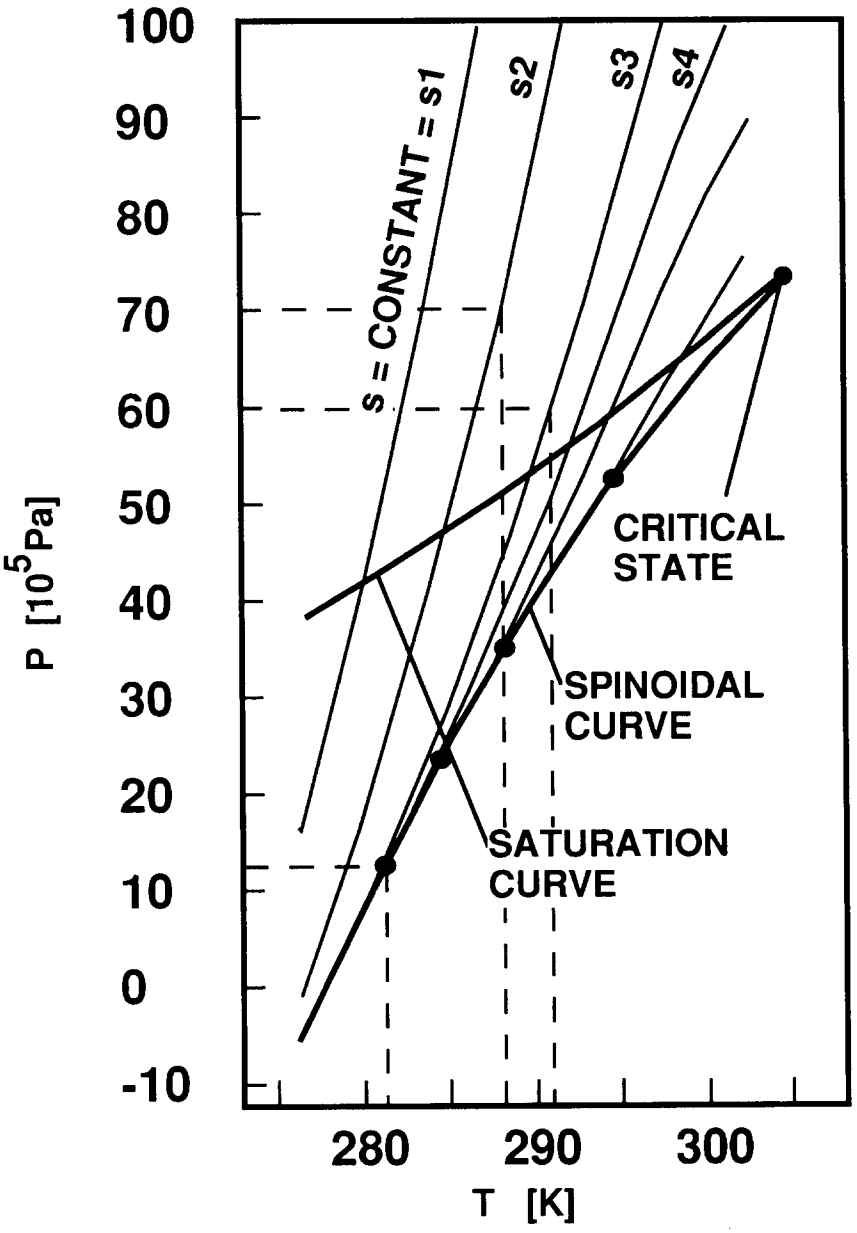

Figure 3. *P-T* diagram for metastable liquid CO_2.

3.2.5 Reduced Dimensionless Equation Set - The Initial Value Problem. Equations (1)-(8) are made dimensionless by introducing a dimensionless time, τ, dimensionless mass of N_2 and liquid agent in the discharge vessel, x_2 and x_3, respectively, and a combined variable, x_1.

$$x_1 = \frac{(1 + \lambda_3 x_2)P_{DV}}{(1 + \lambda_1 x_2)P_{DV,1}}\left[\frac{Z_{DV}}{Z_1} - x_3\right] + \lambda_2\lambda_4(1 - x_2)^\gamma; \quad x_2 = \frac{M_{DV,N2}}{M_{N2}}; \quad x_3 = \frac{M_{DV,AL}}{M_{DV,AL,1}}$$
$$\tau = tC_{D,N}A_N\left[\frac{2P_{DV,1}}{(M_{DV,AL,1}A_{DV}Z_1)}\right]^{1/2} \tag{9}$$

$$\lambda_1 = \frac{M_{N2}}{M_{DV,AG}}\frac{R_{N2}}{R_{AG}}; \quad \lambda_2 = \frac{\dfrac{P_{HT,1}}{P_{DV,1}}}{\left[\dfrac{M_{HT,N2,1}}{M_{N2}}\right]^\gamma}; \quad \lambda_3 = \frac{\lambda_1(\gamma_{AG} - 1)}{(\gamma - 1)}; \quad \lambda_4 = \frac{(\gamma_{AG} - 1)V_{HT}}{(\gamma - 1)Z_1A_{DV}} \tag{10}$$

The initial values of the x's are functions of the various parameters of the particular problem of interest. The dimensionless initial value problem for an arbitrary Figure 1-configuration is

$$\frac{dx_i}{d\tau} = \sigma_i; \quad x_i(0) \textit{ specified}, \; i = 1, 2, 3;$$
$$\sigma_i = \sigma_i(x_1; x_2; x_3; \textit{ parameters of the problem}) \tag{11}$$

The reader is referred to Section 3.2.13 (Appendix) for definitions of the σ_i and for explicit equations to extract values of time-dependent dimensional variables from a solution of Equation (11).

3.2.6 N_2 Jet-Driven Mixing in the Discharge Vessel - Estimating the Resulting Disturbance of the Liquid/Gas Interface. The above model assumes that throughout the pressurization and discharge process the agent gas and the N_2 in the discharge vessel are fully mixed and in a state of thermodynamic equilibrium. It is also assumed that there is no significant heat or mass transfer interactions at the gas/liquid interface, *i.e.*, it is assumed that the interface is relatively quiescent.

In cases where there is no N_2 flow from the holding tank (*e.g.*, the orifice is closed) the initial fully-mixed state of the gases will persist throughout depressurization, the gas volume will be relatively quiescent, and the assumption of negligible interface interactions is expected to hold. This is the case for actual field-deployed systems.

When there is N_2 flow from the holding tank, it is the N_2 jet from the orifice that will drive gas mixing in the discharge vessel. Refer to Figure 4. If jet velocities are too large, the liquid/gas interface disturbance of the jet can be violent enough to invalidate the quiescent interface assumption.

For the configuration of Figure 1 and Figure 4, the significance of the effect of the N_2 jet impinging on the liquid surface can be determined from an estimate of the axial velocity of the orifice jet at the liquid/gas interface. Such an estimate is obtained here from the characteristics of an incompressible submerged jet (*i.e.*, analogous to the N_2 orifice jet) in an unconfined space (analogous to the gas volume of the discharge vessel). The estimate is also useful for other orifice orientations.

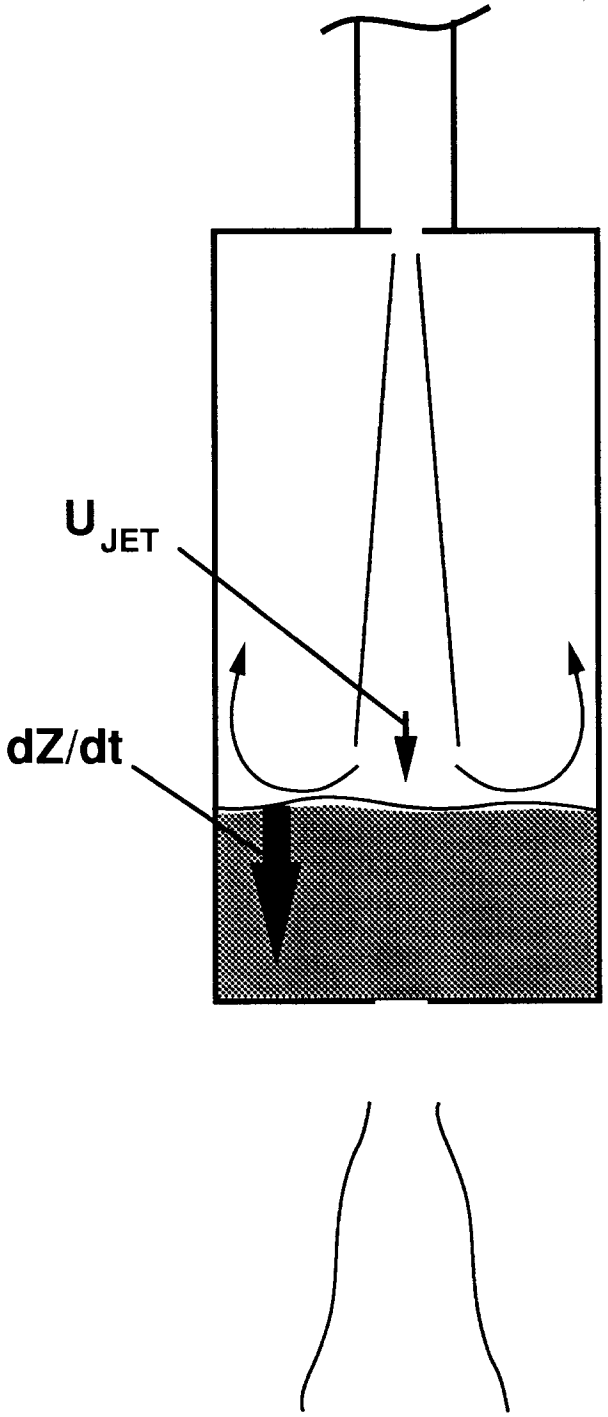

Figure 4. Sketch of the orifice-driven N_2 jet flow in the discharge vessel.

Let the velocity on the jet axis a distance $Z_{JET} = Z_{DV} - Z$ from the orifice (*i.e.*, at the elevation of the liquid/gas interface) be denoted by U_{JET} and assume a uniform velocity, U_O, across the orifice opening,

$$U_O = \frac{\dfrac{dM_{DV,N2}}{dt}}{\dfrac{A_O M_{HT,N2}}{V_{HT}}}. \tag{12}$$

From Abramowitz (1963),

$$\frac{U_{JET}}{U_O} = \frac{0.96}{\left[\dfrac{0.132 Z_{JET}}{D_O} + 0.29\right]} \quad for \quad \frac{Z_{JET}}{D_O} > 5 \tag{13}$$

When the time-dependent solution for $M_{DV,N2}$ is available, U_{JET} can now be estimated from Equations (12) and (13) and the significance of the jetting phenomenon can be assessed.

3.2.7 Solving the Model Equations. A computer program was developed to solve the initial value problem of Equation (11) corresponding to an arbitrary choice of geometric parameters, material properties, and initial conditions, and to determine the value of U_{JET} from Equations (12) and (13). The method of solution is based on the differential equation solver **RKQC** presented by Press (1986). The program was used in the example calculations to follow.

3.2.8 Example Calculations

3.2.8.1 An Experimental Procedure to Simulate the Discharge of Field-Deployed Vessels. As mentioned in Section 3.2.1, the example calculations to be presented here focused on providing guidance for the experimental design and procedure such that a vessel discharge of the experimental system closely simulates the discharge of a field-deployed vessel, while allowing for acquisition of data, including high-speed photography, to characterize the discharge process.

Field-deployed systems use an explosive device to remove, "on demand," a cap covering the exit nozzle/orifice of a prepressurized discharge vessel. Thus, the deployed system is characterized by a Figure 1-type configuration with no holding tank component, *i.e.*, with $A_O = 0$.

The nature of the experimental program at NIST precluded the use of an explosive cap device. The experimental procedure to be evaluated therefore involved a vessel discharge process which was initiated, instead, by the rupture of a nozzle/orifice diaphragm cap at a high cross-diaphragm pressure difference. The pressurization of the discharge vessel from $P_{DV,I}$ to the diaphragm burst pressure, P_{BURST}, was assumed to be achieved with the use of the holding-tank/orifice-flow feature of Figure 1.

As discussed earlier, an experimental run involves sequential processes of vessel pressurization and discharge. Initially, the diaphragm cap prevents flow from the vessel to the outside environment. At $t = 0^+$ the orifice connecting the vessel and the holding tank is opened and pressurization of the vessel is initiated. At the instant the pressure in the vessel reaches the diaphragm burst pressure, the diaphragm ruptures. Nozzle/orifice flow and discharge of the vessel are then initiated. As mentioned

earlier, the pressurization and discharge processes of interest here are expected to occur over time intervals of the order of 10 s and 10^{-2} s, respectively.

Prior to any particular test run, P_{BURST} is only known to an accuracy of approximately 10%. Also, the high-speed camera used to photograph the discharge process during the test procedure could record a total time interval no longer than the order of a few seconds, including an initial interval of approximately 1 s required to bring the camera up to its operating speed.

3.2.8.2 Criteria for Experimental Discharges to Closely Simulate Field-Deployed Discharges. One would hope to determine that an experimental discharge would closely simulate a field-deployed system discharge by obtaining good agreement between results of model simulations of the two processes. The basic criterion would be good reproduction of the predicted time-dependent values of P_{DV} and $M_{DV,AL}$.

Since field-deployed discharges involve no addition of N_2 and no significant heat or mass transfer at the liquid/gas interface, an acceptable Figure 1-type experimental procedure should similarly involve discharges with no significant addition of N_2. In view of this, in addition to the above criterion, two additional criteria must be satisfied if the experimental discharge is to simulate closely a field-deployed discharge: 1) the experiment must include a discharge process during which the total mass of N_2 delivered from the holding vessel to the discharge vessel is small compared to the mass of N_2 in the discharge vessel immediately prior to the onset of discharge, *i.e.*,

$$require \ \frac{(M_{N2} - M_{N2,B})}{M} << 1 \ for \ t > t_{BURST} \tag{14}$$

where $M_{N2,B}$ is the mass of N_2 in the discharge vessel at t_{BURST}; and 2) the addition of N_2 during the entire pressurization/discharge sequence does not lead to gas flows in the discharge vessel gas (where velocities will be of the order of U_{JET}) which are so vigorous as to lead to significant heat or mass transfer at the liquid/gas interface. It is reasonable to expect that interface surface interactions will not be significant if $U_{JET} - dZ/dt$ never exceeds the order of a few m/s. Thus

$$require \ U_{JET} - \frac{dZ}{dt} < 5\text{-}10 \ m/s \ for \ t \geq 0 \ s \tag{15}$$

3.2.8.3 Model Input Parameters. Sets of parameters representative of those for a Figure 1-type experimental design were selected to simulate discharge of a field-deployed system with a 0.5×10^{-3} m^3 discharge vessel half-filled with liquid HCFC-22 and pressurized with N_2 to 41.4×10^5 Pa. Parameters of the field-deployed system are included in Table 1.

The selected parameter sets of Table 1 defined simulations of 18 different experimental systems and the single simulation of the field-deployed system. The parameters sets were used to define and solve the model's initial value problem. Solution results provide time-dependent histories of all model variables and the information necessary to determine whether or not the criteria of Equations (14) and (15) are satisfied during the simulation.

As indicated, the model simulations involve the agent HCFC-22. In solving Equations (11) and (12) the thermodynamic properties listed in Table 2 and Table 3 were used for HCFC-22 and for N_2.

Table 1. Characteristics of Simulated Discharges - Model Input Parameters

agent material	HCFC-22						
$T_{DV,1}$ = $T_{HT,1}$ =	294 K						
diameter of discharge vessel = D_{DV} =	0.05 m						
volume of discharge vessel = V_{DV} =	0.5×10^{-3} m^3						
initial volume of liquid agent in discharge vessel	$V_{DV}/2 = 0.25 \times 10^{-3}$ m^3						
D_N =	0.0191 m						
V_{HT} =	2.5×10^{-3} m^3 (large holding tank)				2.5×10^{-5} m^3 (small holding tank)		field simulation (no holding tank)
$P_{HT,1}$ =	51.7×10^5 Pa				155×10^5 Pa		-
$P_{DV,1}$ =	34.5×10^5 Pa		9.38×10^5 Pa = $P_{SAT}(T_{DV,1})$		34.5×10^5 Pa		41.4×10^5 Pa
P_{BURST}=	37.9×10^5 Pa	44.8×10^5 Pa	37.9×10^5 Pa	44.8×10^5 Pa	37.9×10^5 Pa	44.8×10^5 Pa	41.3×10^5 Pa
D_O =	0.5 mm, 1 mm, and 5 mm	0.5 mm, 1 mm, and 5 mm	0.5 mm, 1 mm, and 5 mm	0.5 mm, 1 mm, and 5 mm	0.5 mm, 1 mm, and 5 mm	0.05 mm 1 mm, and 5 mm	-

Table 2. Properties of HCFC-22

Molecular Weight	86.47 kg/mole
Liquid Density [$\rho_{AL} = \rho_{SAT}(294\ K)$]	1209 kg/m^3
Constant Pressure Specific Heat [$C_{P,AG}$]	57×10^3 Jkg^{-1}mole^{-1}K^{-1}
Saturation Pressure [P_{SAT}]	$6895(T/R)^{-C} \times [F - (T/R)]^{E[F - (T/R)]/[F(T/R)]} 10^{A - B/(T/R) + D(T/R)}$ Pa where A=29.36, B=3845.1, C=7.861, D=0.002190, E=305.8, F=686.1

The following completes the information used to fully define the model equations.

The flow coefficient for the nozzle/orifice (flow of test agent liquid from the discharge vessel to the outside environment) was assigned a value of

$$C_{D,N} = 0.60. \tag{16}$$

The use of Equation (8) and the σ_1 and σ_3 components of Equation (11) require values of P_{SP} for isentropic paths from the time-dependent liquid states in the discharge vessel. For the present calculation it is assumed that throughout the discharge process $P_{SP} < P_{ATM} = 1.01 \times 10^5$ Pa, *i.e.*, spinoidal-curve type instabilities of the metastable exit liquid stream do not occur during the major portion of the discharge-process time interval. However, as seen above in the discussion of CO_2, this assumption can not be expected to hold in general, and actual estimates of P_{SP} will have to be included in more general applications of the mathematical model.

An expression for the flow coefficient, $C_{D,O}$, for the flow through a sharp-edged orifice (flow of N_2 from the holding tank to the discharge vessel) as a function of cross-orifice pressure ratio, P_{DV}/P_{HT}, is taken from Perry (1949). Data points for $C_{D,O}(P_{DV}/P_{HT})$ are plotted in Figure 5. In the present calculations, values of $C_{D,O}$ are estimated by linear interpolation between these data points.

To determine the constant mass of gaseous test agent in the discharge vessel it is assumed that the process of filling the vessel included a time when pure test agent filled the entire vessel with gas and liquid volumes in thermodynamic equilibrium with each other. The mass of gaseous agent at this time is taken to be $M_{DV,AG}$. In the present calculations it is assumed that at this time of equilibrium the agent temperature was 294 K. This is the value taken above for the initial temperatures $T_{DV,1}$ and $T_{HT,1}$.

3.2.9 Relatively Low-Pressure Large-Volume Holding Tank. This section presents results for the pressurization/discharge sequence using a relatively low-pressure large-volume holding tank. Note that experimental safety considerations motivate use of relatively low-pressures in the holding tank, especially when it is of relatively large volume.

$V_{HT} = 2.5 \times 10^{-3}$ m^3 is chosen to be ten times larger than the initial gas volume in the discharge vessel and $P_{HT,1} = 51.7 \times 10^5$ Pa is chosen to be 6.9×10^5 Pa greater than the maximum of the diaphragm burst pressure which can fall within the range 37.9×10^5 Pa $< P_{BURST} < 44.8 \times 10^5$ Pa.

Table 3. Properties of Nitrogen

Molecular Weight	28.01 kg/mole
Constant Pressure Specific Heat [$C_{P,N2}$]	[7.440 - 3.24 × 10^{-3}(T/K) + 6.400 × 10^{-6} $(T/K)^2$ - 2.790 × $10^{-9}$$(T/K)^3$] × 4186 J/(kg-mole·K)

The objective in using the present choice of parameters is to provide for a pressurization process which is slow enough to minimize disturbances of the liquid/gas interface, *i.e.*, satisfy Equation (15), but fast enough to be able to bracket clearly the time of the subsequent discharge process to a known time interval of the order of 1 s. The 1 s time interval is required to guarantee timely triggering of and photographic data acquisition from a high-speed camera during the discharge process. As mentioned above, the latter is expected to occur over a time interval of the order of 10^{-2} s.

The relatively large volume of the holding tank would allow the pressurization/discharge process to be initiated either: 1) from a relatively high-$P_{DV,1}$ state, somewhat below the minimum possible diaphragm burst pressure and with a relatively significant initial mass of N_2 in the discharge vessel; or 2) from a minimum-$P_{DV,1}$ state where there is no N_2 in the discharge vessel (i.e, the discharge vessel initially contains only pure test agent at the saturation pressure $P_{DV,1} = P_{SAT}$, where P_{SAT} is significantly below the P_{BURST} pressures under investigation).

3.2.9.1 Initiating the Pressurization/Discharge Sequence from the Agent's Saturation State; No N_2 in the Discharge Vessel at t = 0. Simulations were carried out for experiments where the pressurization/discharge processes were initiated at the test agent's saturation state, *i.e.*, at $P_{DV,1} = P_{SAT}(T_{DV,1} = 294\ K) = 9.38 \times 10^5$ Pa, *e.g.*, shortly after filling the evacuated vessel with the test agent. In such experiments there is no N_2 in the discharge vessel at t = 0, *i.e.*, $M_{DV,N2,1} = 0$. Results of the calculations are plotted in Figure 6 through Figure 11.

First the pressurization process will be considered. Figure 6 presents plots of P_{DV} and P_{HT} during vessel pressurization, $0 < t < t_{BURST}$. Results are presented for the three orifice diameters, D_O = 0.005 m, 0.001 m, and 0.0005 m.

As seen in Figure 6, for the smallest orifice, D_O = 0.0005 m, the pressurization process, when $P_{DV,1} \leq P_{DV} < P_{BURST}$, takes 4.2 s for $P_{BURST} = 37.9 \times 10^5$ Pa to 5.8 s for $P_{BURST} = 44.8 \times 10^5$ Pa. For the intermediate-size orifice, D_O = 0.001 m, the pressurization process takes 1.0 s for $P_{BURST} = 37.9 \times 10^5$ Pa to 1.4 s for $P_{BURST} = 44.8 \times 10^5$ Pa. For the largest orifice, D_O = 0.005 m, the entire process takes place within 0.1 s.

U_{JET} values corresponding to Figure 6 are presented in Figure 7. For the smallest orifice, D_O = 0.0005 m, U_{JET} starts out at approximately 4 m/s and drops to 2 - 3 m/s at t_{BURST}, the time of diaphragm bursting. For D_O = 0.001 m, U_{JET} starts out at approximately 8 m/s and drops to approximately 4 m/s at t_{BURST}. For D_O = 0.005 m, U_{JET} starts out at approximately 40 m/s and drops to as low as approximately 16 m/s for $P_{BURST} = 44.8 \times 10^5$ Pa at t_{BURST}.

Based on the above results it is concluded that during the pressurization process and relative to the criterion of Equation (15): 1) use of the large orifice would lead to conditions which do not satisfy

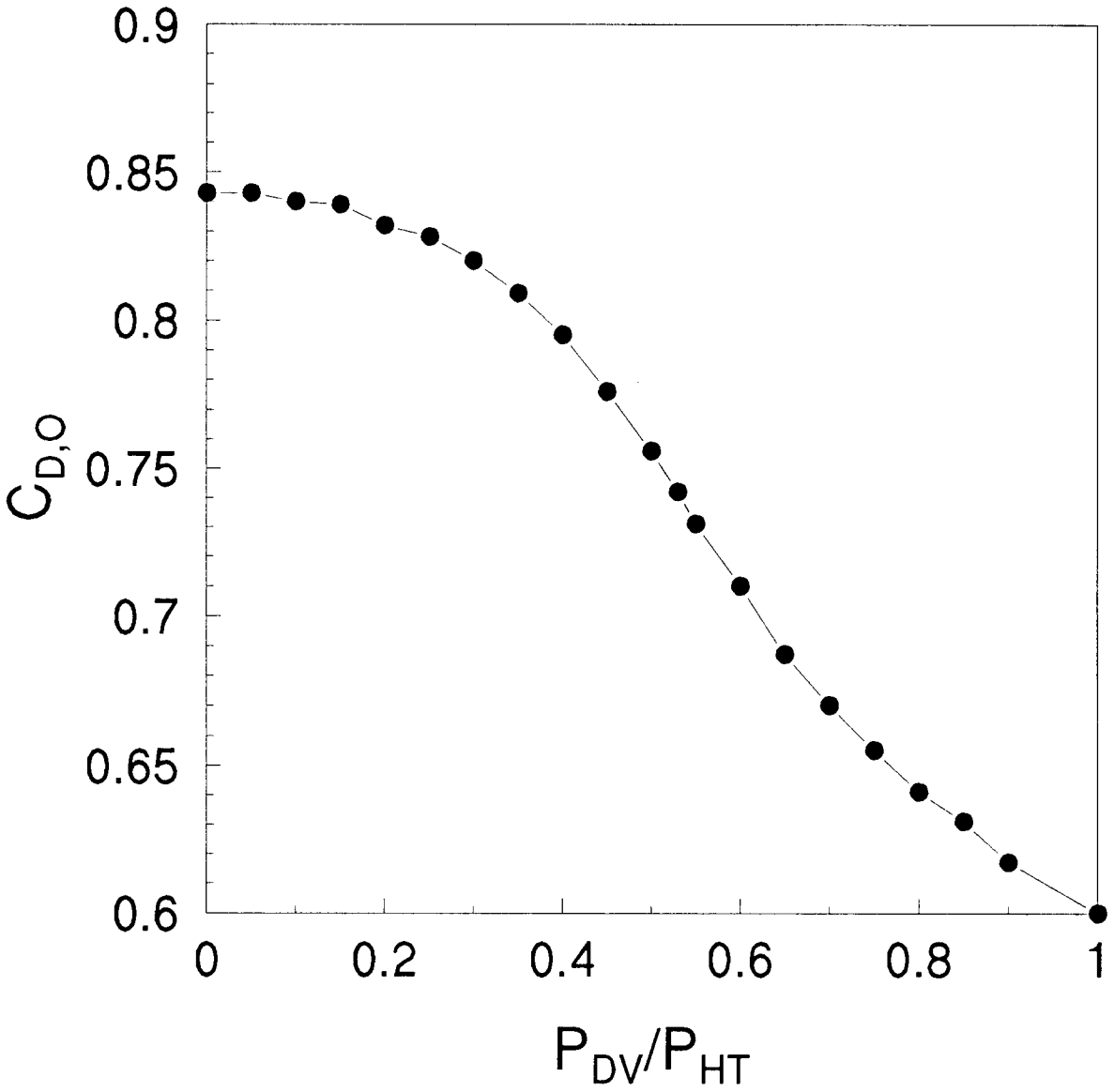

Figure 5. Discharge coefficient, $C_{D,O}$, for compressible flow through a sharp-edged orifice as a function of cross-orifice pressure ratio, P_{DV}/P_{HT} (Perry, 1949).

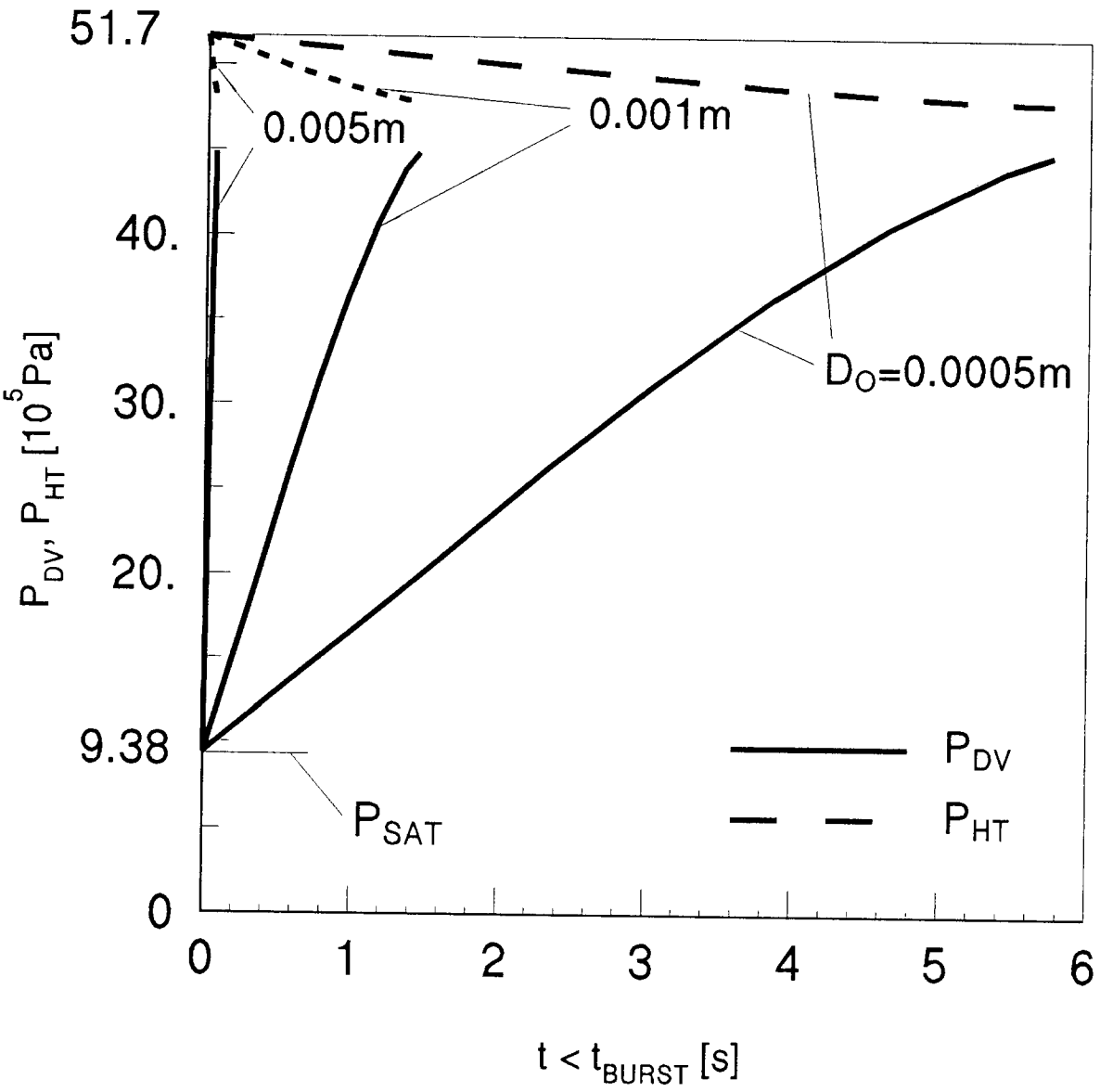

Figure 6. Pressures in the holding tank and discharge vessel for $0 \leq t \leq t_{BURST}$ for a large-volume, low-pressure holding tank and no N_2 in the discharge vessel at $t = 0$.

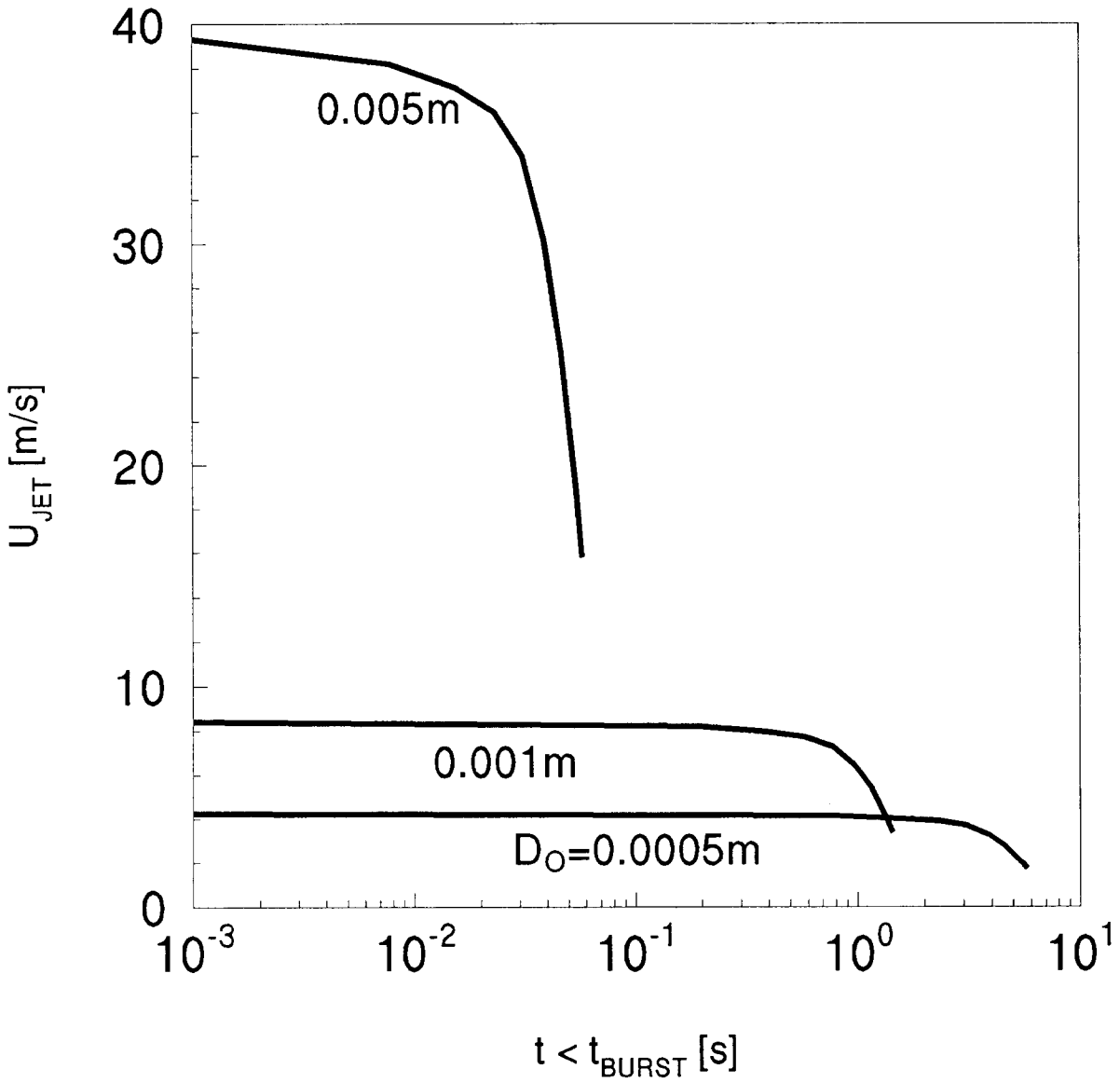

Figure 7. Plots of U_{JET} in the discharge vessel for $0 \leq t \leq t_{BURST}$ for a large-volume, low-pressure holding tank and no N_2 in the discharge vessel at $t = 0$.

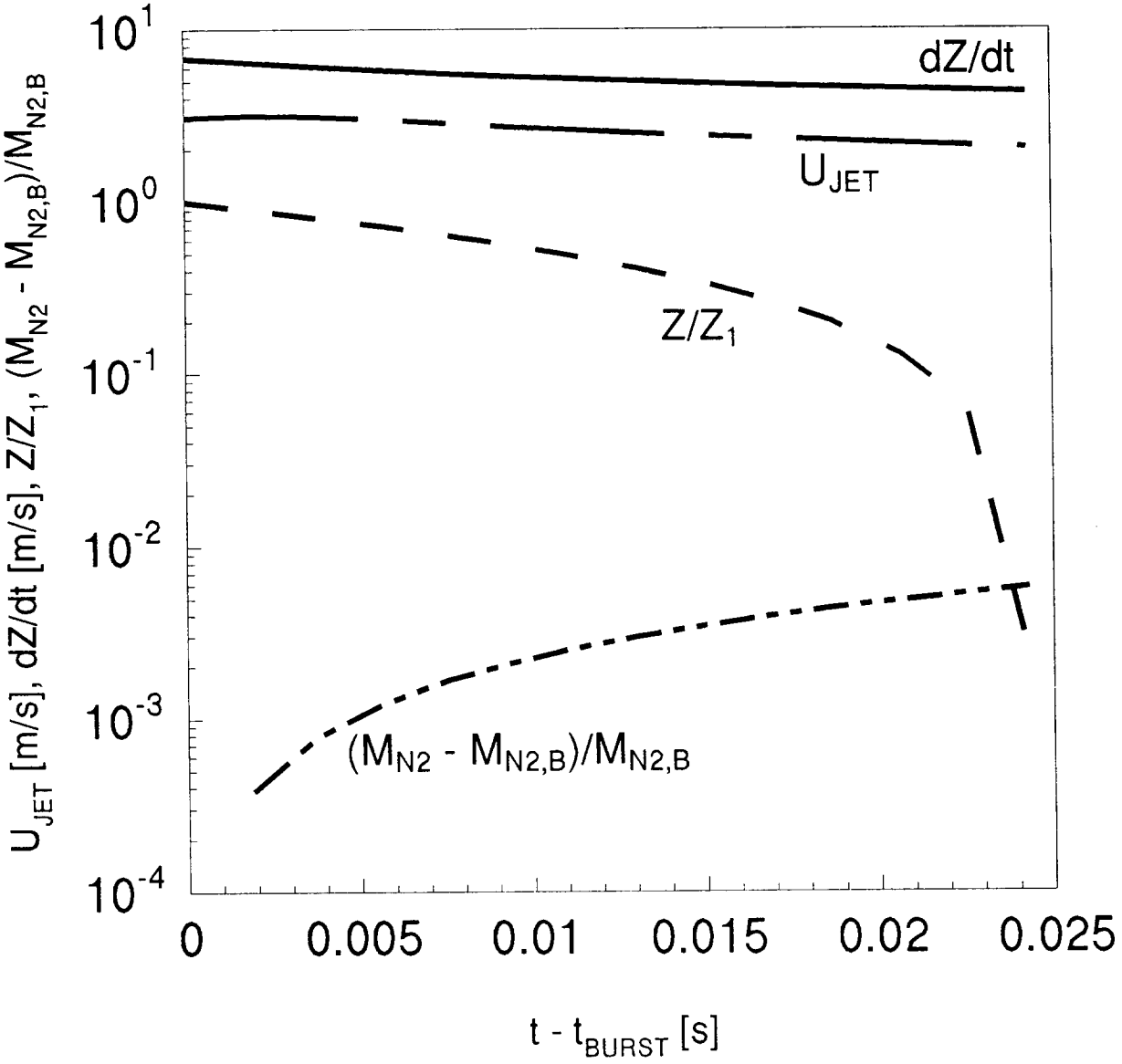

Figure 8. U_{JET}, dZ/dt, Z/Z_1, and $(M_{N2}-M_{N2,B})/M_{N2,B}$ for $t \geq t_{BURST}$; large-volume, low-pressure holding tank; no N_2 in vessel at $t=0$; $D_o=0.5$ mm; $P_{BURST}=3.8$ MPa.

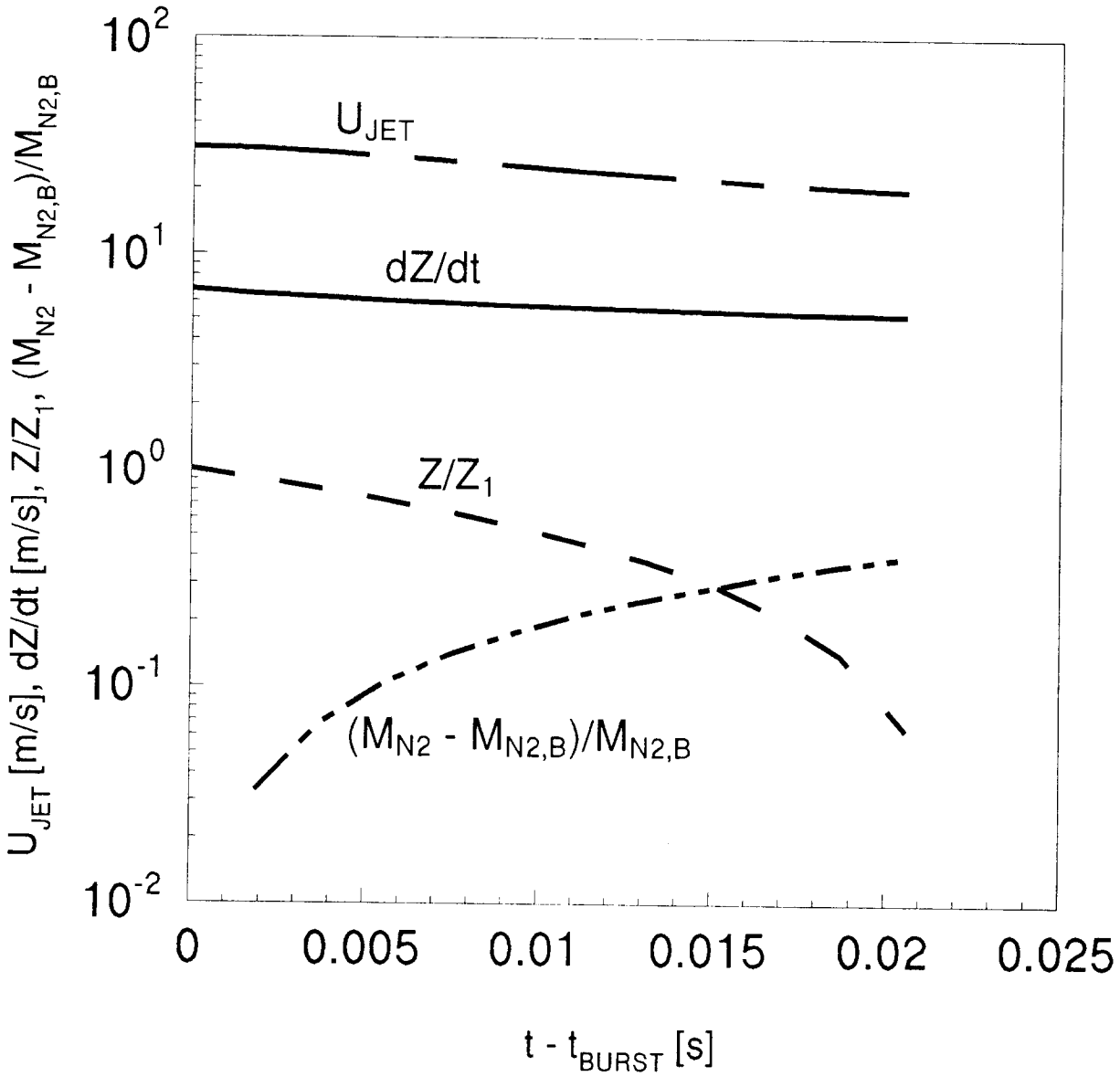

Figure 9. U_{JET}, dZ/dt, Z/Z_1, and $(M_{N2}-M_{N2,B})/M_{N2,B}$ for $t \geq t_{BURST}$; large-volume, low-pressure holding tank; no N_2 in vessel at $t=0$; $D_o=5$ mm, $P_{BURST}=3.8$ MPa.

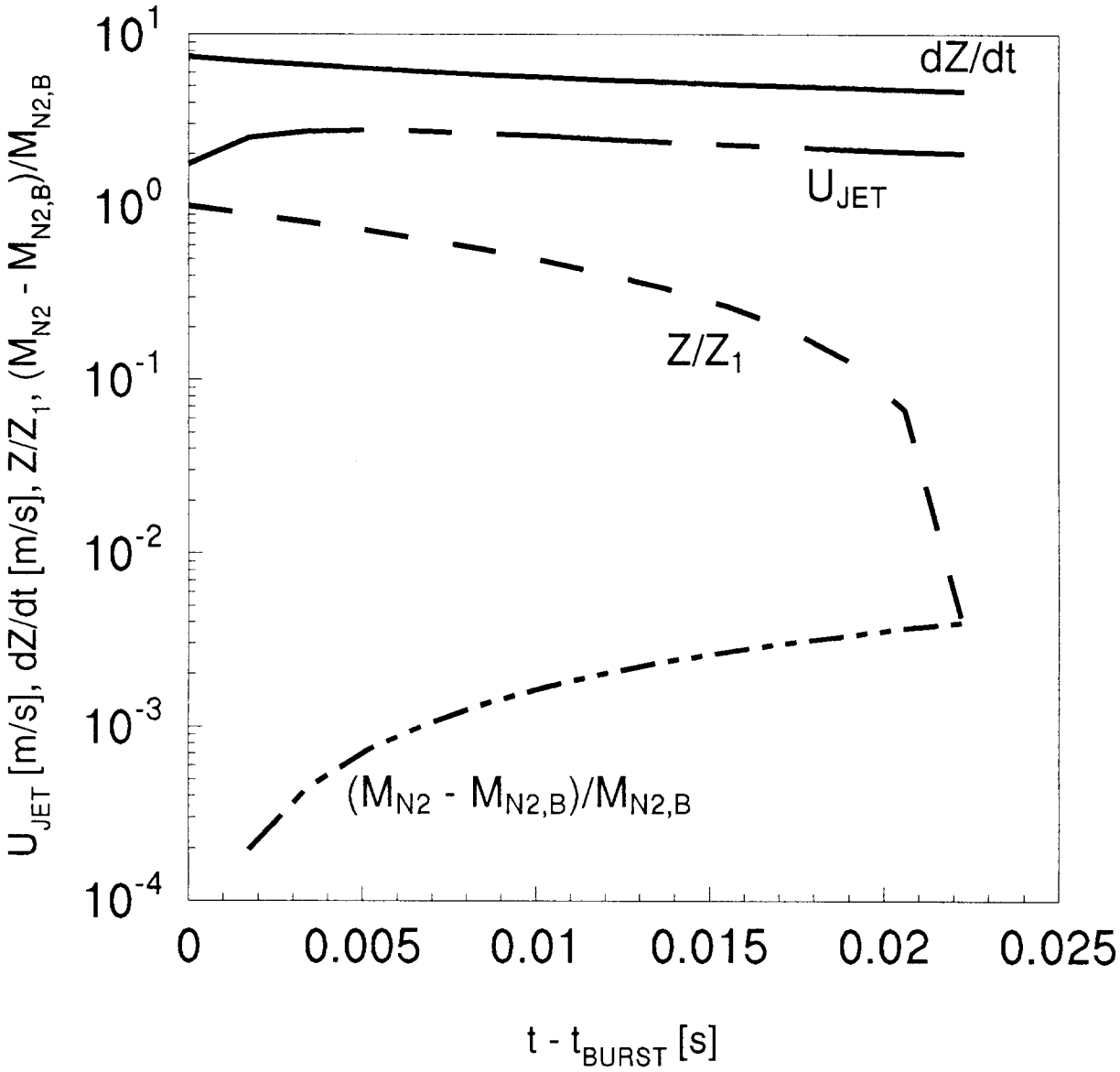

Figure 10. U_{JET}, dZ/dt, Z/Z_1, and $(M_{N2}-M_{N2,B})/M_{N2,B}$ for $t \geq t_{BURST}$; large-volume, low-pressure holding tank; no N_2 in vessel at $t=0$; $D_o=0.5$ mm, $P_{BURST}=4.5$ MPa.

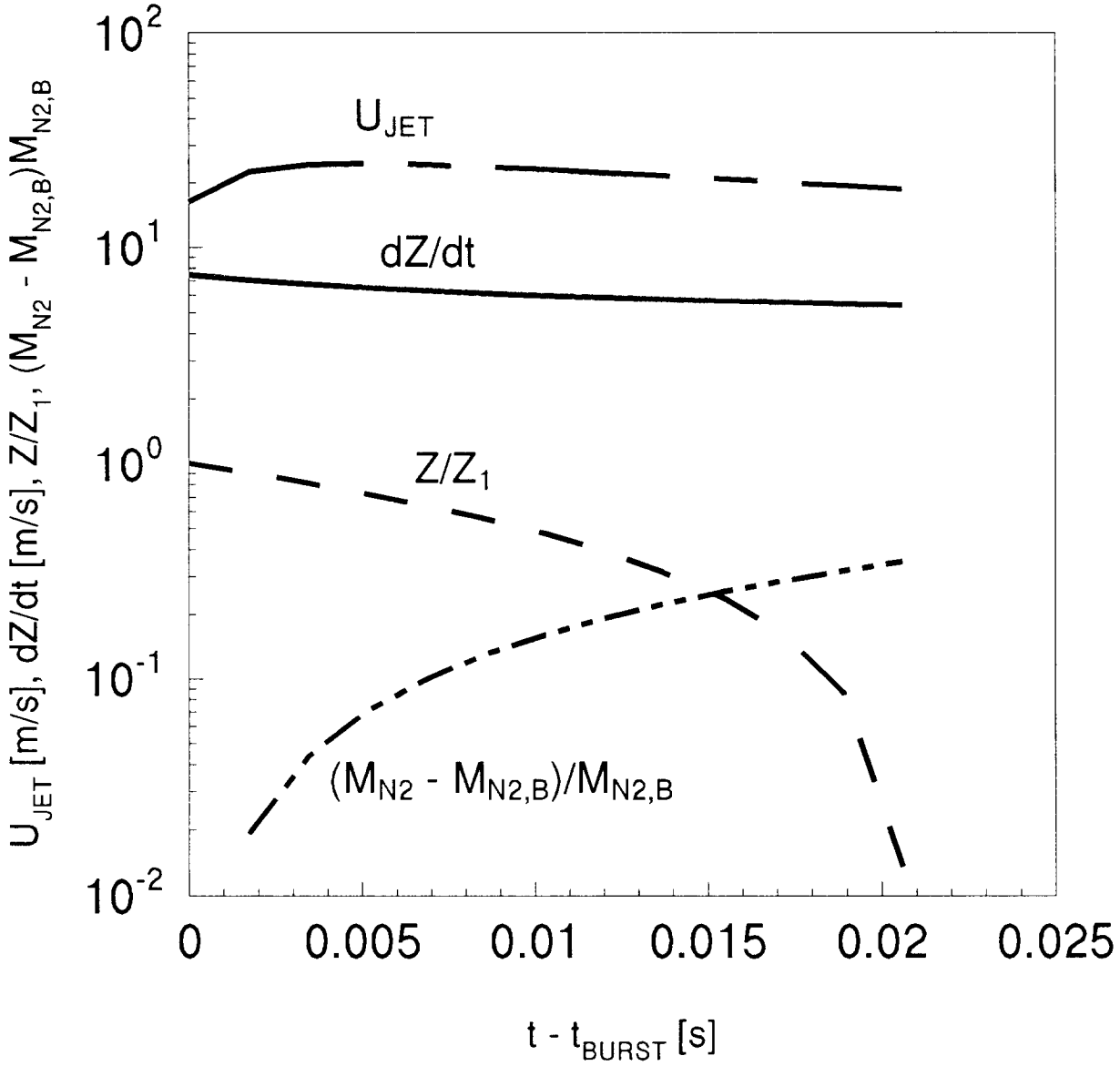

Figure 11. U_{JET}, dZ/dt, Z/Z_1, and $(M_{N2}-M_{N2,B})/M_{N2,B}$ for $t \geq t_{BURST}$; large-volume, low-pressure holding tank; no N_2 in vessel at $t=0$; $D_o=5$ mm, $P_{BURST}=4.5$ MPa.

the criterion; 2) use of the intermediate size orifice would lead to results which are barely acceptable; and 3) use of the small orifice would lead to acceptable performance, provided that pressurization times are consistent with timing requirements of the photographic data acquisition system.

Now the discharge behavior will be discussed. Figure 8 through Figure 11 present plots of U_{JET}, dZ/dt, Z/Z_1, and $(M_{N2} - M_{N2,B})/M_{N2,B}$ during the discharge process. For the limiting burst pressures, $P_{BURST} = 37.9 \times 10^5$ Pa and 44.8×10^5 Pa, results are presented for the small- and large-orifice designs.

Figure 8 presents results for $P_{BURST} = 37.9 \times 10^5$ Pa and $D_O = 0.0005$ m. Once the discharge process is initiated, the liquid is seen to drop from its initial elevation ($Z/Z_1 = 1$) and to be removed entirely from the vessel ($Z/Z_1 \rightarrow 0$) in approximately 0.024 s. Liquid discharge occurs at a relatively uniform rate with dZ/dt dropping from approximately 7.0 to 4.5 m/s during the emptying process. During discharge U_{JET} first rises slightly (because of relatively rapid reductions of P_{DV}, slow reductions of P_{HT}, and resulting increases in cross-orifice pressure difference) from approximately 3 m/s, and then drops (because of the significantly increased length along the jet axis between the source of the jet, at the orifice, and the elevation at the gas/liquid interface - refer to Figure 1 and Figure 4) to the final value of approximately 2 m/s. As can be seen from the plot of $(M_{N2} - M_{N2,B})/M_{N2,B}$, during the entire emptying process the total mass addition of N_2 from the holding tank to the discharge vessel is less than 1% of the initial N_2 mass in the discharge vessel.

Figure 9 presents results for $P_{BURST} = 37.9 \times 10^5$ Pa and $D_O = 0.005$ m. Based on an approximate extrapolation from $t - t_{BURST} = 0.020$ s, once the discharge process is initiated the liquid is seen to drop from its initial elevation and to be removed entirely from the vessel in approximately 0.023 s. Liquid discharge occurs at a relatively uniform rate with dZ/dt dropping from approximately 7.0 to 5.5 m/s during the emptying process. During discharge U_{JET} first rises slightly from approximately 30 m/s, and then drops to the final value of approximately 20 m/s. As can be seen from the plot of $(M_{N2} - M_{N2,B})/M_{N2,B}$, during the entire emptying process the total mass addition of N_2 from the holding tank to the discharge vessel is significant, approximately 45% of the initial N_2 mass in the discharge vessel.

Figure 10 presents results for $P_{BURST} = 44.8 \times 10^5$ Pa and $D_O = 0.0005$ m. Here the discharge is completed in 0.023 s. Liquid discharge occurs at a relatively uniform rate with dZ/dt dropping from approximately 7.5 to 5.0 m/s during the emptying process. During discharge U_{JET} first rises from approximately 1 to 2 m/s, and then drops back to the final value of approximately 1 m/s. During the discharge the total mass addition of N_2 from the holding tank to the discharge vessel is less than 1% of the initial N_2 mass in the discharge vessel.

Figure 11 presents results for $P_{BURST} = 44.8 \times 10^5$ Pa and $D_O = 0.005$ m. From this it is seen that discharge occurs in approximately 0.021 s. Liquid discharge occurs at a relatively uniform rate with dZ/dt dropping from approximately 7.5 to 5.5 m/s during the emptying process. During discharge U_{JET} first rises from approximately 17 to 25 m/s, and then drops to the final value of approximately 20 m/s. During the discharge the total mass addition of N_2 from the holding tank to the discharge vessel is approximately 40% of the initial N_2 mass in the discharge vessel.

Based on the above results it is concluded that during the discharge process and relative to the criteria of Equations (14) and (15) : 1) use of the large orifice would lead to conditions which violate both of the criterion; 2) use of the small orifice would lead to acceptable performance.

3.2.9.2 Initiating the Pressurization/Discharge Sequence From a $P_{DV,1}$ Slightly Below P_{BURST}. Simulations were carried out for experiments initiated from a $P_{DV,1}$ which is slightly below P_{BURST}. Since the minimum possible P_{BURST} is 37.9×10^5 Pa, $P_{DV,1}$ is selected to be 34.5×10^5 Pa.

Figure 12 presents plots of P_{DV} and P_{HT} during vessel pressurization. Results are presented for the three orifice diameters, D_O = 0.005 m, 0.001 m, and 0.0005 m.

As seen in Figure 12, for the smallest orifice, D_O = 0.0005 m, the pressurization process, $P_{DV,1} \leq P_{DV} < P_{BURST}$, takes 0.6 s for $P_{BURST} = 37.9 \times 10^5$ Pa to 1.9 s for $P_{BURST} = 44.8 \times 10^5$ Pa. For the intermediate-size orifice, D_O = 0.001 m, the pressurization process takes 0.1 s for $P_{BURST} = 37.9 \times 10^5$ Pa to 0.5 s for $P_{BURST} = 44.8 \times 10^5$ Pa. For the largest orifice, D_O = 0.005 m, the entire pressurization process takes place in less than 0.02 s.

U_{JET} values corresponding to Figure 12 are presented in Figure 13. For the smallest orifice, D_O = 0.0005 m, U_{JET} starts out at approximately 3.5 m/s and drops to 2.0 - 2.5 m/s at the time of diaphragm rupture. For D_O = 0.001 m, U_{JET} starts out at approximately 7 m/s and drops to approximately 4.5 m/s at the time of diaphragm rupture. For D_O = 0.005 m, U_{JET} starts out at approximately 33 m/s and drops to as low as approximately 21 m/s for $P_{BURST} = 44.8 \times 10^5$ Pa at the time of diaphragm rupture.

Based on the above results it is concluded that during the pressurization process and relative to the criterion of Equation (15), the present results for $P_{DV,1} = 34.5 \times 10^5$ Pa are similar to the earlier results for $P_{DV,1} = P_{SAT} = 9.38 \times 10^5$ Pa.

In the present case where $P_{DV,1} = 34.5 \times 10^5$ Pa, results for the discharge process are very similar to the earlier results where $P_{DV,1} = P_{SAT} = 9.38 \times 10^5$ Pa and are qualitatively well represented by the plots of Figure 8 through Figure 11 and the earlier discussion of these.

3.2.9.3 Comparing the Discharges of a Small-Orifice Test Configuration and a Field-Deployed System. The model equations were also used to simulate the discharge of a field-deployed vessel filled with HCFC-22 and pressurized with N_2. At the onset of discharge the temperature in the vessel was taken to be 294 K and, corresponding to the above calculations, the pressure in the vessel was taken to be 41.4×10^5 Pa, *i.e.*, a nominal $P_{BURST} = 41.4 \times 10^5$ Pa, where simulating tests would involve experiments where 37.9×10^5 Pa $\leq P_{BURST} \leq 44.8 \times 10^5$ Pa. In Figure 14 and Figure 15 calculated values of P_{DV} and Z/Z_1 for the deployed system simulation are compared with the values of these variables obtained in the above test simulations with D_O = 0.0005 m. The $P_{DV,1} = 9.38 \times 10^5$ Pa results are presented in the figures since these compare somewhat less favorably with the field-deployed system results than do the $P_{DV,1} = 34.5 \times 10^5$ Pa results.

As can be seen in the figures, simulated field-deployed system results and simulated test results compare favorably.

3.2.9.4 Summary of Results of Simulations Involving the Relatively Low-Pressure Large-Volume Holding Tank. A Figure 1-type test configuration with a 0.25×10^{-3} m^3 holding tank and a 0.0005 m, and possibly a 0.001 m diameter orifice will provide experimental discharges which can be expected to simulate accurately the discharge of field-deployed systems. Of the two orifice sizes, the smaller orifice is preferable. Use of a 0.005 m diameter orifice can not be expected to adequately simulate field-deployed system discharges under the conditions studied.

It is expected that this result can be extended to a wide range of test parameters and test agents.

3.2.10 Relatively High-Pressure Small-Volume Holding Tank. This section presents results for the pressurization/discharge sequence using a relatively high-pressure small-volume holding tank. $V_{HT} = 2.5 \times 10^{-5}$ m^3 is chosen to be one tenth of the initial gas volume in the discharge vessel and $P_{HT,1} = 155.1 \times 10^5$ Pa is chosen to be large enough to ensure that the amount of N_2 stored in the holding tank will rupture the diaphragm even when P_{BURST} is at its maximum value, 44.8×10^5 Pa.

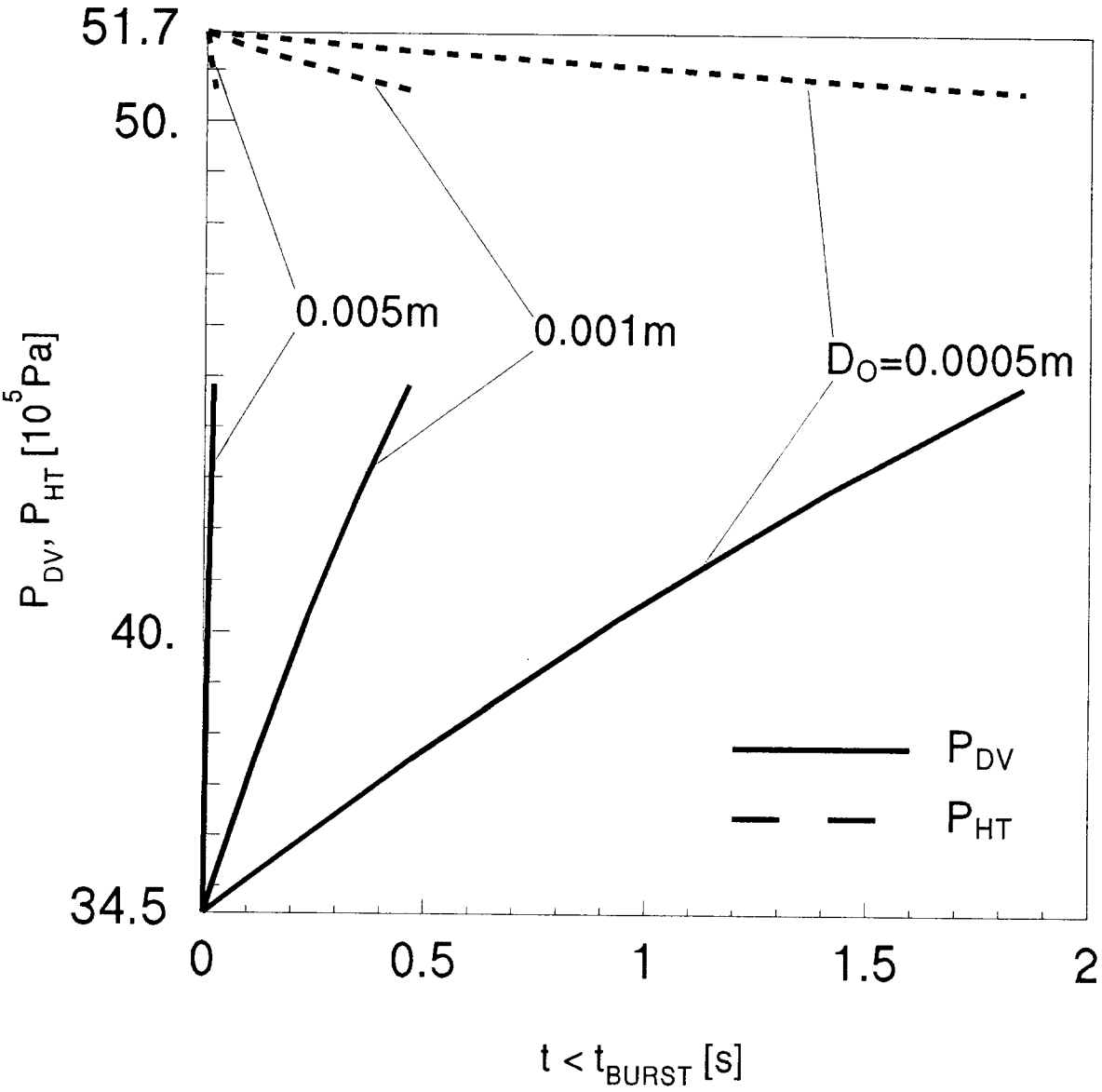

Figure 12. Pressures in the holding tank and discharge vessel for $0 \leq t \leq t_{BURST}$ for a large-volume, low-pressure holding tank; $P_{DV,1}=3.4$ MPa; $P_{HT,1}=5.17$ MPa; $P_{BURST}=4.5$ MPa.

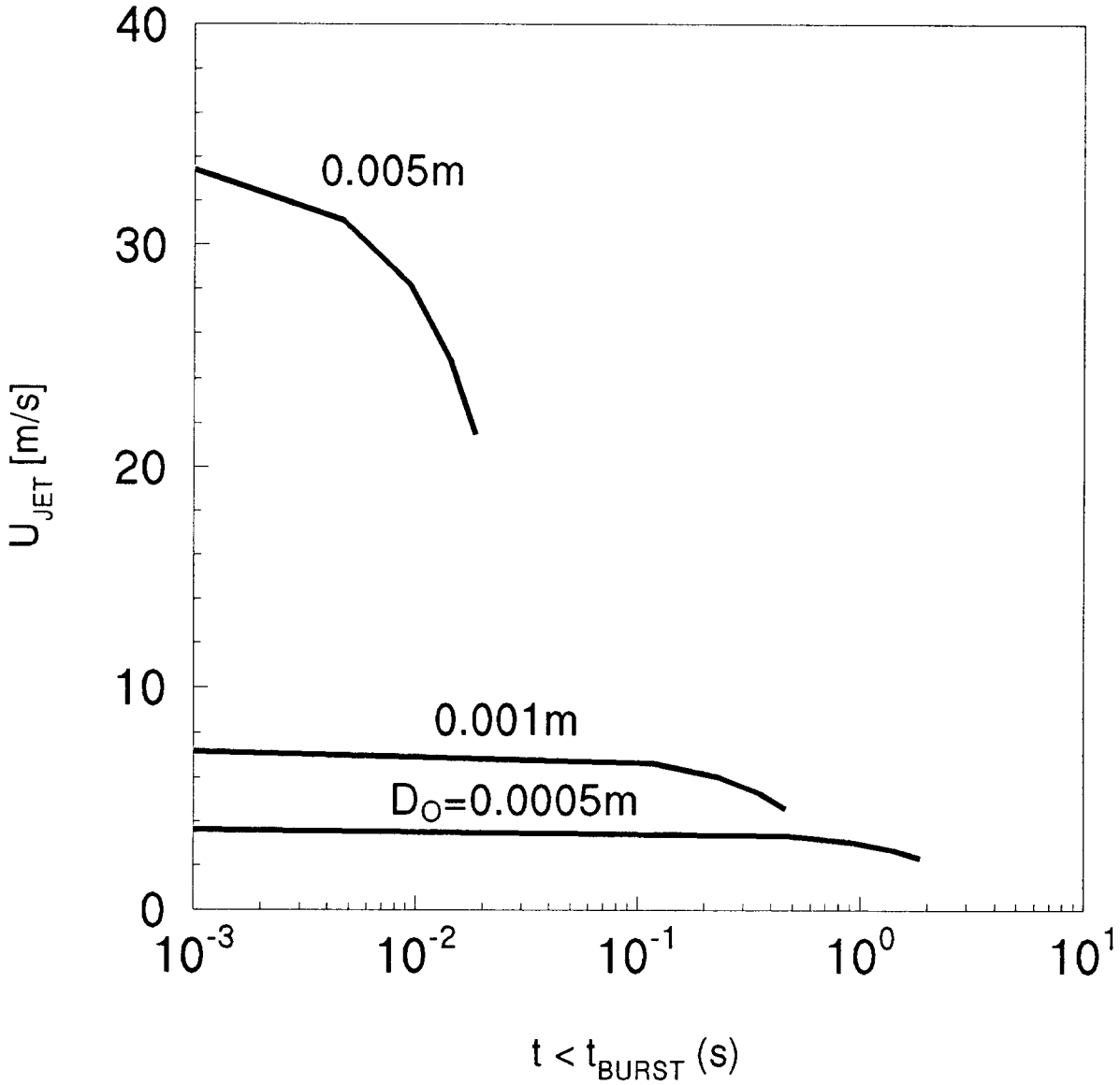

Figure 13. Plots of U_{JET} in the discharge vessel for $0 \leq t \leq t_{BURST}$ for a large-volume, low-pressure holding tank; $P_{DV,1}$=3.4 MPa; $P_{HT,1}$=5.17 MPa; P_{BURST}=4.5 MPa.

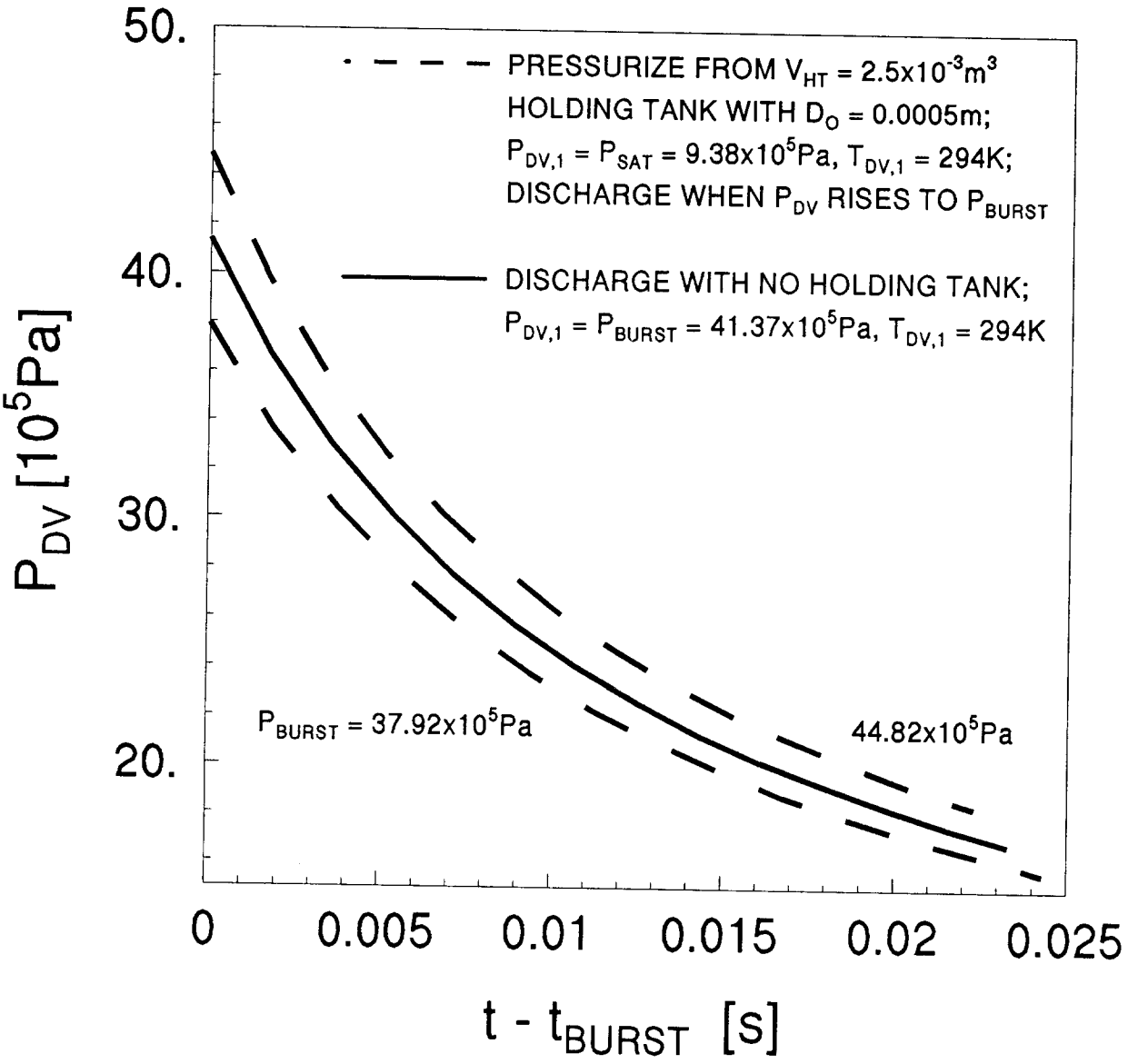

Figure 14. Pressure in the vessel during discharges of the field-deployed vessel and test configuration vessel with a large-volume, low-pressure holding tank and no N_2 in the discharge vessel at t = 0.

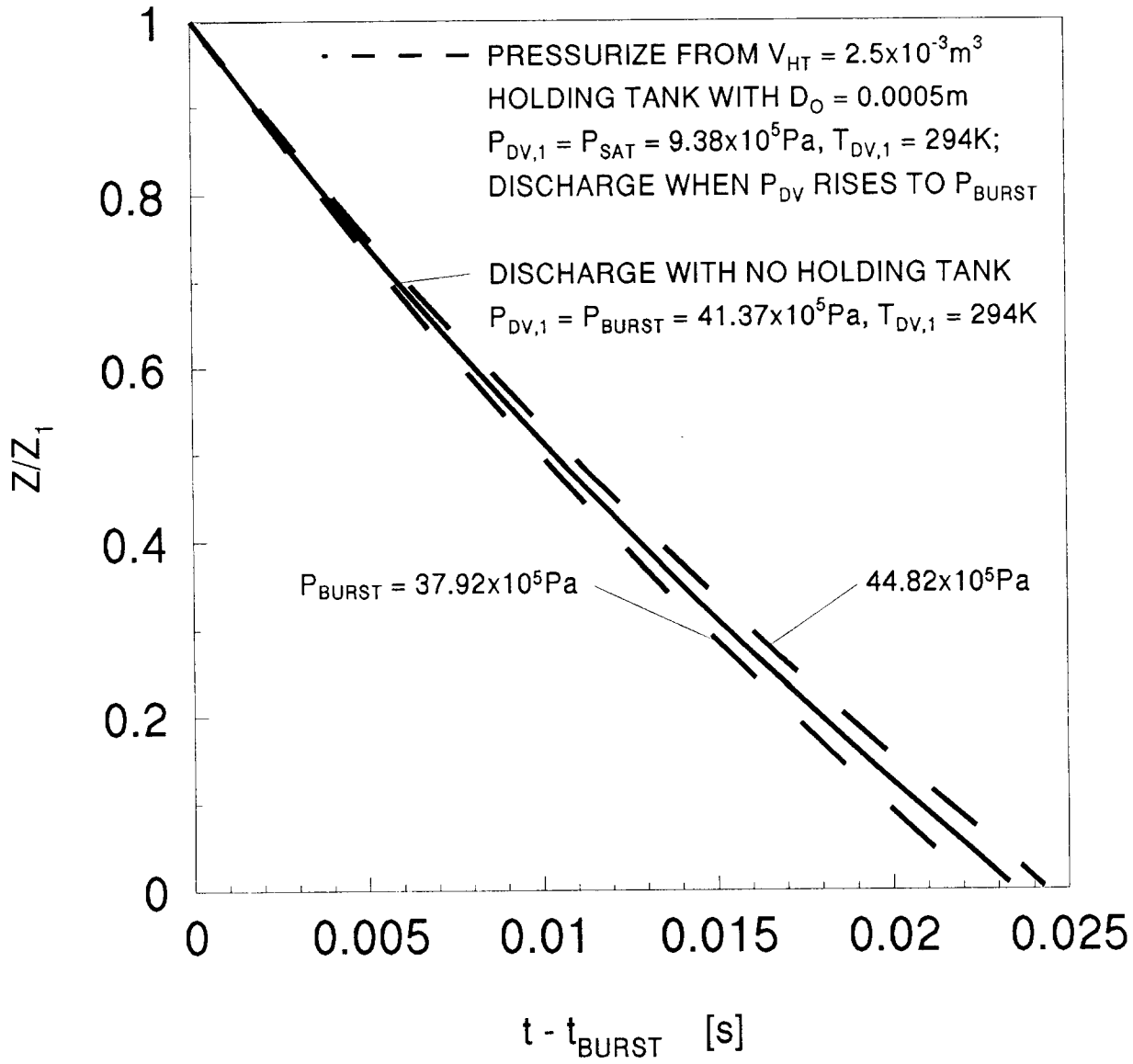

Figure 15. Plots of Z/Z_1 during discharges of the field-deployed vessel and test configuration vessel with a large-volume, low-pressure holding tank and no N_2 in the discharge vessel at t = 0.

The objective of choosing this combination of parameters is to attain a pressurization/discharge sequence which is so rapid, well within the above-mentioned 1 s time interval, as to guarantee, without any significant timing considerations, successful acquisition of high-speed photographic data of the discharge process. The feature of a relatively small initial volume and mass of N_2 in the holding tank is only consistent with test sequences with relatively high initial $P_{DV,1}$'s, values close to the minimum possible diaphragm burst pressure. Thus, the present test parameters would not be expected to be useful in initiating the pressurization/discharge process from an initial state where the vessel contained only pure test agent at its saturation pressure. Here, $P_{DV,1}$ is again chosen to be 34.5×10^5 Pa, slightly below 37.9×10^5 Pa, the minimum value for P_{BURST}.

3.2.10.1 Pressurization and Discharge for the Small Orifice, D_O = 0.0005 m. Simulation results for pressurization/discharge test using the small orifice design are presented in Figure 16 through Figure 20.

For $P_{BURST} = 37.9 \times 10^5$ Pa, plots of P_{DV} and P_{HT} are presented in Figure 16 and plots of U_{JET}, dZ/dt, Z/Z_1, and $(M_{N2} - M_{N2,B})/M_{N2,B}$ in Figure 17. Note that the latter variable is meaningful only during discharge when $t \geq t_{BURST}$. As can be seen in these figures, for this case t_{BURST} = 0.173 s, *i.e.*, this is the time it takes for P_{DV} to rise from $P_{DV,1} = 34.5 \times 10^5$ Pa to the diaphragm rupture pressure. From Figure 17 it is seen that the liquid is nearly all discharged from the vessel (*i.e.*, Z/Z_1 is approaching zero) at approximately t = 0.2 s. From Figure 17 it is also seen that during discharge: the rate of liquid outflow is reduced to about half of its original value, with dZ/dt being reduced from 7.0 m/s to 4.5 m/s; U_{JET} is reduced from an initial predischarge value of approximately 4 m/s to approximately 2 m/s; and $(M_{N2} - M_{N2,B})/M_{N2,B}$ rises from 0 to approximately 0.02, *i.e.*, at the end of the discharge the mass of N_2 in the vessel is increased from its value at t_{BURST} by a factor of approximately 0.02. The latter two results indicate that the criteria of Equations (14) and (15) are both satisfied and, in this sense, as with the relatively large holding tank, the small orifice design can be expected to adequately reproduce field-deployed discharges.

For $P_{BURST} = 44.8 \times 10^5$ Pa, plots of P_{DV} and P_{HT} are presented in Figure 18 and plots of U_{JET} and dZ/dt are presented in Figure 19. Plots of U_{JET}, dZ/dt, Z/Z_1, and $(M_{N2} - M_{N2,B})/M_{N2,B}$ for the times of the discharge process are highlighted in Figure 20. For this case t_{BURST} = 0.94 s. From Figure 18 it is seen that the P_{HT} has almost been reduced to P_{DV} at the time that discharge is initiated. Indeed, if the $P_{HT,1}$ had been much less than 155×10^5 Pa, P_{DV} would not have risen to P_{BURST} and the discharge process would never have occurred! From Figure 19 it is seen that during the pressurization process U_{JET} is reduced from approximately 4.0 m/s to 1.5 m/s. The liquid is nearly all discharged from the vessel at 0.962 s. During discharge: dZ/dt is reduced from 7.5 m/s to 5.0 m/s; U_{JET} rises to approximately 2.5 m/s from its initial value of 1.5 m/s and finally drops to approximately 2 m/s; and $(M_{N2} - M_{N2,B})/M_{N2,B}$ rises from 0 to approximately 0.005. The criteria of Equations (14) and (15) are again satisfied.

As noted, for both $P_{BURST} = 37.9 \times 10^5$ Pa and 44.8×10^5 Pa the above results indicate that both criteria of Equations (14) and (15) are satisfied with the small-holding-tank/small-orifice design and that, in this sense, this design can be expected to adequately reproduce field-deployed discharges. However, for the following three reasons the large-holding-tank design is significantly more robust than the small-holding-tank design: (1) For a given maximum value for P_{BURST} and discharge vessel volume, the minimum acceptable value for $P_{HT,1}$ (approximately 155×10^5 Pa for the present test parameters) is very sensitive to the original amount of liquid in the vessel. For example, in the present simulations the vessel was assumed to be one-half full; but if it were only one-quarter full, the minimum $P_{HT,1}$ that would lead to rupture of the 44.8×10^5 Pa diaphragm would have been approximately 207×10^5 Pa. (2) The small-volume-holding tank configuration does not allow for the

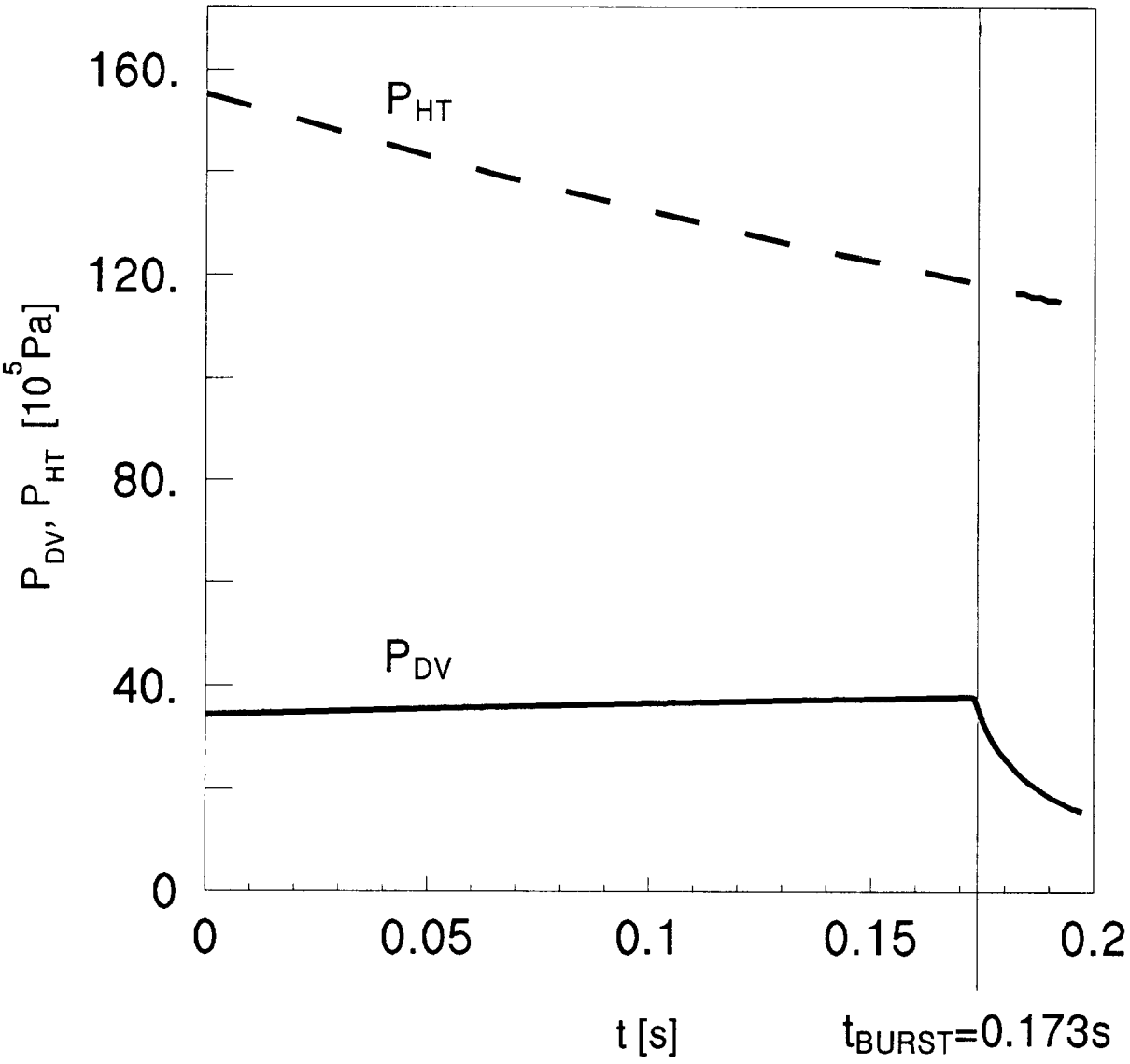

Figure 16. Pressures in the holding tank and discharge vessel for $t \geq 0$ for a small-volume, high-pressure holding tank; D_o = 0.5 mm; $P_{DV,1}$ = 3.45 MPa; $P_{HT,1}$ = 15.5 MPa; P_{BURST} = 3.79 MPa.

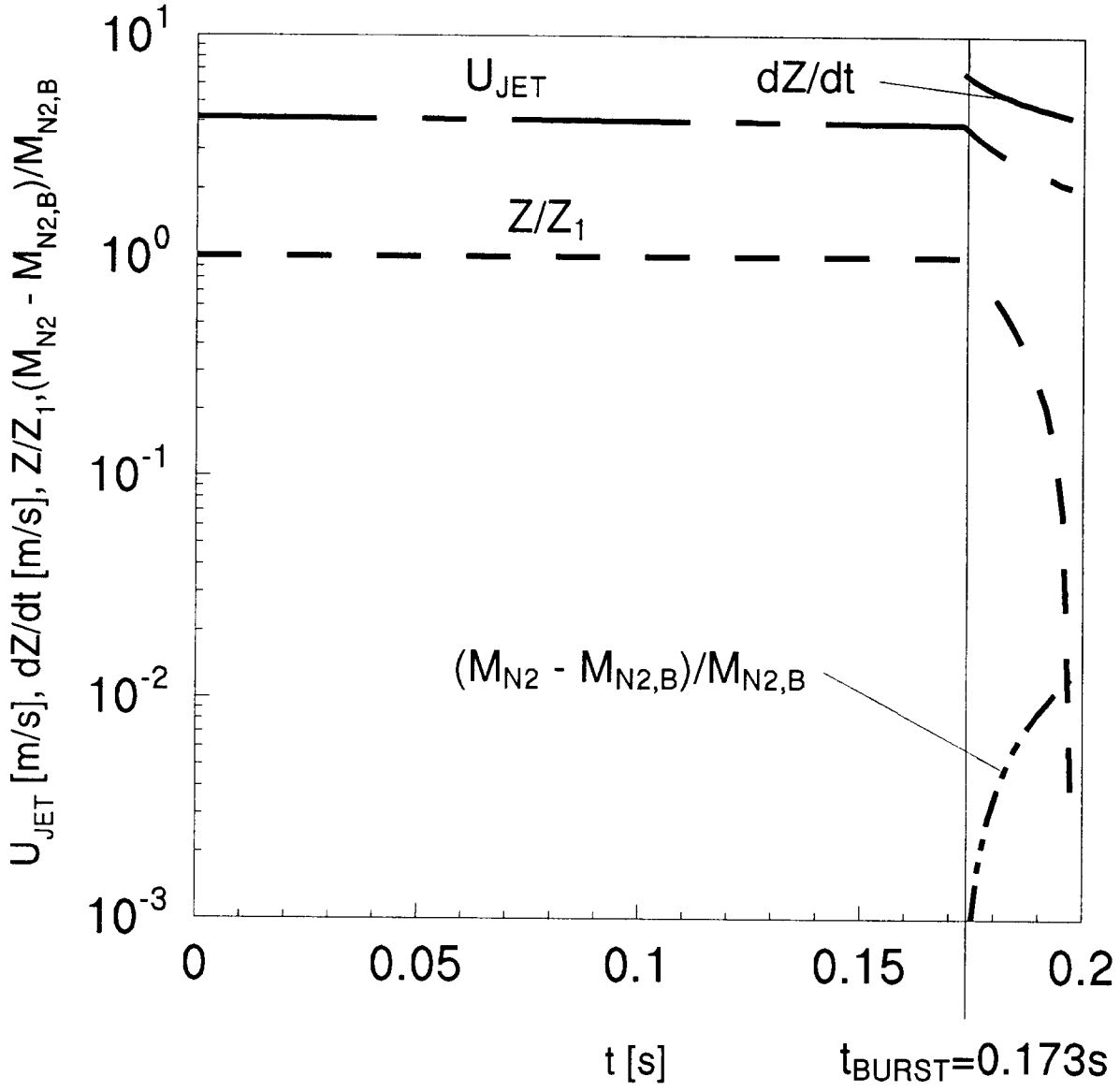

Figure 17. U_{JET}, dZ/dt, Z/Z_1, and $(M_{N2}-M_{N2,B})/M_{N2,B}$ for small-volume, high-pressure holding tank; D_o=0.5 mm; $P_{DV,1}$=3.45 MPa; $P_{HT,1}$=15.5 MPa; P_{BURST}=3.8 MPa.

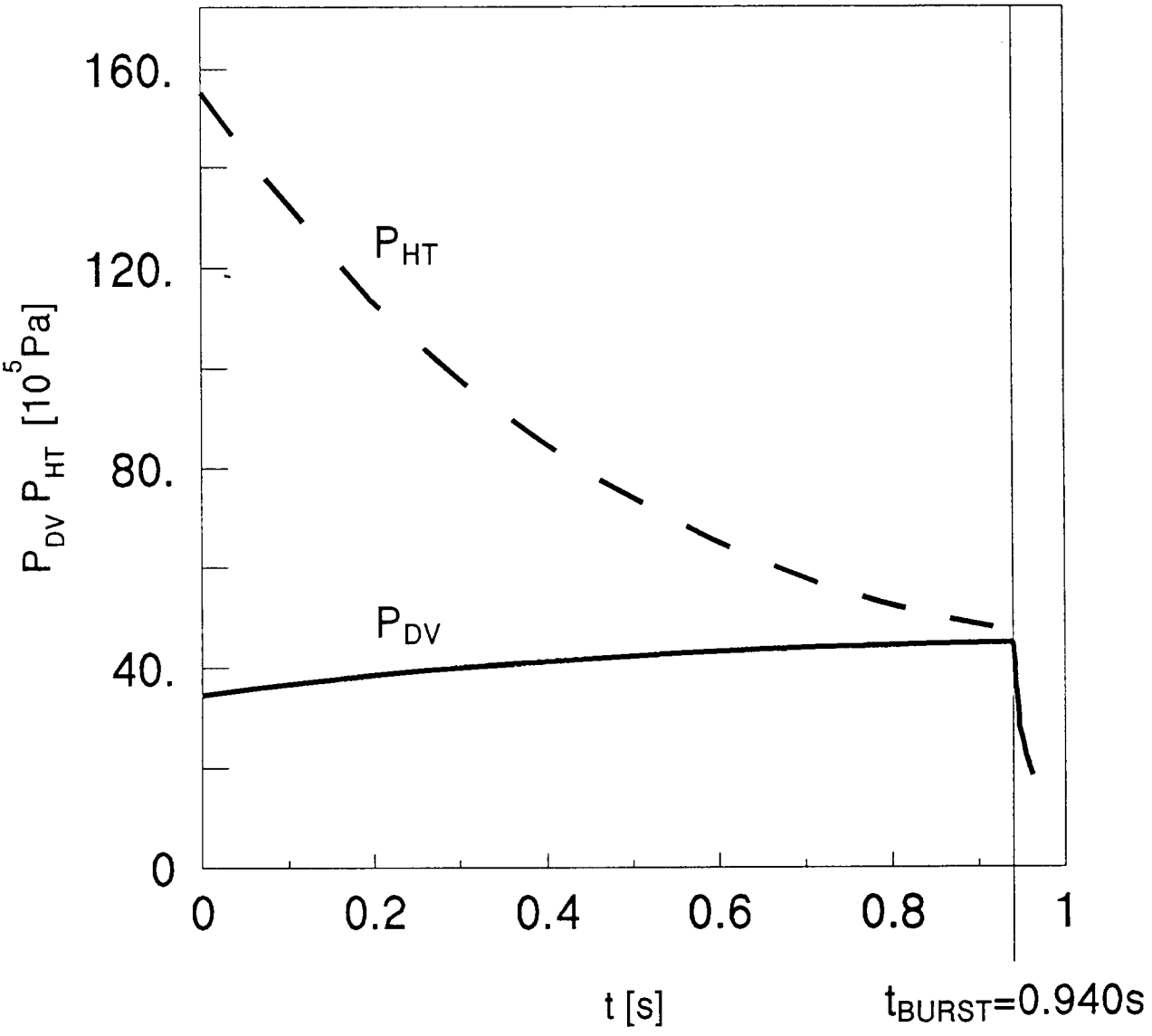

Figure 18. Pressures in the holding tank and discharge vessel for $t \geq 0$ for a small-volume, high-pressure holding tank; D_o = 0.5 mm; $P_{DV,1}$ = 3.45 MPa; $P_{HT,1}$ = 15.5 MPa; P_{BURST} = 4.48 MPa.

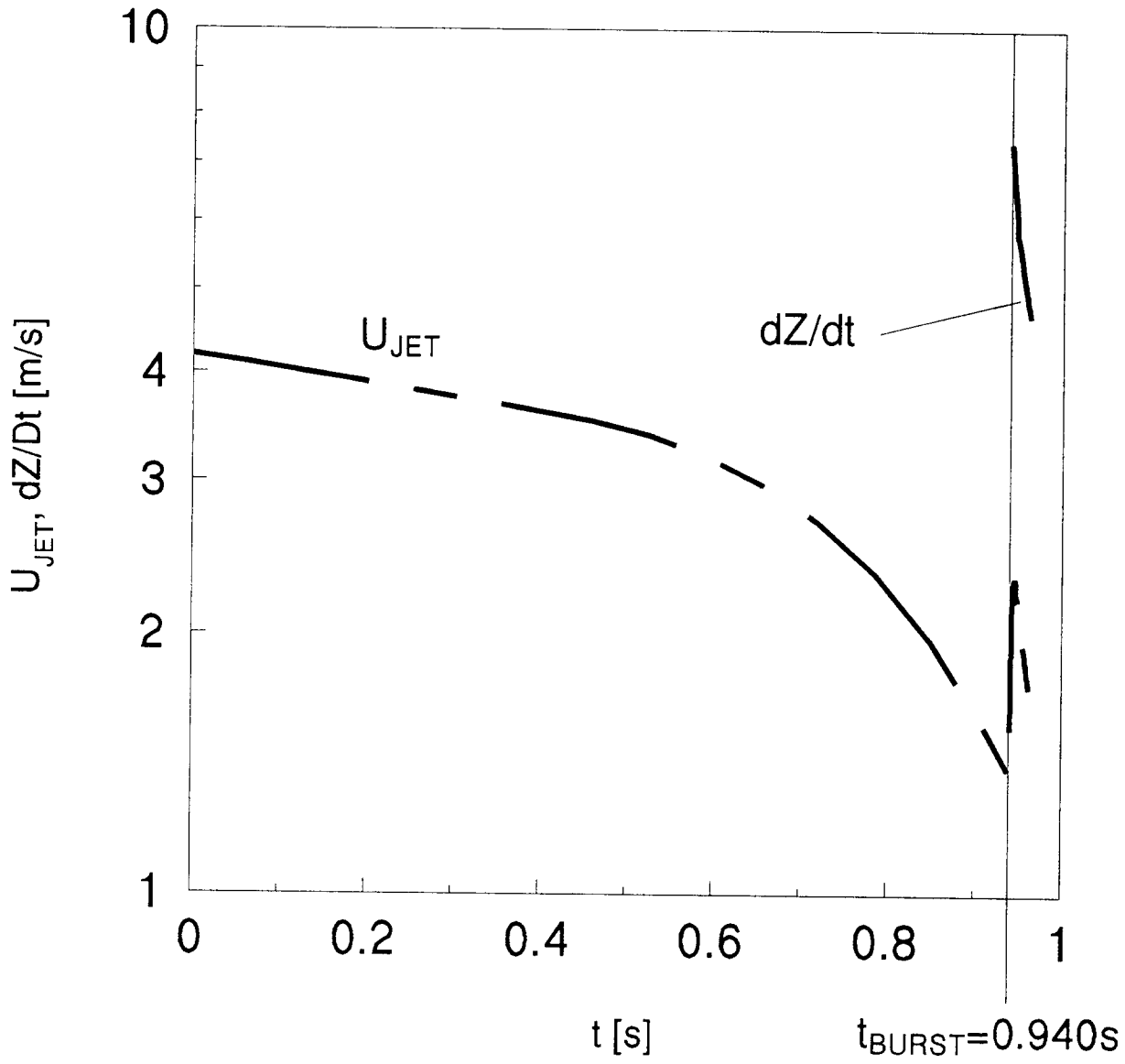

Figure 19. U_{JET} and dZ/dt for $t \geq 0$ for a small-volume, high-pressure holding tank; D_o = 0.5 mm; $P_{DV,1}$ = 3.45 MPa; $P_{HT,1}$ = 15.5 MPa; P_{BURST} = 4.48 MPa.

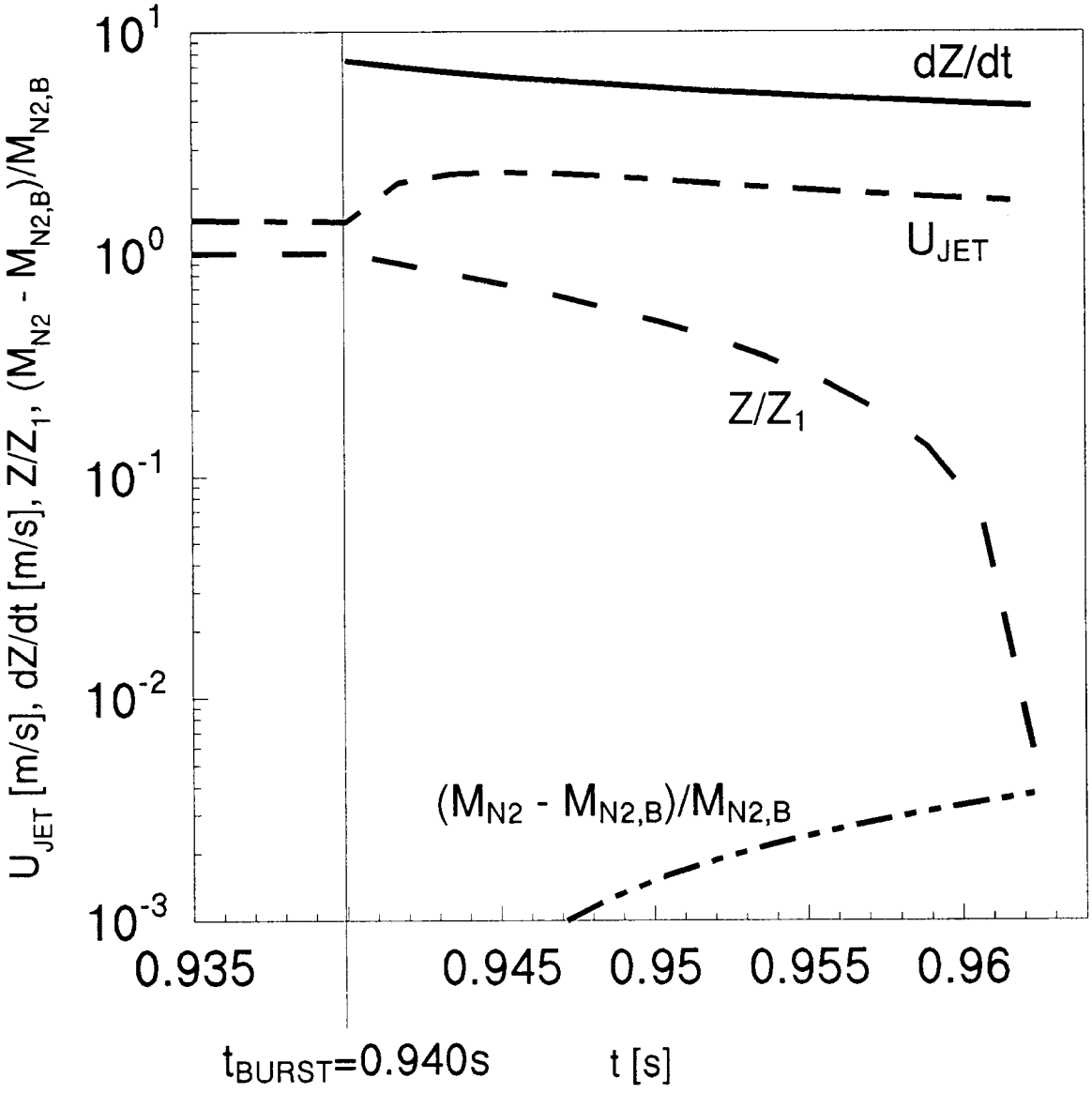

Figure 20. U_{JET}, dZ/dt, Z/Z_1, and $(M_{N2}-M_{N2,B})/M_{N2,B}$ for small-volume, high-pressure holding tank; D_o=0.5 mm; $P_{DV,1}$=3.45 MPa; $P_{HT,1}$ =16 MPa; P_{BURST}=4.48 MPa.

option of initiating tests from relatively-low values of $P_{DV,1}$, *e.g.*, immediately after filling the vessel with the test agent, when $P_{DV,1} = P_{SAT}$. To do so would once again require highly variable and unreasonably large values of $P_{HT,1}$. (3) The large-holding-tank design requires $P_{HT,1}$ values only slightly greater than the maximum P_{BURST} value and it suffers from neither of the above shortcomings.

3.2.10.2 Pressurization and Discharge for the Large Orifice, D_O = 0.005 m. Simulation results for pressurization/discharge test using the large-orifice design are presented in Figure 21 through Figure 24.

For $P_{BURST} = 37.9 \times 10^5$ Pa, plots of P_{DV} and P_{HT} are presented in Figure 21 and plots of U_{JET}, dZ/dt, Z/Z_1, and $(M_{N2} - M_{N2,B})/M_{N2,B}$ in Figure 22. Note that the latter variable is meaningful only during discharge when $t \geq t_{BURST}$. As can be seen in these figures, for this case t_{BURST} = 0.00173 s, *i.e.*, this is the time it takes for P_{DV} to rise from $P_{DV,1} = 34.5 \times 10^5$ Pa to the diaphragm rupture pressure. From Figure 21 is seen that the P_{HT} has almost been reduced to P_{DV} at t = 0.015 s, at which time approximately 40% of the original amount of liquid is still in the vessel, *i.e.*, Z/Z_1 = 0.4 (Figure 22). Also, from Figure 22 it is seen that the liquid is nearly all discharged from the vessel (*i.e.*, Z/Z_1 is approaching zero) at approximately t = 0.023 s. From Figure 22 it is seen that during discharge: the rate of liquid outflow is reduced to about half of its original value, with dZ/dt going from 8 m/s to 4 m/s; U_{JET} is always dropping, being reduced from an initially large predischarge value of approximately 40 m/s to approximately 4 m/s; and $(M_{N2} - M_{N2,B})/M_{N2,B}$ rises from 0 to 0.35, *i.e.*, at the end of the discharge the mass of N_2 in the vessel is increased from its value at t_{BURST} by a factor of approximately 0.35. The latter two results indicate that the criteria of Equations (14) and (15) are not satisfied and, as when used in conjunction with a relatively large holding tank, the large orifice design is not expected to adequately reproduce field-deployed discharges.

For $P_{BURST} = 44.8 \times 10^5$ Pa, plots of P_{DV} and P_{HT} are presented in Figure 23 and plots of U_{JET}, dZ/dt, Z/Z_1, and $(M_{N2} - M_{N2,B})/M_{N2,B}$ in Figure 24. The results are qualitatively similar to those discussed in the last paragraph for $P_{BURST} = 37.9 \times 10^5$ Pa. The quantitative differences can be easily determined from the figures. For this case t_{BURST} = 0.0094 s. From Figure 23 is seen that the P_{HT} has almost been reduced to P_{DV} at the time that discharge is initiated. Indeed, if the $P_{HT,1}$ had been much less than 155×10^5 Pa, P_{DV} would not have risen to P_{BURST} and the discharge process would never have occurred! The liquid is nearly all discharged from the vessel at 0.03 s. During the pressurization process U_{JET} drops from approximately 40 m/s to 15 m/s. During discharge: dZ/dt is reduced from 7 m/s to 5 m/s; U_{JET} is reduced from 15 m/s to 3.5 m/s; and $(M_{N2} - M_{N2,B})/M_{N2,B}$ rises from 0 to 0.1. Although the criterion in Equation (14) is satisfied, that of Equation (15) is not.

3.2.11 Summary and Conclusions. A mathematical model and associated computer program were developed to simulate the discharge of fire extinguishment agents from N_2-pressurized vessels. The model is expected to have three applications. First, to guide the development of an experimental procedure which both 1) simulates depressurization of a field-deployed discharge vessel and 2) allows for acquisition of data, including high speed photography, to characterize adequately the discharge process. Second, to evaluate the discharge characteristics of a wide range of alternative-agent/pressure-vessel configurations, thereby extending the slow and relatively costly experimental method of making such evaluations. Finally, to predict exit flow conditions to be used to solve the problem of agent dispersal outside of the discharge vessel.

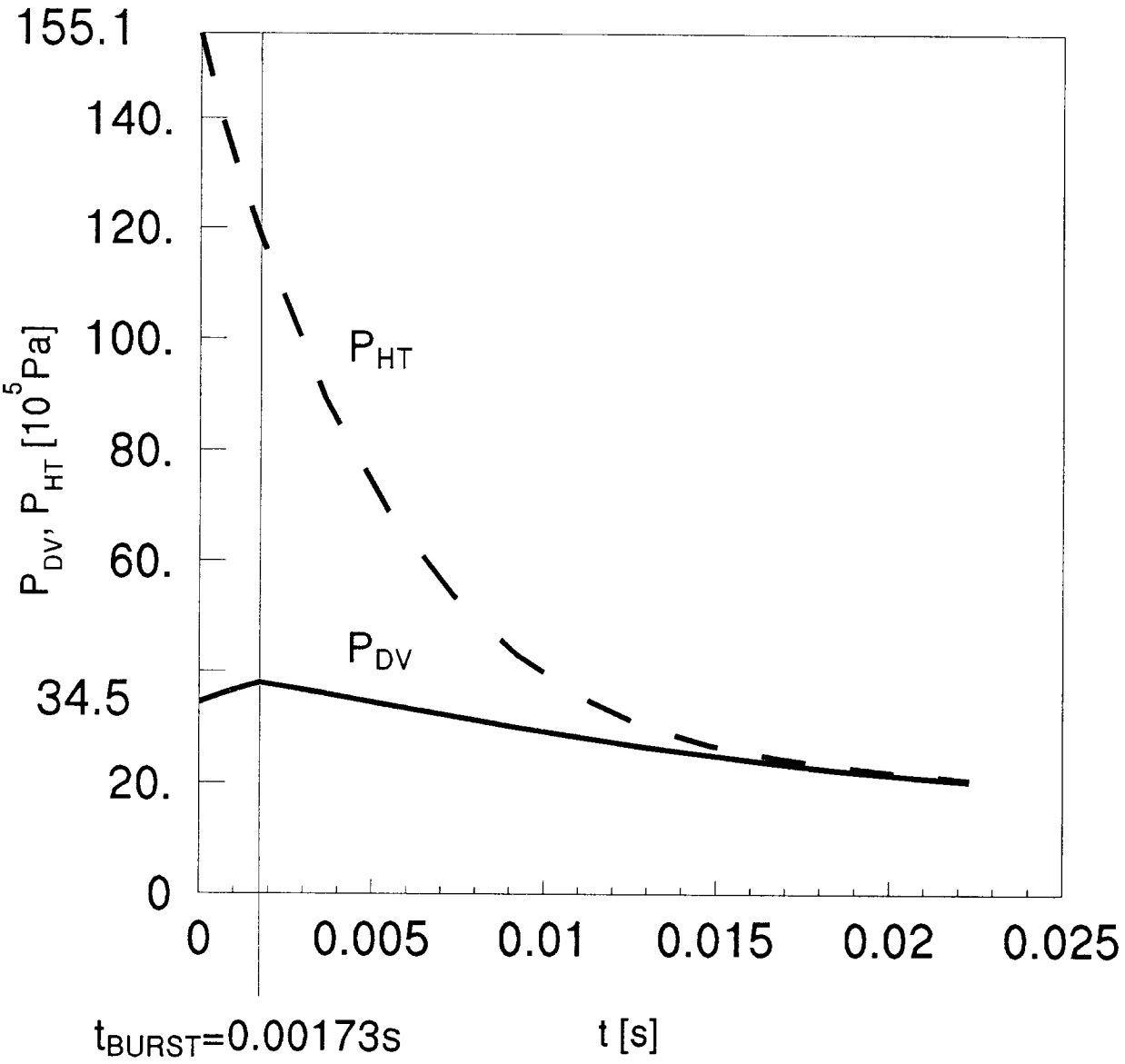

Figure 21. Pressures in the holding tank and discharge vessel for $t \geq 0$ for a small-volume, high-pressure holding tank; D_o = 5 mm; $P_{DV,1}$ = 3.45 MPa; $P_{HT,1}$ = 15.5 MPa; P_{BURST} = 3.79 MPa.

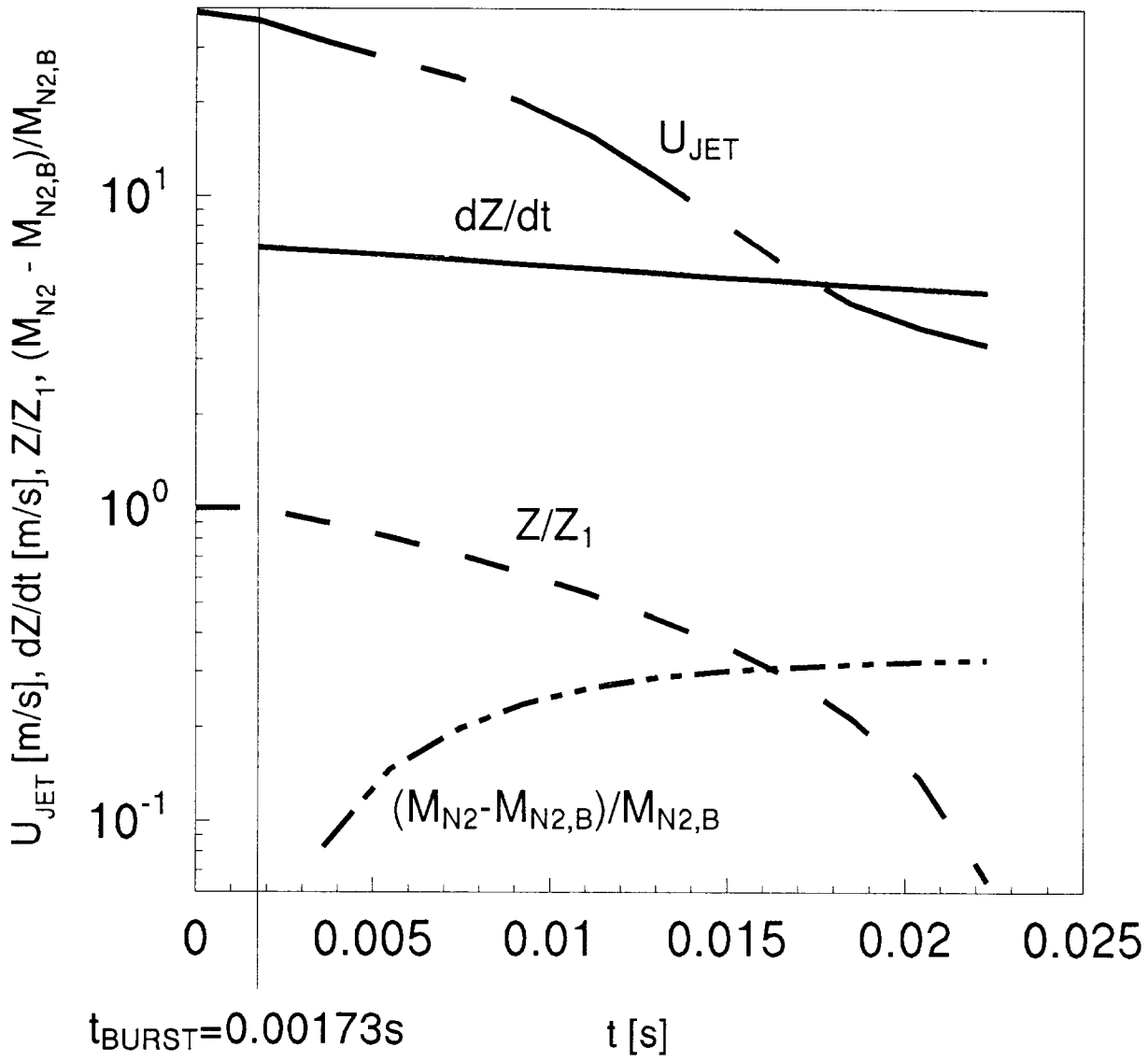

Figure 22. U_{JET}, dZ/dt, Z/Z_1, and $(M_{N2}-M_{N2,B})/M_{N2,B}$ for small-volume, high-pressure holding tank; D_o=5 mm; $P_{DV,1}$=3.45 MPa; $P_{HT,1}$=15.5 MPa; P_{BURST}= 3.79 MPa.

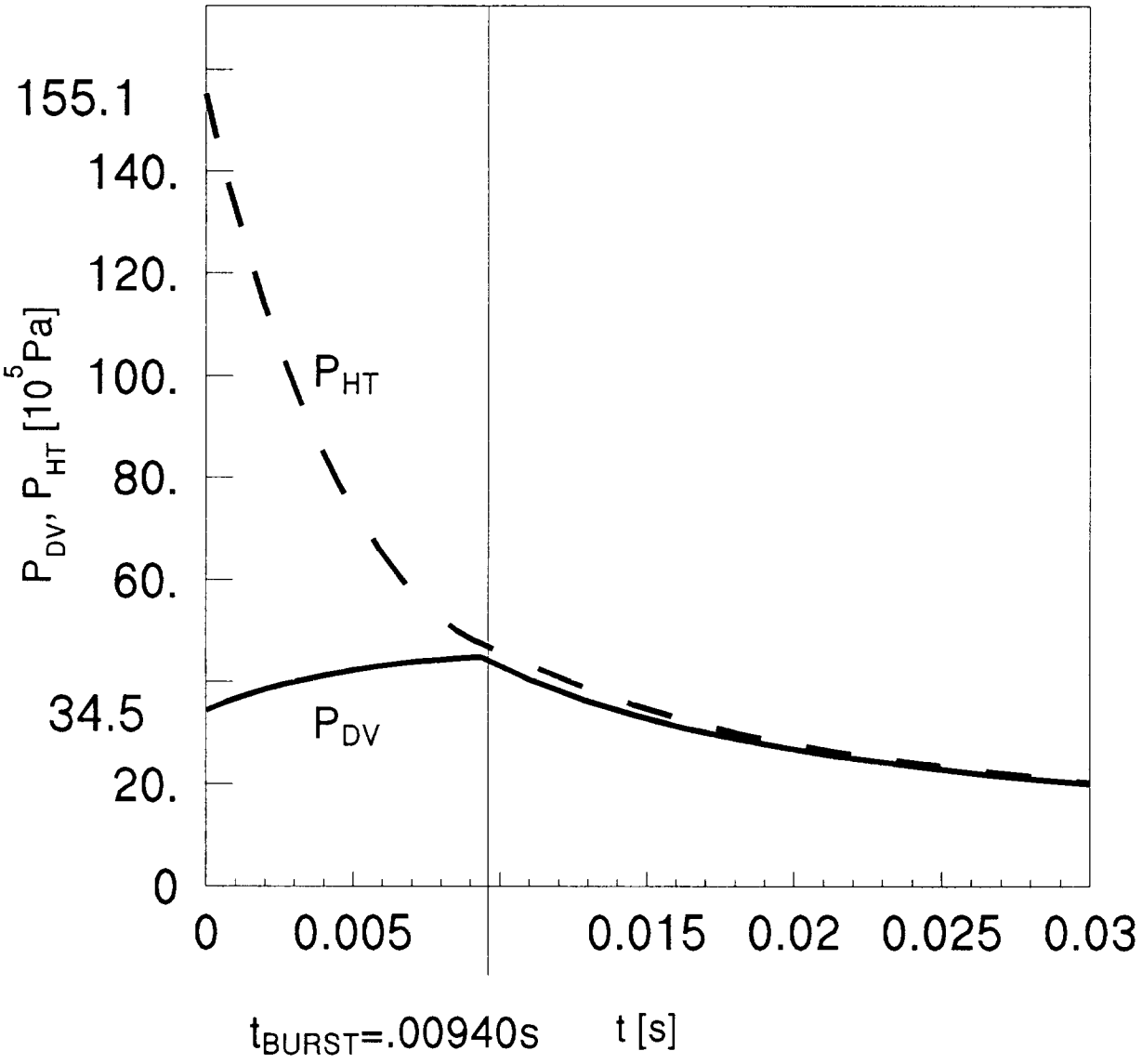

Figure 23. Pressures in the holding tank and discharge vessel for $t \geq 0$ for a small-volume, high-pressure holding tank; D_o = 5 mm; $P_{DV,1}$ = 3.45 MPa; $P_{HT,1}$ = 15.5 MPa; P_{BURST} = 4.48 MPa.

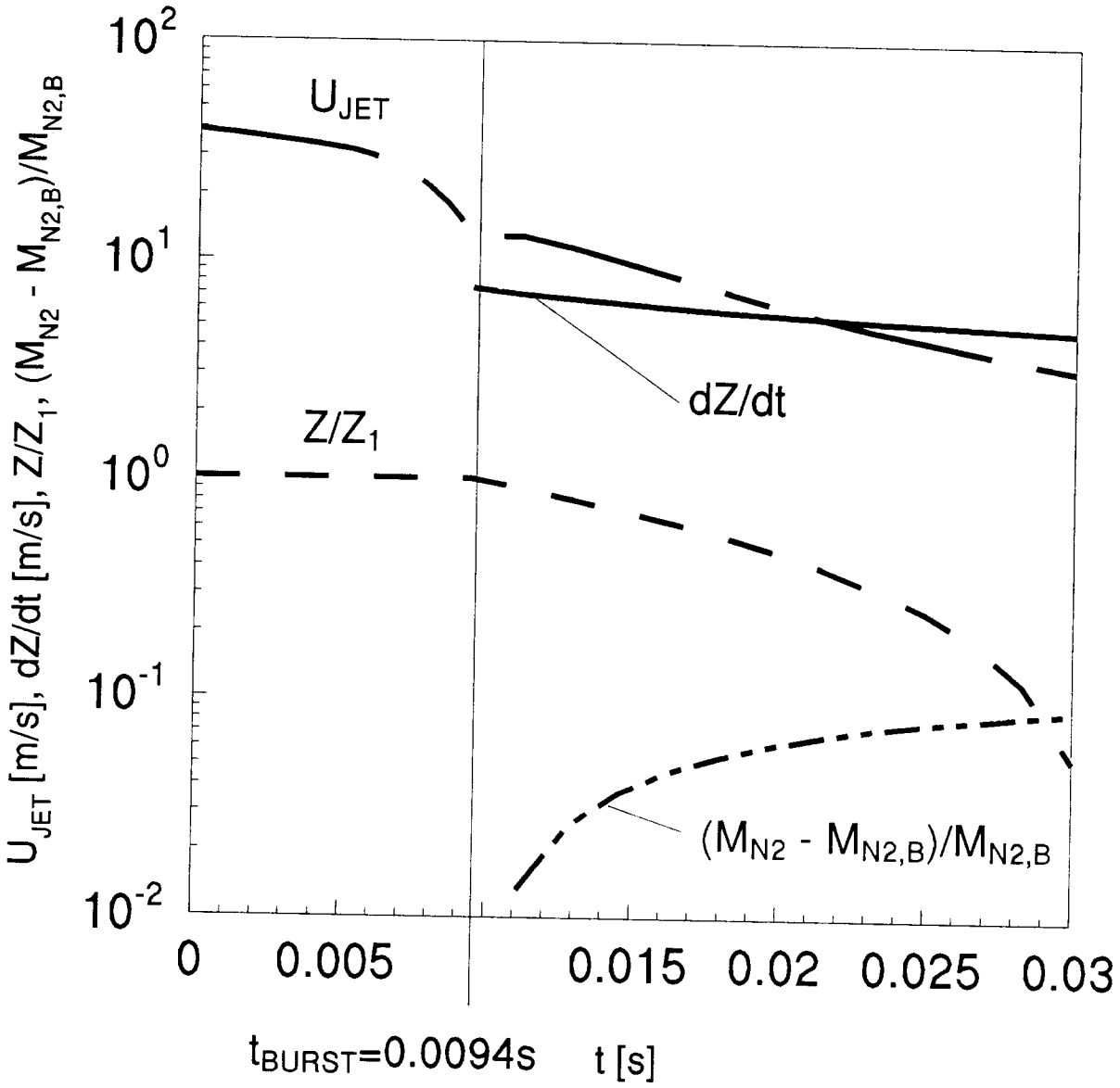

Figure 24. U_{JET}, dZ/dt, Z/Z_1, and $(M_{N2}-M_{N2,B})/M_{N2,B}$ for small-volume, high-pressure holding tank; D_o=5 mm; $P_{DV,1}$=3.45 MPa; $P_{HT,1}$=16 MPa; P_{BURST}=4.48 MPa.

The model is based on the experimental configuration depicted in Figure 1, and the solution method is capable of treating arbitrary choices of geometric parameters, material properties, and initial conditions.

The model was used in example calculations which address the first of the applications, viz., the establishment of a robust experimental design and procedure that would 1) simulate the discharge of field-deployed fire extinguishment systems useable in aircraft and 2) meet additional experimental constraints consistent with a program at NIST in support of aircraft fire safety issues.

In the example calculations, the fixed parameters which characterized the system were a 0.0005 m^3 discharge vessel with a circular exit nozzle/orifice of diameter 0.01905 m half-filled with HCFC-22 in the liquid phase at "room temperature," 294 K.

The deployed system was assumed to be pressurized with N_2 to a total pressure of 41.4×10^5 Pa, where the exit nozzle/orifice is closed with an explosive cap which is released "on demand." In the experimental system, the exit nozzle/orifice is capped with a disk which ruptures at an *a priori*-unknown pressure, between 37.9×10^5 Pa and 44.8×10^5 Pa.

The experimental system, is brought to the rupture/burst pressure, P_{BURST}, from an initial pressure $P_{DV,1}$ by a process of pressurization by flow from the holding tank which is initially filled with N_2 at some pressure, $P_{HT,1}$, higher than P_{BURST}. The holding tank communicates with the discharge vessel through a circular orifice of diameter D_O.

The model was used to simulate the discharge of the deployed system and of the experimental system. Experimental parameters that were varied were $P_{DV,1}$ (9.38×10^5 Pa, the saturation pressure of HCFC-22 at 294 K, or 34.5×10^5 Pa); $P_{HT,1}$ and the volume of the holding tank (51.7×10^5 Pa and 2.5×10^{-3} m^3, or 155.1×10^5 Pa and 2.5×10^{-5} m^3); and D_O (0.005 m, 0.001 m, or 0.0005 m).

Results of the simulations are presented in Figure 6 through Figure 24. Based on the model calculations it was determined that with $P_{DV,1} = 9.38 \times 10^5$ Pa or 34.5×10^5 Pa an experimental configuration/design using the relatively low-pressure (51.7×10^5 Pa), large-volume (2.5×10-3 m^3), holding tank and the smallest-diameter (0.0005 m) orifice would accurately simulate the discharge of the field-deployed system. Furthermore, it is expected that such a design is robust in the sense that it would also simulate well the field-deployed system even when extended to a range of parameters and agent materials well beyond the scope of the present calculations.

Model calculations also indicated that an experimental design which uses the large-diameter orifice (0.005 m) and/or the relatively high pressure small-volume holding tank (155.1×10^5 Pa and 2.5×10^{-5} m^3) would often not provide accurate simulations of field-deployed discharges and would never be expected to be "robust."

3.2.12 Nomenclature

A_{DV}	cross-sectional area of discharge vessel
A_N, A_O	area of discharge nozzle/orifice, orifice from holding tank
$C_{D,N}$, $C_{D,O}$	flow coefficient of discharge nozzle/orifice, orifice from holding tank
$C_{P,AG}$, $C_{P,N2}$	specific heat at constant pressure of agent gas, N_2
$C_{V,AG}$, $C_{V,N2}$	specific heat at constant volume of agent gas, N_2
D_O	diameter of the orifice between discharge vessel and holding tank
$M_{DV,AG}$, $M_{DV,AL}$	mass of gaseous, liquid agent in discharge vessel
$M_{DV,N2}$, $M_{HT,N2}$	mass of N_2 in discharge vessel, holding tank
$M_{DV,N2,1}$, $M_{DV,AL,1}$, $M_{HT,N2,1}$	$M_{DV,N2}$, $M_{DV,AL}$, $M_{HT,N2}$ at t = 0

M_{N2}	total mass of N_2 in discharge vessel and holding tank, see Equation (3)
$M_{N2,B}$	mass of N_2 in discharge vessel when the diaphragm ruptures
P	pressure
P_{AMB}	pressure of ambient environment
P_{BURST}	pressure in discharge vessel when the diaphragm ruptures
P_{DV}, P_{HT}	pressure in discharge vessel, holding tank
$P_{DV,1}$, $P_{HT,1}$	P_{DV}, P_{HT} at t = 0
P_{SAT}	pressure when liquid agent is at saturation
P_{SP}	pressure on agent spinoidal curve
R_{AG}, R_{N2}	gas constants for gaseous agent, N_2
T	temperature
T_{AL}	temperature of liquid agent
T_{DV}, T_{HT}	temperature of gaseous agent in discharge vessel, N_2 in holding tank
$T_{DV,1}$, $T_{HT,1}$	T_{DV}, T_{HT} at t = 0
t	time from beginning of experiment or from onset of discharge of field-deployed system
t_{BURST}	time when diaphragm ruptures
t_D	time at completion of liquid discharge or when P_{DV} reaches P_{SAT} during discharge
U_{JET}, U_O	axial velocity of orifice jet upstream of gas/liquid interface
V_{HT}	volume of holding tank
x_i	variables of dimensionless initial value problem, i = 1, 2, 3, Equation (9)
Z	elevation of gas/liquid interface above bottom of discharge vessel
Z_1	Z at t = 0
Z_{DV}	length of discharge vessel
Z_{JET}	Z_{DV} - Z
γ, γ_{AG}	ratio of specific heats for N_2, gaseous agent
ζ	dimensionless Z, Equation (A-1)
ζ_{DV}	dimensionless Z_{DV}, Equation (A-4)
θ_{DV}, θ_{HT}	dimensionless T_{DV}, T_{HT}, Equation (A-1)
$\theta_{DV,1}$, $\theta_{HT,1}$	dimensionless $T_{DV,1}$, $T_{HT,1}$, Equation (A-1)
ρ_{AL}	density of liquid agent
ρ_{SAT}	density of saturated liquid agent
λ_i	dimensionless parameters, i = 1 to 5, Equations (10) and (A-4)
$\mu_{DV,N2}$, $\mu_{HT,N2}$	dimensionless $M_{DV,N2}$, $M_{HT,N2}$, Equation (A-1)
$\mu_{DV,N2,1}$, $\mu_{HT,N2,1}$	dimensionless $M_{DV,N2,1}$, $M_{HT,N2,1}$, Equation (A-1)
π_{AMB}	dimensionless P_{AMB}, Equation (A-4)
π_{HT}, π_{DV}, $\pi_{HT,1}$	dimensionless P_{HT}, P_{DV}, $P_{HT,1}$, Equation (A-1)
π_{SP}	dimensionless P_{SP}, Equation (A-4)
σ_i	functions of x_i and parameters, i = 1, 2, 3, Equation (11)
τ	dimensionless t, Equations (9) and (A-1)

3.2.13 Appendix: The Dimensionless Initial Value Problem. Define the following dimensionless variables and their initial values:

$$\tau \equiv tC_{D,N}A_N[2P_{DV,1}/(M_{DV,AL,1}A_{DV}Z_1)]^{1/2}$$

$$\pi_{HT} \equiv P_{HT}/P_{DV,1};\ \pi_{HT}(\tau = 0) \equiv \pi_{HT,1} = P_{HT,1}/P_{DV,1} > 1$$

$$\pi_{DV} \equiv P_{DV}/P_{DV,1};\ \pi_{DV}(\tau = 0) = 1$$

$$\mu_{HT,N2} \equiv M_{HT,N2}/M_{N2};\ \mu_{HT,N2}(\tau = 0) = M_{HT,N2,1}/M_{N2} \equiv \mu_{HT,N2,1} = 1 - \mu_{DV,N2,1} \leq 1$$

$$\mu_{DV,N2} \equiv M_{DV,N2}/M_{N2};\ \mu_{DV,N2}(\tau = 0) = M_{DV,N2,1}/M_{N2} \equiv \mu_{DV,N2,1} = 1 - \mu_{HT,N2,1} \leq 1$$

$$\mu_{DV,AL} \equiv M_{DV,AL}/M_{DV,AL,1} = M_{DV,AL}/(\rho_{AL}A_{DV}Z_1);\ \mu_{DV,AL}(\tau = 0) = 1 \qquad \text{(A-1)}$$

$$\theta_{HT} \equiv T_{HT}R_{N2}M_{N2}/(V_{HT}P_{DV,1}) = (T_{HT}/T_{HT,1})(P_{HT,1}/P_{DV,1})/(M_{HT,N2,1}/M_{N2});$$

$$\theta_{HT}(\tau = 0) \equiv \theta_{HT,1} = (P_{HT,1}/P_{DV,1})/(M_{HT,N2,1}/M_{N2}) > 1$$

$$\theta_{DV} \equiv T_{DV}M_{DV,AG}R_{AG}/(Z_1A_{DV}P_{DV,1}) = T_{DV}M_{DV,AG}R_{AG}\rho_{AL}/(M_{DV,AL,1}P_{DV,1});$$

$$\theta_{DV}(\tau = 0) \equiv \theta_{DV,1} = T_{DV,1}M_{DV,AG}R_{AG}/(Z_1A_{DV}P_{DV,1})$$

$$\zeta \equiv Z/Z_1;\ \zeta(\tau = 0) = 1$$

Define the new variable x_1 and introduce x_2 and x_3 as new designations for $\mu_{DV,N2}$ and $\mu_{DV,AL}$, respectively:

$$x_1(\tau) \equiv [(1 + \lambda_3\mu_{DV,N2})/(1 + \lambda_1\mu_{DV,N2})]\pi_{DV}(\zeta_{DV} - \mu_{DV,AL}) + \lambda_2\lambda_4(1 - \mu_{DV,N2})^{\gamma};$$

$$x_1(0) = [(1 + \lambda_3\mu_{DV,N2,1})/(1 + \lambda_1\mu_{DV,N2,1})](\zeta_{DV} - 1) + \lambda_2\lambda_4(1 - \mu_{DV,N2,1})^{\gamma} \qquad \text{(A-2)}$$

$$x_2(\tau) \equiv \mu_{DV,N2};\ x_2(0) = \mu_{DV,N2,1}$$

$$x_3(\tau) \equiv \mu_{DV,AL};\ x_3(0) = \mu_{DV,AL,1}$$

Define also the following functions of the x_i:

$$f_1 \equiv [x_1 - \lambda_2\lambda_4(1 - x_2)^{\gamma}](1 + \lambda_1x_2)/[(1 + \lambda_3x_2)(\zeta_{DV} - x_3)];$$

$$f_2 \equiv \lambda_2(1 - x_2)^{(\gamma - 1)};\ f_3 \equiv \lambda_2(1 - x_2)^{\gamma};\quad f_4 \equiv \lambda_2(1 - x_2)^{\gamma}/f_1; \qquad \text{(A-3)}$$

$$f_5(x_i) \equiv \begin{cases} \lambda_5 f_3\{\gamma[2/(\gamma+1)]^{(\gamma+1)/(\gamma-1)}/f_2\}^{1/2}; & \text{if } f_4 \geq [(\gamma+1)/2]^{[\gamma/(\gamma-1)]} \\ \lambda_5 f_3(1/f_4)^{1/\gamma}\{2\gamma[1-(1/f_4)^{(\gamma-1)/\gamma}]/[(\gamma-1)f_2]\}^{1/2}; & \text{if } f_4 < [(\gamma+1)/2]^{[\gamma/(\gamma-1)]} \end{cases}$$

$$f_6(x_i) \equiv \begin{cases} (f_1 - \pi_{AMB})^{1/2}; & \text{if } \pi_{AMB} \geq \pi_{SP} \\ (f_1 - \pi_{SP})^{1/2}; & \text{if } \pi_{AMB} < \pi_{SP} \end{cases}$$

where

$$\begin{aligned} &\lambda_1 = (M_{N2}/M_{DV,AG})(R_{N2}/R_{AG});\ \lambda_2 \equiv \pi_{HT,1}/(\mu_{HT,N2,1})^{\gamma}; \\ &\lambda_3 = (C_{V,N2}/C_{V,AG})(M_{N2}/M_{DV,AG}) = \lambda_1(\gamma_{AG}-1)/(\gamma-1); \\ &\lambda_4 = [(\gamma_{AG}-1)/(\gamma-1)][V_{HT}/(Z_1 A_{DV})]; \\ &\lambda_5 = (C_{D,O}/C_{D,N})(A_O/A_N)[(M_{DV,AL}/M_{N2})(A_{DV}Z_1/V_{HT})/2]^{1/2}; \\ &\zeta_{DV} = Z_{DV}/Z_1 = \text{constant} > 1;\ \gamma_{AG} = C_{P,AG}/C_{V,AG} = R_{AG}/C_{V,AG} + 1; \\ &\pi_{AMB} = P_{AMB}/P_{DV,1};\ \pi_{SP} = P_{SP}/P_{DV,1} \end{aligned} \tag{A-4}$$

Then the x_i can be determined from the solution of the following initial value problem

$$\begin{aligned} &dx_1/d\tau = -(\gamma_{AG}-1)f_1 f_6;\ dx_2/d\tau = f_5;\ dx_3/d\tau = -f_6 \\ &x_1(0) = [(1+\lambda_3\mu_{DV,N2,1})/(1+\lambda_1\mu_{DV,N2,1})](\zeta_{DV}-1) + \lambda_2\lambda_4(1-\mu_{DV,N2,1})^{\gamma}; \\ &x_2(0) = \mu_{DV,N2,1};\ x_3(0) = \mu_{DV,AL,1} \end{aligned} \tag{A-5}$$

and the solutions for the original dimensionless variables of Equation (A-1) can be retrieved from

$$\begin{aligned} &\pi_{DV} = f_1;\ \pi_{HT} = f_3;\ \mu_{HT,N2} = 1 - x_2;\ \mu_{DV,N2} = x_2;\ \mu_{DV,AL} = \zeta = x_3; \\ &\theta_{HT} = f_2;\ \theta_{DV} = (\zeta_{DV} - x_3)f_1/(1+\lambda_1 x_2) \end{aligned} \tag{A-6}$$

From the latter solutions the dimensional variables can be determined finally from the definitions of Equation (A-1).

The problem formulation of Equation (A-5) and its solution are valid up to the value of τ where $x_3 = 0$ (the last of the liquid is driven from the discharge vessel) or f_1 is reduced to $P_{SAT}/P_{DV,1}$ (the

liquid in the discharge vessel is subjected to a condition where an equilibrium state would lead to flashing).

3.3 Design of Experimental Release Vessel

3.3.1 Introduction. In a conventional halon 1301 bottle, a fixed amount of agent is initially dispensed to the bottle followed by pressurization with nitrogen to a fixed equilibrium pressure at room temperature. Depending upon the application, the amount of agent and the charged pressure can be varied accordingly. Release of the agent from the vessel is normally achieved by a squib or a solenoid valve, either manually or automatically, upon the detection of a fire. For fire protection of dry bays, the agent has to be released from the vessel and suppress the fire in less than 50 ms. The use of a squib or solenoid valve to study discharge dynamics in a laboratory is not appropriate because a squib is an explosive device and the flow path through a solenoid valve is too complex to analyze. In order to obtain fundamental understanding of the discharge processes, an experimental apparatus has to be designed such that it can eliminate the above shortcomings of using either a squib or a solenoid valve and at the same time closely simulate the actual discharge process.
There were two major design criteria that had to be considered: vessel size and release mechanism. Since the experimental condition was at high pressure, the size of the vessel had to be small enough to minimize weight for ease of mounting and handling of the vessel, but not so small that the size of the vessel became unrealistic and that the characteristic emptying time of the agent was so short that it was not possible to characterize the discharge process in sufficient detail. In addition, minimization of the amount of agents used in the discharge tests had to be considered because of the limited availability and high cost of some of the alternative agents. An internal volume of approximately 5×10^{-4} m^3 was selected. This volume was less than a factor of three smaller than the internal volume (14×10^{-4} m^3) of the smallest vessel (type CF-2) specified in the appropriate Military Specification (1965). In addition, this volume was large enough to hold a sufficient amount of agent to perform the discharge experiments. An aspect ratio (length/diameter) of about 5 was used in the vessel design. The selection of this aspect ratio was governed by the dimension of the rupture disk holder (to be discussed).

Since the intent was not to design an actual release mechanism for practical applications, but rather to design a release mechanism that could be used to compare the discharge dynamics of various alternative agents, the device had to have a simple geometry, a simple flow pattern, and quick action. Due to safety consideration in the laboratory, release mechanisms that utilized explosive cartridges to initiate the discharge of the vessel were not considered in the design of the discharge vessel. Solenoid valves were also not considered because of the complex flow path inside the valves (although some valves do have a straight-through design) and a slow response time compared to the emptying time of the vessel. Furthermore, solenoid valves are not designed to operate under extreme high and low temperatures. A rupture disk was chosen as a quick release mechanism because the bursting of the disk is almost instantaneous once a specified pressure has been reached and a simple straight-through and full opening of the non-fragmented burst disk can be obtained. This technique had been successfully used previously in a study of rapid venting of hot, high pressure liquids from a pressure vessel (Kim-E, 1981; Kim-E and Reid, 1983).

3.3.2 Release Vessel Design. A rupture disk (FDI FA scored) with a diameter of 19.1 mm was used as a rapid release mechanism for discharging agents from the pressurized vessel. The disk was

made of stainless steel (SS 316) with a nominal burst pressure of 4.12 MPa at room temperature (22 °C). The actual burst pressure varied less than ± 10% of the nominal burst pressure.

The vessel used in this study was made of either stainless steel or clear acrylic plastic (polymethyl methacrylate). The clear acrylic vessel was used for visualizing the internal behavior of the agents during discharge and for obtaining emptying rates of the agents from the vessel.

The stainless steel (SS 304) vessel was constructed from a tube with an internal diameter of 50.8 mm and a wall thickness of 6.4 mm. One end of the tube was welded with an end plate in which there were four tapped access holes for mounting a piezoelectric dynamic pressure transducer (Kistler Model 603B1), two thermocouples (K-type), and a needle valve (Whitey SS-1RS4) for dispensing the agent into the vessel and for subsequent nitrogen pressurization. The other end of the tube was welded to a flange with an O-ring seal for mounting a rupture disk holder (FDI Model FF). A tapped hole was also made on the lower side wall of the vessel so that a pressure transducer could be mounted to monitor the pressure of the liquid during downward discharge. The internal volume of the vessel was measured by filling the vessel with water and weighing and was found to be 4.97×10^{-4} m^3. The vessel was hydrostatically tested to 17.2 MPa. However, for safety reasons, the vessel was operated at pressures less than or equal to 8.2 MPa. Figure 25 is a schematic of the stainless steel vessel.

The plastic vessel was constructed from a clear acrylic tube with a nominal internal diameter of 50.8 mm and a nominal wall thickness of 9.5 mm. A schematic of the vessel is shown in Figure 26. The tube was sandwiched between two aluminum end plates equipped with O-ring seals using four threaded rods which passed through the plates. The rupture disk holder was attached to one of the end plates. Two tapped holes were drilled for mounting a dynamic pressure transducer and a needle valve on the other end plate. For those agents (all the HCFC's and HFC's) that were found to cause glazing or to dissolve into the wall of the plastic vessel, a new acrylic tube was used for each run. The internal diameter of the plastic tube was found to vary from tube to tube due to the manufacturing process of extruding the tube. The average internal volume of the all plastic vessels was 5.09×10^{-4} m^3 with a standard deviation of 0.15×10^{-4} m^3. Measurements were recorded for each tube used.

3.3.3 Design Validation. The experimental set-up used in this study (to be discussed) resembles closely the conceptual experimental configuration described in Section 3.2. In the conceptual design, a nitrogen holding tank was proposed, whereas in the actual experimental set-up the internal volume (3.38×10^{-4} m^3) of the supply line (not shown in Figure 25 and Figure 26) between the nitrogen cylinder and the pressure vessel acted like a holding tank. In addition, the needle valve used for regulating nitrogen flow into the vessel functioned in a similar way as an orifice plate placed between the holding tank and the pressure vessel. A holding tank was not used in the actual experimental set-up because the combined holding tank/vessel system could not be easily assembled due to the bulkiness of the system. The situation was more critical when changing of the orientation of the system was required in order to study the effect of orientation on the discharge (see Section 3.4).

In an actual discharge vessel, the vessel is a closed system; that is, there is no continuous flow of nitrogen into the vessel. However, the present experimental design depends on the inflow of nitrogen to raise the internal pressure of the vessel in order to rupture the disk (see Section 3.4.2). Furthermore, it was not possible to shut off the nitrogen flow to the vessel at the instant when the rupture disk burst due to the relatively slow response time ($\sim$ 35 ms) of the solenoid used to connect the vessel and nitrogen supply line.

A series of experiments were performed to access the effect of the continuous nitrogen inflow during discharge. It was found that by regulating (less than a 1/4 turn; equivalent to an orifice opening of less than 0.5 mm) the needle valve to minimize the inflow of nitrogen such that the

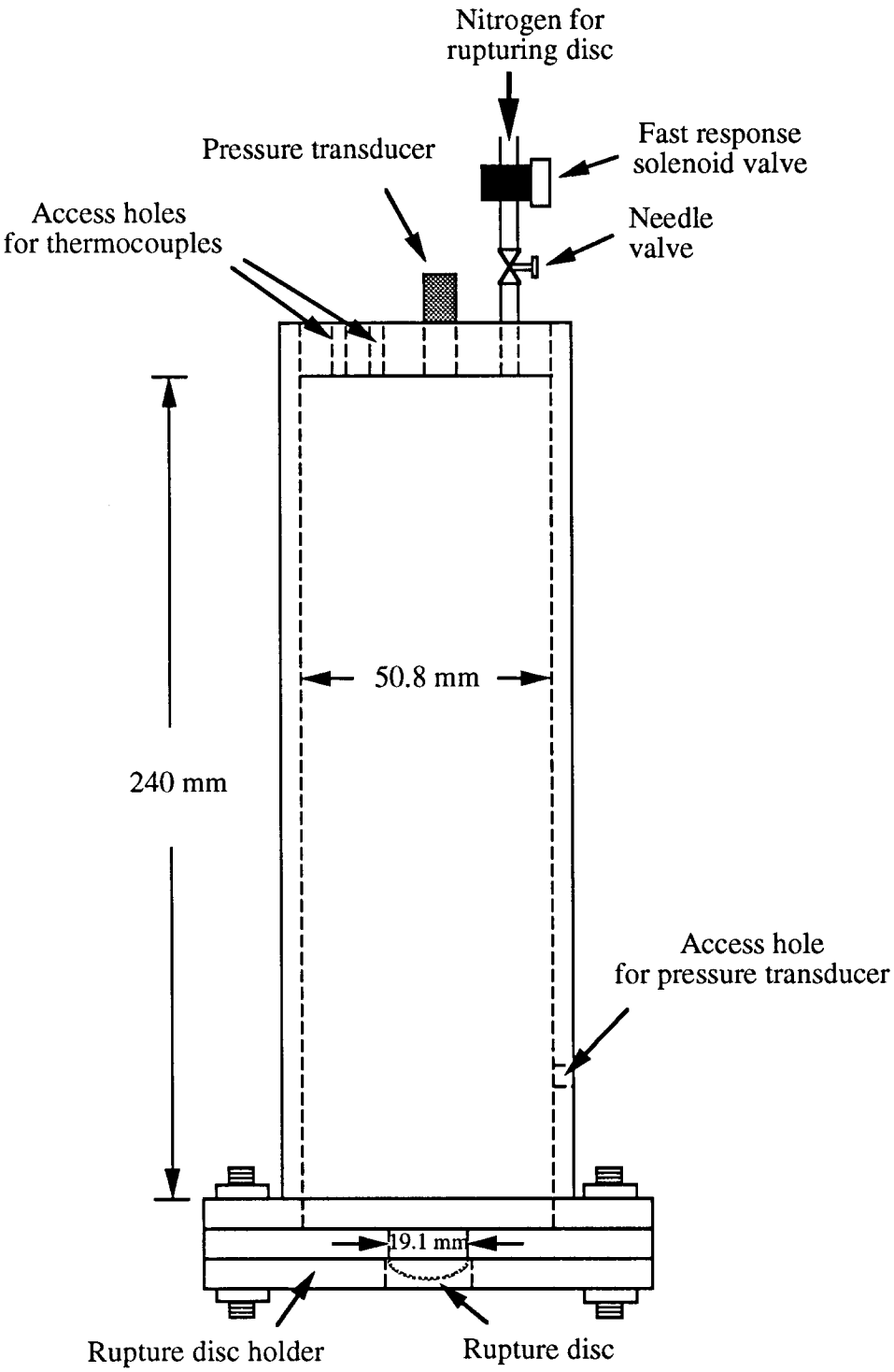

Figure 25. Schematic of the stainless steel vessel.

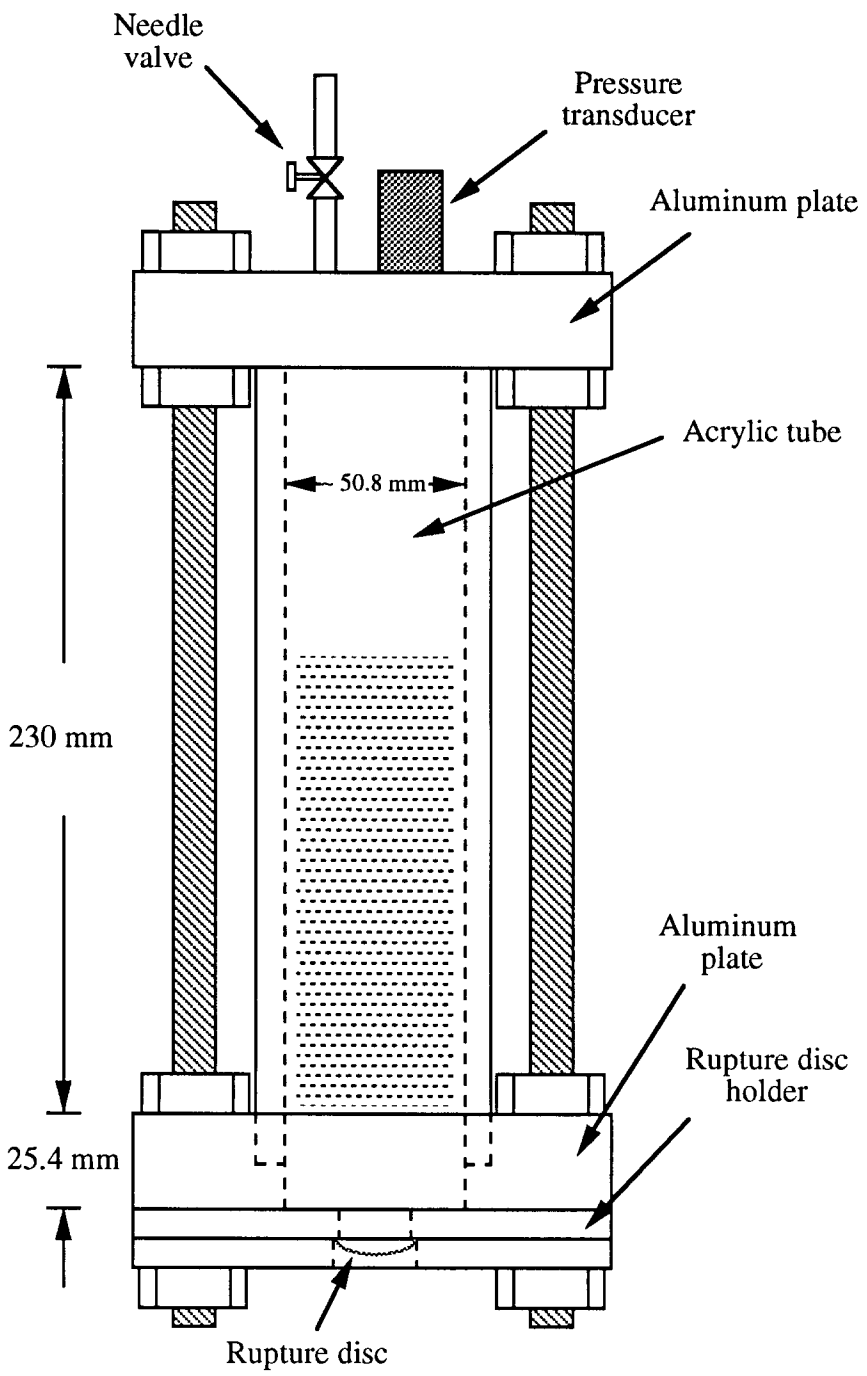

Figure 26. Schematic of the acrylic vessel.

duration from the initiation of nitrogen flow to the rupture of the burst disk was greater than one second, no appreciable differences (within the experimental uncertainty due to the actual burst pressure) were detected in the internal pressure traces during discharge. Therefore, it can be concluded that the continuous flow of nitrogen has an *insignificant* effect on the discharge behavior.

Based on the above discussion, the actual experimental configuration, in essence, incorporates the design recommendations made in Section 3.2 for a generic experimental set-up using a relatively low-pressure large-volume holding tank and a small orifice between the holding tank and the discharge vessel.

Since nitrogen is dissolved in liquid agent in an actual discharge vessel, the effect of dissolved nitrogen on the discharge process needs to be addressed. During discharge, rapid internal depressurization of the vessel could cause degassing of dissolved nitrogen from the liquid which could affect the dynamic behavior of the liquid agent inside the vessel and the flow rate through the vessel opening. Based on observed internal pressure-time histories during discharges of halon 1301, it has been conjectured (with no visual observations) that degassing of nitrogen occurs during the time interval from initiation of discharge to the complete depletion of the liquid (Williamson, 1976, Elliot *et al.*, 1984). However, the characteristic discharge times (order of seconds) for vertically downward release were much longer in these earlier studies than in our experiments ($\sim$ 30 ms). Based on the following argument, it is *hypothesized* that the characteristic discharge time in our experiments is much faster than the time required for degassing of dissolved nitrogen. The time for evolution of dissolved nitrogen in the liquid can be considered to be the sum of the waiting time for nucleation of nitrogen bubbles and the time for nitrogen bubbles to grow (Avedisian, 1985). If the waiting time is assumed to be very short even in the case of rapid discharge, the bubble growth time is then the dominant factor. Assuming the bubble growth is diffusion-controlled, *i.e.*, the growth is due to the diffusion of nitrogen into the bubble, the bubble growth velocity is of the order of 0.1 m/s (Bankoff, 1966). This growth velocity is about two orders of magnitude slower than the velocity of the depleting liquid level during rapid discharge (to be discussed later), implying that the discharge time of the liquid is much faster than that of degassing of dissolved nitrogen. Hence, the presence or absence of dissolved nitrogen would not affect the behavior of the liquid inside the vessel during very rapid discharge. In the experimental procedure used in this work (to be discussed in the next section), the dissolved nitrogen does not play a role due to the short contact time between the liquid and nitrogen in the vessel before initiation of discharge. The above argument is to ensure that the experimental procedure used in this study simulates closely the actual discharge process. Although dissolved nitrogen may not play a role in the behavior of the liquid inside the vessel during vertically downward discharge, it may affect the flashing behavior of the liquid external to the vessel as well as the behavior of the liquid inside the vessel during vertically upward and horizontal release due to longer characteristic discharge time. However, the solubilities of nitrogen in all the liquid agents used in this study were found to be very similar (see Section 2). Therefore, the differences in the overall external behaviors of the liquid agents could still be considered not to be attributable to differences in the solubility of nitrogen in the liquid agents.

3.4 Vessel Discharge Rate Measurements

3.4.1 Introduction. The events occurring inside and outside of a pressurized vessel containing alternative agent during discharge are extremely complicated due to the presence of two-phase flow. The discharge process addresses how the agent is delivered to a fire scene. The effectiveness of an agent in suppressing a fire depends on how fast and how it is transported to the fire. This part of the

task is designed to address the behavior of the proposed alternative agents inside the pressure vessel during *rapid* discharge. The characteristic discharge time is on the order of tens of milliseconds. Various parameters that could influence the discharge process will also be examined in this study. The parameters studied are: (1) orientation of discharge, (2) orifice diameter, (3) presence of an extension tube at the vessel exit, (4) vessel pressure at discharge, and (5) ambient temperature. The behaviors of the agents external to the vessel during discharge are discussed in Section 3.5.

3.4.2 Experimental Method. The experimental procedure involved the following steps. The vessel was evacuated for at least 15 min. The vessel was then connected to the agent supply bottle. For liquid agents, the vessel was filled approximately two-thirds full (by volume). For FC-116, which is a gas at room temperature, the vessel was filled until the pressure in the vessel equilibrated with the pressure in the supply bottle, and the amount of FC-116 in the vessel corresponded to an average fill density of 110 kg/m^3. This number was limited by the pressure of the agent in its supply bottle. The total mass of an agent dispensed to the vessel was obtained by weighing on an electronic scale with an accuracy of 1 g. The vessel was then pressurized with nitrogen to 75% of the nominal burst pressure of the rupture disk through a solenoid valve (Skinner 712X1D1B) and the needle valve (see Figure 25 and Figure 26). To initiate a discharge, the upstream nitrogen pressure in the nitrogen supply line was first raised to approximately 15% above the nominal burst pressure with the solenoid valve closed. The solenoid valve was then opened to start a flow of nitrogen into the vessel through the needle valve and initiate the experiment. The nitrogen flow continuously increased the internal pressure of the vessel to a point where the rupture disk could no longer sustain the rising internal pressure. Bursting and complete opening of the rupture disk followed, thus causing rapid release of the agent from the vessel.

A high-speed movie camera (Photec IV) operating at 2000 frames per second was used to document the events occurring inside the plastic vessel. Kodak Ektachrome high-speed daylight films (ASA 400), some front lighting, and intense backlighting were used. Emptying rates were obtained by using frame-by-frame analysis of the movies taken from the experiments. The high-speed motion picture film acquired for each discharge was analyzed using a slide scanner (Microtek ScanMaker 35t) to digitize the images and digital image processing software (Aldus PhotoStyler Version 1.1). Emptying rates were extracted from the digitized images of the liquid level of the agent in the vessel as a function of time during discharge.

The slide scanner is designed for use with 35 mm slides or film strips, both color and black and white, but is easily adapted for use with 16 mm movie film. It uses a linear array CCD (charge coupled device) and can digitize an image with a resolution of 3656 $\times$ 3656 dpi (dots per inch); twice the resolution (7312 x 7312 dpi) is possible with software interpolation. Dots can be represented by an 8-bit code indicating any one of 256 shades of gray, or by a 24-bit color code indicating any one of over 16 million colors. For this work, two frames per image were scanned as grayscale images with 3656 $\times$ 3656 dpi at 100% scale.

The scanning module incorporated in the digital image processing software (PhotoStyler) is Twain-compliant, which allows software applications and hardware imaging devices to communicate directly. This means that the scanner can be accessed directly from within the digital image processing software; after the scan, the image is placed inside the imaging software, where data processing is performed before the image is archived. The archival method used is to compress the image in JPEG format. In this way, an image that comprises 3.8 Mbyte of disk space can be saved in a file which is 144 kbyte without loss of image quality.

The process for computing the emptying rates is straightforward. The digital image processing software allows the measurement of the position of every pixel in the image, which is typically 2630 pixels wide by 1470 pixels high. Accurate measurements of timing and liquid level position, as seen

through the transparent vessel, allow the computation of volumetric flow rate when the vessel diameter is known.

The edge of the film strip contains a timing mark adjacent to the sprocket holes; the spot appears on the film at a rate of 1 kHz. When the high-speed movie camera is operated at 2000 frames per second, there is a timing spot every 2 frames (nominally 0.5 ms per frame). A more accurate framing rate can be computed by measuring the timing spot relative to the sprocket holes and using linear interpolation. It is estimated that the imprecision in the film speed for the data in this report is $\pm$ 0.001 ms per frame, or $\pm$ 0.2%.

The liquid level and a reference point are measured for each frame with a resolution of $\pm$ 0.5 pixels. Pixels are related to the physical length measurement scale by means of a 25.4 mm steel ball photographed at the beginning of each film reel. The uncertainty in the length calibration is $\pm$ 0.5 pixel, or 0.2 mm. Thus, the uncertainty in the liquid position measurements is typically $\pm$ 0.4 mm.

Two thermocouples, one placed in the ullage and one in the liquid, were used to record the temperature changes in both phases during discharge. The thermocouples used were K-type, fine gage (12 or 25 μm), and unsheathed. The thermocouple were constructed by arc-welding the fine thermocouple to the two bare ends (with the original bead junction removed) of a rugged unsheathed thermocouple (K-type) probe under a microscope. Attempts to record temperatures in the both phases (vapor and liquid) inside the vessel proved to be difficult, although some qualitative information could still be obtained from the temperature measurements. The difficulty lies in the response time and the fragility of the fine wire thermocouples. Even a fine 12 μm unsheathed thermocouple was found to have a time constant which was too slow to follow the events occurring inside the vessel.

The pressure transducer was a Kistler Model 603B1 piezoelectric dynamic pressure transducer which was regulated by a dual mode charge amplifier (Kistler Model 5004). The outputs from the charge amplifier and thermocouples were recorded using a high-speed data acquisition board (Strawberry Tree FLASH-12^{TM} Model 1) at a rate of 25 kHz and stored in a personal computer for subsequent data analysis.

Unless specified, discharge experiments were conducted by discharging vertically downward at room temperature with rupture disks having a nominal burst pressure of 4.12 MPa. This condition will be referred to as the standard discharge in the discussion. The agents studied were the eleven potential replacement agents: HFC-236fa, FC-31-10, FC-318, HCFC-124, HFC-227ea, HFC-134a, FC-218, HCFC-22, HFC-125, HFC-125 (40% by mass)/HFC-32 (60%) mixture, and FC-116. Halon 1301 was also included in the study as a reference agent.

The effect of the size of the opening on the discharge process was assessed by mounting various diameter orifice plates at the base of the discharge vessel to restrict the opening of the rupture disk at the exit of the disk holder. The orifice diameters used in this study were 19.1, 12.7 and 6.4 mm. The plates were 5.08 mm thick.

In order to simulate discharge through a pipe for engine nacelle fire protection applications, experiments were performed using an extension tube 0.5 m long with an internal diameter equal to that of the 19.1 mm rupture disk. The tube was attached to the vessel exit, and the effect of orientation on the discharge dynamics with an extension tube was also studied.

The effect of the initial charge pressure on the discharge was simulated and studied by performing a series of experiments at room temperature using rupture disks with different burst pressures. Rupture disks with nominal burst pressures of 2.76, 4.12, and 5.50 MPa were selected.

A few experiments were also conducted to evaluate the effect of temperature on the discharge characteristics. The temperature effect was evaluated only at -45 °C by using burst disks with nominal burst pressures of 2.76 MPa. Based on the measurements of thermodynamic properties of agent/nitrogen mixture (see Section 2), this burst pressure was chosen in order to simulate the residual pressure in an actual vessel as a result of exposing the vessel to a -45 °C environment. Two agents

(FC-31-10 and FC-218) were evaluated at this temperature. Cooling was achieved by immersing the vessel in dry ice. Due to its large thermal inertia, the stainless steel vessel and its contents could only be chilled to an equilibrium temperature of −45 °C. No experiments were conducted at 150 °C as originally planned because the final pressure exceeded the operating pressure of the vessel even when the vessel was 1/3 fill (see Section 2). However, some general comments will be made in Section 3.4.3.5 with regard to the discharge characteristics at elevated temperatures.

The study on effects of orientation on the discharge dynamics was carried out by discharging the vessel vertically downward and upward or horizontally. Since the horizontal and vertical upward-discharge processes were found experimentally to be slower than the downward discharge, the high-speed movie camera was operated at 500 or 1000 frames per second in these experiments.

Only three agents were used for studying the effect of various parameters on the discharge process. Two representative alternative agents (FC-31-10 and FC-218) and halon 1301 at room temperature. These two alternative agents were chosen among others because they represented the range of boiling points encompassed by most of the eleven proposed fluids. Halon 1301 was included as the baseline agent.

3.4.3 Results and Discussion

3.4.3.1 Standard Discharge. Visual observations of the events occurring inside the vessel during downward discharge are described as follows. Liquid agent is propelled out of the vessel when the rupture disk breaks. In some of the experiments, the inflow of nitrogen disturbs the liquid/vapor interface causing a wavy motion along the liquid surface in a manner similar to that described in Section 3.2. Apparently these disturbances did not affect the agent release behavior. At the end of the liquid discharge the vessel interior becomes foggy, possibly due to the condensation of vapor caused by a decrease in temperature in the ullage due to the adiabatic expansion of the vapor phase. As the discharge of the remaining vapor continues, the vessel becomes clear once again.

Figure 27 shows a photographic sequence of events during a downward discharge of FC-218 from a plastic vessel. The photographs were taken at 2000 frames per second. The frame which corresponds to the time t = 0.5 ms is the first frame where agent is observed outside the vessel. Due to the framing rate, there is a 0.5 ms uncertainty in the times. The dark grey horizontal shadow in the middle of the background was caused by the backlighting set-up. The first photograph shows the plastic vessel, which is located in the middle, the vessel mount, and the liquid level. In this sequence of photographs, the perturbation of the vapor/liquid interface caused by the inflow of nitrogen is evident from the wavy nature of the interface. The photographs also show the behavior (to be discussed in Section 3.5) of the agent outside the vessel during discharge.

Figure 28 through Figure 39 show results for the temporal variation of the internal pressure during downward discharges of all the agents evaluated in this study. Pressures reported in the figures are gauge pressures. The pressure is nondimensionalized by the actual burst pressure, P_i, which is taken to be the pressure at t (time) = 0 s. The time t = 0 s is defined as the time when the first laser (located at the immediate exit of the vessel) signal is attenuated (see Section 3.5) by the agent coming out from the vessel. For most agents (except FC-116, HFC-125/HFC-32 mixture, and halon 1301), there are two distinct regions, separated by an inflection point, in the pressure-time history. The first region corresponds to the time interval during which the liquid agent is being propelled from the vessel; the second region corresponds to the period when the remaining vapor (mostly nitrogen) is being vented from the vessel. Based on observations from the plastic vessel experiments, the inflection point corresponds very closely to the time at which the liquid agent has just been completely expelled from the vessel. Since the pressure-time histories obtained from the pressure transducer mounted on the stainless steel vessel wall in order to monitor the temporal change

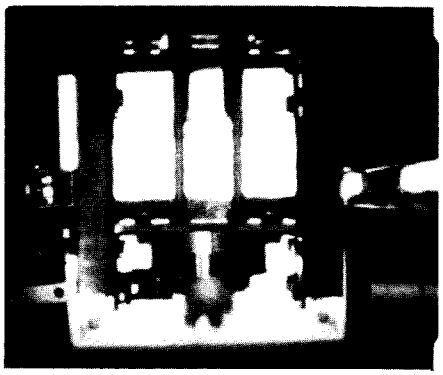

0.5 ms

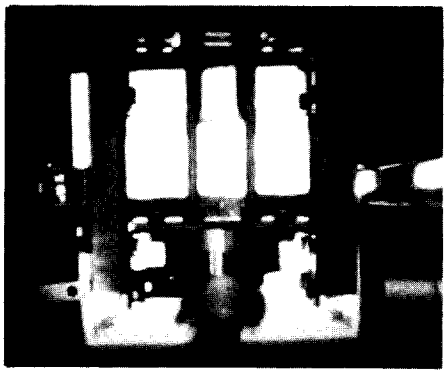

1.0 ms

1.5 ms

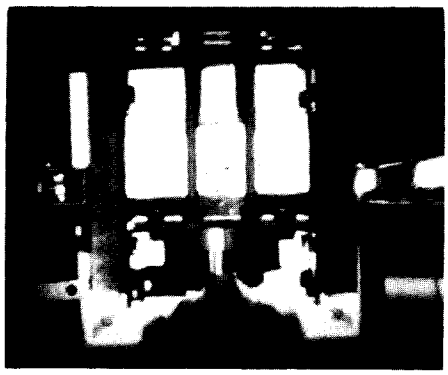

2.0 ms

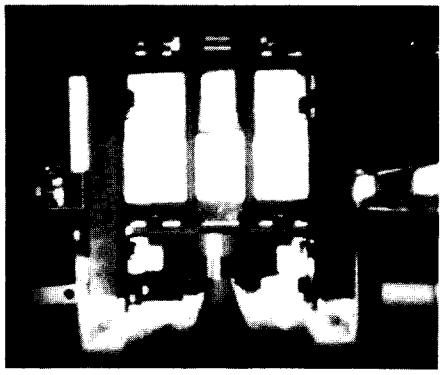

2.5 ms

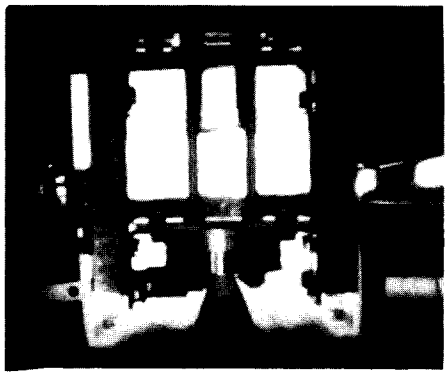

3.0 ms

Figure 27. Photographic sequence of events showing a downward discharge of FC-218 from a plastic vessel.

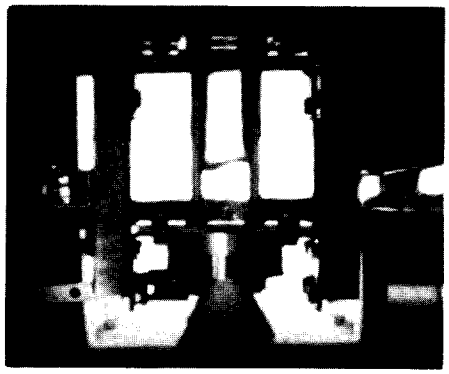

10.0 ms

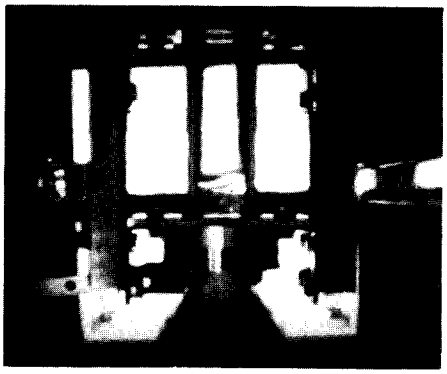

15.0 ms

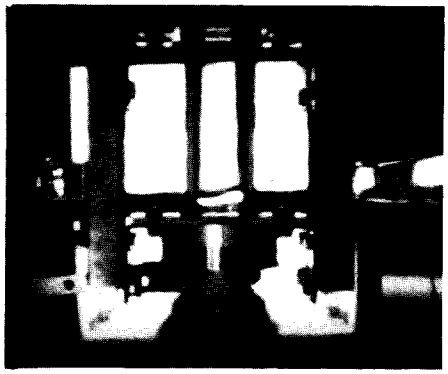

20.0 ms

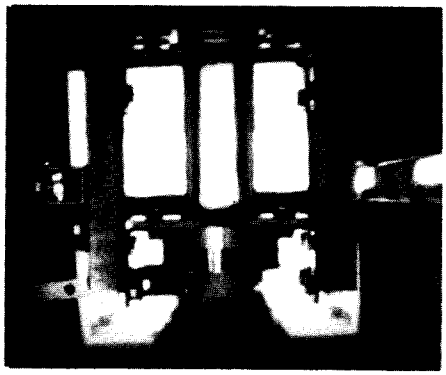

25.0 ms

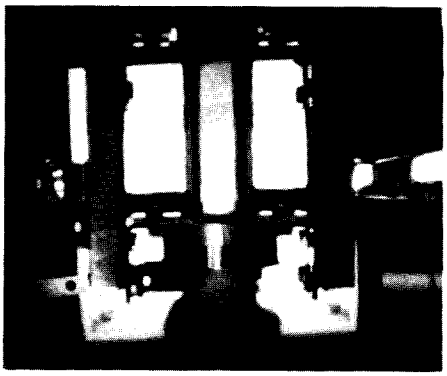

30.0 ms

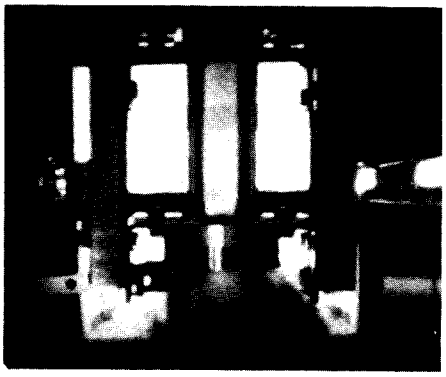

32.5 ms

Figure 27. (continued) Photographic sequence of events showing a downward discharge of FC-218 from a plastic vessel.

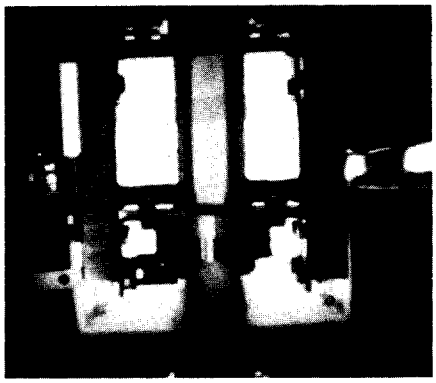

35.0 ms

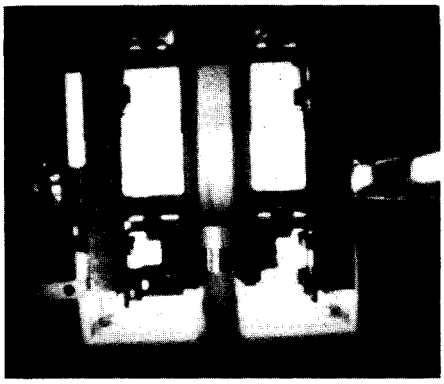

40.0 ms

50.0 ms

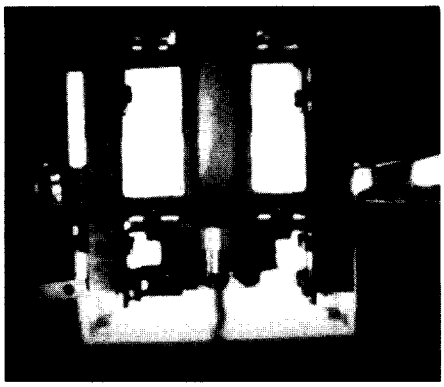

75.0 ms

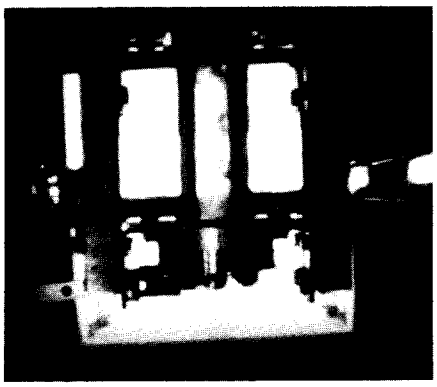

100.0 ms

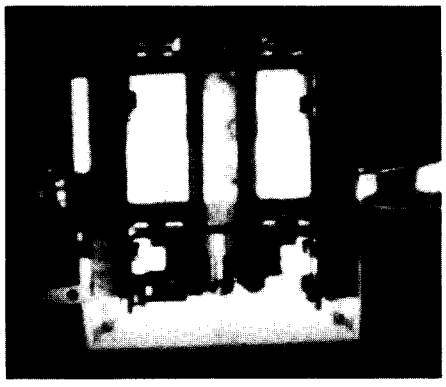

125.0 ms

Figure 27. (continued) Photographic sequence of events showing a downward discharge of FC-218 from a plastic vessel.

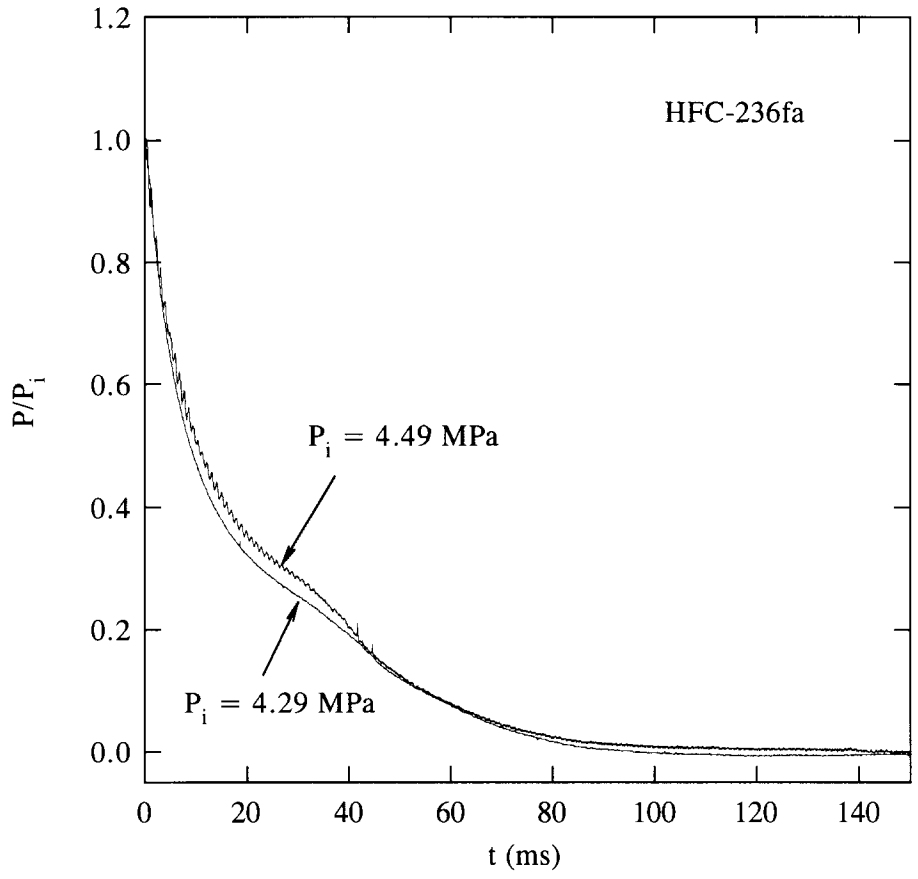

Figure 28. Temporal variations of internal pressure during downward discharges of HFC-236fa.

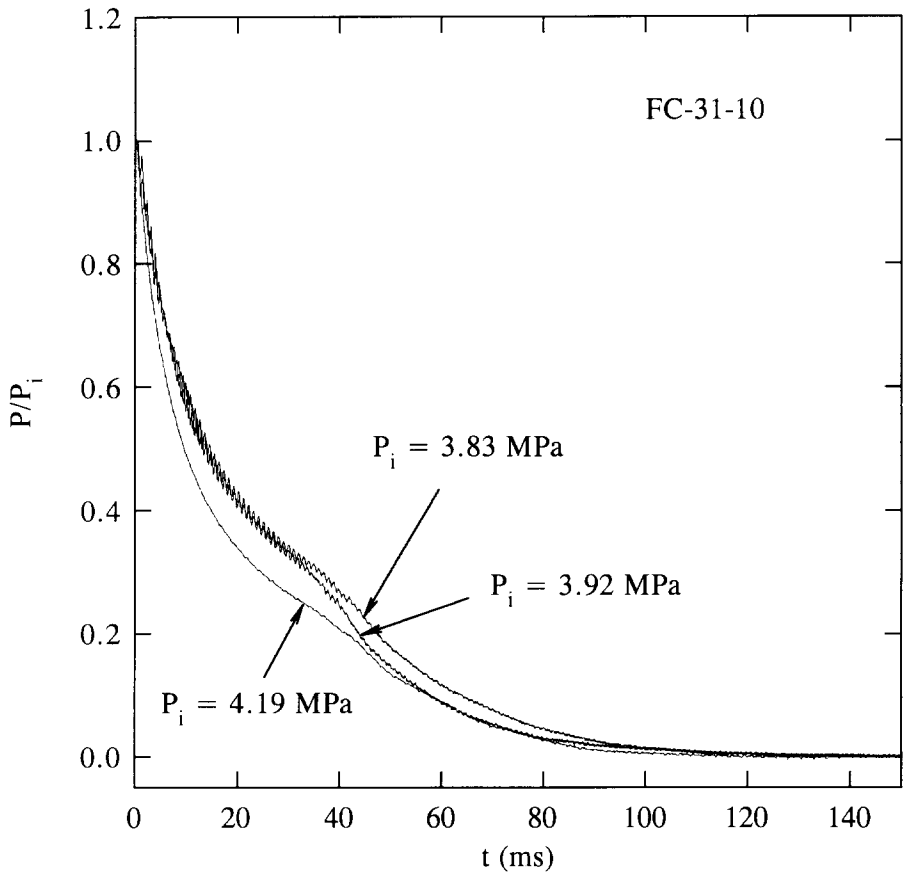

Figure 29. Temporal variations of internal pressure during downward discharges of FC-31-10.

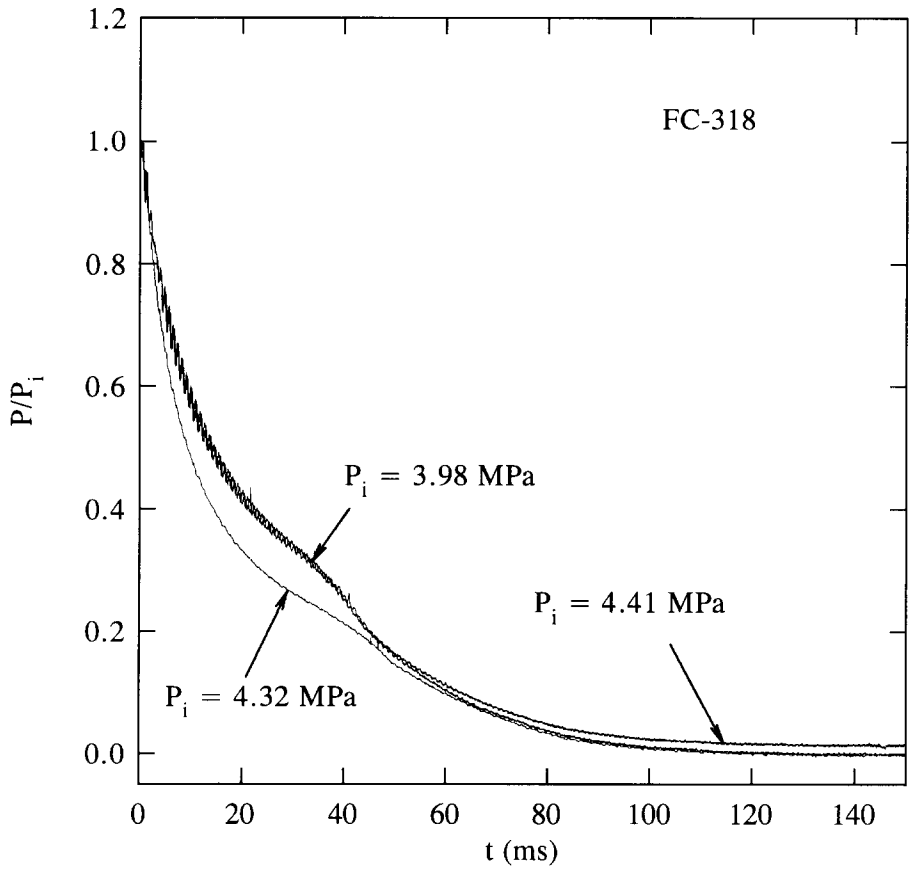

Figure 30. Temporal variations of internal pressure during downward discharges of FC-318.

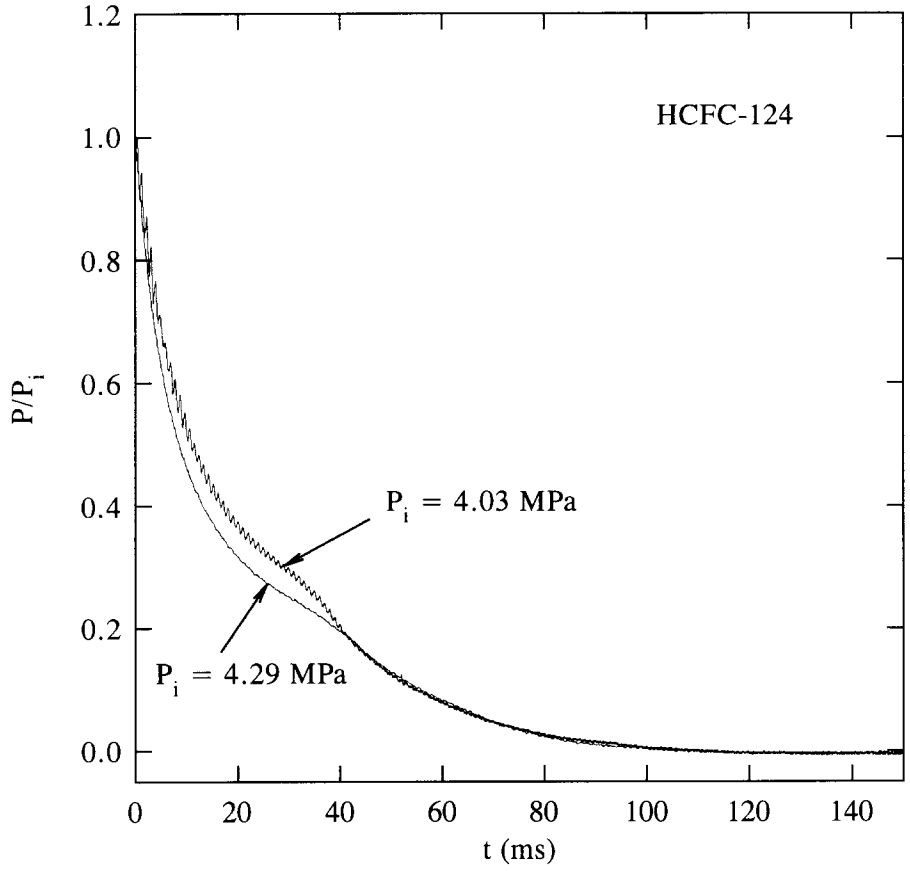

Figure 31. Temporal variations of internal pressure during downward discharges of HCFC-124.

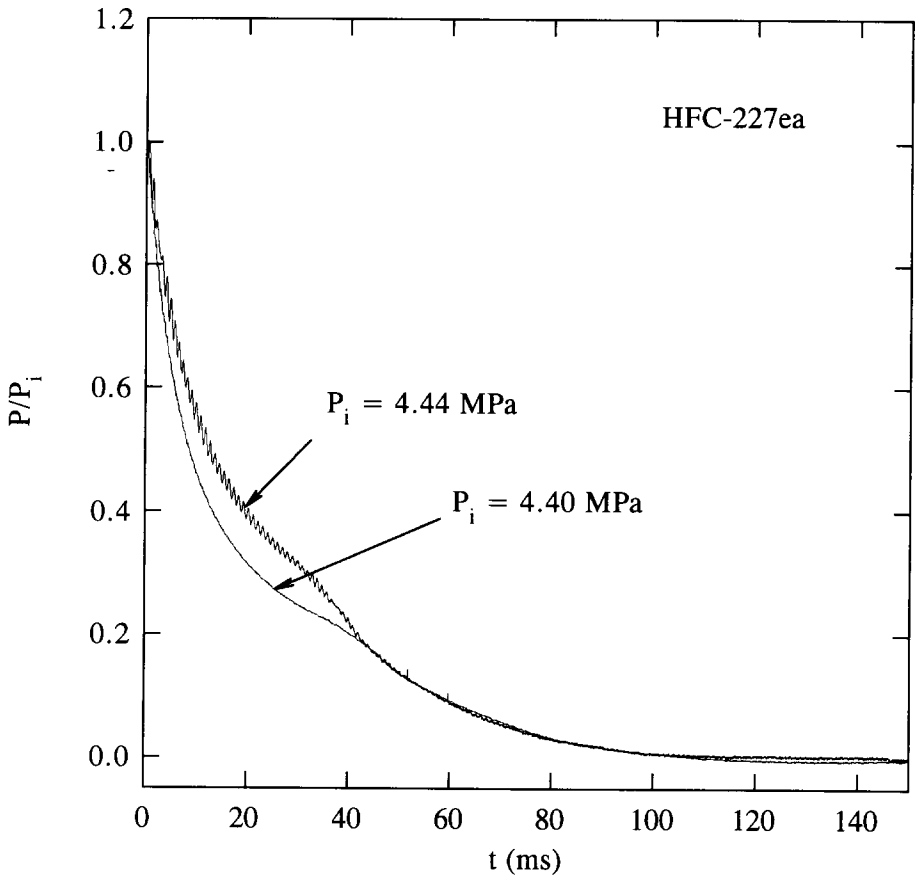

Figure 32. Temporal variations of internal pressure during downward discharges of HFC-227ea.

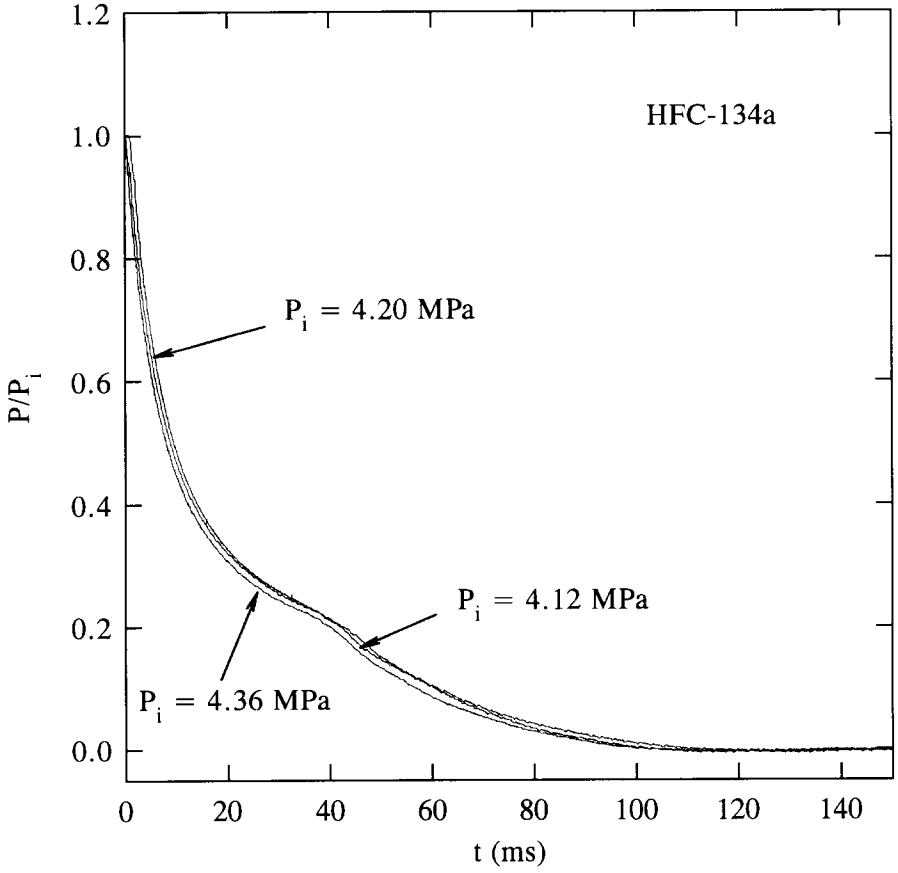

Figure 33. Temporal variations of internal pressure during downward discharges of HFC-134a.

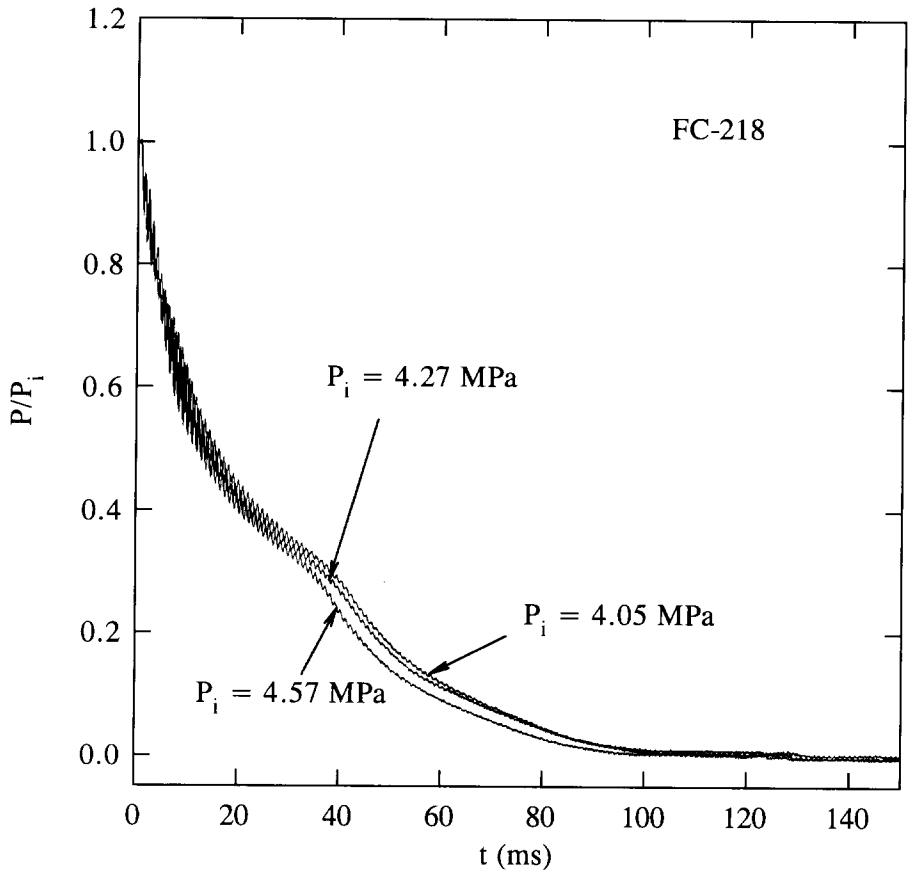

Figure 34. Temporal variations of internal pressure during downward discharges of FC-218.

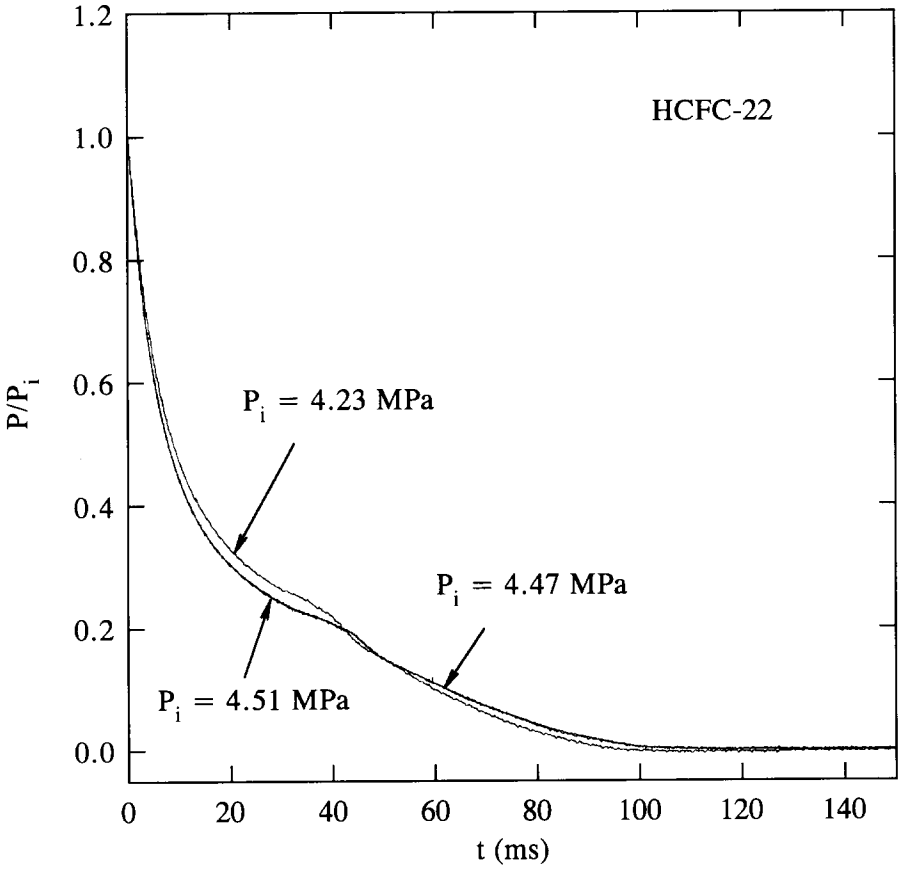

Figure 35. Temporal variations of internal pressure during downward discharges of HCFC-22.

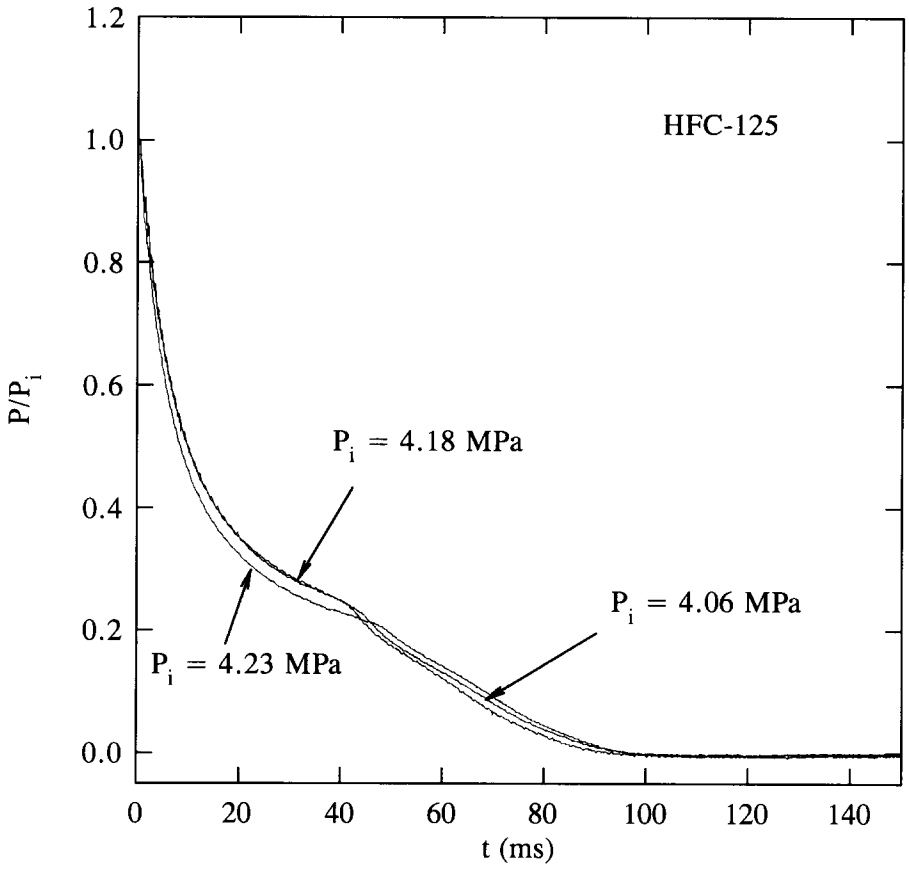

Figure 36. Temporal variations of internal pressure during downward discharges of HFC-125.

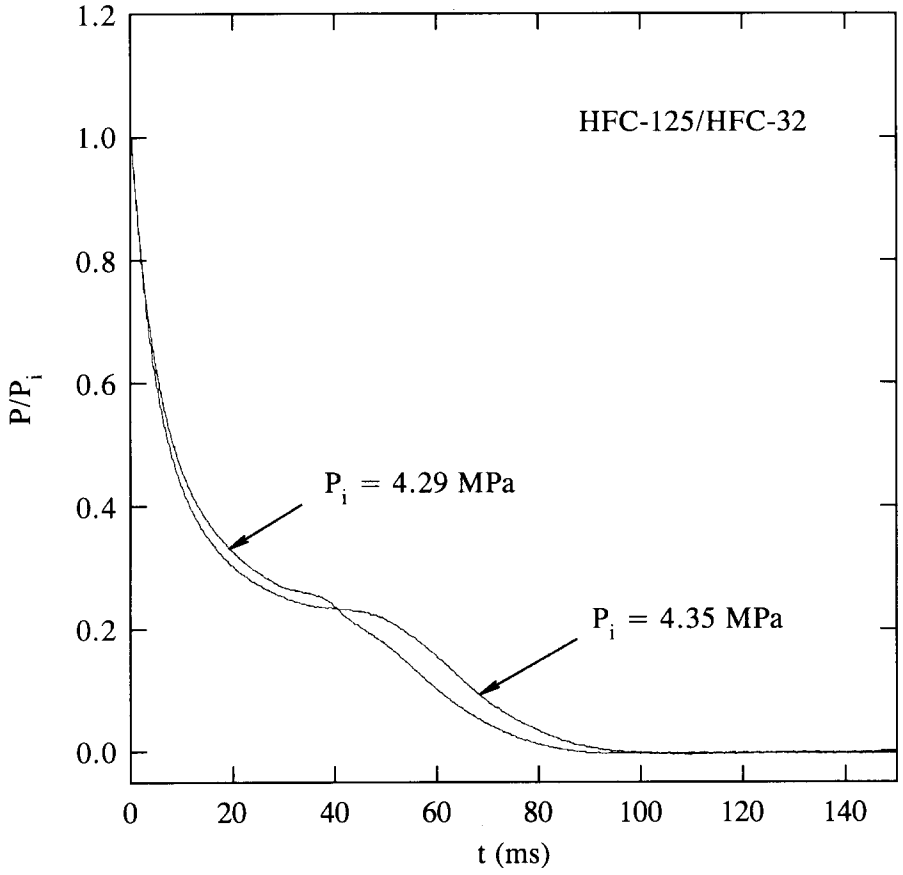

Figure 37. Temporal variations of internal pressure during downward discharges of the HFC-125/HFC-32 mixture.

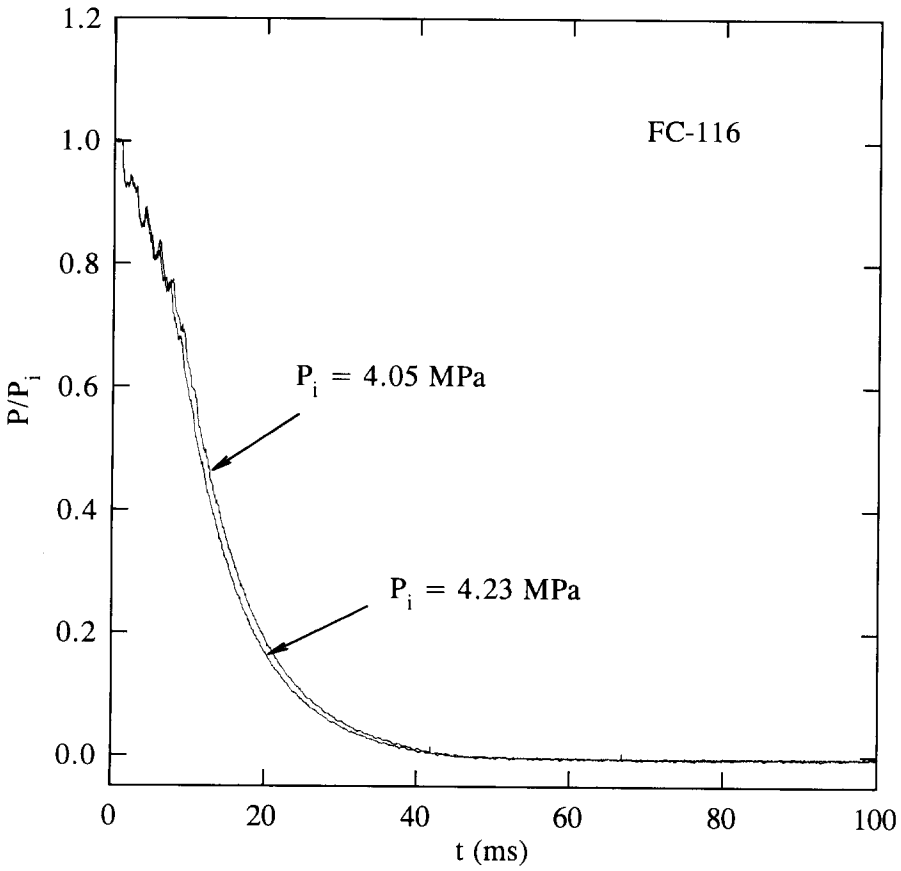

Figure 38. Temporal variations of internal pressure during downward discharges of FC-116.

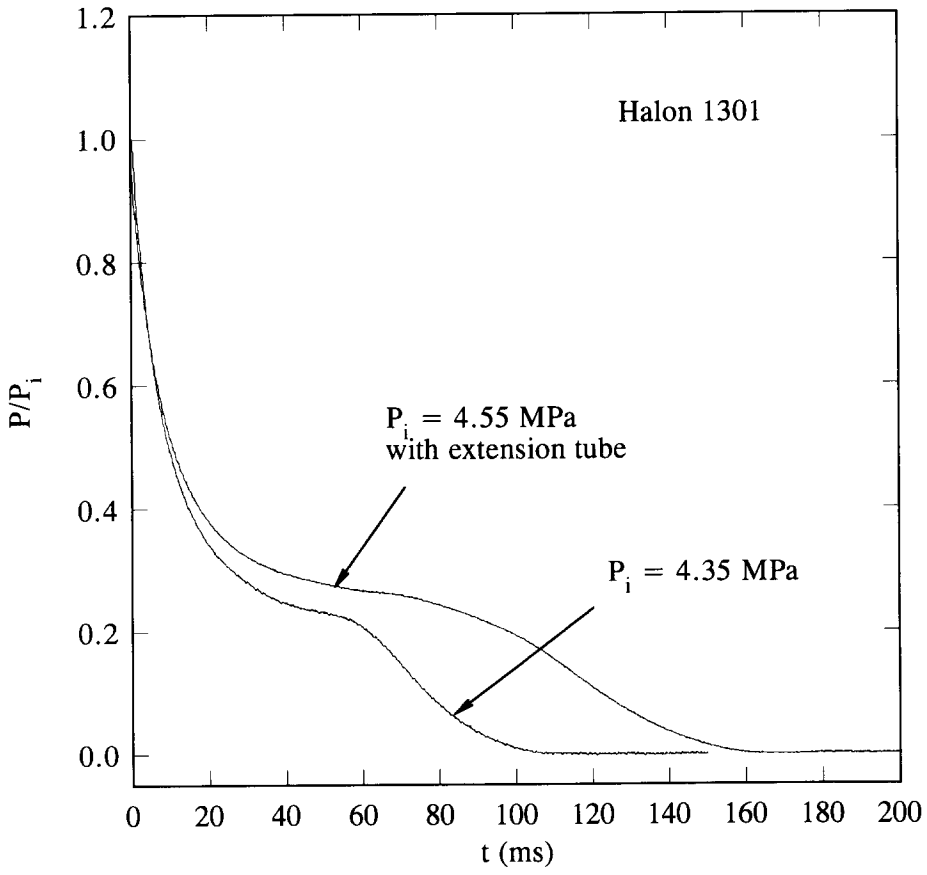

Figure 39. Temporal variations of internal pressure during downward discharges of halon 1301.

of the pressure in the liquid phase followed those obtained from the pressure transducer used to measure pressure change in the vapor phase, only the pressure-time histories from the vapor phase measurements are presented and discussed.

The pressure-time histories obtained using plastic vessels have an oscillatory nature and more noise. Such time traces are easily identified in the figures. This behavior is believed to have been caused by vibration of the vessel mount during discharge. The observed oscillatory frequency of the pressure traces corresponded closely to the natural frequency of the vessel mount, which was estimated by simulating the four threaded rods (see Figure 26) as four springs and the vessel as a mass attached to the springs. Since a different mount was used for the stainless steel vessel, no such oscillatory characteristic in the pressure-time histories was observed. The variations in the pressure-time histories from run to run reflect the nature of the rupture disk, that is, the actual burst pressure of each rupture disk used in the experiments deviated somewhat from its nominal burst pressure. Therefore, different P_i's are anticipated depending on the pressure at which the disk bursts. Differences in the pressure histories obtained from the stainless steel vessel and from plastic vessels are due to the differences in the internal volumes of the vessels.

The visual observation of the internal behavior of liquid agent during discharge from plastic vessels shows that during the time when the liquid level is visible (refer to Figure 26) no internal boiling of the liquid occurs during depressurization. This observation can be explained by examining the temporal variation of the internal pressure. From Figure 28 through Figure 36, for the nine agents with boiling points above -45 °C, the pressures at the time when the liquid empties (at the inflection point in the pressure-time history) is still well above the saturation vapor pressure for all of these agents at room temperature. Although the temperature of the ullage above the liquid is very low because of the expansion of the vapor phase, the characteristic time, t_c, for the interfacial heat transfer between the liquid and the vapor phases is much longer than the discharge time of the liquid, typically O(10 ms). The characteristic time for heat transfer can be estimated (Bird *et al.*, 1960) using

$$t_c \sim \frac{\delta^2}{\alpha}, \tag{17}$$

where α is the thermal diffusivity, typically $O(10^{-7}$ m^2/s) and δ is the thermal penetration distance in the liquid, in our case typically $O(10^{-2}$ m). Hence, t_c is on the order of tens of seconds. Therefore, the liquid agent remains at the initial room temperature and can be considered to undergo an isothermal depressurization during discharge. As shown in Figure 40, this argument is supported by the temperature-time histories in the liquid during discharge of HCFC-22. Figure 40 was obtained using a 25 μm fine wire thermocouple. Data were taken at a rate of 10 kHz.

For FC-116 (see Figure 38), the pressure-time histories show a relatively smooth decay of the internal pressure. Since FC-116 is a gas at room temperature, this behavior is typical of a gas vented from a pressurized vessel. The two regions in the temporal variation of the internal pressure observed for the liquid agents do not exist.

For HCFC-22, HFC-125, HFC-125/HFC-32 mixture, and halon 1301, only the pressure-time histories from the stainless vessel were recorded. Since some of these agents etch plastic and all have relatively high vapor pressures at room temperature, the plastic vessel was not used for fear of rupture of the vessel during its filling and handling.

The experimental results for HFC-125/HFC-32 mixture and halon 1301 deserve further discussion. The pressure-time histories in Figure 37 and Figure 39 show that the transition from the liquid discharge to the venting of the remaining vapor from the vessel is not distinct and abrupt. The transition appears to be gradual. Since no visual observations were made for these agents, the events

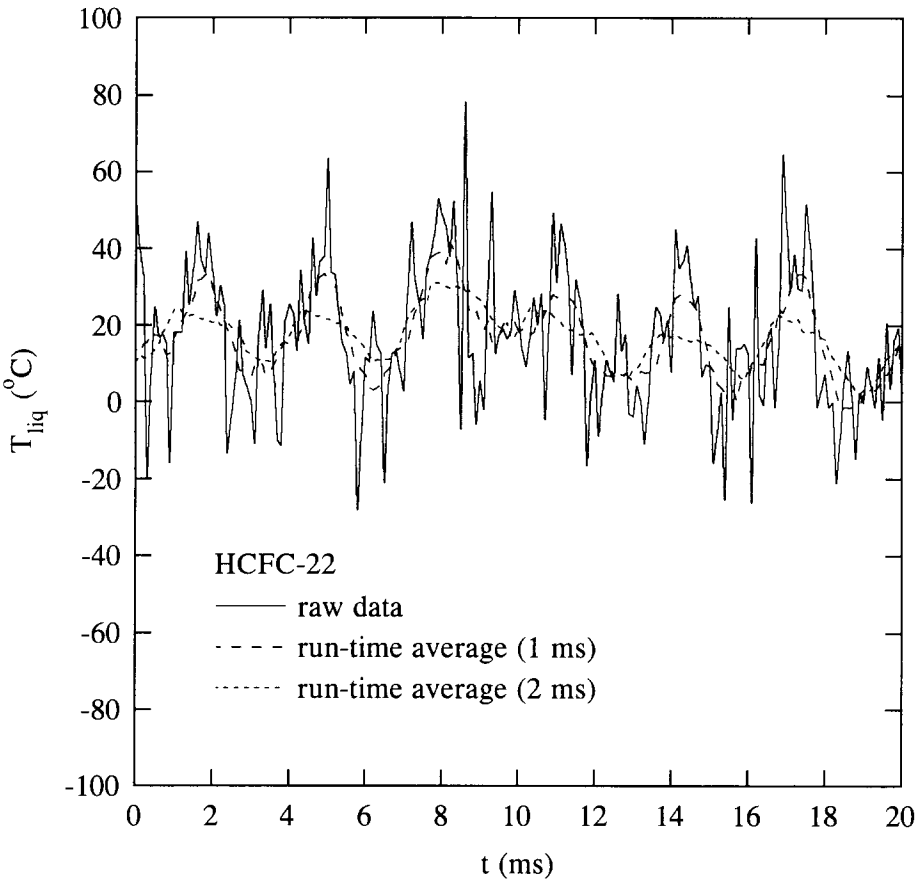

Figure 40. Temporal variation of temperature in the liquid phase during discharge of HCFC-22.

occurring inside the vessel could only be inferred from the experimental pressure-time traces. It can be seen that at some point during the release the internal pressure dropped below the saturation vapor pressure of the agent at room temperature (refer to Section 2). Therefore, it is conjectured that boiling of the liquid occurred near the end of the liquid discharge, thus causing a gradual transition until the remaining liquid had been discharged.

Based on visual observations of the discharges, a simple mathematical model can be formulated to simulate the pressure-time history. As mentioned above, there are two distinct regions, separated by an inflection point, in the pressure-time traces. The first region corresponds to the liquid discharge while the second region corresponds to the discharge of the remaining vapor after the liquid has been released from the vessel. The formulation of the model for liquid discharge will first be presented, followed by a discussion on the simulation of the discharge process of the remaining vapor.

Once the rupture disk bursts, the nitrogen above the liquid agent simply acts as a piston to drive the liquid out of the vessel. The control volume that is being considered is the ullage above the liquid. Since the discharge process is very rapid, the process occurring in the gas phase can be assumed to be adiabatic and reversible, *i.e.*, isentropic. Furthermore, for simplicity the control volume is assumed to be closed in the analysis because the inflow of nitrogen does not influence the discharge process (see Sections 3.2 and 3.3.3). Assuming the vapor phase to be ideal, from the first law of thermodynamics for an isentropic process,

$$PV^{\gamma} = constant \ , \tag{18}$$

where γ is the ratio of the constant pressure and volume heat capacities, P is the pressure, and V is the control volume. Since nitrogen is the dominant species in the vapor phase, the γ of nitrogen with a value of 1.4 is assumed. If a time derivative of Equation (18) is taken, then

$$\frac{dP}{dt} + \frac{P\gamma}{V}\frac{dV}{dt} = 0 \ . \tag{19}$$

Because of the design of the rupture disk holder, there is a short distance, L (25.4 mm), having a diameter of 19.1 mm through which the fluid has to pass before exiting from the release vessel assembly. Because of rapid depressurization, the liquid becomes superheated as it passes through the opening of the disk (Modell and Reid, 1983; Reid, 1976). Superheating of the liquid has been observed in previous studies on the discharge of saturated and subcooled liquid from orifices and nozzles (Benjamin and Miller, 1941; Burnell, 1947; Pasqua, 1953; Hesson and Peck, 1958; Henry, 1970; Prisco *et al.*, 1977; Celata *et al.*, 1983; Van den Akker *et al.*, 1983). If we assume the flow of metastable liquid through the disk opening (D) and the disk holder can be approximated by flow through a short tube ($0 < L/D < 3$) , then the volumetric flow rate of the liquid, expressed in terms of the volumetric expansion rate of the gas above the liquid agent, can be calculated by (Prisco *et al.*, 1977; Tong, 1965)

$$\frac{dV}{dt} = C_d A \sqrt{\frac{2(P - P_{sat})}{\rho_l}} \ , \tag{20}$$

where A is the cross sectional area of the disk opening, ρ_l is the liquid density, P_{sat} is the saturation vapor pressure of agent, and C_d is the discharge coefficient for the liquid, with measured values found

to be between 0.61 to 0.64 in the literature (Prisco *et al.*, 1977; Tong, 1965). Equations (19) and (20) were solved numerically using a fourth order Runge-Kutta method (Carnahan *et al.*, 1969) to obtain the pressure-time histories and the liquid level as a function of time.

Figure 41 through Figure 46 show the temporal variations of liquid level for agents obtained from experiments using plastic vessels. Also shown in the figures are predictions obtained using Equations (19) and (20). The liquid levels were measured from the upper edge of the lower aluminum plate (see Figure 26), and a zero liquid level does not correspond to complete depletion of liquid. The best curve fits were obtained by optimizing the values of C_d, which varied between 0.67 to 0.80. These C_d values are slightly higher than previous experimental values reported in the literature.

After complete depletion of liquid, the discharge process of the remaining vapor can be modeled as follows. If the vapor is assumed to be an ideal gas, the process is again assumed to be isentropic, and the pressure in the vessel is high enough that the flow can be assumed to be choked in the disk opening (which is approximated as a round, sharp-edged orifice), it can be easily shown that the following equation describes the rate of pressure decay in a vessel as a function of time (Kim-E, 1981).

$$\frac{P}{P_{el}} = \left(1 - \frac{C_a A}{V} \left(\frac{R T_{el} \gamma^3 K}{M} \right)^{1/2} \left(\frac{1 - \gamma}{2\gamma} \right) t \right)^{\frac{2\gamma}{1-\gamma}}, \tag{21}$$

with

$$K = \left(\frac{2}{\gamma + 1} \right)^{\left(\frac{\gamma + 1}{\gamma - 1} \right)}, \tag{22}$$

where P_{el} and T_{el} are the pressure and temperature in the vessel at the instant of complete depletion of liquid agent, respectively, C_a is the discharge coefficient for the gas, R is the universal gas constant, and M is the molecular weight of the vapor (assumed to be nitrogen). A choked flow is justifiable because P_e/P, where P_e is the exit pressure (0.101 MPa), is less than the critical pressure ratio most of the time during discharge of the remaining vapor. For an ideal gas undergoing an isentropic process, the critical pressure ratio is given by (Balzhiser *et al.*, 1972)

$$\left(\frac{P_e}{P} \right)_{critical} = \left(\frac{2}{\gamma + 1} \right)^{\frac{\gamma}{(\gamma - 1)}} \tag{23}$$

Optimum values of C_a were found to be between 0.26 and 0.31 (Kim-E, 1981) during depressurization of a vessel initially filled with nitrogen.

Figure 47 through Figure 52 compare the complete pressure-time histories with predictions from Equations (19), (20), (21), and (22). The best curve fits for the duration of vapor discharge were obtained by optimizing the values of C_a, which varied between 0.25 to 0.35. However, if instead of using the P_{el}'s from the liquid discharge calculations, one fits the experimental results of vapor discharge by optimizing both P_{el} and C_a, the values of C_a are found to be $\sim$ 0.6.

The average volumetric flow rates, defined as the initial volume of liquid in the vessel divided by the emptying time of the liquid, are summarized in Table 4. Knowing the framing rate of the high-

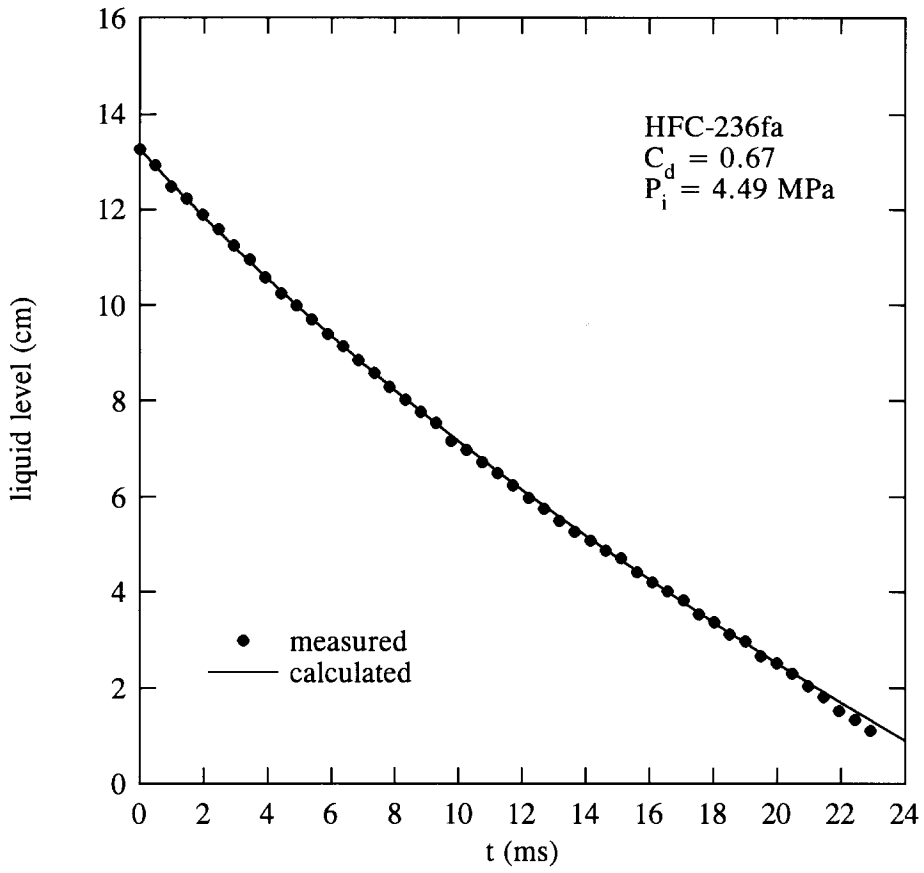

Figure 41. Temporal variation of liquid level obtained from a HFC-236fa discharge.

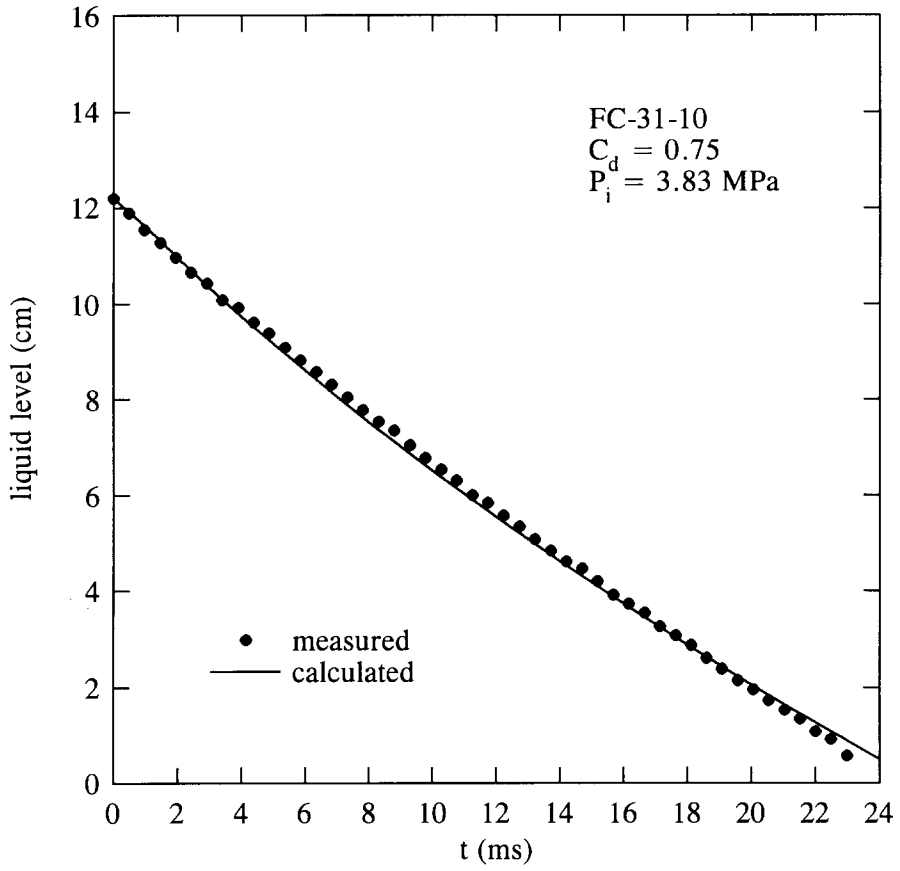

Figure 42. Temporal variation of liquid level obtained from a FC-31-10 discharge.

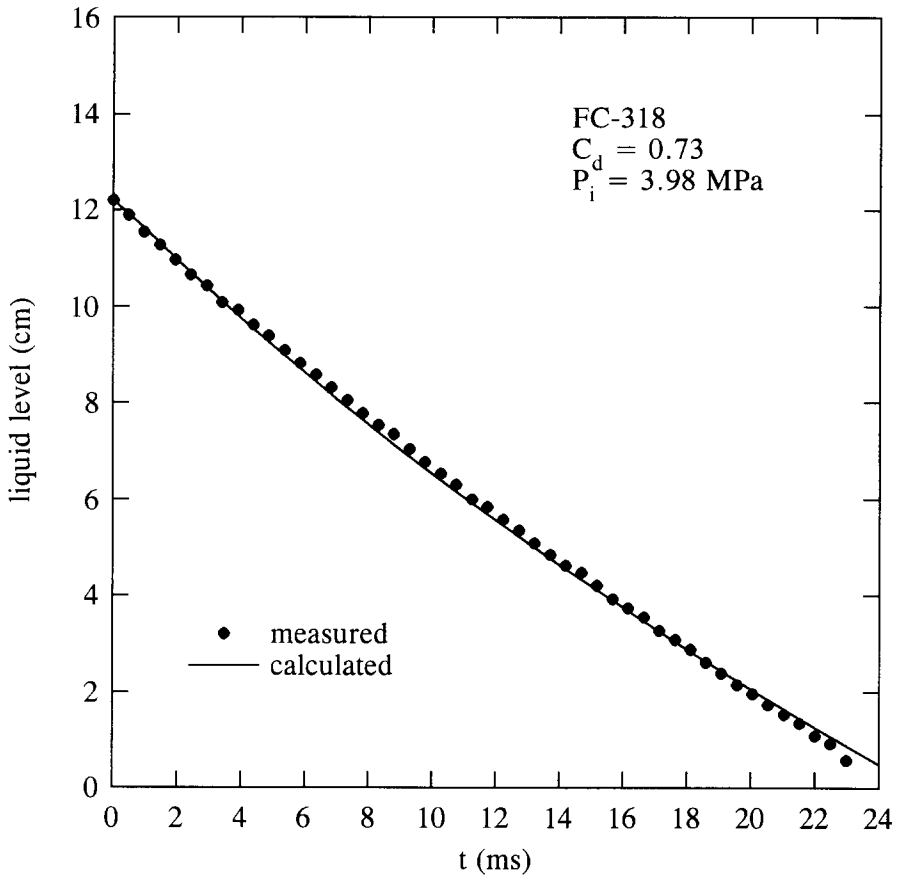

Figure 43. Temporal variation of liquid level obtained from a FC-318 discharge.

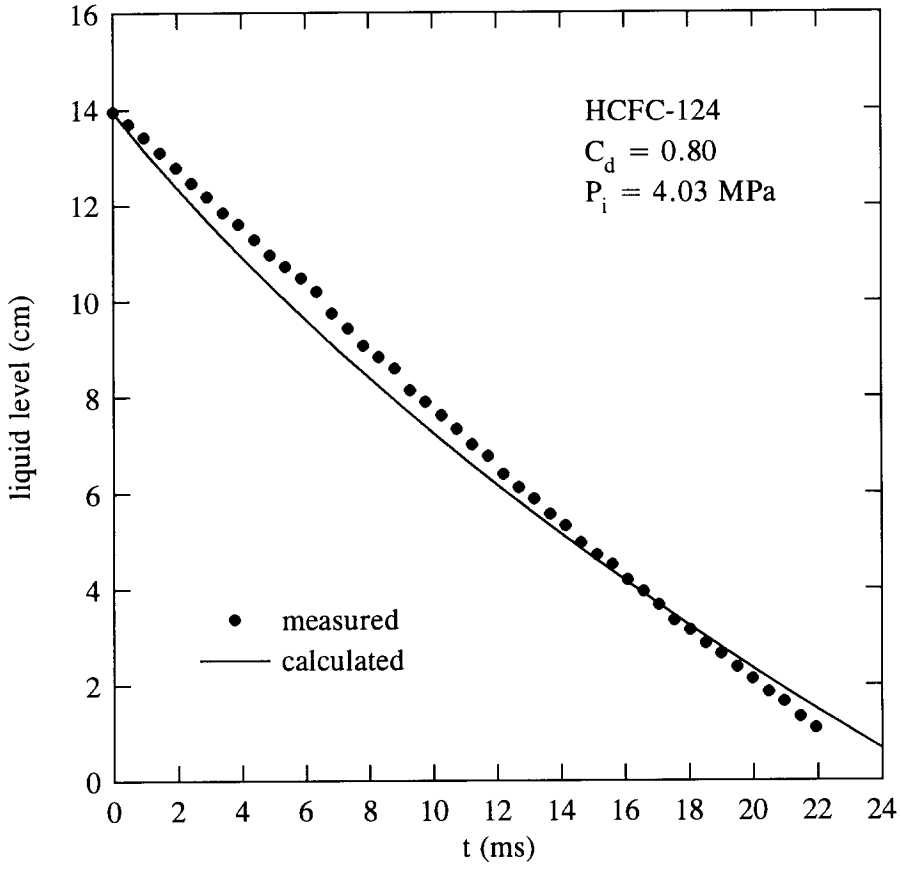

Figure 44. Temporal variation of liquid level obtained from a HCFC-124 discharge.

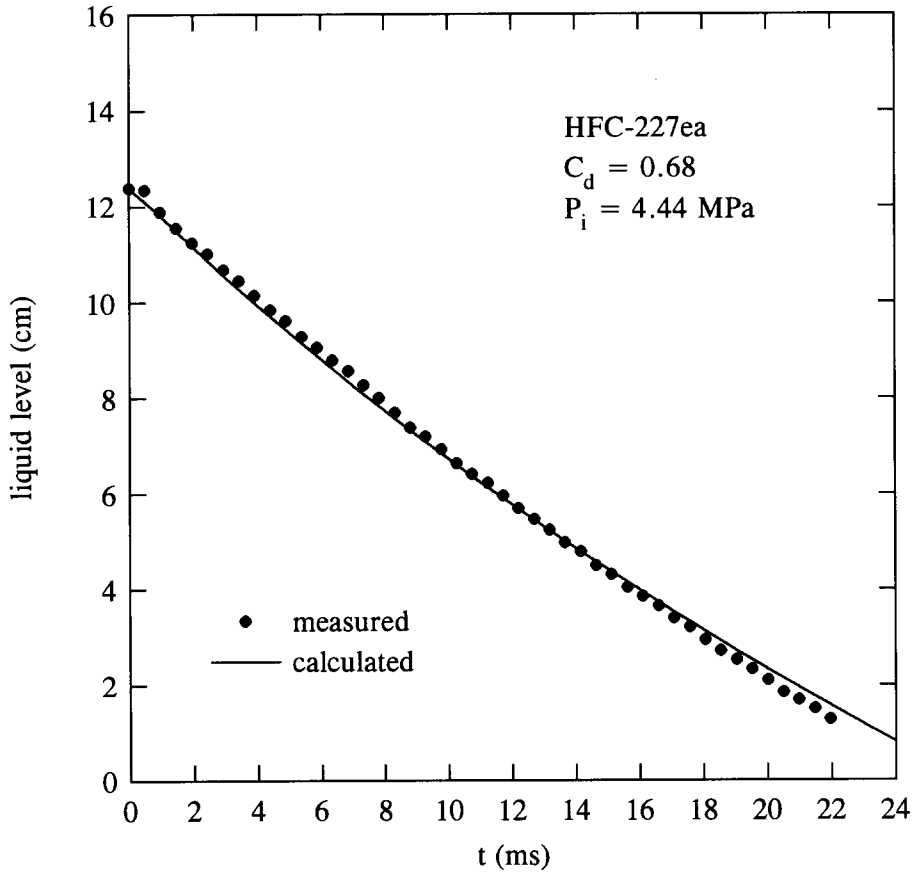

Figure 45. Temporal variation of liquid level obtained from a HFC-227ea discharge.

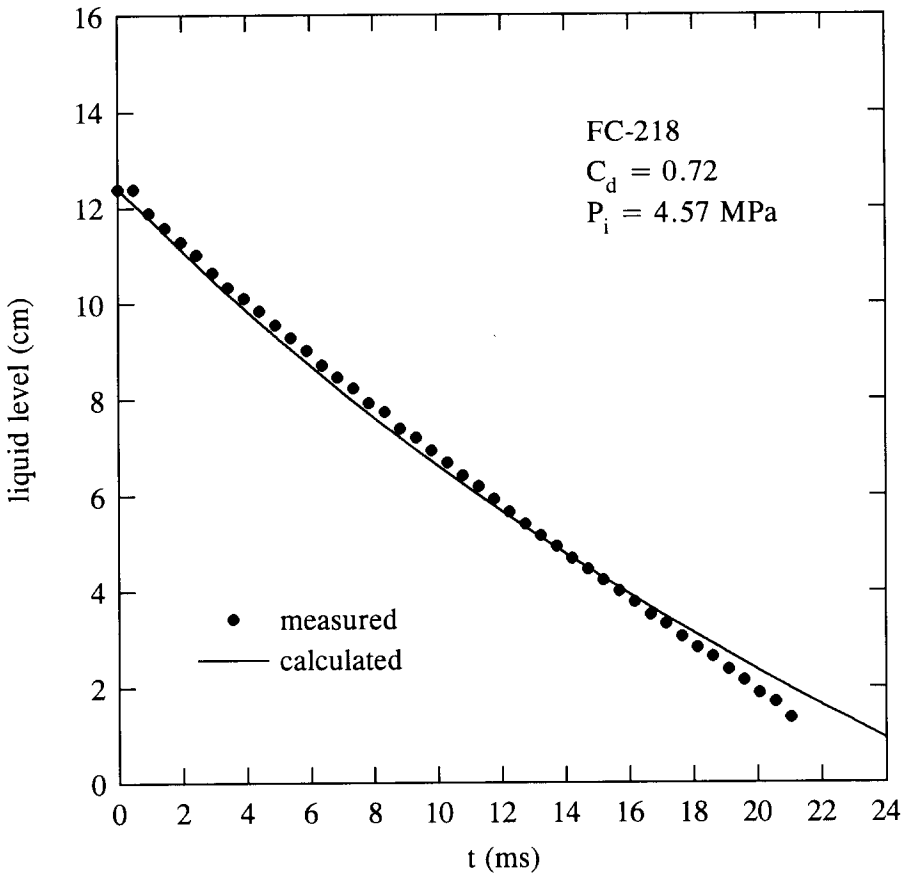

Figure 46. Temporal variation of liquid level obtained from a FC-218 discharge.

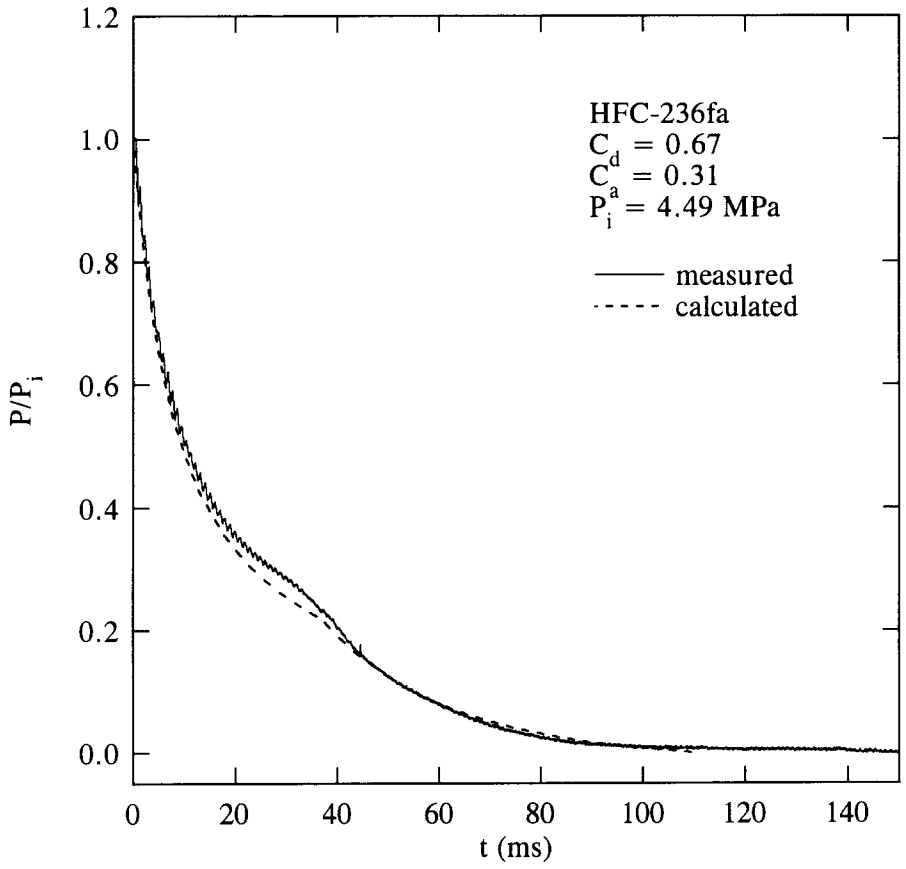

Figure 47. Comparison of measured pressure-time history of a HFC-236fa discharge with prediction.

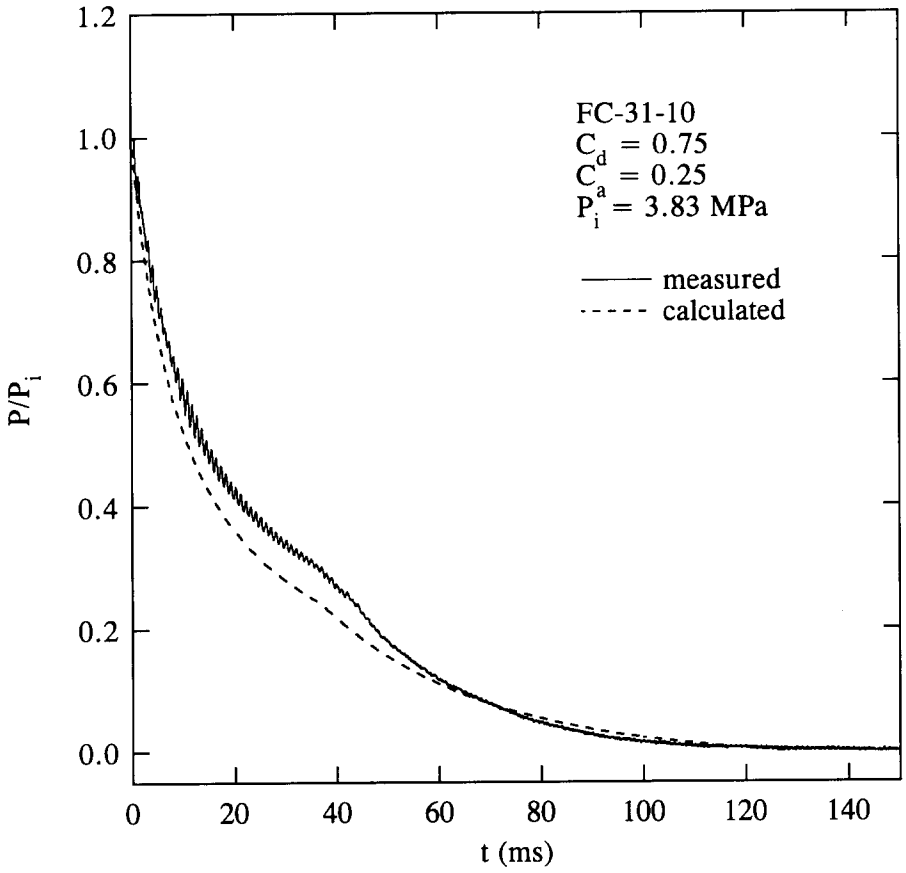

Figure 48. Comparison of measured pressure-time history of a FC-31-10 discharge with prediction.

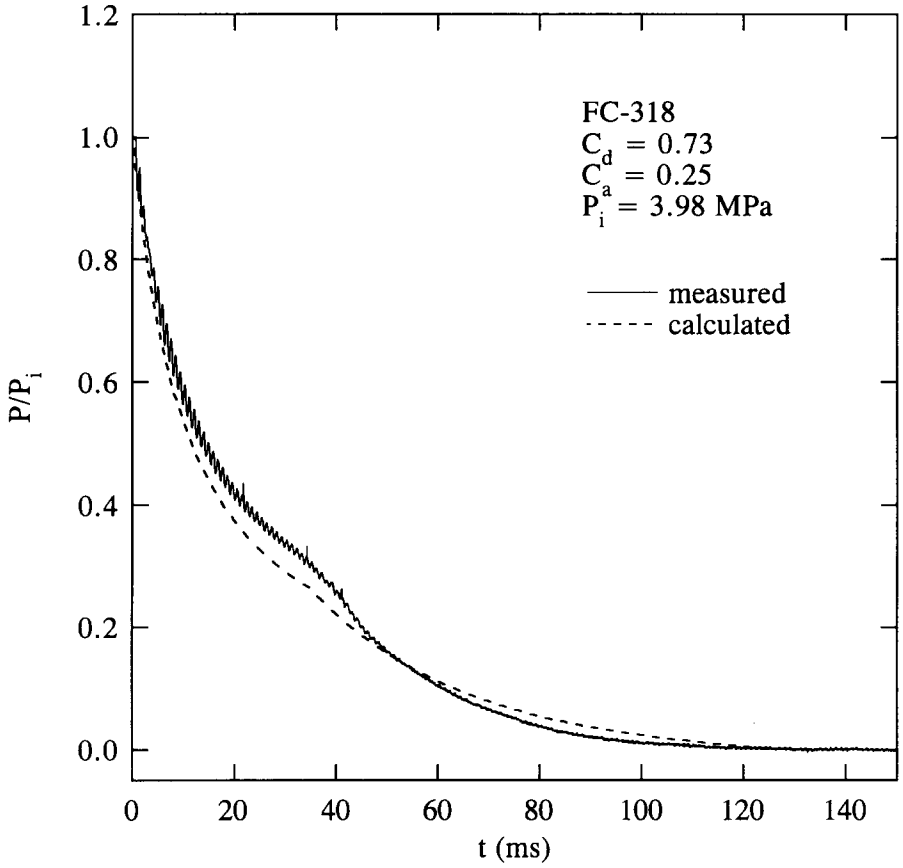

Figure 49. Comparison of measured pressure-time history of a FC-318 discharge with prediction.

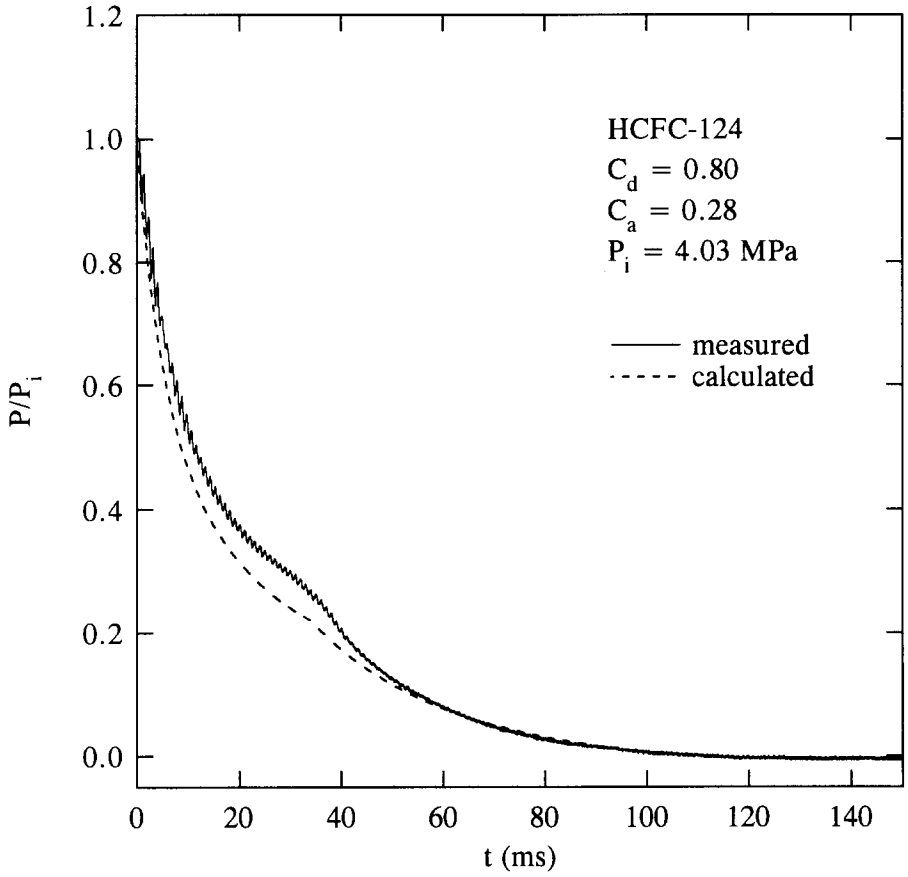

Figure 50. Comparison of measured pressure-time history of a HCFC-124 discharge with prediction.

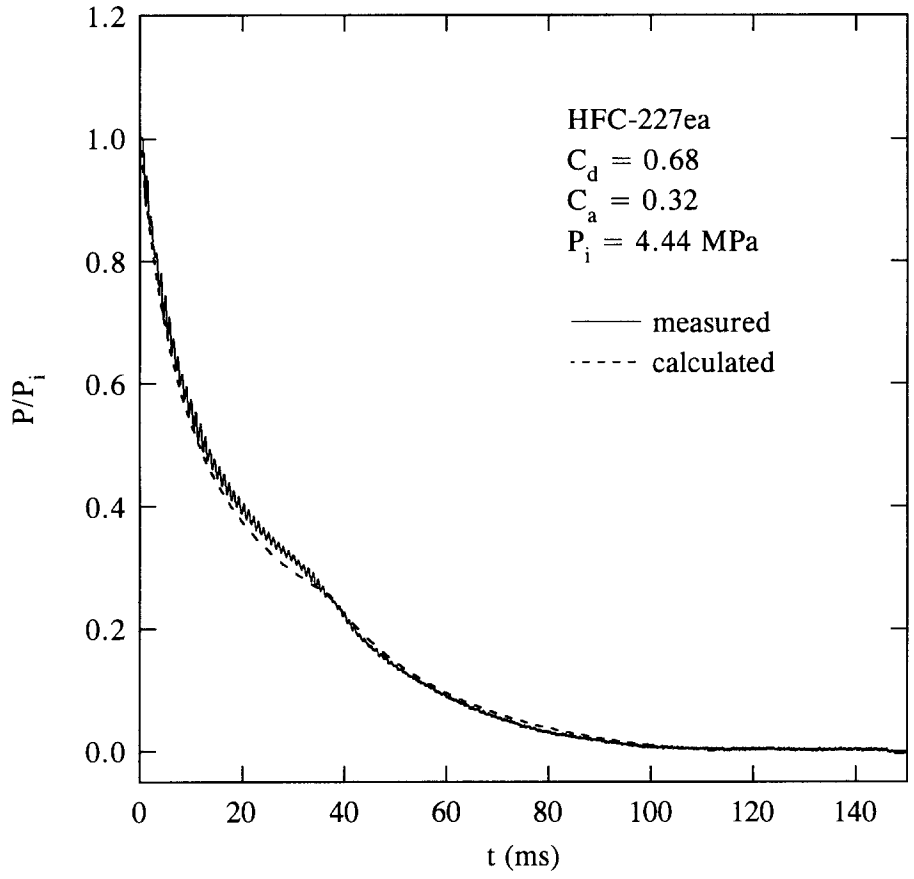

Figure 51. Comparison of measured pressure-time history of a HFC-227ea discharge with prediction.

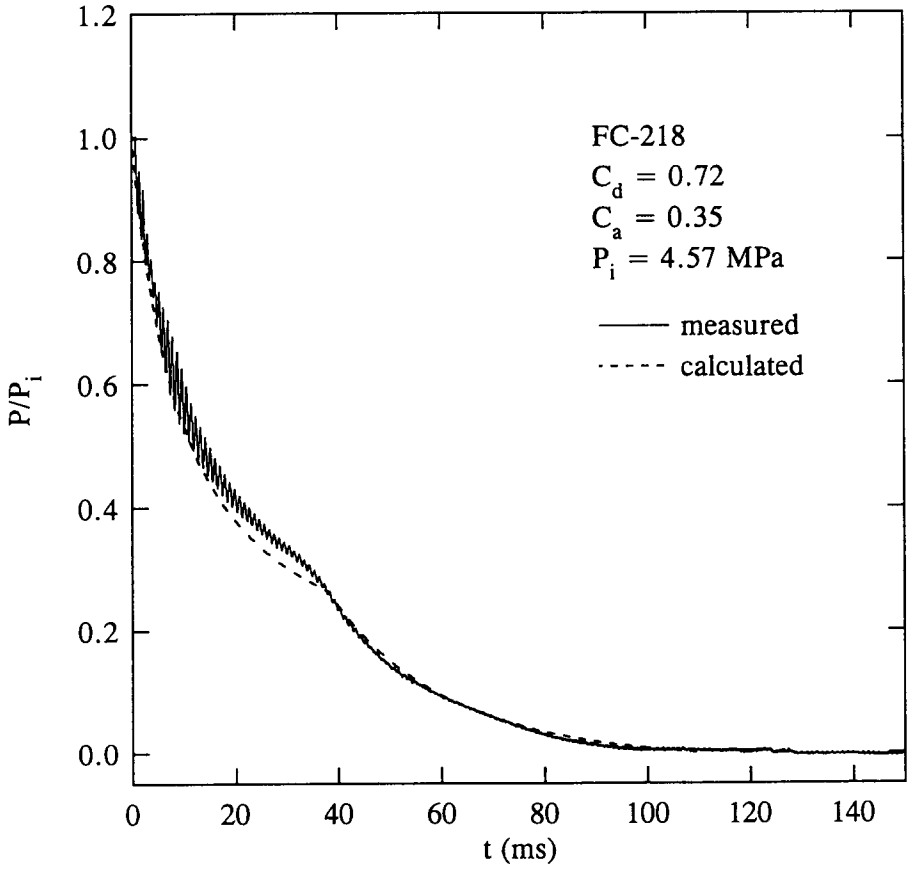

Figure 52. Comparison of measured pressure-time history of a FC-218 discharge with prediction.

Table 4. Initial burst pressures (P_i), initial agent masses (M_i), and average volumetric flow rates (Q) obtained from experiments using plastic and stainless steel vessel

Agent	P_i (MPa)	M_i (g)	Q (m^3/s) x 10^3
HFC-236fa	4.39 ± 0.14[a]	468 ± 5	10.8 ± 0.5
FC-31-10	3.88 ± 0.06	508 ± 18	10.3 ± 0.2
FC-318	4.20 ± 0.30	503 ± 3	10.8 ± 0.2
HCFC-124	4.16 ± 0.18	464 ± 2	10.9 ± 0.8
HFC-227ea[b]	4.44	476	11.1
HFC-134a	4.23 ± 0.12	416 ± 8	10.7 ± 0.9
FC-218	4.31 ± 0.37	462 ± 2	10.8 ± 0.7
HCFC-22	4.40 ± 0.15	411 ± 14	10.2 ± 0.1
HFC-125	4.16 ± 0.09	414 ± 10	9.8 ± 0.7
HFC-125/HFC-32 mixture	4.32 ± 0.04	367 ± 12	10.0 ± 0.8
CF_3Br[b]	4.35	554	7.6

[a]mean ± SD
[b]one run

speed movie camera, the emptying time was obtained by counting the number of frames of the movies for the second flashing of the spray (see Section 3.5) to occur at the vessel exit following the start of the release because the time for the appearance of the second flashing corresponded closely to the inflection point in the pressure-time histories. The scatter in the data reflects the uncertainty in identifying the exact emptying time of the liquid and variations in the initial burst pressure. Except for halon 1301, the average volumetric flow rates of the alternative liquid agents evaluated vary less than 10% among each other. Based on Equations (19) and (20) and given the same initial conditions, the emptying time or the volumetric flow rate of the liquid should be relatively independent of the agents studied because the terms under the square root in Equation (20) do not differ significantly among the agents. This is consistent with the experimental observations made in this work. However, the above simple analysis is only applicable when there is no internal boiling of liquid agent inside the vessel during discharge in a downward orientation; this may not be the case for liquid agents with low boiling points (*e.g.*, halon 1301).

Since FC-116 is a gas at room temperature, Equations (21) and (22) can be used to simulate the discharge of FC-116. In this case, $P_{el} = P_i$ and $T_{el} = T_i$. The predicted and measured pressure decays are given in Figure 53. The predicted values were calculated by assuming an average molecular weight of 83 based on the amount of FC-116 and nitrogen at $t = 0$ and a value of 1.2 for γ. There is a large discrepancy between the measured and predicted temporal variations of internal pressure during discharge. It is conjectured that the assumption of ideal gas behavior which underlies Equations (21) and (22) may not be applicable for FC-116. Support for this conjecture is obtained from studies on releases of nitrogen only (which should behave as an ideal gas). For nitrogen-only releases from the pressurized vessel, Equations (21) and (22) predicted reasonably well the temporal variation of the internal pressure as can be seen in Figure 54. Note that, for both cases

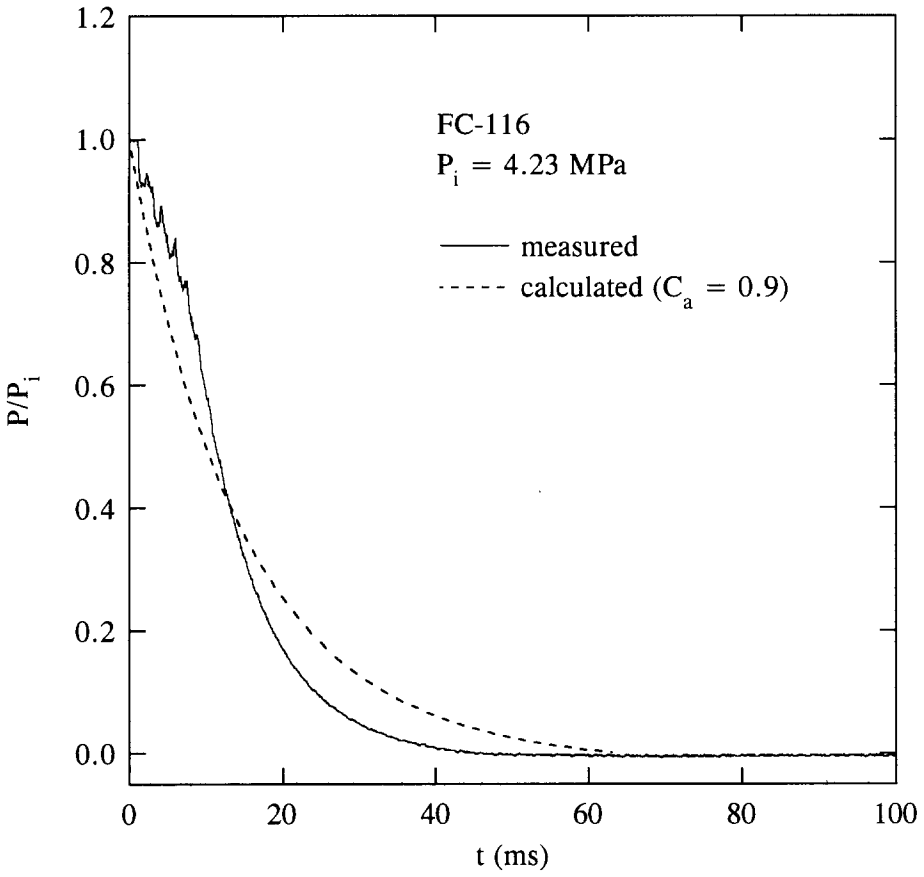

Figure 53. Comparison of a measured pressure-time history of FC-116 discharge with prediction.

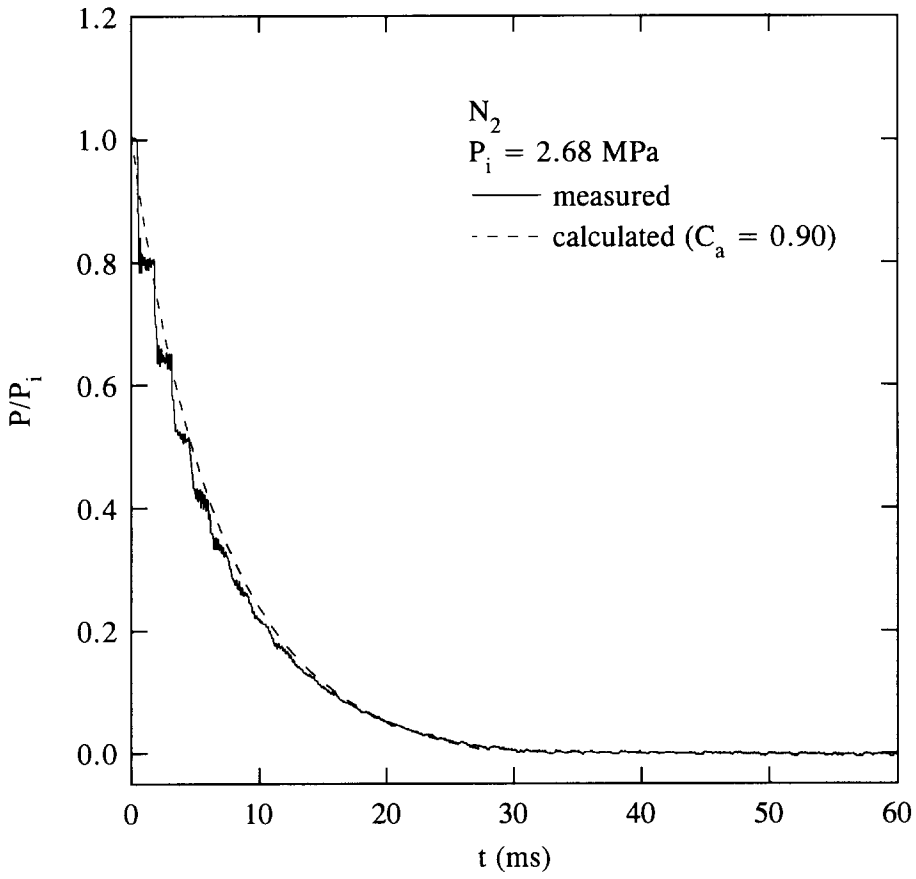

Figure 54. Comparison of a measured pressure-time history of pure nitrogen discharge with prediction.

FC-116 and nitrogen releases, the optimum values of C_a are much higher than the values found in other discharge experiments wherein a liquid agent is initially present and the values in the literature (Kim-E, 1981). The low values of C_a obtained by Kim-E (1981) are possibly due to obstruction of his flow path by a pneumatic plunger. In his experimental set-up, a rupture disk was used as a release mechanism. The plunger which was placed inside the vessel was used to break the rupture disk in order to initiate the discharge process. However, the reason for the low and high values obtained in this study is not known; the low values of C_a were obtained when gas discharge was preceded by liquid release, whereas the high values of C_a were found when liquid was not present initially in the vessel. The value for C_a normally centers around 0.6 (Perry *et al.*, 1984). It can only be conjectured that the edge roughness of the rupture disk opening (Perry *et al.*, 1984) and the transient effect due to the abrupt transition from the discharge of liquid to the release of the remaining vapor may have an effect on the discharge coefficient, and that the assumption of a round, sharp-edged orifice may not be valid because the flow through the disk holder resembles one through a short tube rather than through an orifice. The use of a single value of C_a may also be questionable because C_a can be a function of the pressure ratio across the opening (see Section 3.2). Since the pressure inside the vessel is changing with time during discharge, the pressure ratio is then a function of time. Therefore, it is conceivable that C_a may not be constant during the course of discharge.

3.4.3.2 Effect of an Orifice Plate. The experimental results for internal pressure obtained by restricting the disk opening by means of an orifice plate are shown in Figure 55 through Figure 57. The agent in the vessel remains as liquid during the observation period from the initiation of discharge to the time when the liquid level is no longer visible (see Figure 26) within the plastic vessel. The discharge process is very similar to that without the orifice plate. The key effect of decreasing the diameter of the orifice on the discharge process is to increase the emptying time of the contents, as indicated by the locations of the inflection points in Figure 55 through Figure 57. For the 12.7 mm plate, the average volumetric flow rates are 6.0×10^{-3}, 5.6×10^{-3}, and 3.2×10^{-3} m^3/s for FC-31-10, FC-218, and halon 1301, respectively. For the 6.4 mm plate, the average volumetric flow rates are 1.5×10^{-3}, 1.4×10^{-3}, and 1.3×10^{-3} m^3/s for FC-31-10, FC-218, and halon 1301, respectively. It is found that increasing the diameter of the plate from 6.4 to 12.7 mm increases the average volumetric flow rates of FC-31-10 and FC-218 by approximately fourfold, in accordance with Equation (20), *i.e.*, $dV/dt \sim A$ for a given P. The relationship between the average volumetric flow rate (Q) and the orifice area (A) is clearly seen in Figure 58 for FC-31-10 and FC-218 using burst disks with a nominal burst pressure of 4.12 MPa. Results discussed earlier for standard releases (orifice diameter of 19.1 mm) are included. The symbols in the figure are measured values. The dotted and solid lines in the figure are least-square fits of the data which are forced to pass through the origin. Figure 59 through Figure 62 show the comparisons of measured pressure-time histories of FC-31-10 and FC-218 discharge with predictions using Equations (19) through (22). For the experimental results obtained using a 6.4 mm restrictor plate, the model did not simulate the discharge process well because the flow field is more complicated when a smaller orifice plate is used to restrict the flow at the exit of the short tube section which was part of the rupture disk holder (see Figure 25 and Figure 26). Since it has been conjectured in Section 3.4.3.1 that boiling of liquid halon 1301 inside the vessel occurs near the end of liquid discharge, the above volumetric flow rate-area relationship is not applicable to halon 1301.

3.4.3.3 Effect of an Extension Tube. From visual observations, the presence of an extension tube did not affect the internal behavior of the liquid during discharge. Figure 63, Figure 64, and

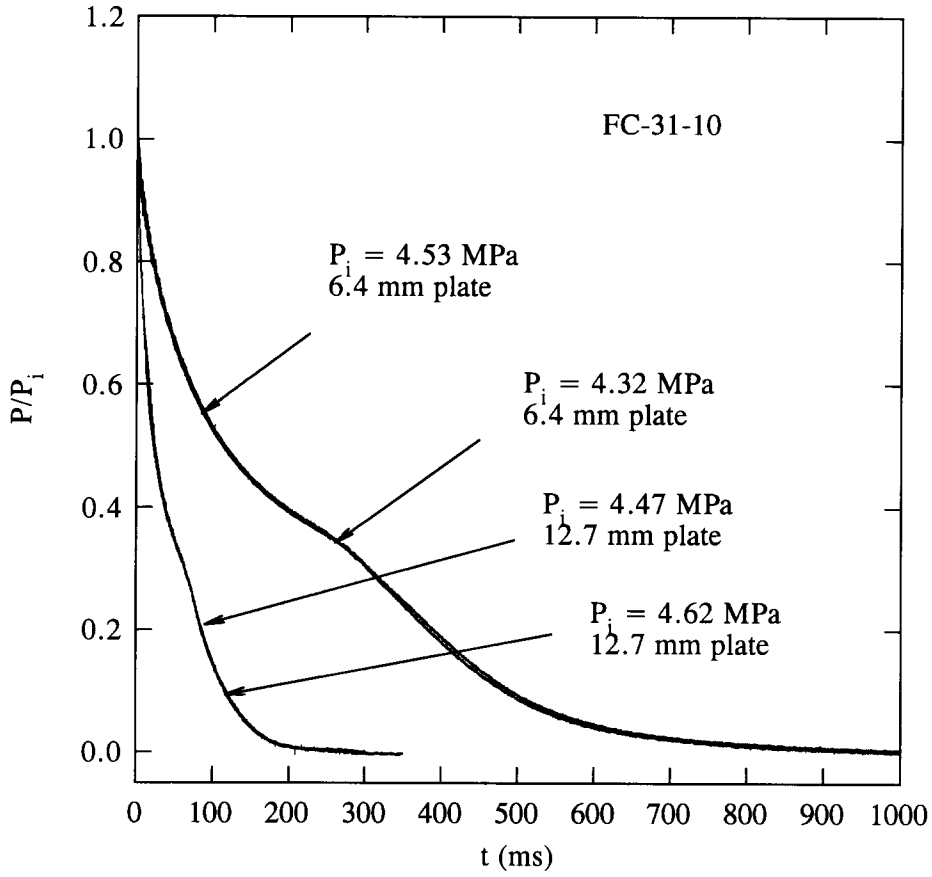

Figure 55. Temporal variations of internal pressure during discharges of FC-31-10 with a restricting orifice plate (6.4 or 12.7 mm).

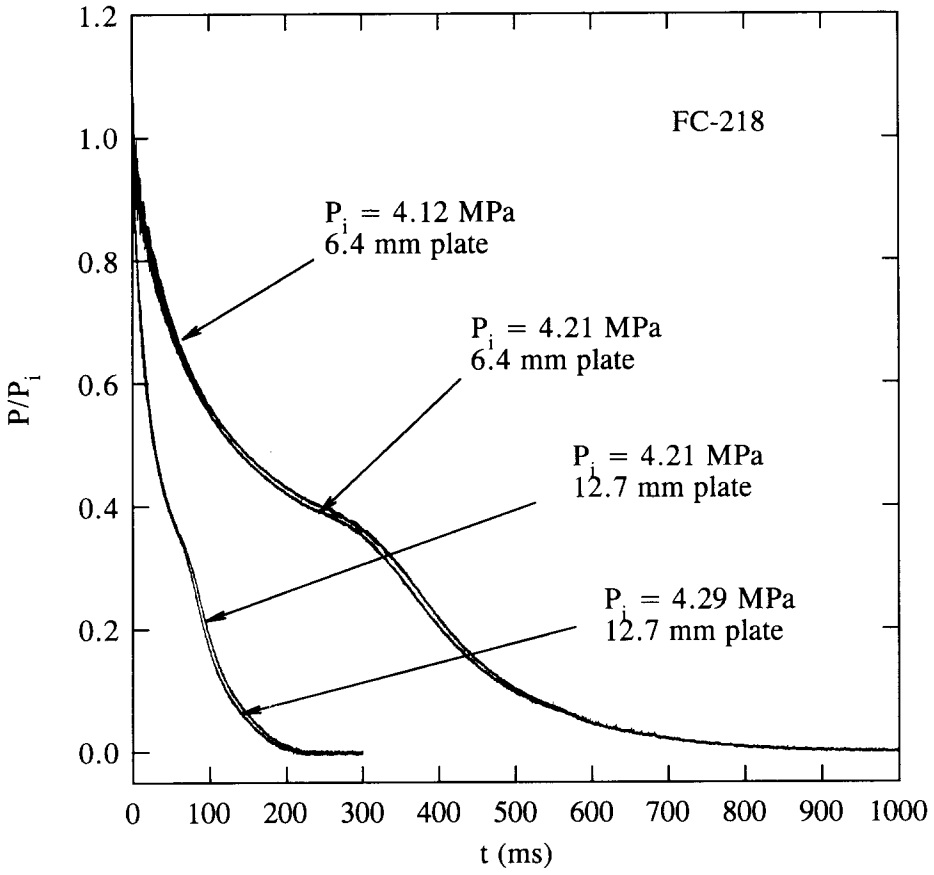

Figure 56. Temporal variations of internal pressure during discharges of FC-218 with a restricting orifice plate (6.4 or 12.7 mm).

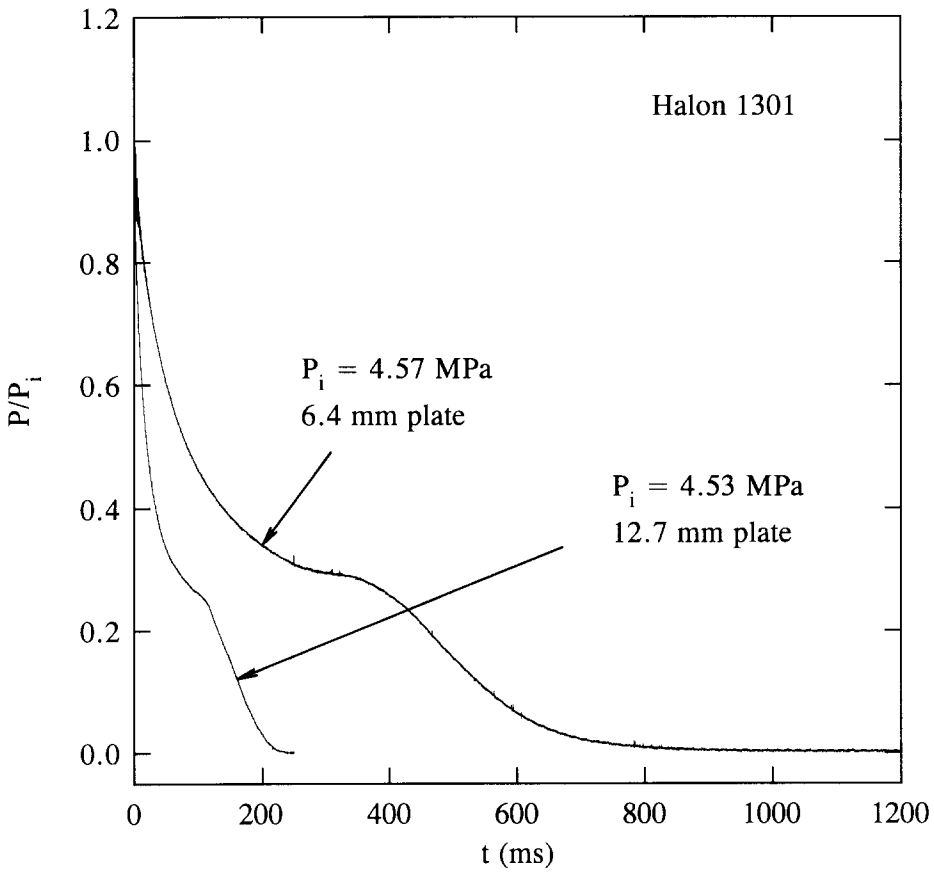

Figure 57. Temporal variations of internal pressure during discharges of halon 1301 with a restricting orifice plate (6.4 or 12.7 mm).

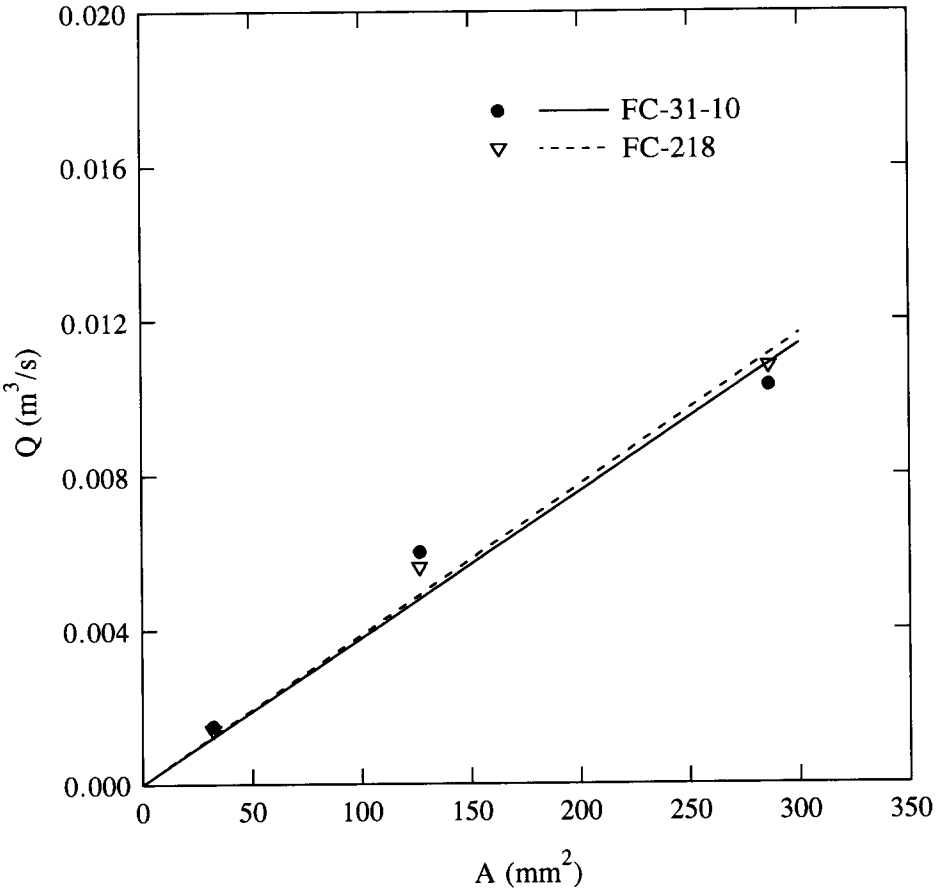

Figure 58. Relationship between average volumetric flow rate and orifice area.

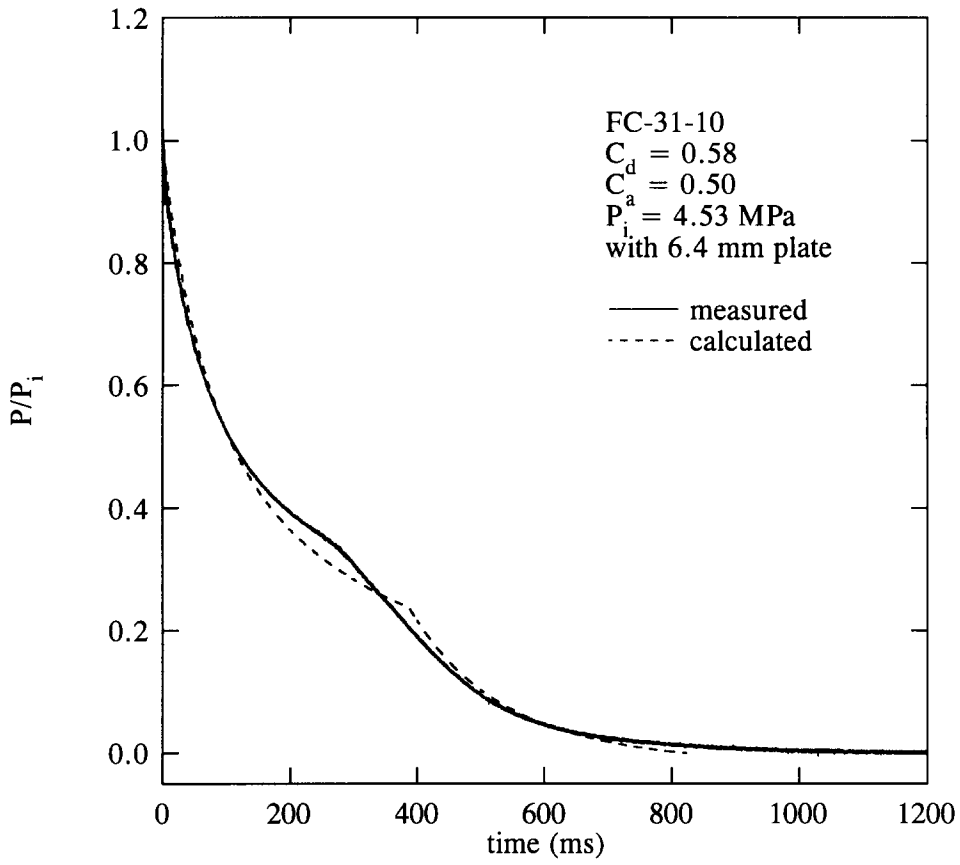

Figure 59. Comparison of a measured pressure-time history of FC-31-10 discharge using a 6.4 mm orifice plate with prediction.

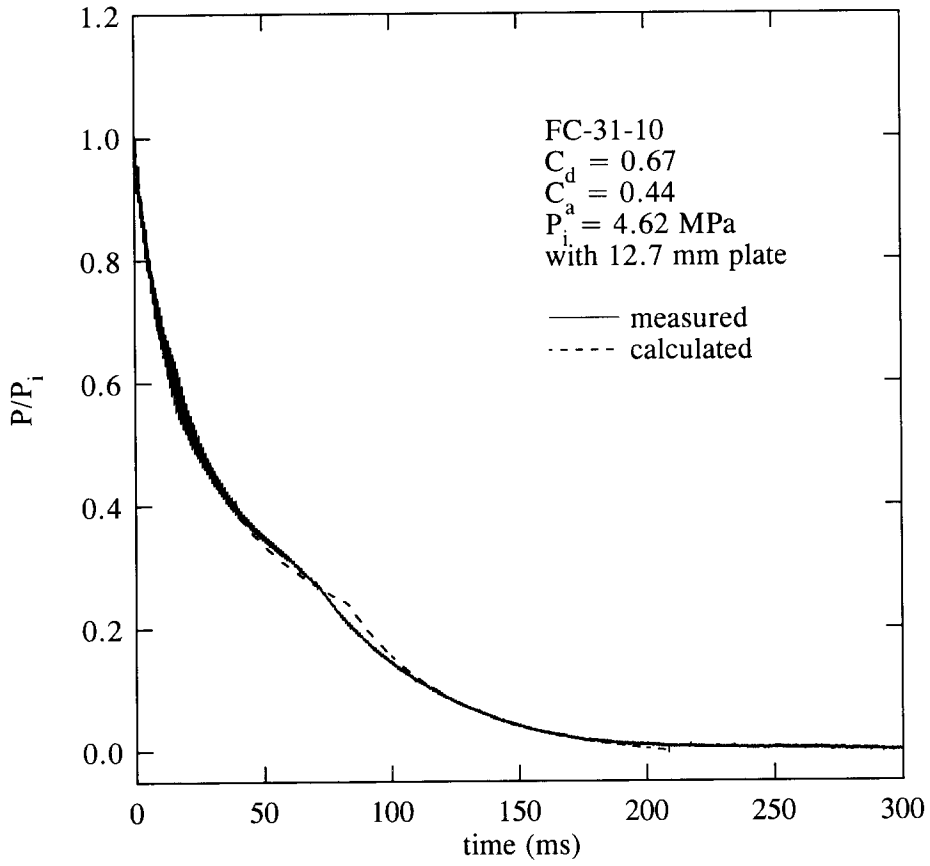

Figure 60. Comparison of a measured pressure-time history of FC-31-10 discharge using a 12.7 mm orifice plate with prediction.

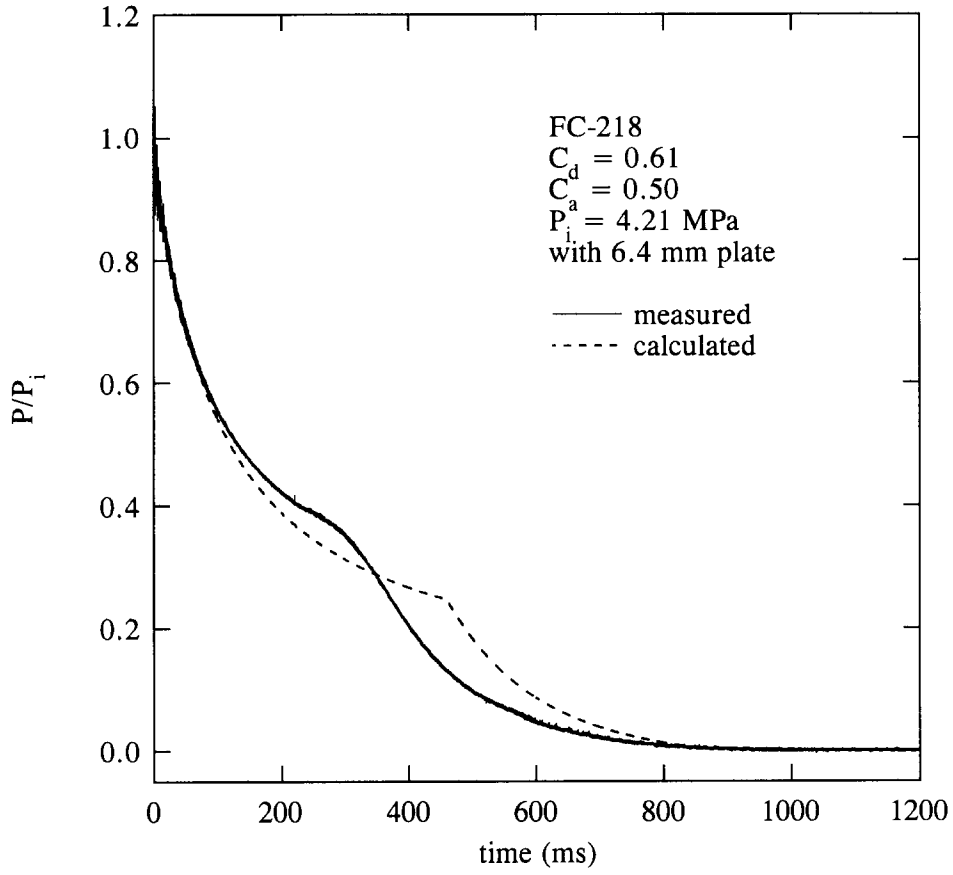

Figure 61. Comparison of a measured pressure-time history of FC-218 discharge using a 6.4 mm orifice plate with prediction.

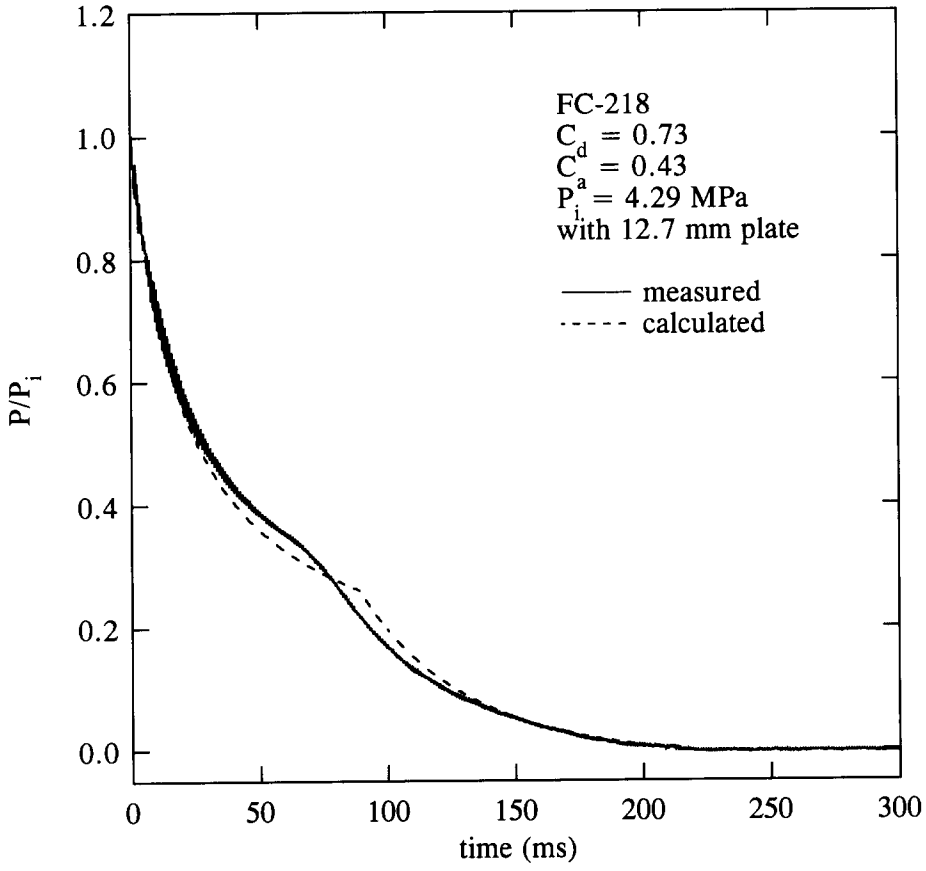

Figure 62. Comparison of a measured pressure-time history of FC-218 discharge using a 12.7 mm orifice plate with prediction.

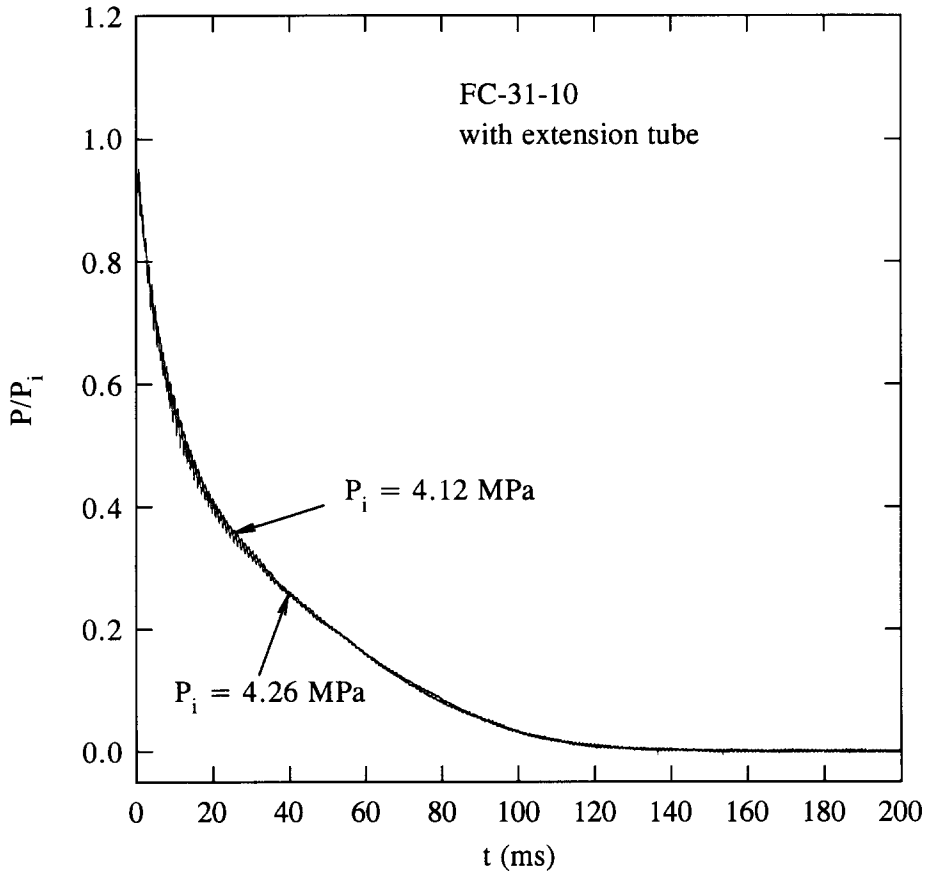

Figure 63. Temporal variations of internal pressure during discharges of FC-31-10 with a 0.5 m long extension tube.

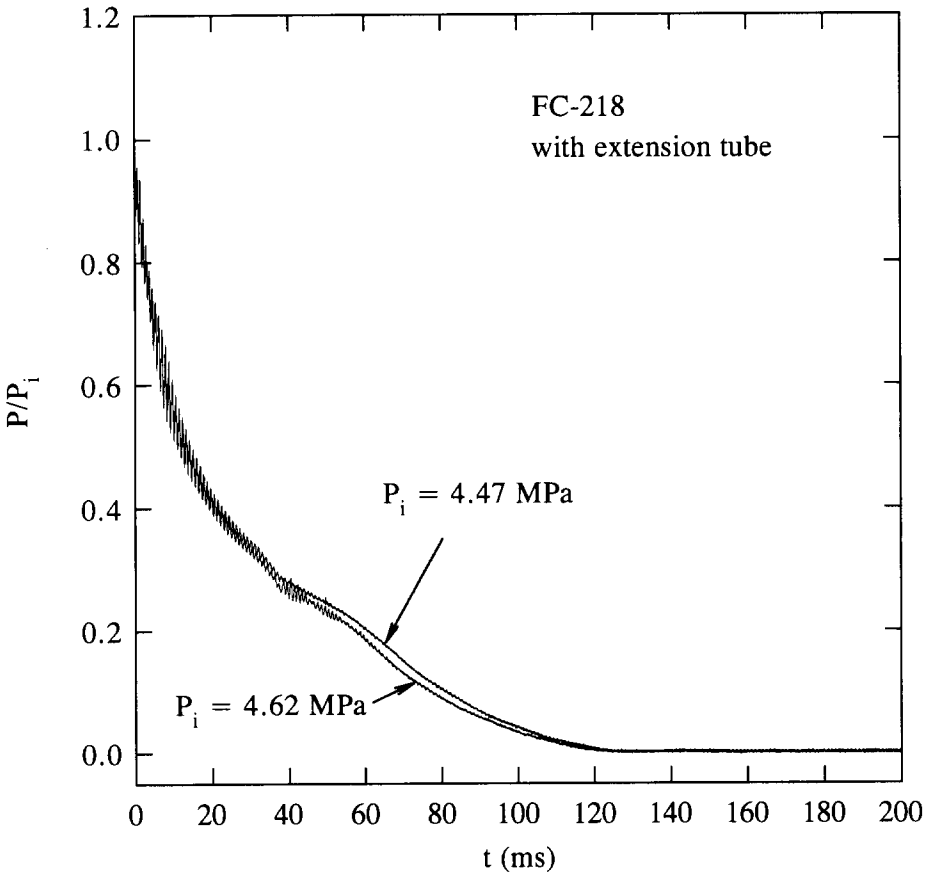

Figure 64. Temporal variations of internal pressure during discharges of FC-218 with a 0.5 m long extension tube.

Figure 39 show the internal pressure results for FC-31-10, FC-218, and halon 1301. For comparison, the results obtained with and without extension tube are shown in Figure 65, Figure 66, and Figure 39. It appears that the presence of an extension tube does not change the temporal behavior of the internal pressure during discharge of liquid FC-31-10 and FC-218. This is indicative of the existence of critical flow at the vessel orifice since the downstream geometry does not affect the pressure upstream (Prisco *et al.*, 1977). The presence of an extension tube slows down the discharge of the remaining vapor from the vessel after liquid depletion because of friction losses in the tube, as can be seen in Figure 65, Figure 66, and Figure 39. In the case of halon 1301, the presence of an extension tube makes the pressure-curve transition from liquid to gaseous discharge more gradual. Such gradual transition is indicative of initiation of boiling within the vessel or extension tube (see discussion in Section 3.4.3.1). Furthermore, when compared to the discharge behavior of halon 1301 without an extension tube, the discharge of the two-phase boiling halon 1301 in the presence of an extension tube is much slower due to additional frictional losses in the tube.

3.4.3.4 Effect of Initial Vessel Pressure. The above discussion is based on results obtained using rupture disks with nominal burst pressures of 4.12 MPa. In order to study the effect of initial pressure on the discharge dynamics, rupture disks with different nominal burst pressures (2.75 and 5.50 MPa) were used. Figure 67 shows pressure-time histories for FC-218 for three initial burst pressures. The oscillation seen in two of the pressure traces reflects the use of a plastic vessel. It is clear that the emptying time of the liquid decreases with increasing initial pressure in the vessel, and that a twofold increase in the initial burst pressure only increases the average volumetric flow rate by approximately a square root of 2. The measured average volumetric flow rates for these three runs are 8.4×10^{-3} m^3/s for $P_i = 2.60$ MPa, 11.3×10^{-3} m^3/s for $P_i = 4.57$ MPa, and 11.9×10^{-3} m^3/s for $P_i = 6.18$ MPa. The results are consistent with the model (Equation (20)), *i.e.*, $dV/dt \sim (P)^{1/2}$ for a given A. The relationship between the average volumetric flow rate (Q) and the initial charge pressure (P_i) is shown in Figure 68 for FC-218 using a 19.1 mm opening. The dotted line in the figure is a least-square fit through the origin, and the symbols represent measured values. The calculated and measured temporal variations of internal pressure for $P_i = 6.18$ MPa, as an example, are shown in Figure 69. The prediction matches the experiment quite well.

3.4.3.5 Effect of Vessel Temperature. The study of the effect of temperature on the discharge dynamics was carried out experimentally with FC-31-10 and FC-218 at −45 °C. Since similar trends were observed for FC-218, only the results for FC-31-10 are shown in Figure 70. The pressure-time histories are very similar to those obtained using the same burst disks but at room temperature. The internal behavior of the agent in the vessel, though not observed visually, should be similar. However, the dispersion characteristics of the agent external to the release vessel were observed to have a less-flashing nature when the agent was discharged at −45 °C (see Section 3.5.3.9). Figure 71 shows a comparison of the measured results with predictions from Equations (19) through (22).

Although no experiments were carried out at 150 °C, the discharge of an agent at this temperature may be characterized as a discharge of a supercritical fluid from the vessel because at this temperature, and its corresponding pressure, the agent/nitrogen mixture is in the supercritical region. If this indeed is the case, then the discharge process should be very similar to that of a FC-116/nitrogen mixture.

Some interesting but important events which may occur when the vessel is rapidly discharged at moderately high temperature and pressure will be discussed. These processes are also discussed in Section 3.2.4. The following is based on the hypothesis proposed by Reid (1979) in an attempt to

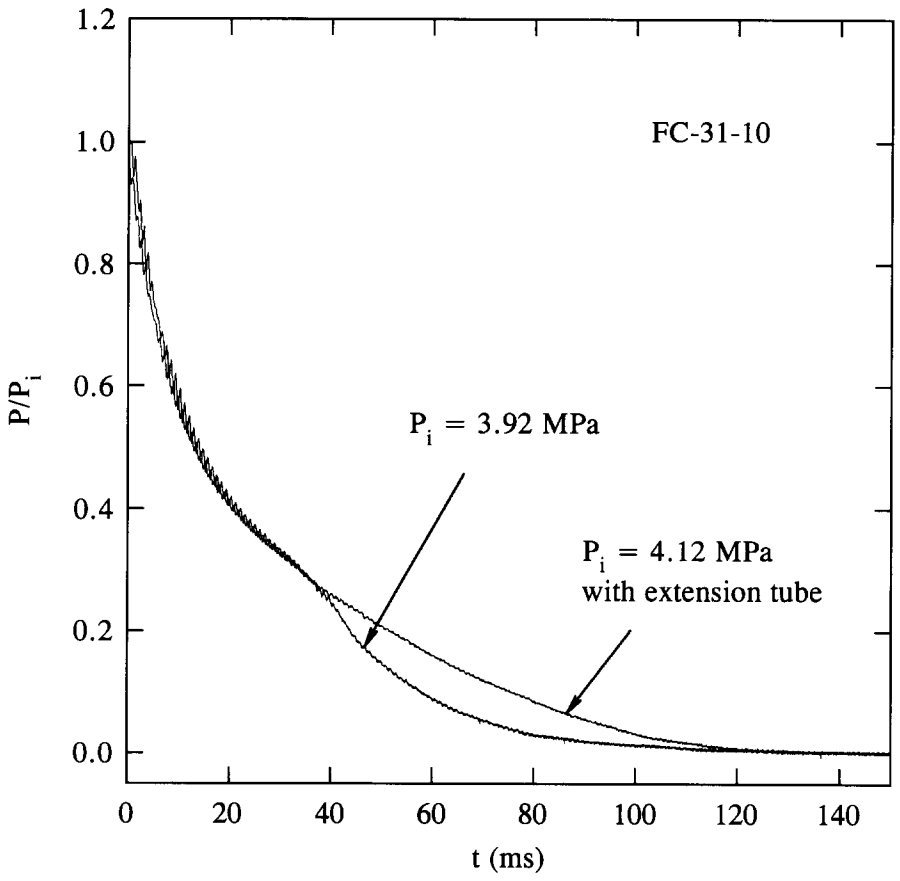

Figure 65. Temporal variations of internal pressure during discharges of FC-31-10 with and without an extension tube.

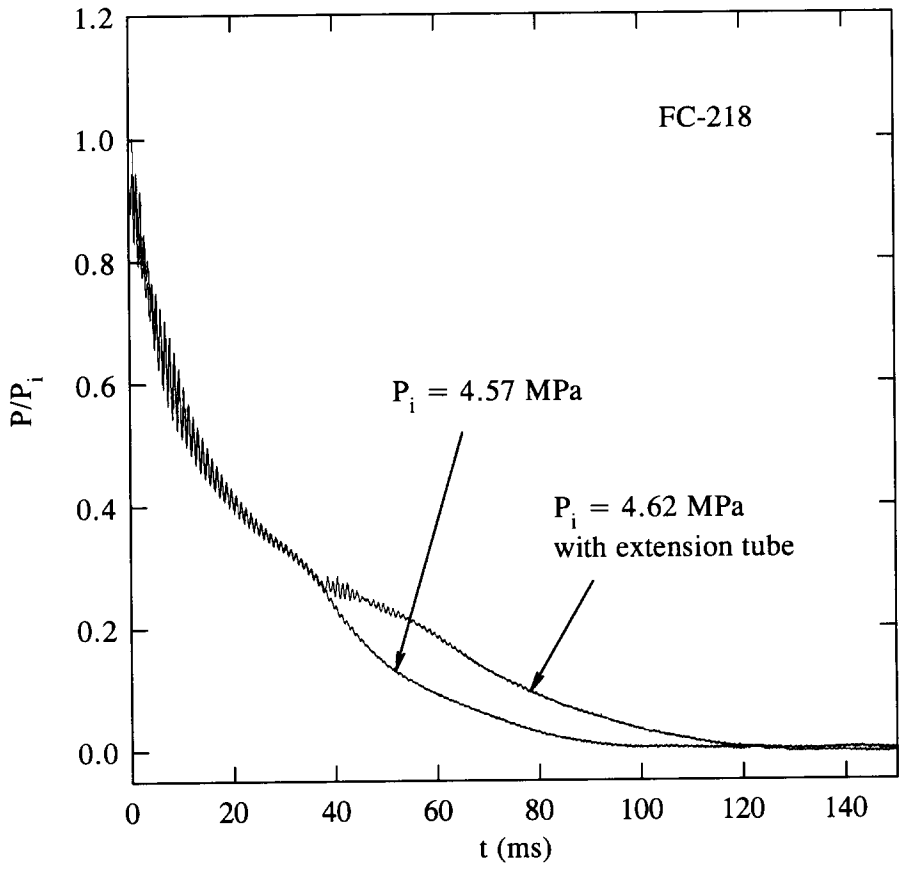

Figure 66. Temporal variations of internal pressure during discharges of FC-218 with and without an extension tube.

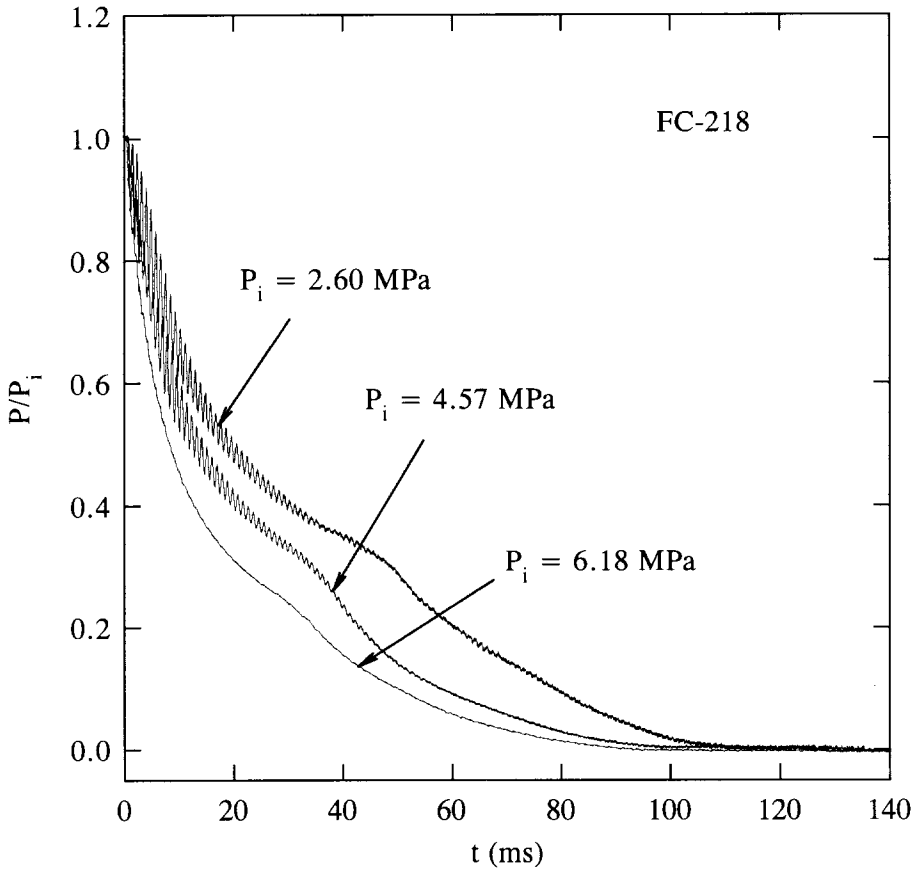

Figure 67. Temporal variations of internal pressure during discharges of FC-218 with different initial burst pressures.

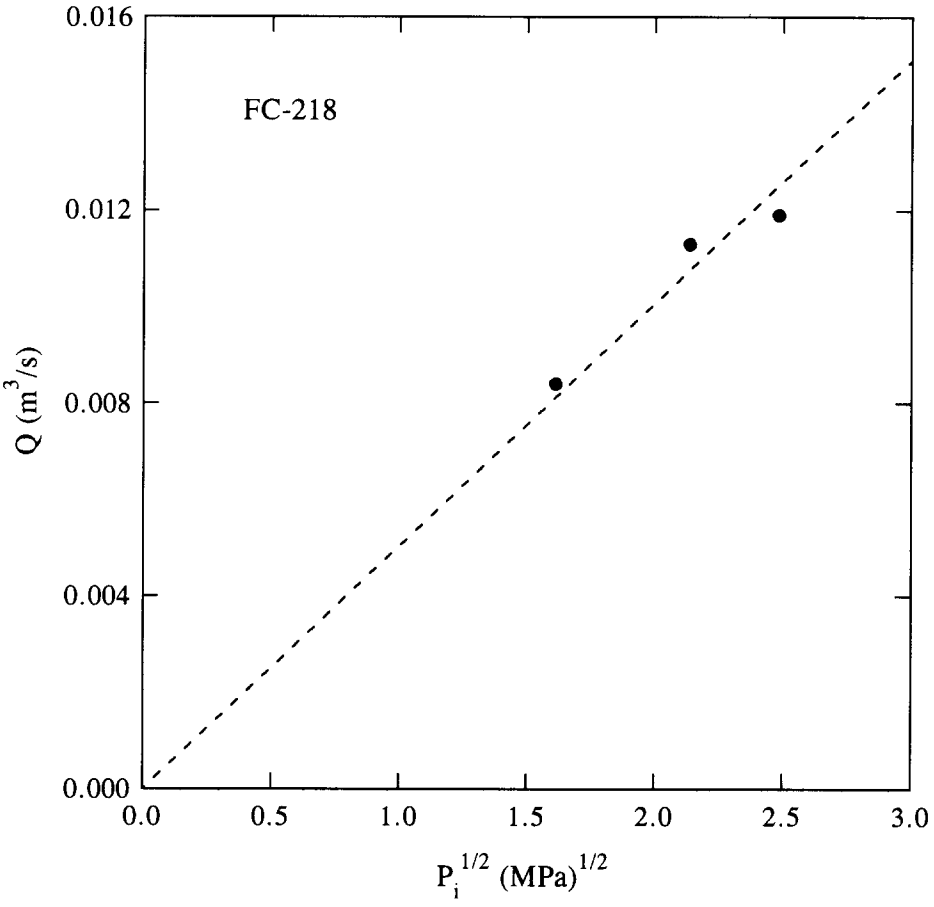

Figure 68. Relationship between average volumetric flow rate and initial charge pressure.

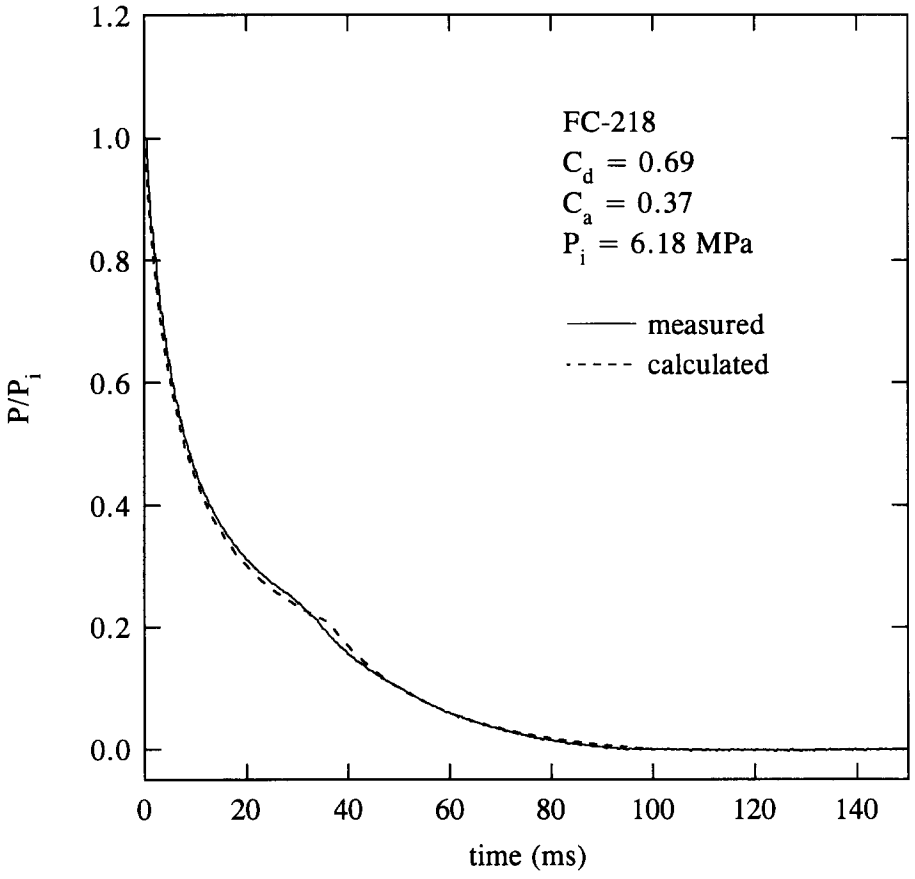

Figure 69. Comparison of measured pressure-time history of a FC-218 discharge at elevated pressure with prediction.

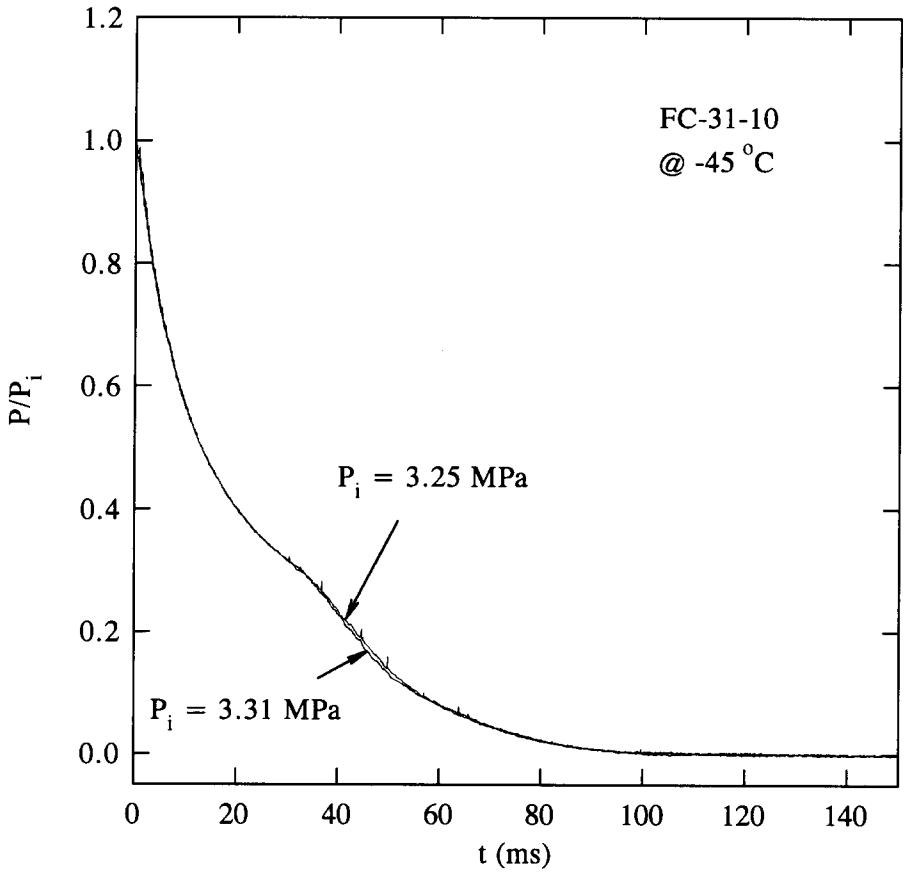

Figure 70. Temporal variations of internal pressure during downward discharges of FC-31-10 at −45 °C.

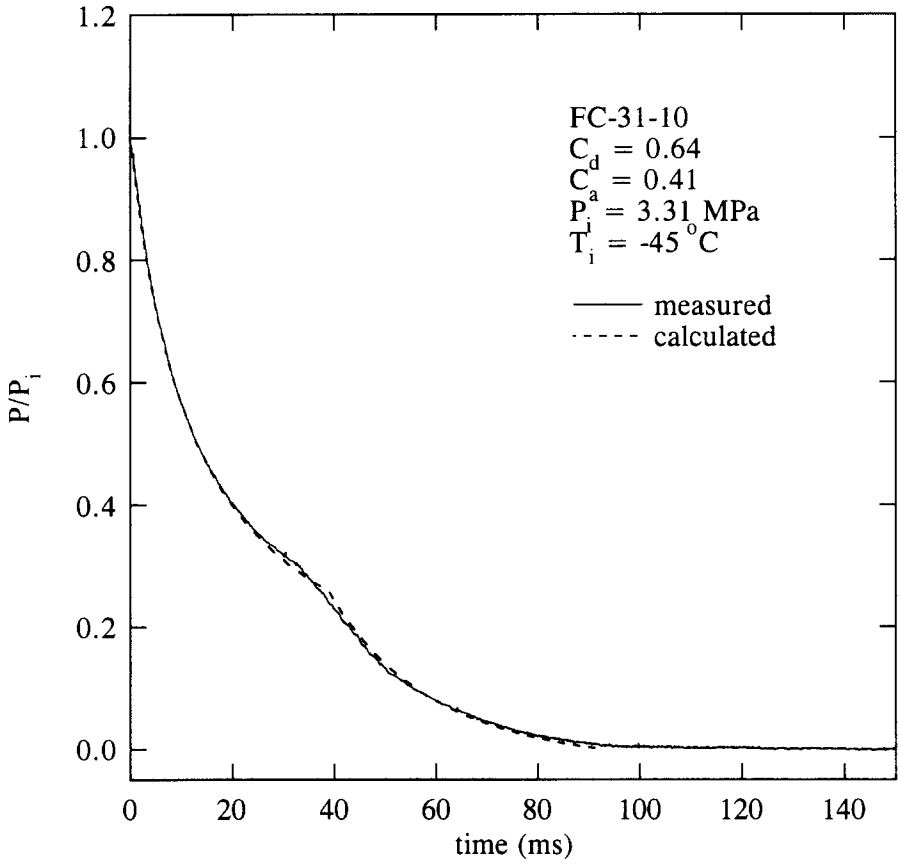

Figure 71. Comparison of measured pressure-time history of a FC-31-10 discharge at −45 °C with prediction.

provide a possible mechanism for pressurized-liquid tank explosions or boiling liquid expanding vapor explosions (BLEVEs).

In order to delineate the important features, and for simplicity and clarity, a fixed initial amount of pure agent in the vessel without pressurization of nitrogen will be considered. For example, say the vessel has an initial fill density (ρ_{fill}) of 0.5 kg of FC-31-10 per 5×10^{-4} m^3 (approximately 2/3 full) at room temperature (22 °C). The vessel is then heated to say T_f = 100 °C. The heating process of the vessel is illustrated in Figure 72 (point *A* to point *B*) which is a pressure-temperature diagram of pure FC-31-10 (Daubert and Danner, 1992). Point *A* represents the initial condition of the vessel, that is, liquid and vapor of FC-31-10 coexist in the vessel at T_i = 22 °C with a saturation vapor pressure of 0.24 MPa). The saturation curve in Figure 72 represents the conditions of pressure and temperature required for the coexistence of liquid and vapor phases. To determine the final state (point *B*) of the heating process, that is, whether point *B* will lie in the single phase (gas or liquid) region or on the saturation curve, one has to compare the saturation vapor and liquid densities at T_f ($\rho_{v,f}$ and $\rho_{l,f}$) with the initial fill density of the vessel (ρ_{fill}). If $\rho_{v,f} < \rho_{fill} < \rho_{l,f}$, then two phases (vapor and liquid) still coexist in equilibrium in the final state (Smith and Van Ness, 1975). In the case of FC-31-10, $\rho_{v,f}$ = 296 kg/m^3 and $\rho_{l,f}$ = 1002 kg/m^3 (Brown and Mears, 1958). Given an initial fill density of 1000 kg/m^3, the final state is still two-phase. Therefore, point *B* lies on the saturation curve, as shown in Figure 72. If the vessel is *rapidly* depressurized or discharged at the final temperature and pressure, the liquid will be superheated, that is, at a temperature higher than the saturation temperature at the corresponding existing pressure (Modell and Reid, 1983). The liquid is superheated as a result of crossing the saturation curve without concomitant phase change. However, there is a pressure limit for how far the metastable liquid can be sustained. This limit is the so-called spinodal curve (Modell and Reid, 1983). The superheated liquid thus lies in the region between the saturation curve and the spinodal curve. Once the superheated liquid reaches the spinodal curve, spontaneous, homogeneous nucleation will occur within the bulk of the liquid. Such rapid nucleation is expected to be accompanied by strong and damaging shock waves and huge pressure increases in the vessel. If this event happens, it is expected that substantial damage would be incurred by the vessel, or in the worst scenario, explosion of the vessel would occur if the vessel was not designed to withstand such a pressure surge.

For a pure agent, the spinodal curve can be calculated (Beegle *et al.*, 1974) by determining where the condition

$$\left(\frac{\partial P}{\partial v}\right)_T = 0 \tag{24}$$

is met. P is the pressure, v is the molar volume, and T is the temperature. The Peng-Robinson equation of state (Peng and Robinson, 1976) is used for illustration (see Section 2.3.1). By applying Equation (24) to the equation of state, the following quartic equation in v results:

$$-\frac{RT}{(v-b)^2} + \frac{2a(v+b)}{[v(v+b)+b(v-b)]^2} = 0 \tag{25}$$

or

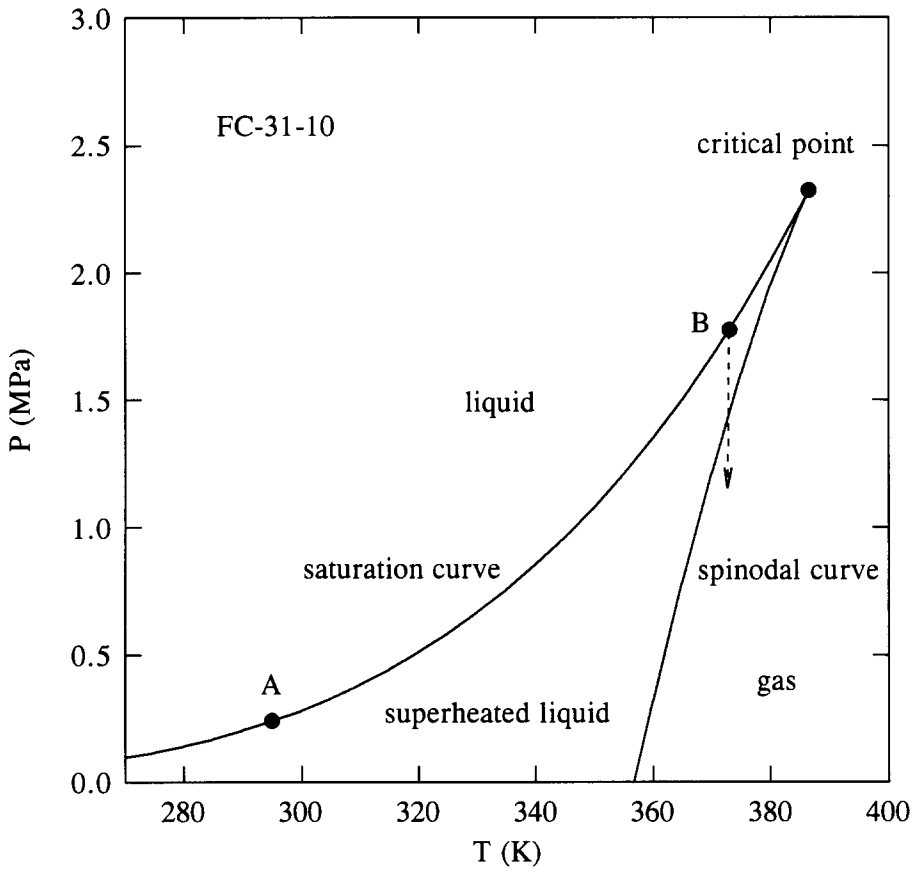

Figure 72. Vapor pressure and calculated spinodal curves for FC-31-10.

$$v^4 + (4b - \frac{2a}{RT})v^3 + 2b(b + \frac{a}{RT})v^2 + 2b^2(\frac{a}{RT} - 2b)v + b^4 - \frac{2ab^3}{RT} = 0 \qquad (26)$$

where a and b are the parameters of the equation of state (see Section 2.3.1). For given temperatures below the critical point, there are four real roots from Equation (26). Two of the roots, one less than the saturated liquid molar volume and the other greater than the saturated vapor molar volume, are nonphysical and are disregarded. The smallest of the remaining two roots corresponds to the v on the liquid spinodal curve, whereas the largest corresponds to the v on the vapor spinodal curve which is not relevant in this discussion. Once v is determined for a given T, P can be obtained from the equation of state. The calculated liquid spinodal curve for FC-31-10 is also shown in Figure 72.

If the vessel is rapidly discharged at the condition corresponding to point B in Figure 72, the discharge process can be approximated by that of an isothermal depressurization (see Section 3.4.3), as depicted by the vertical line in Figure 72. If the homogenous nucleation pressure (P_{hn}) at T_f, which is the pressure corresponding to the intersection of the vertical line and the spinodal curve, is greater than any instantaneous pressure during the interval when the liquid is being discharged, that is

$$P(t) < P_{hn} \qquad 0 < t < t_{el} \qquad (27)$$

where t_{el} represents the time at which complete depletion of liquid occurs, then homogeneous nucleation would be predicted. However, if $P(t) > P_{hn}$ for $0 < t < t_{el}$, then homogeneous nucleation would not occur.

The above discussion is based on a pure agent. If nitrogen is used to pressurize the vessel, nitrogen will be dissolved in the liquid agent. The homogeneous nucleation pressure will then depend not only on the temperature but also on the composition of the liquid mixture. The effect of dissolved gas on the homogeneous nucleation pressure of a liquid was found to raise the homogeneous nucleation pressure (Forest and Ward, 1977). In this case, homogeneous nucleation, if it occurs, would initiate sooner in the presence of the dissolved gas during rapid isothermal depressurization.

Although the hypothesis proposed by Reid (1979) can not be substantiated or disproved at present (Reid, 1979, Kim-E and Reid, 1983), it is prudent to recognize such a potentially hazardous event when the vessel is rapidly discharged at high temperature and pressure, and further study is warranted.

3.4.3.6 Vertically Upward Discharge. When the vapor above the liquid is vented first during depressurization, that is, in the case of upward discharge of the vessel, the discharge process is totally different from that of downward discharge. Visual observation of the discharge process from a plastic vessel reveals several stages. Once the rupture disk breaks, the vapor on top of the liquid is vented out rapidly, during which time the liquid in the vessel remains quiescent. The vapor ullage becomes foggy ($t \sim 10$ ms), possibly due to the condensation of the vapor as the result of cooling by adiabatic expansion. Then, following a delay time ($t \sim 25$ ms), boiling is initiated from the bottom of the vessel, and, because of bubble growth, the liquid-gas mixture level expands all the way through the disk opening. Frothing of the liquid continues for a period of time during which time a two-phase flow emerges from the vessel. The liquid level then settles down ($t \sim 500$ ms). The interior of the vessel becomes clear, and some liquid is observed at the bottom of the vessel. At this point, most of the liquid in the vessel has been expelled. Pool boiling of the liquid then continues until the remaining liquid is boiled off. The complete emptying time of the liquid agent in the vessel is on the order of seconds. The discharge process is much slower for FC-31-10 than for FC-218 because

FC-31-10 has a higher boiling point. The observations, in general, are very similar to those made by Gühler *et al.* (1979) and Fletcher (1982) although the discharge process in both earlier studies is much slower.

Figure 73 shows a photographic sequence of events during a vertically upward discharge of FC-218. The photographs were taken at 1000 frames per second. The frame which corresponds to t = 1 ms is the first frame where the agent first appears outside the vessel. Due to the framing rate, there is a 1 ms uncertainty in the time. The first photograph shows the plastic vessel, a stainless-steel tube inside the vessel for introducing nitrogen in order to burst the rupture disk, vessel mount, and the liquid level. The behavior of the agent inside and outside of the vessel during discharge can be seen in these photographs. The discharge characteristics of the agent outside of the vessel is discussed in Section 3.5.

In Figure 74 the results of pressure measurement for upward discharges of FC-31-10 are shown. In the upward discharge configuration, the pressure transducer measured the temporal variation of the pressure in the liquid phase. When the stainless steel vessel was used in the experiments, the pressure transducer mounted on the side wall of the vessel was used to monitor the pressure change in the vapor phase. Due to its relatively high boiling point, FC-31-10 does not show distinctly in the pressure-time histories the several stages occurring in the discharge process.

Pressure traces for FC-218 and halon 1301 are shown in Figure 75 and Figure 76. The several processes discussed above are clearly depicted. Upon initiation of discharge, the internal pressure decreases rapidly. The following small pressure rise corresponds to the expansion of the liquid. Then, the pressure decreases gradually over a period of time. This time interval corresponds to the continuous frothing of the liquid. Eventually, an abrupt decrease in pressure corresponds to the pool boiling of the remaining liquid in the vessel. The above interpretation is based on comparison of the pressure traces with high-speed movie records obtained from experiments on FC-218 using plastic vessels. Only the stainless steel vessel was used for experiments on halon 1301 due to safety considerations. However, it is conjectured that similar behaviors occurred for halon 1301 because similar pressure-time histories were noted.

When an extension tube was attached to the release vessel assembly exit, the behavior of the liquid agent inside the vessel during vertically upward discharge was very similar to that without an extension tube, as observed in the high-speed movies and noted in Figure 74 through Figure 76.

3.4.3.7 Horizontal Discharge. Observations regarding horizontal discharge of the vessel also show several stages. Once discharge is initiated, the vapor is vented very rapidly from the vessel. Some liquid also flows out of the vessel because the initial liquid level in the horizontally mounted vessel covers a portion of the rupture disk. The flow of vapor causes some wavy motion along the liquid/vapor interface. The sloshing of the liquid could also be caused by the vibration of the vessel mount. A foggy cloud is formed ($t \sim 15$ ms) above the liquid for a period of time. The vessel ullage then becomes clear ($t \sim 400$ ms), and pool boiling is initiated in the remaining liquid pool which still constitutes a significant amount of the initial liquid. Boiling continues until all the liquid is depleted. The emptying time is on the order of seconds. The complete discharge of the remaining liquid is much slower for FC-31-10 than for FC-218 because FC-218 has a lower boiling point.

Figure 77 shows a photographic sequence of events during a horizontal discharge of FC-218. The photographs were taken at 1000 frames per second. The frame which corresponds to t = 1 ms is the first frame where the agent first appears outside the vessel. Due to the framing rate, there is a 1 ms uncertainty in the time. The first photograph shows the plastic vessel (mounted horizontally) with its exit located to the far left and the liquid level. The photographs reveal the behavior of the agent internal and external to the vessel.

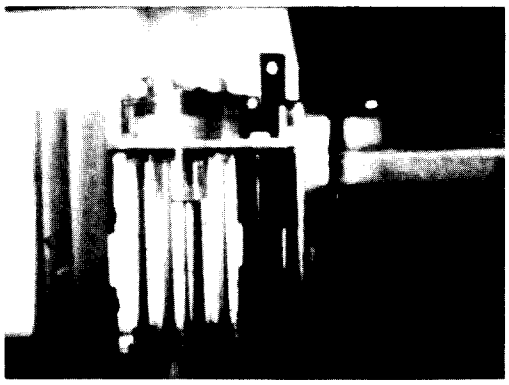

1 ms

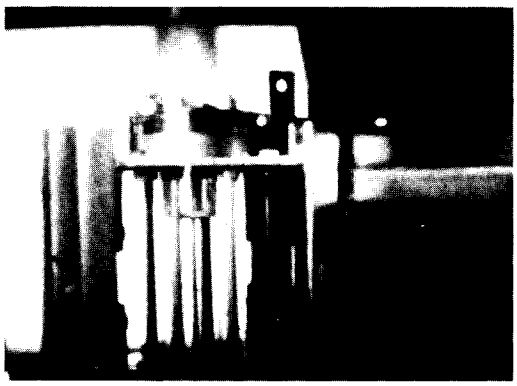

2 ms

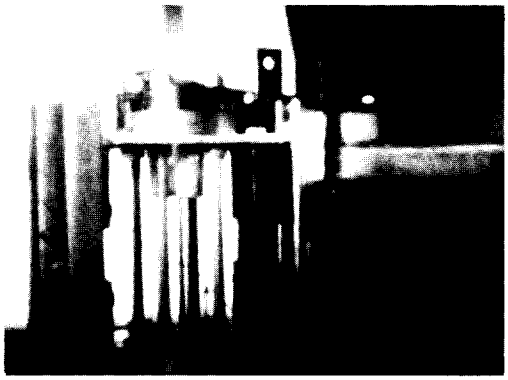

10 ms

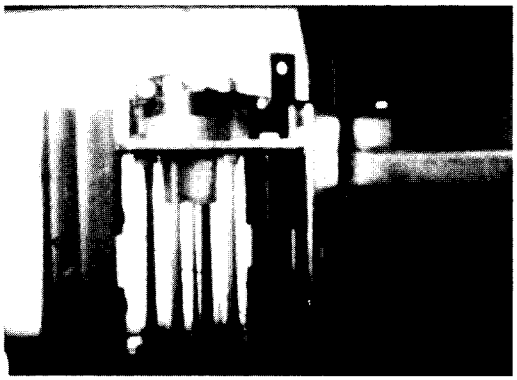

15 ms

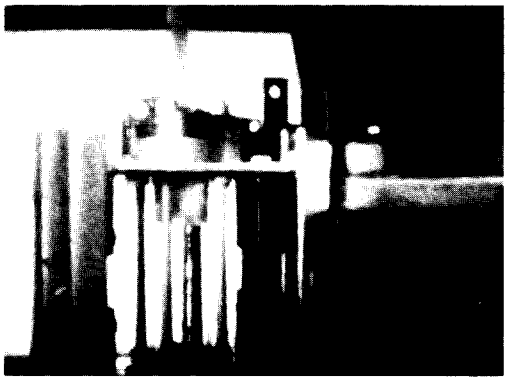

25 ms

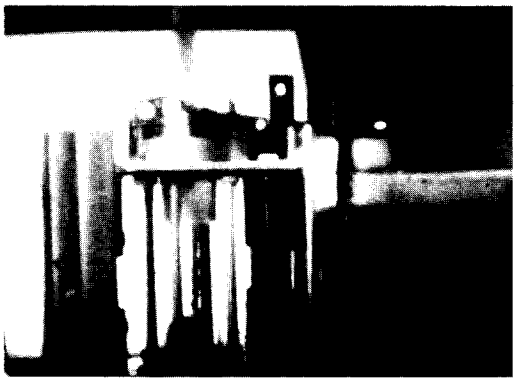

30 ms

Figure 73. Photographic sequence of events showing a vertically upward discharge of FC-218 from a plastic vessel.

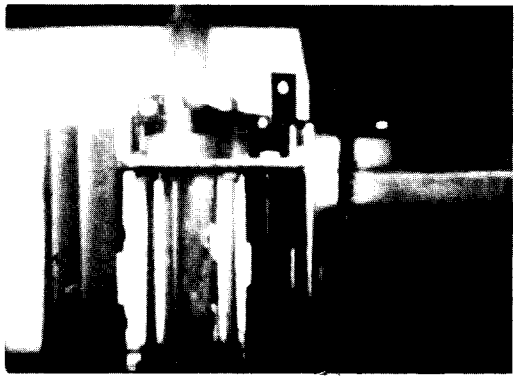

40 ms

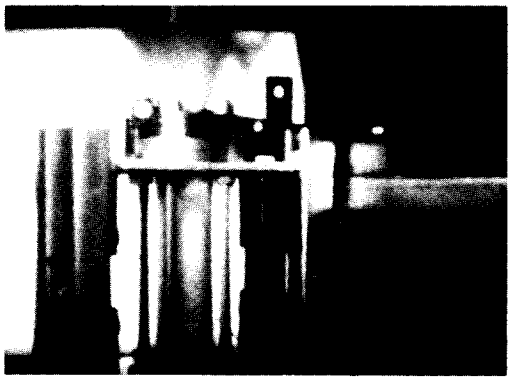

60 ms

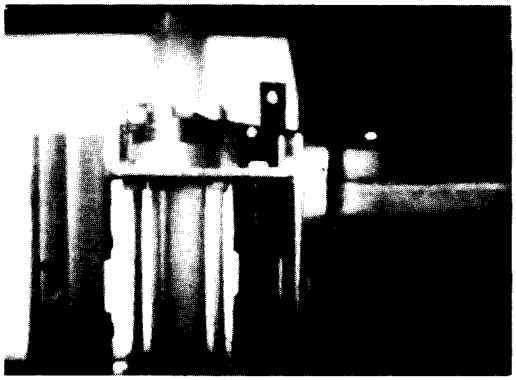

100 ms

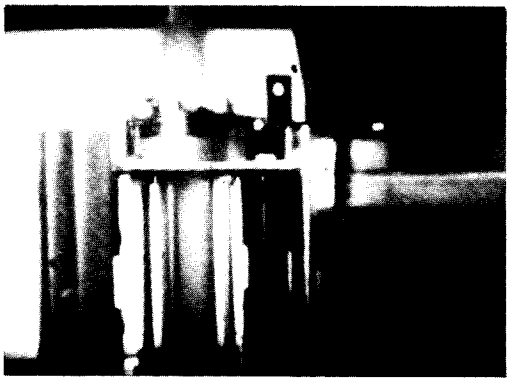

150 ms

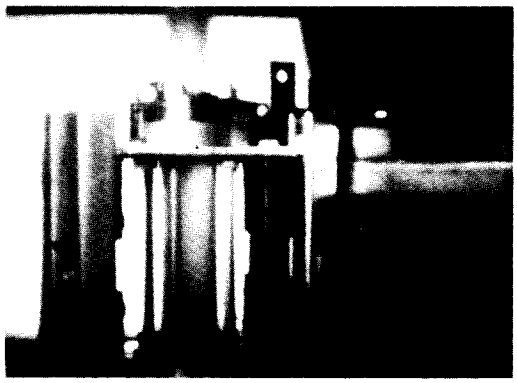

200 ms

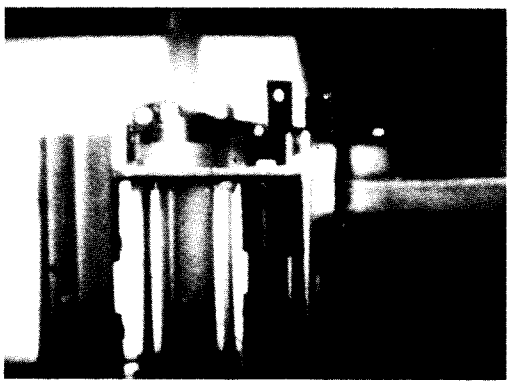

250 ms

Figure 73. (continued) Photographic sequence of events showing a vertically upward discharge of FC-218 from a plastic vessel.

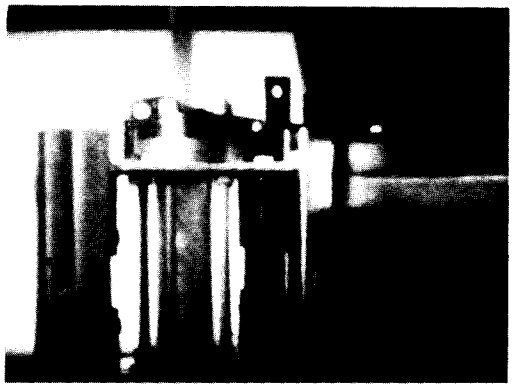

300 ms

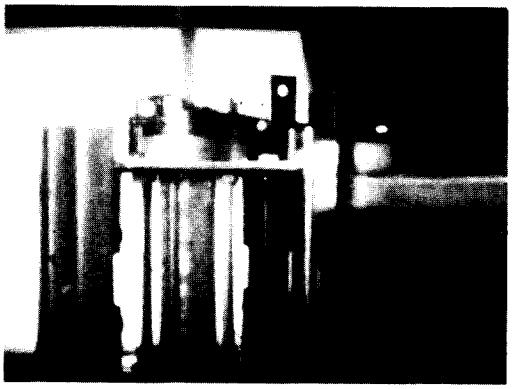

350 ms

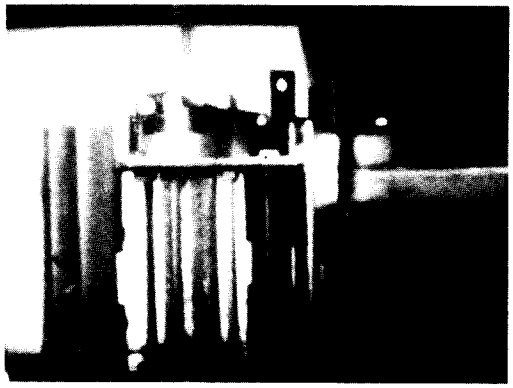

400 ms

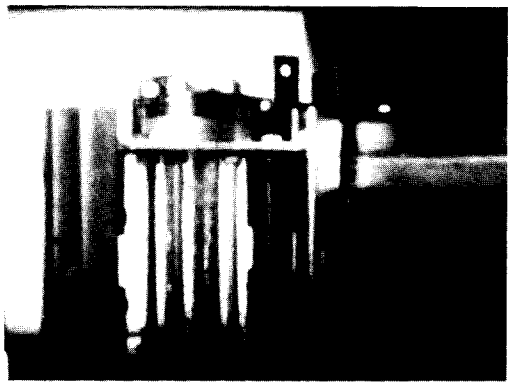

450 ms

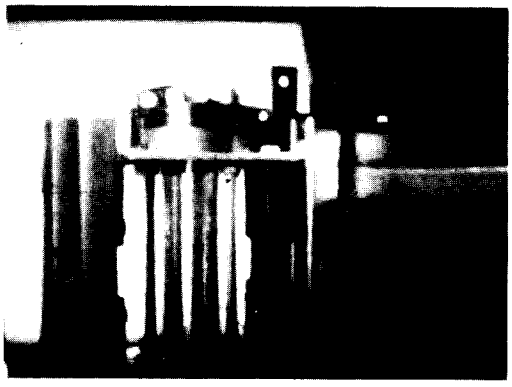

500 ms

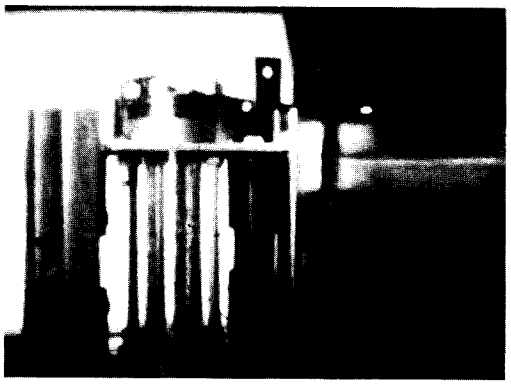

550 ms

Figure 73. (continued) Photographic sequence of events showing a vertically upward discharge of FC-218 from a plastic vessel.

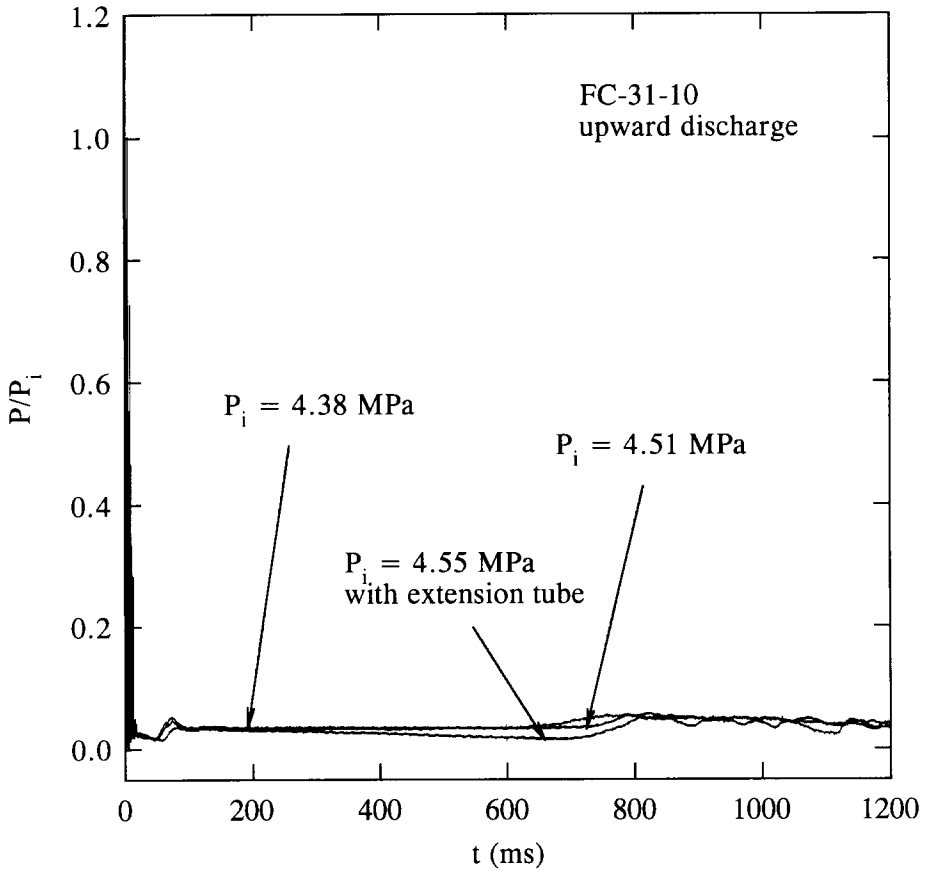

Figure 74. Temporal variations of internal pressure during upward discharges of FC-31-10 with and without an extension tube.

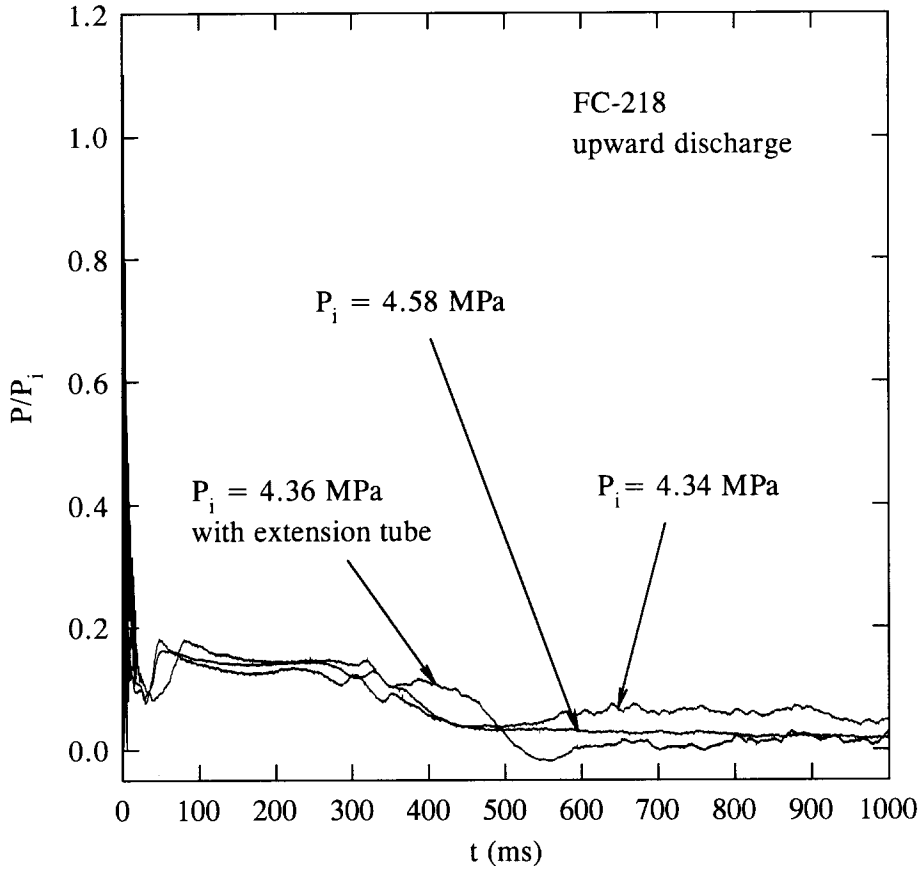

Figure 75. Temporal variations of internal pressure during upward discharges of FC-218 with and without an extension tube.

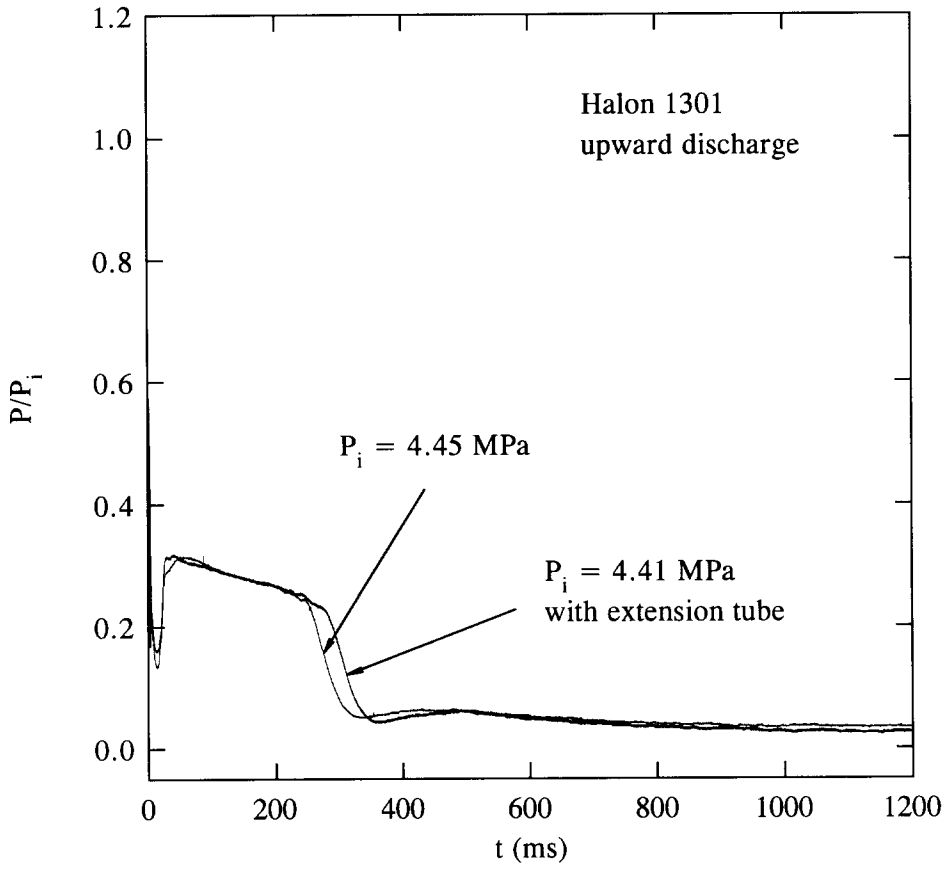

Figure 76. Temporal variations of internal pressure during upward discharges of halon 1301 with and without an extension tube.

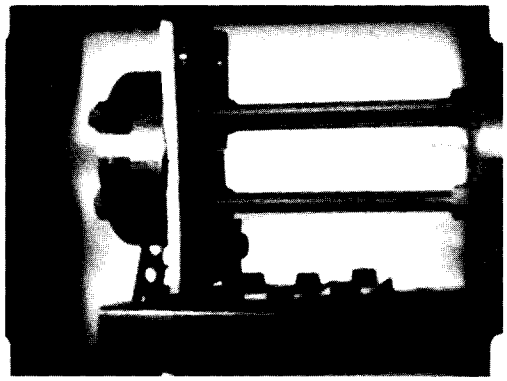

1 ms

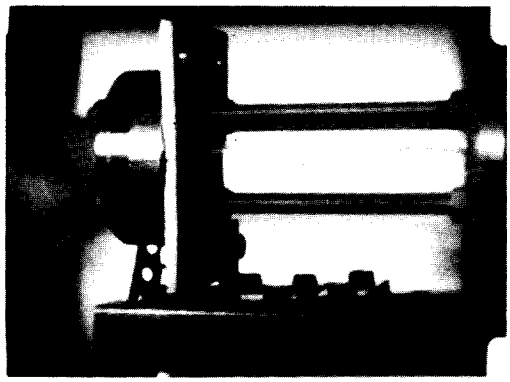

2 ms

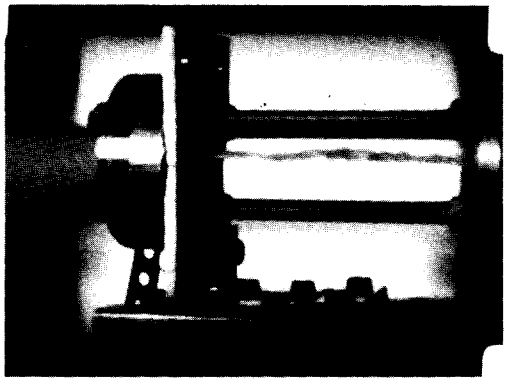

10 ms

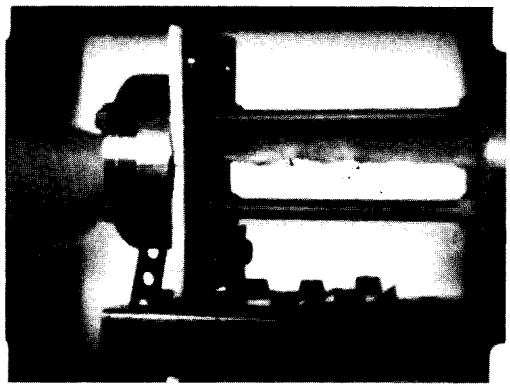

20 ms

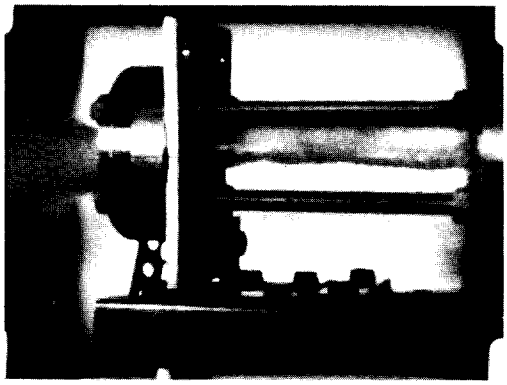

80 ms

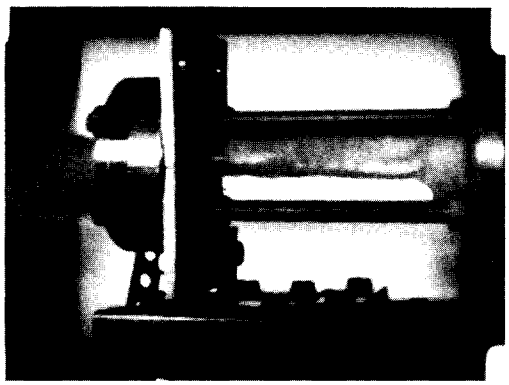

100 ms

Figure 77. Photographic sequence of events showing a horizontal discharge of FC-218 from a plastic vessel.

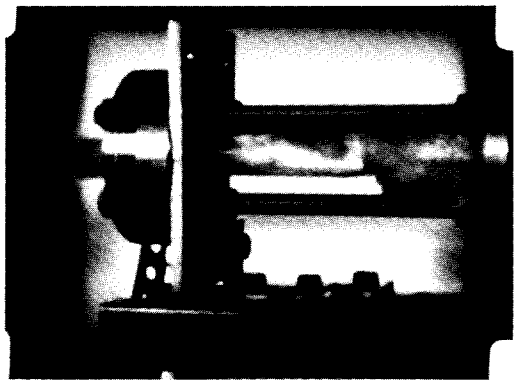

150 ms

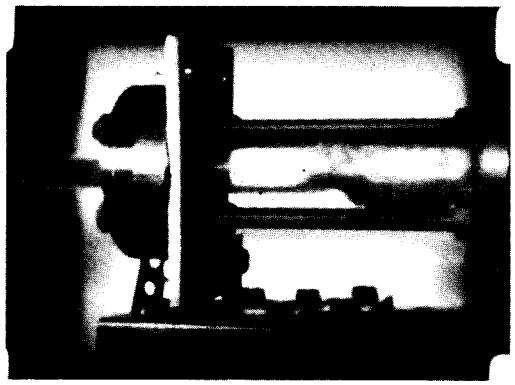

200 ms

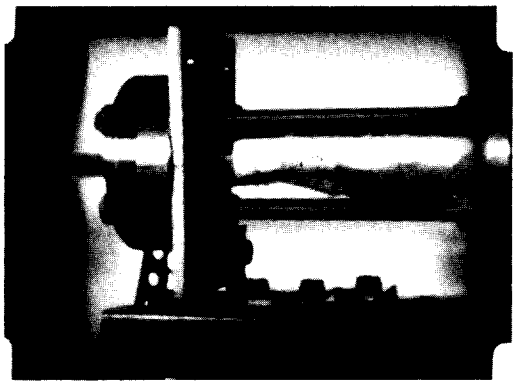

250 ms

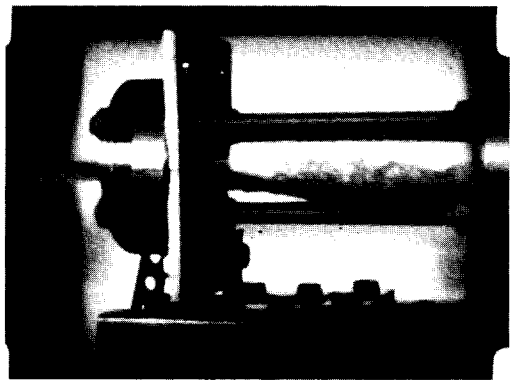

300 ms

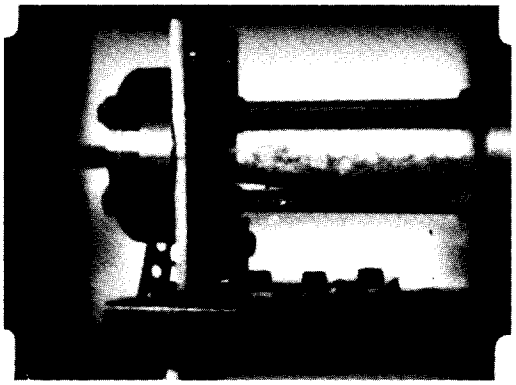

350 ms

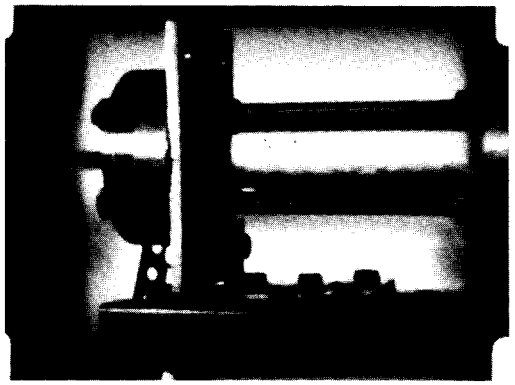

400 ms

Figure 77. (continued) Photographic sequence of events showing a horizontal discharge of FC-218 from a plastic vessel.

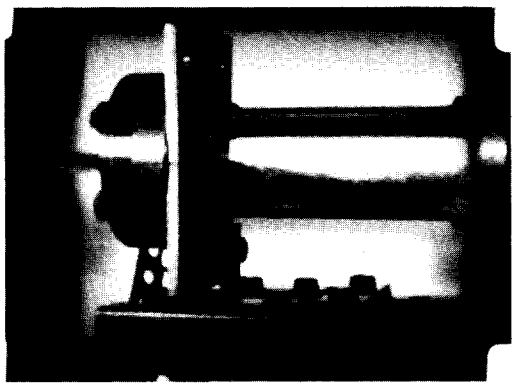

440 ms

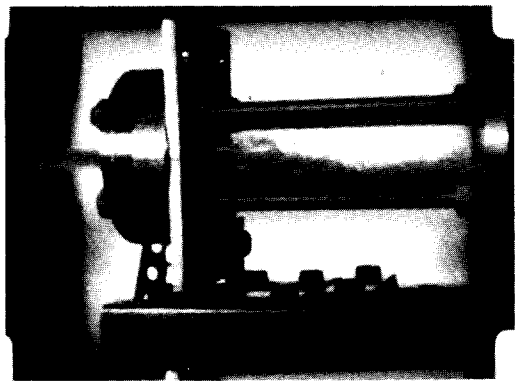

480 ms

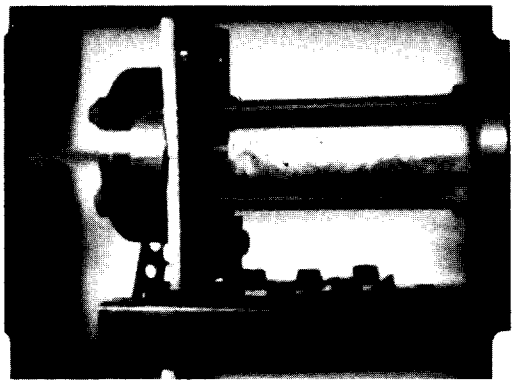

520 ms

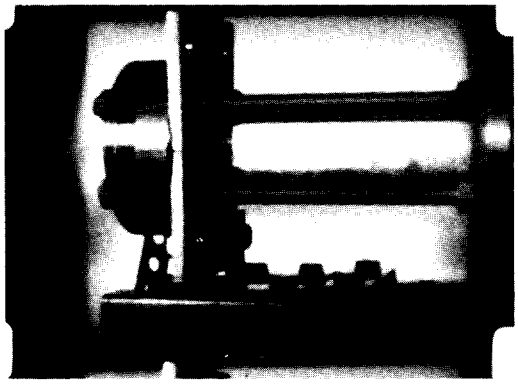

580 ms

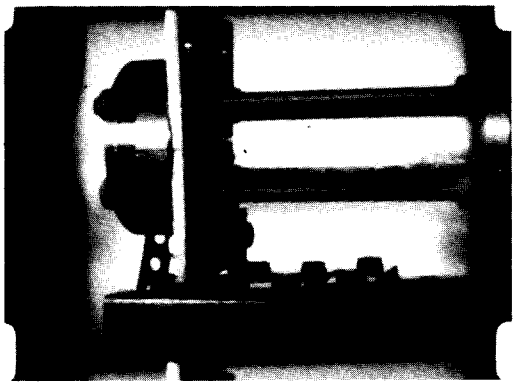

600 ms

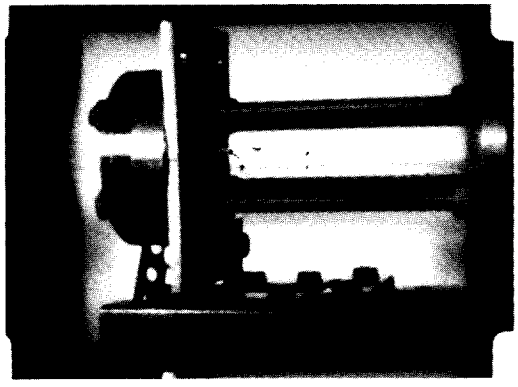

650 ms

Figure 77. (continued) Photographic sequence of events showing a horizontal discharge of FC-218 from a plastic vessel.

Figure 78 and Figure 79 show the pressure-time histories for horizontal releases of FC-31-10 and FC-218. The results were obtained from the pressure transducer that was initially positioned at a location below the liquid level. Therefore, the measured pressure traces represent a combination of the pressure change in two stages during discharge. In the first stage, the pressure measurements were made when the liquid level was still above the position where the transducer was located. In the second stage, the pressure measurements were obtained when the liquid level had dropped below the location of the pressure transducer. In other words, the pressure in the vapor phase was measured.

In Figure 78 and Figure 79, after the initial rapid decrease in pressure, the slight rebound in pressure due to initiation of boiling and bubble growth is not apparent in the case of FC-31-10, but is noticeable in the case of FC-218. Thereafter, the pressure decreases continuously until the liquid is completely boiled off. The reason for the presence of small humps in the pressure traces of FC-31-10 at 500 ms $< t <$ 1000 ms (Figure 78) is unclear. It is conjectured that the liquid level in the vessel during this time interval is still slightly below the location of the pressure transducer because of the relatively slow boiling process of FC-31-10, and that any sloshing of the liquid upon the transducer could raise the pressure reading. The shifting of the location of the hump in the two pressure traces may be indicative of such an event.

Figure 78 and Figure 79 also show results for temporal variations of pressure when an extension tube is connected to the exit of the rupture disk holder. The behaviors are very similar to that when no extension tube is present.

In the case of halon 1301, the results obtained with and without an extension tube are shown in Figure 80. Because a stainless steel vessel was used, no visual observations were made. Therefore, it is unclear at present why the small pressure rebound is apparent in the case of an extension tube but is not present when the extension tube is absent.

3.4.4 Conclusions. In downward discharge, the average volumetric flow rates for all the alternative liquid agents are very similar. No internal boiling was observed for downward discharge of HFC-236fa, FC-31-10, FC-318, HCFC-124, HFC-227ea, HFC-134a, FC-218, HCFC-22, and HFC-125. Based on results for FC-31-10 and FC-218, the behavior of the liquid inside the vessel during discharge was found to be very similar whether an extension tube was present or absent at the vessel exit. A twofold increase in the initial discharge pressure decreases the emptying time of the liquid approximately by half. The effect of a restrictor plate at the vessel exit on the discharge process is to increase the liquid emptying time. A twofold increase in the diameter of the orifice plate increases the average volumetric flow rate by approximately fourfold. Liquid discharged at cold temperature behaves very similarly to that at room temperature. However, when the vessel is discharged vertically upward or horizontally, the discharge process depends on the boiling point of the agent. Agents with higher boiling points remain in the vessel for a considerable amount time before they can be boiled off.

3.4.5 Recommendations. Based on the above findings, it is recommended that in order to empty the liquid contents from the pressure vessel within tens of milliseconds, the vessel should be discharged in a vertically downward position. If the vessel were to be designed to increase release rates and to withstand higher internal pressure, higher initial charge pressures are also recommended. In addition, further study of discharge at high temperatures is needed because of concern regarding boiling liquid expanding vapor explosion (BLEVE).

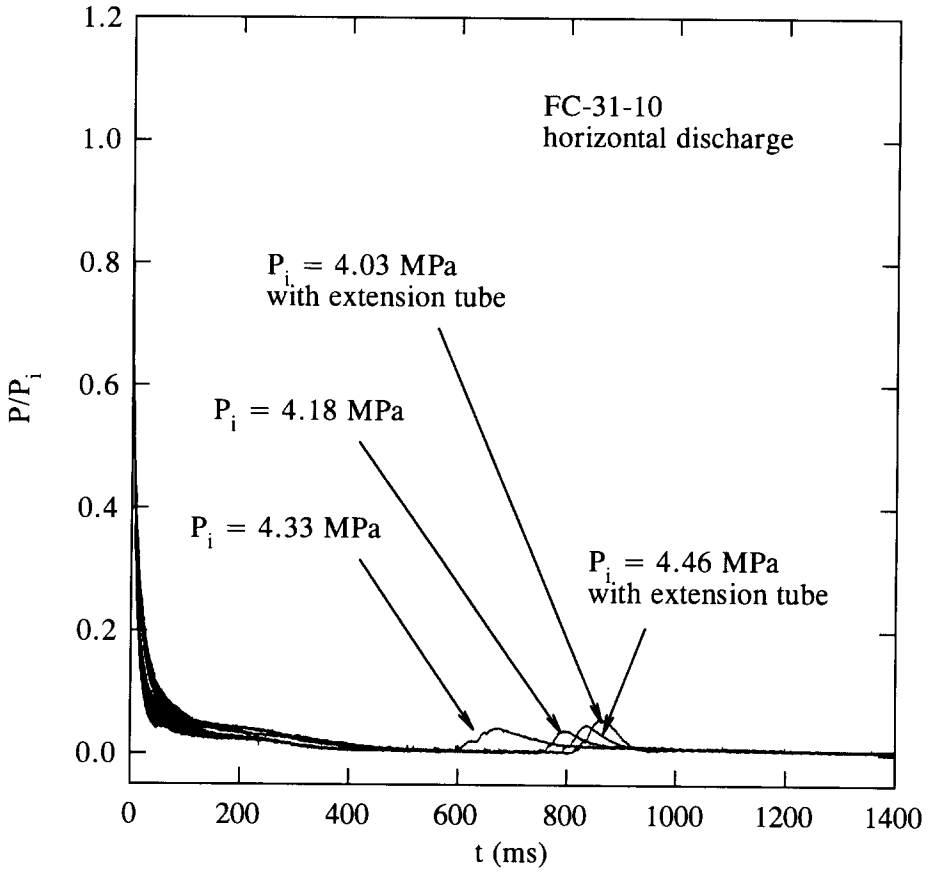

Figure 78. Temporal variations of internal pressure during horizontal discharges of FC-31-10 with and without an extension tube.

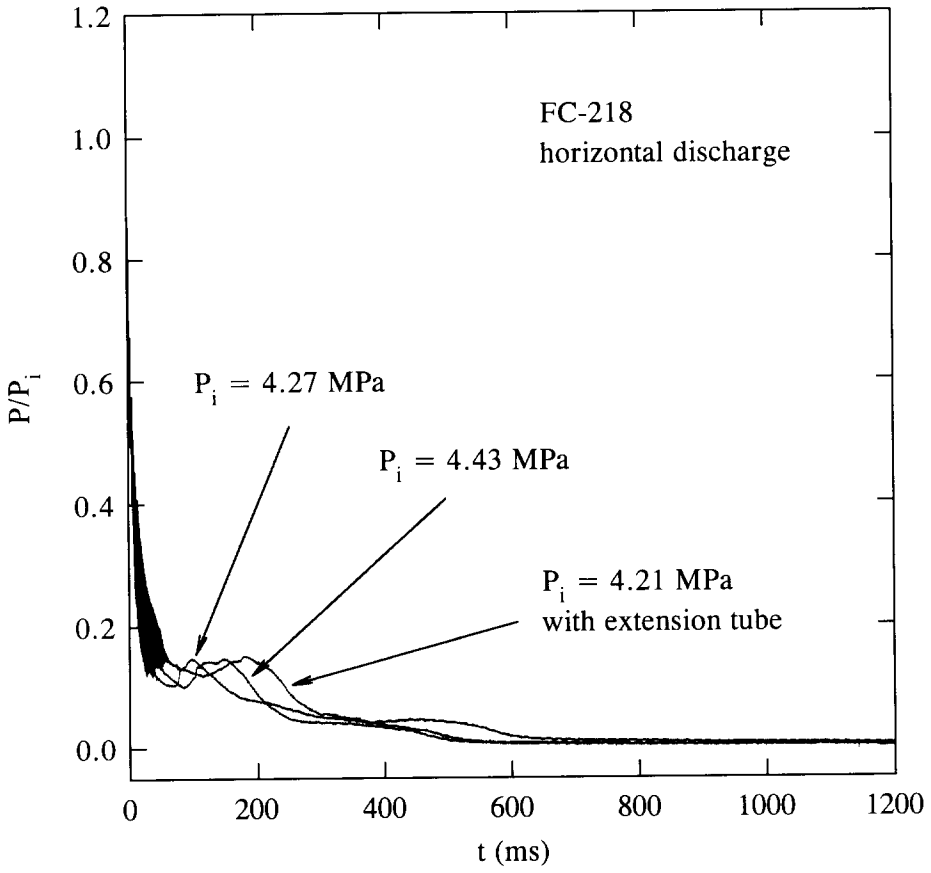

Figure 79. Temporal variations of internal pressure during horizontal discharges of FC-218 with and without an extension tube.

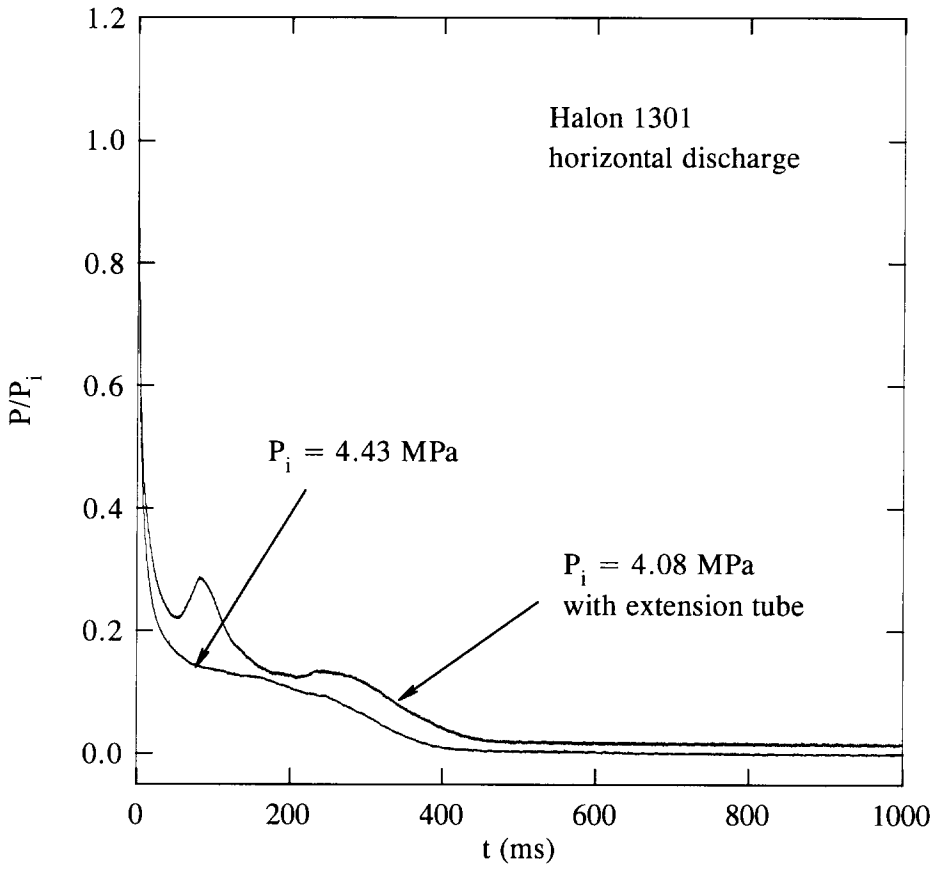

Figure 80. Temporal variations of internal pressure during horizontal discharges of halon 1301 with and without an extension tube.

3.5 Measurements of Agent Dispersion

3.5.1 Introduction. The purpose of this part of the research effort was to characterize experimentally the dispersion and evaporation behavior of the eleven potential replacement fire extinguishing agents. The design of the experiments was based on the reasonable hypothesis that effective fire extinguishment requires both rapid dispersion of the agent within a volume as well as rapid gasification following release of the agent from a pressurized bottle. These properties are expected to be crucial for both the dry bay and engine nacelle applications. However, they are particularly relevant for the dry bay application due to the extremely rapid fire suppression times (on the order of tens of milliseconds) required.

The agent must be dispersed throughout the volume to ensure that all regions of flame are suppressed. This requires that the agent not only be rapidly released from the bottle, but also that it be rapidly and effectively mixed with the surrounding gases. Rapid vaporization of the liquid is desirable for two reasons. While the liquid may, in some circumstances, be dispersed more rapidly as a two-phase mixture, it is also true that it is unlikely to be dispersed evenly throughout the volume. Since the fire location cannot be specified, it is necessary to have full vaporization to ensure a more uniform distribution. The proposed halon replacement agents are not expected to be as effective as halon 1301 for these fire fighting applications since they do not have the effective chemical suppression mechanism associated with the presence of bromine atoms. Principal mechanisms for extinguishment are therefore likely to be heat extraction and dilution as well as the physical effects associated with the rapid release of the agent (*i.e.*, flame extinction due to stretch). Complete vaporization ensures the maximum interaction between the agent and the fire zone.

With the exception of one of the chemicals (FC-116), all of the proposed alternatives are liquids when stored under pressure at room temperature and are superheated when released as liquids into the ambient atmosphere. As a result, partial rapid vaporization is to be expected when these agents are released into an ambient environment at room temperature. A review of the literature indicated that while there have been investigations of flashing liquids reported, none of these previous experiments dealt with the rapid, short-time releases which are characteristic of the current study. Here we summarize the literature which was reviewed during the course of this effort in order to provide an overview of the existing understanding and to provide a basis for later discussion.

One of the earliest investigations of released superheated liquids was the study of Brown and York (1962). These authors investigated sprays formed by the release of water, CFC-11 and water saturated with carbon dioxide. They noted that the flashing of a superheated liquid or a pressurized liquid with dissolved gases provides an additional mechanism for the breakup of a liquid stream (in addition to the classical mechanisms resulting from surface tension forces (Rayleigh, 1878) and aerodynamic forces (Weber, 1931)). They pointed out that for adiabatic conditions the flashing of a superheated liquid would occur by the extraction of latent heat from the liquid to provide the energy necessary to evaporate the liquid. Thermodynamic equilibrium is attained when the fraction of liquid converted to gas is sufficient to cool the remaining liquid to it saturation pressure.

Results reported included the distance required for the liquid jets to break up as well as characterization of the sprays generated. Several of their conclusions are relevant to the current investigation. They reported that a liquid jet does not "shatter" abruptly when the liquid just becomes superheated, but that a well defined amount of superheating is required for shattering to occur. A dependence of the flashing behavior on the jet diameter was characterized by correlating the liquid breakup times with the Weber number (We), defined as

$$We = \frac{\rho_g U_o D}{2\sigma}, \tag{28}$$

where ρ_g is the density of the gas surrounding the liquid jet, U_o is the jet velocity, D is the jet diameter, and σ is the liquid surface tension. The times required for jet breakup increased with decreasing D. A transition in the behavior was observed for $We = 12$.

Brown and York argued that the times required for flashing of pressurized liquid jets containing dissolved gases should be considerably longer than those for superheated jets due to molecular diffusivity considerations. Experimental evidence was provided which supports this conclusion.

Measurements of drop sizes generated by the flashing liquids showed that flashing provided an effective mechanism for atomizing the liquid. The flashing of the liquids resulted in a rapid expansion of the flow.

Lienhard and coworkers (Lienhard, 1964; Lienhard and Stephenson, 1966; Lienhard, 1966; Lienhard and Day, 1970) developed a model for predicting the time required for superheated liquids to flash and compared the findings with experiment. The first of these papers (Lienhard, 1964) considered the conditions for which bubbles growing in a liquid are stable to growth or collapse. Results were based on thermodynamic arguments. Lienhard and Stephenson (1966) considered the kinetics of bubble growth. Their analysis was based on equations for bubble growth developed earlier by Deragarabedian (1953), Forster and Zuber (1954), and Plesset and Zwick (1954). In order for bubbles to grow spontaneously they must attain a critical size. For smaller sizes, bubbles tend to redissolve into the liquid. Nuclei bubbles therefore arise due to fluctuations in the local environment which favor their formation. When such fluctuations result in a bubble with sufficient size to continue growth, a large bubble will form. Generally the formation of a larger bubble will "trigger" the growth of additional bubbles. Using arguments based on the distribution of disturbances in the liquid, Lienhard and Stephenson derived an approximate relation for the period required for a superheated liquid to flash which can be written as

$$t_d \sim \frac{1}{A(P_v - P_{amb})^{7/2}}, \tag{29}$$

where t_d is the delay time for bubble growth, A is the cross sectional area for the liquid flow, P_v is the vapor pressure for the liquid at its release temperature, and P_{amb} is the ambient pressure. Note that P_v-P_{amb} is a measure of the superheat based on pressure. Experimental results were presented for the flashing of superheated water which supported the use of this equation.

In the same paper these authors derived an expression for the amount of work that an isobaric expansion of a superheated liquid can do. For the case where the saturation temperature for the liquid, T_l, is much greater than the superheat expressed in temperature terms, T_l-T_{sat}, the resulting expression is

$$w = C_p \frac{(T_l - T_{sat})^2}{2T_{sat}}, \tag{30}$$

where w is the amount of work which can be done by the flashing and C_p is the constant pressure heat capacity which had been assumed to be constant.

The above analysis for the flashing time was extended by Lienhard and Day (1970) [see also Day (1969)] in order to derive a more general equation applicable to different superheated fluids. They

argued that the delay time for bubble growth should scale with the density of the saturated liquid, ρ_l, D, σ, and the superheat, P_v-P_{amb}. Using the Buckingham Pi-Theorem, they reduced these variables to two dimensionless variables which should correlate the experimental data. These were a dimensionless dwell time, Φ,

$$\Phi \equiv \frac{(P_v - P_{amb})^{5/2} D t_d}{\sigma^2 \sqrt{\rho_f}}, \tag{31}$$

where ρ_f is the liquid density, and a dimensionless jet diameter, Ψ,

$$\Psi \equiv \frac{D(P_v - P_{amb})}{\sigma}. \tag{32}$$

By using Equation (29) and eliminating t_d and $(P_v$-$P_{amb})$ from the equations one finds that

$$\Phi\Psi = constant \tag{32}$$

Once the constant in Equation (32) is determined experimentally, it should be possible to predict t_d for any superheated fluid. Based on measurements of delay times for jet flashing with water and liquid nitrogen, the constant in Equation (32) was found to equal 2.12×10^{13}. This paper also has a detailed discussion of the conditions under which liquid jet break up occurs as the result of capillary and aerodynamic instability.

In a brief paper, Lienhard (1966) considered how the spreading of a flashing liquid jet can be understood in terms of the amount of work which the flashing can do on the system (Equation (30)). The analysis was done in terms of the radial velocity, U_r, imparted to the spray by the flashing. The maximum such velocity, $U_{r,max}$, is

$$U_{r,\max} = \left(\frac{C_p}{T_{sat}}\right)^{1/2} (T_l - T_{sat}) \tag{33}$$

Lienhard argued that all of the available work would not be used to impart radial momentum and that only a fraction, C, would be available. Based on experimental spreading angles for flashing superheated water jets he estimated that $C \approx 0.04$.

Solomon *et al.* (1982) reported limited measurements for a flashing jet of CFC-11 and superheated fuels. They found that flashing due to small amounts of superheating was very effective in generating atomized liquid flows.

Celata *et al.* (1982) have provided a very brief description of experiments on the release of superheated water. They found that flashing took place very rapidly, and that the spreading angle of the two-phase flow increased with increasing superheat. Using a probe, they recorded dynamic pressures within the flow field. Unlike previous investigations, they concluded that evaporation was occurring on the outside of the flow and that there was a narrow liquid core in the center of the flow surrounded by a two-phase shell.

Moodie and Ewan (1990) provide a nice introduction to the release behavior of liquid jets. They discussed the behavior of flashing jets and showed a photograph of a flashing CFC-11 jet. The analysis was complicated because flashing seemed to occur within the vessel orifice. They measured

the peak droplet sizes which suggested that the droplet size decreased with increasing superheating. Time-averaged temperature measurements were also provided. The temperature profiles seem to suggest that the entire jet is flashing unlike the findings of Celata *et al.* (1982). The temperature measurements also indicate that the entrainment of air plays a critical role in the ultimate evaporation of the superheated liquid.

These authors also made mass fraction measurements of CFC-11 and air in the flow field. These measurements also suggest the two-phase flow covered a large extent of the flow. Velocity measurements were also reported. These measurements showed that measured flow velocities were considerably higher than expected based on liquid flow rates at the vessel exit. Radial velocity profiles in the region near the vessel were non Gaussian, but tended to attain a Gaussian profile as the measurement location was moved further downstream.

Superheated releases of CFC-11, chlorine, methylamine, and cyclohexane have been investigated by Johnson and Diener (1991). In these experiments the liquid fraction of the two-phase flow was captured. The data indicated that there were well defined superheat points for which the liquids flashed near the vessel exit. Under these conditions the amounts of liquid trapped decreased significantly. Comparisons were made with a model designed to predict the behaviors. In general, the agreement was not very good.

There are a variety of systems employed for the release of halon 1301 into dry bays and nacelles. It was beyond the scope of this study to investigate a wide range of release configurations. For this reason, the decision was made to characterize the spreading and mixing characteristics of the agents following release from a generic system based on the vessel developed to study the release rate of agents (see Section 3.3).

3.5.2 Experimental Methods. As mentioned above, there were very few investigations available in the literature to guide the design of a system for characterizing the dispersion and evaporation behavior of the agents. As a first step in the design process a high-speed video system[1] was used to record a downward release of HCFC-22 from the vessel at a rate of 1000 frames/s. A burst disk providing a nominal pressure of 4.1 MPa was employed and the 0.0005 m^3 vessel was filled one-third full. A series of sequential photographs from the high-speed video are reproduced in Figure 81. Lighting for the camera was provided from the rear and front of the release.

As can be seen from Figure 81, the mixing process is extremely complex. When the burst disk first opens, a flashing is observed which results in a rapid expansion of the agent in both the downward and radial directions. The lighting from behind the flow is attenuated by the flow. Shortly afterwards a vortex structure forms at the downstream edge of the release and the flow field looks very much like an impulsively started axisymmetric gas jet. Such structures have been observed in liquid jets (Shirakashi *et al.*, 1984) and combustion torch ignition experiments (Cattolica and Vosen, 1987). As the flow develops behind the leading edge it has a nearly linear spreading behavior. This is true near the orifice as well as the far field. The linear expansion seems to be initiated immediately at the orifice of the vessel. At 13 ms into the release a second flashing starts near the vessel orifice and one ms later this flashing has resulted in a very rapid radial expansion. Analysis of the emptying rate of the vessel for these conditions indicates that the second flashing occurred very close to the time when the liquid was completely released from the vessel. Following

---

[1]Kodak Ektapro 1000 Motion Analyzer. The authors thank Michael Howachyn of Kodak for arranging a demonstration of this instrument and for allowing us to record an initial series of high-speed images of the releases.

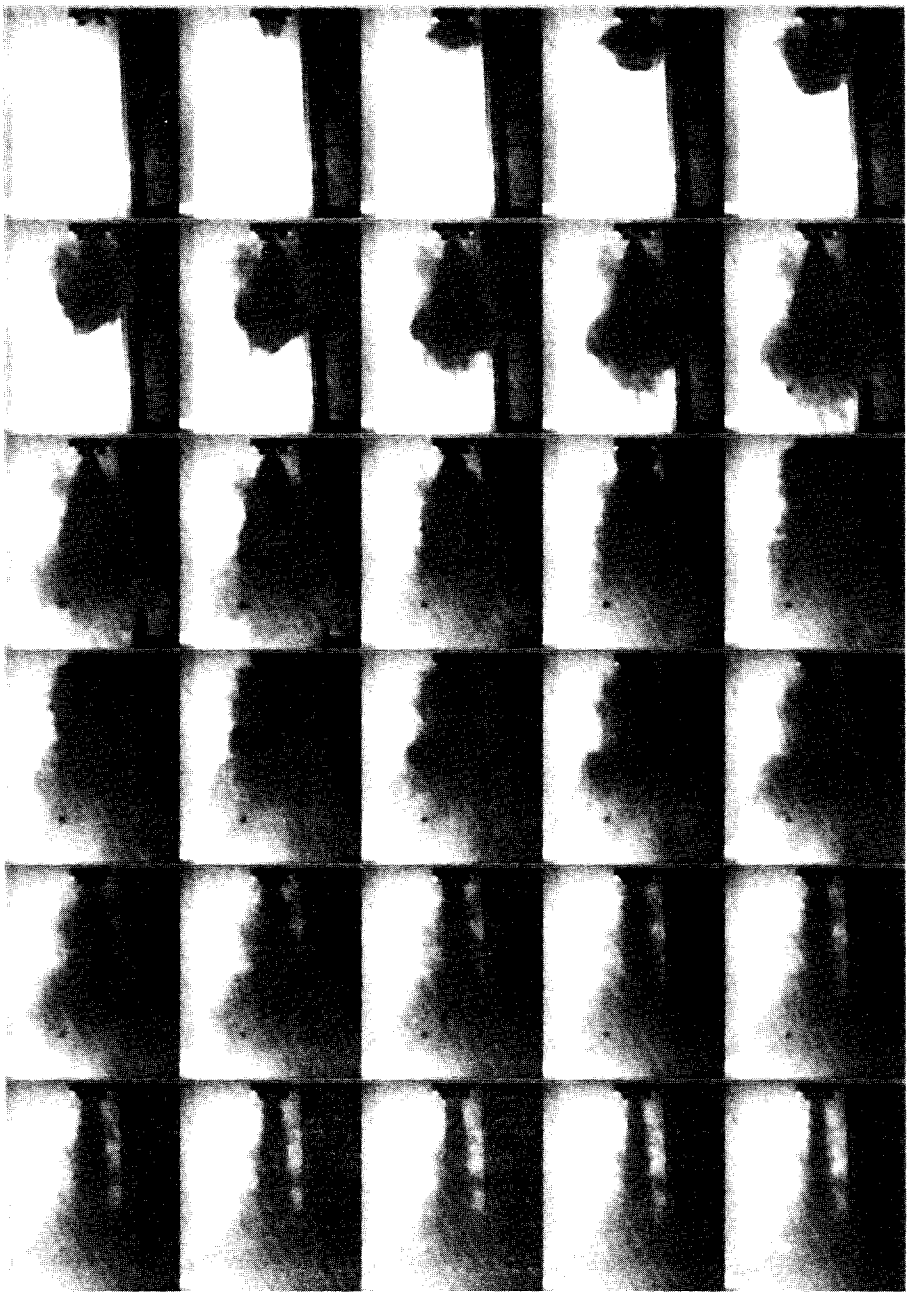

Figure 81. Sequence from a high-speed video (1000 frames/s) of the flow formed by a release of 245 g (1/3 full) of HCFC-22 from the 0.0005 m^3 test vessel. Time increases to the right and from top to bottom.

the second flashing, the release becomes obviously slower and within 30 ms the flow has cleared up and the backlighting is again transmitted.

Additional high speed films indicated that the double flashing behavior identified from Figure 81 was typical for downward releases of all of the agents, with the exception of FC-116 which was not investigated since this agent is not a liquid under the storage conditions. All of the agents resulted in nearly total attenuation of a laser beam when they were present in a two-phase state. This observation ultimately determined the type of diagnostics which could be employed to characterize the mixing and vaporization behavior.

Our initial intention was to record the concentration of agent as a function of time using either Rayleigh light scattering (gas concentrations only) (Pitts and Kashiwagi, 1984) or aspirated hot-film probes (Brown and Rebollo, 1972). However, the early visualization studies indicated that these techniques are inappropriate due to the two-phase nature of the flows and their high optical density. A consideration of possible diagnostics revealed that there were no techniques available which would allow quantitative concentration measurements or two-phase flow characterization over the short time periods required.

The discussion above indicates that the two most important flow properties determining the ability of an agent to extinguish a flame are rapid mixing and agent vaporization. A simple, but effective, experimental system was developed to characterize the agents with regards to these two variables. This system combined high speed flow visualization, laser attenuation measurements, dynamic pressure measurements, and an aspirated hot-film concentration probe. To our knowledge, this is the first time that such a system has been used to characterize the behavior of the short period, two-phase flow generated by a release from a pressurized bottle. Figure 82 shows a schematic of the overall system.

The system was used to characterize the flows formed by releases of the agents from the vessels developed to study their release rates (see Section 3.3). Data were recorded for the various release conditions performed during these investigations (see Section 3.4).

3.5.2.1 High-Speed Filming. The same high-speed camera which was used to record the fluid level inside the transparent vessel (see Section 3.4.2) simultaneously recorded the release of the agent in regions near the vessel exit. This was accomplished by placing the camera such that it recorded the liquid behavior inside the transparent vessel as well as locations immediately downstream of the vessel exit. The field of view imaged by the camera could be varied by adjusting the camera placement and distance from the vessel. Most data were recorded with a field of view of roughly 0.40 m width and 0.10 m height.

Selected frames of these films were used to estimate the axial and radial velocities of the agents immediately following release. The approach used image analysis (see Section 3.4.2) to locate the downstream and radial edges of the release at different times and calculate the corresponding velocity. The radial velocity was determined for the downstream location (13 mm from orifice) where the pressure transducer (see ahead) was located. Due to the relatively small area of the near-field release which was imaged, normally only two such measurements could be made before the agent covered an area larger than the field-of-view. Note that frame 1 is defined as the frame where it is clear that the release of the agent has begun. As a result, the time for frame 1 can be anywhere from 0 to 0.49 ms (for a framing rate of 2000 frames/s) following the bursting of the disk.

3.5.2.2 Laser Attenuation Measurements. This part of the system was designed to measure the rate at which the downstream edge of the released agent moved away from the vessel exit and to provide estimates for the period required for the agent to evaporate. Five laser beams were aligned downstream of the vessel exit and perpendicular to the flow direction. Simple helium neon lasers

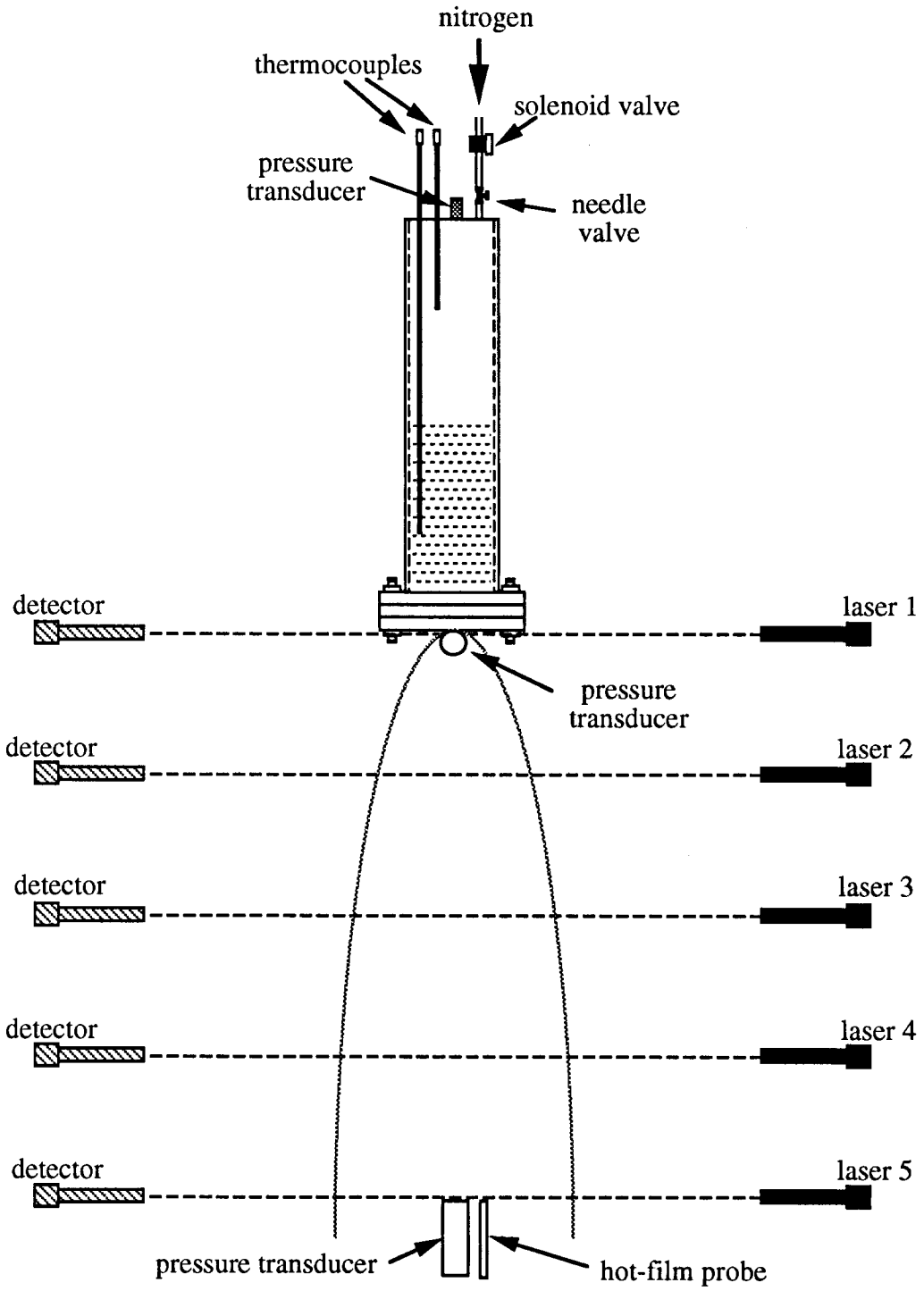

Figure 82. A schematic of the experimental system is shown. Helium-neon lasers and silicon photodiodes are used for the extinction measurements. The piezoelectric pressure transducers and aspirated hot-film probe are described in the text.

(Melles Griot 05-LLR) were mounted on a vertical strut located 1.3 m from the vessel such that the spacing between lasers was nominally 0.3 m. The laser closest to the vessel was positioned across the center of the orifice within 1 mm of the rupture disk holder.

After traversing the flow field the lasers were detected by a series of five photodiodes. The photodiode amplifier circuits and mountings were based on a design by Bryner (1993). Each detector was a silicon photodiode (Hamamatsu S1337-1010BQ) having an active surface area of 100 mm^2. An operational amplifier circuit (Figure 83) was used to generate a voltage proportional to the light intensity striking the photodiode. Each photodiode and amplifier was placed in a rigid mount with a connector for power input and signal extraction. The mount was drilled and tapped so that a rod could be attached for positioning the photodiode. A tube having an inside diameter of 22 mm and a length of 0.23 m was placed in front of the detector in order to shield the photodiode from ambient light in the room. In some cases neutral density filters were used to ensure that the outputs of the photodetectors were not saturated. Circuits housed in a single box were built to provide power for the photodiodes and signal outputs on BNC connectors for a maximum of eight detectors. For the experiments reported here only five detectors were used.

The photodetectors were mounted on a vertical strut located on the opposite side of the room from the lasers. Each photodiode system was aligned with one of the laser beams in such a way that the beam was centered on the active area. Figure 84 is a photograph of the photodiode detectors.

The voltage outputs for the photodiodes (numbered 1 to 5 with 1 closest to the vessel) were recorded using the data acquisition system described below. Tests showed that laser #1 was totally attenuated very rapidly (in less than 40 μs) when the disk burst. The attenuation of this laser beam was used to define time 0 for the experiments. It is interesting that this laser beam was normally found to be totally attenuated several hundred microseconds before a pressure drop was recorded by the pressure transducers within the vessel.

3.5.2.3 Dynamic Pressure Measurements. Two piezoelectric pressure transducers were used external to the vessel to record the dynamic pressure of the releases. The transducers were Kistler 603B1 models used with Model 5004 amplifiers. The amplifiers included 180 kHz frequency filters and were operated in the "long" integration mode to allow the pressure to be tracked over the relatively long time (generally several hundred milliseconds) of a release. The output of the amplifier is a voltage proportional to the pressure. Usually a range of 687 kPa/V was used.

One of the pressure transducers was located near the vessel exit at a distance 13 mm downstream of the rupture disk holder of the vessel and 46 mm from the centerline defined by the center of the orifice. It was oriented so that it was perpendicular to the centerline. Note that the orifice was nominally 19.1 mm in diameter, and the pressure transducer was located 4.8 orifice radii from the centerline.

The second pressure transducer was positioned along the centerline of the release at a downstream position just beyond the point where the fifth laser beam crossed the centerline (1.3 m downstream of the vessel exit). It was oriented perpendicular to the flow direction.

Both pressure transducers were mounted in the center of conically shaped pieces of aluminum designed to protect the transducers and, at the same time, minimize their interaction with the flow field. The near-field transducer and its mount were attached to a rod which allowed positioning of the transducer. This pressure transducer and its mount can be seen in the early frames of the high-speed films which are shown later. The downstream transducer and its mount were attached to a plate which was capable of surviving the large dynamics pressures sometimes generated by the flow fields at this position. Figure 85 is a photograph showing the pressure transducer mounted in the experimental system.

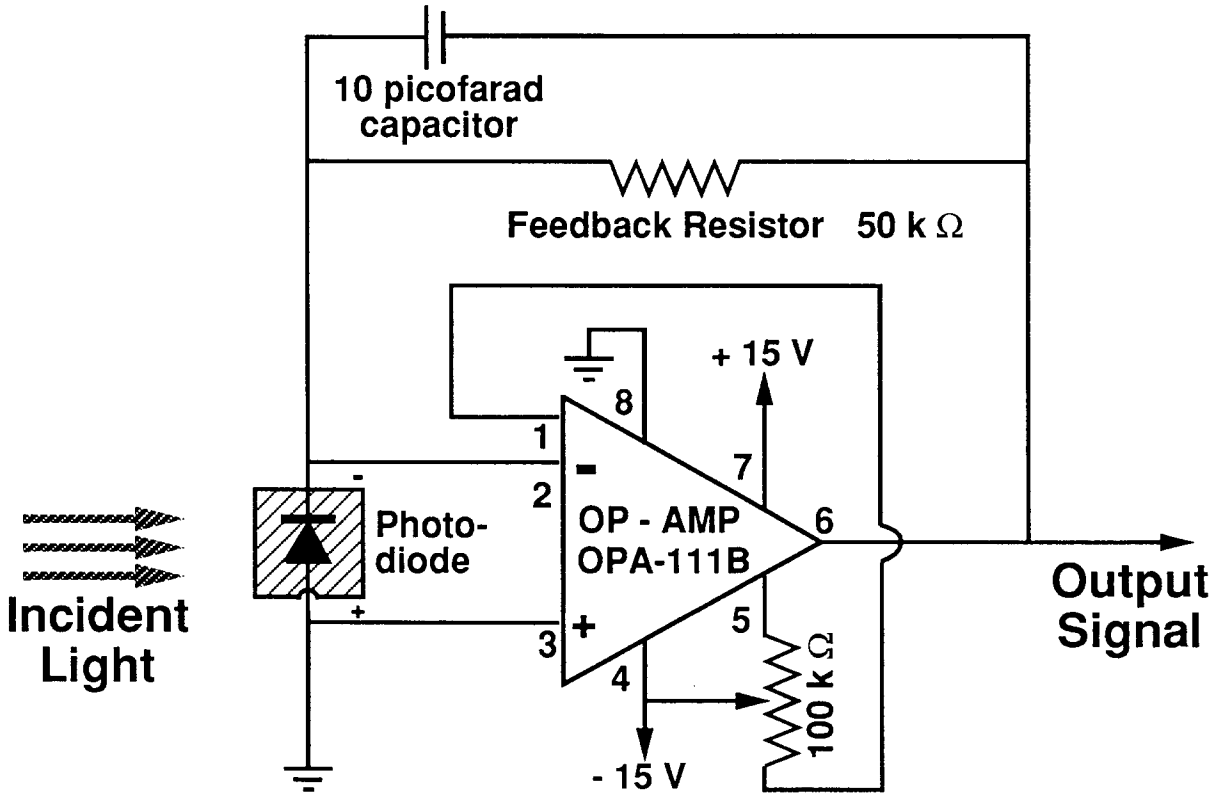

Figure 83. The circuit used to power a photodiode and generate a voltage proportional to the current generated by light striking the detector. The output is a signal proportional to the laser intensity reaching the detector.

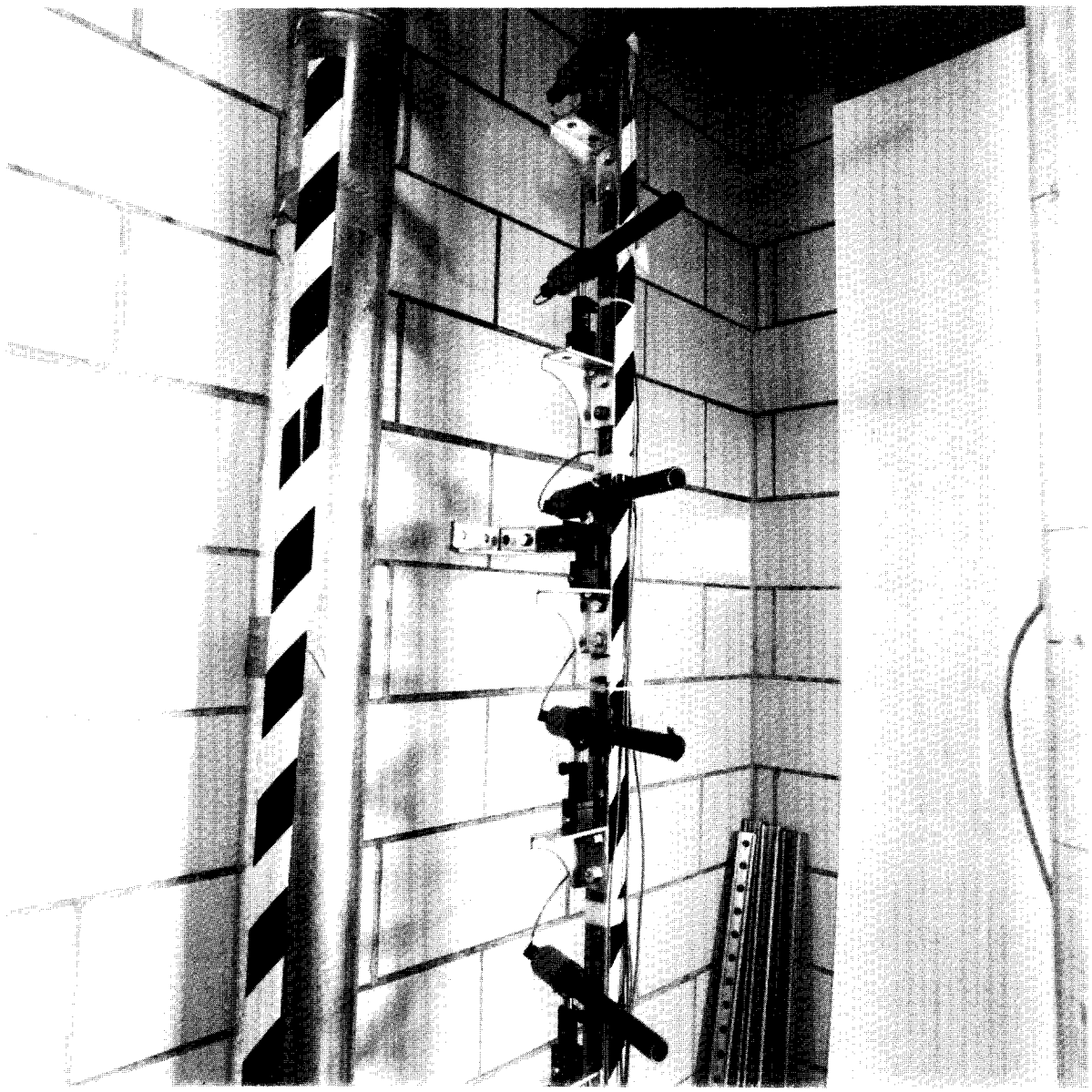

Figure 84. A photograph of the array of five photodiodes and mounts used to record transmitted laser intensities across the flow. The nominal spacing between detectors is 0.3 m.

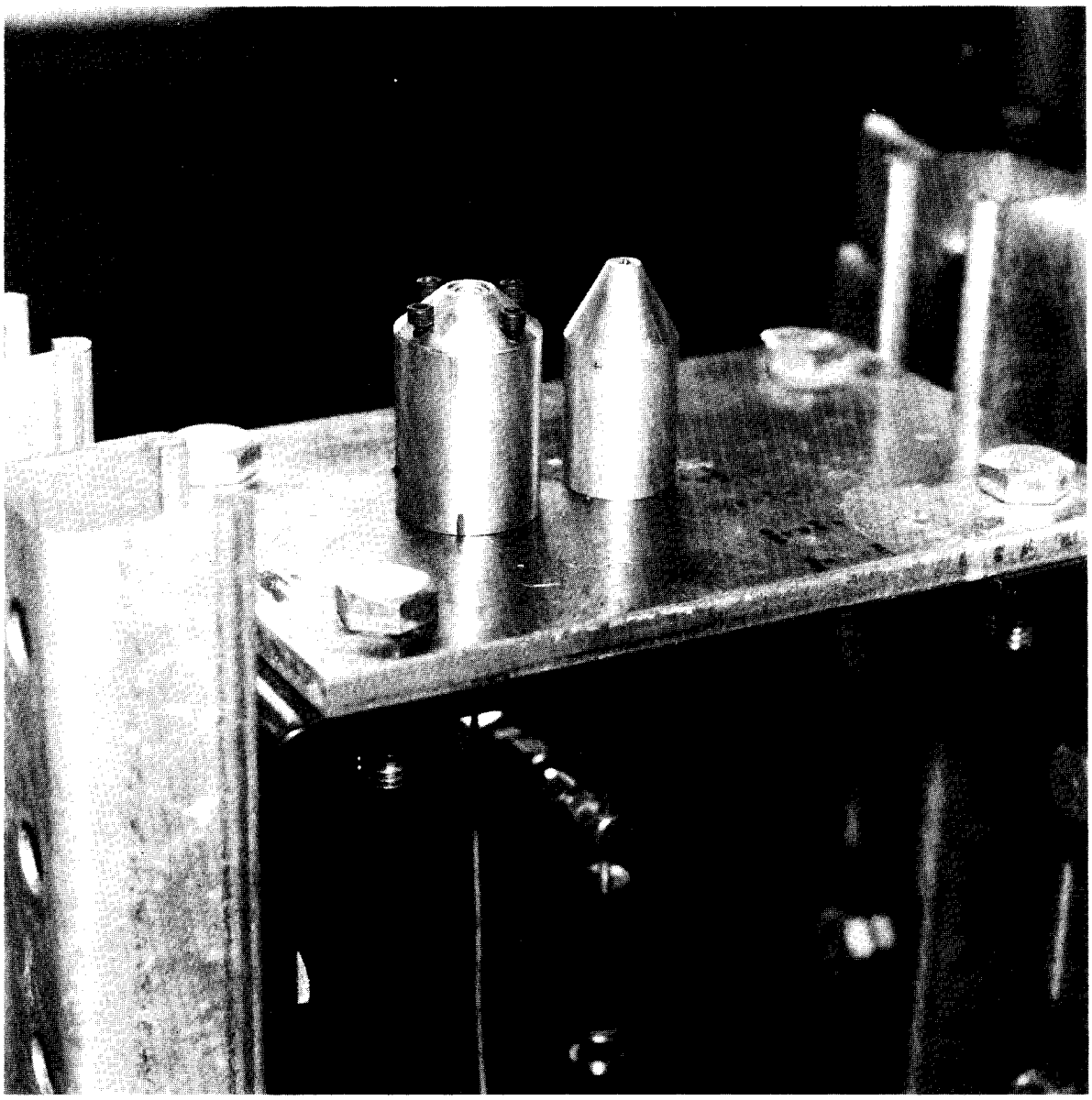

Figure 85. Photograph of the dynamic pressure transducer (left) and aspirated hot-film (right) located 1.3 m downstream of the agent vessel. Probes are placed in metal housings for protection and to provide a means for mounting to an aluminum plate.

An important point with regard to the use of these transducers is the expected response of the transducer to the flow. Davis (1980) used pitot tubes to make similar measurements of dynamic pressure in a gas-liquid mixture flow. He reported that pressure probes respond partially to the incident flow momentum flux with pressure rises of

$$P_m = \tfrac{1}{2}\varepsilon \rho_m U^2 \tag{34}$$

where P_m is the measured dynamic pressure, ε is a factor which varies between 1.0 and 1.85, ρ_m is the density of the mixture, and U is the local flow velocity. Note that Equation (34) reduces to the standard Bernoulli equation form for a pitot tube (Roberson and Crowe, 1980) when ε equals 1. Davis argues that the variation in ε is the result of the relative motion of the gas and liquid in the region of the probe tip. For the case of the piezoelectric transducers used in the current investigation, the stagnation point is very close to the probe and such effects should not be important. Equation (34) with $\varepsilon = 1$ will therefore be used.

3.5.2.4 Aspirated Hot-Film Probe. The aspirated hot-film probe is a device which is designed to record real-time concentrations in isothermal binary gas mixtures. The response time depends on a number of system parameters, but is generally less than 1 ms. The active part of the device consists of a thin quartz rod which is coated with platinum. A small current is passed through the platinum film and resistively heats the surface. The resistance of the device changes with temperature. Feedback electronics are provided which maintain the resistance, and hence the temperature, constant. This is known as the constant-temperature mode. A bridge circuit provides the current necessary to balance the heat losses from the rod. By monitoring this current it is possible to characterize these heat losses which vary with the flow velocity over the rod, the thermal conductivity of the gases surrounding the rod, and the fluid temperature. (Bradshaw, 1971)

The most common use of hot-films is for velocity measurement in a single fluid where proper calibration allows the measured heat losses to be related to velocity. Brown and Rebollo (1972) showed that these devices could be utilized for accurate concentration measurements in isothermal binary gas mixtures by placing the hot-film in the flow generated by extracting gases through a small orifice with a sufficient backing pressure that the gas becomes sonically choked. In this case the velocity only depends on the fluid properties. Since the flow velocity is always constant for a given composition, it is possible to calibrate the instrument with mixtures of the two gases having a range of concentration, and then make accurate concentration measurements in unknown mixtures.

The use of an aspirated hot-film for concentration measurements in the current investigation is complicated by the variations in temperature which occur as the result of the vaporization of the superheated agents and the presence of two-phase flow, which dramatically alters the heat loss behavior of the fluid. For this reason, in the current investigation, these probes were not used for quantitative measurements, but rather provided qualitative indications of the presence of an agent and whether or not a single or two phase fluid was present.

The system employed was commercially available from TSI, Inc. It consisted of a Model 1440-20 aspirating probe used in conjunction with a Model 1053B constant temperature anemometer and Model 1051-2 power supply. The necessary vacuum source for the probe (7 l/m @ 33 kPa) was provided by a small vacuum pump. The probe was placed in a conically shaped aluminum holder to protect it and allow easy mounting. It was positioned near the centerline just downstream of the fifth laser beam by mounting on a plate placed in the flow. It can be seen in the photograph in Figure 85. The voltage output of the anemometer circuit was recorded in the manner described below.

3.5.2.5 Data Acquisition System. The data acquisition requirements for this experiment were demanding. Counting the sensors employed within the vessel, a maximum of eleven sensors were used for a single run. The processes of interest occur at submillisecond time scales. A data acquisition rate of 25 kHz per channel was ultimately used. Note that this corresponds to a total maximum data rate of 275 kHz. Total data collection times varied up to a maximum of 2 s.

The design of the agent release vessel presented an additional difficulty. Due to variations in the pressure required to rupture the disk and the need to flow the pressurization nitrogen into the vessel at a reasonably slow rate, it was not possible to know exactly when the experiment would be initiated. This meant that it was necessary to "trigger" data acquisition using some property of the experiment itself. It was also desirable to record some data prior to the initiation of the experiment in order to provide baselines. This was done by continuously recording the data until a trigger was received and then saving a specified number of data points before and after the trigger signal. This type of data acquisition is referred to as "pretriggering."

The system chosen for the experiments was the Flash 12-Model 1 digitizer from Strawberry Tree. This system provides 16 channels of 12 bit data acquisition at a maximum total data rate of 1 MHz. Voltage ranges can be specified for each channel, and provisions are available for making thermocouple measurements. A daughter board was attached which provided a total high-speed memory of 1 Mbyte. The board was mounted in a 486 personal computer, and data acquisition functions were controlled using Workbench 4.0 software.

The system was operated in the pretrigger mode with the trigger signal provided by the near-total attenuation of laser #1 which was located immediately downstream of the vessel orifice. All of the transducer outputs described above as well as those internal to the vessel (see Section 3.4.2.) were connected to the digitizer, and the voltage ranges adjusted to match the expected signals. Following the conclusion of an experiment, the data was stored for later analysis using SigmaPlot 5.0 software.

3.5.2.6 Test Conditions. These experiments were performed in conjunction with the release experiments summarized in Section 3.4. The majority of these experiments were downward releases at room temperature using nominally 4.1 MPa burst disks and a vessel orifice of 19.1 mm. However, additional runs were performed with a cooled vessel exhausting into a room temperature environment, using burst disks set for higher and lower pressure, and smaller orifices. In a few cases, a half-meter extension tube was attached to the vessel. In this case, the near-field pressure measurements were not made, but the transmitted intensities of the three downstream lasers, the downstream dynamic pressure, and the aspirated hot-film response were recorded. Some measurements were also made for upward releases. In this case laser #5 was placed just above the vessel orifice and provided the timing for the experiment.

3.5.3 Experimental Results

3.5.3.1 High-Speed Filming. The high-speed films provide excellent qualitative insights into the behavior of the agents upon release from the pressure vessel. Figure 86 and Figure 87 show time series taken from films recorded at 2000 frames/s for releases of FC-31-10 and halon 1301. These films were recorded primarily to monitor the behavior of the released agent. The region imaged is 0.19 m (downstream) x 0.33 m (radial). Remarkable differences are observed in the mixing behaviors of the two agents.

The behavior of the FC-31-10 (Figure 86) is summarized as follows. At time 0 the disk bursts and the agent appears as a white plume. During the next 3 ms the agent spreads rapidly in both the radial (maximum of 0.14 m) and axial directions (0.17 m). The flow then develops a mushroom shape which is characteristic of an impulsively started axisymmetric jet. As the flow further

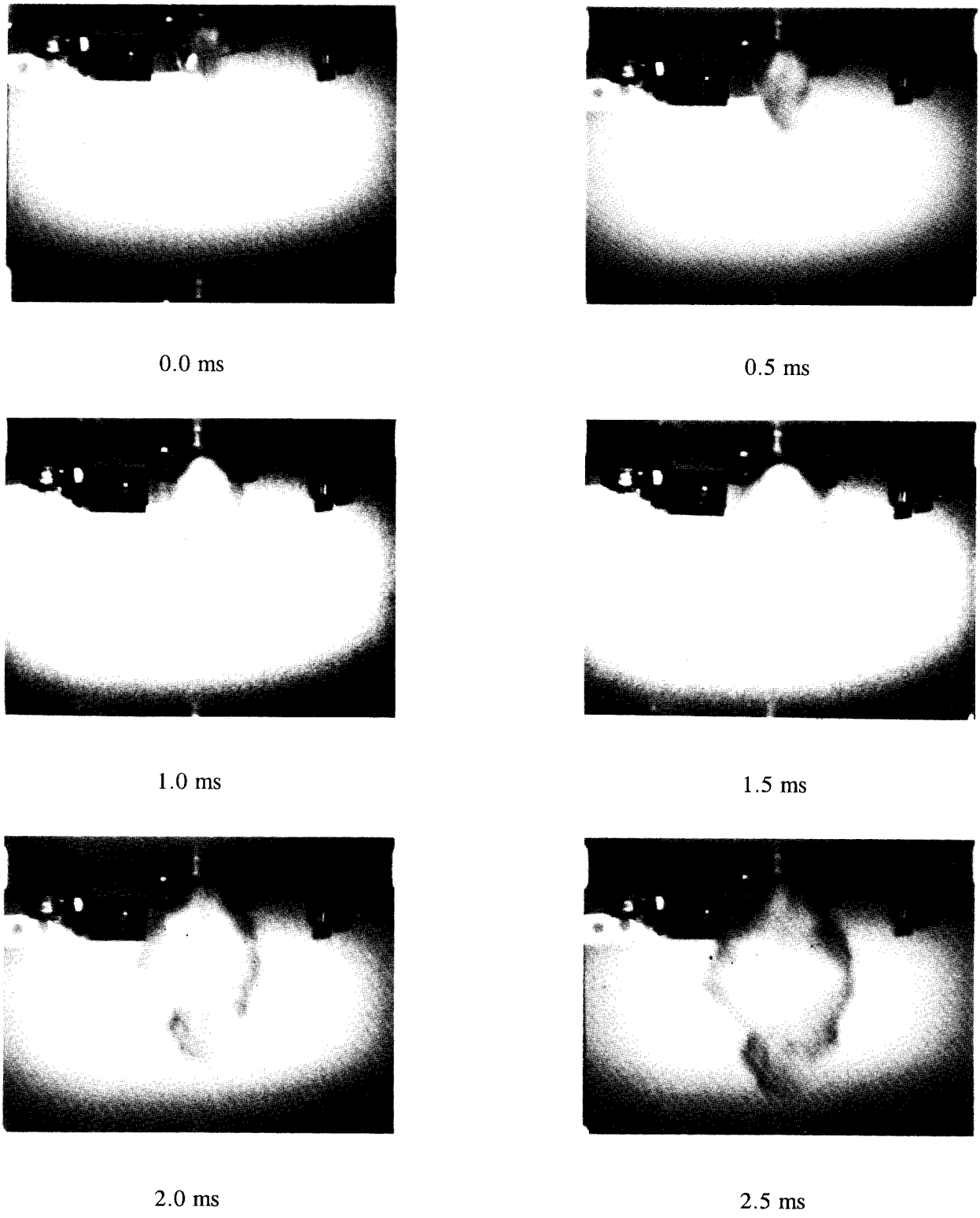

Figure 86. A sequence from a high-speed film (2000 frames/s) of the flow formed by a release of 386 g of FC-31-10 from the vessel. The times indicate the period since the initiation of the release.

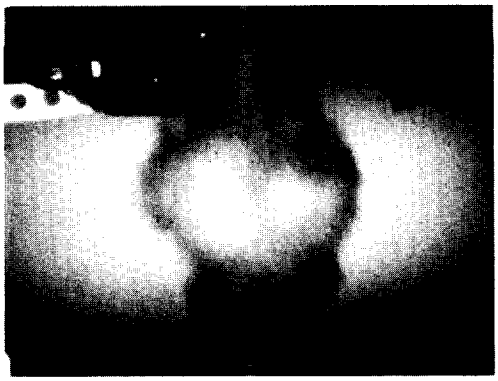

3.0 ms

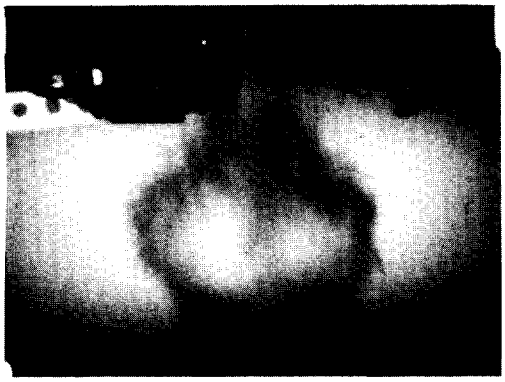

3.5 ms

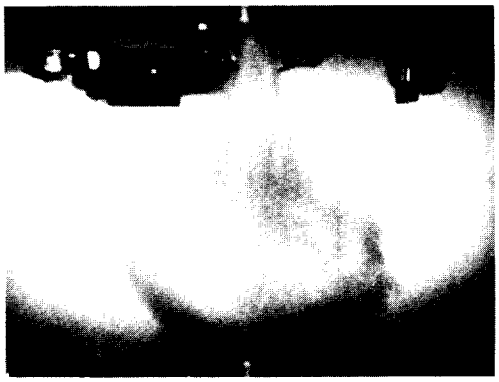

4.0 ms

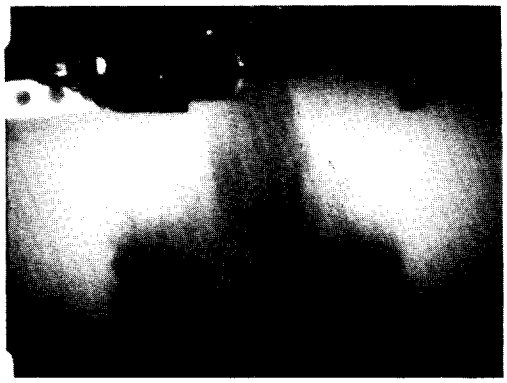

4.5 ms

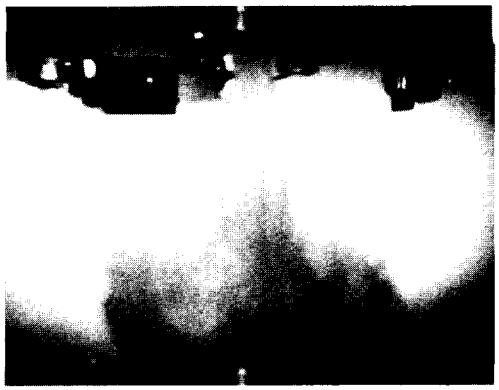

5.0 ms

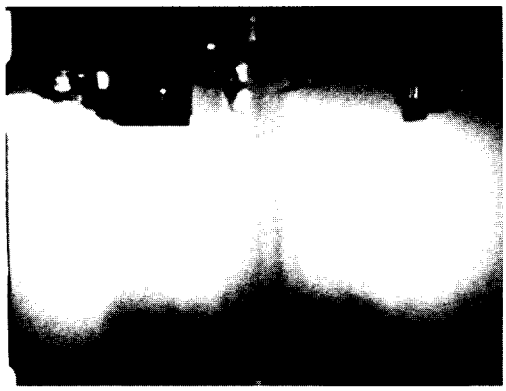

5.5 ms

Figure 86. (continued) A sequence from a high-speed film (2000 frames/s) of the flow formed by a release of 386 g of FC-31-10 from the vessel. The times indicate the period since the initiation of the release.

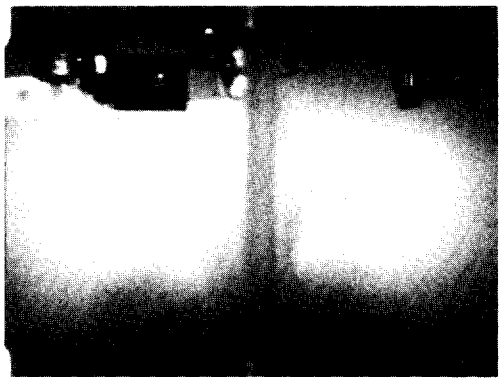

6.0 ms

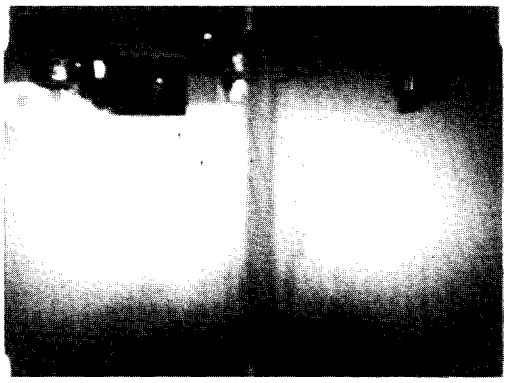

6.5 ms

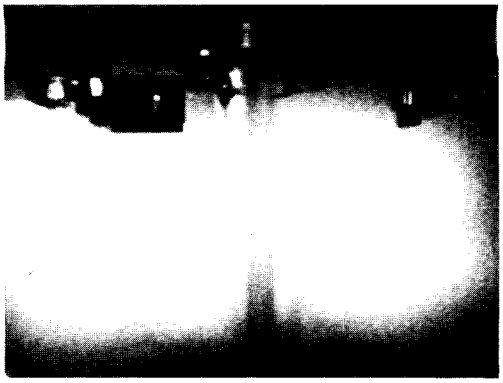

7.0 ms

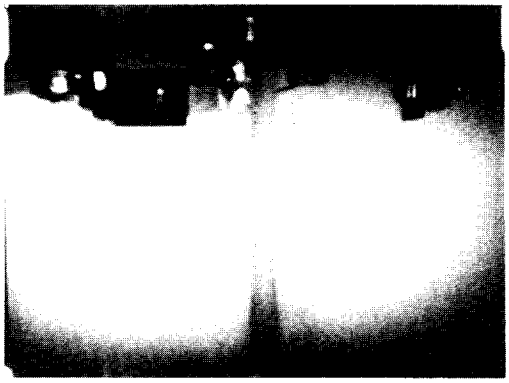

7.5 ms

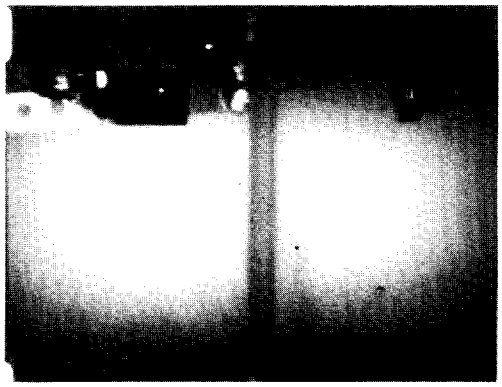

8.0 ms

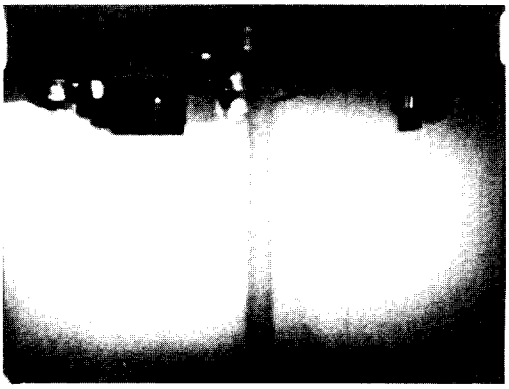

8.5 ms

Figure 86. (continued) A sequence from a high-speed film (2000 frames/s) of the flow formed by a release of 386 g of FC-31-10 from the vessel. The times indicate the period since the initiation of the release.

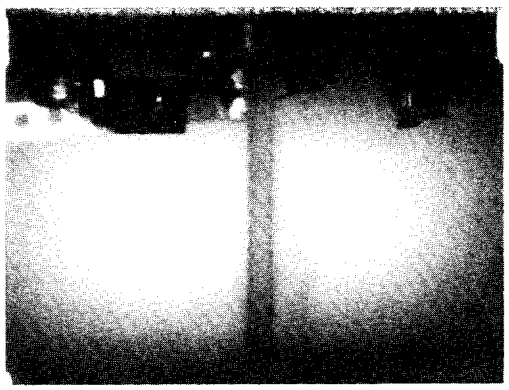

9.0 ms

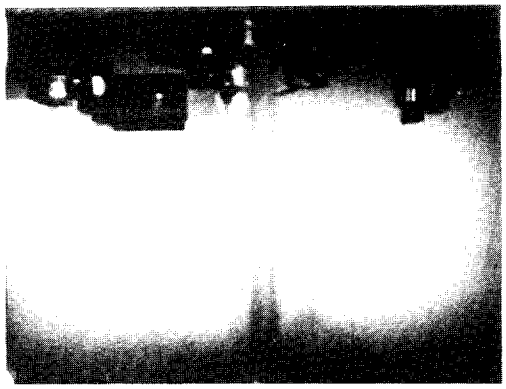

9.5 ms

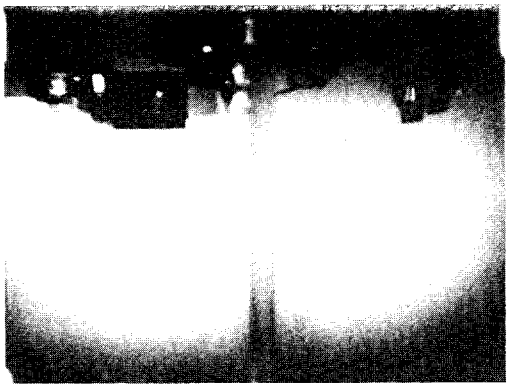

10.0 ms

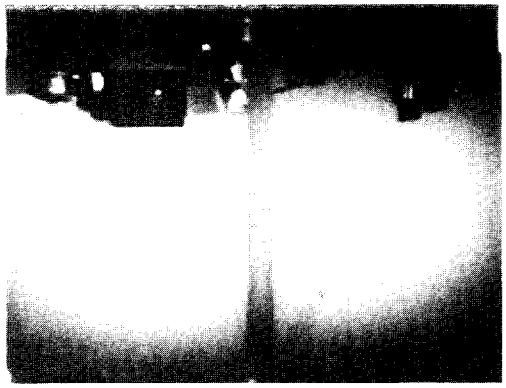

10.5 ms

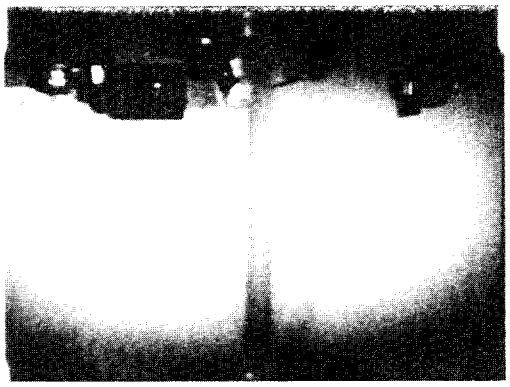

11.0 ms

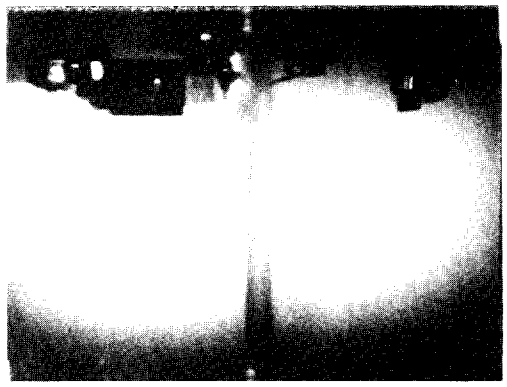

11.5 ms

Figure 86. (continued) A sequence from a high-speed film (2000 frames/s) of the flow formed by a release of 386 g of FC-31-10 from the vessel. The times indicate the period since the initiation of the release.

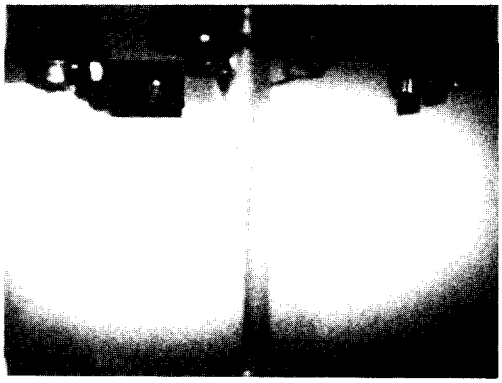

12.0 ms

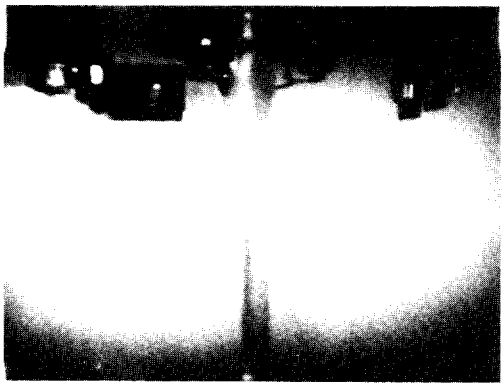

12.5 ms

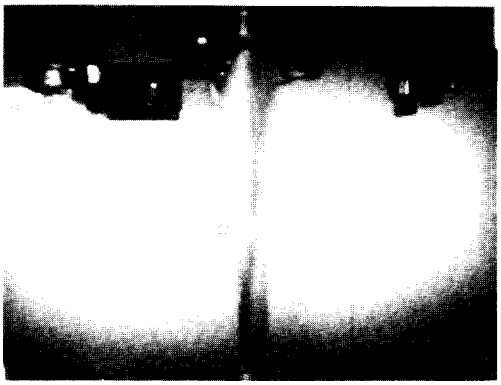

13.0 ms

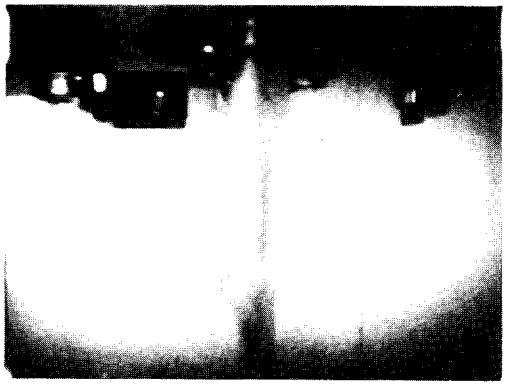

13.5 ms

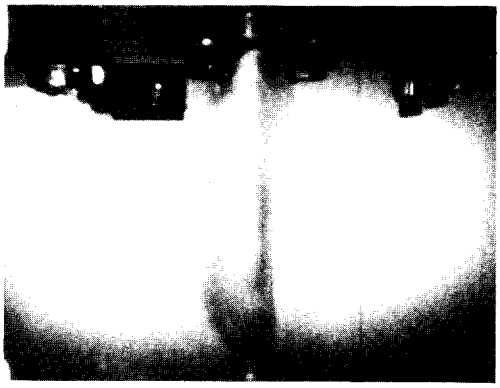

14.0 ms

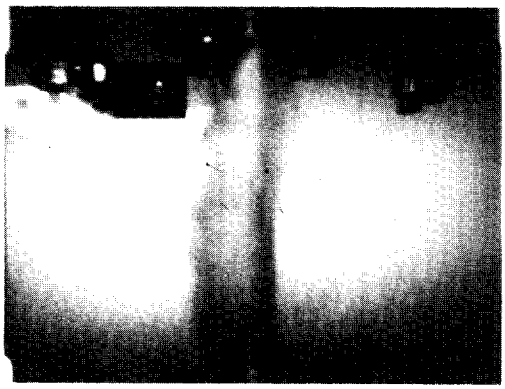

14.5 ms

Figure 86. (continued) A sequence from a high-speed film (2000 frames/s) of the flow formed by a release of 386 g of FC-31-10 from the vessel. The times indicate the period since the initiation of the release.

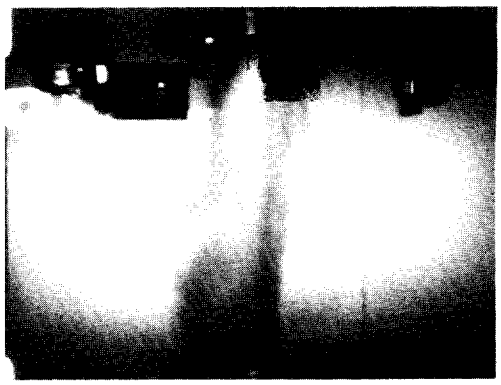

15.0 ms

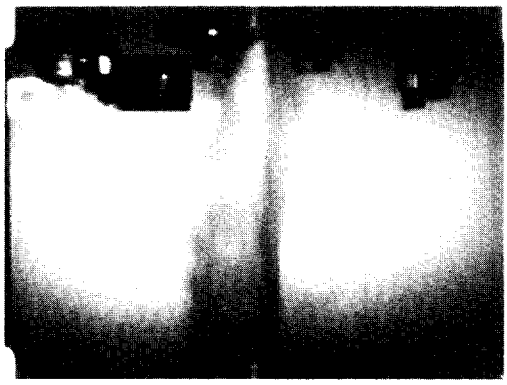

15.5 ms

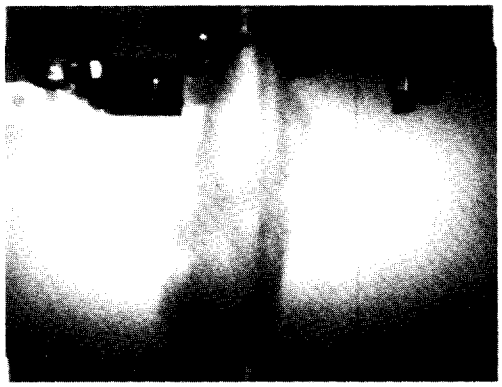

16.0 ms

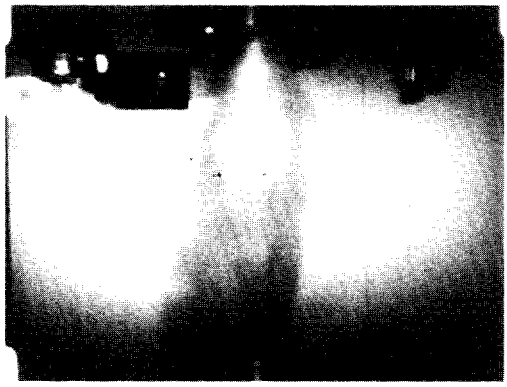

16.5 ms

17.0 ms

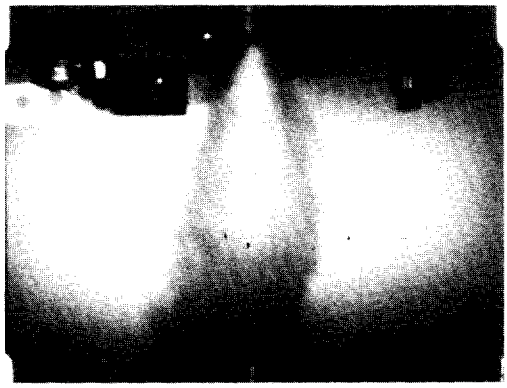

17.5 ms

Figure 86. (continued) A sequence from a high-speed film (2000 frames/s) of the flow formed by a release of 386 g of FC-31-10 from the vessel. The times indicate the period since the initiation of the release.

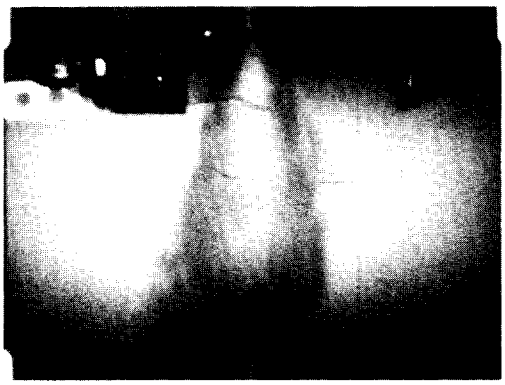

18.0 ms

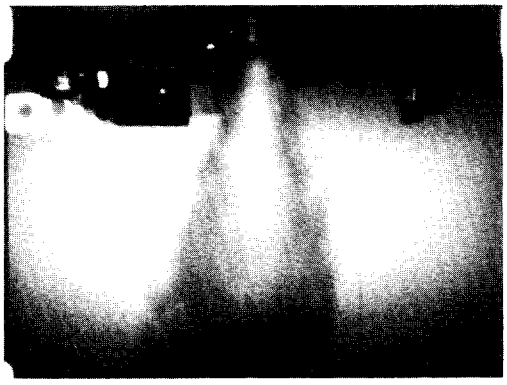

18.5 ms

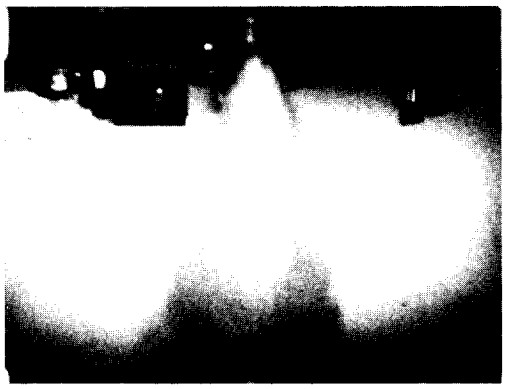

19.0 ms

19.5 ms

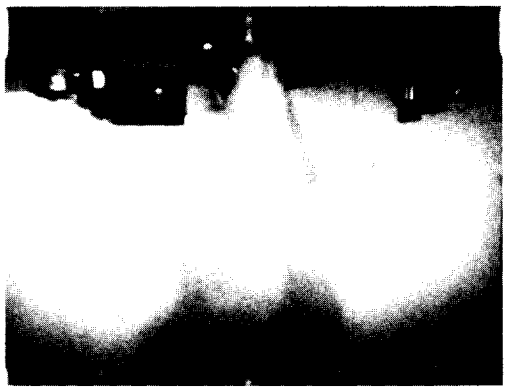

20.0 ms

20.5 ms

Figure 86. (continued) A sequence from a high-speed film (2000 frames/s) of the flow formed by a release of 386 g of FC-31-10 from the vessel. The times indicate the period since the initiation of the release.

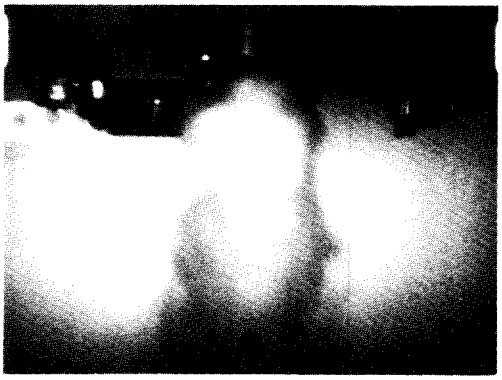

21.0 ms

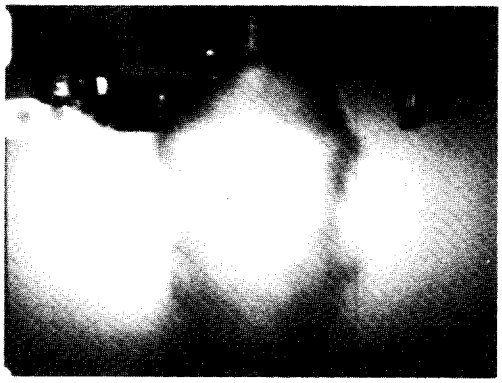

21.5 ms

22.0 ms

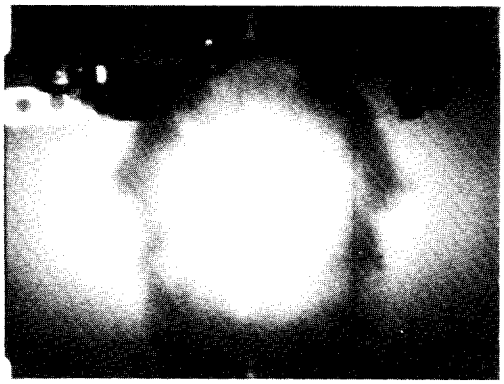

22.5 ms

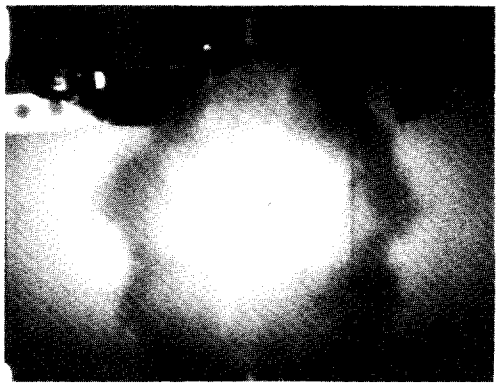

23.0 ms

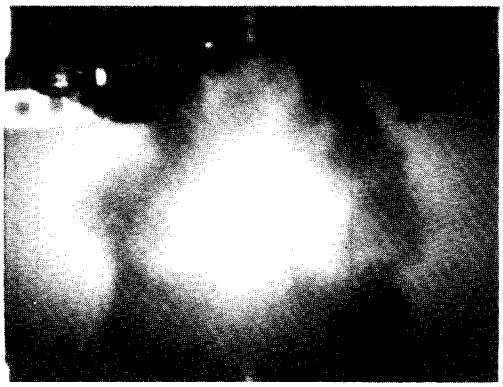

23.5 ms

Figure 86. (continued) A sequence from a high-speed film (2000 frames/s) of the flow formed by a release of 386 g of FC-31-10 from the vessel. The times indicate the period since the initiation of the release.

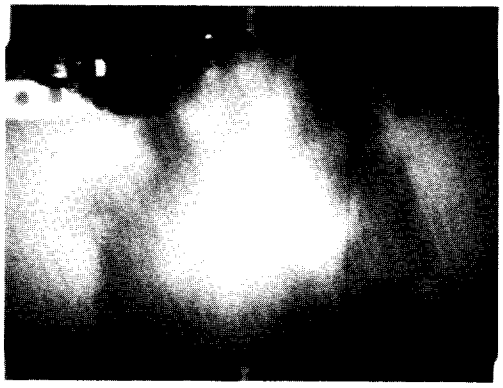

24.0 ms

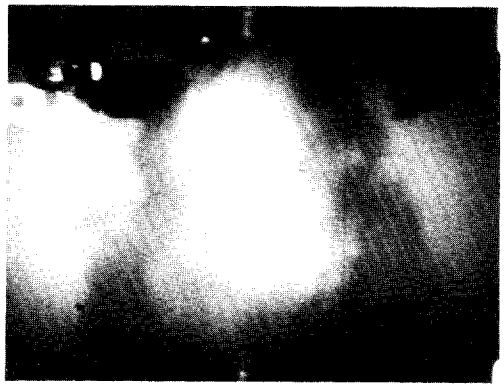

24.5 ms

25.0 ms

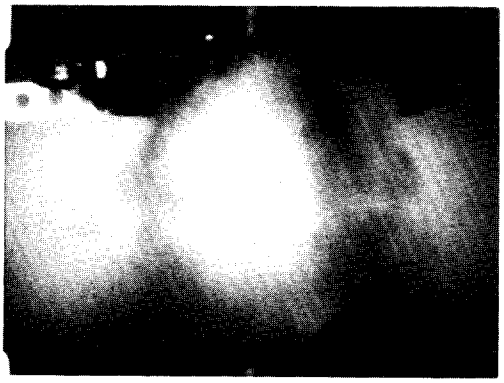

25.5 ms

26.0 ms

26.5 ms

Figure 86. (continued) A sequence from a high-speed film (2000 frames/s) of the flow formed by a release of 386 g of FC-31-10 from the vessel. The times indicate the period since the initiation of the release.

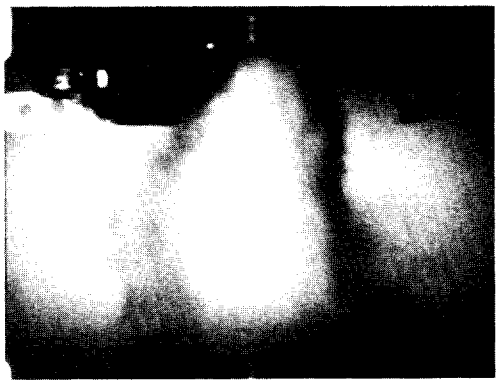

27.0 ms

27.5 ms

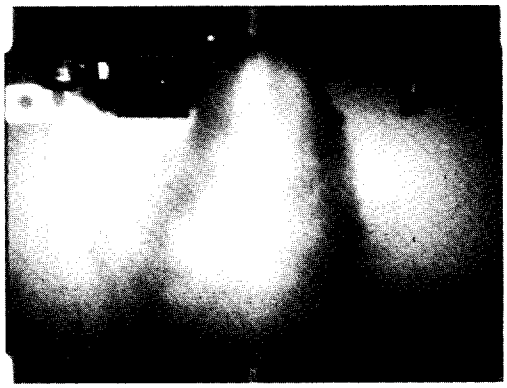

28.0 ms

28.5 ms

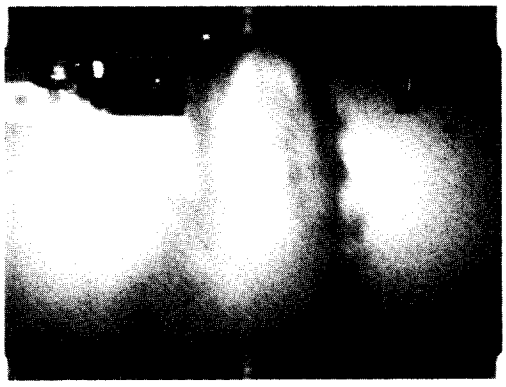

29.0 ms

29.5 ms

Figure 86. (continued) A sequence from a high-speed film (2000 frames/s) of the flow formed by a release of 386 g of FC-31-10 from the vessel. The times indicate the period since the initiation of the release.

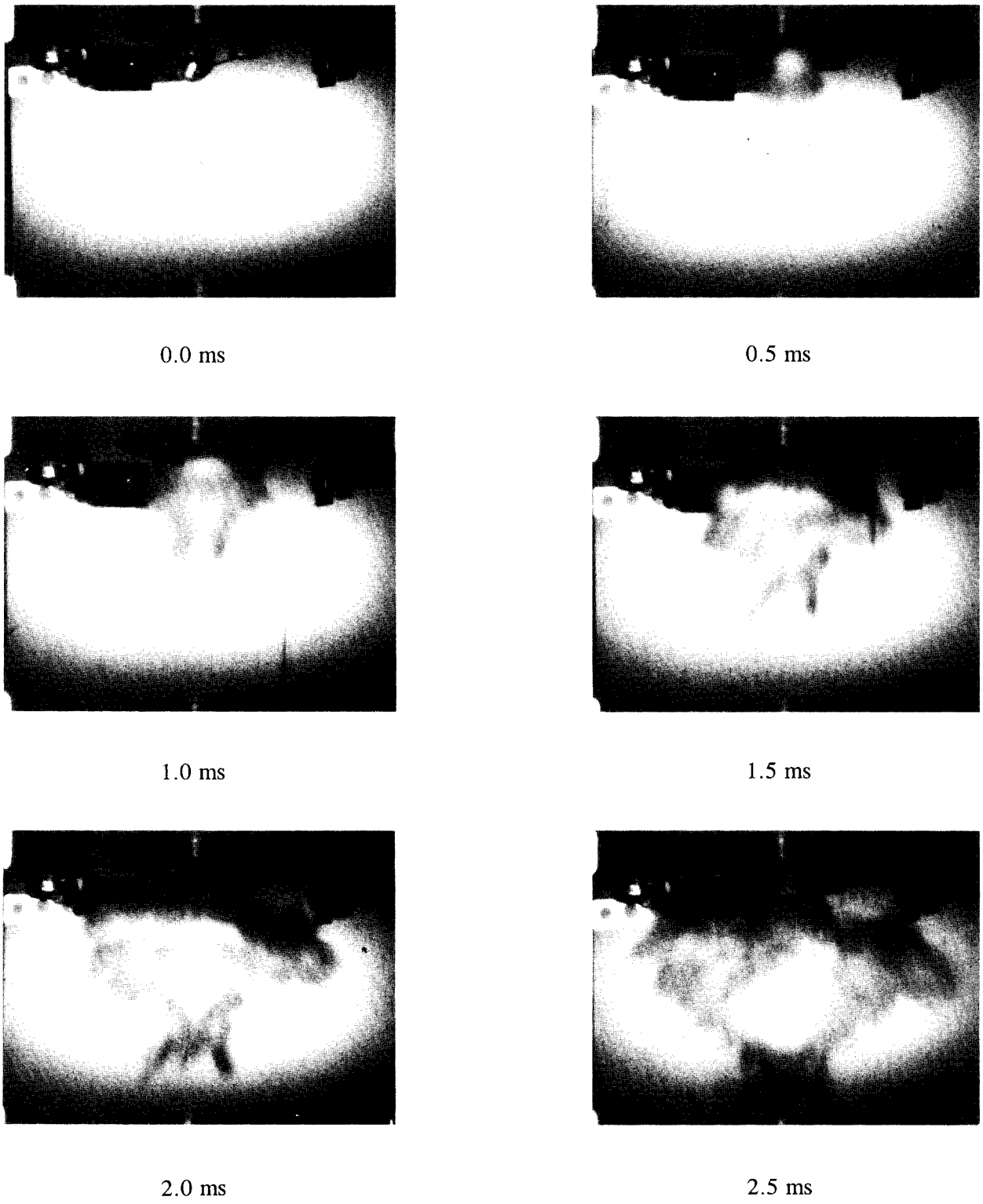

Figure 87. A sequence from a high-speed film (2000 frames/s) of the flow formed by a release of 270 g of halon 1301 from the vessel. The times indicate the period since the initiation of the release.

3.0 ms

3.5 ms

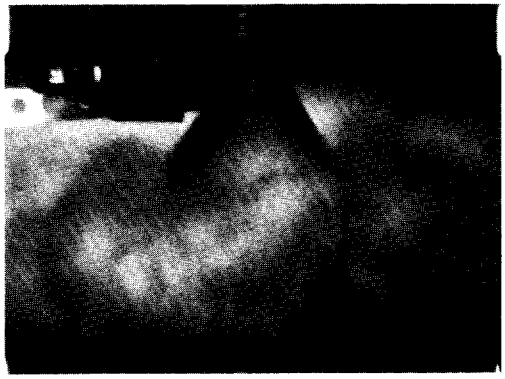

4.0 ms

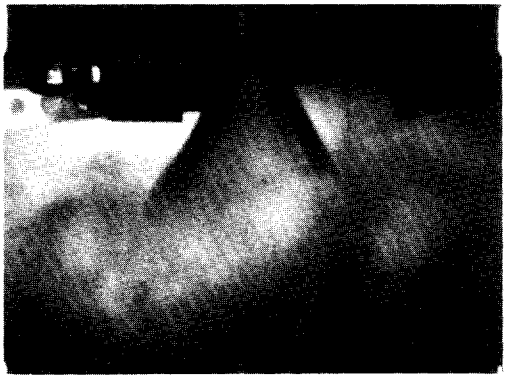

4.5 ms

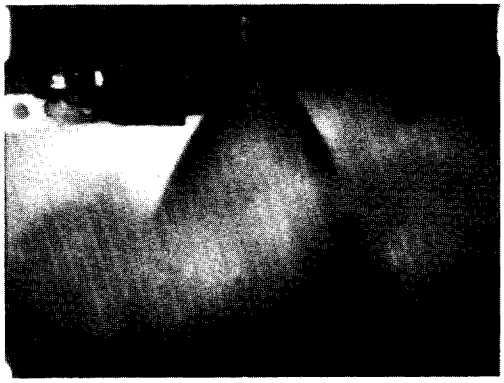

5.0 ms

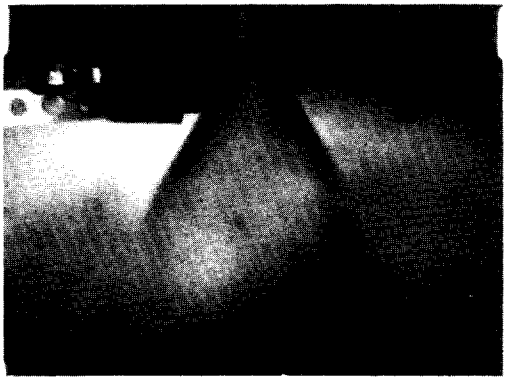

5.5 ms

Figure 87. (continued) A sequence from a high-speed film (2000 frames/s) of the flow formed by a release of 270 g of halon 1301 from the vessel. The times indicate the period since the initiation of the release.

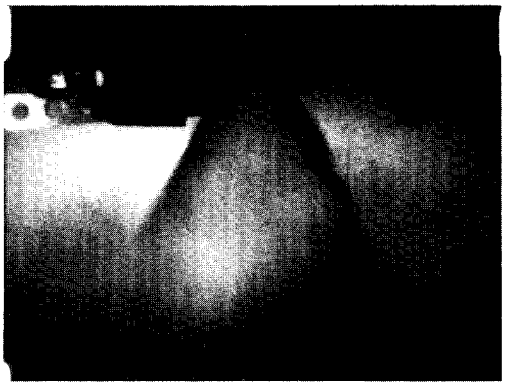

6.0 ms

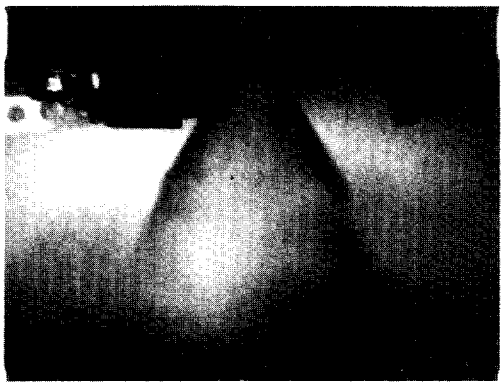

6.5 ms

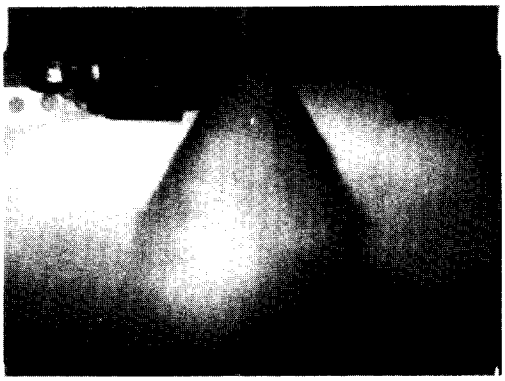

7.0 ms

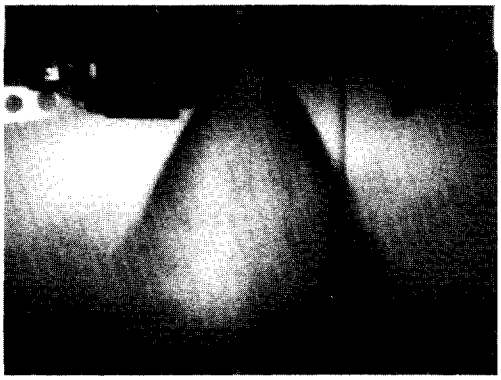

7.5 ms

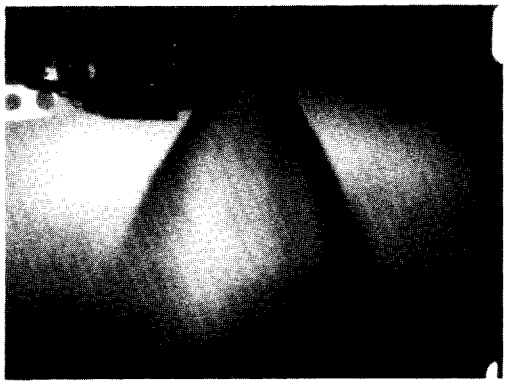

8.0 ms

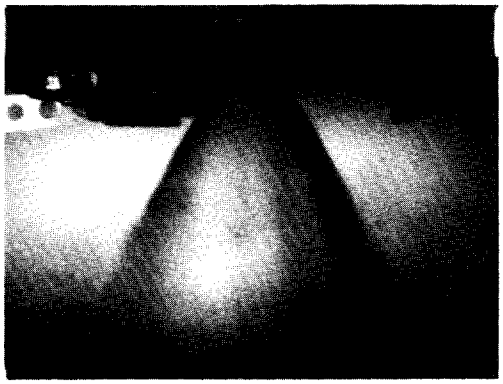

8.5 ms

Figure 87. (continued) A sequence from a high-speed film (2000 frames/s) of the flow formed by a release of 270 g of halon 1301 from the vessel. The times indicate the period since the initiation of the release.

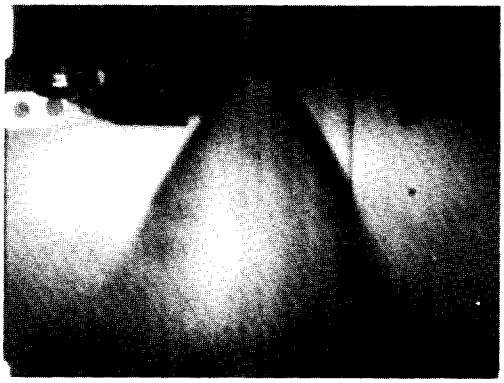

9.0 ms

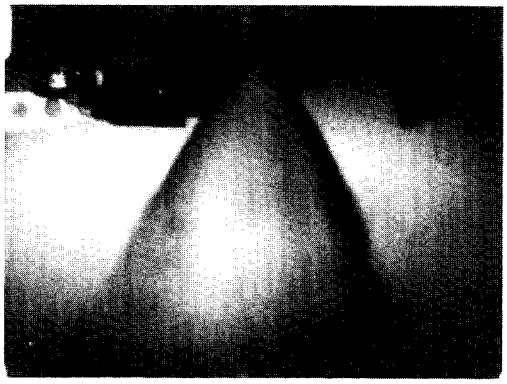

9.5 ms

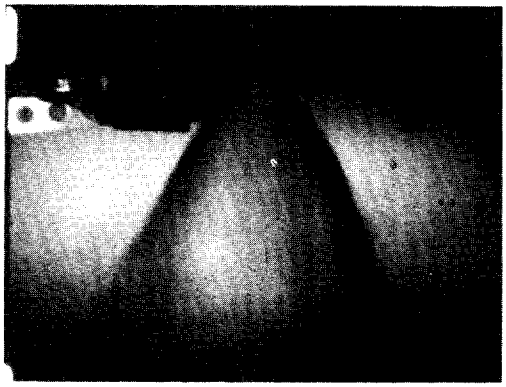

10.0 ms

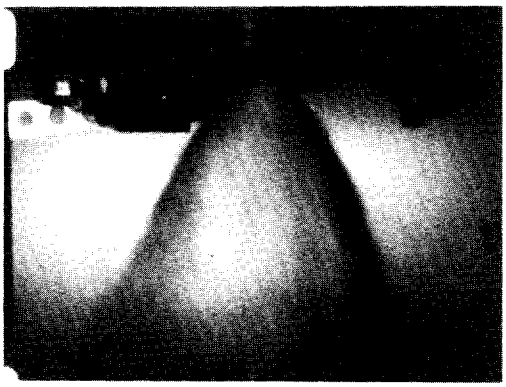

10.5 ms

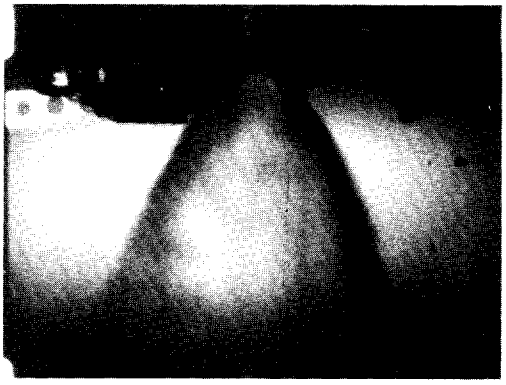

11.0 ms

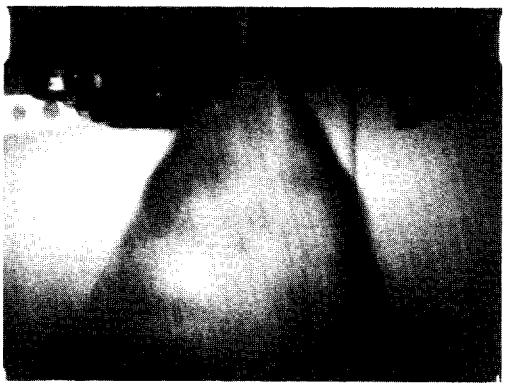

11.5 ms

Figure 87. (continued) A sequence from a high-speed film (2000 frames/s) of the flow formed by a release of 270 g of halon 1301 from the vessel. The times indicate the period since the initiation of the release.

12.0 ms

12.5 ms

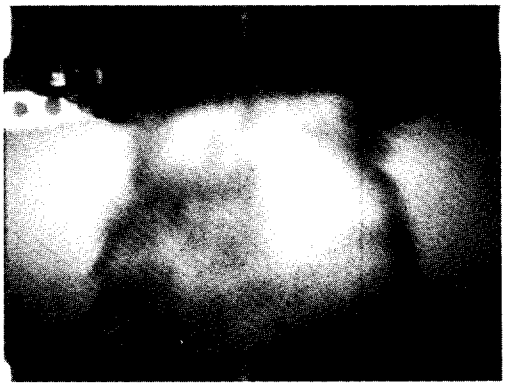

13.0 ms

13.5 ms

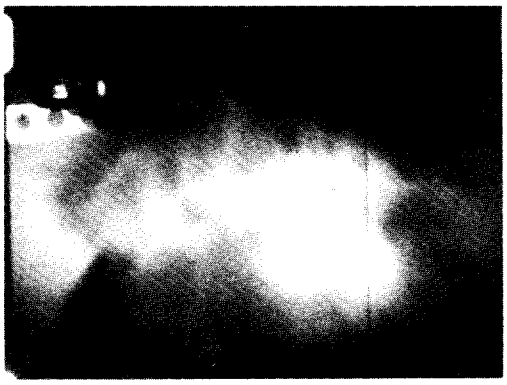

14.0 ms

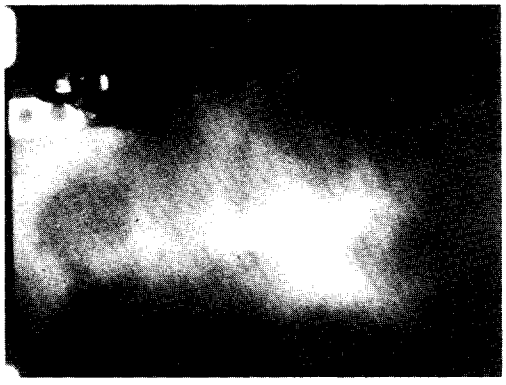

14.5 ms

Figure 87. (continued) A sequence from a high-speed film (2000 frames/s) of the flow formed by a release of 270 g of halon 1301 from the vessel. The times indicate the period since the initiation of the release.

15.0 ms

15.5 ms

16.0 ms

16.5 ms

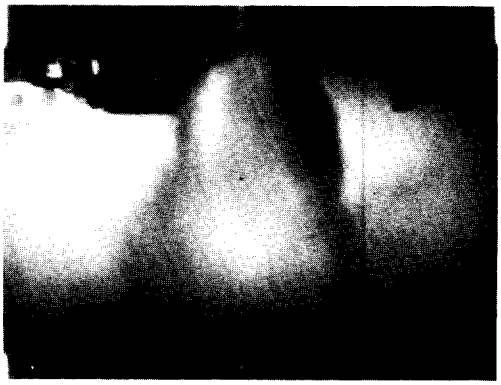

17.0 ms

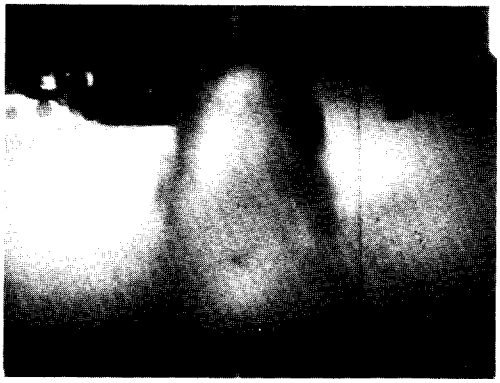

17.5 ms

Figure 87. (continued) A sequence from a high-speed film (2000 frames/s) of the flow formed by a release of 270 g of halon 1301 from the vessel. The times indicate the period since the initiation of the release.

18.0 ms

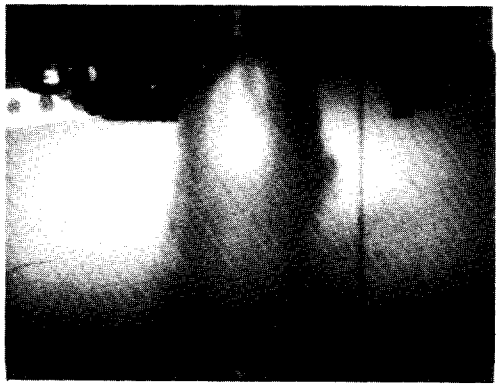

18.5 ms

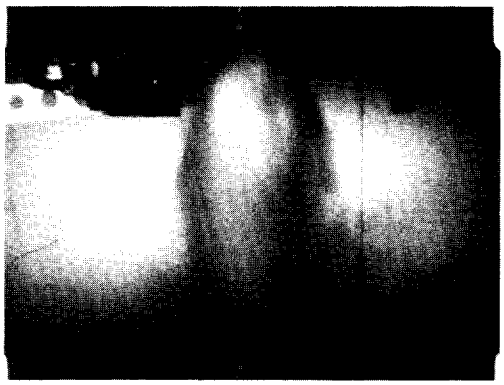

19.0 ms

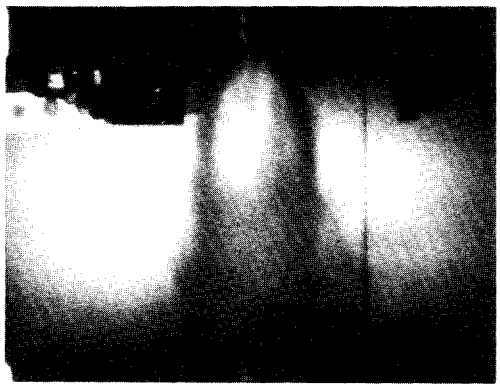

19.5 ms

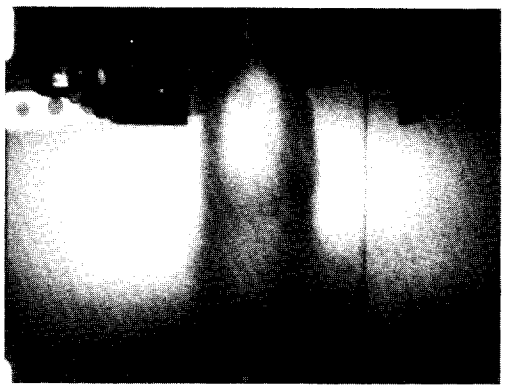

20.0 ms

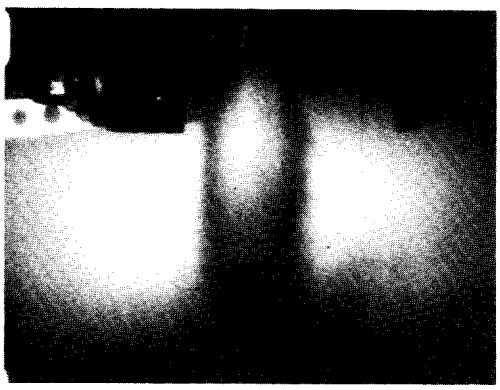

20.5 ms

Figure 87. (continued) A sequence from a high-speed film (2000 frames/s) of the flow formed by a release of 270 g of halon 1301 from the vessel. The times indicate the period since the initiation of the release.

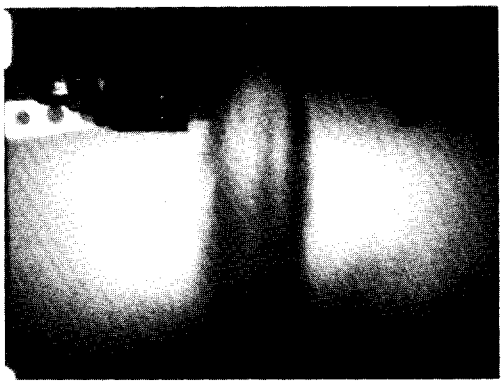

21.0 ms

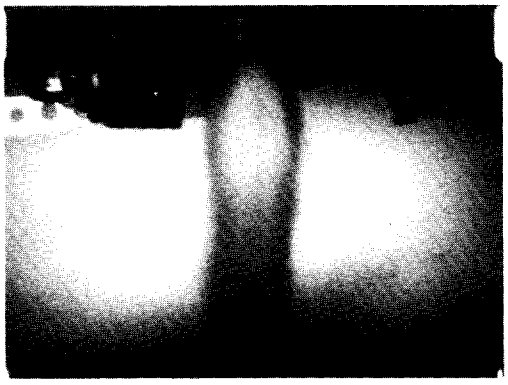

21.5 ms

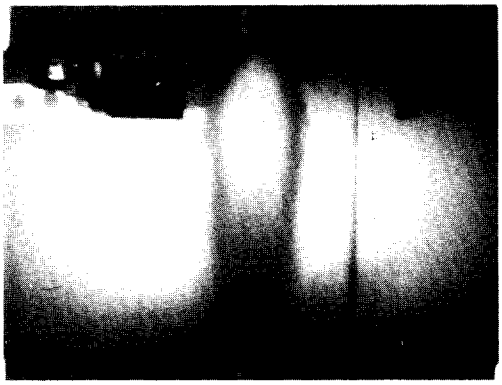

22.0 ms

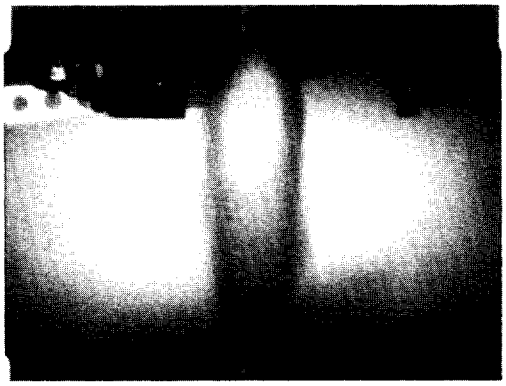

22.5 ms

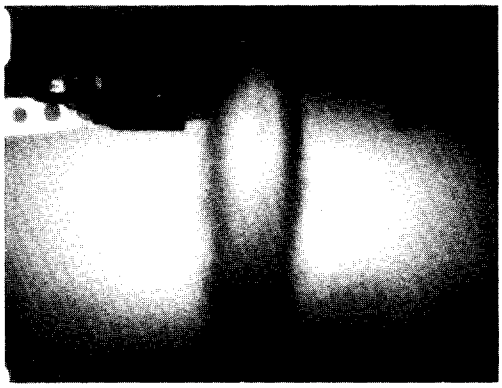

23.0 ms

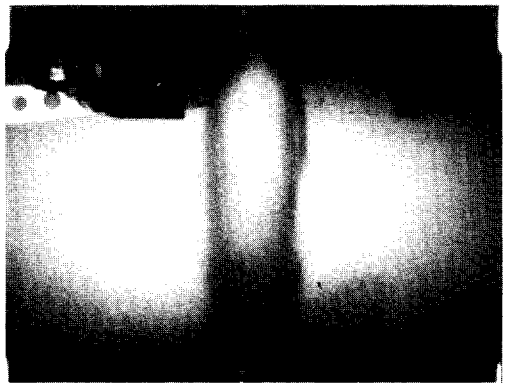

23.5 ms

Figure 87. (continued) A sequence from a high-speed film (2000 frames/s) of the flow formed by a release of 270 g of halon 1301 from the vessel. The times indicate the period since the initiation of the release.

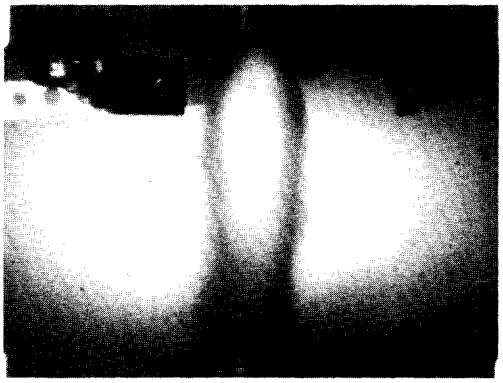

24.0 ms

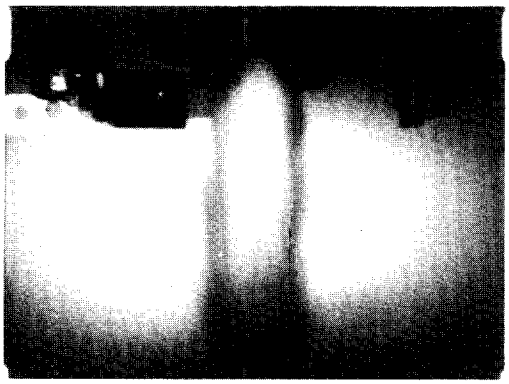

24.5 ms

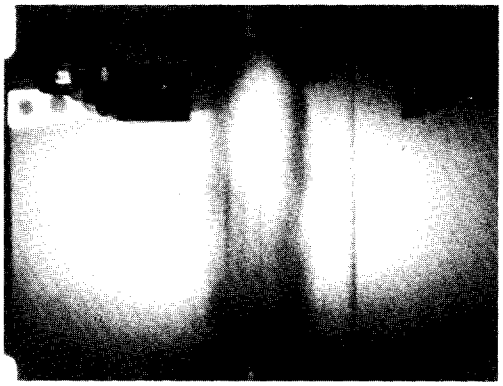

25.0 ms

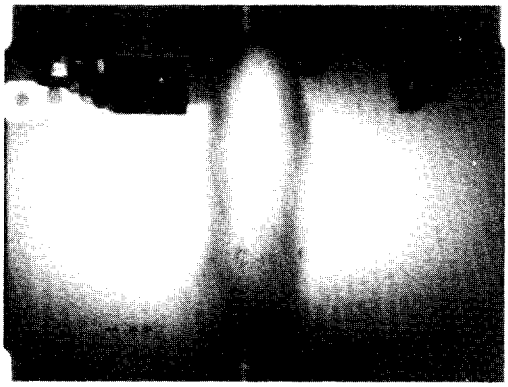

25.5 ms

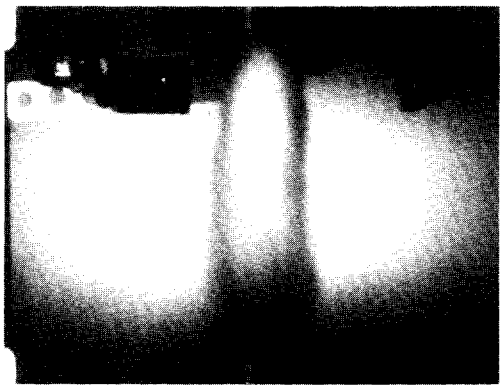

26.0 ms

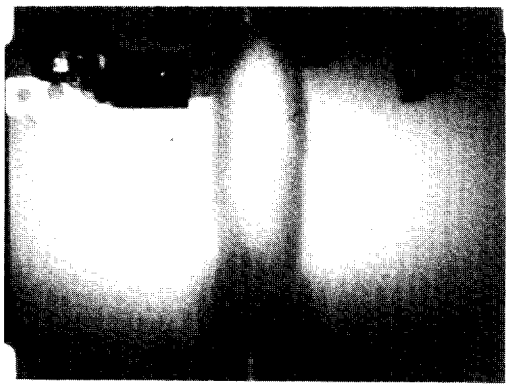

26.5 ms

Figure 87. (continued) A sequence from a high-speed film (2000 frames/s) of the flow formed by a release of 270 g of halon 1301 from the vessel. The times indicate the period since the initiation of the release.

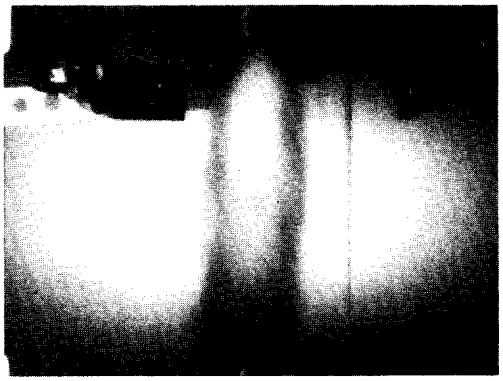

27.0 ms

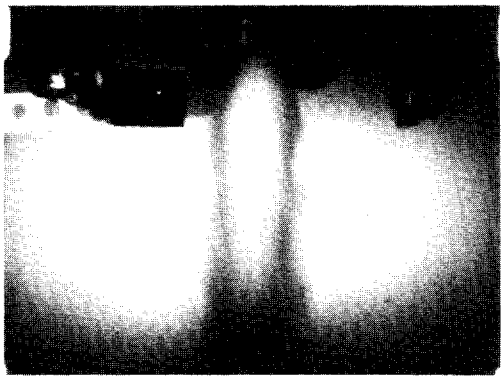

27.5 ms

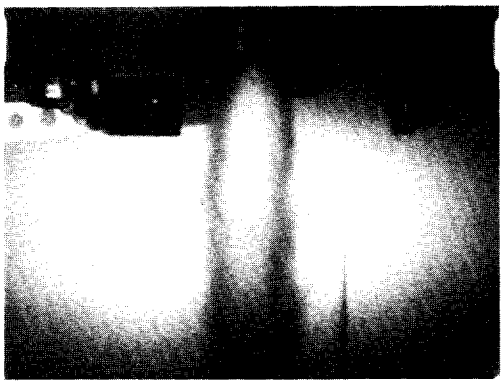

28.0 ms

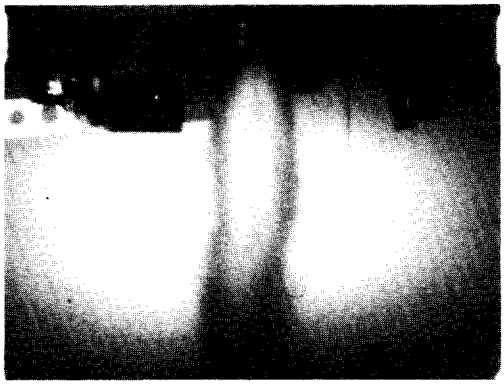

28.5 ms

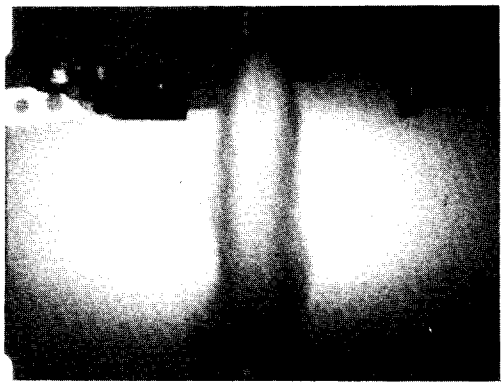

29.0 ms

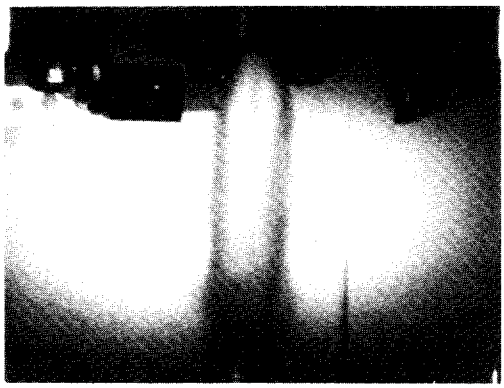

29.5 ms

Figure 87. (continued) A sequence from a high-speed film (2000 frames/s) of the flow formed by a release of 270 g of halon 1301 from the vessel. The times indicate the period since the initiation of the release.

develops, the neck of the flow grows thinner until at roughly 6 ms following release the agent is exiting the vessel as a liquid stream which exists over the entire observed downstream length. At approximately 10 ms partial flashing of the liquid jet occurs near the orifice and subsequently grows in time and space. Even after 15 ms the two-phase flow is compact and has not spread substantially over the observed downstream distance. At later times the jet begins to spread slowly until a very strong expansion occurs 21 ms after release. This point corresponds closely to the emptying time estimated from pressure measurements recorded internal to the vessel. This strong flashing behavior lasts a few milliseconds before only condensed vapor in the nitrogen flow is observed to exit the vessel.

The halon 1301 (Figure 87) is released in a very different way. The initial release of the agent from the bottle is much more violent than observed for the FC-31-10. The flow develops fingers which look almost like an explosion. By 3.5 ms the agent covers a wider radial extent (approximately 0.29 m) than it has moved downstream. The flow near the nozzle seems to be assuming a conical shape. The jet continues to spread in the radial direction as the flow field moves beyond the farthest observed downstream position. For the next 8 ms the flow seems to settle down into a flow condition for which the flow leaves the nozzle and spreads rapidly with downstream distance. The spreading angle is roughly 60°. During this period the material ejected to large radial positions at earlier times seems to have evaporated. This behavior can be contrasted to that for FC-31-10 where the released agent appears to form a liquid stream during this phase of the release. Fourteen milliseconds after the release a very strong flashing is observed which disperses material over extremely wide radial distances for short downstream distances. Again, internal pressure measurements indicate that this is roughly the time when all of the liquid has been emptied from the vessel.

Films were recorded for all of the agents over the smaller 0.40 m × 0.10 m view area. Table 5 lists measured values of radial and axial velocities calculated from the films for the ten proposed alternative agents which are liquid at room temperature and halon 1301. Due to the limited number of measurements the data do not show definite trends. However, it is clear that the axial near-field velocities increase with decreasing boiling point (*i.e.*, the amount of superheating).

3.5.3.2 Near-Field Dynamic Pressure Measurements. These measurements were intended to test two aspects of the released agent behaviors. The first was whether or not there were shock waves generated by either the bursting of the disk or the sudden flashing of the liquid. The second was to detect the presence of the agent at the transducer and, if possible, estimate the degree of vaporization.

The high-speed films showed that during an agent release there were two flashings which might expel liquid to a distance where it could strike the pressure transducer. Time records of pressure traces all show signals corresponding to the second flashing near the end of the release. The lower boiling-point liquids also showed pressure rises shortly after the disk burst (recall that time 0 is defined as the time when laser #1 is strongly attenuated). Interestingly, no pressure changes were generally detected for the higher boiling-point liquids at short times.

Figure 88 shows a time plot of pressure from the near-field pressure transducer for two room temperature releases of HFC-236fa from a vessel which is 2/3 full of the liquid agent. The two sets of data are in good agreement. No pressure increases are observed until near the time when the fluid is emptied from the vessel. Apparently, the flashing observed in the high-speed films when the disk burst did not generate shock waves or impart sufficient momentum to the HFC-236fa to reach the pressure transducer which was 46 mm from the centerline. In contrast, the strong flashing observed near the ends of the releases generated a very large dynamic pressure at the transducer. Table 6 lists the maximum pressures observed for the two releases.

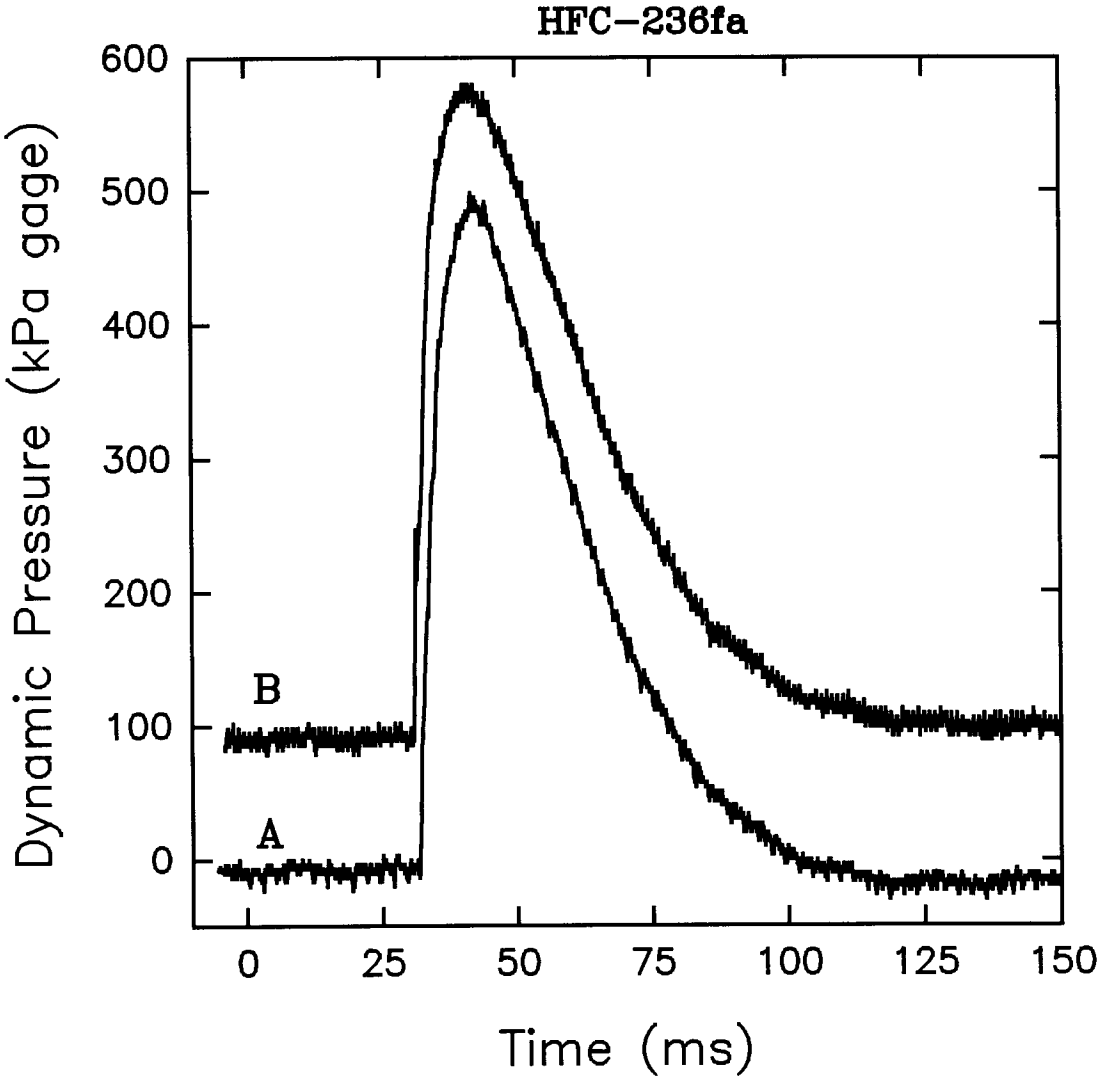

Figure 88. Two time traces of near-field dynamic pressure for releases of HFC-236fa. For clarity, trace B is offset by 100 kPa. Conditions are: A, 464 g of agent, release pressure of 4.30 Mpa; B, 471 g agent, release pressure of 4.51 MPa.

Table 5. Values of Velocity Determined from High Speed Films of Liquid Agents Released from Pressurized Vessels

AGENT	Radial Velocity Frame 2-3 (m/s)	Radial Velocity Frame 3-4 (m/s)	Axial Velocity Frame 2-3 (m/s)	Axial Velocity Frame 3-4 (m/s)
HFC-236fa	9	[a]	42	57
FC-31-10	12	2.4	49	[a]
FC-318	14	0	67	[a]
HCFC-124	10	0	57	[a]
HFC-227ea	[a]	2	55	57
HFC-134a	10	5	69	63
FC-218	6	11	86	[a]
HCFC-22	[a]	[a]	58.1	49.3
HFC-125	2.1	18	76	[a]
HFC-125/HFC-32 mixture	17	9	80	[a]
halon 1301	11	1.5	> 80	[a]

[a] Measurements could not be made for these conditions due to poor contrast in the images

A number of releases with various vessel fill levels have been made for FC-31-10. Figure 89 shows time plots of pressures from the near-field pressure transducer for three runs having initial vessel fill levels of 1/3, 1/2, and 2/3. The observed behaviors are very similar to those found for HFC-236fa. Table 6 summarizes the pressure increases observed during the second flashings for a number of experiments. There are no clear trends in the maximum pressure with burst pressure or the mass of agent in the bottle. A range of values are observed which are likely to be characteristic of run-to-run variations.

Figure 90 shows two pressure time traces for FC-318. The results are similar to those for HFC-236fa and FC-31-10 except that one of the pressure traces has a slight jump with a maximum of 41 kPa starting 3.48 ms after the agent release. This pressure rise indicates that for this release the initial flashing behavior was strong enough to eject material as far as the pressure transducer. A total of six experiments were run with this agent. Only one recorded the initial flashing behavior. Pressure increases associated with the second flashing are listed in Table 6. A fairly wide range of pressures is observed.

Two time traces for the near-field pressure behavior are shown in Figure 91 for HCFC-124. No signals were recorded immediately following the opening of the vessel orifice. The relevant data for observed dynamic pressures as a result of the second flashing are summarized in Table 6.

Table 6. Maximum Dynamic Pressures Observed by the Near-Field Transducer During the Second Flashings of Agent Releases

Agent	Mass of Agent (g)	Internal Pressure at Release (MPa)	Maximum Dynamic Pressure (kPa)
HFC-236fa	464	4.30	499
	471	4.51	480
FC-31-10	261	4.50	314
	262	4.45	293
	263	3.98	364
	266	4.33	314
	386	4.21	448
	387	4.52	397
	495	3.93	557
	515	4.20	312
	520	3.85	315
FC-318	257	3.90	487
	270	4.25	469
	404	3.92	516
	501	4.43	647
	505	3.99	561
	521	4.34	629
HCFC-124	465	4.30	708
	462	4.05	668
HFC-227ea	476	4.45	900
	489	4.41	792
HFC-134a	419	4.21	1176
	418	4.13	1101
	423	4.38	1317

Table 6. (continued) Maximum Dynamic Pressures Observed by the Near-Field Transducer During the Second Flashings of Agent Releases.

Agent	Mass of Agent (g)	Internal Pressure at Release (MPa)	Maximum Dynamic Pressure (kPa)
FC-218	468	4.28	559
	463	4.06	421
	460	4.58	579
HCFC-22	412	2.81	572
	421	4.48	1402
	417	4.52	1271
HFC-125	423	4.24	1047
	403	4.19	367
	416	4.07	566
HFC-125/HFC-32 mixture	375	4.36	1508
	358	4.31	1626
halon 1301	270	4.43	602
	554	4.36	113

Figure 92 and Table 6 contain similar results for HFC-227ea. One of the releases showed a quite substantial pressure increase starting 1.12 ms after the initial release of the agent. The pressure reached a maximum of 304 kPa.

Results for HFC-134a are given in Figure 93 and Table 6. Three sets of data were recorded for this agent. Two of these showed pressure increases (169, 102 kPa) shortly after (1.80 ms and 1.52 ms) the initiation of the experiments. The experiment which isn't shown in Figure 93 did not have a pressure increase at the short delay time.

Three sets of data were also recorded for FC-218. Figure 94 and Table 6 summarize the findings. As found for the HFC-134a, two of the releases resulted in small pressure increases (28 and 31 kPa) shortly following the release time (1.92 and 1.60 ms). As can be seen by comparing entries in Table 6, the pressure increases as a result of the second flashing observed for the FC-218 are considerably smaller than those found for the HFC-134a.

HCFC-22 generated pressure traces which were quite complicated and variable. Examples of two of the traces are shown in Figure 95. The pressure time histories are quite different than those for the agents discussed up to this point. Not only are pressure increases observed near the beginnings and ends of the releases, there also indications of some flashing behavior at intermediate times. Table 6 summarizes the findings for three releases of HCFC-22. The dynamic pressures observed for the releases using nominal 4.14 burst disks were the highest recorded during the study. The pressure increase was found to be considerably smaller for the one case using a lower-pressure burst disk (see Table 6).

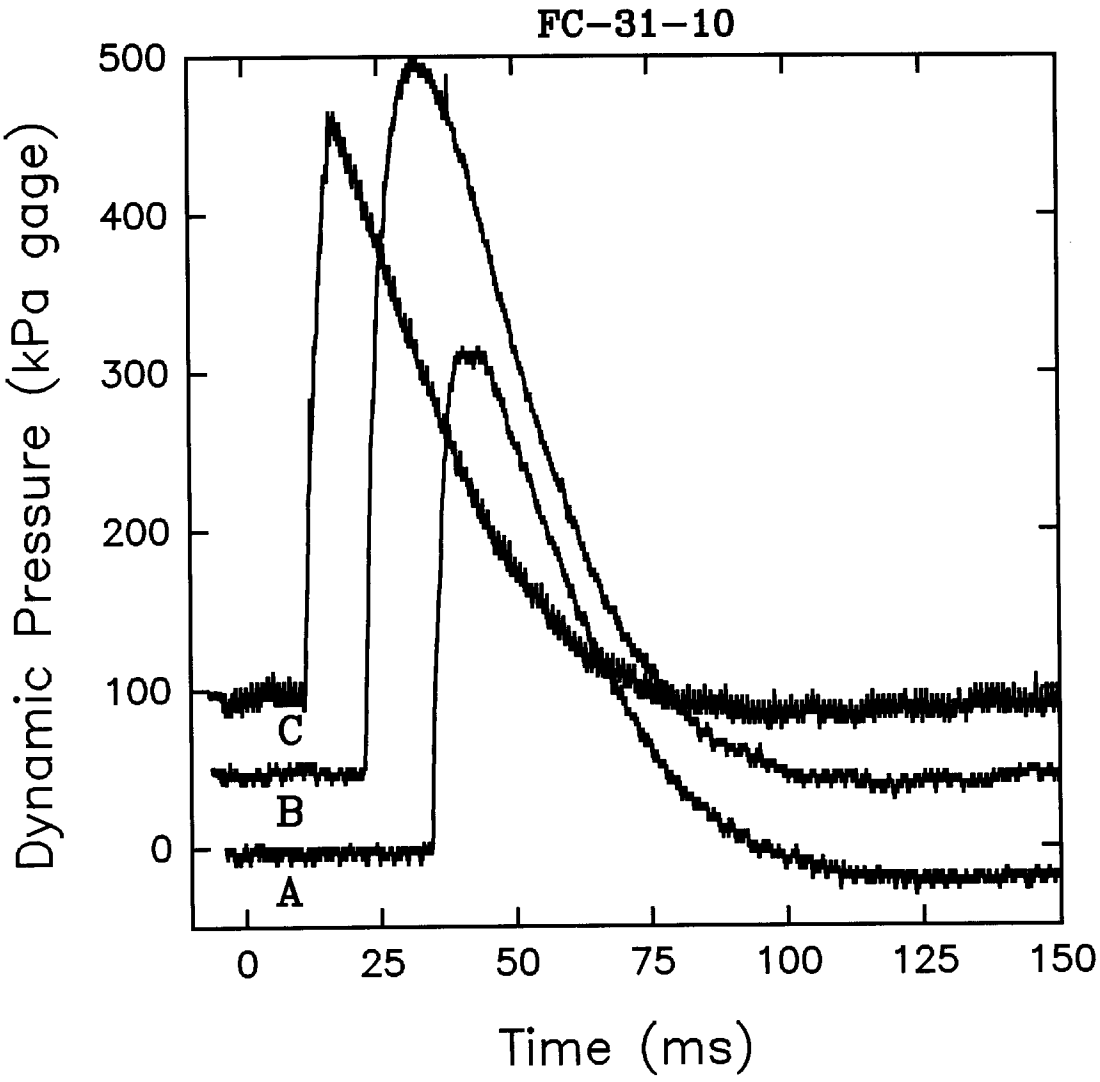

Figure 89. Three time traces of near-field dynamic pressure for releases of FC-31-10. Traces B and C are offset by 50 kPa. Conditions: A, 515 g, release pressure 4.20 MPa; B, 386 g, release pressure 4.21 MPa; C, 263 g, release pressure of 3.98 MPa.

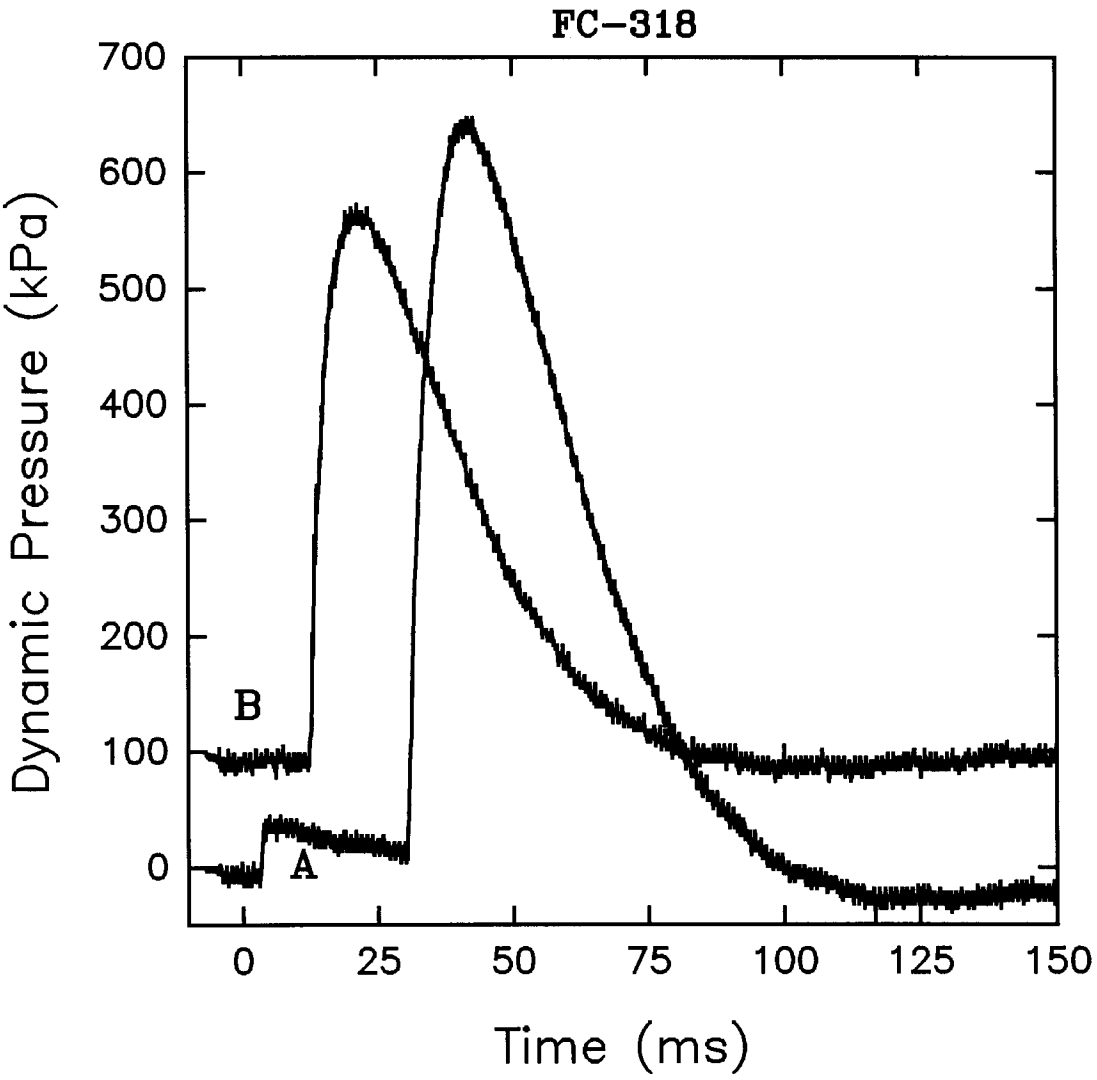

Figure 90. Two time traces of near-field dynamic pressure for releases of FC-318. Trace B is offset by 100 kPa. Conditions: A, 501 g, release pressure 4.43 MPa; B, 270 g, release pressure 4.25 MPa.

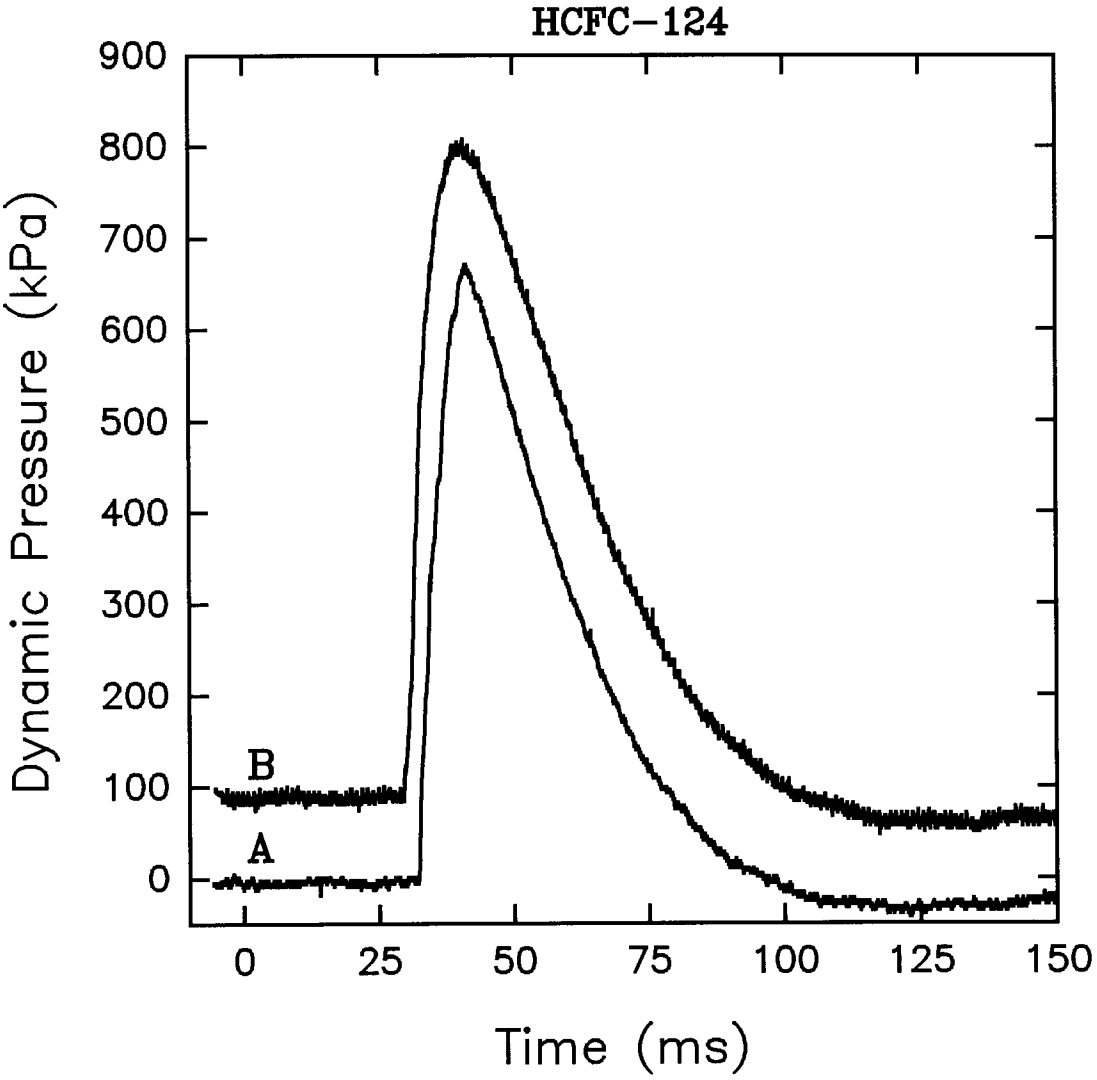

Figure 91. Two time traces of near-field dynamic pressure for releases of HCFC-124. Trace B is offset by 100 kPa. Conditions: A, 465 g, release pressure 4.30 MPa; B, 462 g, release pressure 4.05 MPa.

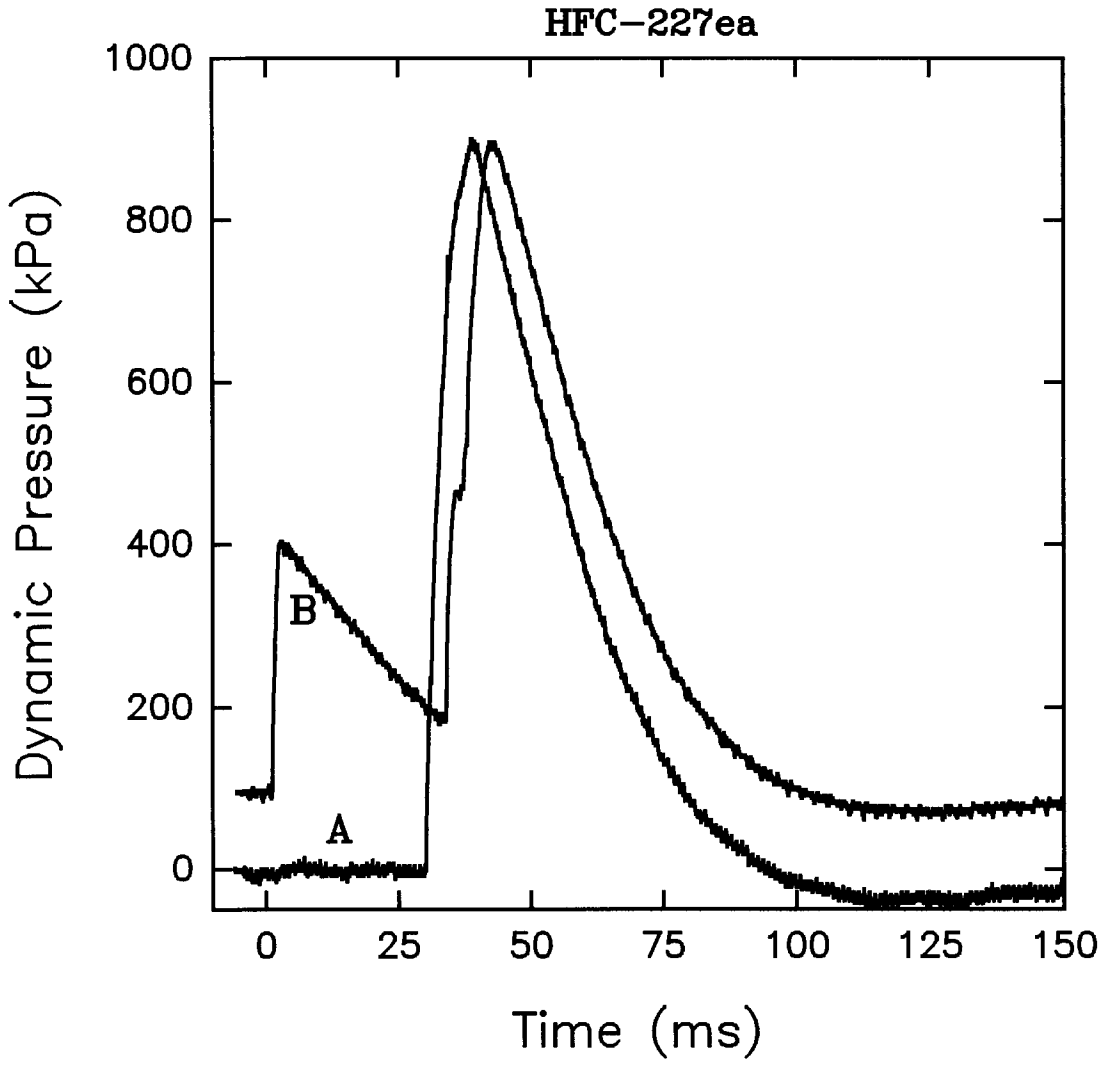

Figure 92. Two time traces of near-field dynamic pressure for releases of HFC-227ea. Trace B is offset by 100 kPa. Conditions: A, 476 g, release pressure 4.45 MPa; B, 489 g, release pressure 4.41 MPa.

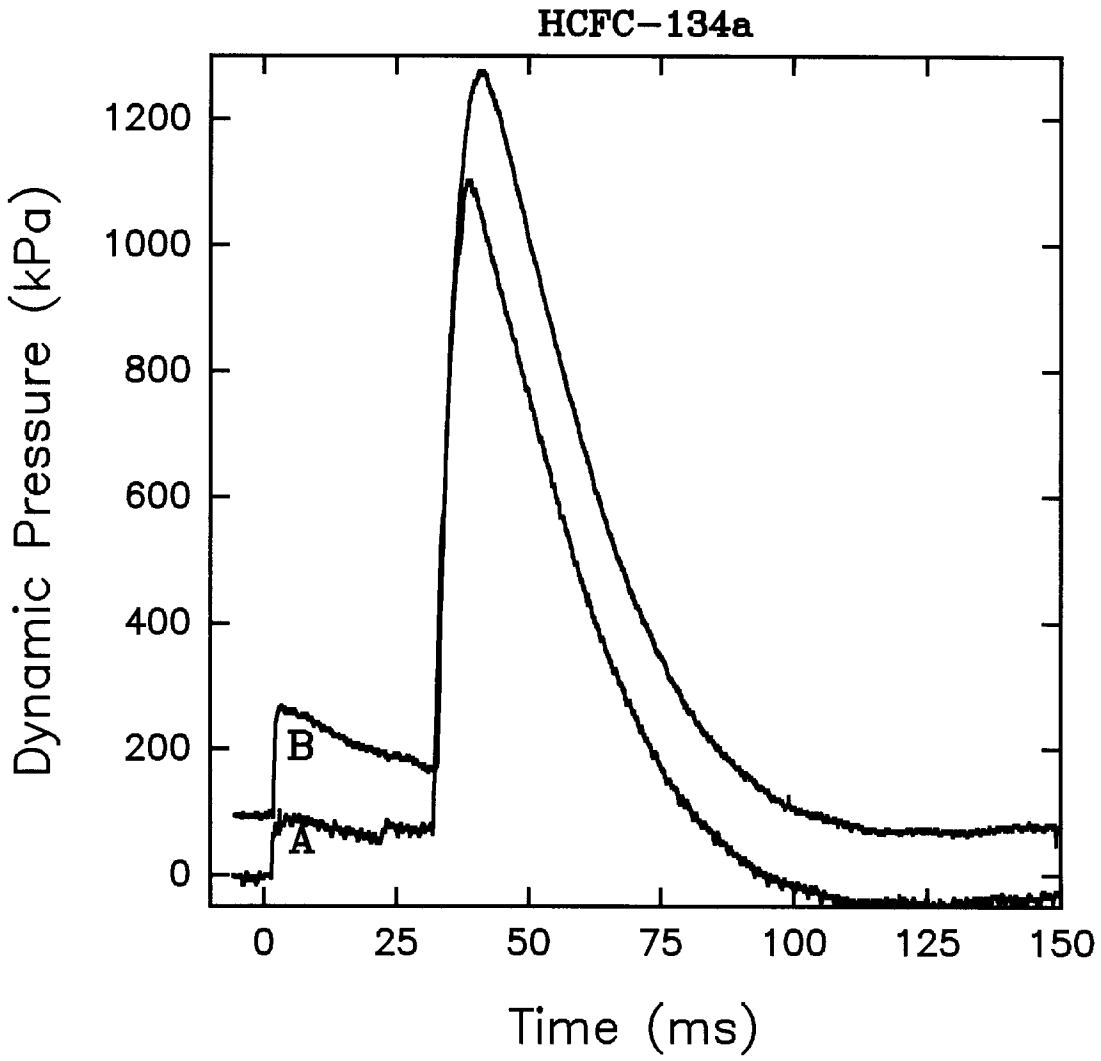

Figure 93. Two time traces of near-field dynamic pressure for releases of HFC-134a. Trace B is offset by 100 kPa. Conditions: A, 423 g, release pressure 4.38 MPa; B, 418 g, release pressure 4.13 MPa.

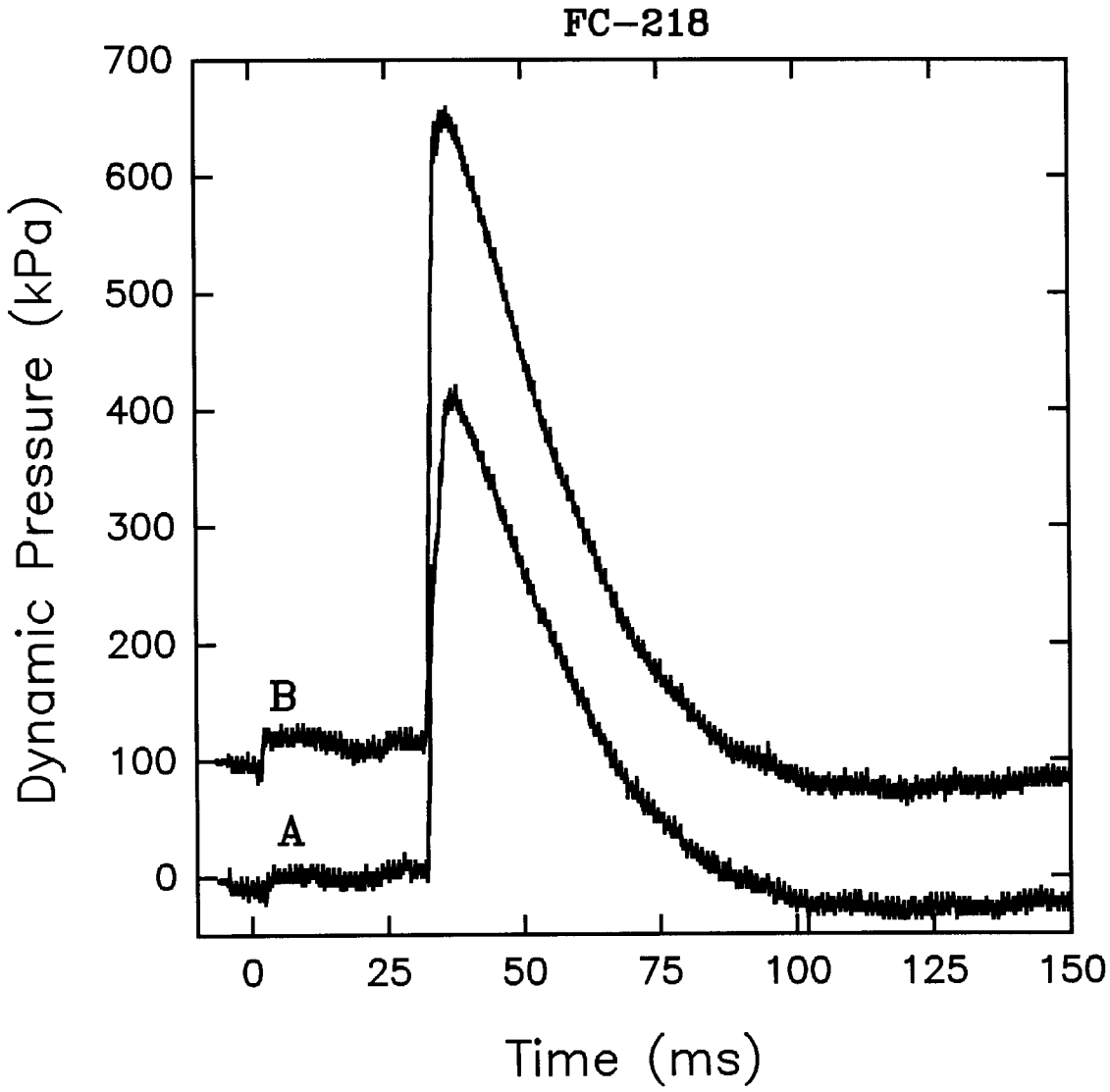

Figure 94. Two time traces of near-field dynamic pressure for releases of FC-218. Trace B is offset by 100 kPa. Conditions: A, 463 g, release pressure 4.06 MPa; B, 468 g, release pressure 4.28 MPa.

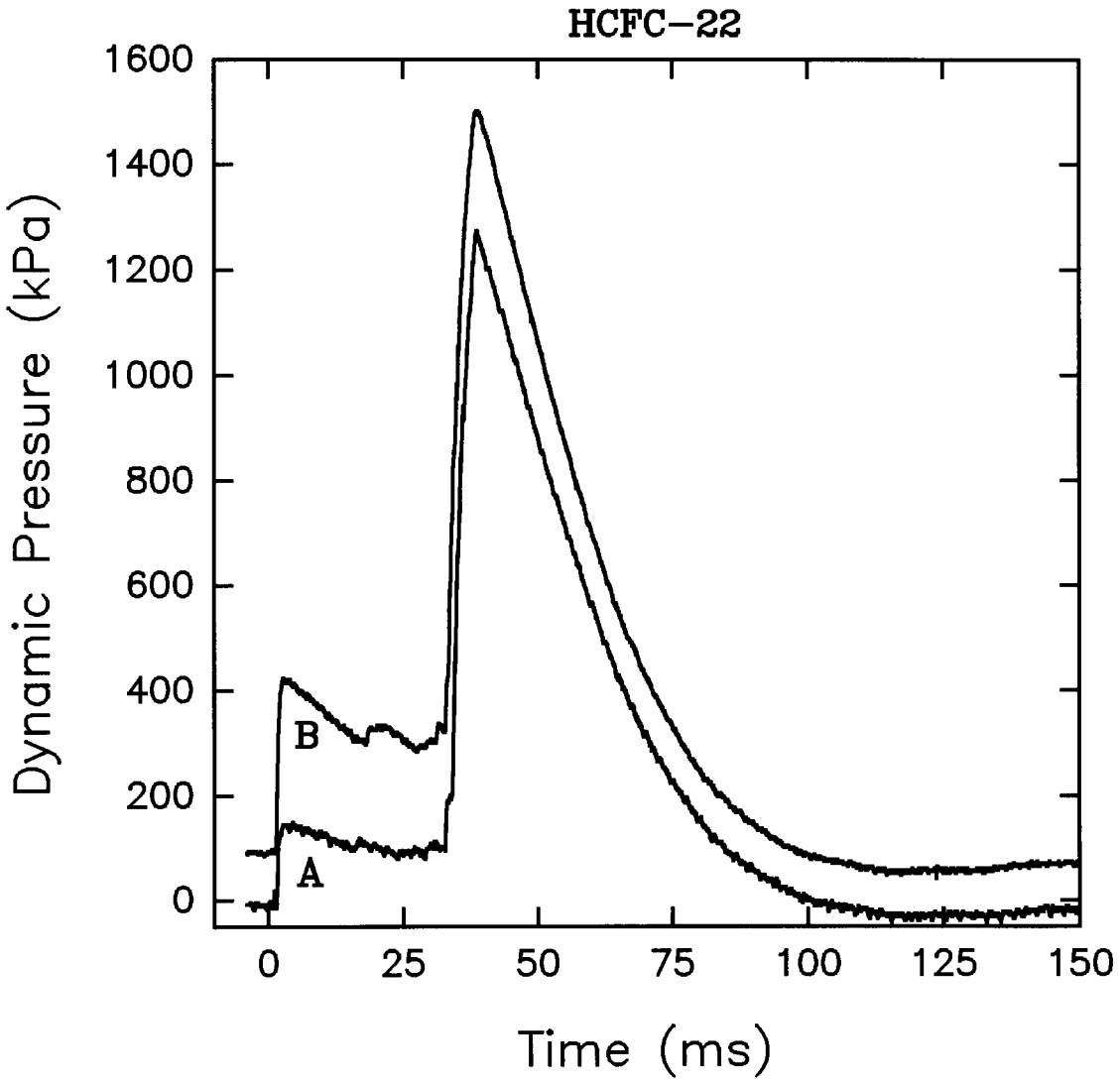

Figure 95. Two time traces of near-field dynamic pressure for releases of HCFC-22. Trace B is offset by 100 kPa. Conditions: A, 412 g, release pressure 4.52 MPa; B, 417 g, release pressure 4.48 MPa.

HFC-125 also generated pressure traces which varied from release to release. Figure 96 shows two examples. Both plots indicate that flashing occurred at the beginning and end of the releases, but there were indications that flashing also took place at intermediate times. The third set of data summarized in Table 6 was similar. Each release has a pressure rise at early times. The maximum pressures observed were 20, 81, and 122 kPa.

The HFC-125/HFC-32 mixture has the lowest boiling point of all of the potential replacement agents except FC-116. Time traces for two releases of this agent (see Figure 97) indicate that the liquid tends to flash strongly during most of time the liquid is exiting the vessel. Pressure increases (249 and 293 kPa) first appear immediately (1.24 and 1.12 ms) following the release. These are followed by a short quiet period before the dynamic pressure begins to increase rapidly. The maximum pressure readings occurred near the end of the releases, reaching values greater than 1500 kPa. Table 6 summarizes the findings.

For comparison purposes, releases of halon 1301 were also performed. Figure 98 and Table 6 summarize the findings. Note that trace B was recorded for a release in which the vessel was only 1/3 full of liquid. In both cases, the pressure traces indicate that flashing occurred immediately following (1.16 and 1.84 ms) the opening of the orifice. Early pressure increases of 91 and 43 kPa were observed. Trace A indicates that the liquid flashed near the orifice during most of the release. The flashing associated with the emptying of the vessel is also obvious. Despite the fact that the boiling point of halon 1301 is 20 K lower than for the HFC-125/HFC-32 mixture, the dynamic pressures measured are considerably lower for the halon 1301. The maximum pressures observed due to the second flashing are quite different for the two experiments shown in Figure 98.

These measurements will be discussed further in Section 3.5.4. However, a few general conclusions can be drawn from the results summarized in Table 6 and the figures. The data for the various agents have been presented in order of decreasing boiling point. Only for the lowest boiling-point agents are dynamic pressures generated by the flashing observed immediately following the opening of the burst disk. For agents having boiling points higher than HCFC-22 (232 K), flashing is only detected near the beginning and end of the releases. Pressure increases observed for HCFC-22 and agents having lower boiling points suggest that strong flashing is taking place at intermediate times as well. With the exceptions of FC-218, HFC-125, and halon 1301, the pressure increases observed near the time when the vessel empties increase with decreasing boiling point.

3.5.3.3 Laser Attenuation Measurements. Laser attenuation measurements were made at the five downstream positions listed in Table 7 for each of the agents investigated. Figure 99 through Figure 109 show examples of the laser signals recorded for releases of all of the alternative agents, with the exception of FC-116, and halon 1301. In each case the vessel was 2/3 full of the liquid agent and a nominal 4.14 MPa burst disk was used.

For the higher boiling-point agents, the arrival of the agent at a laser beam fully extinguishes the beam nearly instantaneously (within 40 μs). This is clearly seen in Figure 99 through Figure 104 where sharp drops are seen in the laser intensities at successively later times as the agent moves away from the vessel orifice. Recall that time 0 corresponds to the extinguishment of laser #1. The light extinguishment is the result of scattering by the two-phase flows generated by the releases. For the lower boiling-point agents, the fall off in light intensity with time is not as sharp. This is most clear for lasers #3, #4, and #5 for the halon 1301 release (see Figure 109). This observation is evidence that these liquid agents are evaporating at a sufficient rate on the leading edges of the releases that the two-phase flow is not optically dense enough to fully extinguish the laser beams. Even for the low boiling-point liquids, the laser beams are eventually fully attenuated as the flow develops further.

At varying times following the complete attenuation of the laser beams, the optical density of the flows decreases and the laser beams are partially transmitted. The exact nature of the optical density

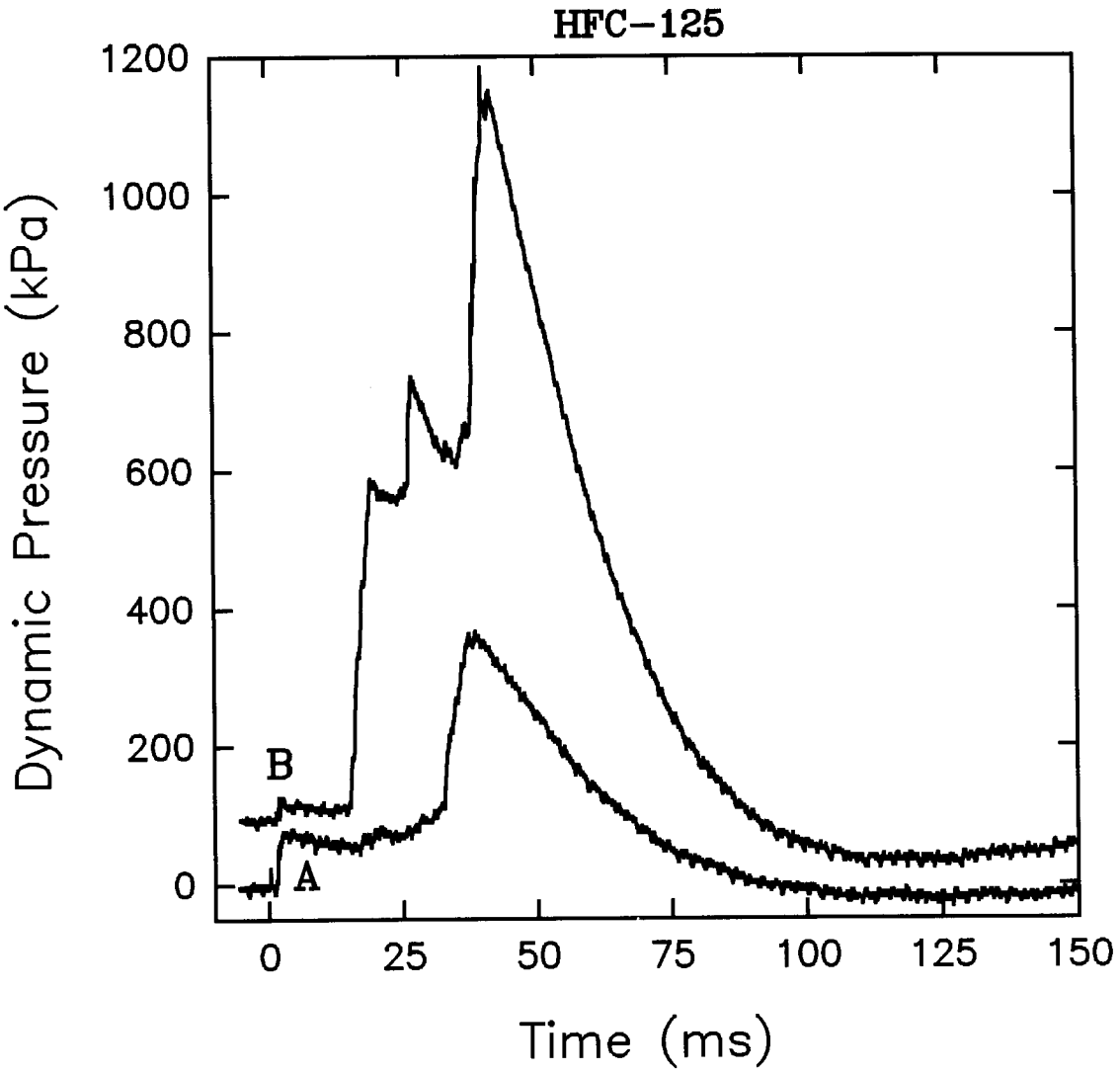

Figure 96. Two time traces of near-field dynamic pressure for releases of HFC-125. Trace B is offset by 100 kPa. Conditions: A, 416 g, release pressure 4.07 MPa; B, 423 g, release pressure 4.24 MPa.

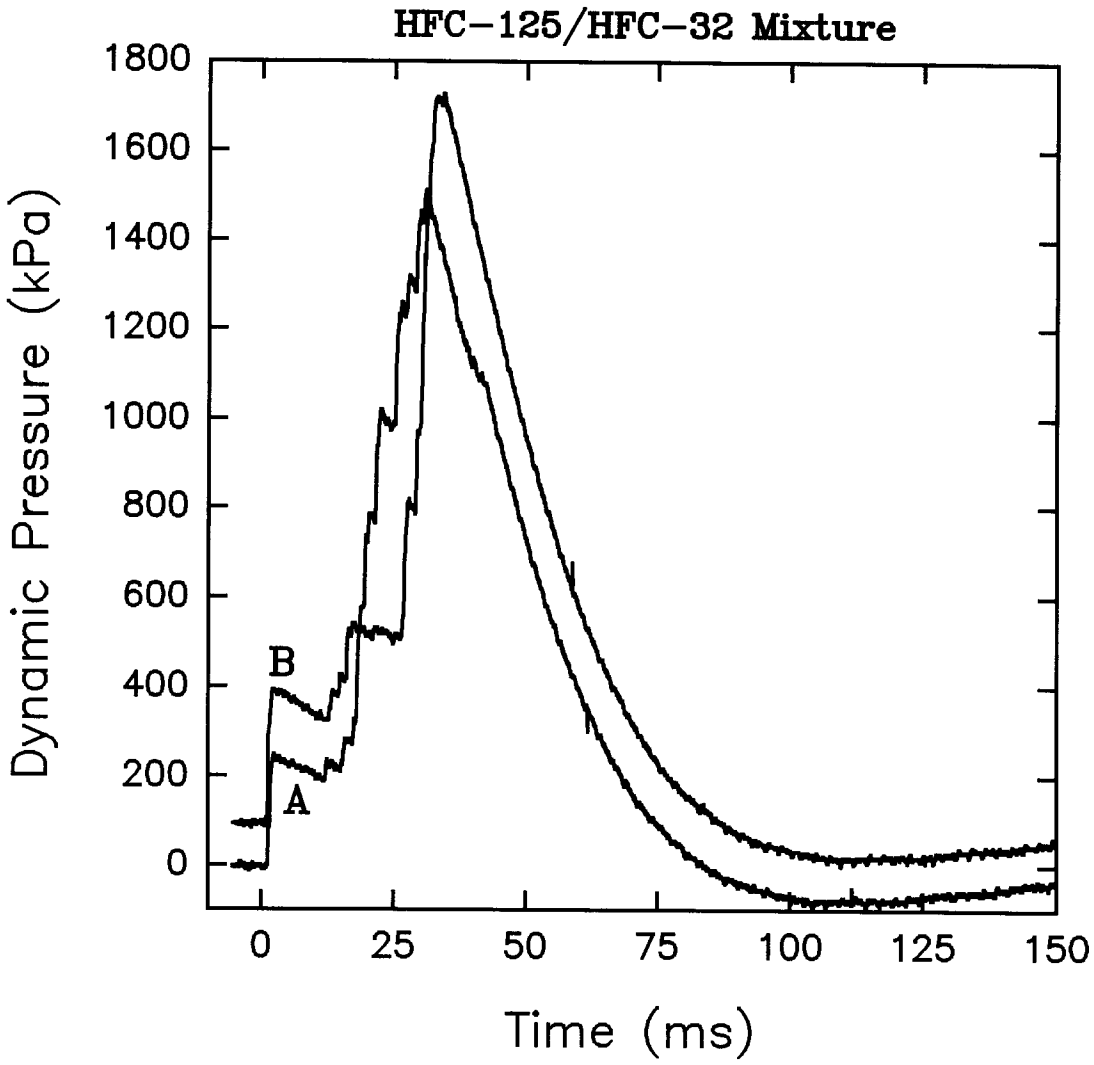

Figure 97. Two time traces of near-field dynamic pressure for releases of the HFC-125/HFC-32 mixture. Trace B is offset by 100 kPa. Conditions: A, 375 g, release pressure 4.36 MPa; B, 358 g, release pressure 4.31 MPa.

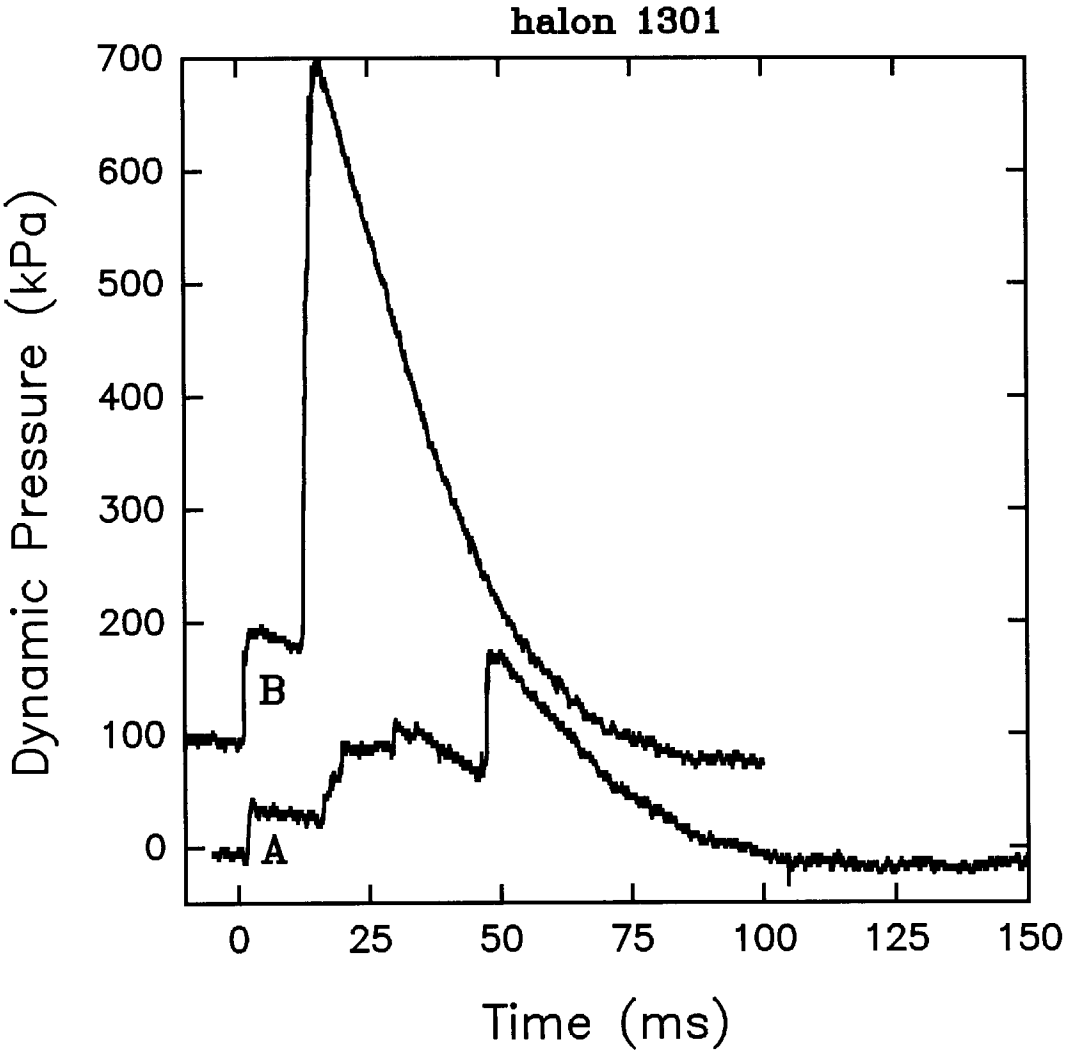

Figure 98. Two time traces of near-field dynamic pressure for releases of halon 1301. Trace B is offset by 100 kPa. Conditions: A, 554 g, release pressure 4.36 MPa; B, 270 g, release pressure 4.43 MPa.

Table 7. Downstream Distances from the Orifice of the Release Vessel for the Five Laser Beams. Distances Between the Laser Beams are also Indicated.

	Downstream Position (m)	Separation Distance (m)
Laser #1	0.0	0.320
Laser #2	0.320	0.335
Laser #3	0.655	0.305
Laser #4	0.960	0.340
Laser #5	1.300	

of a flow is expected to be quite complex. It should be a function of the total mass concentration of the agent, the degree of vaporization of the agent, the size of droplets in the liquid phase, and the degree to which the agent has cooled and condensed water vapor from the surrounding air entrained by the flow. Even so, there are clear trends in the data. The total attenuation of laser #1 lasts for much longer than the agent release time (30-40 ms). The explanation for this behavior is available from the high-speed films of the behavior of the agents inside the vessel (see Section 3.4.1). These show that agent condensation occurs in the nitrogen above the liquid in the vessel during a release. This is attributed to the cooling of the nitrogen and gaseous agent by the adiabatic expansion of the gas (see Section 3.4). Due to the gas used to pressurize the vessel, there is a slow flow of nitrogen even after a release is complete and eventually the condensed agent is swept from the vessel.

The time behaviors of laser #2 transmission for releases of different agents provide insight in the evaporation characteristics of the various agents. For all of the agents except FC-218, the time of total laser beam attenuation is on the order of 60 ms or roughly 50% longer than the total release time of the liquid. The total attenuation time for FC-218 is roughly the same as its release time. The total attenuation times of the beam for laser #3 tend to be somewhat shorter than for laser #2. The recovery of light transmission tends to be quicker for the lower boiling-point agents.

The periods of total light attenuation for lasers #4 and #5 are longer and the recovery of light transmission takes place more slowly. It is likely that this observation is the result of the condensation of water vapor which should require a longer period to evaporate than the agents.

As can be seen in Figure 99 through Figure 109, the arrival time of an agent release at a laser beam is easily detected as a rapid, near-total attenuation of the transmitted light. It is a simple exercise to accurately determine these arrival times. For example, for the data shown in Figure 99 the arrival times are 0, 5.88, 10.55, 15.31, and 20.01 ms for lasers #1-#5, respectively. Since the distances between the laser beams are known, four average velocities can be calculated from these results. Such calculations have been made for the series of releases from 2/3 filled vessels. In the figures which follow, the average velocities are plotted as a function of downstream distance defined as the midpoints of the laser beam locations.

Figure 110 through Figure 120 show results for the ten agents which are liquids at room temperature and halon 1301. There are dramatic differences among the results. HFC-236fa, FC-31-10, FC-318, HCFC-124, and HFC-227ea (Figure 110 through Figure 114) are similar. Average velocities measured at the first measuring station fall in a range of 50 to 60 m/s. As the

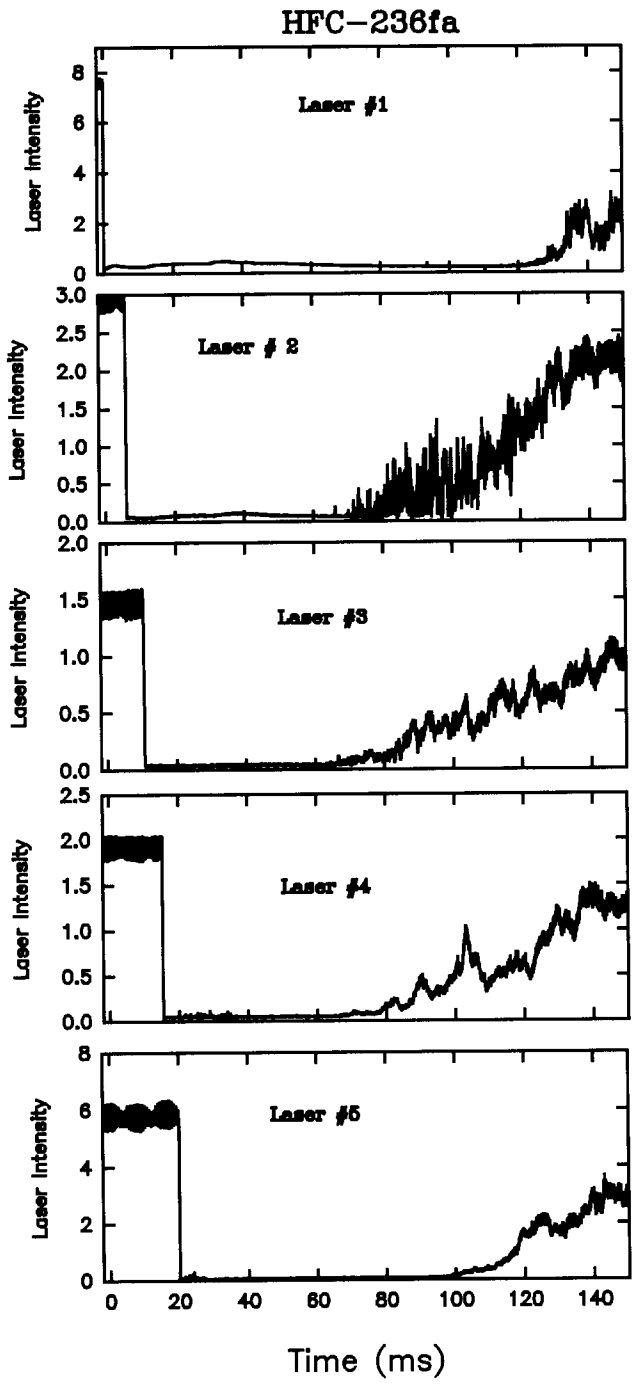

Figure 99. Time behaviors for transmission of laser beams #1-#5 spaced as shown in Table 7 following a release of HFC-236fa at 0 s. Conditions: 464 g agent, 4.30 MPa release pressure.

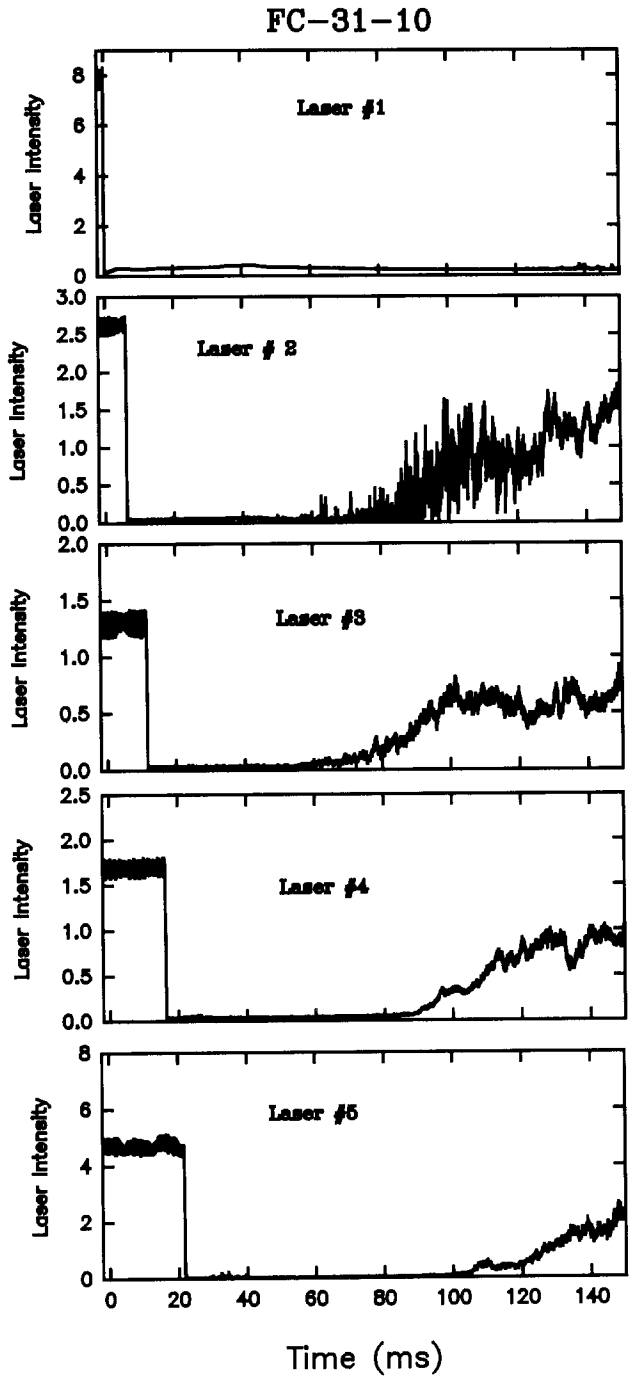

Figure 100. Time behaviors for transmission of laser beams #1-#5 spaced as shown in Table 7 following a release of FC-31-10 at 0 s. Conditions: 520 g agent, 3.85 MPa release pressure.

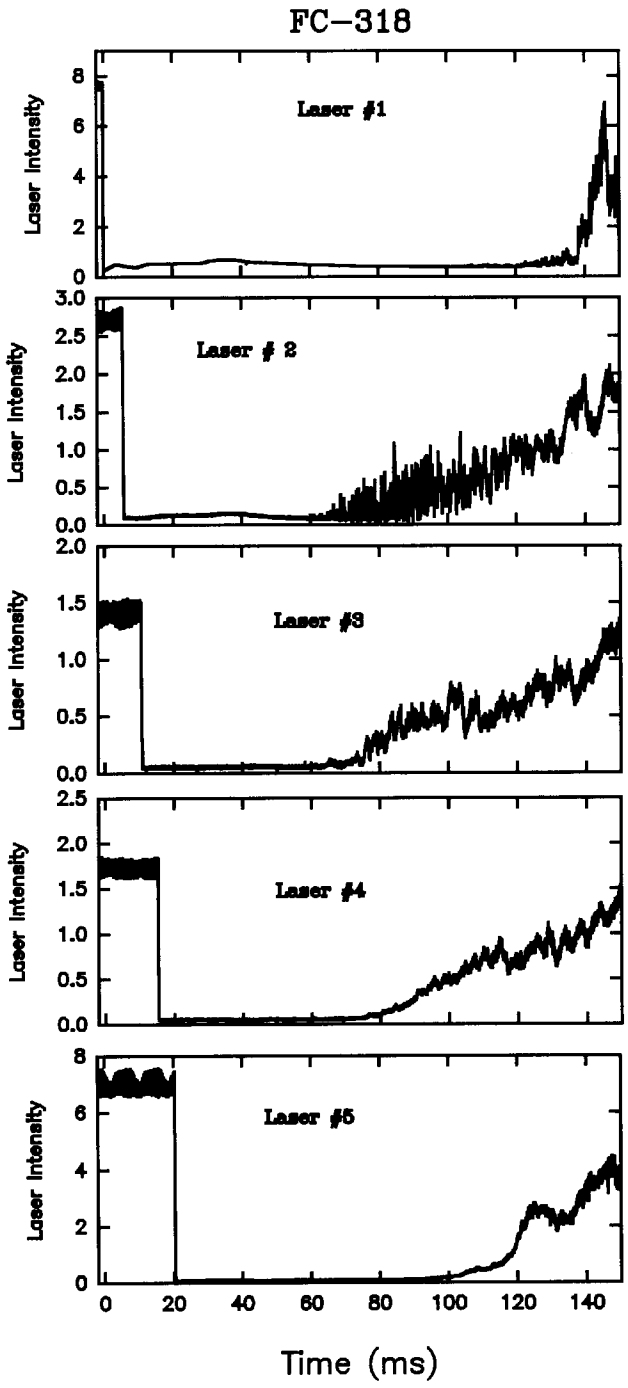

Figure 101. Time behaviors for transmission of laser beams #1-#5 spaced as shown in Table 7 following a release of FC-318 at 0 s. Conditions: 501 g agent, 4.43 MPa release pressure.

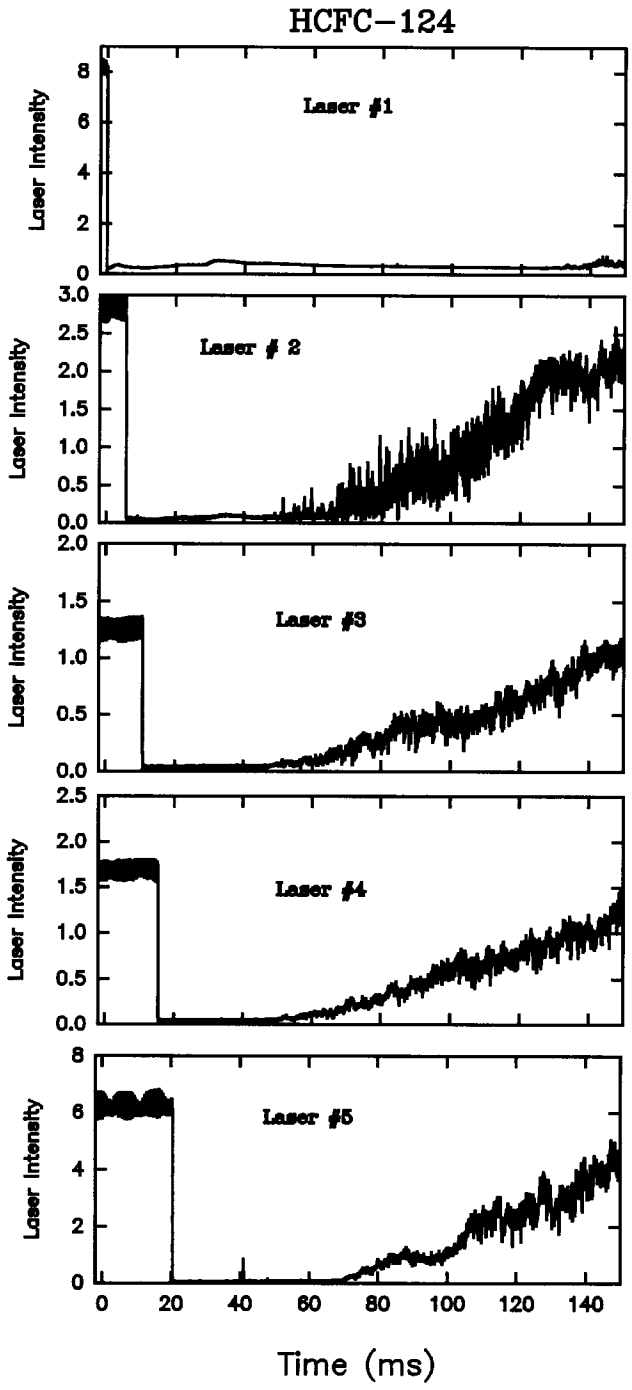

Figure 102. Time behaviors for transmission of laser beams #1-#5 spaced as shown in Table 7 following a release of HCFC-124 at 0 s. Conditions: 462 g agent, 4.05 MPa release pressure.

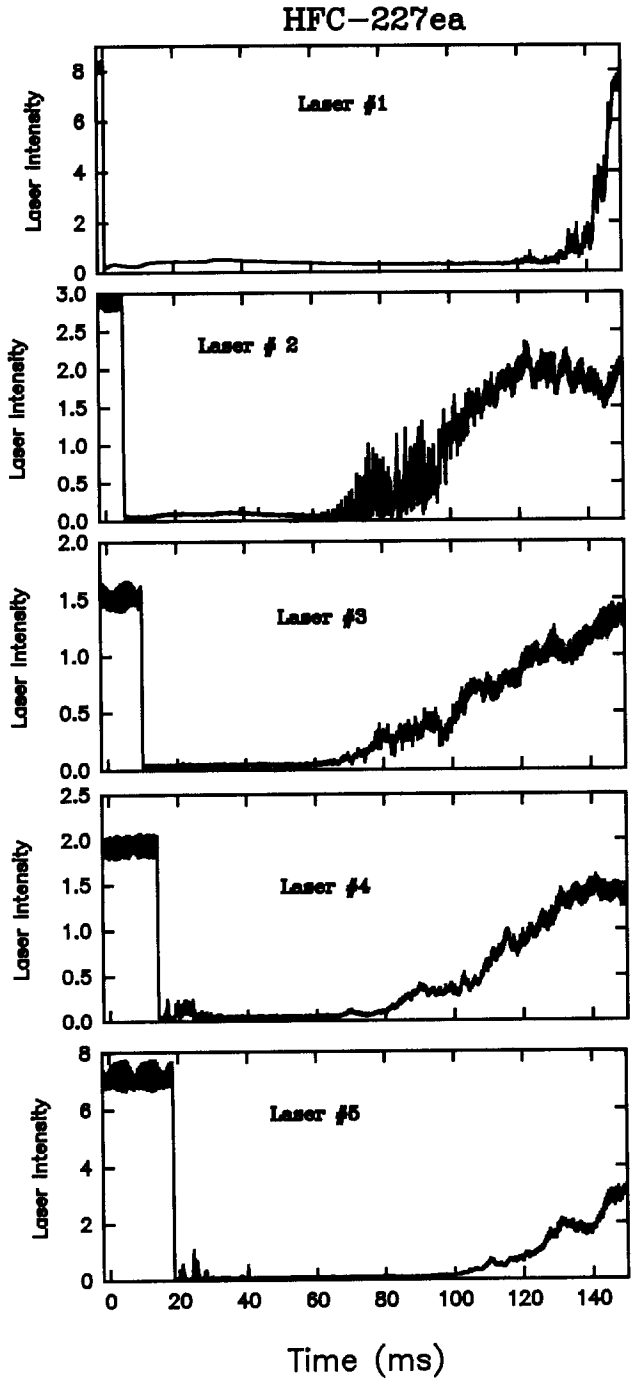

Figure 103. Time behaviors for transmission of laser beams #1-#5 spaced as shown in Table 7 following a release of HFC-227ea at 0 s. Conditions: 476 g agent, 4.45 MPa release pressure.

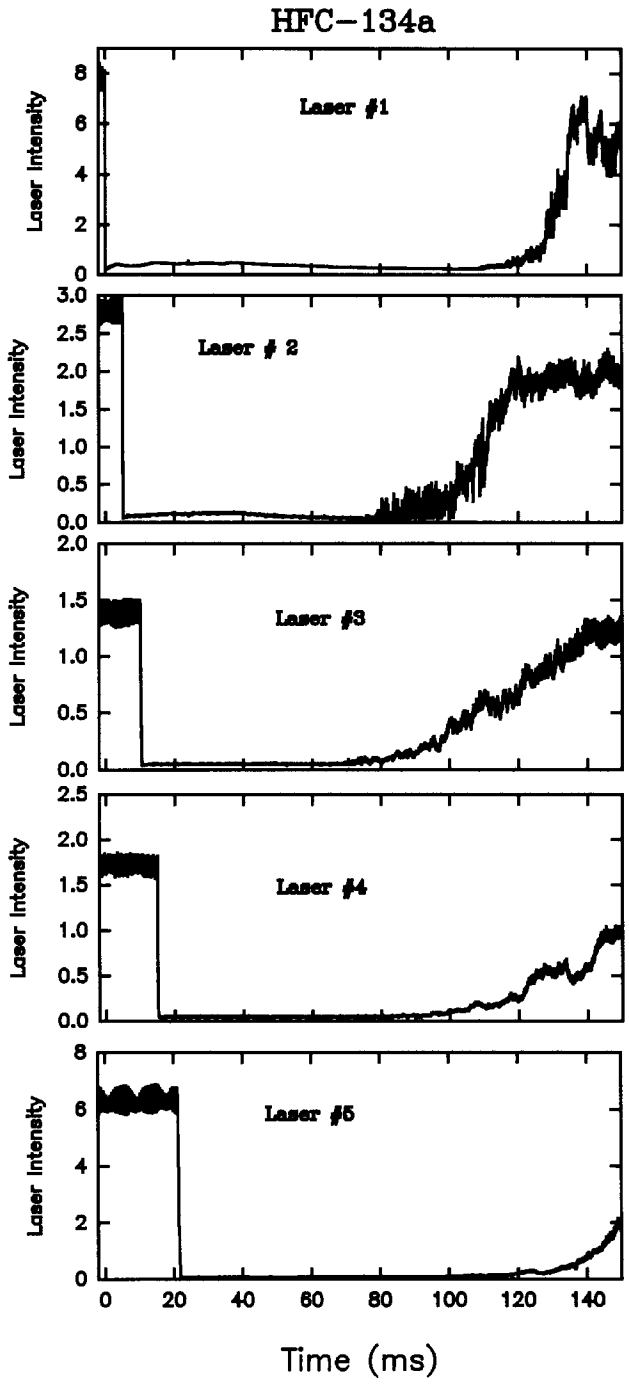

Figure 104. Time behaviors for transmission of laser beams #1-#5 spaced as shown in Table 7 following a release of HFC-134a at 0 s. Conditions: 418 g agent, 4.13 MPa release pressure.

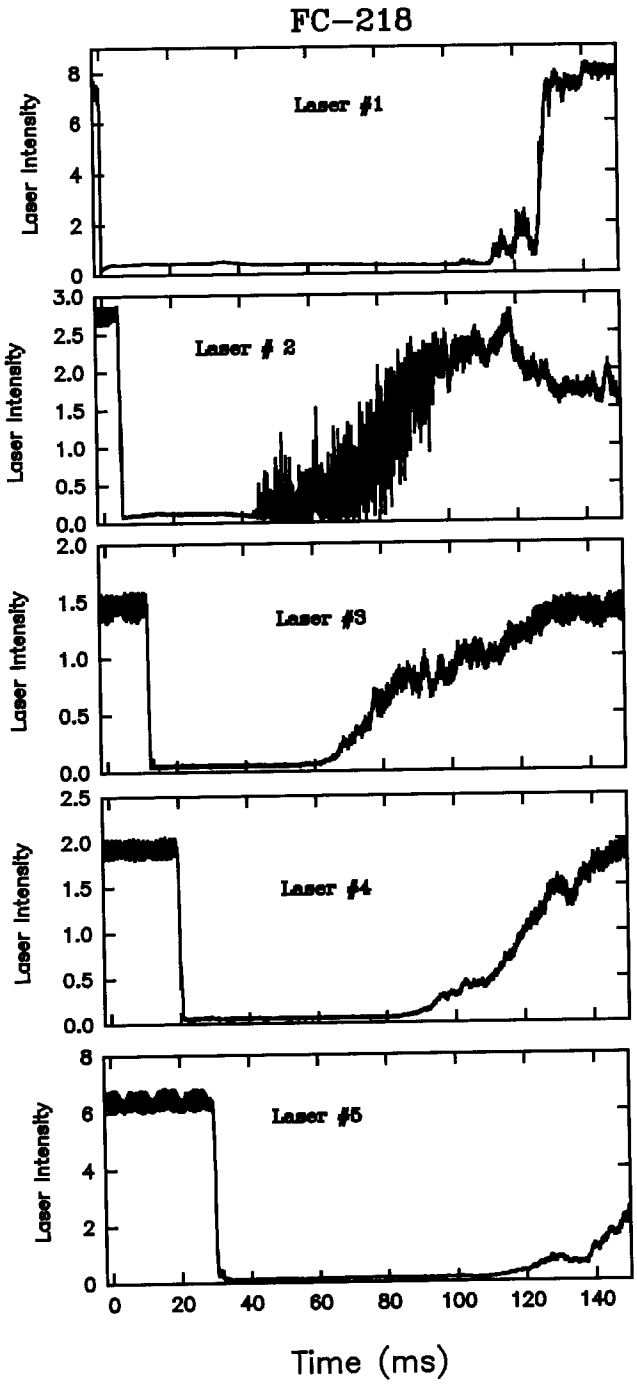

Figure 105. Time behaviors for transmission of laser beams #1-#5 spaced as shown in Table 7 following a release of FC-218 at 0 s. Conditions: 463 g agent, 4.06 MPa release pressure.

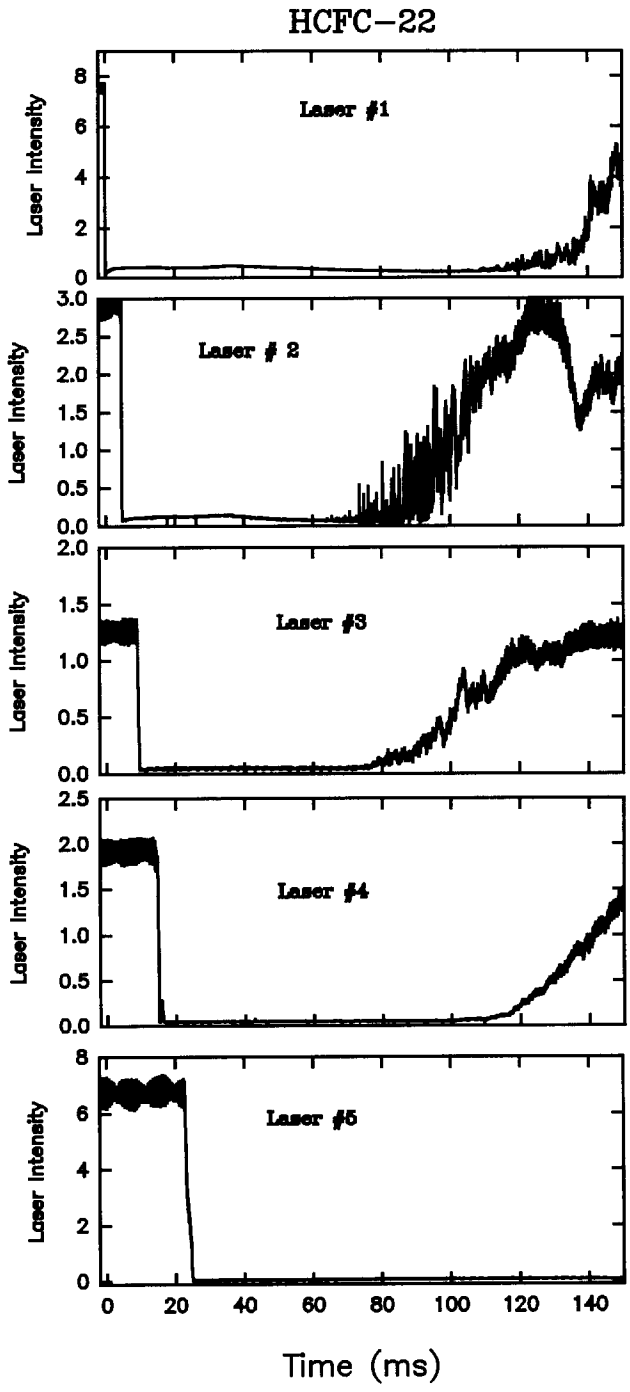

Figure 106. Time behaviors for transmission of laser beams #1-#5 spaced as shown in Table 7 following a release of HCFC-22 at 0 s. Conditions: 417 g agent, 4.52 MPa release pressure.

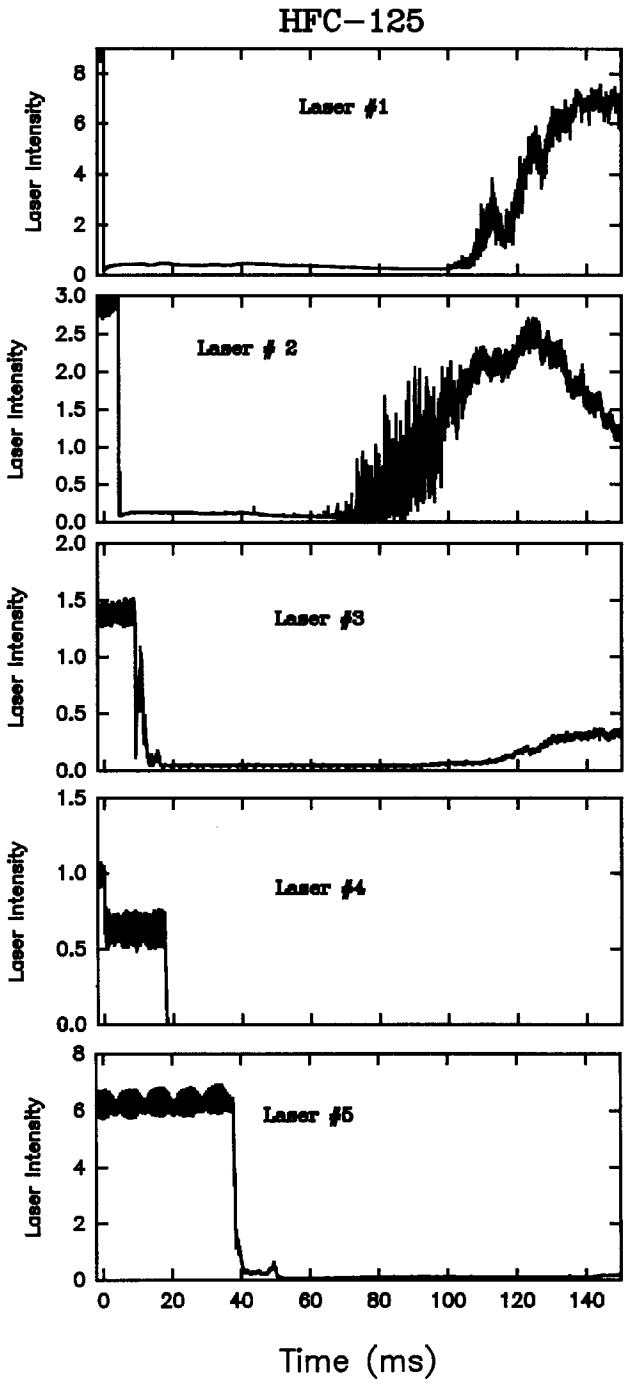

Figure 107. Time behaviors for transmission of laser beams #1-#5 spaced as shown in Table 7 following a release of HFC-125 at 0 s. Conditions: 423 g agent, 4.24 MPa release pressure.

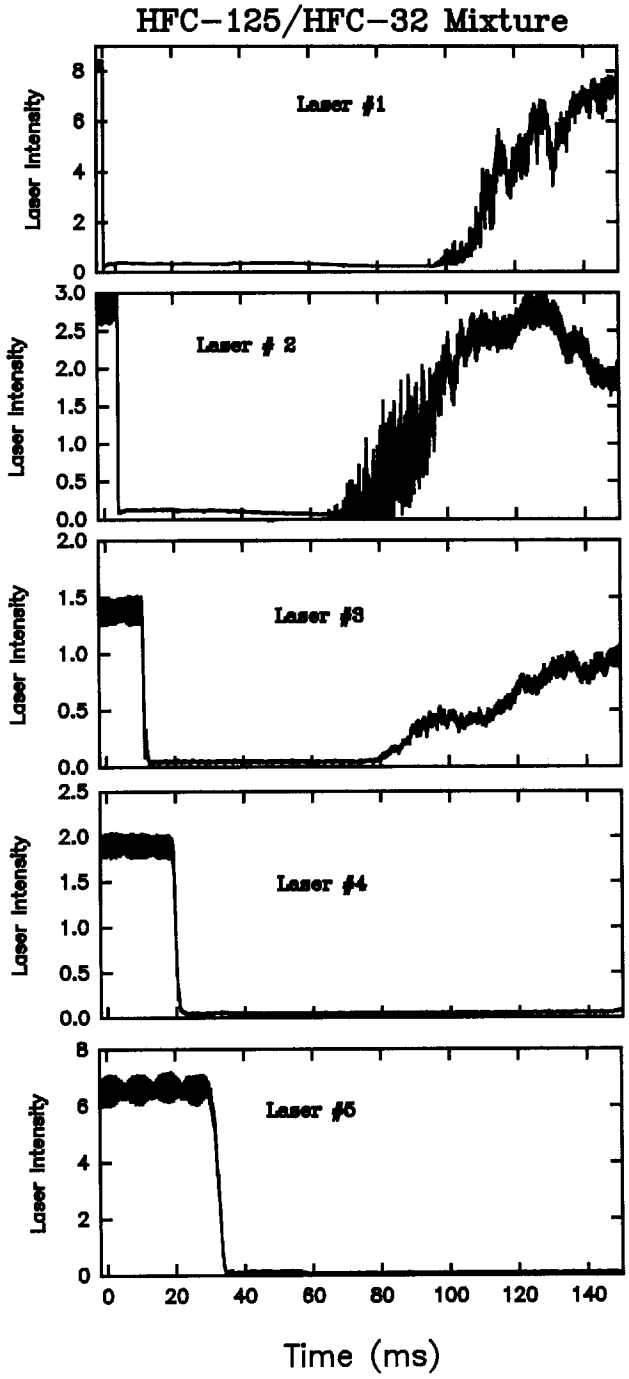

Figure 108. Time behaviors for transmission of laser beams #1-#5 spaced as shown in Table 7 following a release of the HFC-125/HFC-32 mixture at 0 s. Conditions: 375 g agent, 4.36 MPa release pressure.

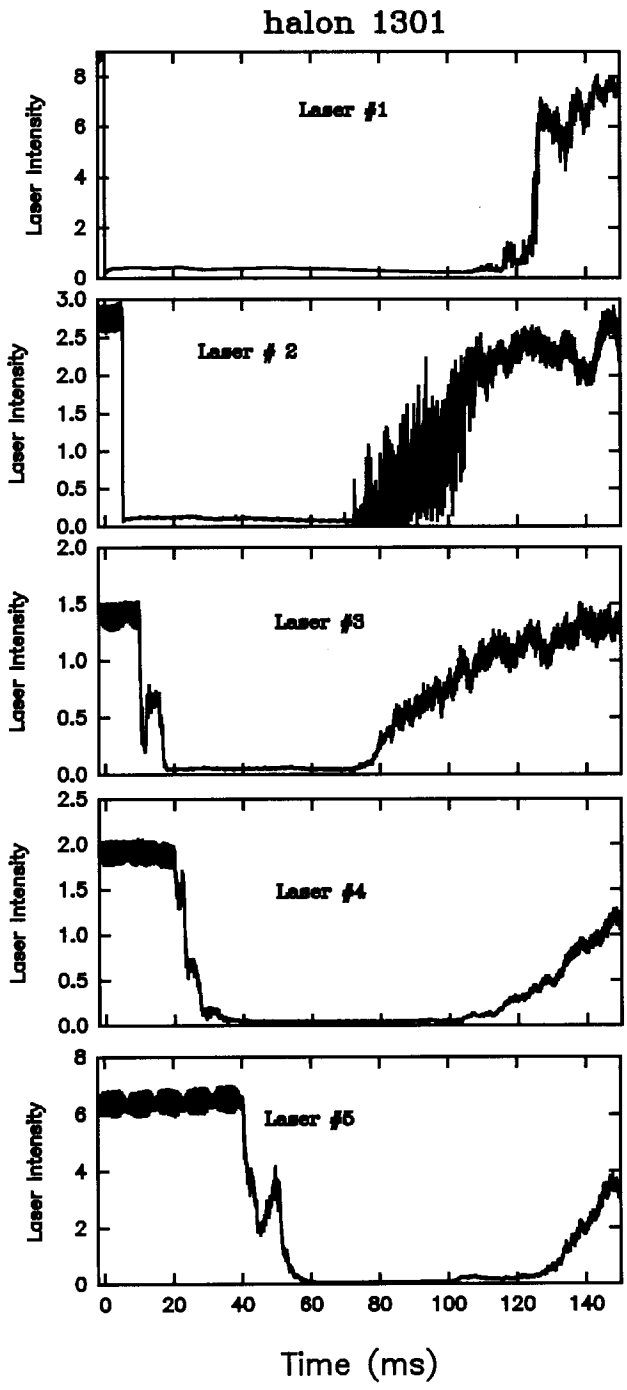

Figure 109. Time behaviors for transmission of laser beams #1-#5 spaced as shown in Table 7 following a release of halon 1301 at 0 s. Conditions: 554 g agent, 4.36 MPa release pressure.

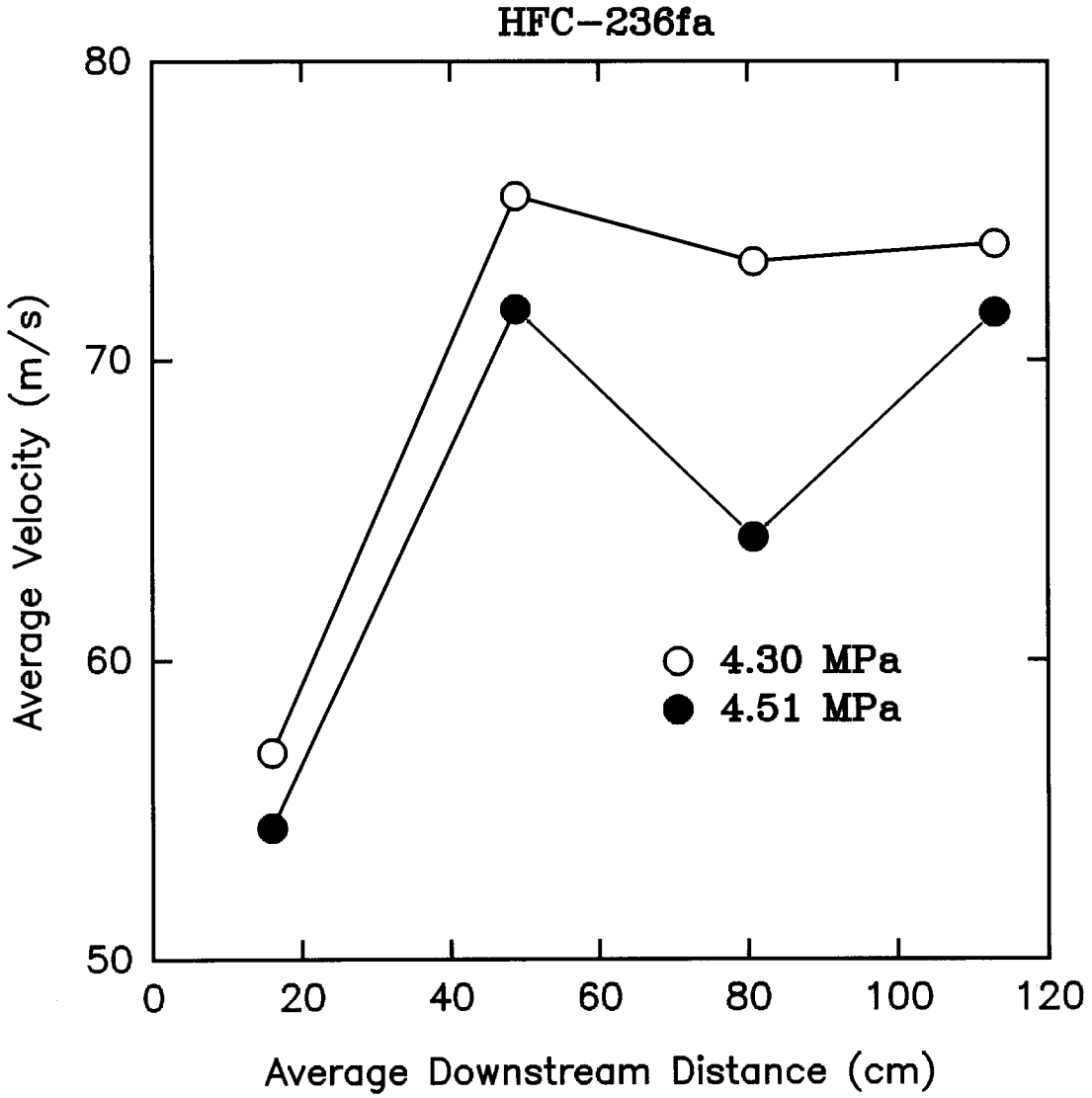

Figure 110. Average velocities for releases of HFC-236fa determined by the time of arrival at laser beams #1-#5 plotted as a function of average downstream distance. Pressures are those inside the vessel at disk bursting.

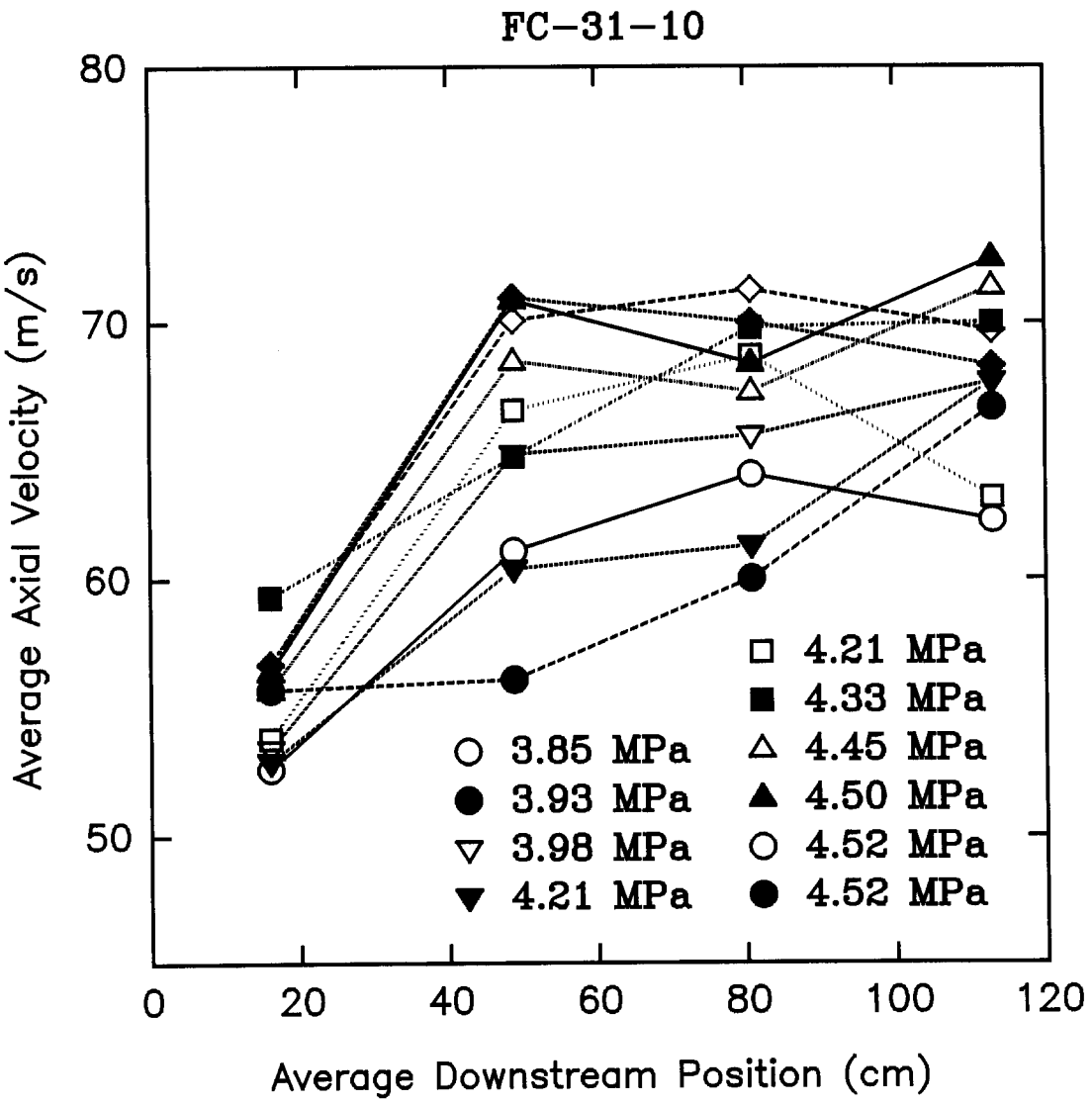

Figure 111. Average velocities for releases of FC-31-10 determined by the time of arrival at laser beams #1-#5 plotted as a function of average downstream distance. Pressures are those inside the vessel at disk bursting.

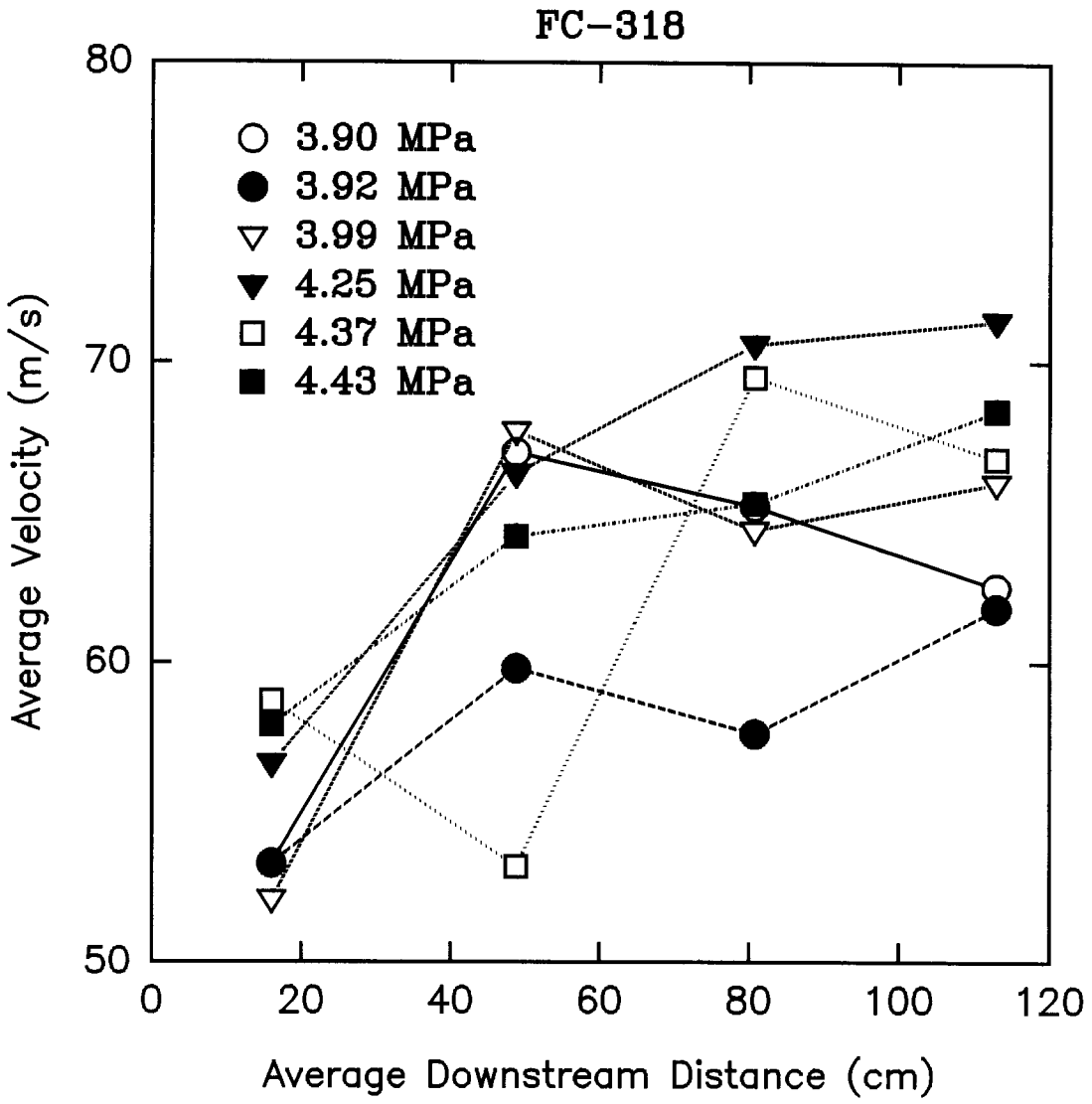

Figure 112. Average velocities for releases of FC-318 determined by the time of arrival at laser beams #1-#5 plotted as a function of average downstream distance. Pressures are those inside the vessel at disk bursting.

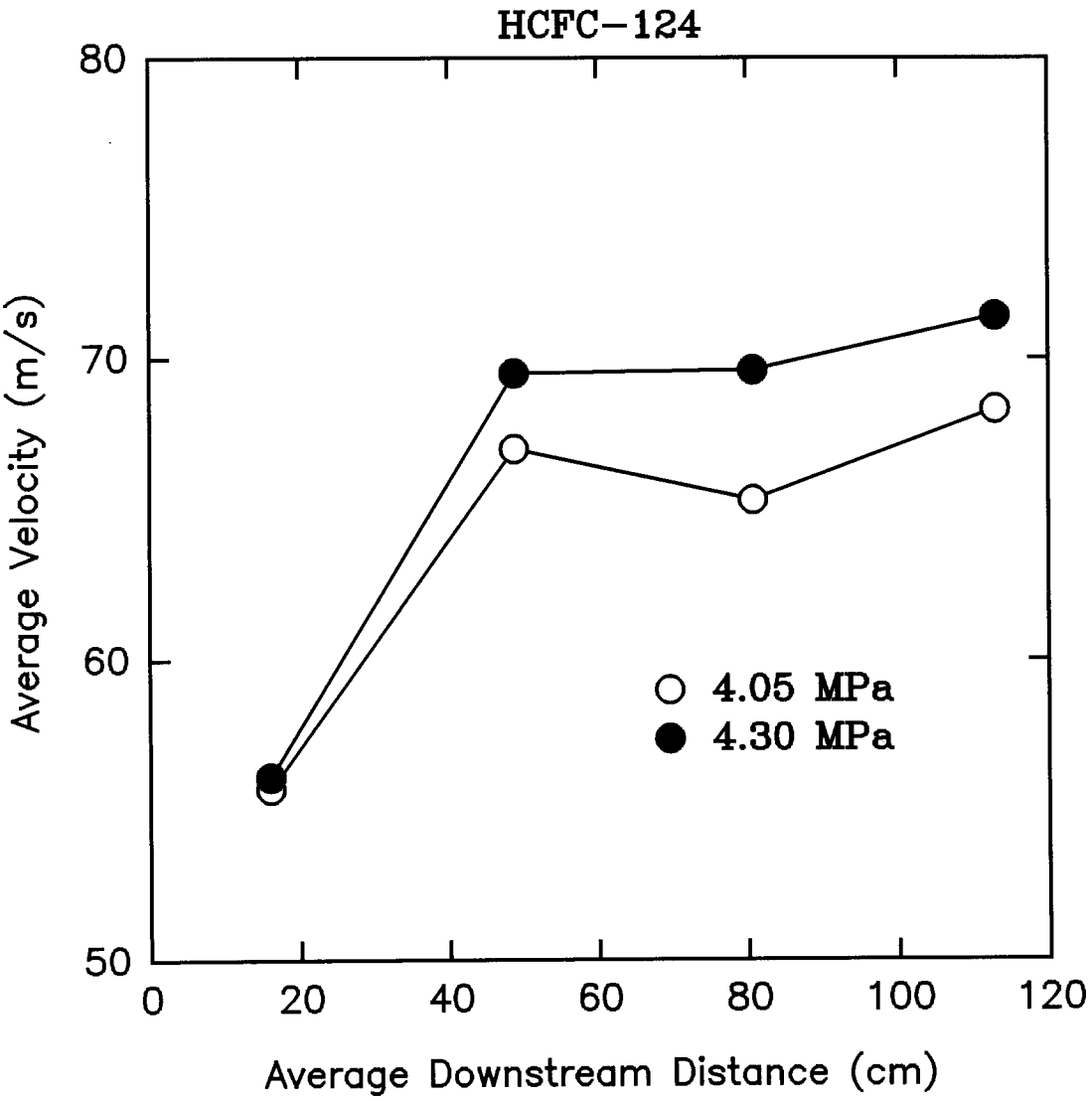

Figure 113. Average velocities for releases of HCFC-124 determined by the time of arrival at laser beams #1-#5 plotted as a function of average downstream distance. Pressures are those inside the vessel at disk bursting.

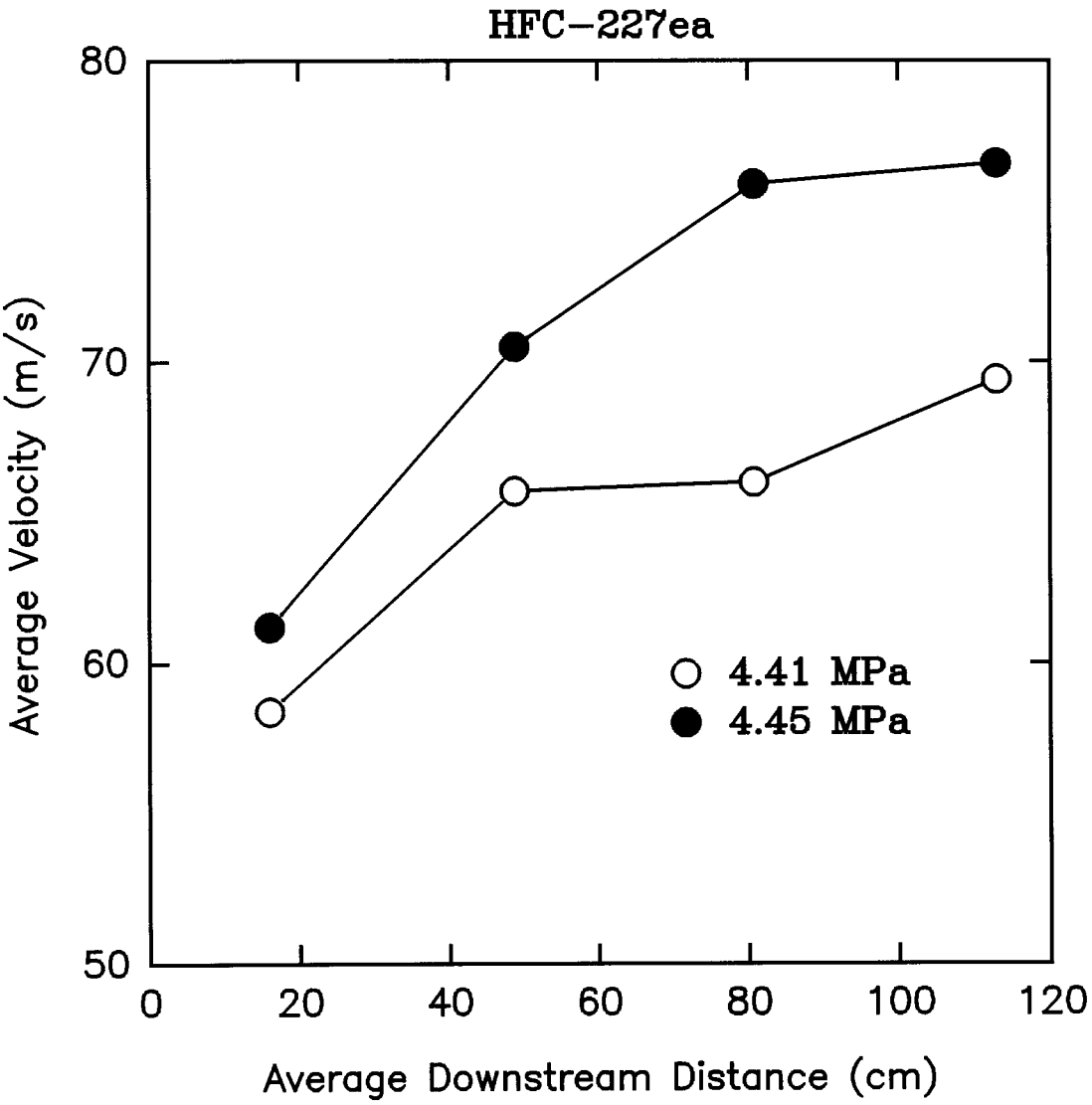

Figure 114. Average velocities for releases of HFC-227ea determined by the time of arrival at laser beams #1-#5 plotted as a function of average downstream distance. Pressures are those inside the vessel at disk bursting.

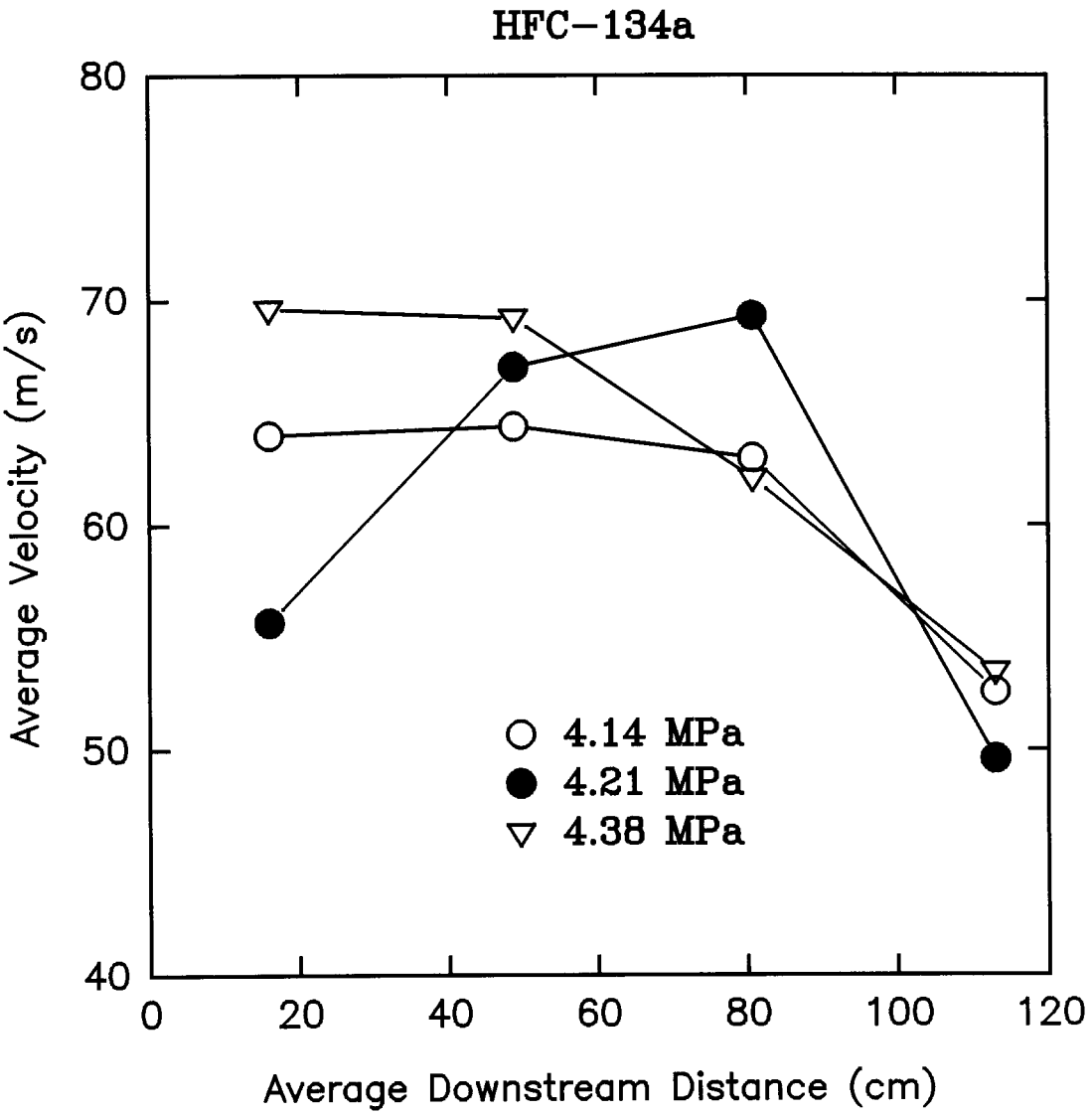

Figure 115. Average velocities for releases of HFC-134a determined by the time of arrival at laser beams #1-#5 plotted as a function of average downstream distance. Pressures are those inside the vessel at disk bursting.

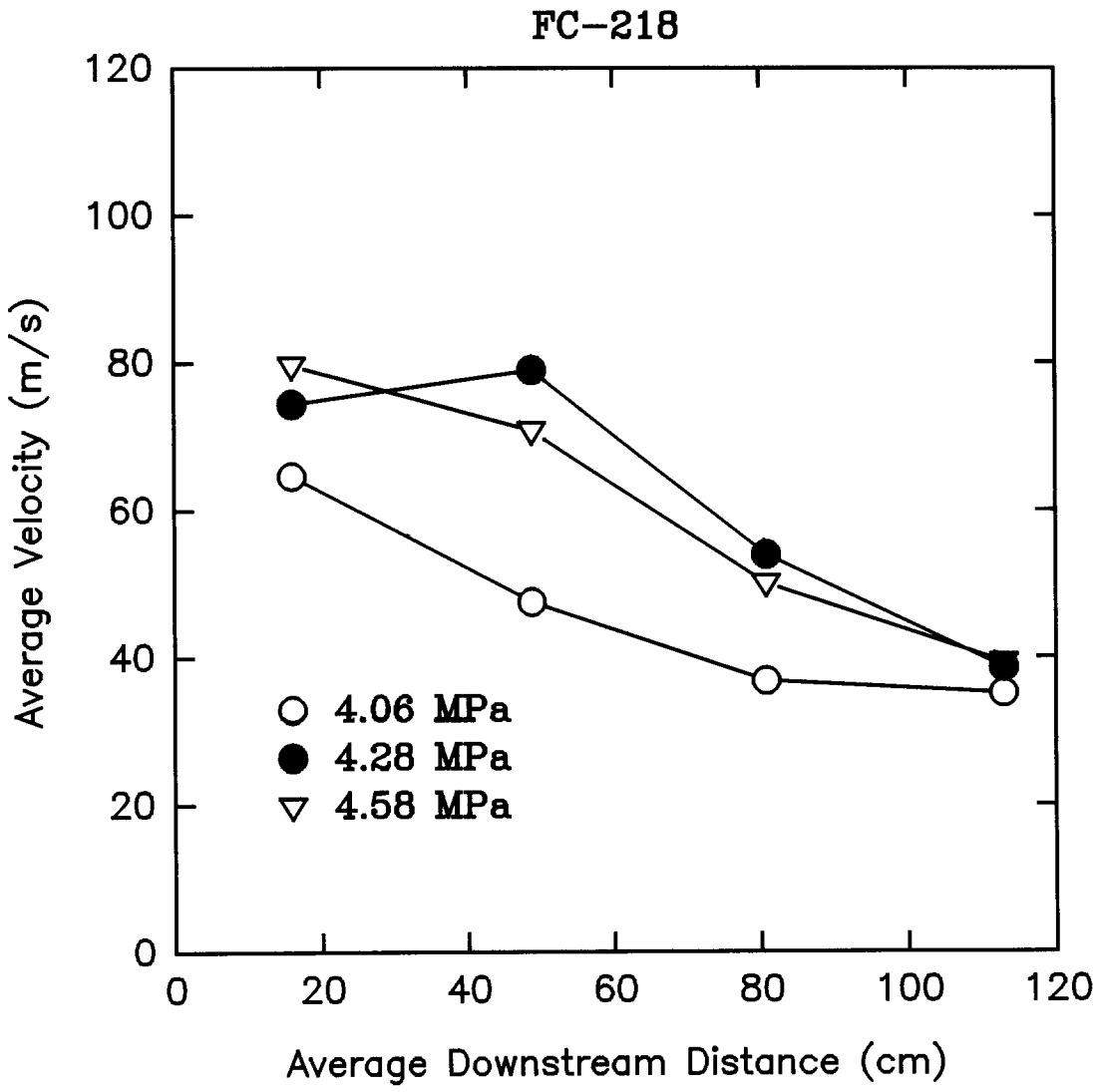

Figure 116. Average velocities for releases of FC-218 determined by the time of arrival at laser beams #1-#5 plotted as a function of average downstream distance. Pressures are those inside the vessel at disk bursting.

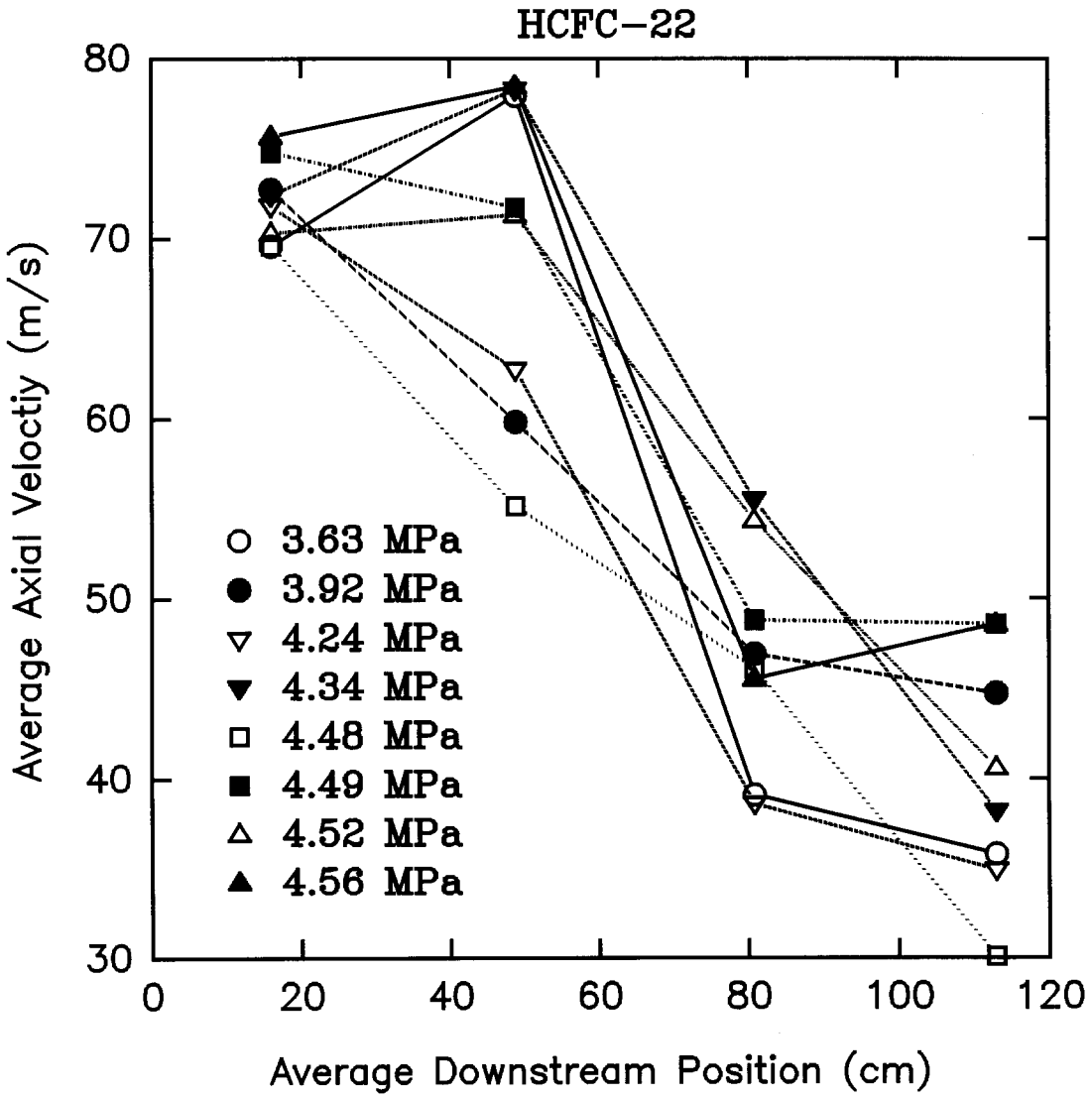

Figure 117. Average velocities for releases of HCFC-22 determined by the time of arrival at laser beams #1-#5 plotted as a function of average downstream distance. Pressures are those inside the vessel at disk bursting.

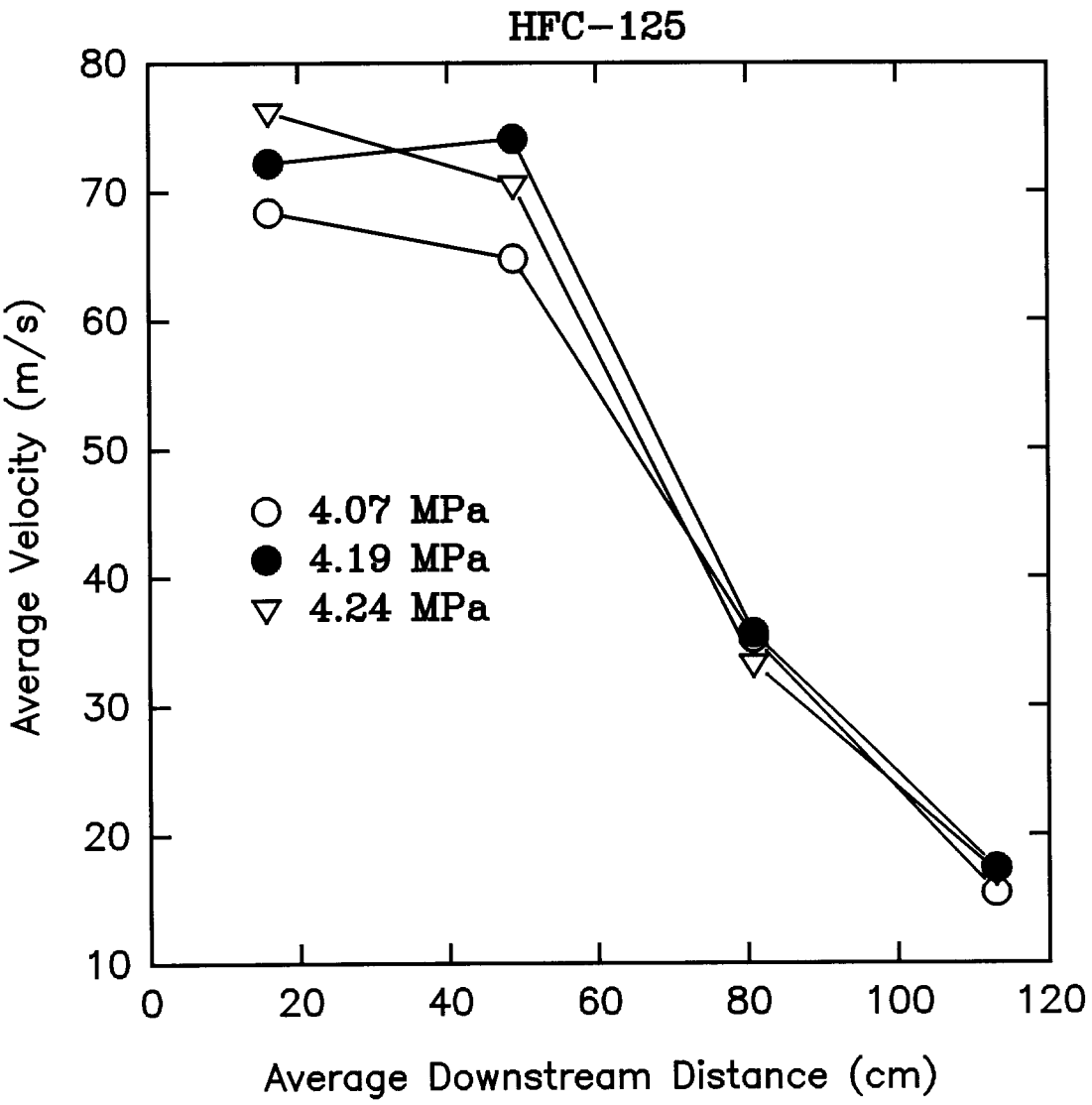

Figure 118. Average velocities for releases of HFC-125 determined by the time of arrival at laser beams #1-#5 plotted as a function of average downstream distance. Pressures are those inside the vessel at disk bursting.

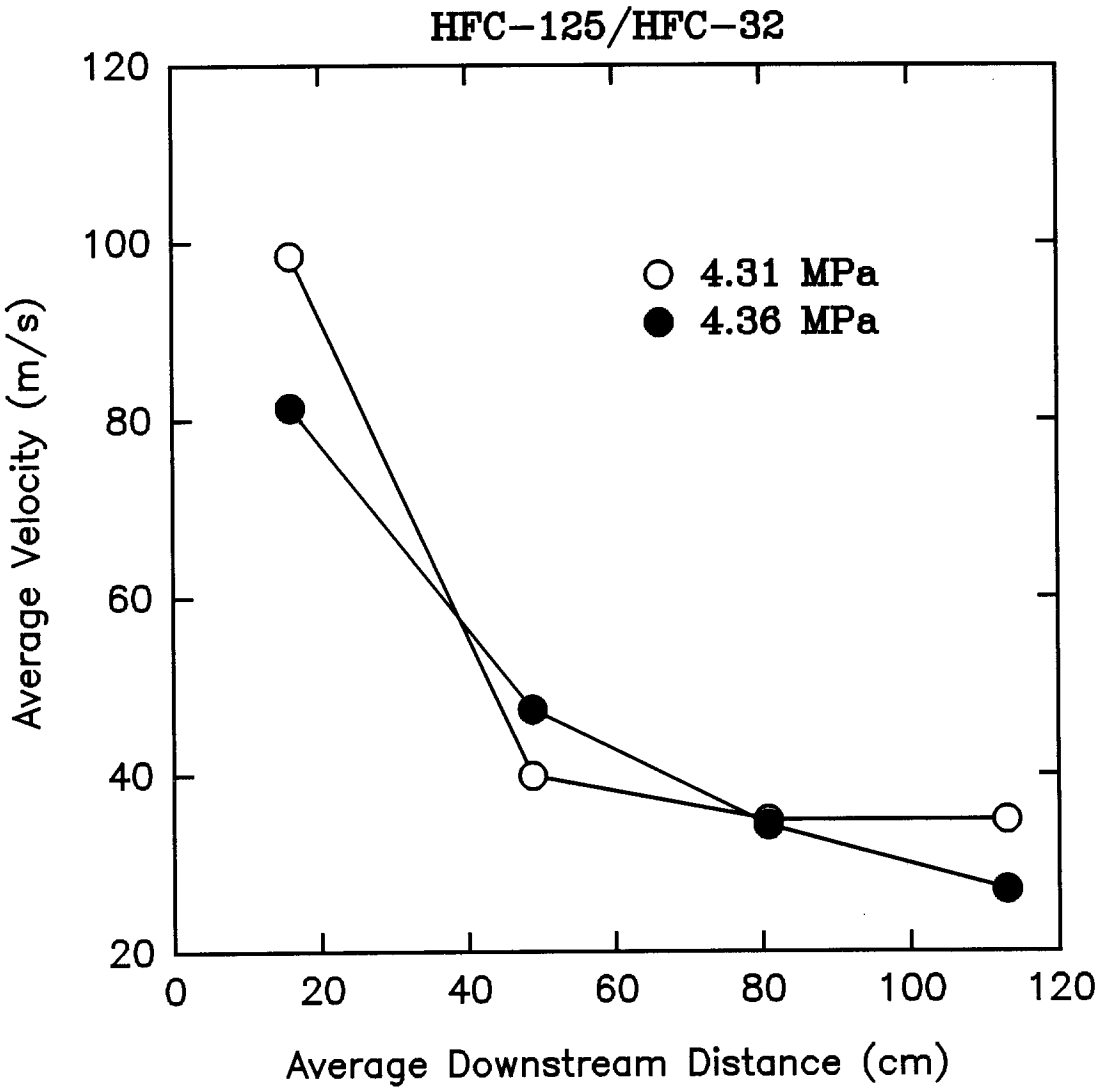

Figure 119. Average velocities for releases of the HFC-125/HFC-32 mixture determined by the time of arrival at laser beams #1-#5 plotted as a function of average downstream distance. Pressures are those inside the vessel at disk bursting.

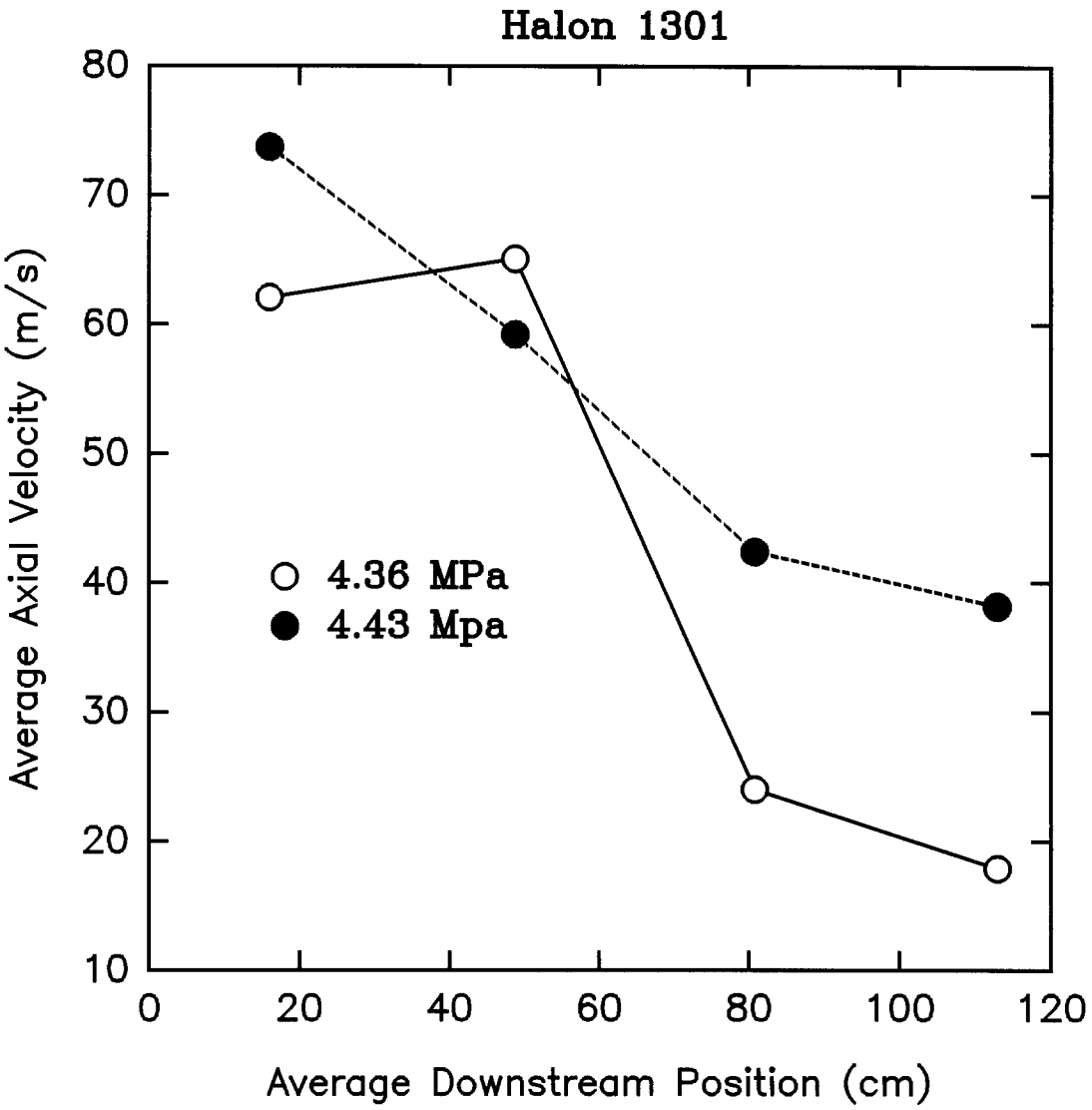

Figure 120. Average velocities for releases of halon 1301 determined by the time of arrival at laser beams #1-#5 plotted as a function of average downstream distance. Pressures are those inside the vessel at disk bursting.

agent moves further away from the vessel, the average velocities actually increase, remaining roughly constant at approximately 70 m/s.

HFC-134a (Figure 115) has a different velocity dependence on downstream distance. Two of the releases had high velocities (65-70 m/s) near the vessel which stayed roughly constant over the two nearest measurement locations. At the third and fourth locations the velocities actually decreased to values of roughly 50 m/s. Note that these results are nearly exactly the opposite of those for the higher boiling-point agents discussed above. A third release of HFC-134a looks similar to the higher boiling-point agents (*i.e.*, the measured velocity near the nozzle is roughly 56 ms/s and increases to roughly 70 m/s) except that the velocity again decreases at the furthest measuring station.

The velocity results for FC-218 (Figure 116) are similar to those for HFC-134a. Velocities for the two locations near the nozzle are on the order of 80 ms/s. As the agent moves further from the exit the velocity begins to fall off, decreasing to approximately 40 m/s for the last station. The results for HCFC-22 (Figure 117) are similar, but there is substantial scatter in the results.

For HFC-125 (Figure 118) the velocities near the vessel are again roughly 70 m/s. However, these velocities decrease faster with downstream distance becoming less than 20 m/s at the most distant location. The HFC-125/HFC-32 mixture (Figure 119) displays a similar, but enhanced behavior. Velocities near the vessel exit are very high, approaching 100 m/s. By the second measuring station the velocity has dropped rapidly and eventually falls to less than 30 m/s. Interestingly, the results for halon 1301 (Figure 120) are similar to those for FC-218 and HFC-125.

These measurements have been made for a range of pressures in the release vessel due to variations in burst disks. Close examination shows that the measured velocities depend somewhat on pressure, with higher pressures yielding higher velocities. However, for the range of pressures shown the dependence is relatively weak and on the order of experiment-to-experiment variation.

3.5.3.4 Far-Field Dynamic Pressure Measurements. These measurements were made on the centerline of the releases at a distance 1.3 m from the vessel exit. The pressure transducer was oriented such that it faced the release direction. Figure 121 through Figure 131 show examples of the dynamic pressures recorded as a function of time for the ten room-temperature liquid replacement agents as well as halon 1301.

Figure 121 shows time plots of downstream dynamic pressure for two releases of HFC-236fa. In both cases a rapid pressure rise is observed at approximately 20 ms following release. This agrees closely with the arrival of the agent at laser #5 as determined by strong beam attenuation (18.8 ms and 20.1 ms). The pressure jumps roughly 200 to 300 kPa immediately following the arrival of the agent at the transducer. The pressure then continues to increase over the next 25 ms. Maximum pressures observed in the two cases were 1,100 kPa and 1,420 kPa. As we will be discussed shortly, such pressure increases are indicative of a two-phase flow striking the transducer.

Similar pressure traces for FC-31-10 are shown in Figure 122. The behaviors are similar to those for HFC-236fa with maximum pressures reaching 820 and 1029 kPa. The pressure traces for FC-318 (Figure 123) also have a similar behavior except the initial pressure increase is somewhat higher (500 to 700 kPa) with maximum observed values of 1000 and 1200 kPa. Results for HCFC-124 are shown in Figure 124. This agent generates strong pressure increases (500 to 700 kPa) immediately upon arrival at the transducer which then grow to very high levels (1200 to 1500 kPa). The results for HFC-227ea (Figure 125) are very similar to those for HCFC-124. The pressure traces for HFC-134a (Figure 126) have very rapid and large increases ($>$ 1000 kPa) upon arrival at the transducer and reach the highest values (1900-2100 kPa) of any of the high boiling-point agents.

The dynamic pressure measurements for FC-218 (Figure 127) have a very different behavior than those discussed thus far. A rapid pressure increase is observed at roughly 25 ms corresponding to the time when the agent reaches the transducer. A maximum value is quickly reached. This maximum

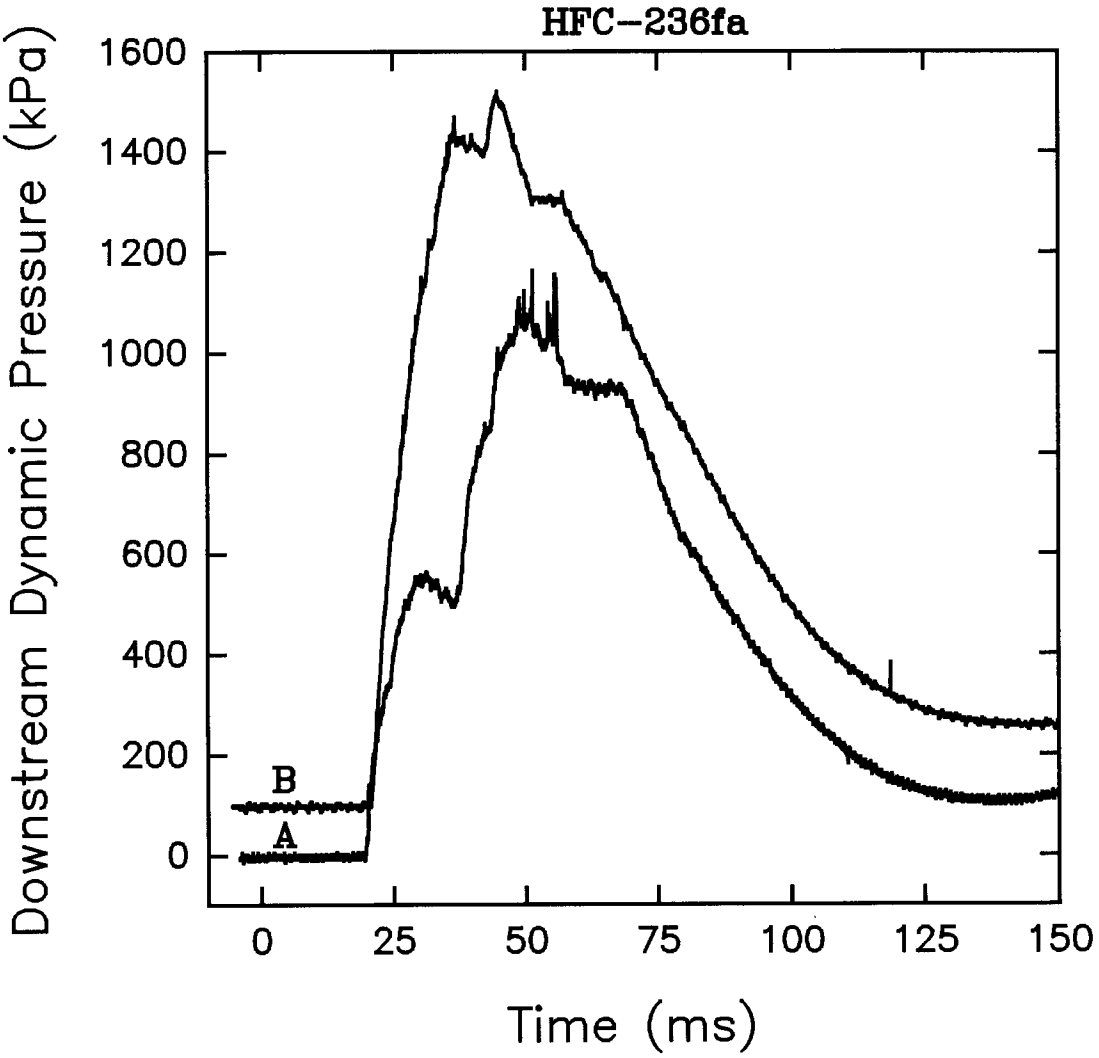

Figure 121. Dynamic pressure measured 1.3 m from the vessel for HFC-236fa. For clarity, trace B is offset by 100 kPa. Conditions are: A, 471 g agent, release pressure of 4.51 MPa ; B, 464 g of agent, release pressure of 4.30 MPa.

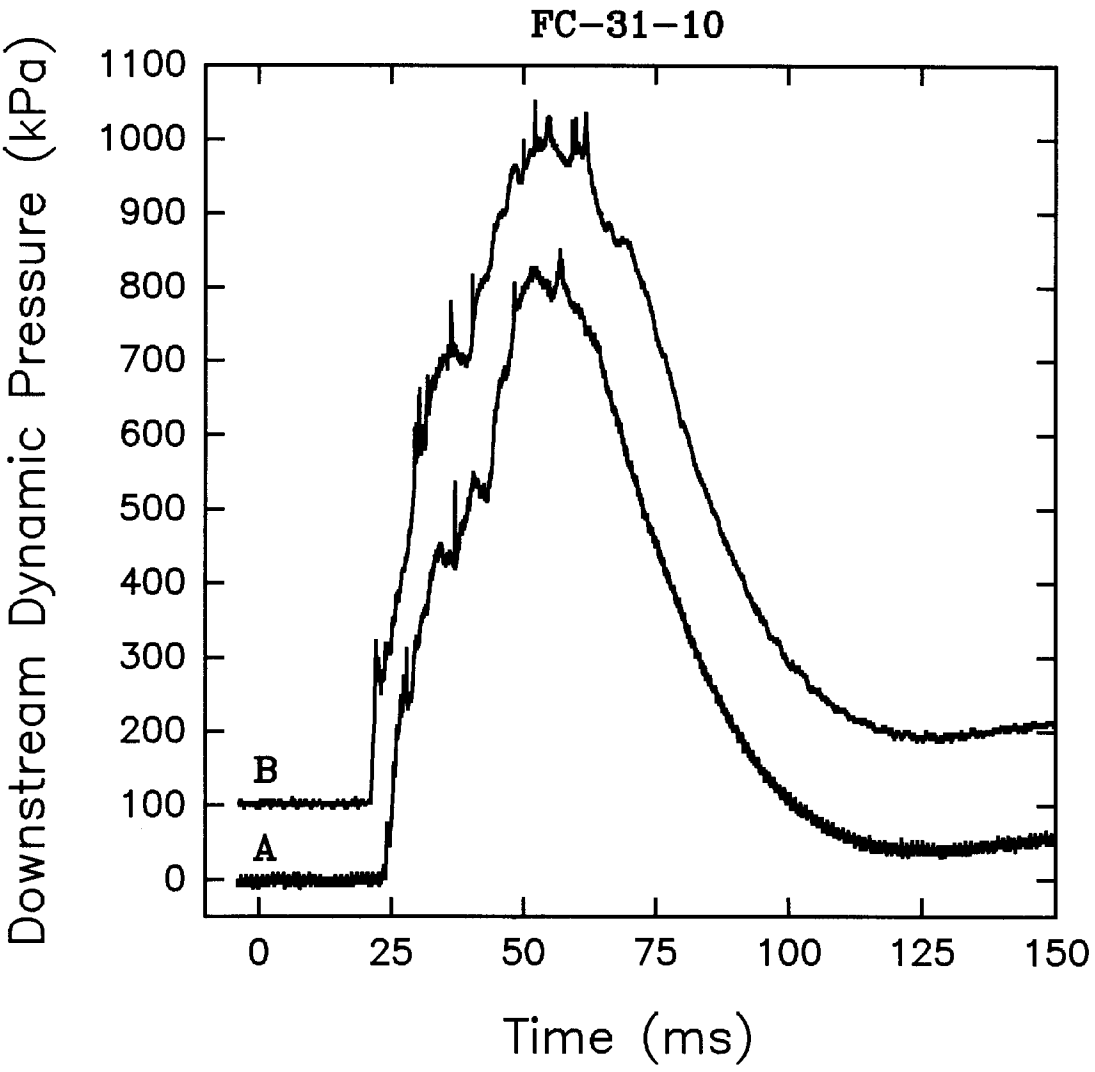

Figure 122. Dynamic pressure measured 1.3 m from the vessel for FC-31-10. For clarity, trace B is offset by 100 kPa. Conditions are: A, 495 g agent, release pressure of 3.93 MPa ; B, 515 g of agent, release pressure of 4.20 MPa.

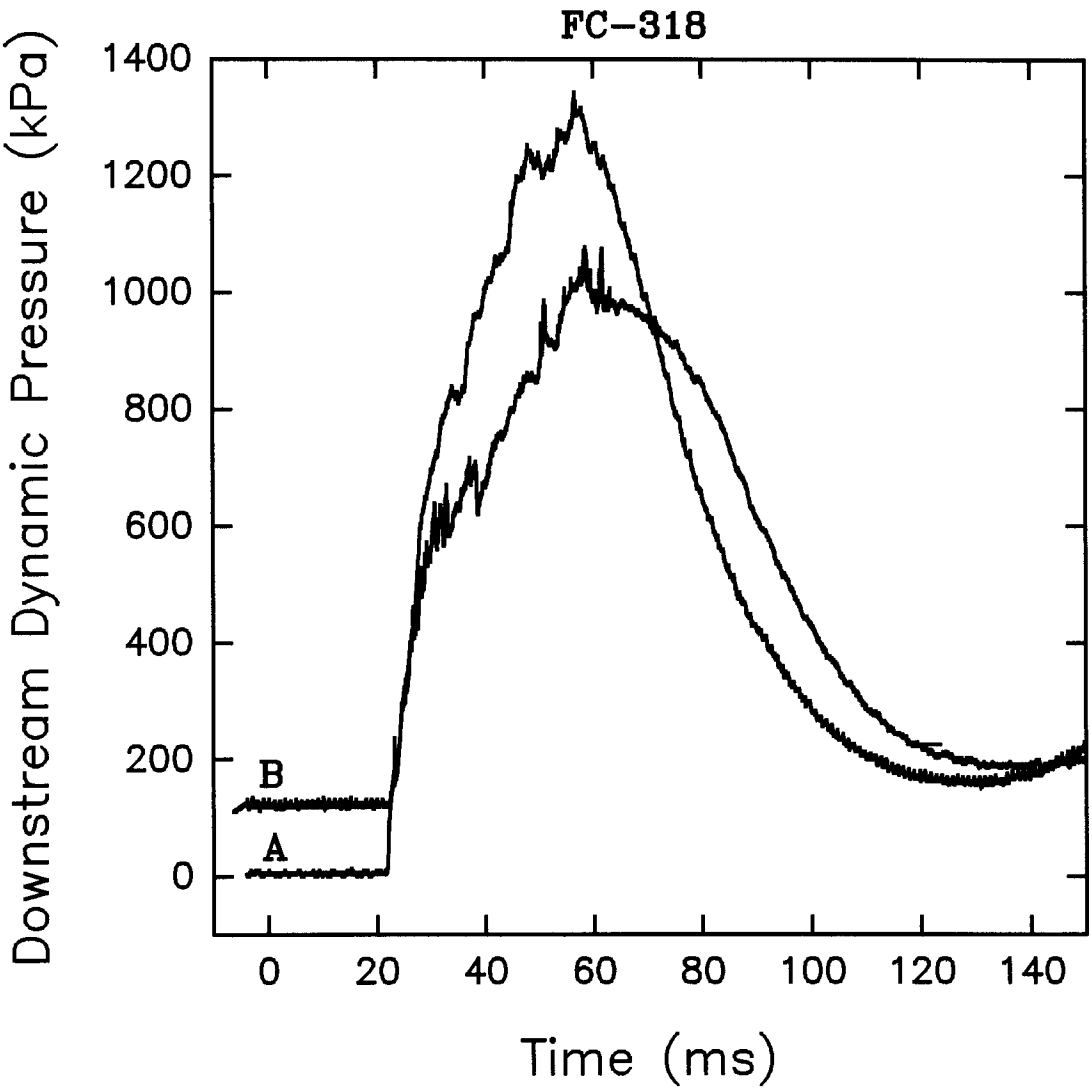

Figure 123. Dynamic pressure measured 1.3 m from the vessel for FC-318. For clarity, trace B is offset by 100 kPa. Conditions are: A, 521 g agent, release pressure of 4.34 MPa ; B, 505 g of agent, release pressure of 3.99 MPa.

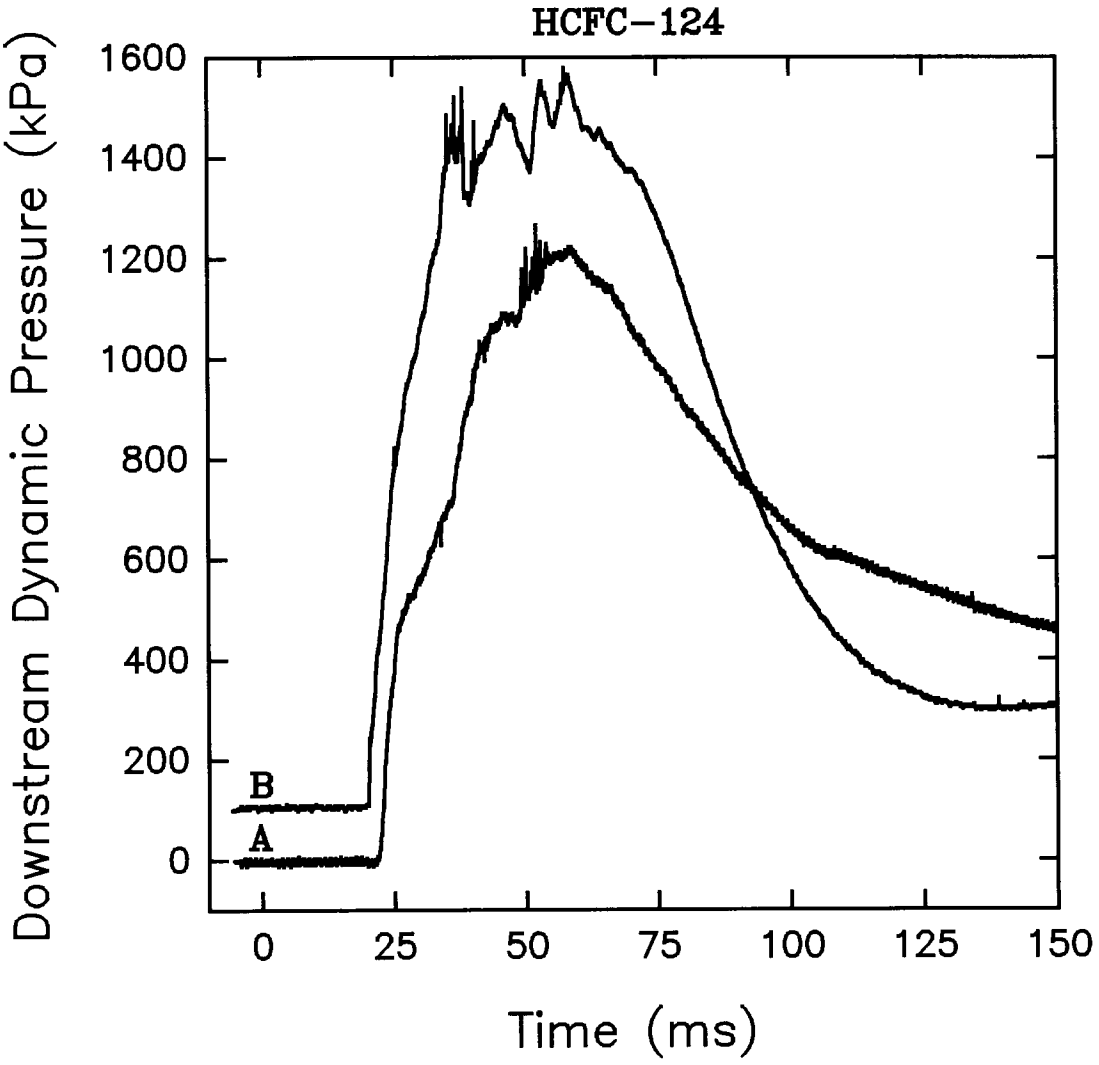

Figure 124. Dynamic pressure measured 1.3 m from the vessel for HCFC-124. For clarity, trace B is offset by 100 kPa. Conditions are: A, 462 g agent, release pressure of 4.05 MPa ; B, 465 g of agent, release pressure of 4.30 MPa.

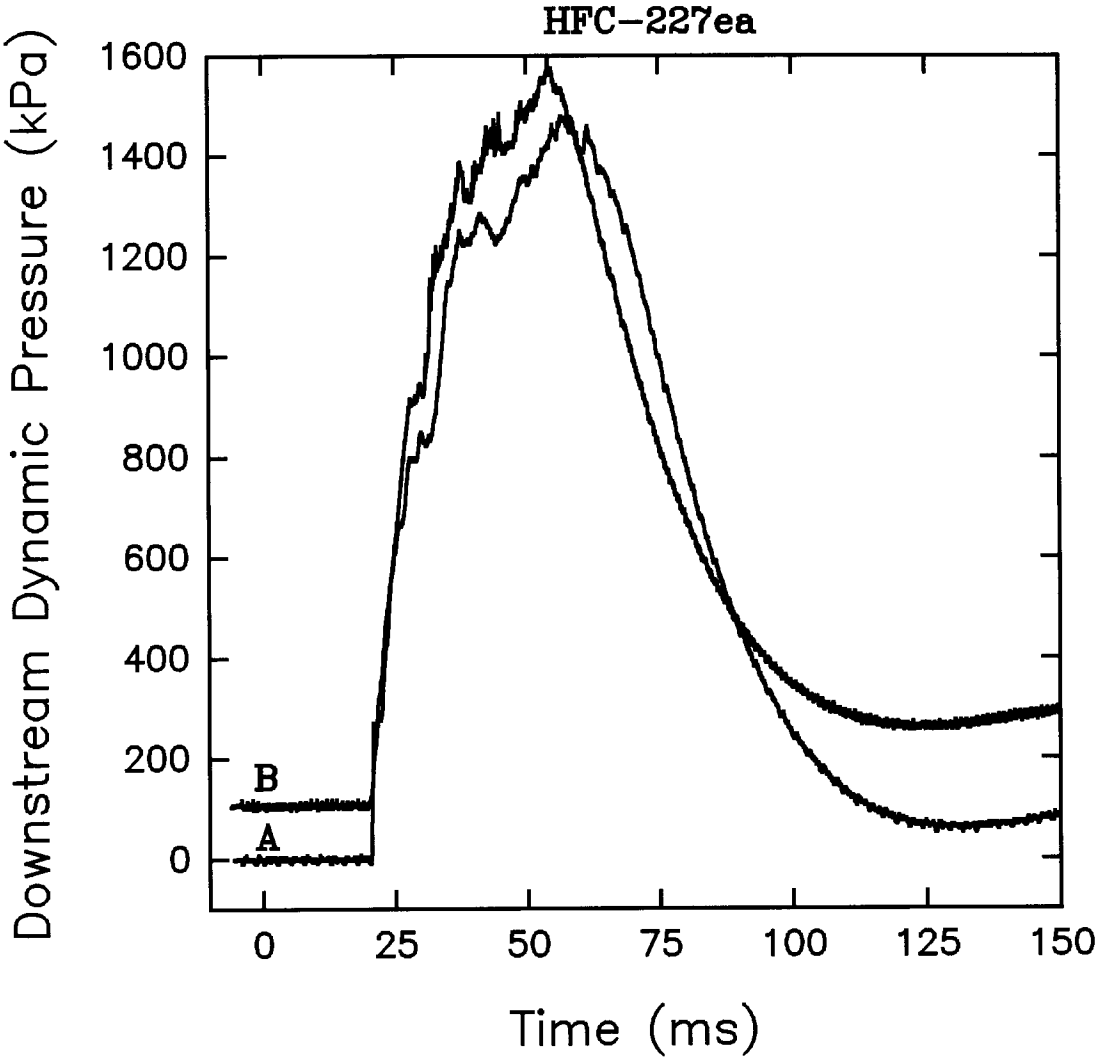

Figure 125. Dynamic pressure measured 1.3 m from the vessel for HFC-227ea. For clarity, trace B is offset by 100 kPa. Conditions are: A, 489 g agent, release pressure of 4.41 MPa ; B, 476 g of agent, release pressure of 4.45 MPa.

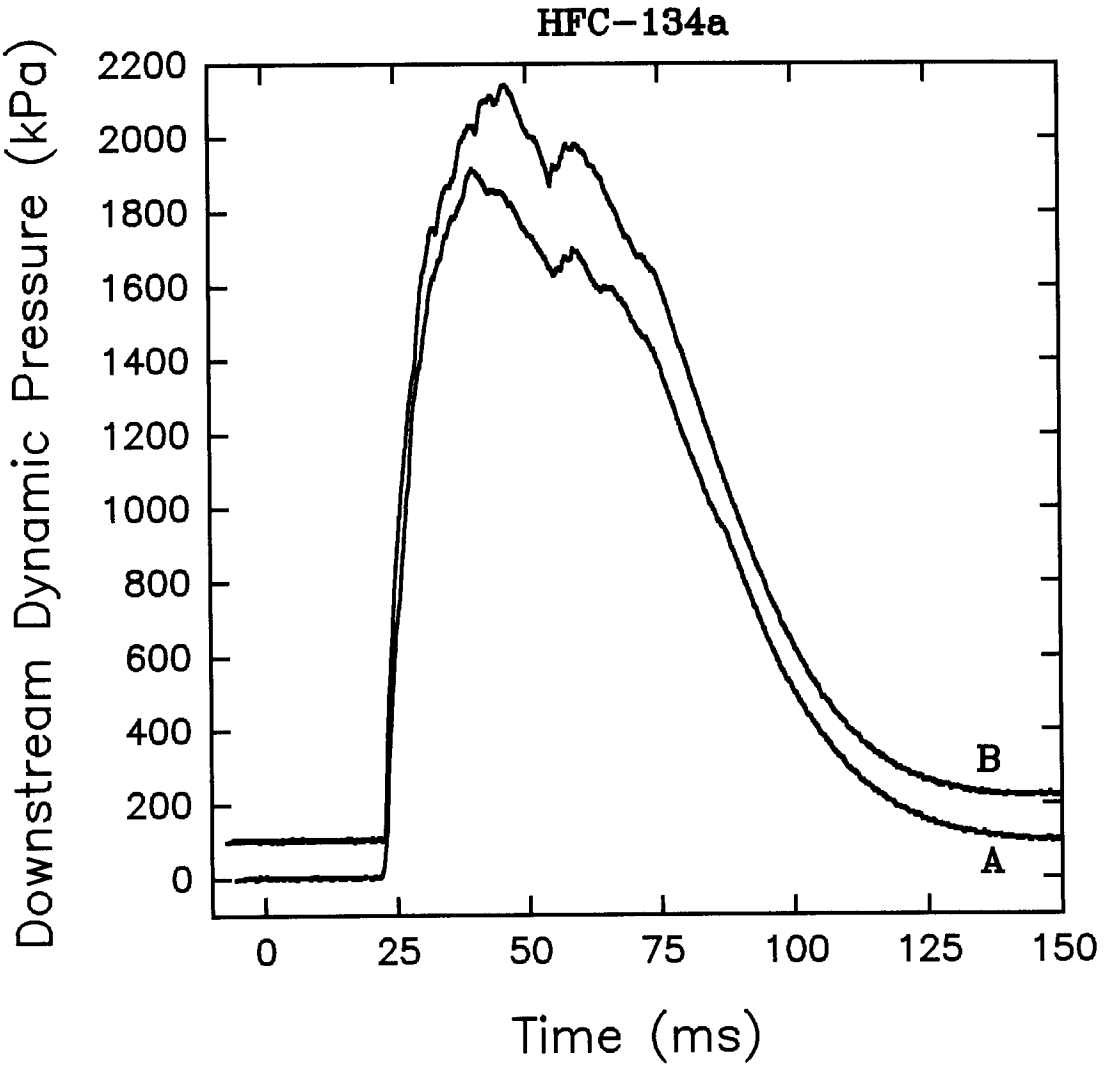

Figure 126. Dynamic pressure measured 1.3 m from the vessel for HFC-134a. For clarity, trace B is offset by 100 kPa. Conditions are: A, 418 g agent, release pressure of 4.13 MPa ; B, 419 g of agent, release pressure of 4.21 MPa.

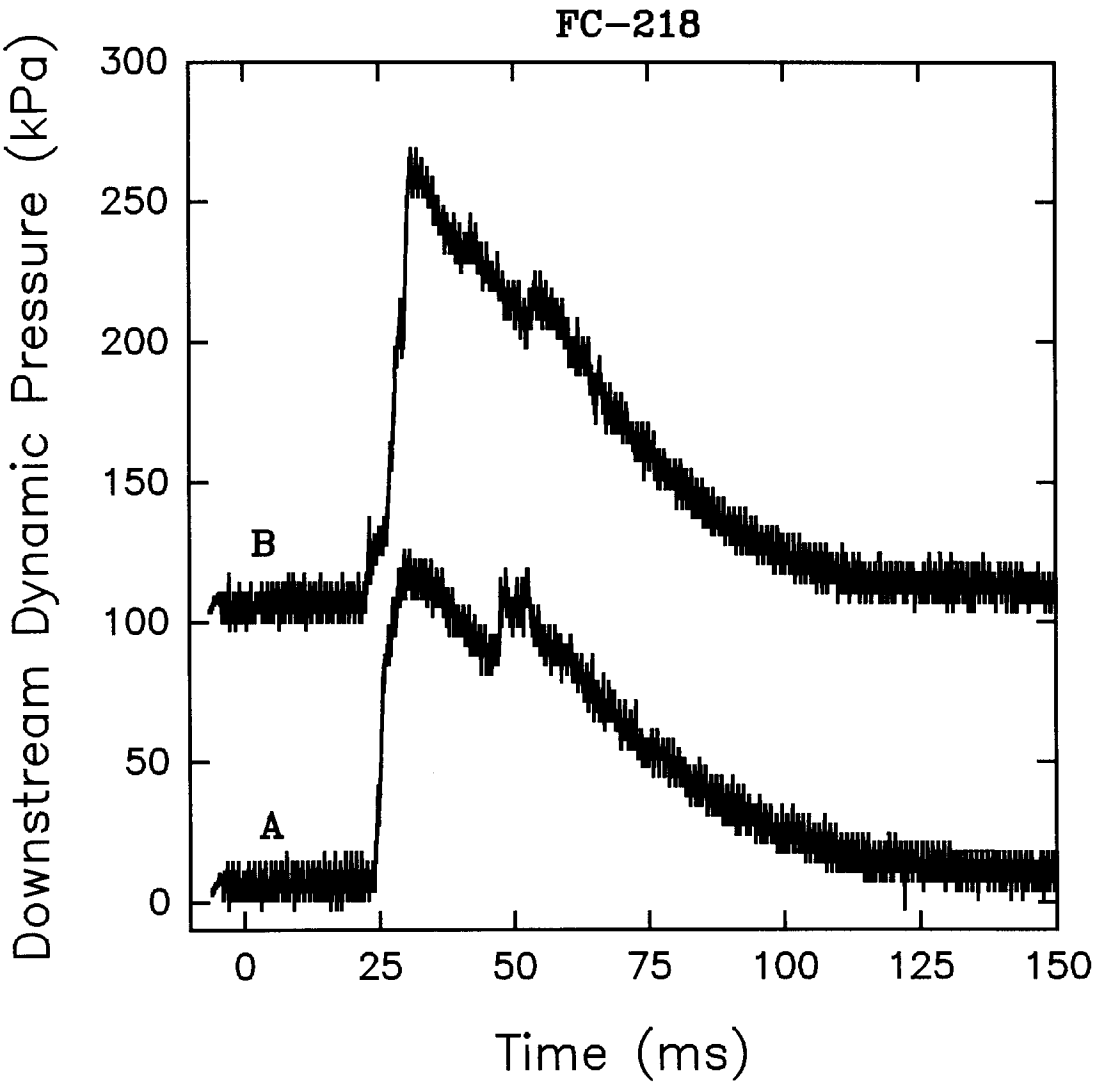

Figure 127. Dynamic pressure measured 1.3 m from the vessel for FC-218. For clarity, trace B is offset by 100 kPa. Conditions are: A, 460 g agent, release pressure of 4.58 MPa ; B, 468 g of agent, release pressure of 4.28 MPa.

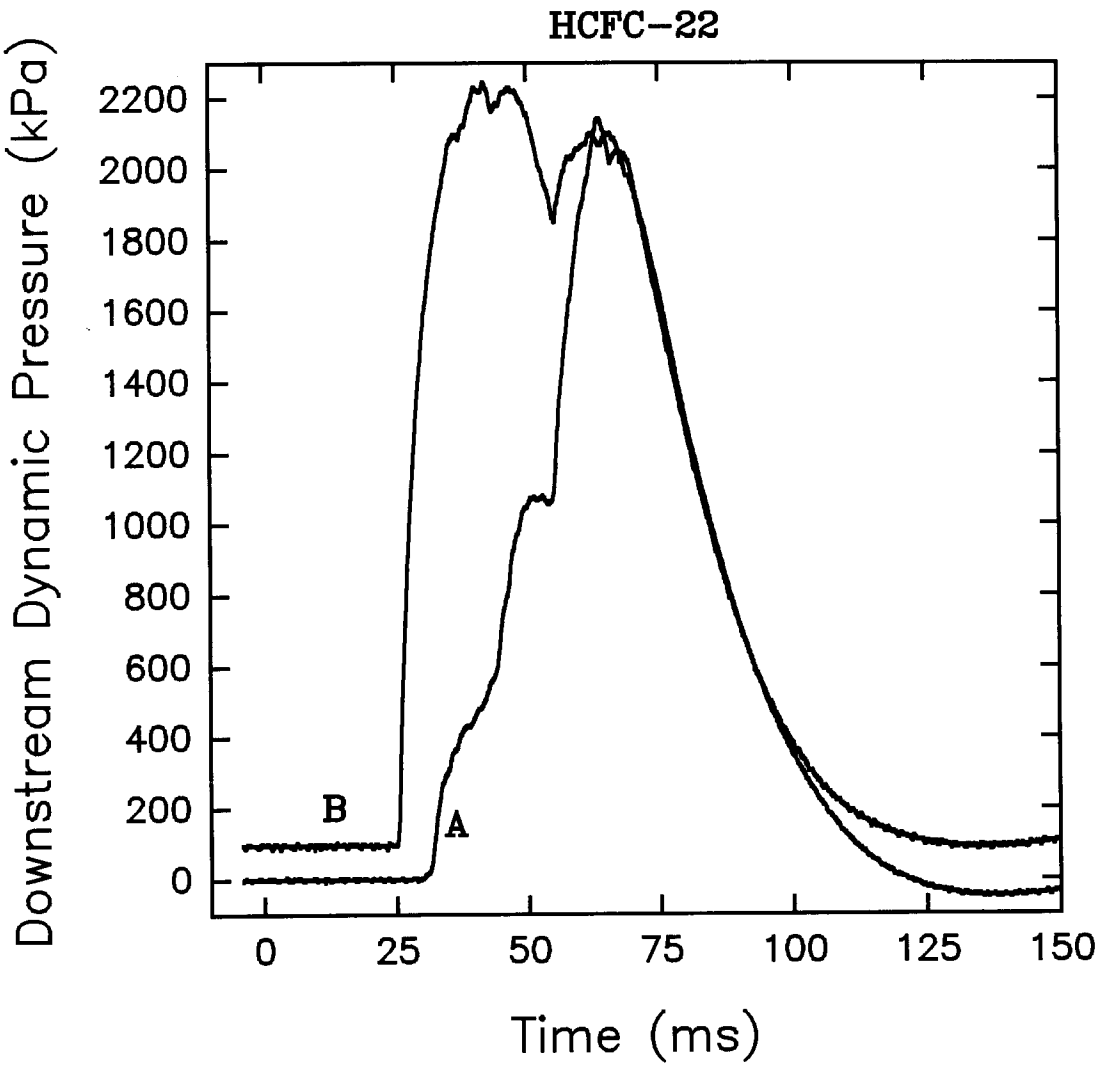

Figure 128. Dynamic pressure measured 1.3 m from the vessel for HCFC-22. For clarity, trace B is offset by 100 kPa. Conditions are: A, 421 g agent, release pressure of 4.48 MPa ; B, 417 g of agent, release pressure of 4.52 MPa.

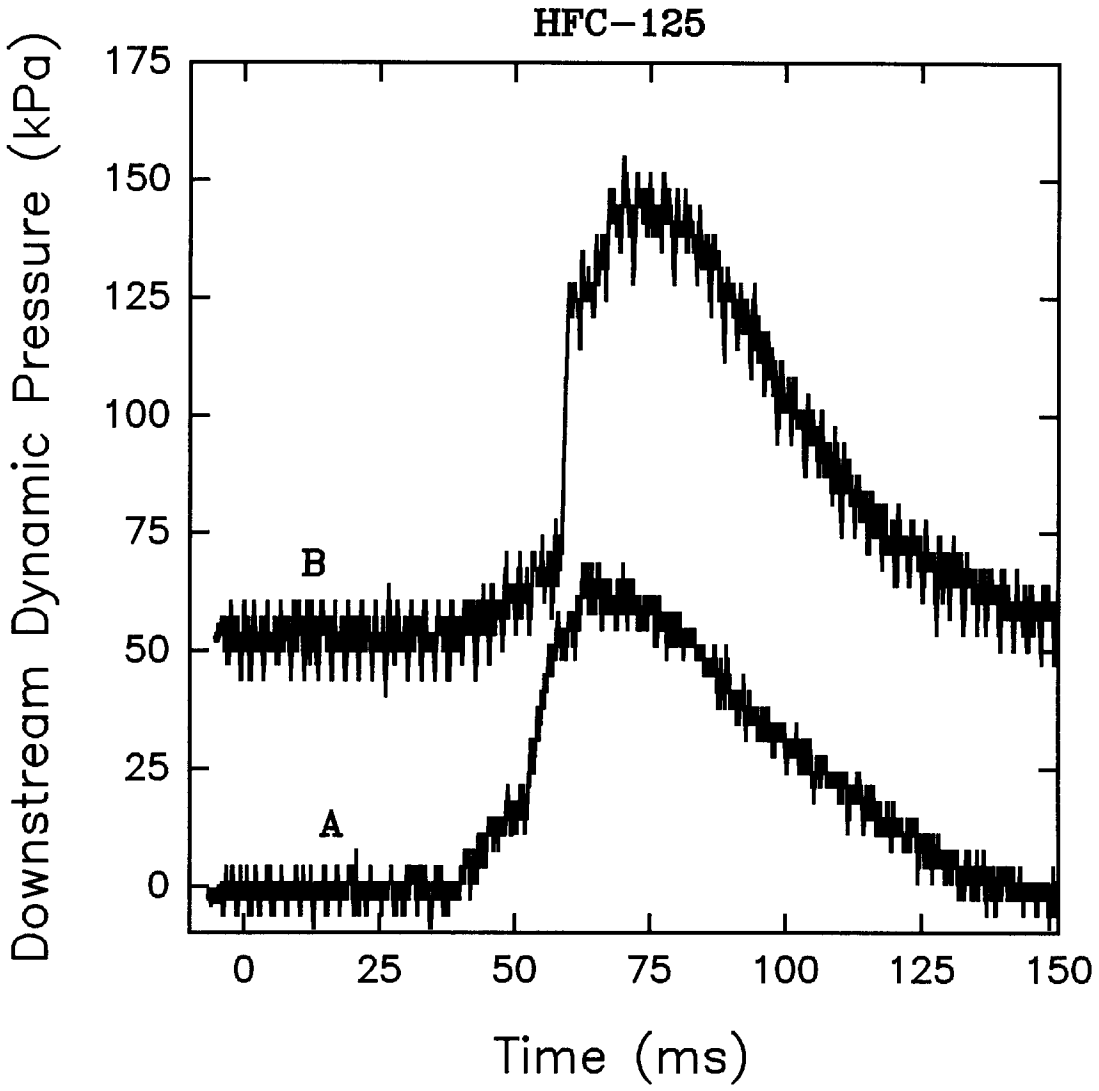

Figure 129. Dynamic pressure measured 1.3 m from the vessel for HFC-125. For clarity, trace B is offset by 50 kPa. Conditions are: A, 403 g agent, release pressure of 4.19 MPa ; B, 423 g of agent, release pressure of 4.24 MPa.

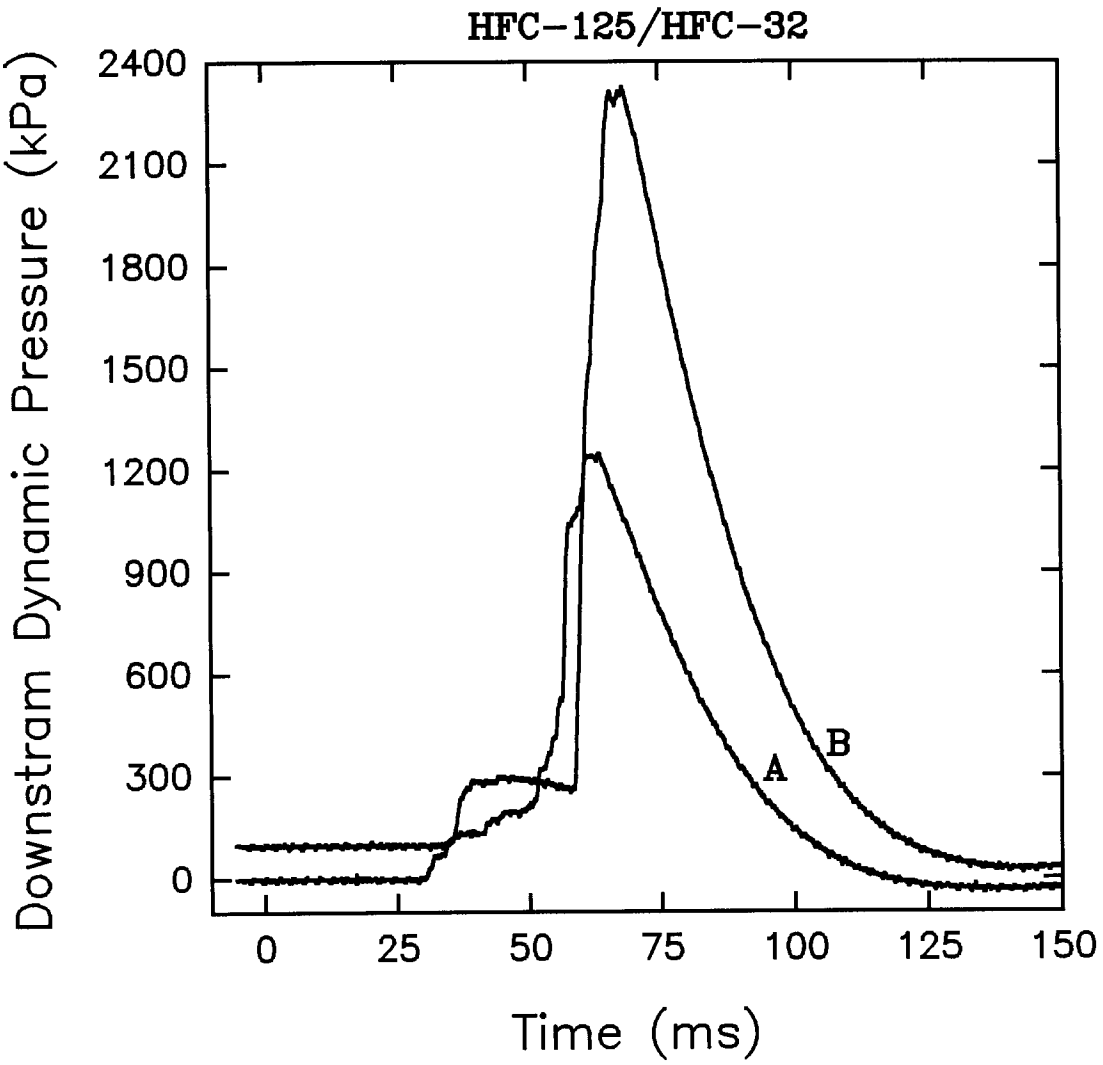

Figure 130. Dynamic pressure measured 1.3 m from the vessel for the HFC-125/HFC-32 mixture. For clarity, trace B is offset by 100 kPa. Conditions are: A, 358 g agent, release pressure of 4.31 MPa ; B, 375 g of agent, release pressure of 4.36 MPa.

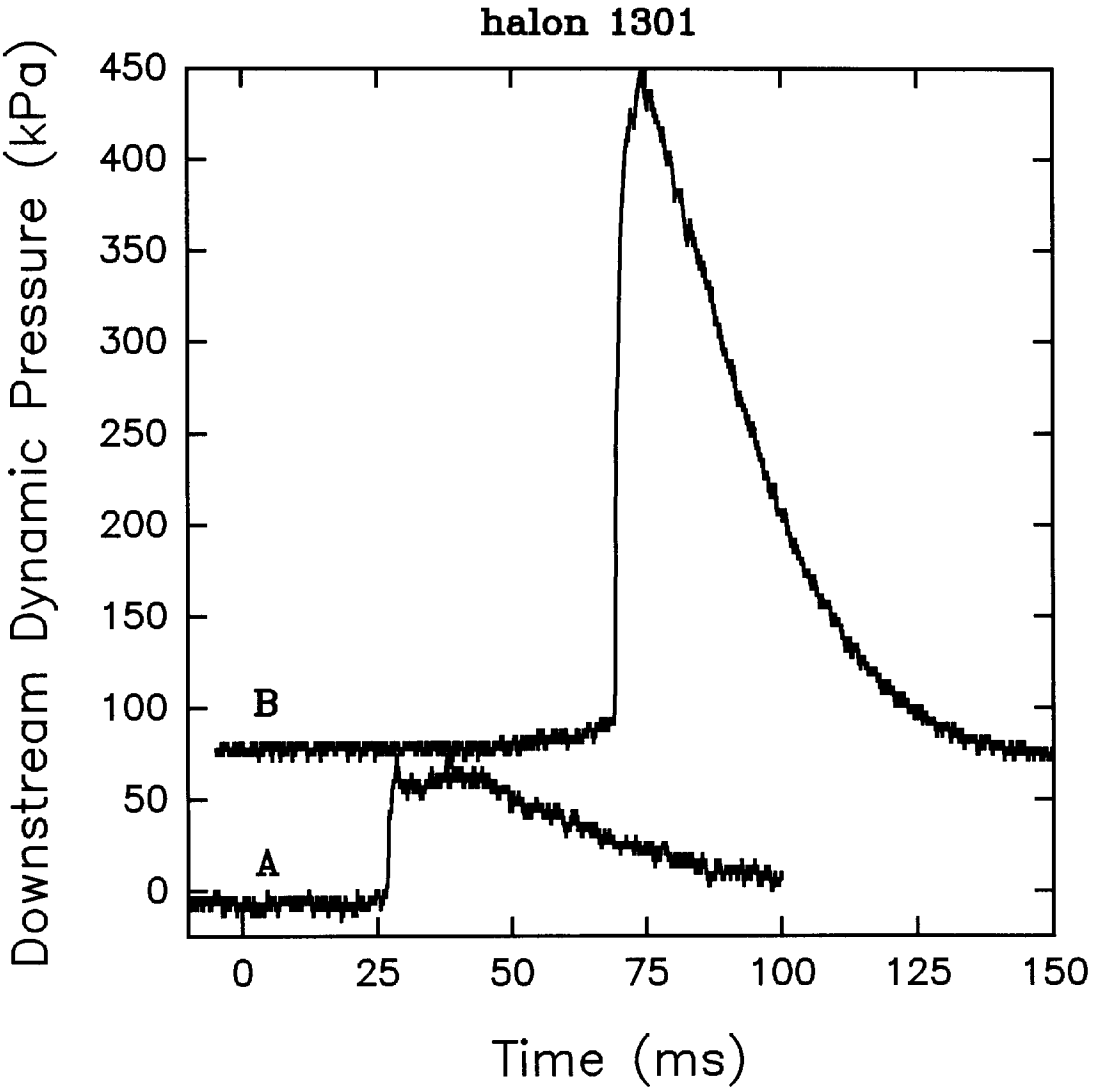

Figure 131. Dynamic pressure measured 1.3 m from the vessel for halon 1301. For clarity, trace B is offset by 75 kPa. Conditions are: A, 1/3 full, 270 g agent, release pressure of 4.43 MPa ; B, 554 g of agent, release pressure of 4.36 MPa.

value is considerably smaller (100-150 kPa) than observed for any of the higher boiling-point agents. The pressure time traces for HFC-125 (Figure 129) are similar except for the fact that the maximum observed pressures are even lower (on the order of 50 kPa). Dynamic pressures observed for halon 1301 (Figure 131) were also quite low, except near the end of one of the releases where a rapid increase to 375 kPa was observed.

While the pressure increases for the low boiling-point agents FC-218, HFC-125, and halon 1301 tended to be smaller than observed for higher boiling-point cases, the results were quite different for HCFC-22 (Figure 128) and the HFC-125/HFC-32 mixture (Figure 130). Both of these agents showed substantial variation between experiments. For HCFC-22 the time required for the pressure to reach its maximum value differed somewhat between releases, but the maximum values reached were greater, being on the order of 2100 kPa for both cases shown. The data for the mixture are also variable. In one case the maximum pressure was in excess of 2200 kPa, while in the other the maximum only reached 1200 kPa.

To summarize, the results for the high boiling-point liquids seem to be consistent and show that very high dynamic pressures are generated at a distance of 1.3 m from the vessel by the release of this type of agent. Two distinct types of pressure curves are found for the lower boiling-point liquids. HCFC-22 and the HFC-125/HFC-32 mixture generate maximum pressures which are similar to those observed for the higher boiling-point agents even though they have more complex time histories, and there are larger variations among experiments. FC-218, HFC-125, and halon 1301 releases generate maximum pressures which are considerably reduced from those observed for all of the other tested liquids.

3.5.3.5 Aspirated Hot-Film Measurements. The aspirated hot-film has only been used to characterize qualitatively the nature of the flows reaching the 1.3 m downstream position. It should be noted that the these probes can be calibrated to accurately measure concentration in isothermal binary mixtures of gases. If the temperature is changing, or if two phases are present the response of these probes is more complex. An ongoing project at NIST is evaluating the utility of aspirated hot-film probes for concentration measurements under these complex conditions.

Since the results are qualitative, only a few representative examples are reported here. Even so, it will become clear that the hot-film response provides useful information for detecting the present of an agent and for determining whether it is a single or two-phase flow.

Figure 132 shows an example of the aspirated hot-film output observed during the release of HFC-236fa. A nearly constant signal (roughly 6.3 V) is observed until 20 ms following release at which time an abrupt increase in voltage is observed. Figure 99 and Figure 121 show that 20 ms is the time when the agent first reaches the probe. Thus the constant signal is that representative of room temperature air. The signal induced by the arrival of the agent is very "spikey" and reaches values of nearly 10 V. Such voltages are much higher than would be expected for a 100% concentration of the gaseous agent (Pitts and McCaffrey, 1986). The large heat transfer from the hot-film probe which these voltages represent is attributed to the presence of two-phase flow in the probe. Evaporative cooling of the droplets requires large amounts of heat. The large voltage spikes are observed for roughly 40 ms. This period is on the order of the period required for release of the agent. Afterwards, much smaller voltages are observed which decay slowly toward that expected for air. This is taken as evidence that the mixture is becoming more gaseous due to evaporation of the agent as it mixes with the air. This is consistent with the transmission observed for laser #5 (Figure 99) which indicates that the flow becomes partially transmitting at roughly 100 ms following the release.

The hot-film responses for FC-31-10, FC-318, HCFC-124, HFC-227ea, and HFC-134a are very similar to those for HFC-236fa. During the period when the releases are passing the probe there are

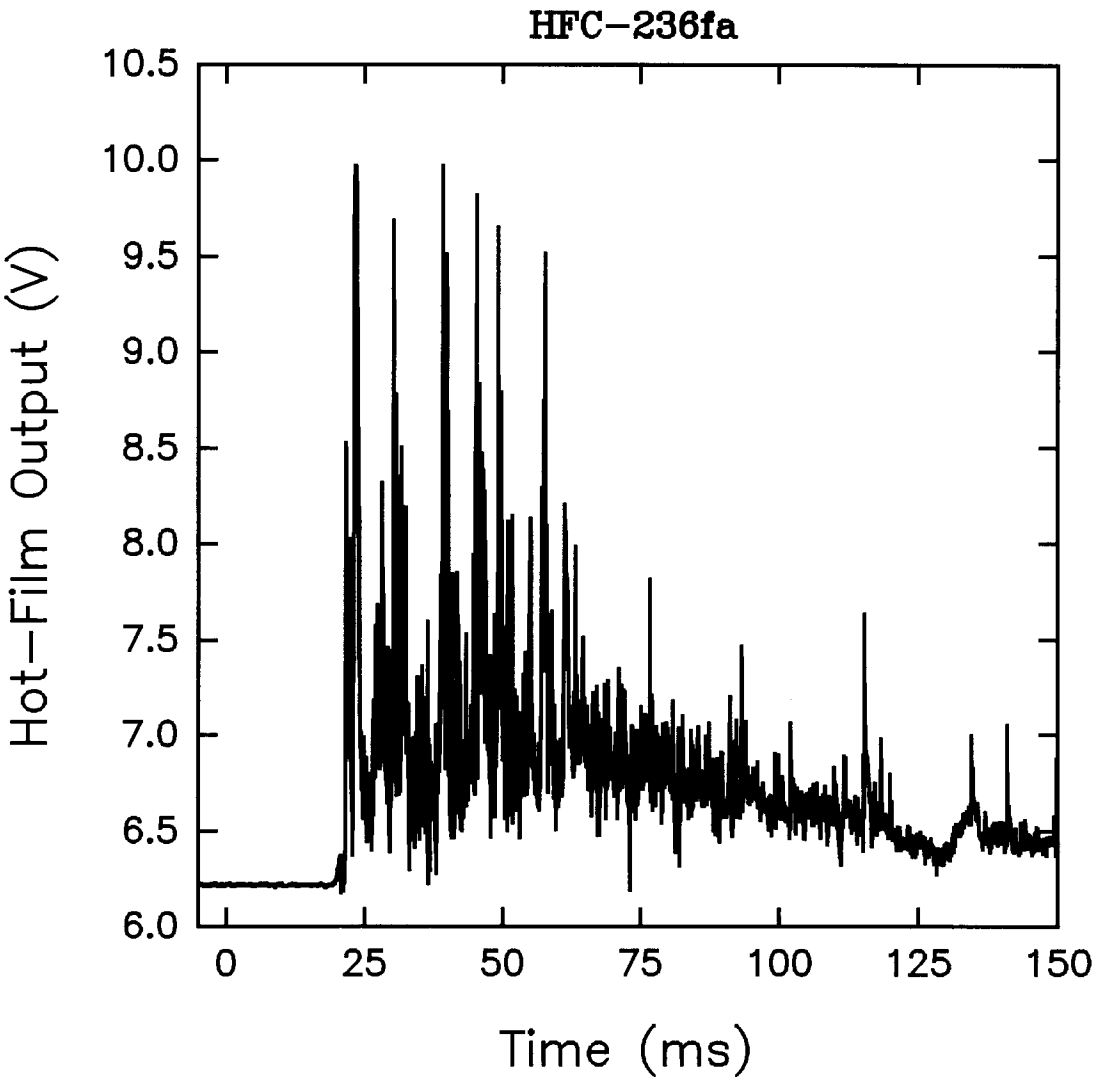

Figure 132. The voltage output of the aspirated hot-film located 1.3 m from the vessel is plotted as a function of time for a release of HFC-236fa. Conditions: 464 g of agent, release pressure of 4.30 MPa.

voltage signals which must be associated with two-phase flow. Afterwards, the voltages begin to fall and approach those for room-temperature air.

The hot-film response for FC-218 releases was quite different. Figure 133 shows an example of the hot-film voltage plotted as a function of time. The signal begins to rise at the time when laser beam #5 is strongly attenuated (Figure 105) and the downstream pressure transducer (Figure 127, curve A) detects the arrival of the agent. The signal changes rapidly with time indicating the presence of highly turbulent flow, but during the initial part of the signal following the arrival of the agent the voltage increases are relatively small and consistent with those expected for a binary gas mixture. At roughly 50 ms following the release, there is a rise in the hot-film voltage and spiking appears which suggests the presence of a two-phase flow. Interestingly, the downstream pressure transducer recorded a small rise in dynamic pressure at the same time. These results suggest that near the end of the release a small amount of two-phase fluid reached the 1.3 m downstream position, but the responses of the detectors suggest that the FC-218 was much more completely vaporized than the higher boiling-point agents.

Figure 134 shows simultaneous plots of downstream dynamic pressure and hot-film output as functions of time for a release of HFC-125. The flow of this agent results in relatively small increases in both dynamic pressure and hot-film voltage. Roughly 20 ms after the agent arrives at the measurement location there are sharp increases in both signals. It is difficult to determine whether this is the result of the arrival of two-phase flow or a higher concentration (*i.e.*, density) or velocity of gaseous agent. In either case, it is clear that this agent arrives nearly completely vaporized. Figure 135 shows a similar plot for halon 1301. Here there is a significant increase in dynamic pressure associated with the end of the release which appears to have two-phase behavior. However, it is clear from the traces that during most of the release primarily gas-phase agent is reaching this downstream position.

Recall that releases of HCFC-22 and the HFC-125/HFC-32 mixture resulted in large downstream dynamic pressures. Figure 136 and Figure 137 show time plots for the hot-film outputs for these two agents. In both cases there is evidence for two-phase flow near the beginning and ends of the releases. This conclusion is consistent with the observed dynamic pressure behaviors (see Figure 128 and Figure 130).

3.5.3.6 Effects of Orifice Diameter. Experiments were done for FC-31-10, FC-218, and halon 1301 using plates with orifices of 12.7 and 6.4 mm. The same flow characterizations recorded for the standard release conditions were used.

For the FC-31-10 the near-field pressure transducer recorded a pressure rise of roughly 450 kPa when the 12.7 mm orifice was used and no measurable increase when the 6.4 mm orifice was used. These results can be compared with the results in Table 6 for the 19.1 mm opening where maximum dynamic pressures were between 300-400 kPa. The pressure behavior for a release of FC-218 through the 12.7 mm orifice is shown in Figure 138. It can be seen that the transducer responded shortly after the start of the release and that the dynamic pressure remained high over the remaining release period of approximately 75 ms. Comparison with Figure 94 shows that the maximum pressures reached are lower for this orifice diameter than for the 19.1 mm opening, but that the pressures are sustained over a much longer period. For the 12.7 mm orifice, the fluid seems to be flashing continuously. For the smallest orifice no pressure increase was detected. The dynamic pressure time behaviors recorded for releases of halon 1301 had very similar behaviors to those for the FC-218.

The size of the orifice has a strong effect on flashing behavior. For the higher boiling-point FC-31-10 no flashing is observed for the smaller orifices. For the lower boiling-point liquids, the maximum dynamic pressure observed decreases when the 19.1 mm orifice is reduced to 12.7 mm, but

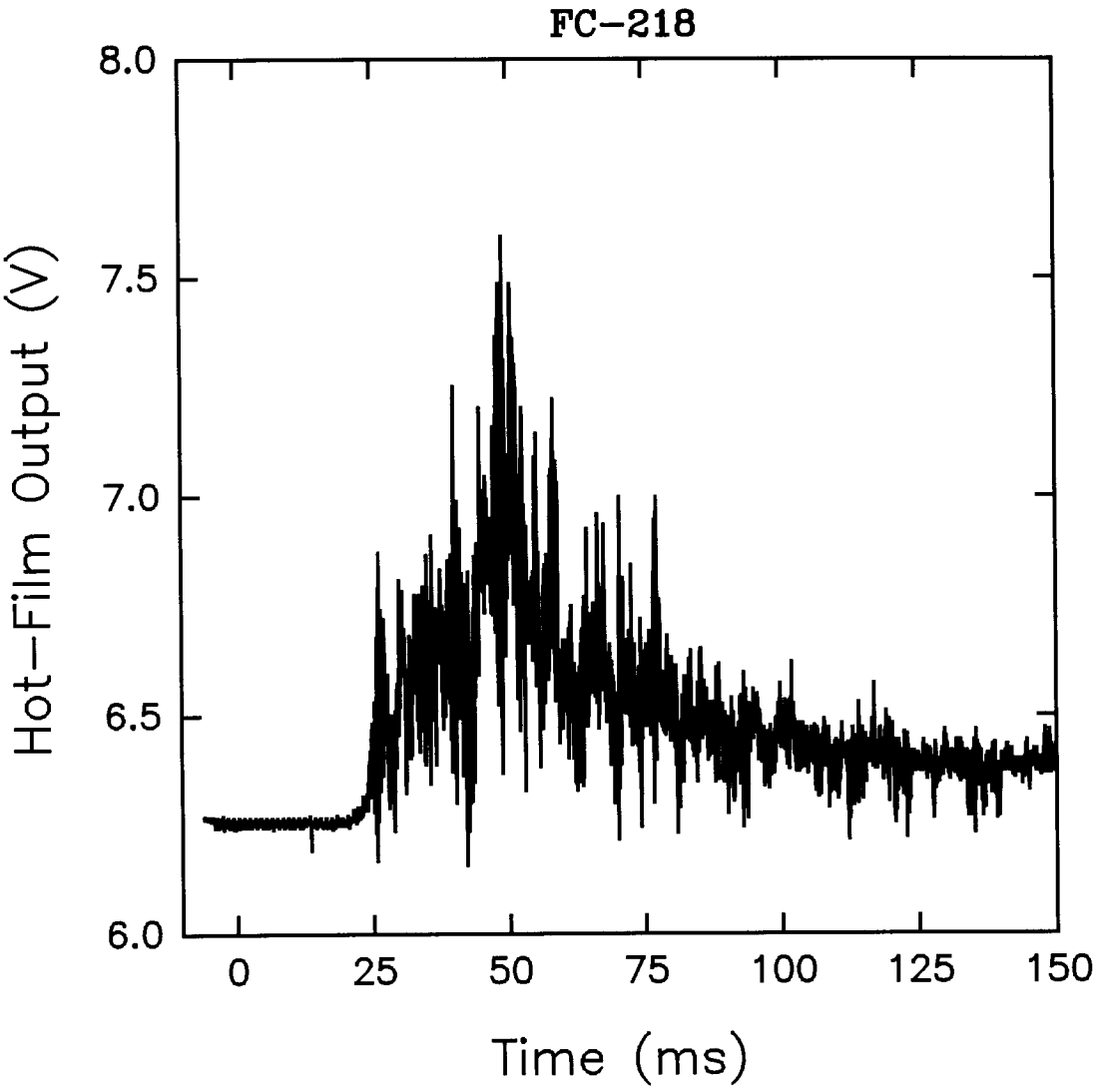

Figure 133. The voltage output of the aspirated hot-film located 1.3 m from the vessel is plotted as a function of time following a release of FC-218. Conditions: 460 g of agent, release pressure of 4.58 MPa.

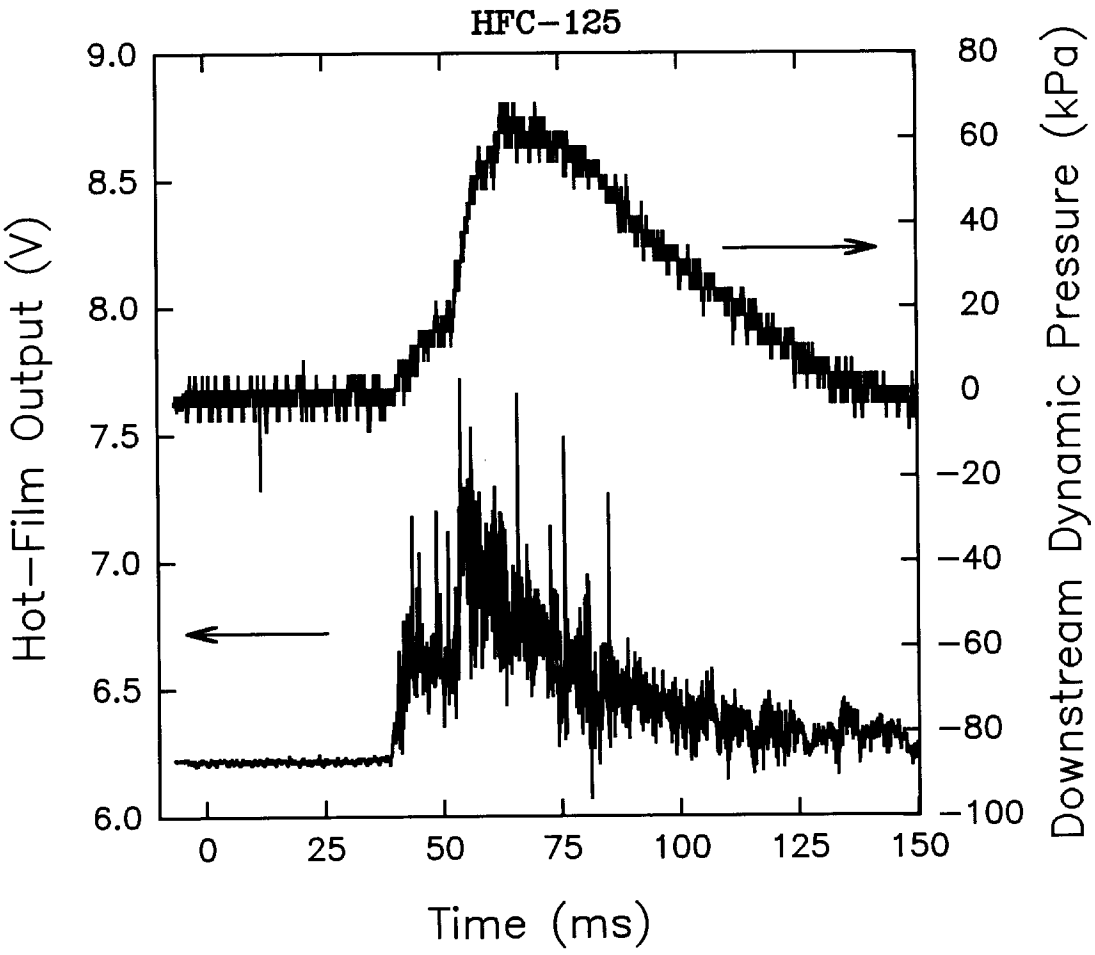

Figure 134. The voltage output of the aspirated hot-film and the dynamic pressure for probes located 1.3 m from the vessel are plotted as a function of time following a release of HFC-125. Conditions: 403 g of agent, release pressure of 4.19 MPa.

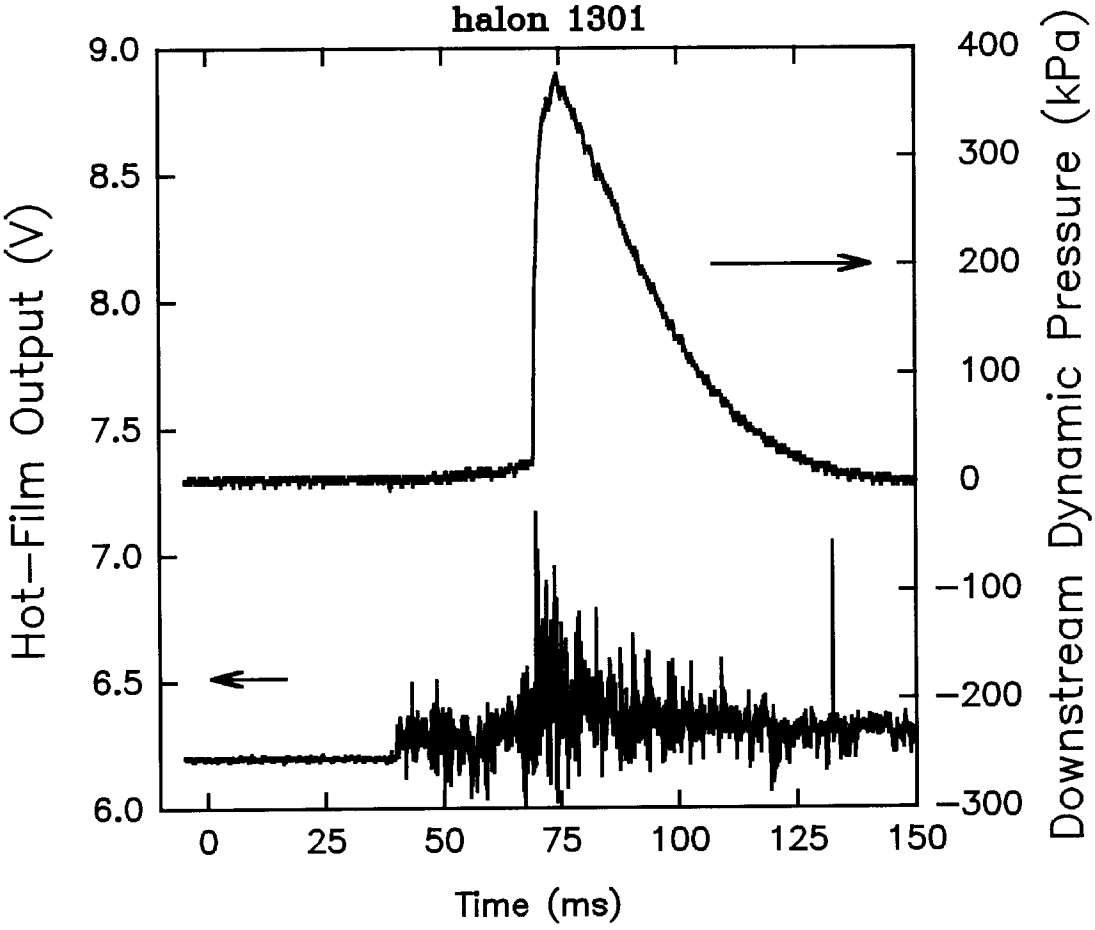

Figure 135. The voltage output of the aspirated hot-film and the dynamic pressure for probes located 1.3 m from the vessel are plotted as a function of time following a release of halon 1301. Conditions: 554 g of agent, release pressure of 4.36 MPa.

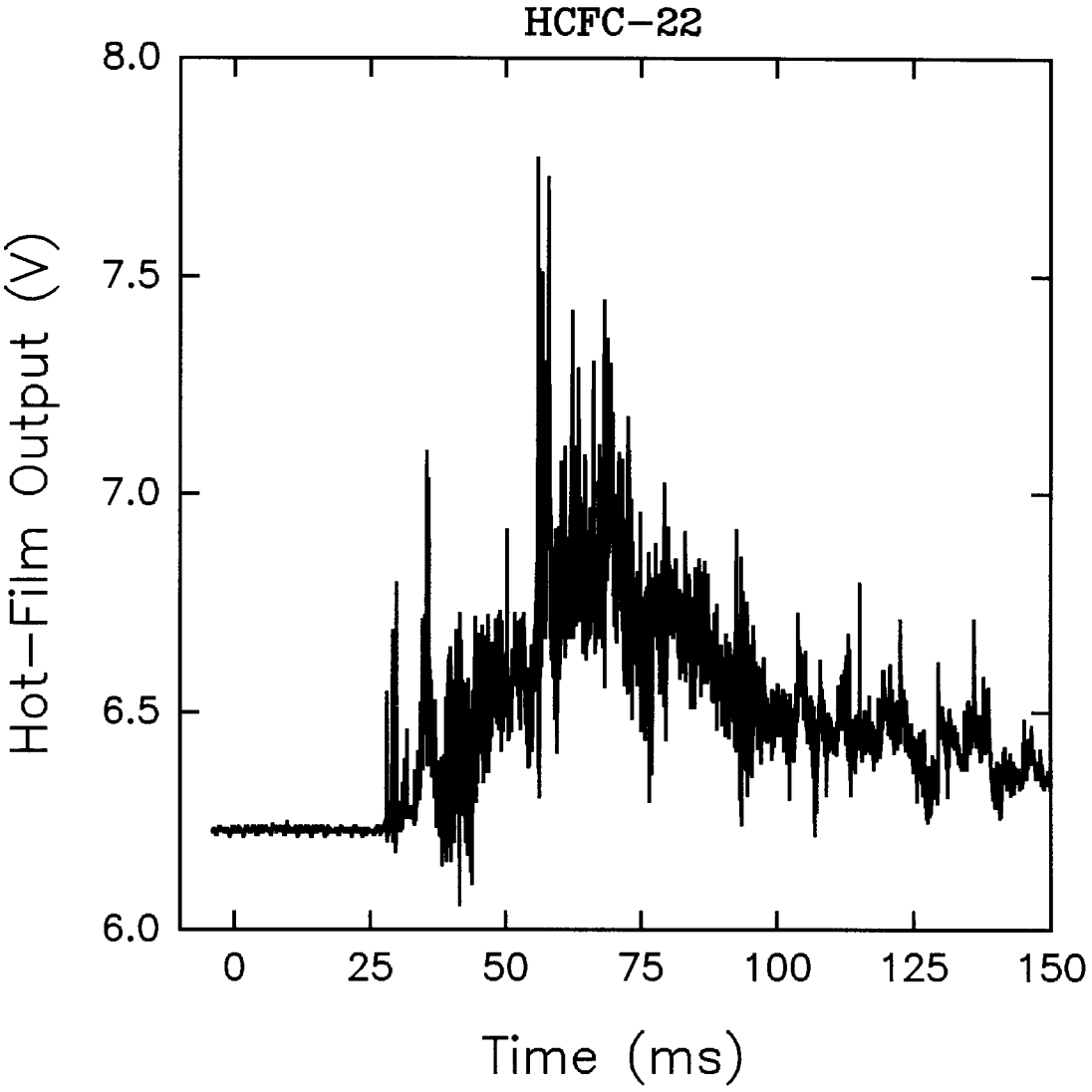

Figure 136. The voltage output of the aspirated hot-film located 1.3 m from the vessel is plotted as a function of time following a release of HCFC-22. Conditions: 421 g of agent, release pressure of 4.48 MPa.

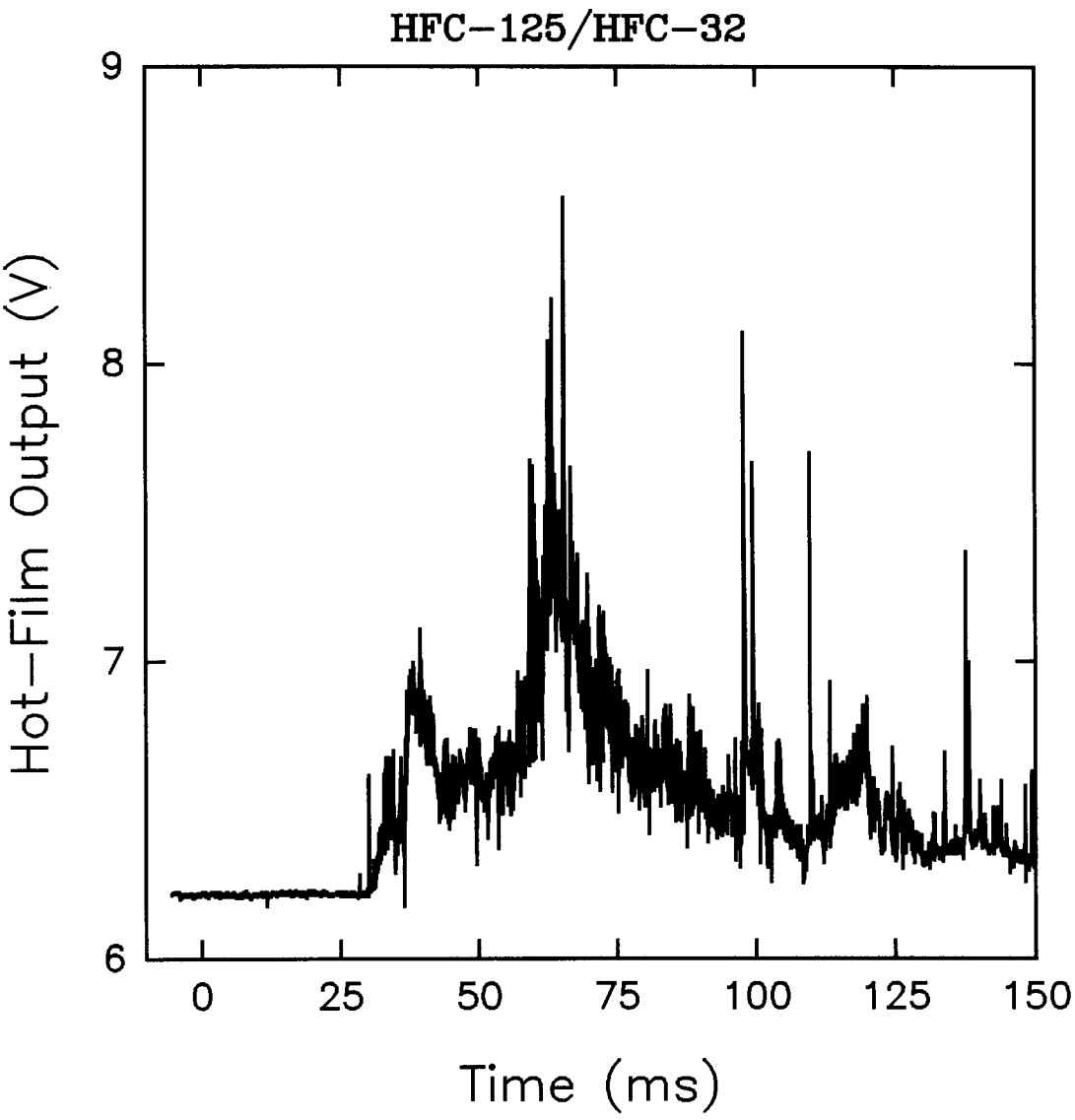

Figure 137. The voltage output of the aspirated hot-film located 1.3 m from the vessel is plotted as a function of time following a release of the HFC-125/HFC-32 mixture. Conditions: 375 g of agent, release pressure of 4.36 MPa.

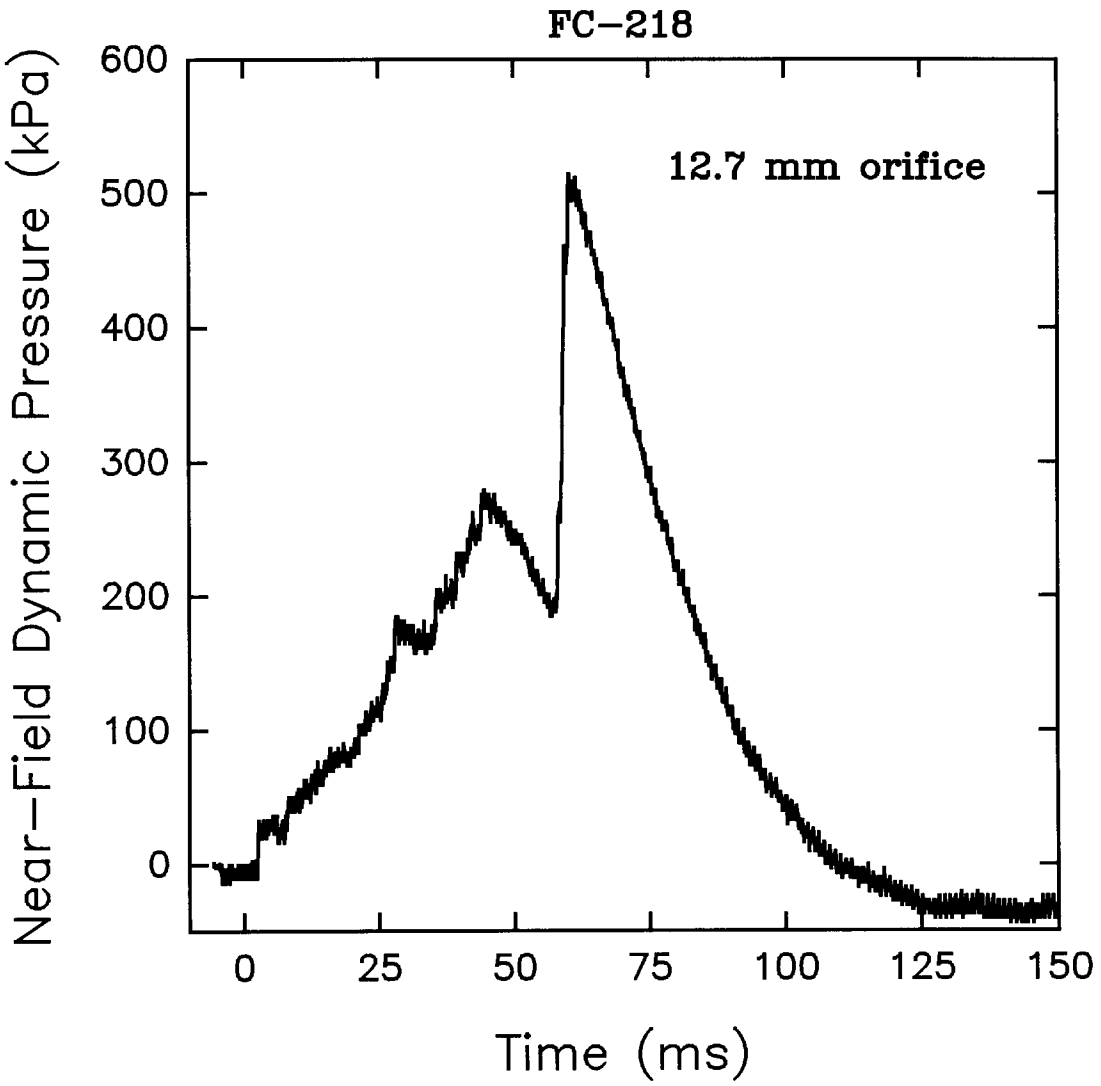

Figure 138. Time trace of near-field dynamic pressure for a release of FC-218 through a 12.7 mm orifice. Conditions: 457 g of agent, 4.30 MPa release pressure.

the period of flashing is substantially extended. No increases in dynamic pressure are observed for the smallest orifice.

Figure 139 through Figure 141 compare the average velocity variations with average downstream position for releases of FC-31-10, FC-218, and halon 1301 through the three orifices. For FC-31-10 releases, smaller orifices result in significant changes in the velocity development. With the 19.1 mm opening (Figure 111 and Figure 139) the velocity first increases and then levels off at values near 70 m/s. For the two smaller orifices the initial velocity is on this order, but it then decreases with increasing downstream distance. The smallest velocity is observed at the farthest position using the 6.4 mm orifice.

Velocities near the vessel exit are roughly the same for each orifice size when FC-218 is considered (Figure 140). The velocities drop off in each case with increasing downstream distance. Once again the smallest orifice results in the lowest velocity at the last measuring position.

The results for halon 1301 (Figure 141) are similar to those for FC-218 except that the velocities nearest the orifice vary somewhat with the smaller orifices producing higher velocities. Overall, the smaller orifices generate higher velocities near the vessel and lower velocities further downstream.

The evaporation characteristics of the flows for releases of the three agents are indicated by Figure 142 through Figure 145 where the time behaviors for the far-field pressure transducer and hot-film aspirated film voltages are plotted as functions of time. The responses for the release of FC-31-10 from the 12.7 mm orifice (Figure 142) indicate that this agent is a two-phase mixture 1.3 m from the vessel. This is clear from the high dynamic pressures and spikey nature of the hot-film signal. The period required to empty the bottle is roughly 65 ms. This is also roughly the length of the two-phase flow period at the downstream position. The plots for the release from the 6.4 mm orifice indicate that the agent first arrives in the gas phase and remains so throughout the release period.

The data for the release of FC-218 through the 12.7 mm orifice (Figure 143) suggest that this agent is fully vaporized when it reaches the sampling position, except, perhaps, at the very end of the release. Both the low dynamic pressures and small increases in hot-film voltages support this conclusion. Similar results were obtained for the 6.4 mm orifice.

Halon 1301 has a behavior which is very much like that for FC-218 except that a very strong two-phase component is observed near the end of the release when the 12.7 mm orifice is used (Figure 144). Both the dynamic pressure and hot-film signals indicate the presence of two-phases. It is possible that this change in flow composition is associated with the strong flashing which occurred near the vessel as the liquid emptied from the vessel. Figure 145 shows results for a release of halon 1301 through the 6.4 mm orifice. Here the signals from both transducers are small indicating that only gaseous agent is present 1.3 m from the orifice. A small pressure increase was recorded at the end of the release which may be associated with the presence of a small amount of liquid agent or a higher concentration or velocity of the gaseous agent. Note the long time period required for release through this small opening.

3.5.3.7 Effect of Vessel Pressurization Level. The effect of the vessel pressurization level on the mixing and dispersion behavior of an agent was investigated for releases of FC-218 using burst disks designed to break at nominal pressures of 2.76, 4.14, and 5.52 MPa. Figure 146 and Figure 147 show examples of the results for near-field dynamic pressure as a function of time for vessels having high and low internal pressures, respectively. Figure 94 shows two examples of results for releases having intermediate levels of pressurization. None of the releases indicated a pressure rise associated with the first flashing following the release of the FC-218. Interestingly, the highest dynamic pressure associated with the second flashing is observed for the release with an

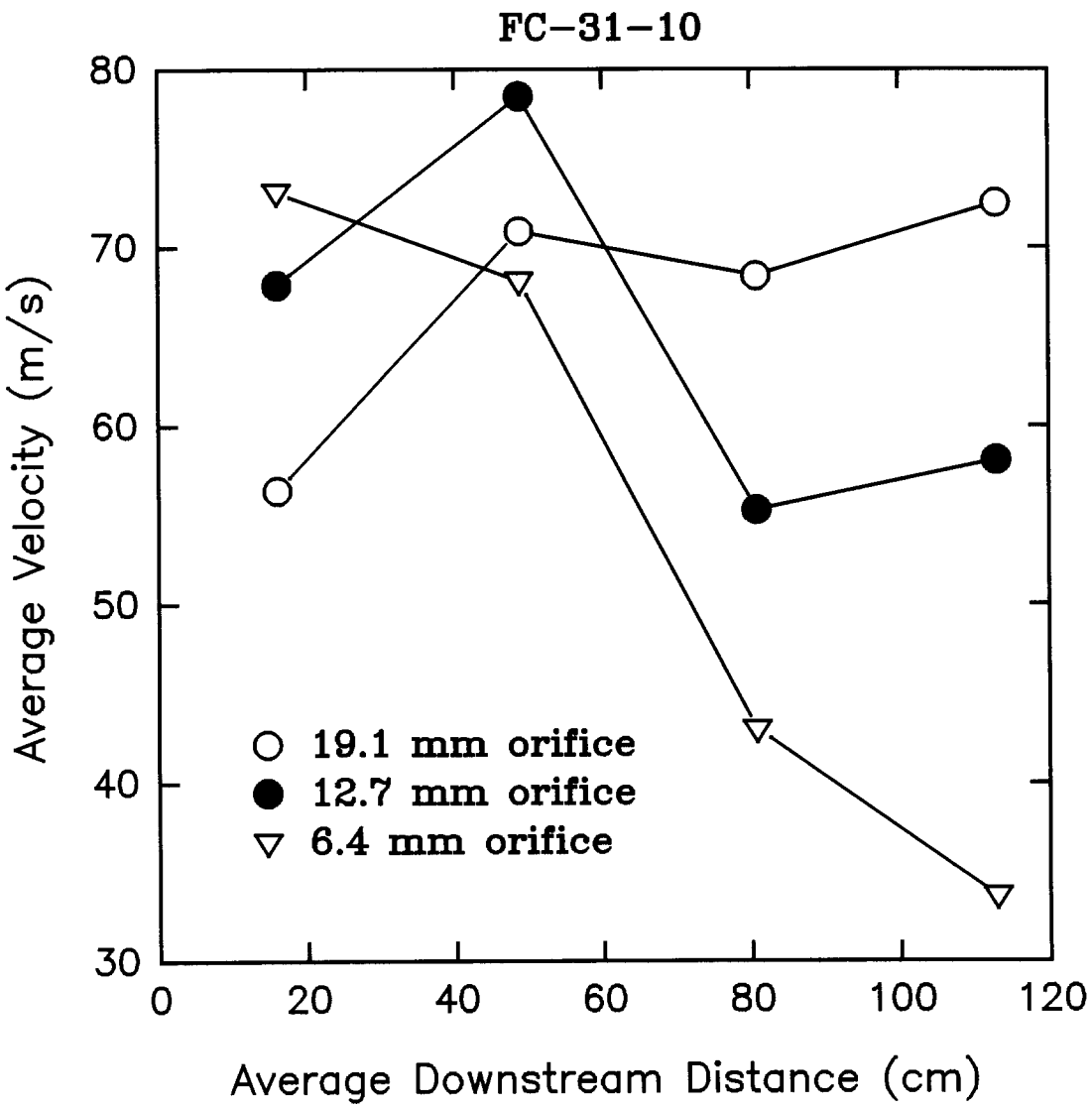

Figure 139. Average velocities determined by the time of arrival at laser beams #1-#5 plotted as a function of average downstream distance for releases of FC-31-10 through 19.1, 12.7, and 6.4 mm orifices.

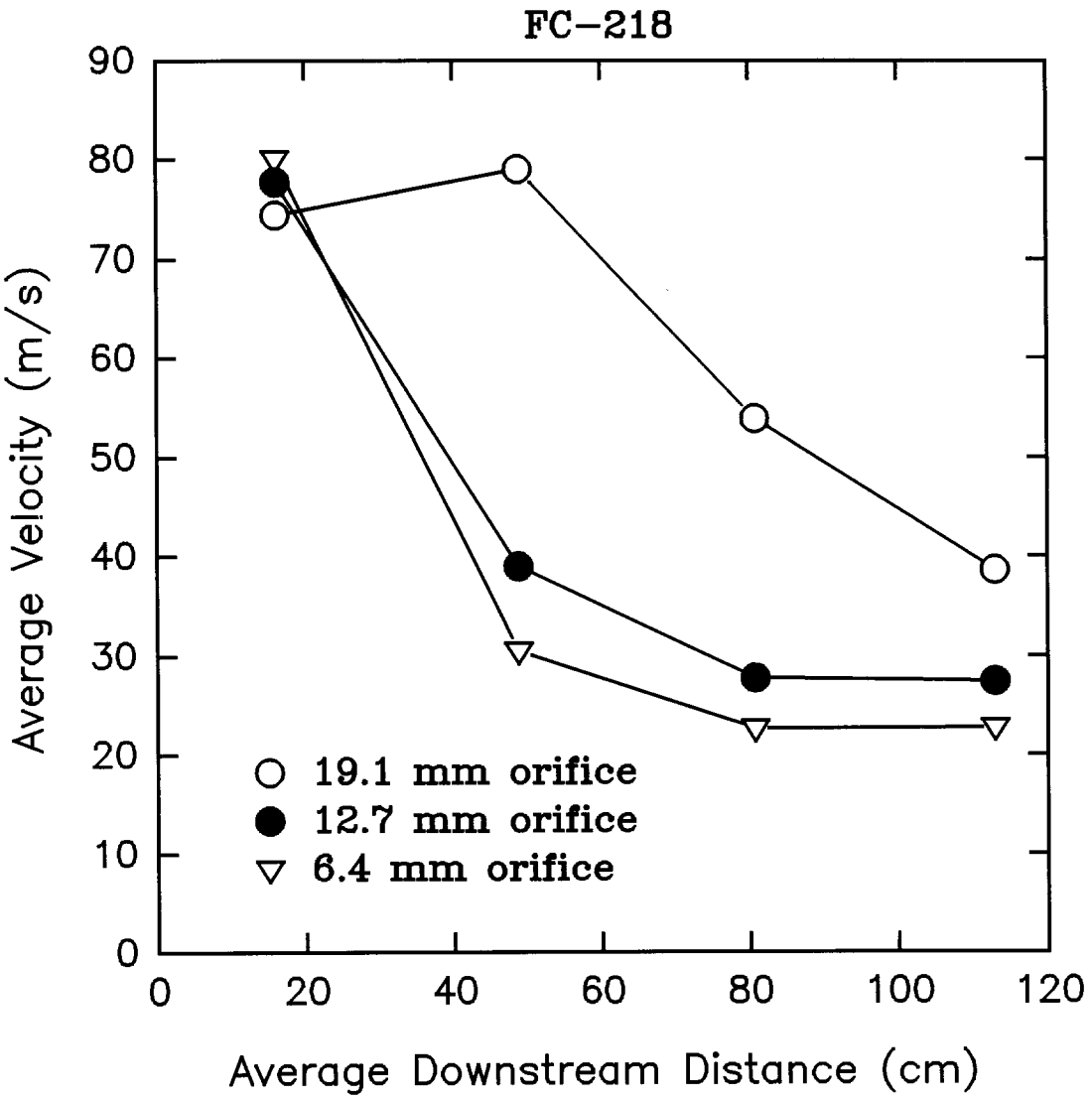

Figure 140. Average velocities determined by the time of arrival at laser beams #1-#5 plotted as a function of average downstream distance for releases of FC-218 through 19.1, 12.7, and 6.4 mm orifices.

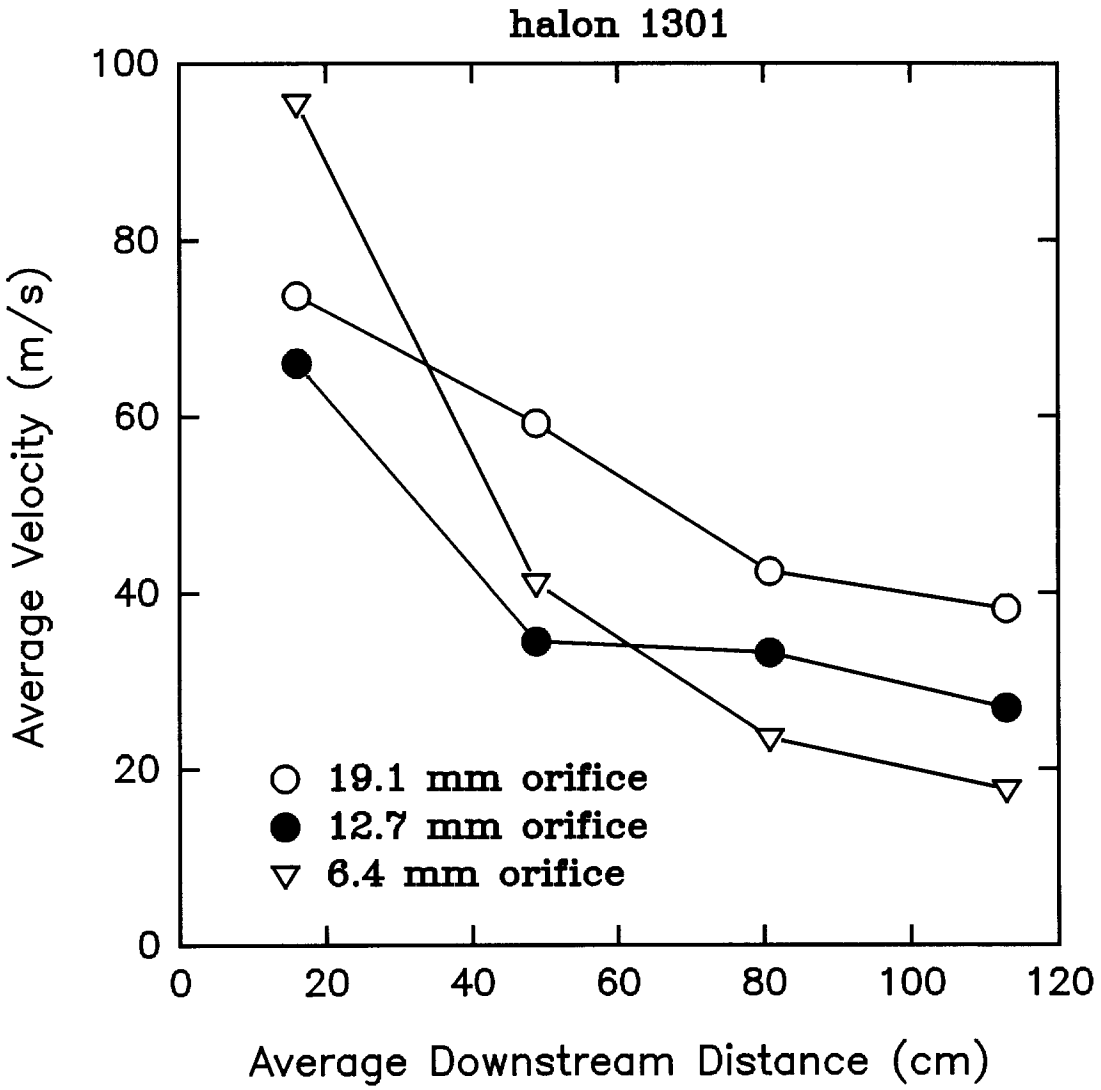

Figure 141. Average velocities determined by the time of arrival at laser beams #1-#5 plotted as a function of average downstream distance for releases of halon 1301 through 19.1, 12.7, and 6.4 mm orifices.

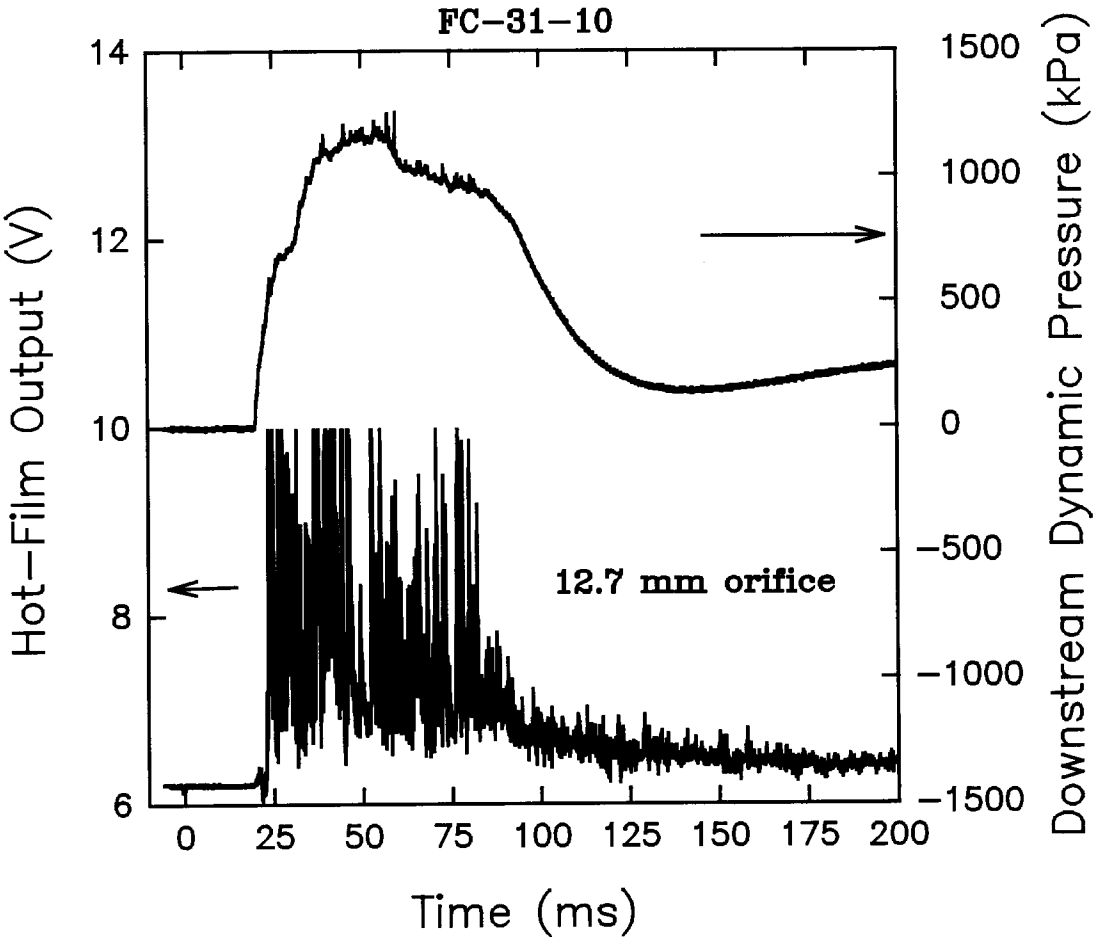

Figure 142. Voltage output of the aspirated hot-film and dynamic pressure for probes placed 1.3 m from the vessel as a function of time following a release of FC-31-10 through a 12.7 mm orifice. Conditions: 521 g of agent, release pressure of 4.48 MPa.

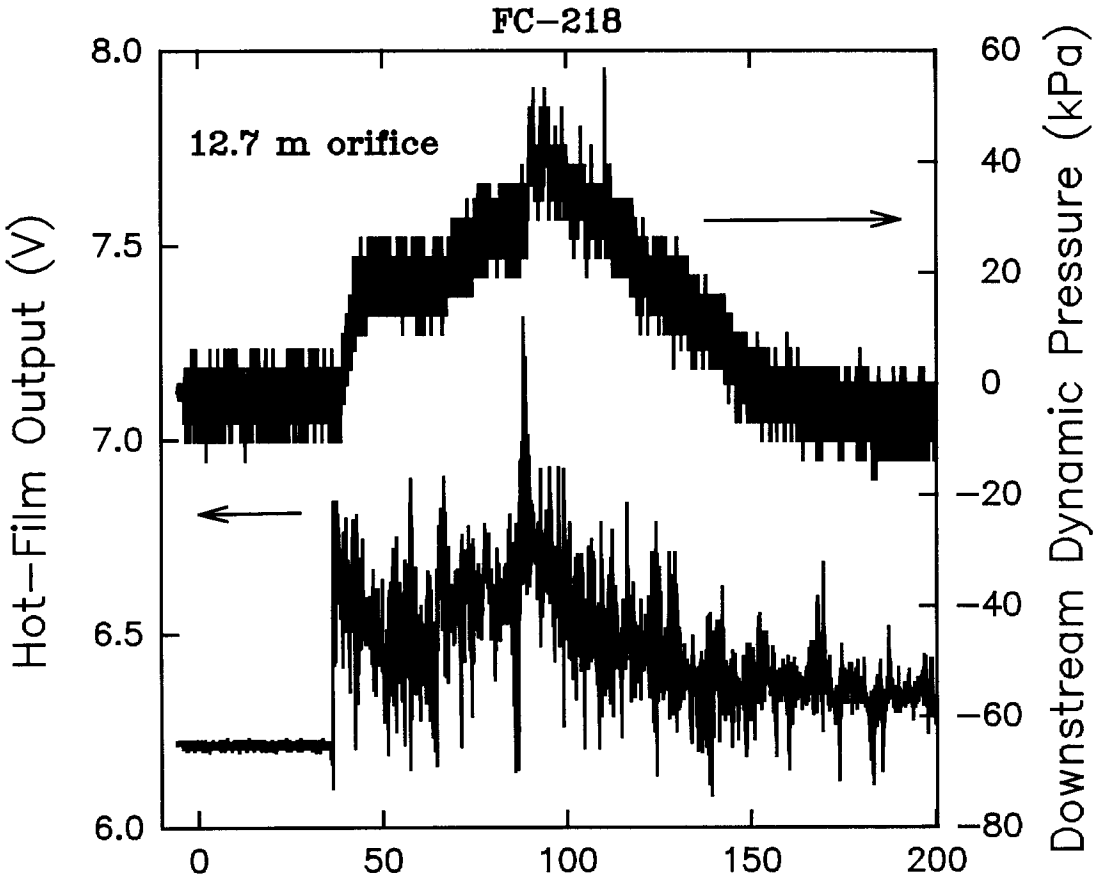

Figure 143. Voltage output of the aspirated hot-film and dynamic pressure for probes placed 1.3 m from the vessel as a function of time following a release of FC-218 through a 12.7 mm orifice. Conditions: 463 g of agent, release pressure of 4.23 MPa.

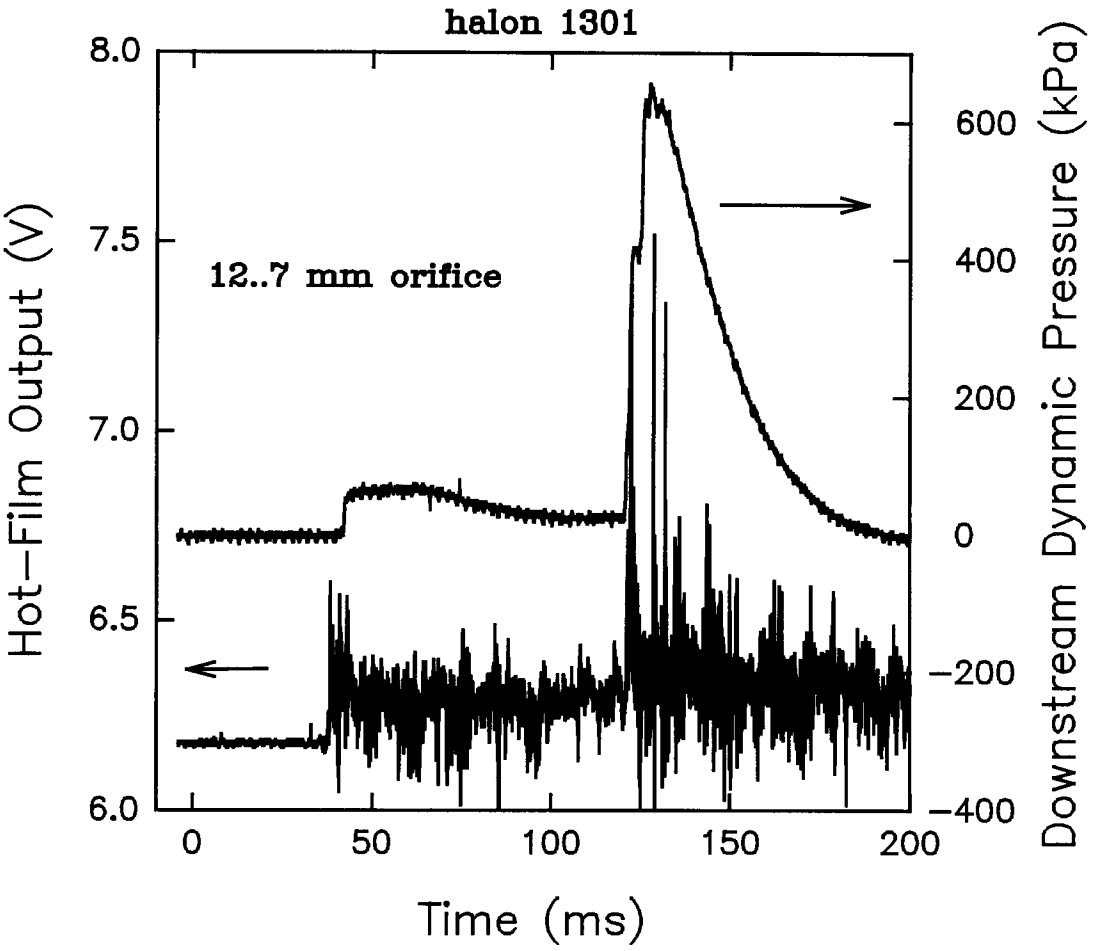

Figure 144. Voltage output of the aspirated hot-film and dynamic pressure for probes placed 1.3 m from the vessel as a function of time for a release of halon 1301 through a 12.7 mm orifice. Conditions: 537 g of agent, release pressure of 4.54 MPa.

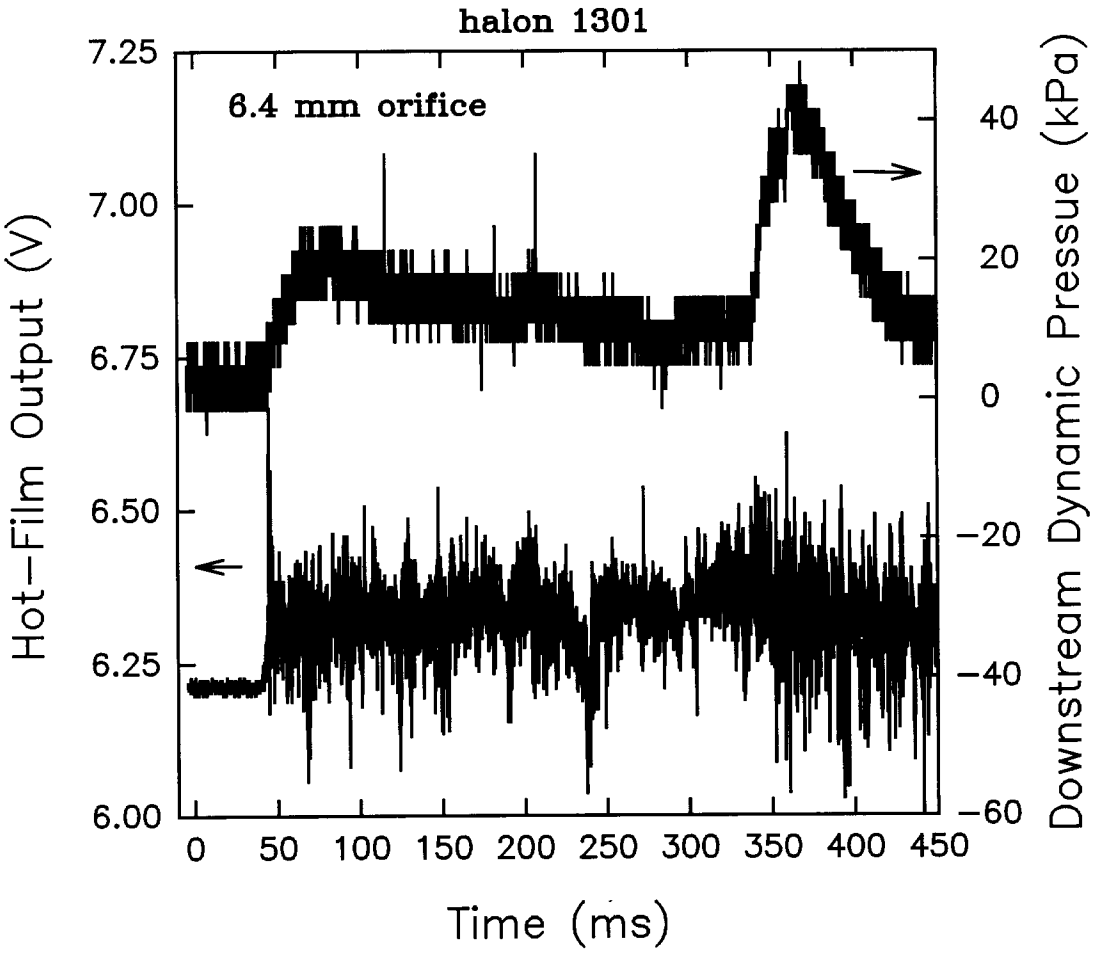

Figure 145. Voltage output of the aspirated hot-film and dynamic pressure for probes placed 1.3 m from the vessel as a function of time for a release of halon 1301 through a 6.4 mm orifice. Conditions: 546 g of agent, release pressure of 4.62 MPa.

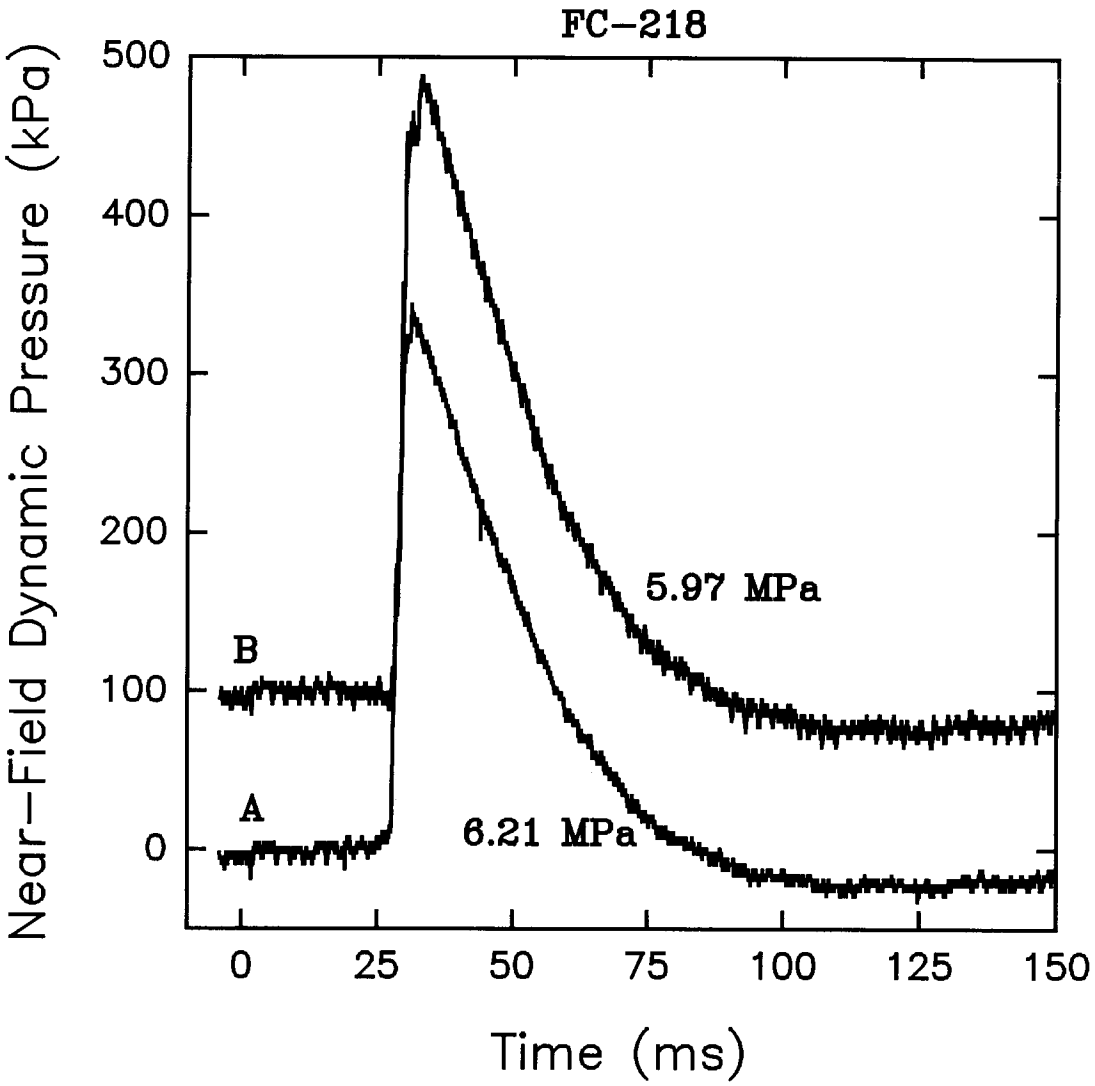

Figure 146. Two time traces of near-field dynamic pressure for releases of FC-218 using nominal 5.52 MPa burst disks. Trace B is offset by 100 kPa. Conditions: A, 455 g, release pressure 6.21 MPa; B, 457 g, release pressure 5.97 MPa.

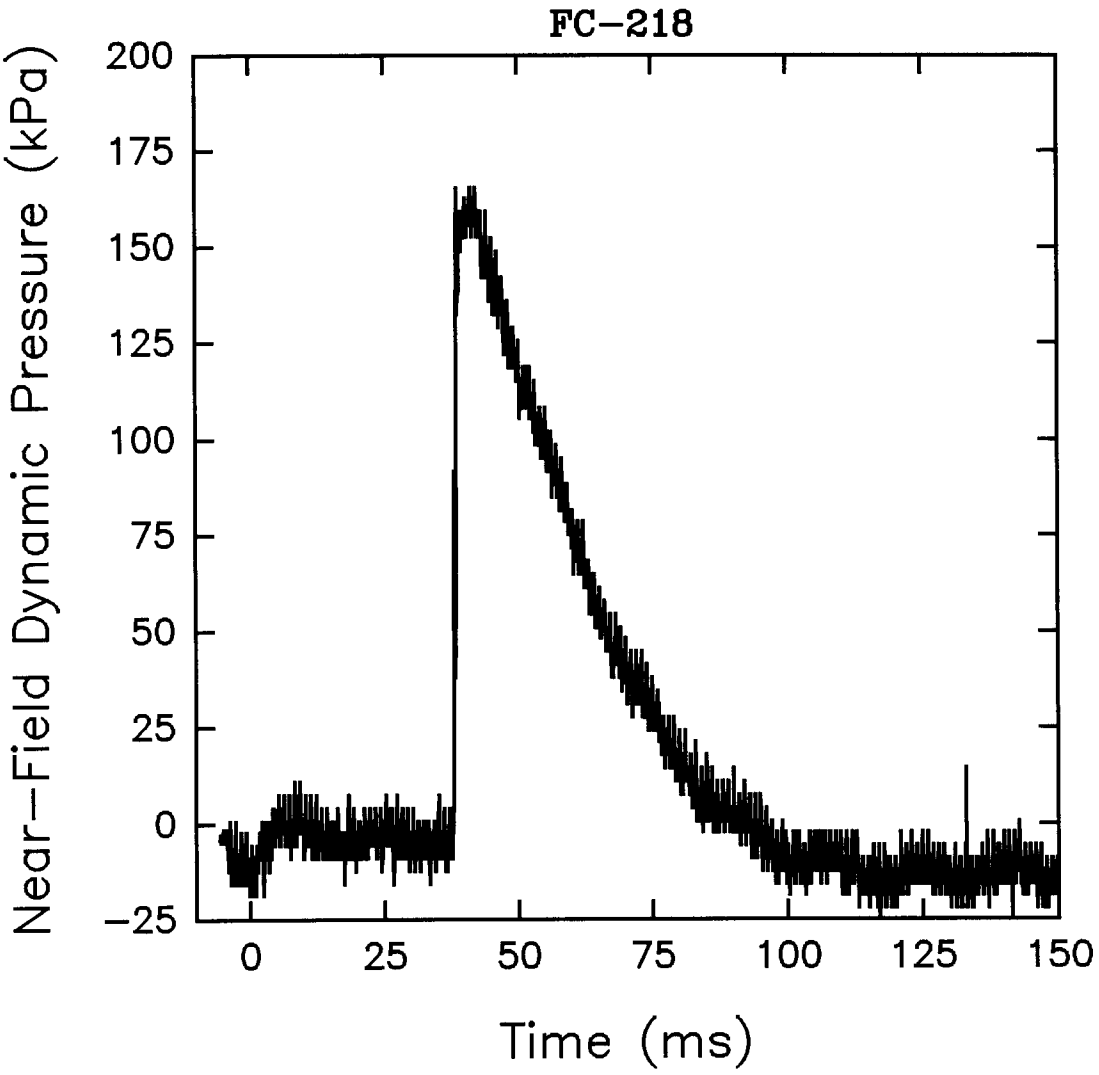

Figure 147. Time trace of the near-field dynamic pressure for a release of FC-218 using a nominal 2.76 MPa burst disk. Conditions: 436 g, release pressure 2.61 MPa.

internal pressure of 4.28 MPa. The releases at higher internal pressures resulted in somewhat lower dynamic pressures. The smallest pressure rise was observed when the vessel pressure was 2.61 MPa.

Measurements discussed in Section 3.4.3.4 showed that the agent was expelled from the vessel at higher rates as the internal pressure was increased. Figure 148 shows the average velocities measured for three releases of FC-218 subject to a range of vessel pressures. Consistent with the emptying rate measurements, the velocities increase with internal pressure. The largest difference is observed when reducing the internal vessel pressure from 4.28 MPa to 2.61 MPa.

3.5.3.8 Effect of Attaching a 0.5 m Extension Tube to the Vessel. A 0.5 m tube having a 19.1 mm inside diameter was attached to the orifice of the vessel. The near-field pressure transducer was not employed in these experiments. The tube blocked lasers #1 and #2. As a result, average velocity measurements are only available for the two measurement locations farthest from the vessel. Note that the exit for the tube was located 0.8 m from the downstream position of laser #5. Measurements were made for FC-31-10, FC-218, and halon 1301.

Figure 149 through Figure 151 show measurements of average velocities for the three agents with the tube in place. For comparison purposes the results for releases without the tube are also shown. In each case the velocities observed with the tube are considerably higher than when the tube is absent. For the higher boiling-point FC-31-10 the increase is only 20 to 30%. However, for the two lower boiling-point agents the increase is more than a factor of two.

The downstream dynamic pressures and hot-film responses recorded for releases of the three agents are shown in Figure 152 through Figure 154. In each case very high dynamic pressures are measured suggesting that the agents are arriving as two-phase flows. The spikey nature of the hot-film signals support this conclusion. For the two low boiling-point agents, FC-218 and halon 1301, the hot-film detects the presence of the agents before a large pressure increases is observed. This suggest that the initial agent reaching the detectors is primarily vapor. However, after only a few milliseconds, the flow displays two-phase character.

Comparison of Figure 154 with Figure 152 and Figure 153 shows that the two-phase flow period is considerably longer for the halon 1301 ($\sim$ 100 ms) than for the other two agents. This, in turn, implies that the time required for the release of the agent from the vessel is substantially longer. In the absence of the extension tube (see Section 3.4.3.1) the liquid release period for the three agents is on the order of 40 ms. The presence of the extension tube therefore more than doubles the liquid release period for halon 1301. The same conclusion was reached in Section 3.4.3.3 based on internal vessel pressure measurements. The longer liquid release period is attributed to the generation of a two-phase flow of halon 1301 in the tube.

3.5.3.9 Effect of Cooling the Agent Prior to Release. Two releases of FC-31-10 were studied in which the agent inside the vessel was cooled to 228 K, *i.e.*, a temperature far below its boiling point of 271 K. As would be expected, the high-speed films indicated that there was very little flashing of the liquid as it exited the vessel. No near-field dynamic pressure measurements were made, but no pressure increase would be expected due to the absence of flashing behavior.

Figure 155 is a plot of the measured average velocity as a function of distance from the vessel. These results can be compared with similar plots shown in Figure 111 for releases of FC-31-10 with the vessel at room temperature. The velocities near the vessel exit are much lower for the cooled agent as expected for the lower release pressure. There are small increases in these velocities with downstream distance, but the increases are much smaller than observed for the room temperature releases (roughly 10 m/s versus 15 m/s).

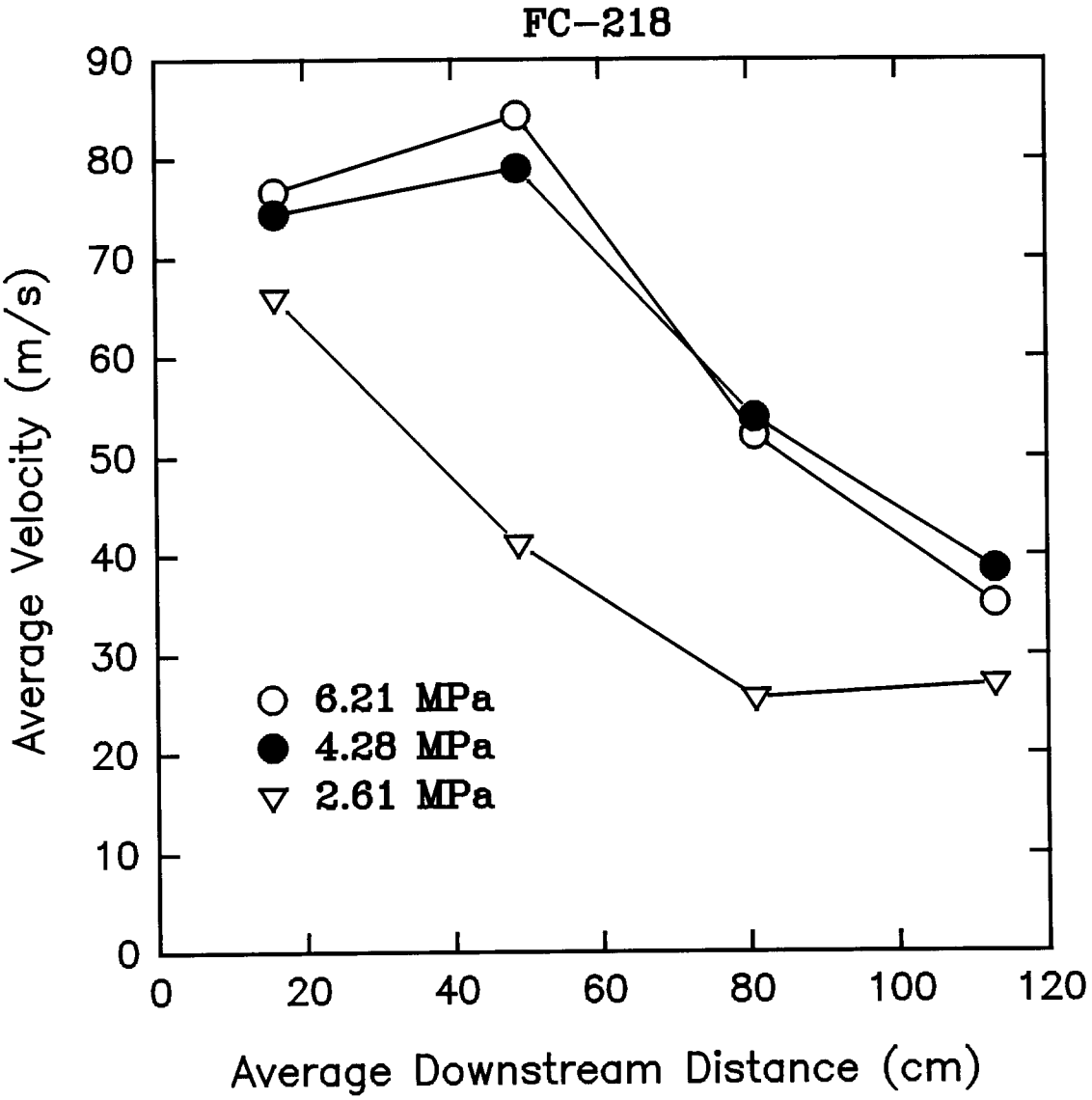

Figure 148. Average velocities as a function of downstream distance determined by time of arrival at laser beams #1-#5 for releases of FC-218 with burst disks covering a range of nominal pressures. Pressures are those inside the vessel at disk bursting.

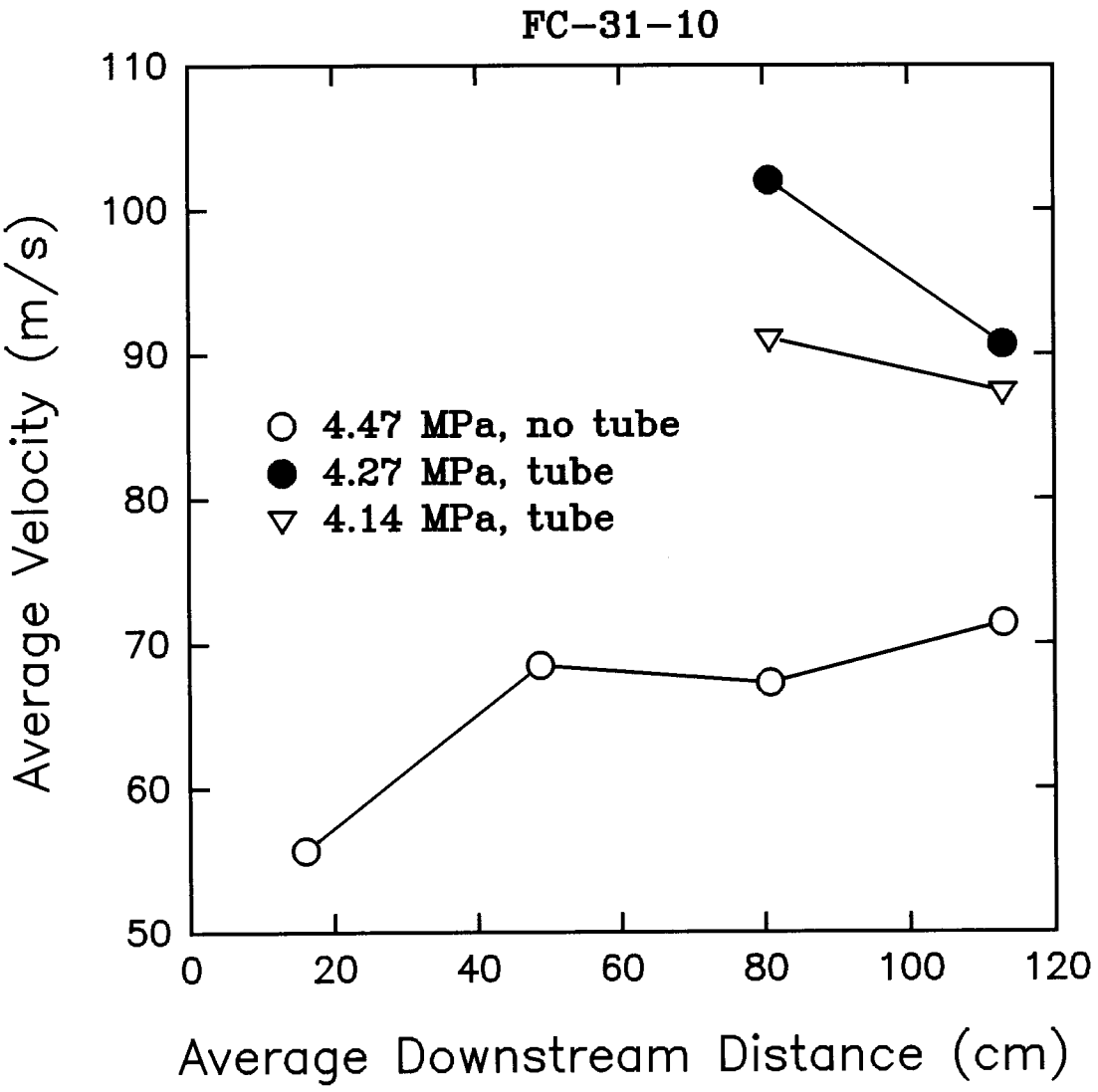

Figure 149. Average velocities determined by the time of arrival at laser beams #1-#5 as a function of downstream distance for releases of FC-31-10 with and without an extension tube. Pressures are those inside vessel at disk bursting.

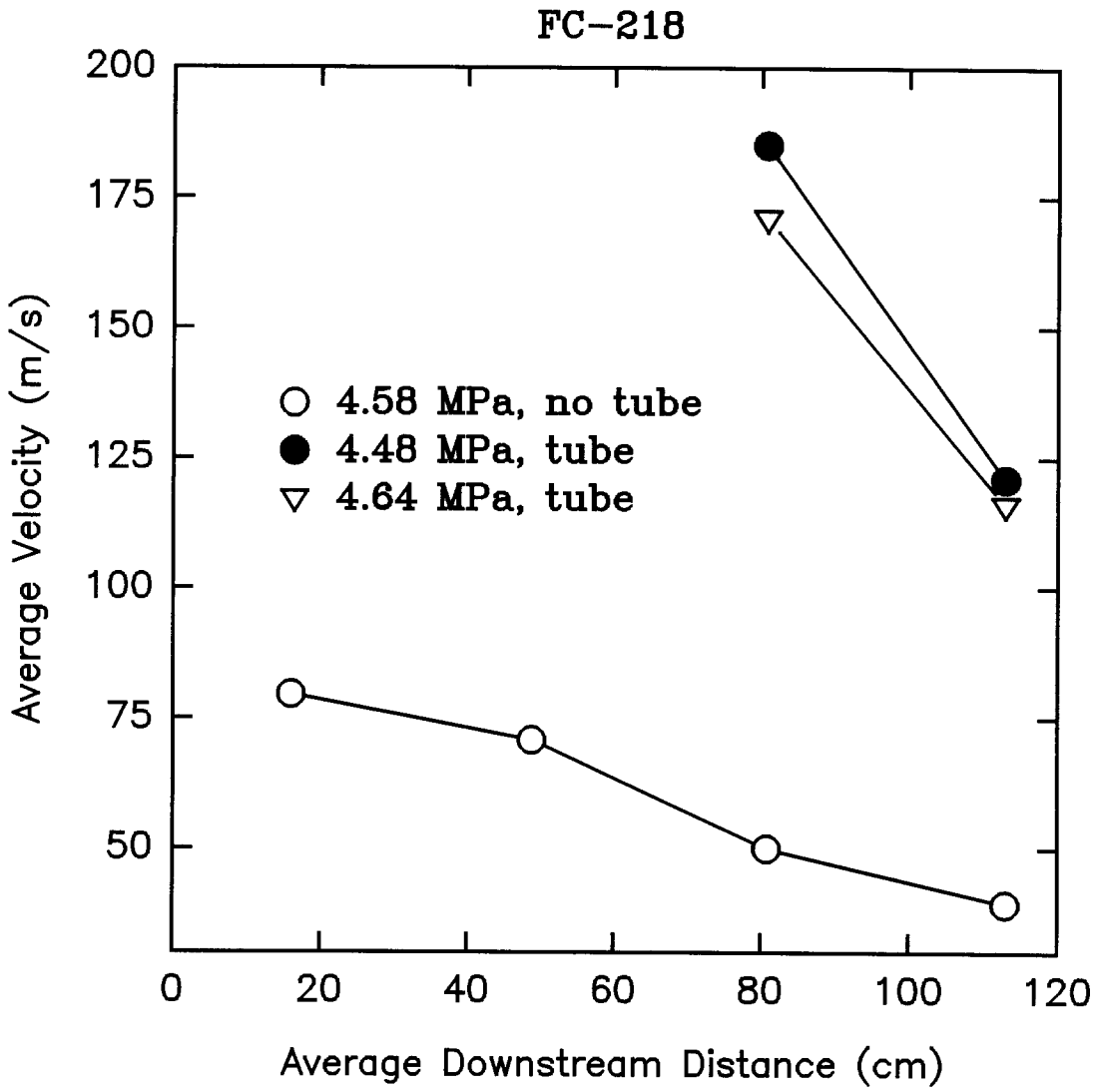

Figure 150. Average velocities determined by the time of arrival at laser beams #1-#5 as a function of downstream distance for releases of FC-218 with and without an extension tube. Pressures are those inside vessel at disk bursting.

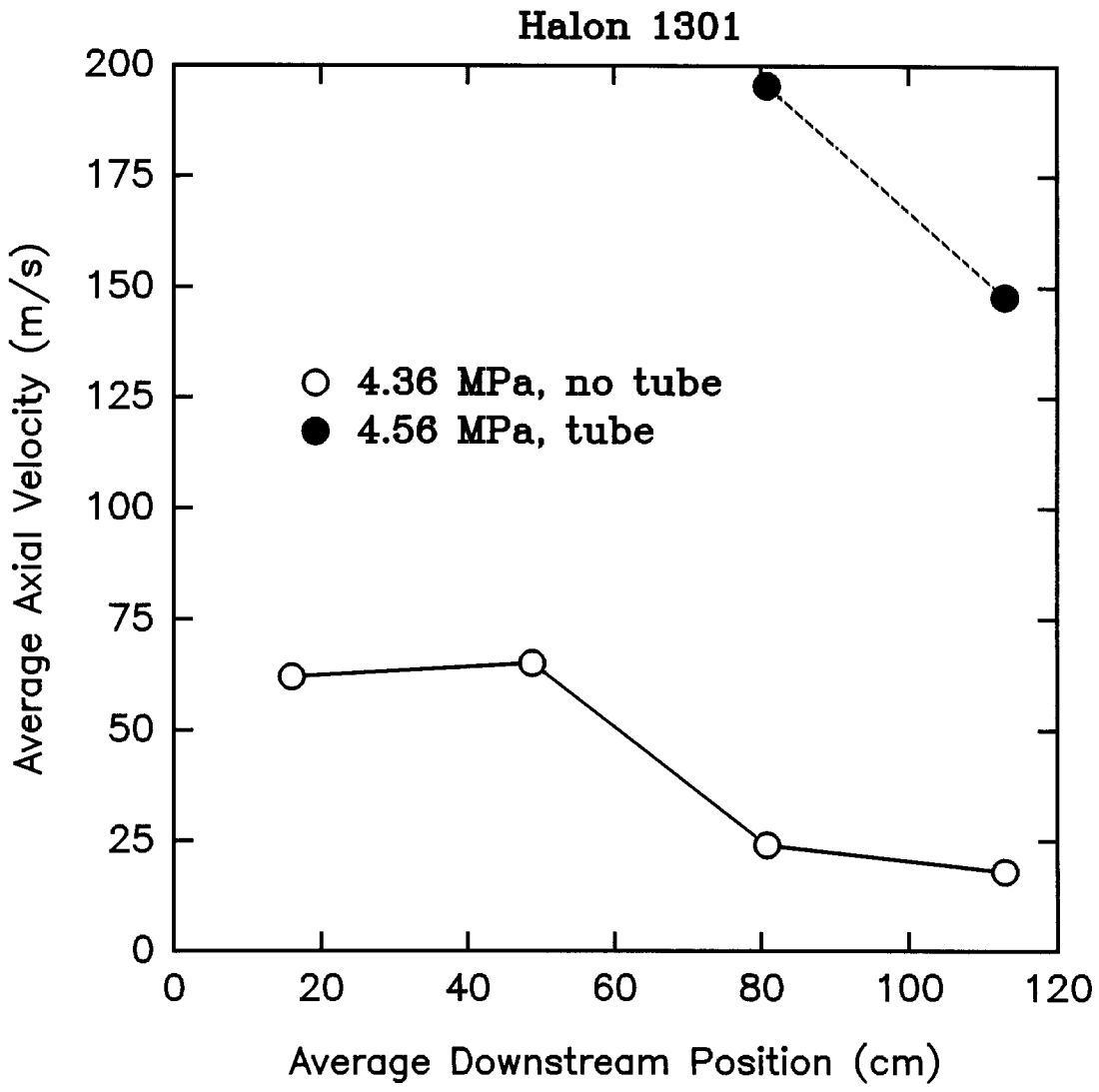

Figure 151. Average velocities determined by the time of arrival at laser beams #1-#5 as a function of downstream distance for releases of halon 1301 with and without an extension tube. Pressures are those inside vessel at disk bursting.

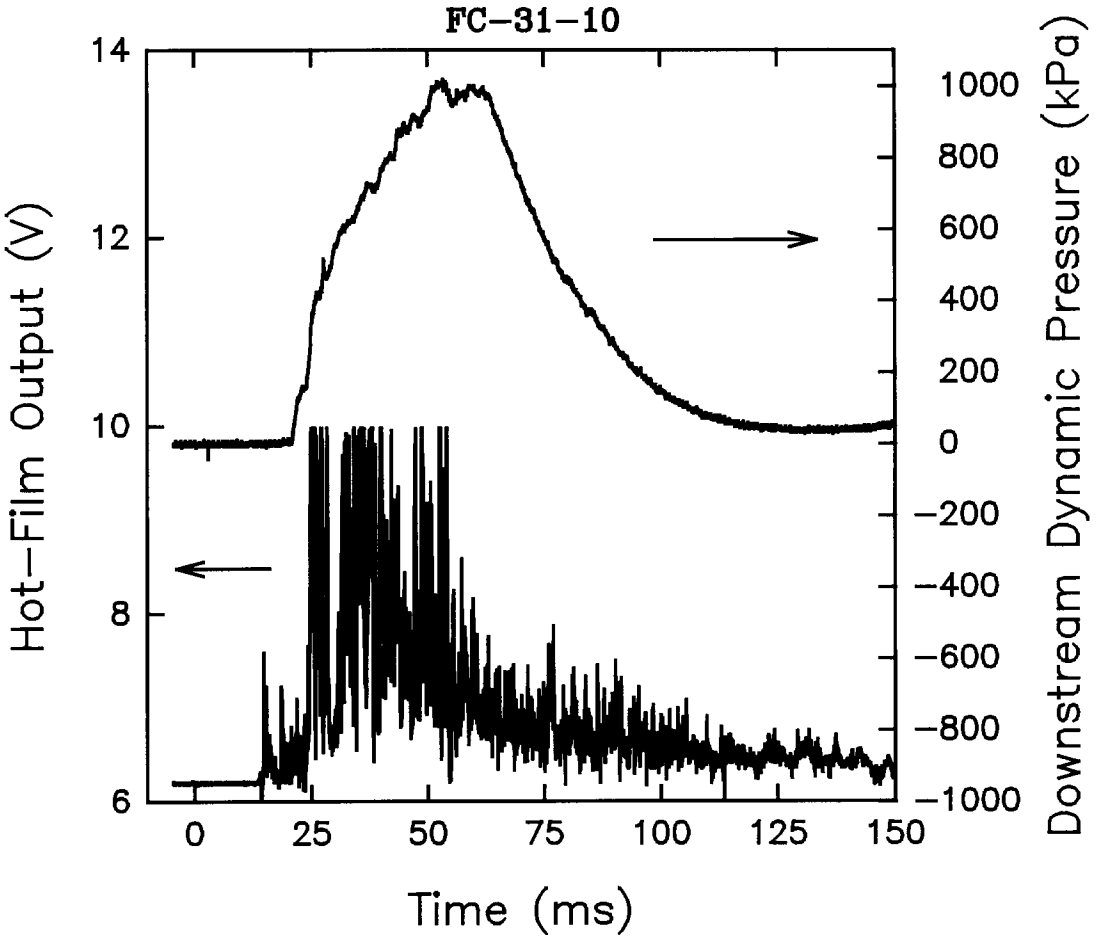

Figure 152. Aspirated hot-film voltage and dynamic pressure for probes located 1.3 m from the vessel with an attached 0.5 m tube plotted as functions of time following release of FC-31-10. Conditions: 513 g of agent, release pressure of 4.14 MPa.

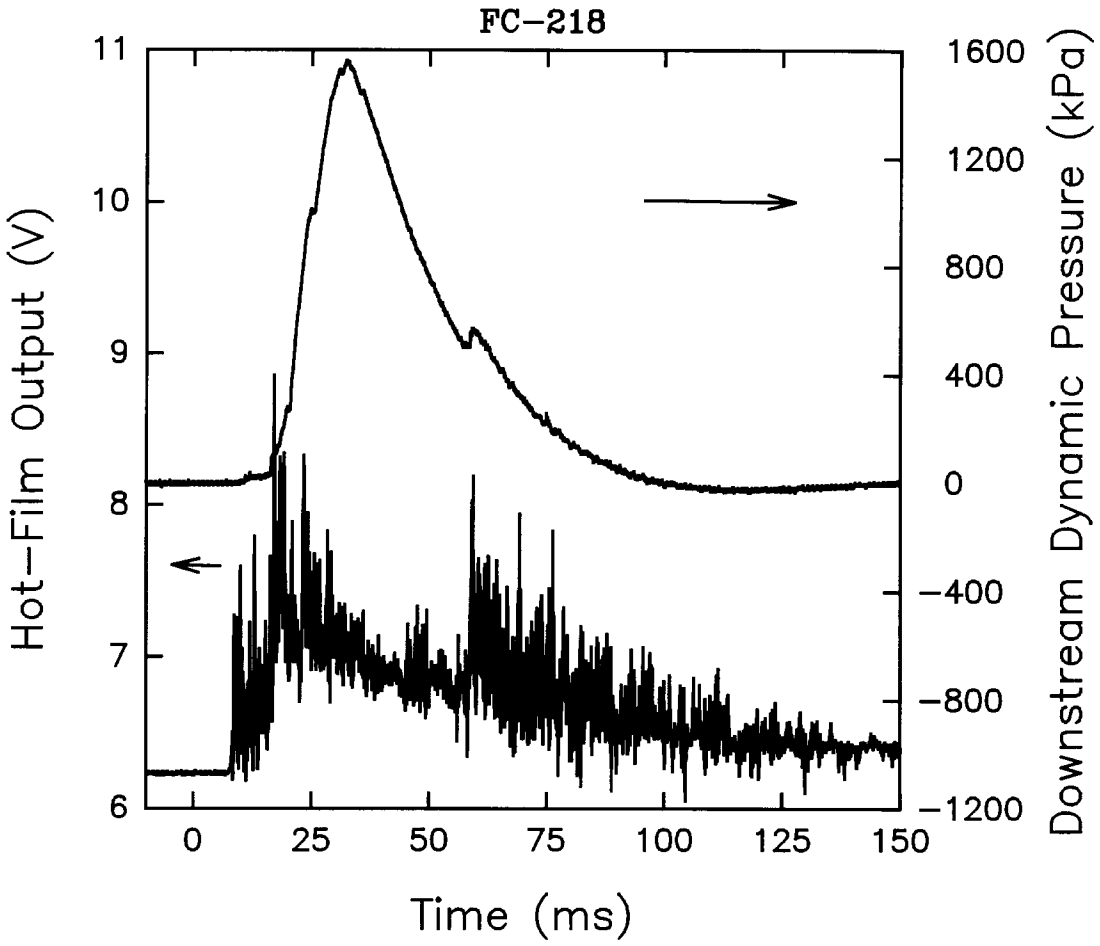

Figure 153. Aspirated hot-film voltage and dynamic pressure for probes located 1.3 m from the vessel with an attached 0.5 m tube plotted as functions of time following release of FC-218. Conditions: 465 g of agent, release pressure of 4.48 MPa.

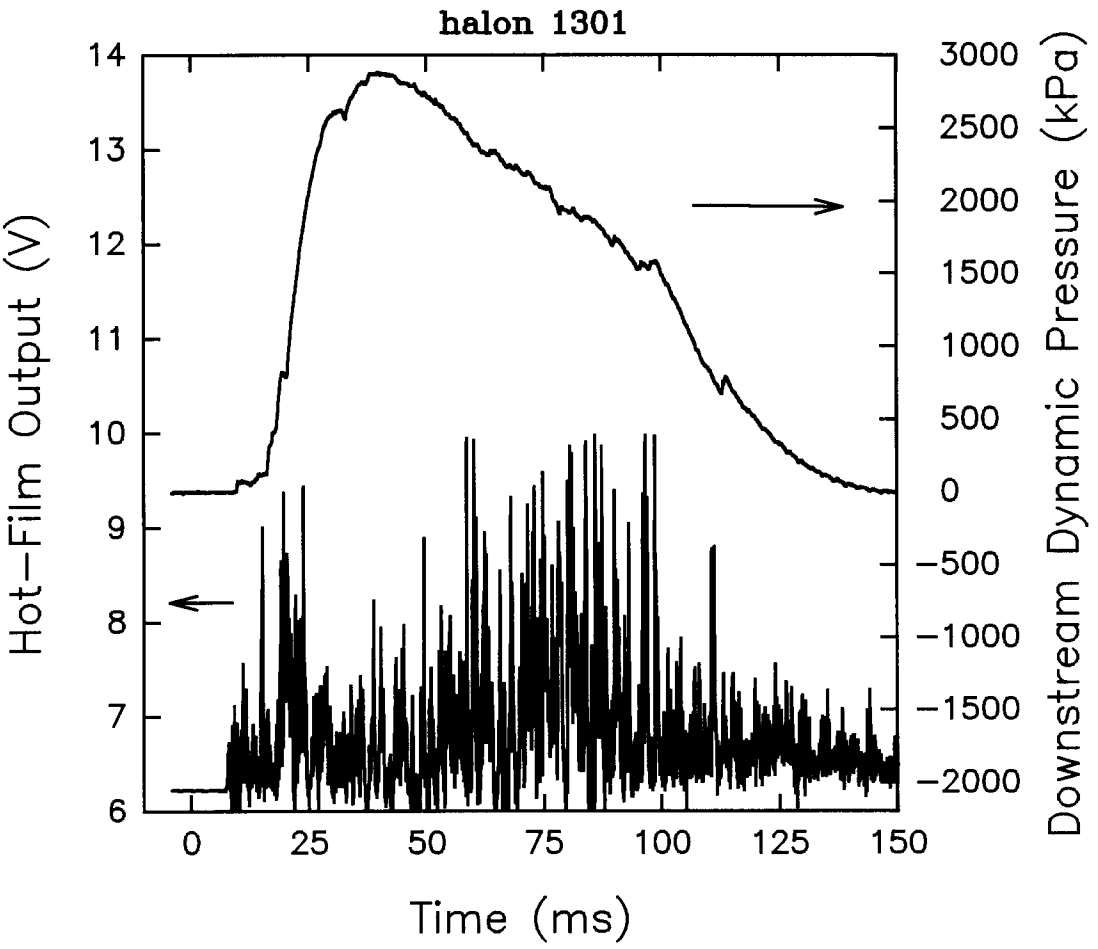

Figure 154. Aspirated hot-film voltage and dynamic pressure for probes located 1.3 m from the vessel with an attached 0.5 m tube as functions of time following release of halon 1301. Conditions: 523 g of agent, release pressure of 4.56 MPa.

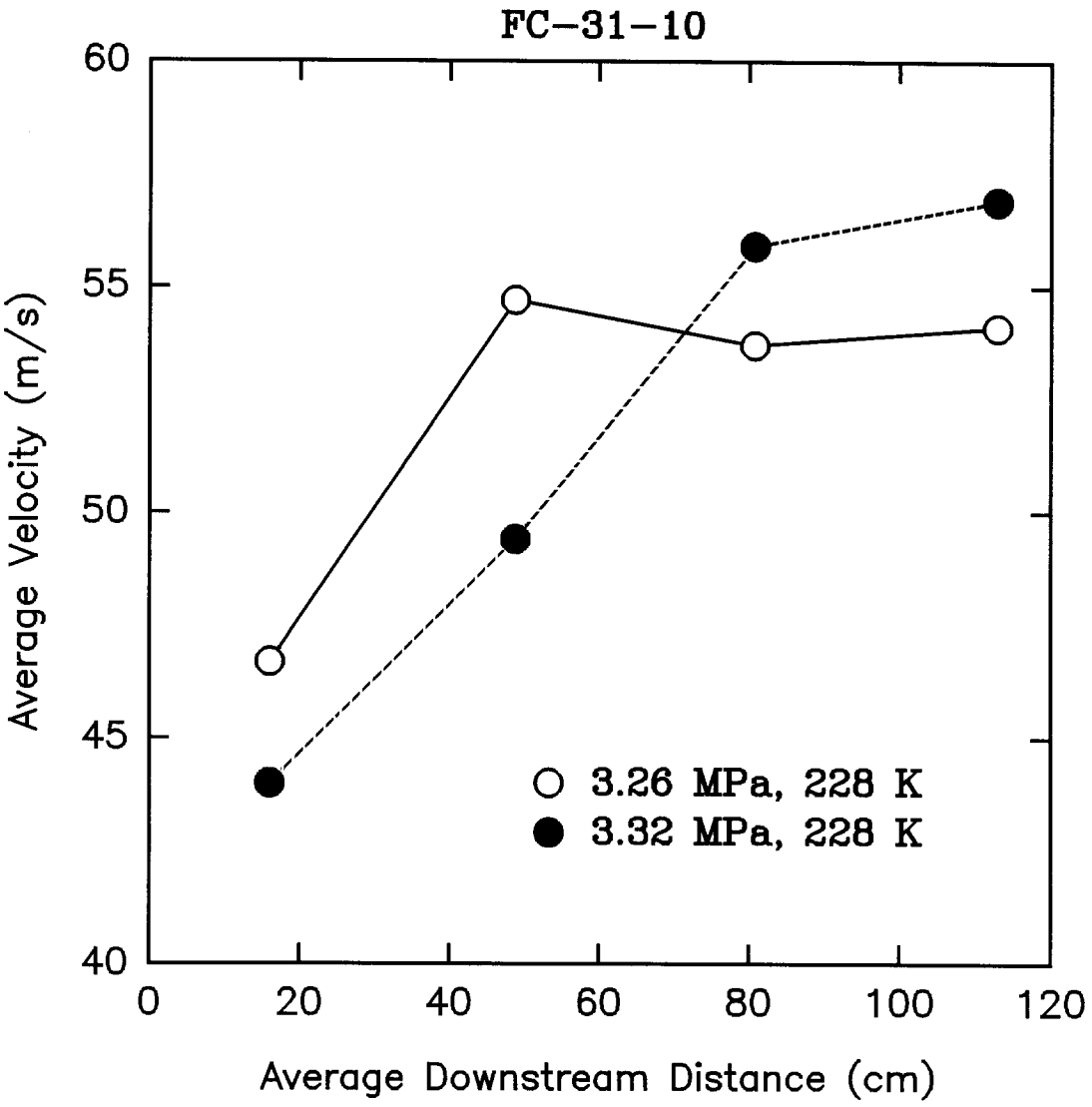

Figure 155. Average velocities for releases of cooled FC-31-10 determined by the time of arrival at laser beams #1-#5 plotted as a function of average downstream distance. Vessel internal temperatures and pressures are indicated.

The downstream dynamic pressure and aspirated hot-film voltage time plots shown in Figure 156 indicate that when the agent arrives at the 1.3 m sampling position it has a great deal of two-phase character. This is consistent with a slow evaporation due to its initial cold temperature.

A single release of FC-218 cooled to 228 K was run. At times during releases of agents which reached the downstream detectors as mostly liquid, a strong interference was recorded on all of the data channels. This was the case for the release of cold FC-218. For this reason, plots of the data are not shown. However, the results are discussed because they provide important insights as to the importance of superheating on the agent behavior. The release pressure was 3.34 MPa. Due to the positioning of the vessel, laser #1 was located 60 mm from the vessel orifice. The initial pressure drop inside the vessel was noted 1 ms before laser #1 detected any attenuation. This suggests agent began flowing immediately and achieved a near-vessel velocity on the order of 60 m/s. This estimate is consistent with measurements of the average velocity determined from laser beam attenuation measurements shown in Figure 157. For comparison, the results for a room temperature release are also included in the figure. The most remarkable finding from Figure 157 is the nearly constant flow velocity at positions removed from the vessel. A steady stream of fluid is detected with a velocity of 57 m/s.

Strong interferences in the signals were detected when the release reached the 1.3 m sampling position. The aspirated hot-wire signal was very large and saturated the digitizer. The dynamic pressure measurement was also quite noisy, however, it is possible to estimate that the dynamic pressure rose quickly and reached a level of roughly 1.4 MPa that persisted over the period of the release. Using the velocity of 57 m/s from the laser measurements, this dynamic pressure corresponds to a density of 860 kg/m^3. The room temperature density of the liquid is 1321 kg/m^3 suggesting that very little of the liquid was evaporated over the 1.3 m length of the flow.

Recall that for room temperature releases of FC-218, the degree of vaporization was quite high, approaching 100%. These results demonstrate the dramatic effect that the degree of superheating can have on the vaporization of these agents.

3.5.3.10 Effect of Orientation--Upward Releases. Releases of the agents were made with the vessel orifice oriented upward and horizontally. Measurements of the mixing behavior have only been recorded for the vessel oriented upwards. High-speed films, near-field dynamic pressure, laser attenuation, downstream dynamic pressure, and aspirated hot-film measurements have all been made. The experimental system was modified by moving the vessel to a location just below laser #5 and the downstream pressure transducer and aspirated hot-film to a location just upstream of laser #1. Keep in mind for the figures which follow that laser #5 is closest to the vessel exit. Releases of FC-31-10, FC-218, and halon 1301 were studied.

The high-speed films demonstrated that releases of the agents upward were quite different from downward releases. The behaviors of the agents within the vessel are described in Section 3.4.3.6 There it is noted that for an upward release the nitrogen first exited the vessel. During this period some gaseous agent was condensed. After a fairly substantial delay the agent in the bottle began to boil and froth, filled the vessel, and generated a two-phase flow exiting the vessel. Approximately 20 ms was required for the agent to begin to boil and a longer period to fill the vessel and generate the two-phase flow. The periods required to expel the agent completely were substantially longer for the upward releases than when the agents were released downward.

The films show related behaviors for the released agents near the vessel orifice (*e.g.*, see Figure 73). A plume is easily observed when the disk first opens. After a short period of time the plume seems to disappear, only to reappear when the fluid inside the vessel begins to boil.

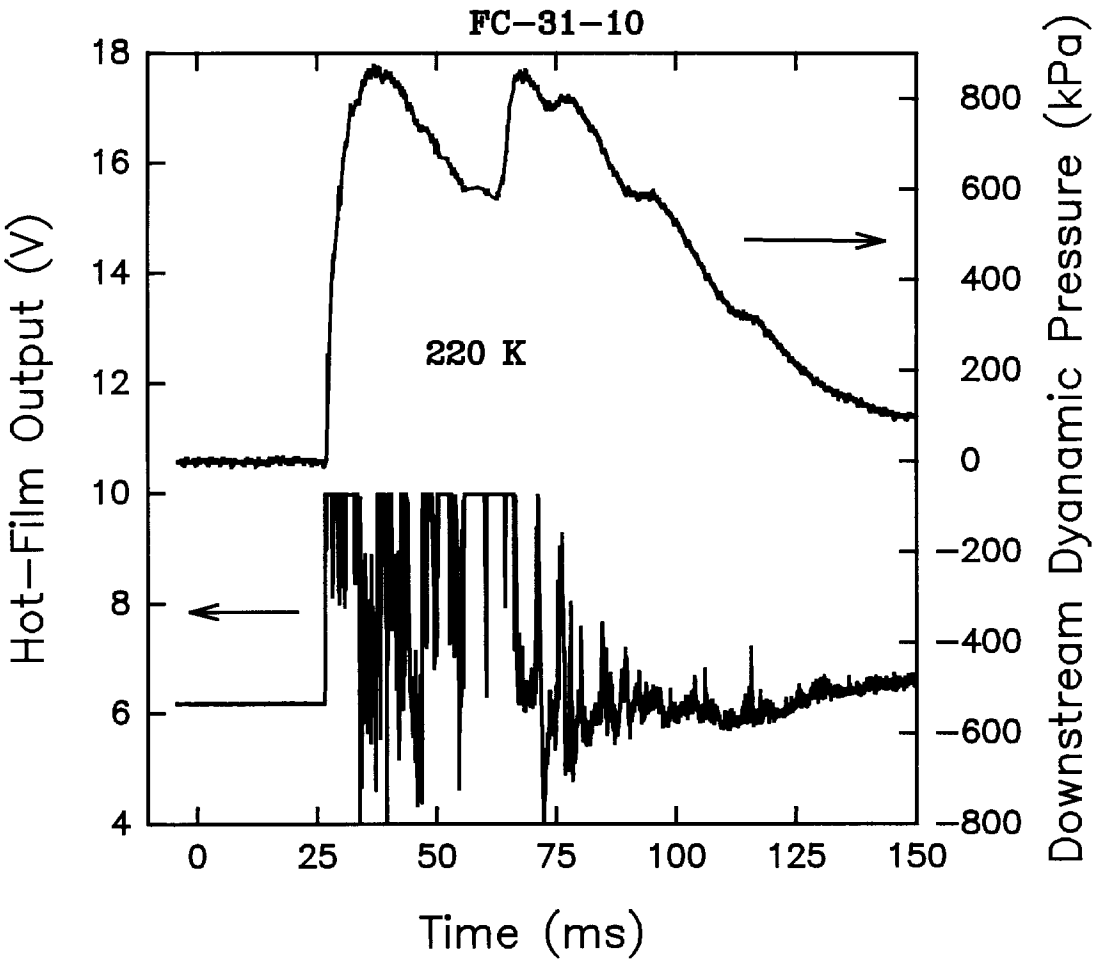

Figure 156. Aspirated hot-film voltage and dynamic pressure for probes located 1.3 m from the vessel plotted as functions of time following release of FC-31-10 cooled to 228 K. Conditions: 517 g of agent, release pressure of 3.34 MPa.

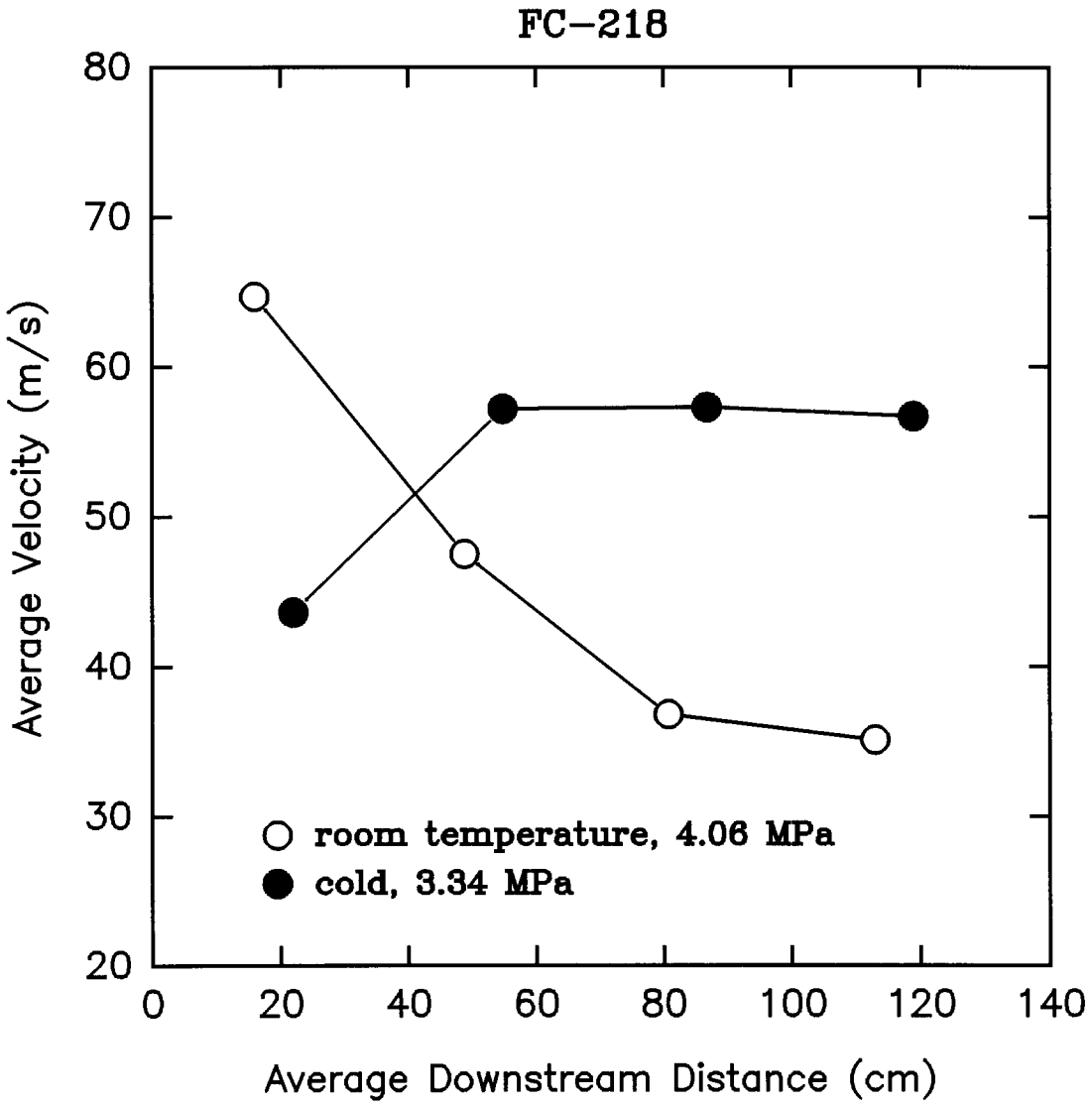

Figure 157. Average velocities for releases of room temperature and cooled FC-218 determined by the time of arrival at laser beams #1-#5 plotted as a function of average downstream distance. Vessel pressures are indicated.

None of the time plots of near-field dynamic pressure showed an increase following the bursting of the disk. This indicates that the disk bursting does not generate a shock wave, and that the strong flashing behaviors which are characteristic of downward releases do not occur for the upward cases.

Figure 158 shows the laser attenuation signals over the first 200 ms for a release of FC-31-10. Laser #5 is totally attenuated very rapidly when the disk bursts. The flow then allows light to pass for a very short period before extinguishing the beam once again. The high-speed film shows that the second attenuation occurs as the result of an increase in optical density in the gas within the vessel which is subsequently transported through the orifice. Presumably this is agent vapor which condensed as the nitrogen cooled during expansion. At roughly 18 ms the flow becomes partially transmitting for a brief period. The film shows the same behavior. It appears as if the nitrogen flow has ceased before the agent begins to boil in the vessel. At roughly 24 ms following release, the liquid begins to boil at the bottom of the vessel and vapor is once again forced through the orifice leading to total attenuation of laser #5. At approximately 54 ms after release the boiling liquid fills the vessel and the flow from the orifice begins to spread much more rapidly. Since laser #5 is already totally attenuated, no effect is observed on the laser signal.

Further downstream the lasers are attenuated in different ways. Laser #4 is nearly totally attenuated very shortly after the disk opens, but then is partially transmitted for a period before the two-phase flow arrives. The degree of laser beam attenuation due to the initial flow of nitrogen decreases with increasing distance from the nozzle, but is still observable at laser #1. The furthest laser detects the flow very shortly (approximately 5 ms) after the release indicating the flow velocity is quite high. Figure 159 shows the average velocities determined for the initial gas flow as a function of distance from the orifice. At progressively later times, lasers #4-#1 show a strong extinguishment which is attributed to the arrival of condensed agent from the vessel. Estimates of the arrival times for this flow have been made and used to calculate average velocities which are also included in Figure 159. Lasers #3-#1 become partially transmitting after the initial arrival of the two-phase flow. The flow continues to transmit light for periods of tens of milliseconds before all three lasers are again totally attenuated. The later attenuations are attributed to the arrival of the two-phase flow generated by the boiling liquid filling the vessel. The arrival times of this third flow at lasers #3-#1 have also been estimated and used to calculate average velocities. Results are shown in Figure 159.

Three points should be noted concerning Figure 159. First, the velocities of the two-phase flows are considerably less than the velocities associated with the nitrogen release. Second, the average two-phase flow velocities are much lower than observed for comparable downward releases of FC-31-10 (see Figure 111). Three, the velocities of the two two-phase flows are similar.

Figure 160 shows a similar time plot for the laser signals over a much longer period of time. It is now clear that an optically dense flow is present until roughly 800 ms after the disk opens and the period required for full release of the agent approaches 1 s. This result contrasts dramatically with the observed emptying times when this agent is released downward which are on the order of 40 ms for a two-thirds full vessel.

The signals recorded by the downstream pressure transducer and aspirated hot-film are consistent with the above conclusions. Results over short and longer time periods are shown in Figure 161 and Figure 162. The arrival of the released nitrogen at the position 1.3 m from the vessel is clearly detectable in the hot-film signal even though it causes only a very small dynamic pressure rise (Figure 161) despite the high velocity. The response of the hot-film requires that this initial gas flow either contains some of the agent, or that it is substantially cooled by the nitrogen. On the other hand, when the first flow identified as consisting of two phases arrives at 75 ms following release, there is a substantial increase in both the hot-film and pressure signals consistent with the presence of a two-phase flow. Note that the velocity of the two-phase flow is considerably lower than the flow

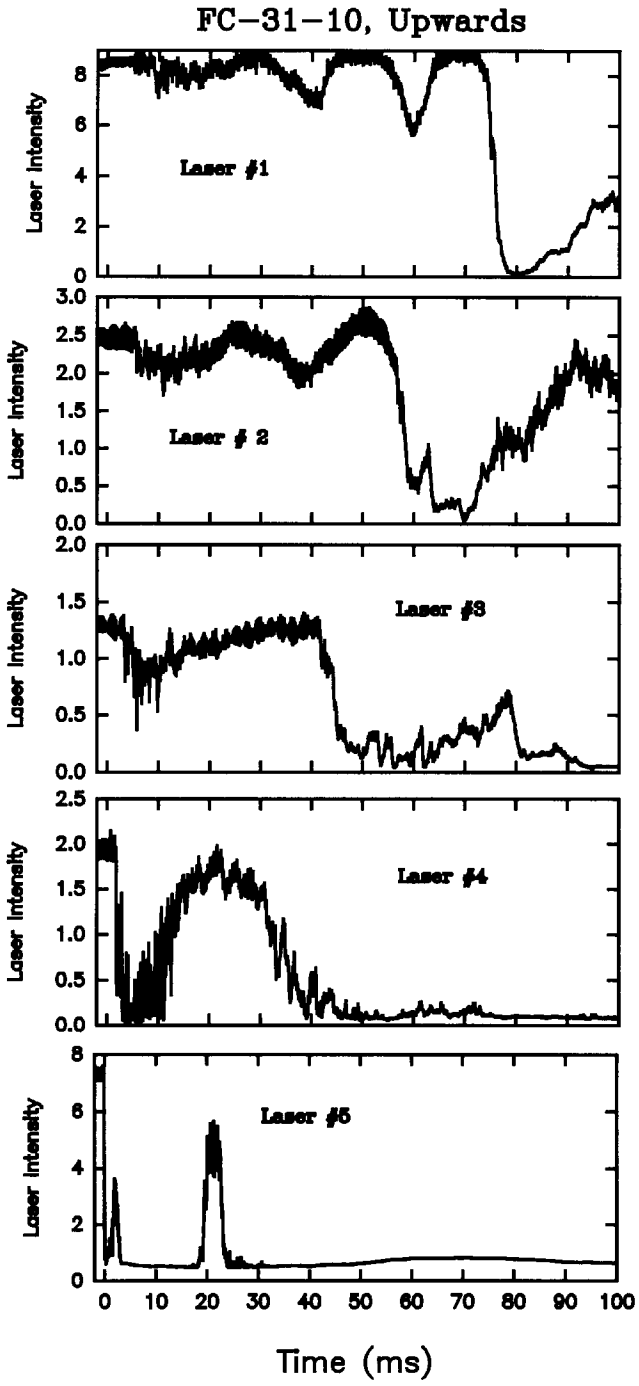

Figure 158. Short time behaviors for transmission of laser beams #5-#1 spaced as shown in Table 7 following an upward release of FC-31-10 at 0 s. Conditions: 505 g agent, 4.40 MPa release pressure.

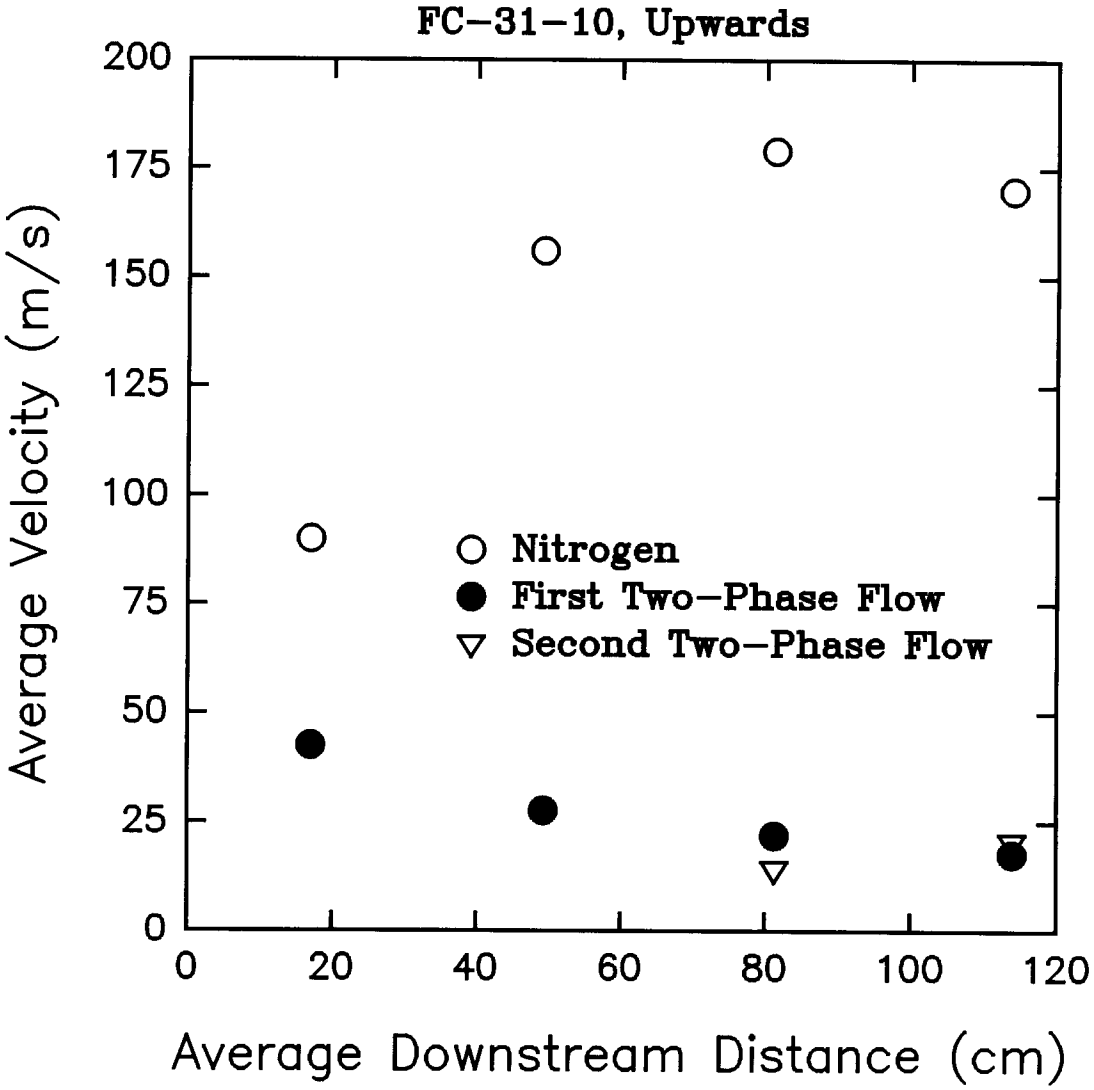

Figure 159. Average velocities for upward releases of FC-31-10 determined by the time of arrival at laser beams #5-#1 plotted as a function of average downstream distance. Results for arrival of nitrogen and two two-phase flows are indicated (see text).

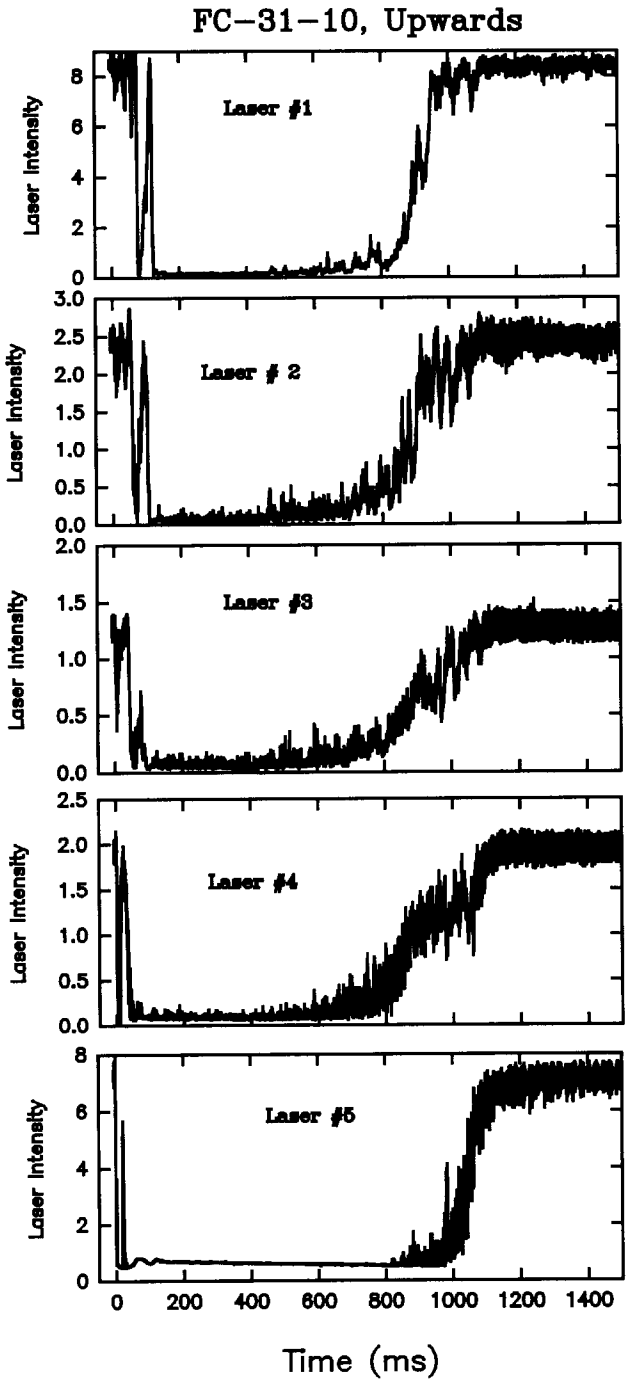

Figure 160. Long time behaviors for transmission of laser beams #5-#1 spaced as shown in Table 7 following an upward release of FC-31-10 at 0 s. Conditions: 505 g agent, 4.40 MPa release pressure.

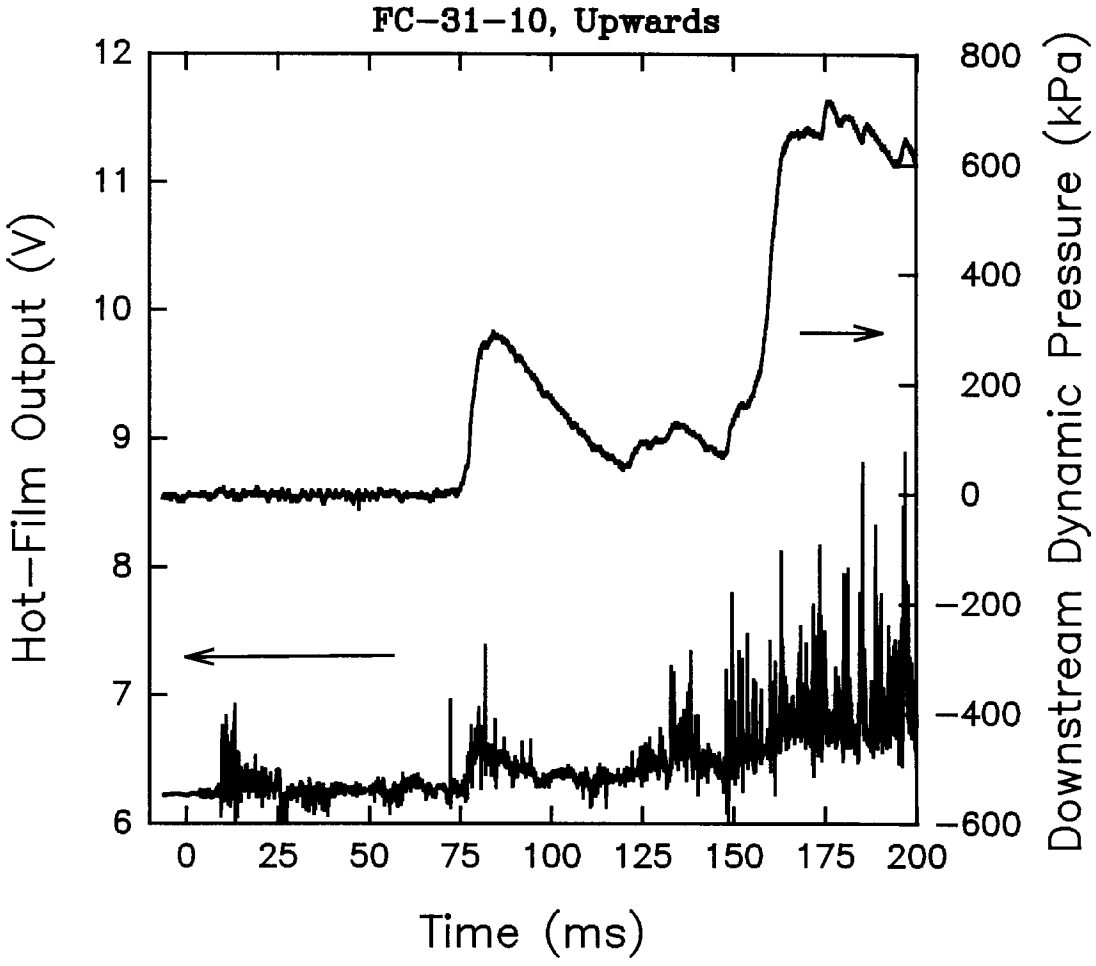

Figure 161. Voltage output of the aspirated hot-film and the dynamic pressure for probes located 1.3 m from the vessel are plotted for a short time period following an upward release of FC-31-10. Conditions: 505 g of agent, release pressure of 4.40 MPa.

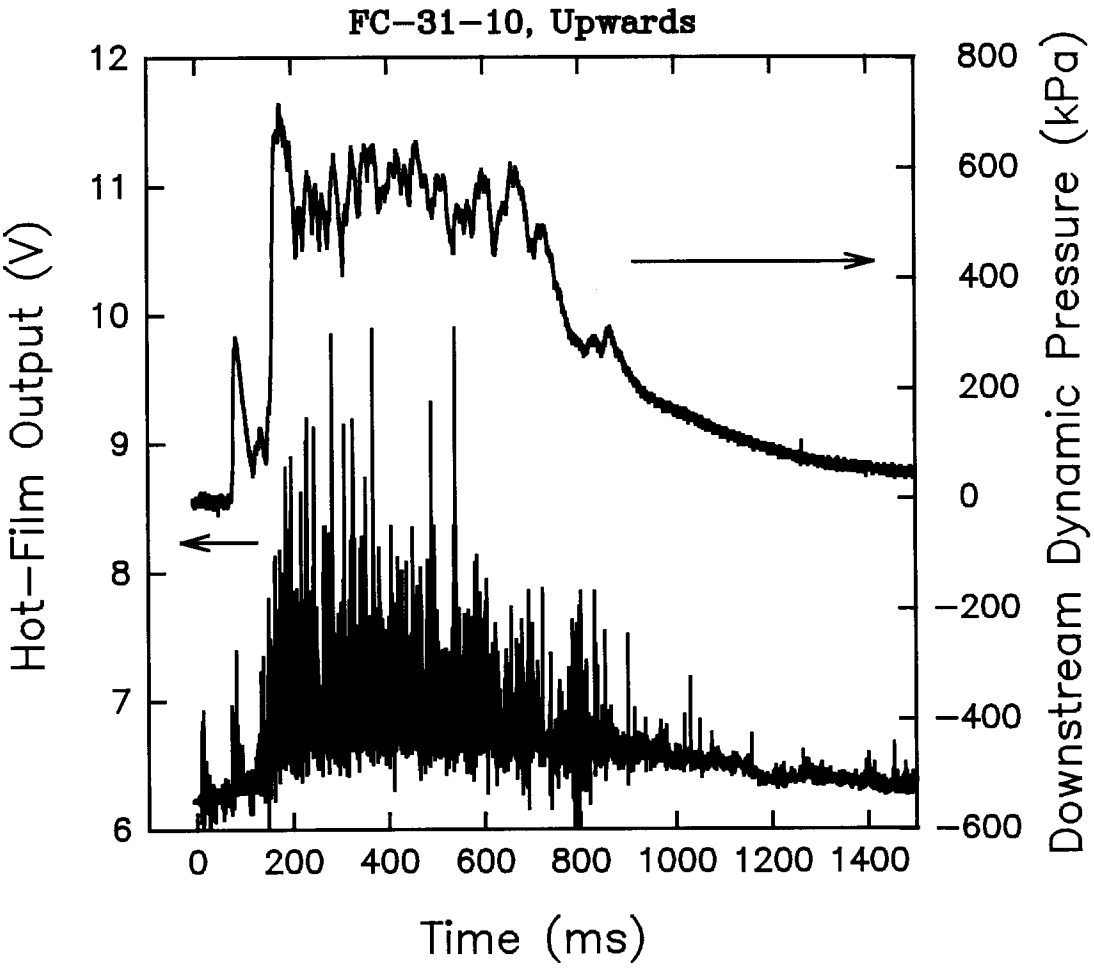

Figure 162. Voltage output of the aspirated hot-film and the dynamic pressure for probes located 1.3 m from the vessel are plotted for a long time period following an upward release of FC-31-10. Conditions: 505 g of agent, release pressure of 4.40 MPa.

resulting from the nitrogen release (see Figure 159). Following the first arrival of two-phase flow, both signals fall consistent with laser #1 being transmitted during this period. The arrival of the second two-phase flow is accompanied by a large dynamic pressure jump and much stronger indications of two-phase flow in the aspirated hot-film signal. Figure 162 shows that the later two-phase flow persists until roughly 800 ms, again consistent with the attenuation behavior of laser beam #1.

Figure 163 and Figure 164 show the laser intensity behaviors observed for upward releases of FC-218. For short times (Figure 163), the results are similar to those for the FC-31-10. When the disk bursts, laser #5 is immediately fully attenuated. Some transmission is then observed shortly after the disk opens before the laser is totally attenuated a few milliseconds later due to condensation of the agent vapor in the nitrogen. Transmission is observed for a period from roughly 12 to 20 ms following the nitrogen release. At this point, boiling in the vessel begins from the bottom and expulsion of gas from the vessel again extinguishes the laser beam. Note that the boiling begins at a somewhat shorter time than observed for the FC-31-10. High-speed films indicate the vessel is filled with boiling liquid at 39 ms following release and the more vigorous two-phase flow should form at this time.

The attenuation signals for lasers #4-#5 do not show the distinct arrival of two separate types of two-phase flow. However, it is possible to estimate roughly when the flow generated by the two-phase flow formed when the vessel is completely filled with boiling liquid reaches the lasers. For the position of laser #5 we have used the high-speed film to provide the starting time for the flow. The arrival times have been used to calculate the average velocities for the downstream edge of the two-phase flow shown in Figure 165. Velocities for the nitrogen release are also included in this figure. The results are very similar to those for FC-31-10 shown in Figure 159.

Figure 164 shows that the total attenuation of the laser beams lasts until roughly 250 ms after the release and that the laser beams are nearly completely transmitted at 500 ms. These results suggest that the upward release of FC-218 from the vessel requires only 1/3 as long as a similar release of FC-31-10.

Time plots of the downstream dynamic pressure and aspirated hot-film voltage for the FC-218 release are shown in Figure 166 and Figure 167. Figure 166 indicates that the two-phase flow reaches the sampling position roughly 55 ms following release. This is attributed to the two-phase flow which extinguishes laser #5 at 20 ms following release. A much higher pressure rise appears starting at roughly 80 ms. This time is consistent with the attenuation behavior seen for laser #1. The hot-film signal is consistent with the arrival of a strong two-phase flow. The plots of these signals over longer time periods (Figure 167) show that the two-phase flow is present until roughly 250 ms following release, consistent with the conclusion based on laser measurements.

The plastic vessel was not used for releases of halon 1301 so the internal behavior cannot be described. However, high-speed films of releases outside of the vessel indicated that the behaviors for halon 1301 were similar to those already described. The first two-phase flow appeared at 16 ms following release and the two-phase flow from the filled vessel appeared at approximately 30 ms. Figure 168 through Figure 171 show measurement results for a release of halon 1301. Short and long time plots of laser intensities are given in Figure 168 and Figure 169. For the short time data (Figure 168), the behaviors observed are similar to those described for FC-31-10 and FC-218. It is difficult to estimate arrival times for the two-phase flow at the positions nearer the orifice so velocities will not be reported. However, it is clear that two different two-phase flows reach laser #5 at roughly 30 and 50 ms. The effects of these flows are also evident in the hot-film and dynamic pressure signals shown in Figure 170. As found for the other agents, the second flow generates much higher dynamic pressures and hot-film response. This is attributed to the arrival of a two-phase flow generated by boiling when the vessel is totally filled with a two-phase mixture. Figure 169 and

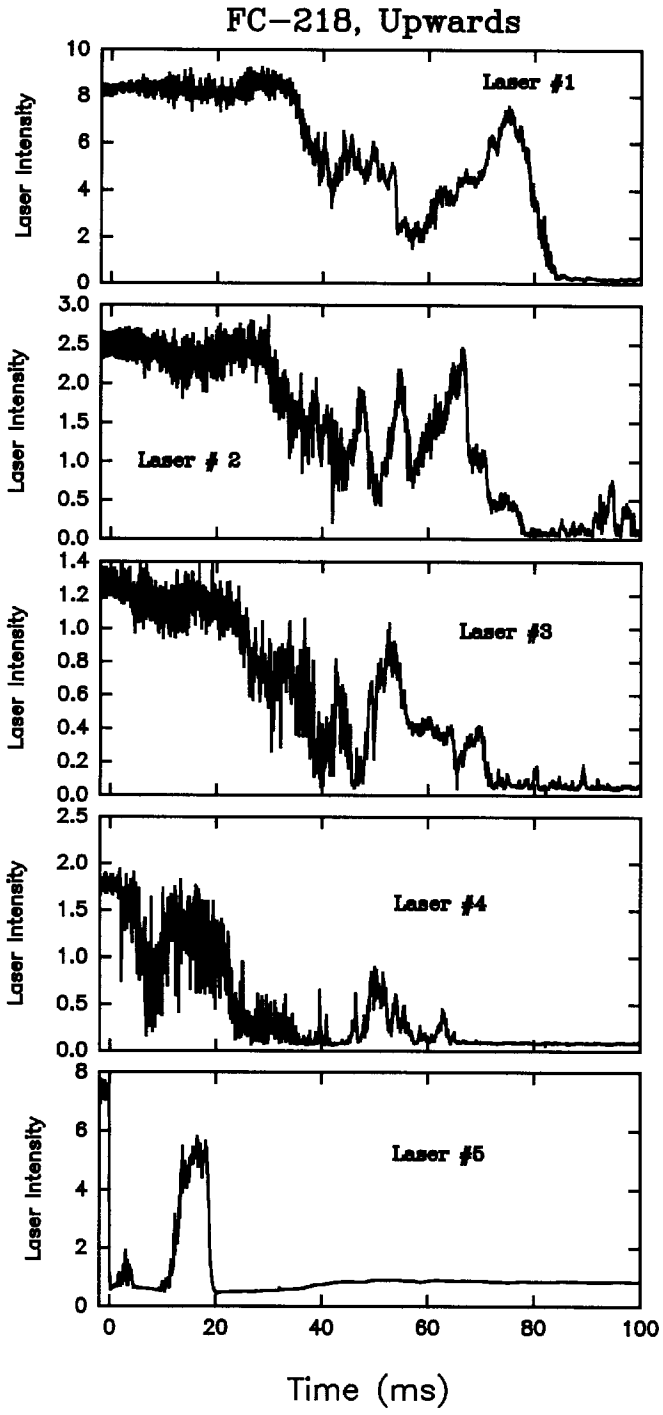

Figure 163. Short time behaviors for transmission of laser beams #5-#1 spaced as shown in Table 7 following an upward release of FC-218 at 0 s. Conditions: 461 g agent, 4.35 MPa release pressure.

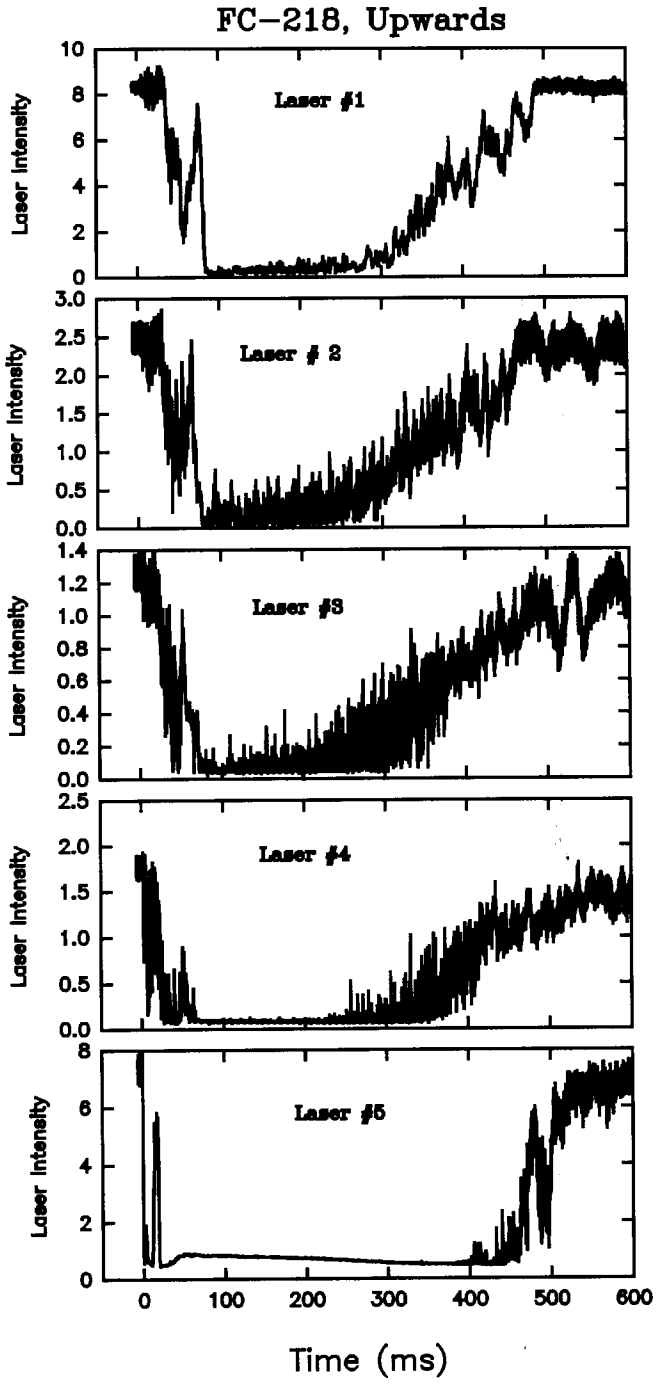

Figure 164. Long time behaviors for transmission of laser beams #5-#1 spaced as shown in Table 7 following an upward release of FC-218 at 0 s. Conditions: 461 g agent, 4.35 MPa release pressure.

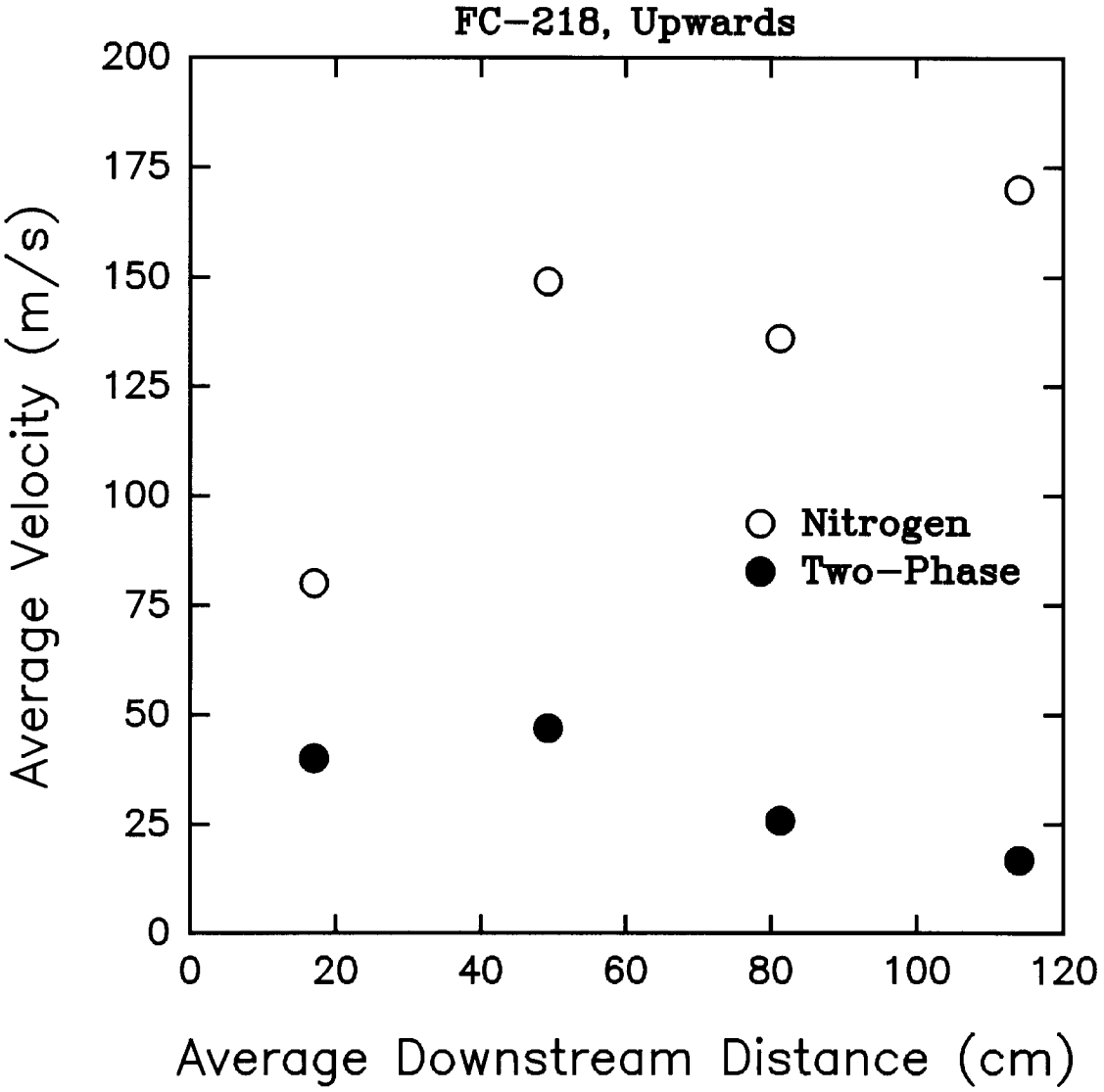

Figure 165. Average velocities for upward releases of FC-218 determined by the time of arrival at laser beams #5-#1 plotted as a function of average downstream distance. Results for arrival of nitrogen and the two-phase flow are indicated (see text).

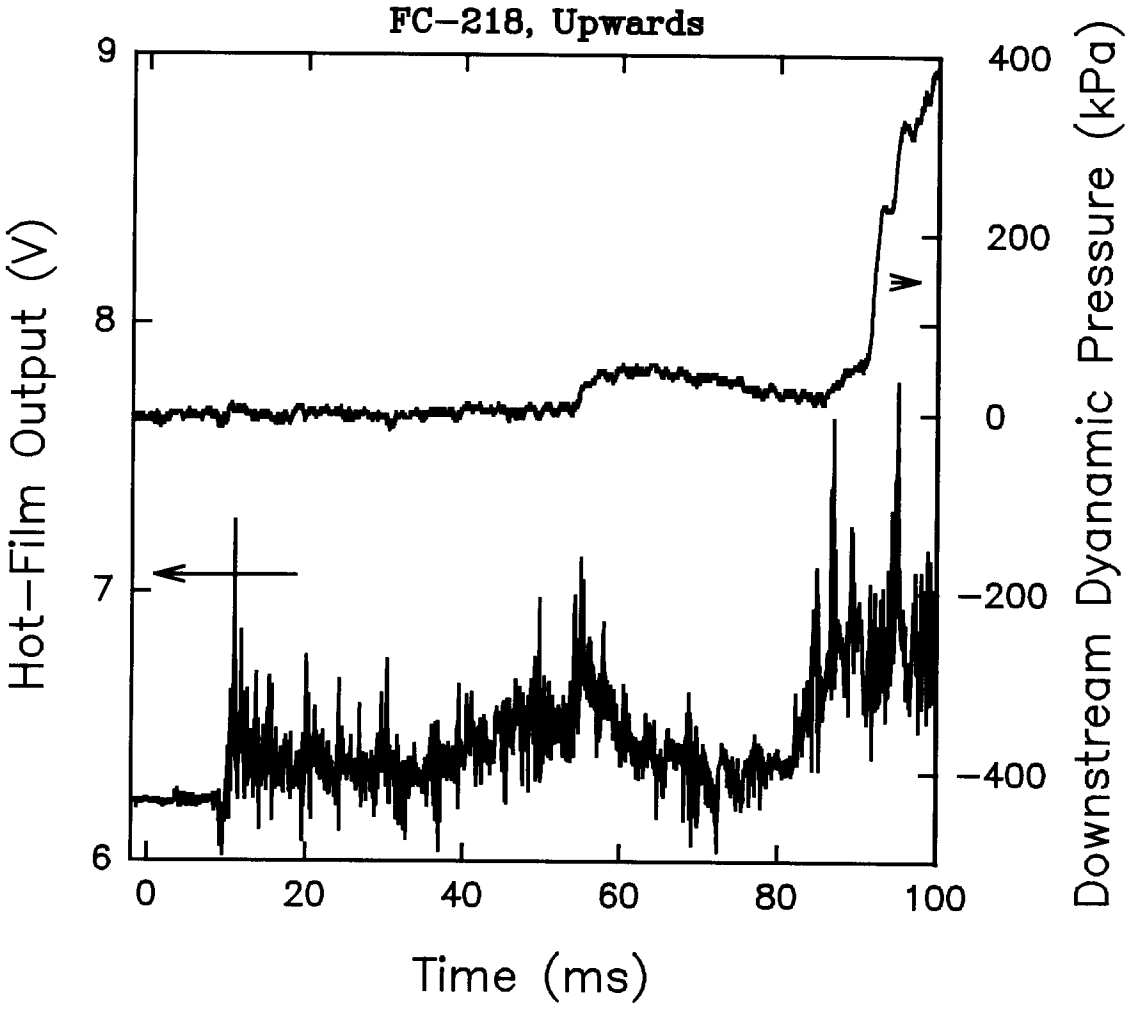

Figure 166. Voltage output of the aspirated hot-film and the dynamic pressure for probes located 1.3 m from the vessel are plotted for a short time period following an upward release of FC-218. Conditions: 461 g of agent, release pressure of 4.35 MPa.

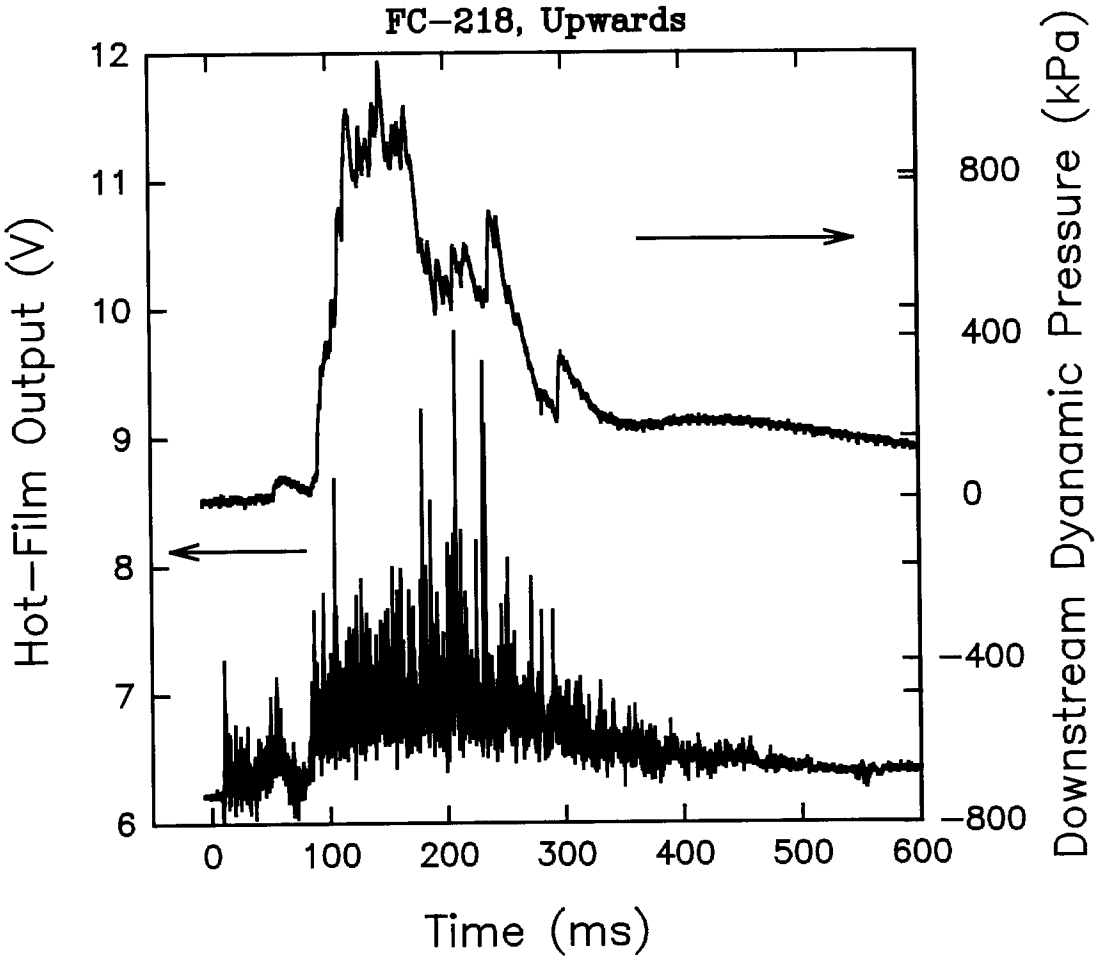

Figure 167. Voltage output of the aspirated hot-film and the dynamic pressure for probes located 1.3 m from the vessel are plotted for a long time period following an upward release of FC-218. Conditions: 461 g of agent, release pressure of 4.35 MPa.

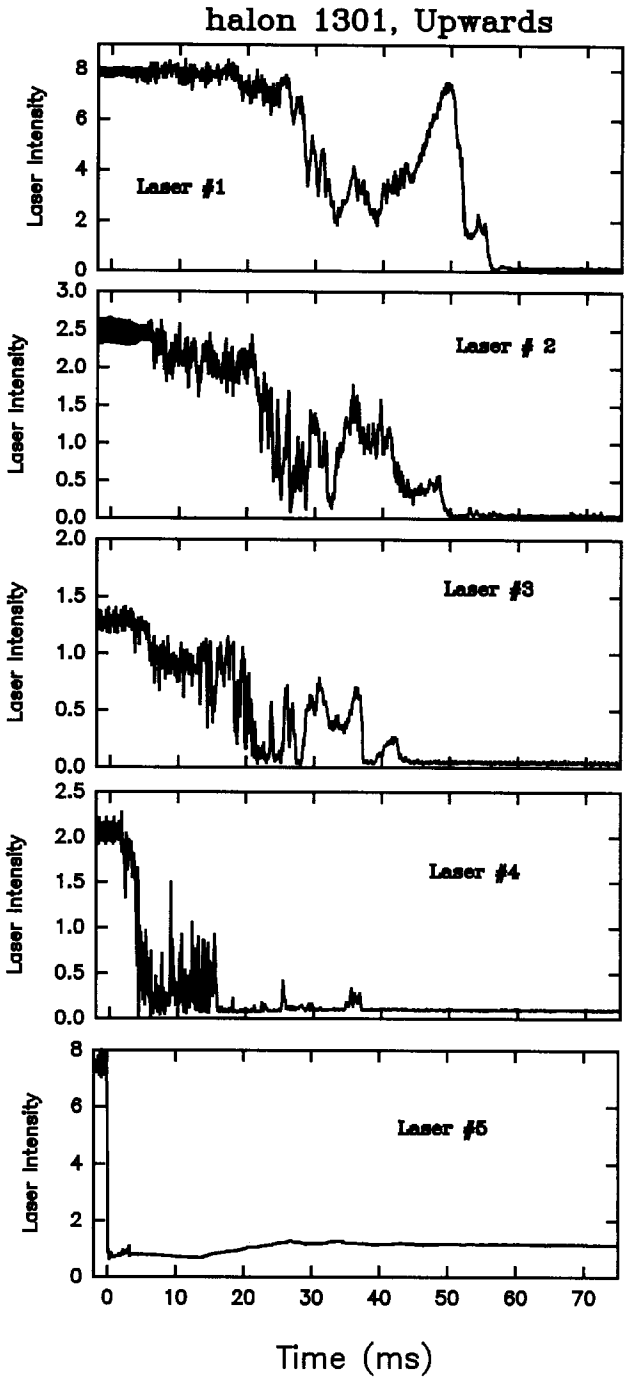

Figure 168. Short time behaviors for transmission of laser beams #5-#1 spaced as shown in Table 7 following an upward release of halon 1301 at 0 s. Conditions: 545 g agent, 4.46 MPa release pressure.

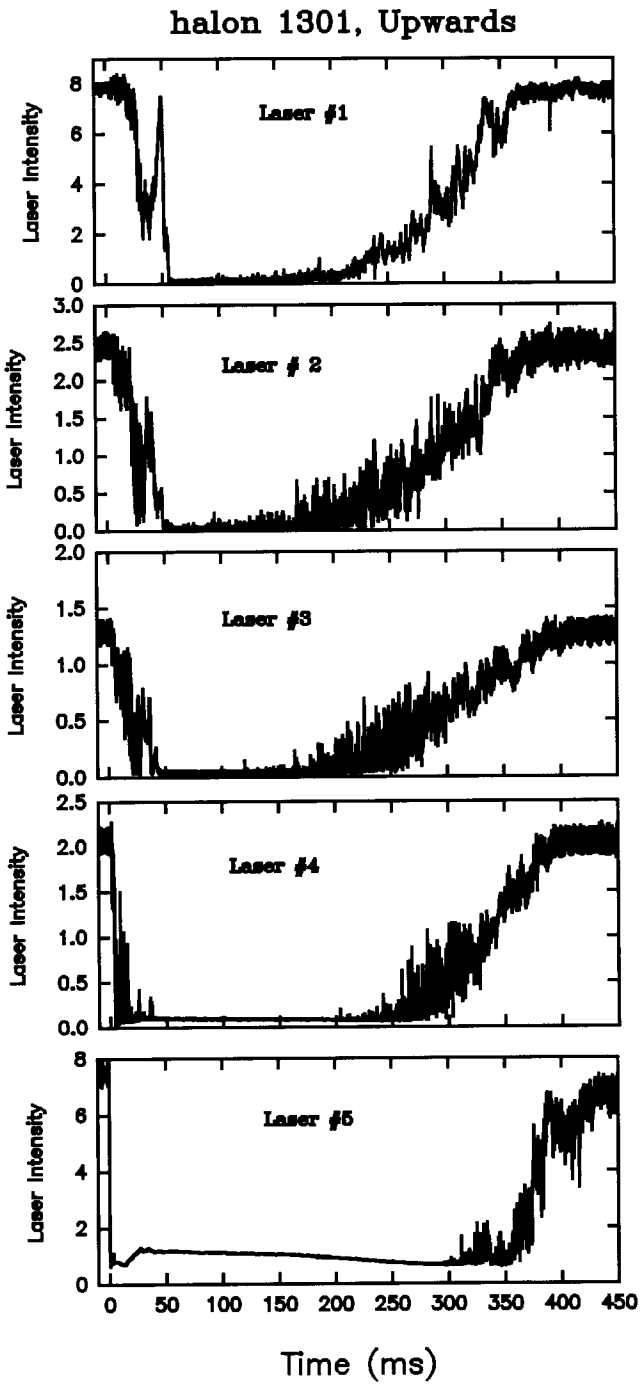

Figure 169. Long time behaviors for transmission of laser beams #5-#1 spaced as shown in Table 3 following an upward release of halon 1301 at 0 s. Conditions: 545 g agent, 4.46 MPa release pressure.

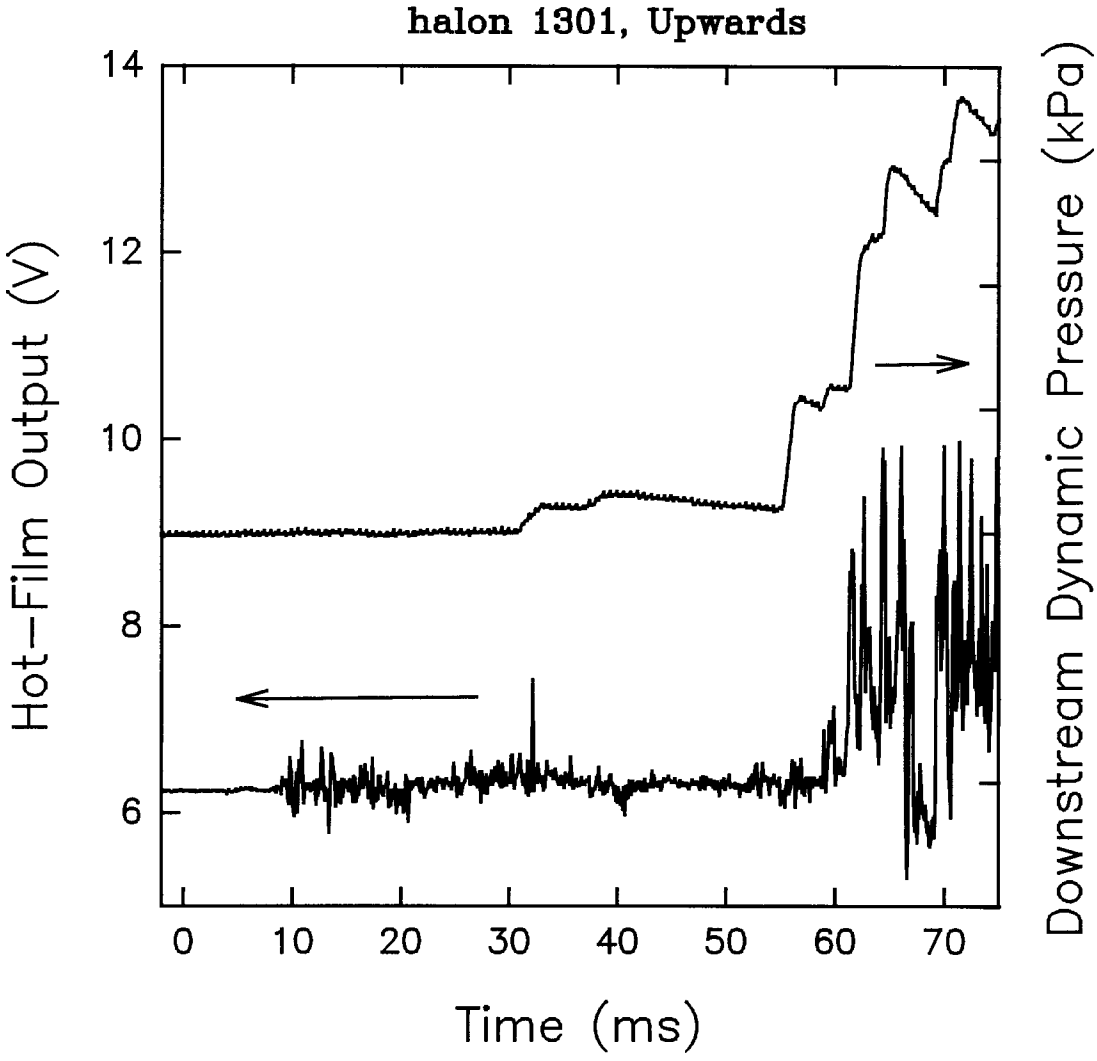

Figure 170. Voltage output of aspirated hot-film and dynamic pressure for probes located 1.3 m from the vessel are plotted for a short time period following an upward release of halon 1301. Conditions: 545 g of agent, release pressure of 4.46 MPa.

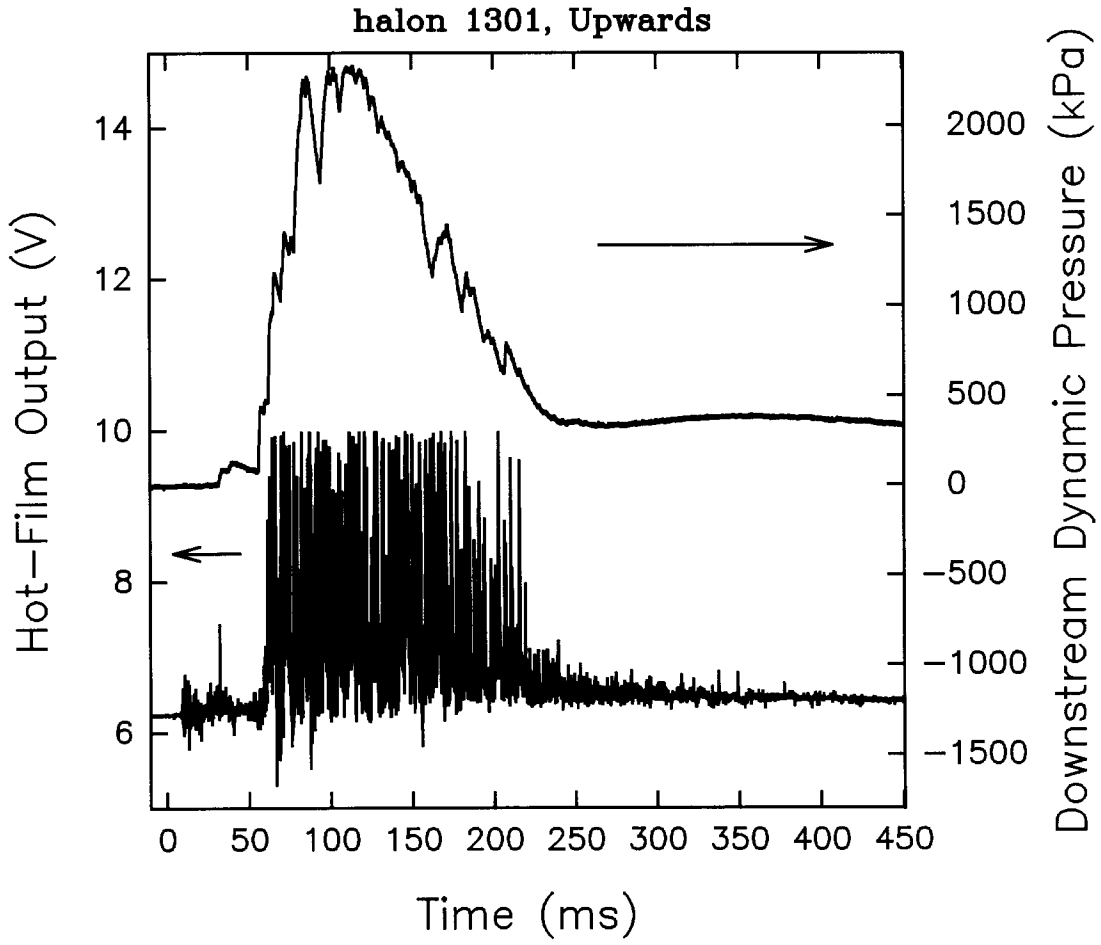

Figure 171. Voltage output of aspirated hot-film and dynamic pressure for probes located 1.3 m from the vessel are plotted for a long time period following an upward release of halon 1301. Conditions: 545 g of agent, release pressure of 4.46 MPa.

Figure 171 show that the two-phase flow from the vessel lasts until roughly 200 ms following the start of the release.

3.5.4 Discussion

3.5.4.1 Downward Release of Pressurized Superheated Liquids. The experimental findings provide a great deal of insight into the mechanisms responsible for the dispersion and vaporization of superheated liquids from pressurized bottles. To our knowledge, this investigation represents the first systematic investigation of these important physical processes which are expected to be crucial in the ability of an agent to extinguish a fire in a compartment. These findings are particularly relevant for the aircraft dry bay application. In the following we will summarize the important conclusions of the study and attempt to provide physical explanations for the observations.

The following discussion will be clearer if one considers the following figures which show calculated values of Jakob number (Figure 172) for each agent as a function of agent boiling point and the dynamic pressures (Figure 173 and Figure 174) expected for a given velocity and a range of densities chosen to span pure air to those typical of the liquid agents.

The Jakob number (*Ja*) is a dimensionless number which estimates the fraction of a superheated liquid which can be vaporized adiabatically. In other words, it is the ratio of the sensible heat within the liquid, which can be extracted from the liquid by cooling to its boiling point for the ambient pressure, and the heat of vaporization, ΔH_{vap}, for the liquid. Mathematically, it is defined as

$$Ja = \frac{\Delta h}{\Delta H_{vap}}, \tag{35}$$

where Δh is the change in enthalpy of the liquid on cooling from the ambient temperature (T_{amb}) to the boiling point of the liquid (T_{sat}) for the ambient pressure,

$$\Delta h = \int_{T_{amb}}^{T_{sat}} C_{p,l}(T)dT. \tag{36}$$

$C_{p,l}$ is the constant pressure heat capacity for the liquid which varies slightly with temperature. Values of *Ja* calculated for each of the potential replacement agents, with the exception of FC-116, and halon 1301 have been calculated. The results are plotted in Figure 172 and listed in Table 8.

In order to calculate the specific heats at a constant pressure of one atmosphere for temperatures ranging from room temperature to the liquid boiling point, the specific heat was assumed to be independent of pressure. The specific heats were fit to a second- or third-order polynomial and integrated from the boiling point to room temperature (293 K) to yield the change in internal energy. The specific heat was also fit by a spline fit technique. Results for the two approaches are included in Table 8. The two sets of calculations are in excellent agreement.

The required specific heats of HFC-227ea, HCFC-22, HFC-134a, HCFC-124, HFC-125, FC-218, FC-318, and halon 1301 were obtained from the PROZPER program (Ely and Huber, 1993). The values for FC-31-10 were estimated by the method of Tarakad, Danner, and Lee-Kesler (Daubert and Danner, 1992). The specific heat of the HFC-125/HFC-32 mixture was calculated using Rowlinson's corresponding states method (Reid *et al.*, 1987) coupled with the Genetron equation (Allied Signal, 1991) for the ideal heat capacity. Values for HFC-236fa were calculated using Rowlingson's corresponding states method and the method of Joback (Reid *et al.*, 1987). Heats of vaporization are those listed in Table 1 of Section 2.1.

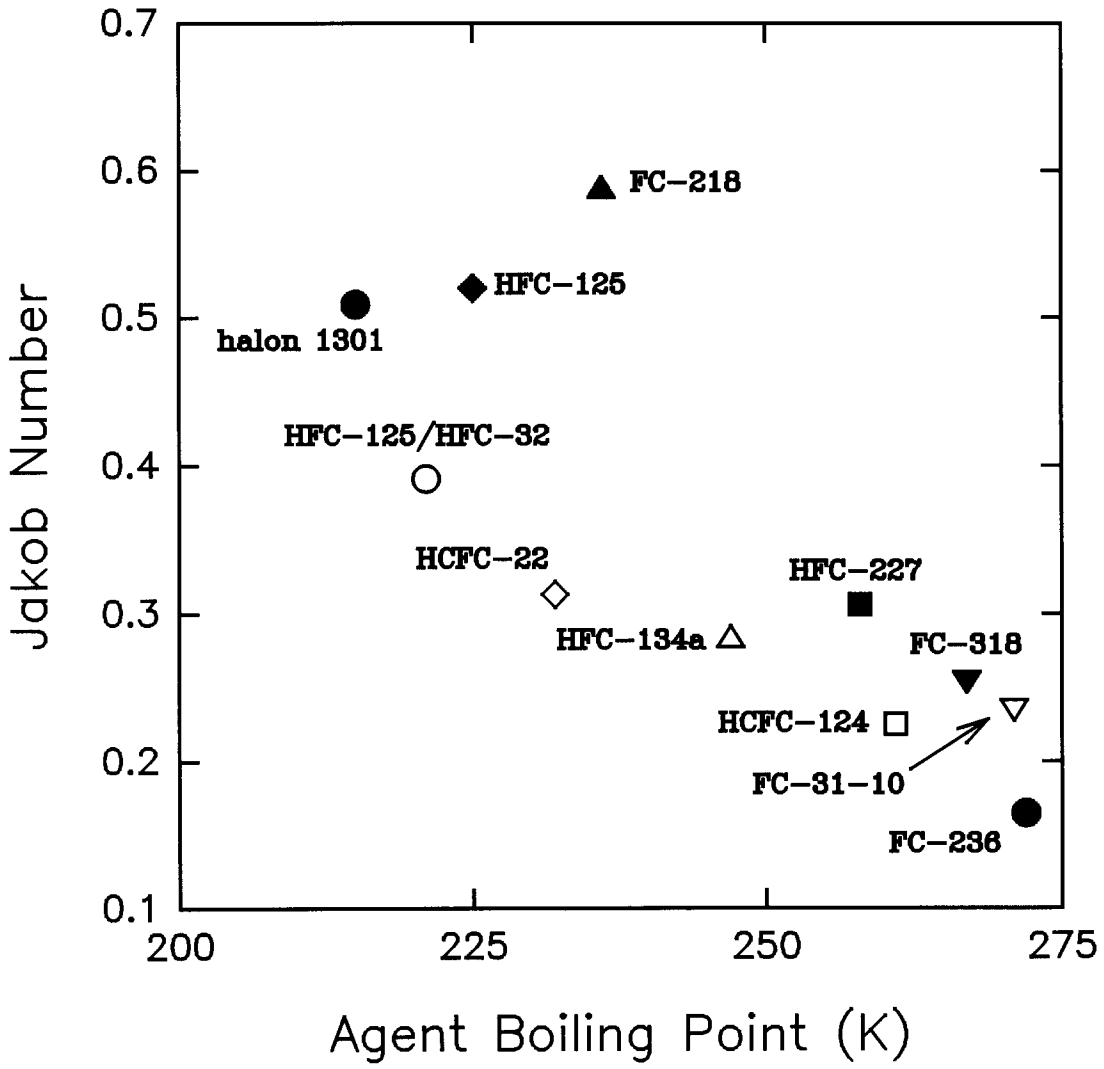

Figure 172. Values of Jakob number are plotted as a function of boiling point for each of the potential replacement agents, except FC-116, and halon 1301.

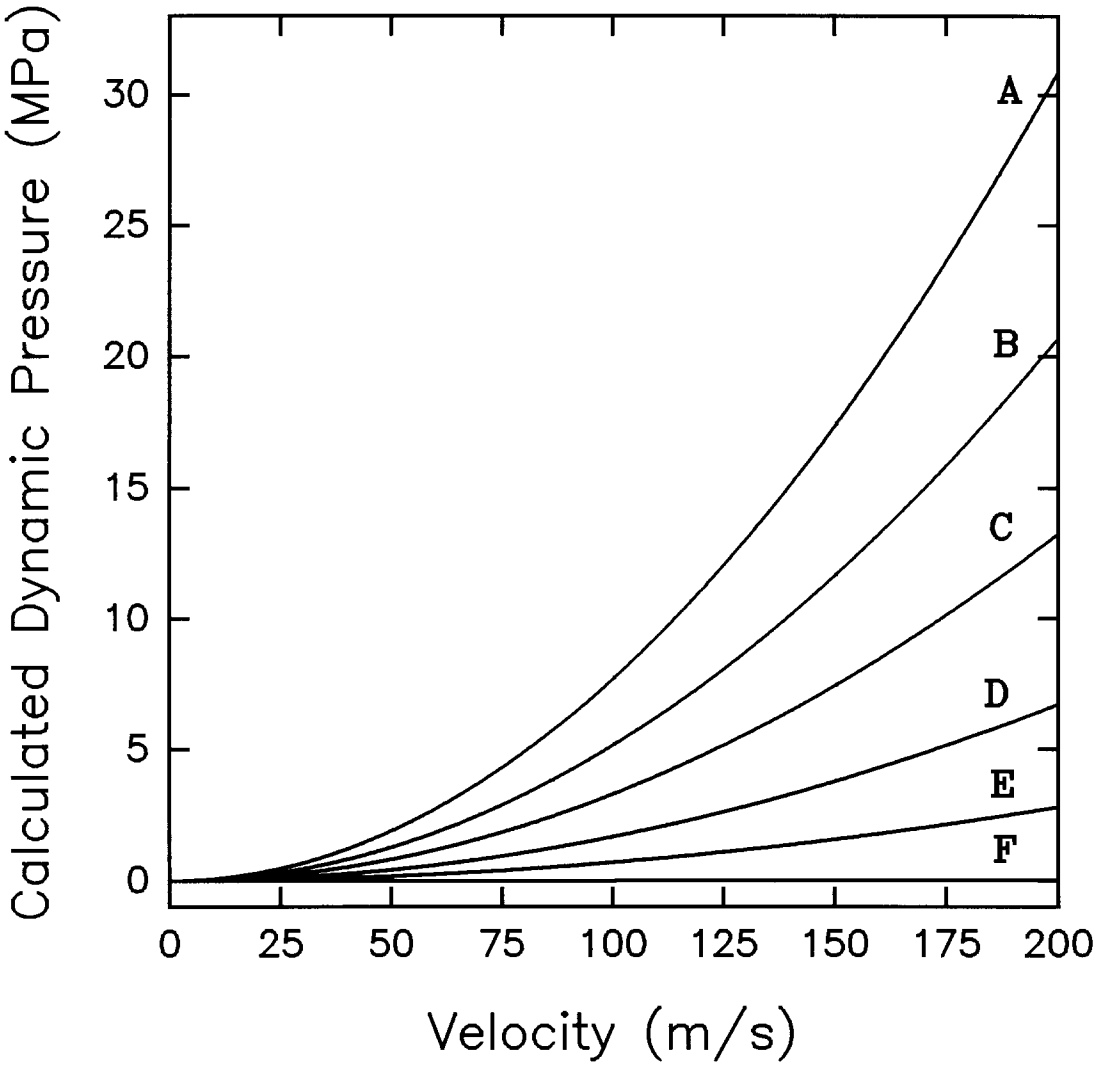

Figure 173. Calculated dynamic pressures for: A) liquid halon 1301, B) liquid HFC-125/HFC-32 mixture, C) 50% liquid/50% vapor mixture FC-218, D) 25% liquid/75% mixture FC-218, E) 10% liquid/90% gas mixture FC-218, and F) room-temperature air.

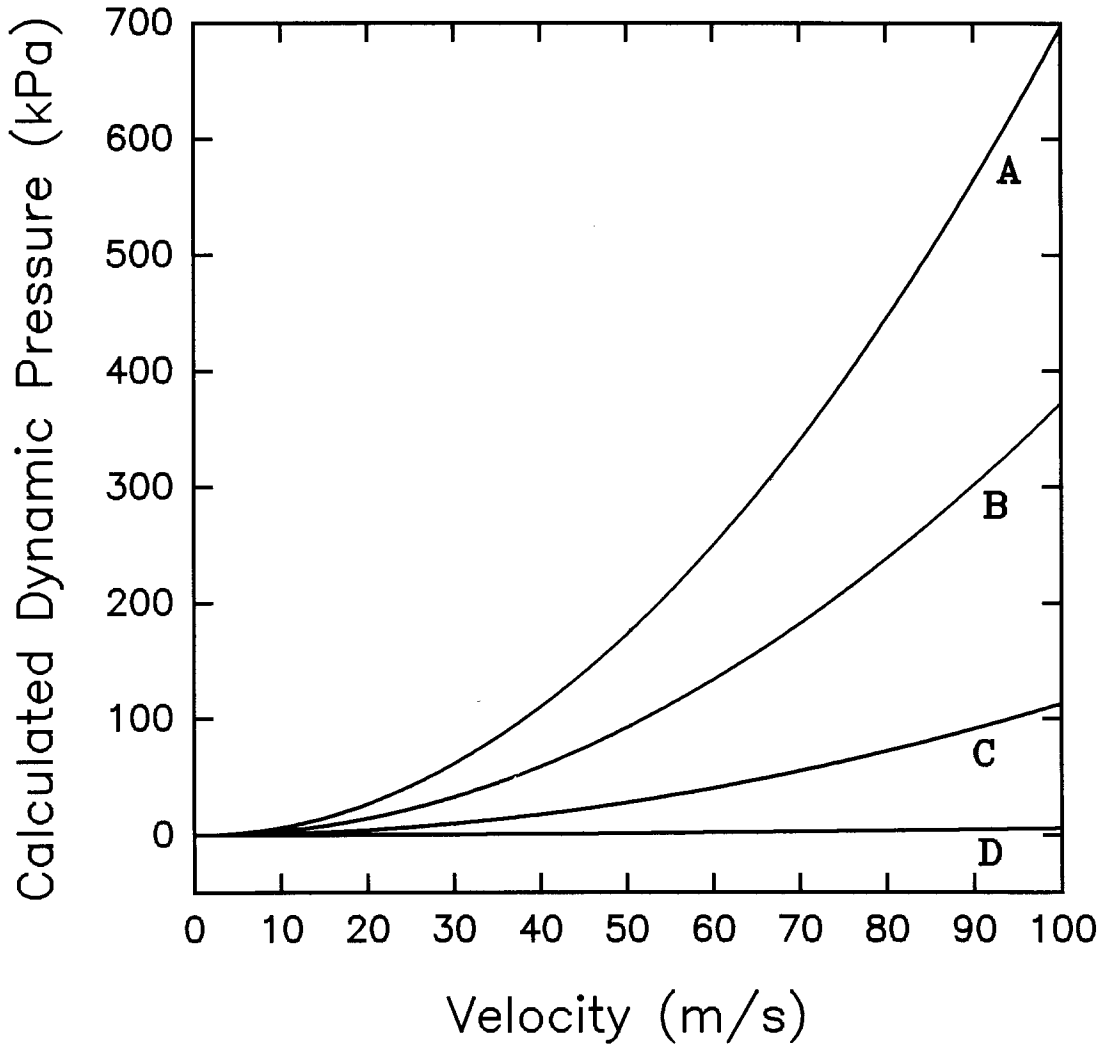

Figure 174. Calculated dynamic pressures for: A) 10% liquid/90% mixture FC-218, B) 5% liquid/95% mixture FC-218, C) 1% liquid/99% mixture FC-218, and D) room-temperature air.

Table 8. Jakob Numbers for Room Temperature (293 K) Releases of Ten Potential Replacement Agents and Halon 1301. Heat Capacity Temperature Dependencies have been Fit Using Polynomial and Spline Fits.

AGENT	*Ja* (Polynomial Fit)	*Ja* (Spline Fit)
HFC-236fa	0.165	0.165
FC-31-10	0.236	----
FC-318	0.255	0.255
HCFC-124	0.228	0.228
HFC-227ea	0.306	0.306
HFC-134a	0.283	0.283
FC-218	0.587	0.578
HCFC-22	0.313	0.313
HFC-125	0.520	0.520
HFC-125/HFC-32	0.391	0.391
halon 1301	0.509	0.509

Note that three of the agents, HFC-125, FC-218, and halon 1301, have higher *Ja* than the remaining agents. The value for the HFC-125/HFC-32 mixture is intermediate. All of the other agents have values which fall below 0.35.

During the course of this investigation dynamic pressures were recorded near the vessel exit and on the flow centerline 1.3 m from the vessel orifice. Since actual velocities or densities are not available, it is not possible to derive density or velocity information from these measurements using Equation (34). However, the magnitudes of the dynamic pressures do provide insights into the nature of the flows. This becomes clear when one considers Figure 173 and Figure 174.

Figure 173 shows the calculated dynamic pressure as a function of velocity for densities corresponding to those for liquid halon 1301 (1551 kg/m^3), liquid HFC-125/HFC-32 mixture (1040 kg/m^3), a 50% liquid/50% vapor mixture of FC-218 (665 kg/m^3) at its boiling point temperature, a 25% liquid/75% gas mixture of FC-218 (338 kg/m^3), a 10% liquid/90% gas mixture of FC-218 (141 kg/m^3), and room-temperature air (1.20 kg/m^3). The dependencies of the calculated dynamic pressures on density and velocity are clear. Note that for high velocities and densities, very large dynamic pressures are attained, while for air the pressures are relatively low for the entire velocity range.

Figure 174 is a similar plot of dynamic pressure, but the velocity and density ranges have been reduced. Results are for a 10% liquid/90% gas mixture of FC-218 (141 kg/m^3), a 5% liquid/95% gas mixture of FC-218 (75.3 kg/m^3), a 1% liquid/99% gas mixture of FC-218 (22.8 kg/m^3), and room-temperature air (1.20 kg/m^3). The effect of even a small fraction of liquid phase agent on measured dynamic pressures is obvious from this figure.

The two most dramatic events that were identified in the high-speed films of the releases were the violent mixing of agents with their surroundings observed at the initiation of a release and at times close to when the final liquid agent exits the containment vessel. These events were termed "flashings" even though it will become clear that term is most likely inappropriate for the later of these events.

The initial rapid spreading of the agent as the burst disk opens is fairly easy to explain qualitatively by considering the events when the disk opens, even though the actual behaviors are exceedingly complex to describe quantitatively. Immediately following the rupture of the disk, the liquid agent in proximity to the orifice experiences a rapid depressurization to the outside ambient pressure. At this point the liquid is not in motion. Pressure measurements in the liquid within the vessel indicate that this pressure drop is not transmitted into the vessel which means the drop must occur within the orifice. The liquid at the interface should undergo a rapid flashing. This flashing may be induced by local perturbations associated with the bursting of the disk or may even take place as a miniature boiling liquid expanding vapor explosion (BLEVE). Such processes have been discussed in Sections 3.2.4 and 3.4.3.5.

The first detectable pressure drops inside the vessel within the nitrogen occur 0.36 to 0.76 ms following the near-total attenuation of laser beam #1, with the majority requiring roughly 0.4 ms. Since pressure changes are expected to be transmitted at the speed of sound, less than 1 ms is required for pressure fluctuations to travel from the orifice to the internal pressure transducer at the top of the vessel. The observed delay is therefore attributable to the period required for the liquid to begin to accelerate through the orifice and thus drop the nitrogen pressure due to a volume increase of the ullage. The internal pressure fits discussed in Section 3.4.3.1 indicate that the liquid flow reaches a choked condition in a very short period of time.

Even though the initial flashing behavior is evident in all of the high-speed movies of the releases, it was only detected by the near-field pressure transducer for the lower boiling-point liquids. This demonstrates that shock waves are not generated by the disk bursting, and that any signals recorded by the transducer must either result from shock waves generated by liquid flashing or direct impingement of a two-phase flow on the transducer. The periods required for the near-field external pressure transducer to sense the releases varied from 1.28 to 1.84 ms. Such time delays are consistent with estimates for radial velocities listed in Table 5 based on high-speed-films measurements.

Once the pressure at the orifice is released, the liquid in the vessel begins to accelerate and flow through the orifice. The high-speed films indicate that the flows quickly form a liquid stream. Based on measurements given in Section 3.4.3.1, the flow velocities are on the order of 60 m/s.

The "flashing" near the conclusion of the release of the liquid agent is at first glance more difficult to understand. The films show a very vigorous event which appears to occur as the result of very rapid boiling of the agent. For all of the agents the near-field pressure transducer recorded sharp increases in dynamic pressure which varied from several hundred to 1600 kPa (see Figure 88 through Figure 98).

Reference to Figure 173 and Figure 174 shows that the fluid striking the pressure transducer must have high velocities and densities. Such a behavior is difficult to attribute simply to flashing of the liquid. The key is to recognize that a release of a vessel's contents is not complete once the liquid is expelled. A significant pressure of nitrogen and vaporized agent remains. These gases will now exit the vessel. The question is: How are the gases released from the vessel? The answer has already been provided in Section 3.4.3.1. The flow becomes that of a sonically choked gas flow through the orifice.

By assuming that there is only ideal-gas nitrogen in the vessel, it is straightforward to estimate a flow velocity for the gas. Assuming an initial pressure of 4.14 MPa and that the liquid fills two thirds of the vessel, the expression for the adiabatic expansion of a gas,

$$P_i V_i^{\gamma} = P_f V_f^{\gamma}, \tag{37}$$

allows the initial temperature for the gas release to be calculated. Here P and V are pressure and volume, the subscripts i and f refer to initial and final conditions, and γ is the ratio of constant pressure and constant volume heat capacities. Using the ideal gas law this becomes

$$T_f = T_i \left(\frac{P_f}{P_i}\right)^{(1-\frac{1}{\gamma})}, \tag{38}$$

where T is the temperature. For $V_i = 0.000333$ m^3 and $V_f = 0.000500$ m^3, these equations yield $P_f = 2.40$ MPa and $T_f = 251$K. With these values, it is now possible to calculate the sonic velocity using

$$U_{sonic} = \sqrt{\gamma R T_f M}, \tag{39}$$

where R is the gas constant and M is the molecular weight for the gas. Substituting in Equation (39) gives $U_{sonic} = 323$ m/s.

It is now clear that the flow leaving the vessel will accelerate dramatically once the liquid has been expelled. This rapidly expanding gas quickly catches up with the slower moving, but much denser, liquid or two-phase jet. To the gas stream, the liquid will appear much as a solid body due to its much higher density. As a result, the gas should pass around the agent flow which explains the very rapid expansion of the jet observed in the films. The nitrogen flow is also expected to interact with the liquid or two-phase flow, both fragmenting it and mixing with it. As a result of this mixing, a two-phase mixture will be generated. It is presumably such mixtures which are detected by the dynamic pressure transducer. These flows can be both high speed and relatively high density due to their two-phase character, thus explaining the very high dynamic pressures which are observed.

To our knowledge, this is the first report of such an aerodynamic mechanism for rapidly dispersing releases of liquid agents. It is unclear how significantly this process will affect the overall dynamics for the mixing of an agent with its surroundings. However, it seems likely that for short-period releases, such as those investigated here, the effects can be substantial, and that the release of high pressure nitrogen can substantially augment the mixing of a released liquid agent as the result of its own velocity and flashing behavior.

The velocities measured from the extinguishment of the laser beams provide insights into the flashing behaviors of the various agents. The measured velocities nearest the vessel exit were between 50 and 60 m/s for HFC-236fa, FC-31-10, FC-318, and HCFC-124 (see Figure 110 through Figure 113). The results for HFC-227ea (Figure 114) are only slightly higher. These velocities are consistent with the flow velocity of the liquid stream from the vessel suggesting that for these agents the liquid stream extends at least 0.32 m downstream of the orifice. These observations are also consistent with the observation of a liquid stream in the high-speed films (*e.g.*, see Figure 86).

For each of these high boiling-point agents the velocity was higher at the second measurement position indicating that flashing had begun and the flow was accelerating due to the volume expansion associated with the flashing. Assuming an average liquid flow velocity of 60 m/s, this means that the period required for these agents to flash lies somewhere between 5 and 10 ms.

As noted earlier, the measured velocities for HFC-134a (Figure 115) suggested that this agent was an intermediate case. In two experiments the highest velocities were observed between lasers #1 and #2 suggesting that flashing of the liquid jet occurred somewhere in between. One case showed the flashing taking place between lasers #2 and #3. For the two cases where flashing occurred near the vessel, the velocity then fell off with increasing distance for distances beyond laser #3. This suggests that flashing is complete and the resulting two-phase flow is slowing down as it mixes with surrounding air as would be expected for a gas jet.

The remaining low boiling-point liquids, FC-218, HCFC-22, HFC-125, the HFC-125/HFC-32 mixture, and halon 1301 all have high velocities near the vessel exit, and then slow down significantly with increasing distance. Again, this is taken to mean that the agents rapidly expand near the exit due to rapid boiling and then spread more slowly as two-phase flows entraining air. The fact that all have increased velocities near the vessel exit indicates that the time required for flashing must be significantly less than 5 ms.

Additional evidence for this conclusion is found in the near-field pressure traces for FC-218, HCFC-22, HFC-125, the HFC-125/HFC-32 mixture, and halon 1301 (Figure 94 through Figure 98). These traces show that dynamic pressures are recorded not only at the start and end of a release, but during the release. This can only be the case if the fluid leaving the vessel is flashing over a very short flow distance. This flashing generates the two-phase flows necessary for the observed pressure increases. The pressure increases for the intermediate times are strongest for the HFC-125/HFC-32 mixture and halon 1301 consistent with their low boiling points. A very rapid expansion of halon 1301 is also consistent with the rapid spreading of this flow which can be seen in Figure 87.

The general trends observed for the flashing times are consistent with those discussed by Day (1969) and Lienhard and Day (1970). The times decrease with increasing superheat which is directly related to the difference in pressure between the ambient and saturated values. Using Equations (31)-(32), it is possible to derive the following expression for the flashing time,

$$t_d = 2.12X10^{13}(P_v - P_{amb})^{-7/2} D^{-2} \sigma^3 \sqrt{\rho_f} \tag{40}$$

This equation has been tested for those agents for which surface tension value estimates were available from Daubert and Danner (1992). Other values for the variables in Equation (40) are taken from Table 1 of Section 2. Table 9 lists the values of surface tension used along with calculated values of t_d.

It is clear that Equation (40) vastly underestimates the times required for the liquid streams to flash. At the present time we are unable to provide an explanation for this failure. On the basis of this finding, it is concluded that the prediction of flashing lengths for these agents is currently not possible.

The discussion thus far has shown how flashing of the agents leads to enhanced mixing of the two-phase flow with its surroundings. It is clear that the amount of superheating is crucial to the speed and violence of this flashing. As noted earlier, it is also necessary for the agents to be vaporized in order to be effective. The downstream dynamic pressure measurements and hot-film response provide insights here.

All of the high boiling-point agents show similar behaviors. When the agent first reaches the pressure transducer there is a rapid jump in the pressure. Following this jump the pressure continues to increase for a period roughly equal to the time required for release of the liquid agent from the containment vessel. This observation suggests that velocity measured from the propagation of the downstream edge of the release should provide a good estimate for the entire release period.

For HFC-236fa, FC-31-10, FC-318, HCFC-124, and HFC-227ea these velocities were on the order of 70 m/s. The maximum dynamic pressures observed for these agents were in range of 800 to

Table 9. Values of Time Required for Flashing of Superheated Liquid Streams Calculated Using Equation (40)

Agent	Surface Tension (N/m)	Calculated t_d (s)
FC-31-10	0.0153	4.0×10^{-6}
FC-318	0.0117	8.5×10^{-7}
HFC-134a	0.0230	2.7×10^{-8}
FC-218	0.0159	1.3×10^{-8}
HCFC-22	0.0184	1.1×10^{-8}
HFC-125	0.0171	3.3×10^{-8}
halon 1301	0.0156	2.1×10^{-9}

1600 kPa with a typical value being 1200 kPa. Using Equation (34), the density necessary to generate such a pressure rise is on the order of 430 kg/m^3. The densities of these liquids range from 1356 to 1499 kg/m^3. This suggests that roughly 30% of the mass for these agents reaching the 1.3 m downstream position on the centerline of the flow is not vaporized. As discussed in the experimental section, the aspirated hot-film responses were consistent with the presence of two-phase flows at this downstream location for all of the releases.

The HFC-134a results are somewhat different. The laser measurements (Figure 115) indicate the velocity for this flow at the 1.3 m position is on the order of 50 m/s, but the dynamic pressures observed were on the order of 2000 kPa yielding a density of roughly 1600 kg/m^3. This estimate is higher than the original density of the liquid which is 1209 kg/m^3. This suggests that this agent is only slightly evaporated over the flow distance and its velocity must be somewhat higher than estimated. It is difficult to understand this finding given the behavior of the other agents. However, the experimental results were repeatable.

The results for the low boiling-point liquids varied dramatically from agent to agent. When FC-218 reached the pressure transducer there was a fairly rapid increase in dynamic pressure to values on the order of 100 to 200 kPa (Figure 127). Figure 116 indicates the flow velocities are on the order of 40 m/s. This suggests that the local density is roughly 125-250 kg/m^3. Since the liquid density is 1321 kg/m^3, this suggests that 10-20% of the agent is present as liquid (also see Figure 173 and Figure 174).

For HFC-125 the dynamic pressures recorded when the agent first reached the pressure transducer (Figure 129) were very low, being less than 10 kPa. Measured velocities (Figure 118) were on the order of 18 m/s. This indicates that the flow density was less than 60 kg/m^3. Based on the liquid density for HFC-125 (1190 kg/m^3), this suggests that much less than 5% of the flow is in the liquid state.

The results for halon 1301 were variable. One of the releases (B in Figure 131) gave no measurable pressure increase when the agent first arrived. The pressure eventually began to rise slowly after 20 ms and then increased at the end of the release to almost 400 kPa. The hot-film response (Figure 135) indicates that two-phase flow is associated with the large pressure rise. Flow velocities are on the order of 30 m/s (Figure 120). These observations suggest that the flow initially

arrives nearly fully vaporized, but that near the end of the release the flow density increased to roughly 900 kg/m^3. This observation is difficult to understand until one realizes that the large dynamic pressure increase is likely associated with the flow generated by the release of nitrogen from the vessel. Flow velocities are expected to be much higher for this case. It seems likely that the high pressure results from a high-speed flow of nitrogen, which has entrained some two-phase halon 1301, striking the pressure transducer. Recall it was concluded that a two-phase mixture of halon 1301 is released from the vessel near the end of the liquid release due to flashing within the nozzle or vessel (see Section 3.4.3.1). The high-speed nitrogen flow would be likely to entrain the resulting two-phase flow.

The results for FC-218, HFC-125, and halon 1301 indicate that most of the liquid agent is vaporized over the 1.3 m flow length. This is in sharp contrast to HCFC-22 where very high dynamic pressures are generated during most of the time the agent flow is striking the transducer (Figure 128). Maximum dynamic pressures were on the order of 2000 kPa. Using an average velocity of 40 m/s (Figure 117), these pressures yield calculated densities on the order of 2500 kg/m^3 which can be compared to a liquid density of 1192 kg/m^3. This is another case where the flow velocity estimate must be low. However, it seems clear that a large fraction of the agent arrives in the liquid state at the 1.3 m location.

The HFC-125/HFC-32 mixture also generated complicated dynamic pressure time dependencies (Figure 130). When the agent first reached the transducer there were pressure increases on the order of several hundred kPa. Using an estimate for the flow velocity of 30 m/s from Figure 119, this yields densities on the order of 700 kg/m^3 or roughly 60% liquid. The aspirated hot-film response (Figure 137) for this agent also indicated the presence of a strong two-phase flow. Near the end of the releases there were strong pressure increases which are likely associated with an increase in flow velocity, perhaps as a result of the nitrogen release.

The conclusions from the above discussion can be summarized as:

- The high boiling-point agents generate flows which consist of roughly 30% liquid on the centerline at 1.3 m from the vessel.
- FC-218, HFC-125, and halon 1301 produce flows which have most of the agent ($> 90\%$) in the gas state.
- HCFC-22 and the HFC-125/HFC-32 mixture yield pressure traces which suggest that a large fraction of their mass is still liquid at the measurement location.

It is impossible to provide a detailed description of the physical processes which are occurring during the mixing following a high pressure release of a superheated liquid due to the complex and interactive nature of the physical processes which are taking place. Flashing generates a two-phase flow at some unknown position which has unknown velocity, temperature, and droplet size distributions. This two-phase flow then begins to entrain room-temperature air. For temperatures near 295 K, the entrained air will also introduce heat into the flow which can evaporate additional liquid. The short duration of the flows further complicates attempts to understand the behavior since flow development is likely to last for a large fraction of the total flow time. As an example, the impulsively started flow should immediately interact directly with room temperature air. However, as the flow develops, the flow volume will contain more and more agent and air will enter only from outer regions of the flow. As a result, the amount of agent which is vaporized as a function of downstream distance is expected to vary with time. This may explain some of the time dependencies observed in the downstream dynamic pressure measurements.

The lack of detailed measurements also makes a complete understanding impossible. Most of the downstream measurements are only valid for the centerline of the flow and the fraction of two-phase flow is only estimated for two locations. No information is available concerning the radial structure of the flow.

Despite the limitations of the measurements, it is possible to draw some general conclusions concerning the evaporation of the agents. The measurements suggest that the high boiling-point agents are only roughly 70% vaporized at the 1.3 m downstream position. Referring to Figure 172 it can be seen that these six agents, including HFC-134a, are clumped together at the lower right-hand side of the plot of *Ja* versus agent boiling point. The *Ja* numbers are all 0.3 or less indicating that the superheating of these agents is sufficient to vaporize only a small fraction of the agent. In order for the remainder of the agent to be vaporized, additional heat must be absorbed from the surroundings. The fact that these agents reach the pressure transducer as two-phase flows indicates that insufficient heat is available to fully vaporize the agents. Since it was estimated that roughly 30% of the agent flows was liquid at the transducer, this suggests that sufficient air was entrained to vaporize half of the remaining liquid.

It should be pointed out that the actual dynamic pressure which is measured will be a complicated function of flashing behavior and the degree of vaporization. This is due to the different dependencies of the dynamic pressure on density and velocity (see Equation (34)). Flashing of an agent increases its velocity and decreases it density due to the accompanying volume expansion. As a result, it is possible to either increase or decrease the measured dynamic pressure. This effect may explain the high densities calculated for some of the flows such HFC-134a.

Based on this discussion, it is now possible to gain some insight into the vaporization behaviors of the low boiling-point liquids. The three liquids which seemed to be nearly fully vaporized were FC-218, HFC-125, and halon 1301. Figure 172 shows that these three liquids have the highest *Ja* numbers of any of the agents tested. In each case, the agent can provide over 50% of the heat required for full evaporation. They also have quite high superheats, and, as a result, they tend to flash strongly near the vessel exit. The resulting two-phase flow has a relatively long distance over which to entrain air. The wide dispersion of the agent due to flashing also aids in the evaporation process. Apparently, sufficient air is entrained into these flows to provide the heat necessary to complete the evaporation for these agents.

HCFC-22 is an interesting case. Even though its boiling point is lower than that for FC-218, its *Ja* is only slightly more than 0.3. As a result, flashing vaporizes considerably less of the fluid than for the low boiling-point liquids just discussed. Another peculiarity of this agent is that for constant fill level in the vessel (generally 3.33×10^{-4} m^3), significantly higher number of moles of this agent are released during the same liquid flow period (4.6 moles versus 2.3, 3.3, and 3.6 for FC-218, HFC-125, and halon 1301, respectively). This means the amount of expansion and acceleration of the liquid will be higher for a given percentage of vaporization. This expansion will tend to shield the liquid from entrained air and may well contribute to a slower rate of agent evaporation. The combination of low *Ja* and high number of moles most likely accounts for the very high downstream dynamic pressures observed for this agent (see Figure 128).

The same arguments provide an explanation for the two-phase character of the HFC-125/HFC-32 mixture which was observed. Its *Ja* number is intermediate between that of halon 1301 and HCFC-22. The liquid itself only provides 40% of the heat necessary to vaporize all of the liquid. In addition, this agent provides, by far, more moles of agent (5.2 moles) than any other for a release from the 2/3 full vessel. Again, the degree of expansion and acceleration associated with this large number of moles is likely to limit the entrainment of air and complete vaporization of this agent.

On the basis of the mixing results, three parameters have been identified which control the degree of vaporization of an agent. These are the amount of superheat, Jakob number, and the number of moles contained in the liquid release. Efficient evaporation is favored by high superheat, high *Ja*, and a low number of moles of fluid in the vessel.

3.5.4.2 Effects of Orifice Diameter on Mixing and Evaporation. The orifice size affects the dynamic pressure measurements in the near field, the dispersion velocities, and the degree of evaporation at the far stream position. For FC-31-10 the maximum dynamic pressure associated with the release of the nitrogen using the 12.7 mm opening was roughly the same as for the 19.1 mm opening, while the 6.4 mm opening generated no pressure increase. For FC-218 and halon 1301 the intermediate size orifice yielded lower maximum overpressures, but also provided indications that flashing was taking place over much of the liquid release periods. Such an indication of continual flashing for the largest nozzle was not observed for FC-218. For both of the low boiling-point liquids no near-field pressure increases were observed when the smallest orifice was used.

These dynamic pressure results can be understood in terms of the expected flashing behavior of the agents and the effects of the released nitrogen. Due to the low superheat of the FC-31-10, this agent never flashes in the near field. The pressure rise detected for the 12.7 mm orifice is the result of high-speed nitrogen striking the slower moving liquid. For the smaller orifice, no pressure rise is detected due to the reduced mass flow of both the liquid and the nitrogen gas. The flow simply does not expand sufficiently to reach the pressure transducer.

The most interesting observation for the FC-218 was the flashing of the liquid for flow through the 12.7 mm opening, which was not observed when the 19.1 mm opening was used. This is likely due to a reduction in the flashing time for the smaller orifice which caused the flashing to occur nearer the nozzle with the result that two-phase flow struck the transducer. Such a behavior is consistent with the dependence of flashing time on liquid stream diameter reported by Lienhard and Day (1970). The reduction of the maximum dynamic pressure associated with the release of nitrogen on going from the 19.1 to 12.7 mm orifices and the absence of a pressure rise for the 6.4 mm orifice are explained by the reduction in mass flows of the liquid and nitrogen as discussed above for FC-31-10. The near-field pressure behaviors for halon 1301 are consistent with the conclusions for FC-218.

The average velocity measurements with downstream position shown in Figure 139 through Figure 141 indicate that, in general, the velocities nearest the vessel increase as the orifice size is decreased and that those at the farthest downstream position decrease. These higher velocities are consistent with the liquid flashing earlier and more strongly near the vessel when the liquid stream diameter is reduced as predicted by Lienhard and Day (1970). Due to the smaller diameters and lower mass flows of the liquid jet through the smaller orifices, the two-phase flows will mix with air and spread faster over shorter distances in a manner similar to turbulent axisymmetric jets (see Richards and Pitts (1993) and references therein). As a result of air entrainment they slow down as observed experimentally.

The measurements of downstream dynamic pressure and aspirated hot-film response confirm the above conclusions. Due to the low superheat of FC-31-10 it reached the 1.3 m downstream position as a two-phase flow for releases through both the 19.1 mm and 12.7 mm orifices. However, due to the shorter flow distance required for the entrainment of a sufficient mass of air to evaporate the agent, the 6.4 mm orifice release reached these detectors as a gas-phase flow. The FC-218 seems to be fully vaporized for each of the orifice sizes. Interestingly, halon 1301 showed (Figure 144) two-phase character near the end of the release when the intermediate orifice size was used. This was also the case for the 19.1 mm orifice. The smallest orifice yields single-phase flow due to the more efficient entrainment of air as can be seen in Figure 145.

3.5.4.3 Effects of Vessel Pressurization Level on Mixing and Evaporation. The effects of vessel pressurization are only available for FC-218. The near-field dynamic pressure traces are qualitatively similar when using nominal 5.51 MPa, 4.14 MPa, and 2.76 MPa burst disks. No pressure rise is observed until very near the time when liquid is completely expelled from the vessel.

In each case the pressure rise is attributed to the collision of high-speed nitrogen with the liquid stream. The actual magnitudes of the dynamic pressure increases are difficult to interpret physically due to the complex interactions involved.

The average flow velocities observed for the FC-218 as a function of downstream distance were very similar for overpressures of 6.21 MPa and 4.28 MPa (Figure 148). This suggests that the flashing behavior is similar for these two flows and that the velocities resulting from the flashing are dominating the flow behavior. On the other hand, the velocities were lower at each station for a release at the lowest pressure (2.61 MPa). It would appear that the significantly lower liquid velocities near the vessel exit in this case resulted in significantly slower mixing.

3.5.4.4 Effects of an Extension Tube on Mixing and Evaporation. The addition of a 0.5 m extension tube on the vessel had very little effect on the release behavior of the agents, but it significantly modified the mixing behavior. Figure 149 through Figure 151 show that measured velocities at the two locations furthest from the vessel exit were much higher when the tube was in place than when no tube was used for FC-31-10, FC-218, and halon 1301. These observation can be easily understood if one makes the reasonable assumption that each of these liquids flashed somewhere within the tube due to a reduction in pressure. The flashing liquids must expand. For a free expansion, the gas is free to expand in all directions. However, for the liquids in a tube the expansion is constrained to occur only along the tube direction. Much as for a bullet constrained within the barrel of a rifle, the mass of the fluid is highly accelerated down the tube. For flashing liquids with high *Ja* number, the accelerations are quite dramatic indeed. Velocities approaching 200 m/s were observed.

The dynamic pressures measured 1.3 m from the vessel opening were extremely high for each of the fluids (Figure 152 through Figure 154), and, in the case of halon 1301, approached 3 MPa. Even assuming very high velocities, this suggests that a significant amount of the liquid was unevaporated. The measured responses of the aspirated hot-films support this conclusion. To our knowledge, the extremely high velocities and overpressures generated by using a tube to dispense superheated fire-fighting agents have not been previously documented.

3.5.4.5 Effects of Agent Cooling on Mixing and Evaporation. Cooling of the agents has a very large effect on the dispersion and evaporation of the released liquid. FC-31-10 has a boiling point close to room temperature and, as a result, does not flash or evaporate rapidly. At the 1.3 downstream measurement position, the flow generated by a room temperature release of this agent has a large percentage of the agent in the liquid phase. Cooling will slow down the mixing and evaporation and increase the liquid fraction of the two-phase flow. In fact, very nearly 100% of the agent is expected to arrive at the 1.3 m position as liquid.

The effects of cooling FC-218 are considerably more dramatic than for FC-31-10. A room temperature release of FC-218 flashes very close to the vessel exit rapidly evaporating and dispersing the agent. By the time the agent reaches the 1.3 m downstream position the flow has entrained sufficient air to essentially evaporate all of the released agent. Upon cooling to a temperature of 228 K, which is below its boiling point of 236 K, these advantages of FC-218 for mixing disappear. Flashing no longer takes place and the agent reaches the downstream location mostly as a liquid flow. It should be noted that for these tests the agent entered room temperature air. If the ambient environment was also cooled, the liquid would not be expected to vaporize at all, and the release would be a liquid stream which would eventually pool somewhere within the space.

3.5.4.6 Effects of Release Orientation on Mixing and Evaporation The effects of releasing the agents upwards instead of downward are dramatic. The observations are easily understood in

terms of the changes in release behavior which were observed inside the vessel (see Section 3.4.3.6). It was noted that for downward releases the nitrogen acts on the liquid inside the vessel much as a pressure applied to a piston. It pushes the liquid rapidly from the vessel where it subsequently flashes if the liquid at the vessel temperature is superheated. The behavior for upward releases is completely different. Since the nitrogen is now at the top of the vessel next to the orifice, it is immediately released from the vessel upon the opening of the burst disk. The pressure within the vessel drops very rapidly to close to that of the ambient surroundings. There is no force to drive the liquid agent from the vessel. If the pressure in the vessel falls below the ambient saturation pressure of the agent, the agent will begin to boil, ultimately filling the vessel with a two-phase mixture. As the pressure rises due to expanding bubbles, this two-phase mixture is expelled from the vessel.

The measurements of nitrogen velocity shown in Figure 159 and Figure 165 show that downstream velocities are on the order of 175 m/s. These high velocities are due to the very large velocities (estimated to be on the order of 300 m/s) expected for choked flows of nitrogen through the 19.1 mm orifice. There is very little agent vapor in the nitrogen and the fraction of the total agent mass released initially is quite small. The very small laser attenuations (Figure 158, Figure 163, and Figure 168) observed downstream of the vessel when the nitrogen flows arrived are consistent with this conclusion.

Once the nitrogen was expelled from the vessel, delay times were observed before the liquid agent began to flow. For FC-31-10 this delay time was 24 ms and for FC-218 it was 19 ms. It was not possible to measure a time accurately for the halon 1301 release, but the behavior of laser #4 in Figure 168 suggests a value on the order of 16 ms. These initial releases of agent are attributed to the expulsion of condensed vapor above the liquid as the superheated liquids in the vessel begin to boil following depressurization. The decreasing delay times observed with increasing superheat are consistent with the behaviors expected for flashing of superheated liquids (see the discussion in Section 3.5.1). It is interesting that the observed delay times are significantly longer than those estimated for streams of liquid outside of the vessel, which were much less than 5 ms for the two low boiling-point liquids.

The initiation of boiling does result in the release of some agent from the vessel. However, the laser beam attenuation, downstream dynamic pressure, and aspirated hot-film measurements all indicated the mass of the agents released during these release periods were fairly low. Only when the two-phase mixture fully filled the vessel did significant agent begin to leave the bottle. These times were estimated as 54, 39, and 30 ms for FC-31-10, FC-218, and halon 1301, respectively. For FC-31-10 the time before significant mass of agent was released during an upward release was longer than required for the complete downward release of this agent. Even for the lower boiling-point agents the times required for release of a significant mass of the agents were quite long for upward releases as compared to downward releases.

The change in release mechanism for upward releases as compared to downward releases also has significant effects on the mixing and evaporation behavior of the agents. The results shown in Figure 159 and Figure 165 show that both of the two-phase flows have velocities which are significantly lower than observed for downward releases. As a result, much longer times are required for an agent to reach the 1.3 m downstream distance. Even though the two-phase flows are moving more slowly and therefore provide longer times for evaporation, the very high dynamic pressures and aspirated hot-film responses measured indicate that much of the agent mass is still liquid. Estimates of densities for FC-31-10 and FC-218 based on the measured velocities and dynamic pressures are significantly higher than the densities of the pure liquid agents. This suggests that velocities later during the flow period are somewhat higher than estimated based on the leading edge measurements. This does not contradict the conclusion that the flows must consist of large fractions of unevaporated liquid. For the low boiling-point liquids this result is completely the opposite to that for downward

releases, where it was observed the FC-218 and halon 1301 were nearly fully vaporized over this distance.

The change in evaporation behavior can be understood in terms of the release mechanism. The pressure necessary to expel the liquid from the vessel is generated by boiling of the liquid at a pressure close to atmospheric. As a result, the temperature of the liquid drops to levels close to it boiling point. The gas-liquid mixture leaving the vessel is expected to have a similar temperature. No additional flashing will occur to evaporate liquid. The only way that additional vaporization can occur is through entrainment of room temperature air into the flow with subsequent heat transfer to the agent mixture. The downward releases demonstrated that insufficient air is entrained to vaporize a large fraction of the agent.

The times required for complete release of the agents estimated from the laser beam attenuation measurements, 800 ms for FC-31-10, 500 ms for FC-218, and 250 ms for halon 1301, are consistent with estimates based on measurements within the vessel. (see Section 3.4.3.6).

These results demonstrate how detrimental the effects of changing the release direction of a pressurized agent from a downward to upward orientation can be on the time required for the start of the release, the release rate, the effectiveness of agent dispersion, and the degree of evaporation. It should be noted that while no tests were performed using cooled agents, it is extremely likely that essentially no agent would be expelled from the vessel by an upward release of one of these agents cooled below it boiling point.

3.5.5 Summary and Agent Ranking. The primary purpose of the work described in this section was to allow the proposed halon-alternative agents to be ranked with regard to their dispersion behaviors and evaporation rates following release from pressurized bottles. It has been argued that fire extinguishment capability is enhanced by efficient dispersion and mixing and rapid evaporation. The measurement techniques developed during the study provide sufficient data to allow the proposed alternative agents to be ranked based on these criteria.

It is significant that the current fire extinguishing agent, halon 1301, was found to be efficiently dispersed following release from a pressurized vessel at room temperature as the result of the rapid and strong flashing of the superheated liquid. Rapid vaporization was also observed due to its high Jakob number and relatively low number of moles per unit volume of the liquid. During the course of this investigation a workshop was held with a selected group of representatives of manufacturers (Walter Kidde Aerospace, Pacific Scientific, and Systron Donner) of fire-extinguishment systems for aircraft in an effort to obtain practitioners' viewpoints on desirable dispersion, mixing, and evaporation behaviors for alternative agents. Their conclusion was that the replacement agent's physical properties should resemble as nearly as possible those for halon 1301. This conclusion is consistent with our own, which is based on our understanding of the fire extinguishment process.

The experimental findings show that agents which are relatively high boiling--FC-236fa, FC-31-10, FC-318, HCFC-124, HFC-227ea, and HFC-134a--have dispersion, mixing, and evaporation properties following downward release which are not well suited for rapid fire extinguishment. This results from their relatively high-boiling points and low Jakob numbers. In the case of the lower boiling alternative agents--FC-218, HCFC-22, HFC-125, and the HFC-125/HFC-32 mixture--important differences were observed. HCFC-22 and the HFC-125/HFC-32 mixture were shown to have strong flashing behaviors due to their low boiling points, but also were found to vaporize relatively slowly due their low Jakob numbers and relatively high number of moles per unit volume of liquid. As a result, their mixing and vaporization behaviors are quite different than observed for halon 1301. On the other hand, FC-218 and HFC-125 were found to mix very efficiently by flashing and to vaporize rapidly since they have higher Jakob numbers and fewer moles per unit volume of the liquid than HCFC-22 and the mixture.

Table 10. Relative ranking of ten alternative agents based on dispersion, mixing, and evaporation behavior. Note that FC-116 has not been included since it is a critical fluid at room temperature.

Agent	Relative Ranking
FC-218	1
HFC-125	1
HFC-125/HFC-32 Mixture	3
HCFC-22	4
HFC-134a	5
HFC-227ea	6
HCFC-124	7
FC-318	8
FC-31-10	9
FC-236fa	10

On the basis of the above discussion it is possible to rank the alternative agents based on their dispersion, mixing, and evaporation behaviors as shown in Table 10. Boiling point alone has been used to rate agents having boiling points which are higher than FC-218. Note that FC-116 is not included in the table. This is because this agent is not a liquid at room temperature.

This investigation has yielded a number of findings which provide an improved understanding of the physical processes which are responsible for the dispersion, mixing, and evaporation behaviors of the agents and may be useful for the engineering design of practical fire extinguishment systems.

The importance of the boiling point, Jakob number, and number of moles of agent per unit volume of liquid for determining the behaviors during downward releases have already been discussed. To our knowledge, this is the first time that these parameters have been identified as the controlling physical properties for short-period releases of pressurized agents. Also for the first time, it has been shown that the release of the nitrogen pressurization gas following expulsion of an liquid agent from the vessel interacts strongly with the agent flow and provides an additional mechanism for dispersion and mixing of the agent. This mechanism is expected to be important for releases having very short periods.

The effects of variations in a variety of system parameters on the mixing behavior have been characterized. Modifications in dispersion and evaporation behaviors with changes in the pressurization level of the vessel and diameter of the vessel orifice for downward releases can be understood in terms of the understanding of these processes obtained during the current investigation. Higher vessel pressurization of the agents results in more rapid discharges of the liquids from the containment vessel and, therefore, more rapid mixing. The higher pressures of nitrogen present result in more intense mixing when the high-speed nitrogen exits the vessel following depletion of the liquid.

Changes in the mixing and evaporation behavior with orifice diameter result from a number of dependencies. Use of smaller diameters significantly reduces the mass flow rate of the liquids. As a result, the mixing times are increased. Reduction of the orifice diameter also reduces the time required for the liquid flow to flash. In some cases, this effect improves mixing even though the total release time has been increased. The known mixing behavior for gaseous axisymmetric jets indicates that downstream mixing behavior scales with jet diameter. For this reason, flows through smaller orifices mix over much shorter flow distances than flows from larger orifices. Keep in mind that this apparent advantage is offset by the reduced agent mass-flow rate.

The effects of adding an extension tube to the vessel are dramatic. When flashing occurs within the tube very high exit velocities are observed. The resulting two-phase flows are capable of generating quite high dynamic pressures. Even for the low boiling liquids, mixing and evaporation are inhibited in this configuration.

The system parameter which has been found to have the most profound effect on the mixing and evaporation behavior is the liquid temperature. This is a direct result of the dominant role of the degree of superheating on the flashing and evaporation. It is interesting that the role of agent temperature has been characterized as being underappreciated with regard to testing of halon 1301 dispersion in nacelles (Chamberlain, 1970). The current investigation has considered the effects of cooling the agent. Particularly for FC-218, the dispersion and evaporation were drastically degraded by cooling below the boiling point. It is likely that cooling drastically reduces the effectiveness of an agent for suppression of nacelle or dry bay fires.

As an example of the possible effects which might result from cooling, Figure 175 shows the calculated Jakob number for superheated FC-218 liquid for a range of liquid temperatures at atmospheric pressure. It is clear that Ja decreases rapidly with temperature. Most measurements for this investigation were for 294 K for which Ja $\approx$ 0.6. A decrease in temperature of less than 30 K results in a decrease of the Ja number to 0.3. This value is similar to those the high boiling liquids at room temperature which were found to vaporize very slowly. Clearly, relatively minor cooling will result is dramatic variations in flashing and evaporation behavior.

Effects of heating the liquid agent were not considered during this work. However, dramatic changes, which might aid or hinder fire-fighting effectiveness are to be anticipated.

The significance of these findings for designing fire extinguishment systems for aircraft are discussed further in Section 3.7.

Another parameter which significantly changes the mixing and evaporation behavior is the vessel orientation. In general, highly effective dispersion and evaporation is only observed for an orientation where the nitrogen pressurization gas is located such that the agent is expelled from the vessel as a liquid driven by the gas pressure. If an orientation allows the pressurization gas to exit the vessel before the liquid, the release rate is substantially reduced. Due to the slower release rates, mixing is less effective. Furthermore, in these cases the agent is generally expelled as a two-phase flow which does not flash on exiting the vessel. A significant mechanism for mixing and rapid evaporation is thus eliminated.

3.6 Transient Spray Computations

3.6.1 Introduction. Over the past three decades, an increasing acceptance of and reliance upon numerical solutions for transient fluid flow problems have taken place. In many cases, experimental studies are prohibitively expensive, whereas high-speed computers are comparatively economical and allow a wide range of parameters to be examined in a short time. As a result, computational fluid

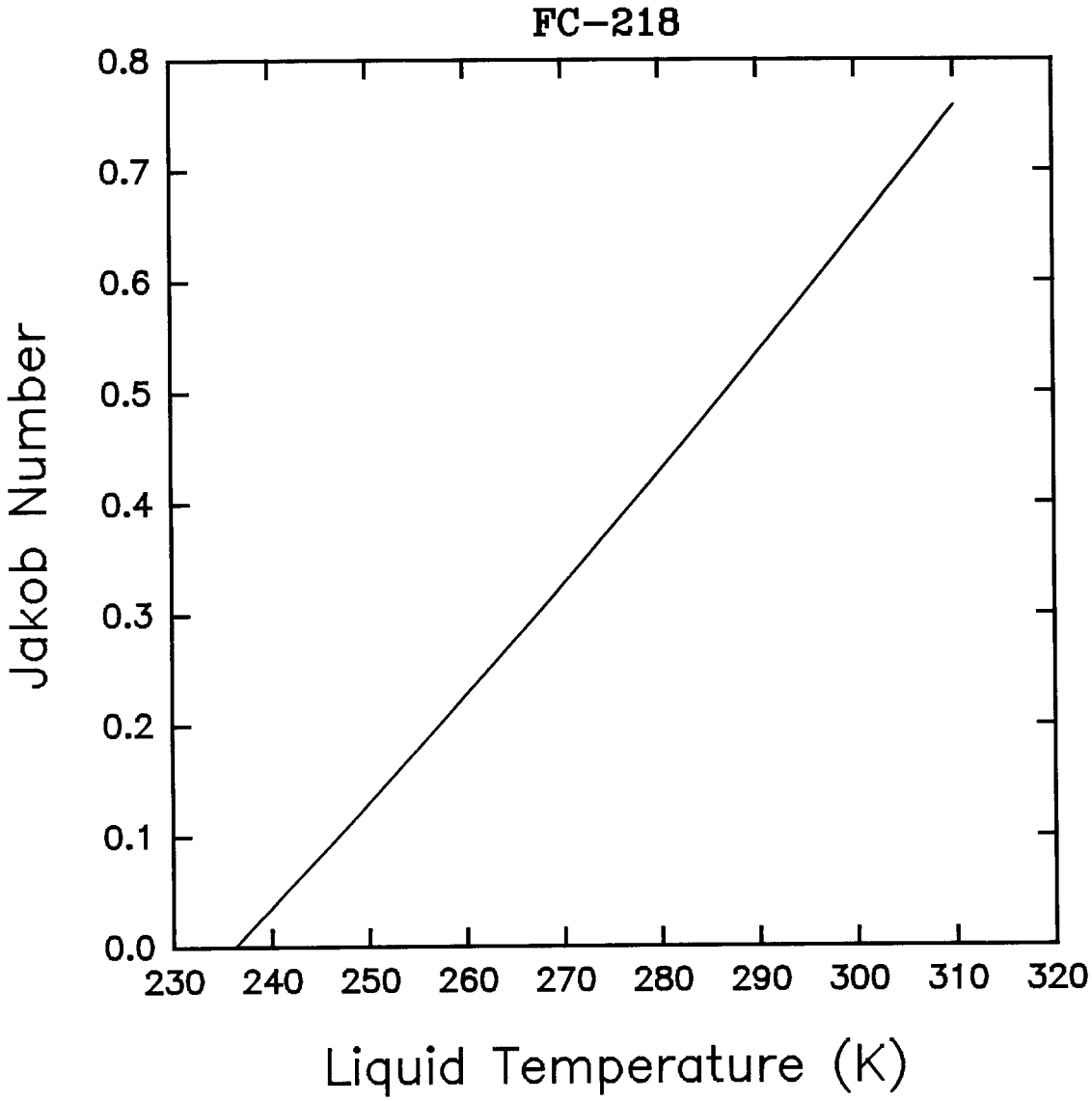

Figure 175. Calculated values of Jakob number for releases of FC-218 as a function of liquid temperature over a range of 310 to 235 K.

dynamics (CFD) has become a powerful tool for both basic and design studies in a broad range of physics and engineering problems. CFD refers mainly to the use of computers for numerically solving the nonlinear equations governing fluid motion. Pioneering work in this field first employed hand computations to demonstrate that nonlinear equations of fluid motion could be solved numerically. Computers have automated, improved, and dramatically sped up what was first done by hand.

The basic CFD equations express the balances of mass, momentum and energy of a fluid, and can be solved analytically for only a limited number of simplified situations. The success of CFD is often based on innovative numerical algorithms which discretize either the full set of equations or some simplified set derived from them, forming a large but finite number of algebraic or ordinary differential equations which can be solved by computers (Oran, 1988). The fundamental idea in CFD is that spatial dimensions are divided into discrete contiguous cells, usually called finite volumes or finite elements, and time is discretized in short intervals called timesteps. This discretization is forced by conventional computers having finite-sized memories segmented into floating-point words of data. The numerically determined values of the fluid variables in each cell are advanced from one timestep to the next using the nearby fluid variables determined at the previous timestep. While such marching techniques are developed with time-dependent problems in mind, they are also used to find steady-state solutions when appropriate.

The number of possible CFD algorithms is enormous and the correct choice depends on many properties of the problem being solved and the computer resources available. In all cases, however, only a finite number of discrete values comprise the representation, and each value is only specified to finite precision. This means that information is inevitably lost in the computational solution relative to the continuous problem being approximated. The result is uncertainty and errors in the computation arising from the discretization. The source of the uncertainty is the missing information about the detailed solution structure within the discrete spatial cells and timesteps. All approaches which use a finite number of values to represent a continuous profile have this problem. Nowadays, computers with hundreds of millions of high-precision floating-point calculations per second are readily available, and this translates into computations which can simulate some real fluid flows more accurately than can be validated by modern experimental diagnostic techniques. Three-dimensional simulations with several million cells are possible giving spatial resolution on the order of 1% of the size of the physical system. Two-dimensional solutions, where they are appropriate, can provide even higher spatial resolution.

In this section preliminary efforts to extend the use of existing CFD codes for the computation of the flows generated by the release of halon 1301 and alternative agents are summarized. Also included is an approach for predicting the initial conditions for the two-phase flow generated by the release of superheated liquids into an ambient environment.

3.6.2 Numerical Simulation of Discharge Sprays

3.6.2.1 Models Considered and General Capabilities. The fundamental CFD problem for an extinguishing agent discharge and dispersion is to develop the capability of qualitatively and quantitatively predicting the time evolution of the agent concentration field. It inherently involves a multidimensional analysis of a one- or two-phase, multi-component, compressible medium where thermodynamic effects and transport phenomena are important. This, in turn, imposes even more stringent requirements on the numerical algorithms used and computational times.

The dispersion of sprays of halon and halon-alternative fire extinguishing agents throughout a protected space is a very complex process involving many physical phenomena occurring simultaneously and affecting each other. The agent stored in the liquid state is discharged from nitrogen-pressurized vessels through a simple, nozzle/orifice-like exit. The systems under consideration

involve vessel volumes of the order of 10^{-3} m^3, with required discharge times of the order of 10^{-2} s. To achieve such rapid discharge times, the initial pressurization levels must typically be of the order of several megapascals. As the liquid agent exits from the vessel, thermodynamic and fluid-dynamic instabilities lead to flashing and break the agent into a two-phase droplet/gaseous jet mixture. This occurs in a short transition region which starts at the vessel exit and ends where thermodynamic and fluid-dynamic equilibrium has been achieved. If the temperature of the discharged liquid agent is far above its normal boiling point, the liquid very quickly evaporates and creates a cloud of agent vapors surrounding the moving spray with remaining liquid having a temperature equal to its boiling point. In the transition region the spray consists of a flowing mixture of liquid-agent fragments of various shapes and sizes and gaseous agent. This flow then entrains initially-quiescent air from the surrounding environment.

Downstream of the transition region the flow begins to develop as a mixed, two-phase, agent/air jet where thermodynamic equilibrium is maintained and where droplet collision and agglomeration do not play an important role in the ensuing jet dynamics and in the dispersal of the agent throughout the protected space. The entrainment, mixing and evaporation continue as the spray is dispersed throughout the space.

For advanced multi-dimensional mathematical models describing complex transient flow problems, numerical methods solving sets of nonlinear partial differential equations as well as relevant computer codes have been developed at the Los Alamos National Laboratory. Two of these codes--CONCHAS-SPRAY (Cloutman *et al.*, 1982) and KIVA-II (Amsden *et al.*, 1985a,b,c; 1987; 1989)--have been considered during the present study. The reader is referred to the cited references for complete details concerning these models.

CONCHAS-SPRAY was the first computer code developed at Los Alamos National Laboratory to solve the equations of transient, multi-component, dissipative, chemically reactive fluid dynamics, together with those for the dynamics of an evaporating liquid spray. It was a descendant of an earlier experimental code called CONCHAS (Butler *et al.*, 1979), which did not include the spray modeling capability. The code is quite general, but has been designed with applications to internal combustion engines specifically in mind. The formulation is spatially two-dimensional, which requires that the dependent variables depend on only two of the three spatial coordinates because of symmetry. The option is provided to select either rectangular or cylindrical coordinates, corresponding to linear or axial symmetry, respectively. All the transport coefficients such as dynamic viscosity, heat conductivity and mass diffusivity as well as heat capacities are assumed to be temperature dependent. The effects of turbulence are represented by an optional subgrid scale (SGS) turbulence model (Deardorff, 1971). This model was found to be very useful for parabolic flows which occur in, as an example, jet flows (*e.g.*, Gmurczyk *et al.*, 1992). The code allows a Lagrangian, Eulerian, or mixed description, and is particularly useful for representing curved or moving boundary surfaces.

Evaporating liquid sprays are represented by a discrete-particle technique (Dukowicz, 1980), in which each computational particle represents a number of similar physical particles. The radius and other attributes of a particle are statistically assigned using a Monte Carlo sampling technique. The evaporation rate is obtained from a quasi-steady model (Dukowicz, 1979). The particles and fluid interact by exchanging mass, momentum and energy. These interactions are treated by implicit coupling procedures to avoid the prohibitively small time steps that would otherwise often be necessary. The spray is assumed to be thin, as defined by O'Rourke (1981).

KIVA-II (a descendent of KIVA) is one of the latest in a sequence of multidimensional numerical models (Amsden *et al.*, 1985a,b,c; 1987; 1989) designed to solve the dynamics of evaporating fuel sprays interacting with flowing multicomponent gases undergoing mixing and heat transfer in a manner similar to CONCHAS-SPRAY, but extended into full three-dimensional situations, including droplet break-up/coalescence phenomena. Turbulence modeling is more sophisticated than in

CONCHAS-SPRAY. A standard k-ϵ model (Amsden *et al.*, 1989; Launder and Spaulding, 1972) extended to variable density flows is used to simulate turbulence effects in the calculations. Transport equations for the turbulence kinetic energy and turbulence dissipation rate are solved with appropriate source terms for the spray interaction.

The spray model is fundamentally based and, as such, has broad applicability. The dynamics of the atomized fuel spray are handled by a Monte Carlo based discrete-particle technique (Dukowicz, 1980). The spray is considered to be composed of discrete computational particles, each of which represents a group of droplets of similar physical properties. The distribution functions for droplet size, velocity, and spray pattern produced by the fuel injector are statistically sampled and the resulting Lagrangian parcels are followed as they locally interact and exchange mass, momentum, and energy with the surrounding gas. The model accounts for turbulence effects and interactions between droplets (O'Rourke, 1981) but other dense spray effects are neglected. When a computational parcel is selected to be injected into the flow field, its size is determined by sampling from a chi-squared distribution function (Bracco, 1985). The masses of the injected parcels are constant, thereby permitting each parcel to represent a different number of actual droplets depending on its size. The influence of droplet collisions on the spatial variation of the droplet mean size is taken into account by a sampling procedure. Collision frequency is then calculated and used to determine the probability that a droplet in a given parcel undergoes a collision with a droplet in a nearby parcel. All droplets in the given parcel behave in the same manner; either they do or do not collide and no new computational parcels are created. However, if a collision occurs and the resulting parcel has more than twice the original injection mass of the parcel, it is broken into two identical parcels with half the number of droplets as the original. Trajectories of these two parcels subsequently diverge because of their different interactions with the local turbulence field.

3.6.2.2 Calculational Approach and Code Modification. As a first step in the development of codes capable of modeling releases of halon 1301 and alternative agents, it was decided to focus on the use of CONCHAS-SPRAY. The two-dimensional axisymmetric variant of the generalized model was adapted as a subset of the KIVA-II code to accommodate the needs of the specific problem under consideration. The set of time-dependent equations is expressed in a two-dimensional form since the experimental discharges were designed to be axisymmetric. It should be noted, however, that the experiments discussed earlier in Section 3 were in a large rectangular room, while those which were modeled are for much smaller closed volumes. The choice to model a smaller closed volume was dictated by practical computational time limitations.

CONCHAS-SPRAY consists of a set of 26 primary subroutines controlled by a short main program. In addition to the primary subroutines there are thirteen supporting subroutines that perform tasks for the primaries. For various applications, all required geometrical specifications, initial and boundary conditions may be specified using input data alone. In other cases where the input data is inadequate to define the problem of interest, the required specifications must be inserted directly into the appropriate subroutines. The modular structure of the program enables such modifications.

The CONCHAS-SPRAY code was used almost as received from Los Alamos. However, the evaporation routine was judged to be inadequate. As a result, the following expression for the agent equilibrium vapor pressure, $P_a(T_l)$, at liquid temperature T_l suggested by Daubert and Danner (1992),

$$P_a(T_l) = \exp\left(A+\frac{B}{T_l}+C\ln T_l+DT_l^E\right), \tag{41}$$

was incorporated into the expression for the mass fraction of agent vapor, Y_l^*, at the droplet surface,

$$Y_l^* = M_a\left[\frac{PM_{air}}{P_a(T_l)} + M_a - M_{air}\right]^{-1}. \quad (42)$$

where M_{air} and M_a are the molecular weights for air and agent, respectively, and P is the total pressure in the gas. A, B, C, D, and E are empirical constants chosen to fit the temperature variation of a given agent. When the vapor pressure data of HCFC-22 were modeled, CONCHAS-SPRAY was unable to compute beyond the first timestep because the liquid vapor pressure exceeded 101 kPa for a temperature corresponding to the boiling point of HCFC-22. A different set of coefficients was chosen in subsequent calculations to maintain a vapor pressure below the ambient. Rather than a flashing spray, the results are more applicable to an evaporating spray. Special attention to this issue will be required to properly model the flashing process which was experienced by many of the agents in the experimental discharges.

Several other minor modifications to the code were necessary to ensure numerical stability. For instance, strong temperature and pressure gradients were generated by the rapid evaporation of the liquid that prevented convergence of the calculations. This type of numerical instability was removed by the introduction of a viscous pressure (Thompson, 1972), which was added to individual pressures within a computational cell and also to the pressure-volume work term appearing in the energy equation. Following these modifications, it was found that stable calculations could be carried out.

The situation investigated was the discharge of a hypothetical liquid agent through an orifice located on the centerline of a 0.42 m diameter cylindrically shaped volume. Agent inflow boundary conditions were derived from the results of the discharge vessel experiments (see Section 3.4), in which the agent mass flow rate was measured. The initial pressure was 101 kPa, and the liquid was assumed to be a mono-sized spray at a temperature of -41 °C. Computational parcels representing the droplets were introduced at the injector with an axial velocity of 61.4 m/s directed at an angle of 0° relative to the symmetry axis. The corresponding mass flow rate was 21.2 kg/s. A zero azimuthal component of velocity was assumed for the droplets at the injector. All of the gas and liquid parameters were taken as uniform across the orifice exit. The air in the compartment was specified to be quiescent and uniform in temperature at time equals zero. The surrounding walls were treated as solid, free-slip boundaries maintained at a constant temperature of 21 °C. The subsequent penetration and shape of the spray resulted solely from the interactions of the liquid droplets with the ambient air.

A zero-order model of the transitional region between the nozzle exit and a fully-developed spray is described in Section 3.6.4. Because the details of the actual fluid flow were not measured and are essentially unknown, it has been assumed that a spray of uniform droplet size is already established at the discharge orifice exit and is injected into the area at a prescribed rate. It should be noted that, due to these assumptions, the model does not reproduce many critical aspects of the discharge process, and cannot be directly compared to the experiments. The value of the calculations has been in the identification of the limitations of CONCHAS-SPRAY and the clarification of the experimental parameters which must be measured or controlled before a realistic representation of the discharge process can be expected. Six cases were chosen for the numerical simulations: a chamber length of 1.0 and 2.5 m, an initial air temperature of 21 and -30 °C, and an initial droplet diameter of 200 or 600 μm.

3.6.2.3 Sample Calculations and Results. All the computations were performed on a Convex supercomputer with a UNIX operating system. The wall clock computational time for one case (around 15 ms of the real process) required three hours on the average. The data were collected in

the form of large ASCII files (typically 12 Mb/file/case) which were converted subsequently into small graphics subfiles. The results were then plotted as contours of constant velocity, density, pressure, temperature, gas species mass fraction, vorticity, kinematic viscosity, mass flux, and liquid phase mass fraction. In order to demonstrate the types of effects which were observed, results for the vapor phase mass fraction of agent into the one meter long volume are described.

Figure 176 shows the time behavior of the agent vapor mass fraction distribution for four times following release. Assuming that the mass fraction of agent vapor follows the two-phase jet flow (likely to be an excellent assumption), it can seen that the downstream edge of the flow field moves away from the orifice with increasing time and that the jet spreads with increasing downstream distance. By 14.3 ms the flow has moved roughly 0.9 m from the source. An interesting feature is the "head" which grows on the downstream edge of the flow field. Recall that a similar structure was observed in high speed films of the experimental agent releases. Calculated velocity fields indicate that the head forms as the result of a vortical motion developed by the flow field. As a result, this is a region of efficient heat transfer from the air to the flow which evaporates the liquid droplets. The resulting agent evaporation causes a volume expansion which further enlarges the head.

Figure 177 shows the results of an identical calculation except that the diameter of the injected liquid droplets is increased from 200 μm to 600 μm. The downstream penetration of the two-phase flow is little changed from that found when smaller droplets are injected. However, the spreading rate of the jet is decreased and the head at the downstream edge of the flow is much narrower. Larger droplets are expected to result in lower evaporation of the liquid due to their smaller surface area. The reduction in spreading rates for Figure 177 is likely due to a combination of a smaller volume expansion and the lesser entrainment of air associated with fewer large rather than many small droplets.

The effect of the ambient temperature on the mixing behavior can be seen by comparing Figure 176 and Figure 178. The overall shapes of the mass fraction contours are very similar even though the air temperature has been decreased over 50 °C. At first glance this appears to be counter to what one would expect; *i.e*, a lower ambient temperature should diminish the vaporized agent mass fraction. The explanation is that the vapor pressure curve used in the calculation ensures that the agent pressure is less than the ambient pressure even for the higher temperature computation. For an agent like HCFC-22, an increase in temperature has a much more dramatic impact on the vapor pressure, which most likely would lead to a significantly higher vapor fraction when the ambient temperature is increased as much as 50 °C. This could not be verified, however, because of numerical instabilities which occurred under more realistic flashing conditions.

As noted above, the calculations generate two-dimensional predictions for a wide range of variables including velocity, pressure, temperature, density, species mass fraction and spray contours. A few additional characteristics of the results are summarized here to give an indication of what physical processes may be important in these systems. At certain regions in the flows very high velocities were calculated due to the rapid evaporation of the liquid droplets. These velocities were sufficient at times to generate shock waves which subsequently interacted with the two-phase flow and modified its mixing and evaporation behavior. It should be noted that shock waves were not detected in the experiments, but this may have been the result of differences in geometry between the experiment and calculation. Since the vessel was closed, major modifications were found when the vessel length was increased from 1.0 m to 2.5 m. This is to be expected due to the higher pressures and stronger shock waves which occur in the smaller volume.

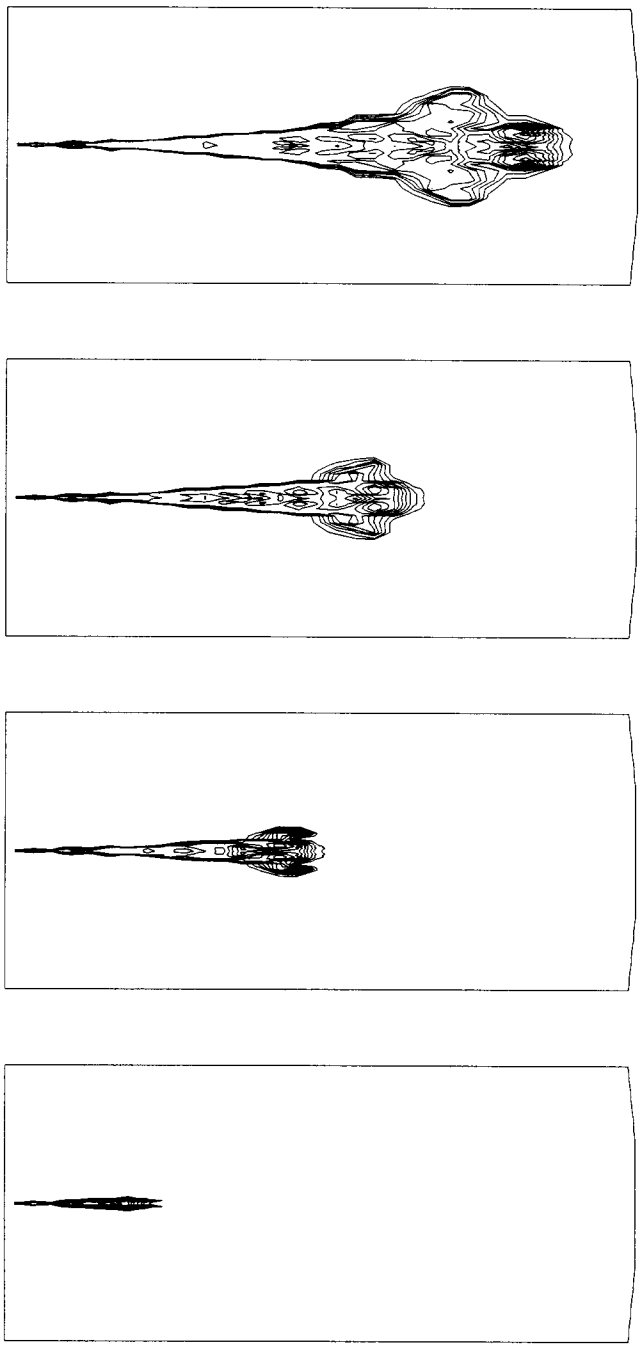

Figure 176. Agent vapor mass fraction contours at 3.5, 8.3, 10.7, 14.3 ms following spray release at 0 ms. Maximum mass fraction=0.15, contour interval=0.0188, spray mean Sauter diameter=200 μm, ambient T=294 K, P=101 kPa, compartment length=1 m.

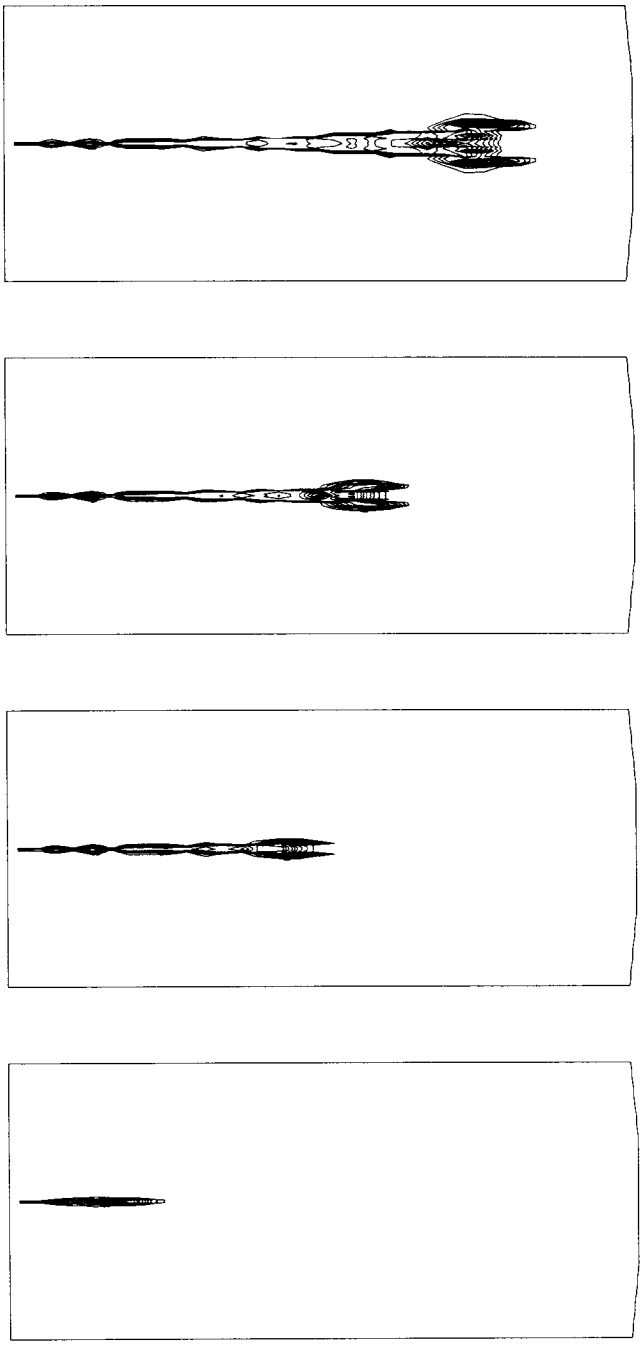

Figure 177. Agent vapor mass fraction contours at 3.5, 8.3, 10.7, 14.3 ms following spray release at 0 ms. Maximum mass fraction=0.14, contour interval=0.0175, spray mean Sauter diameter=600 μm, ambient T=294 K, P=101 kPa, compartment length=1 m.

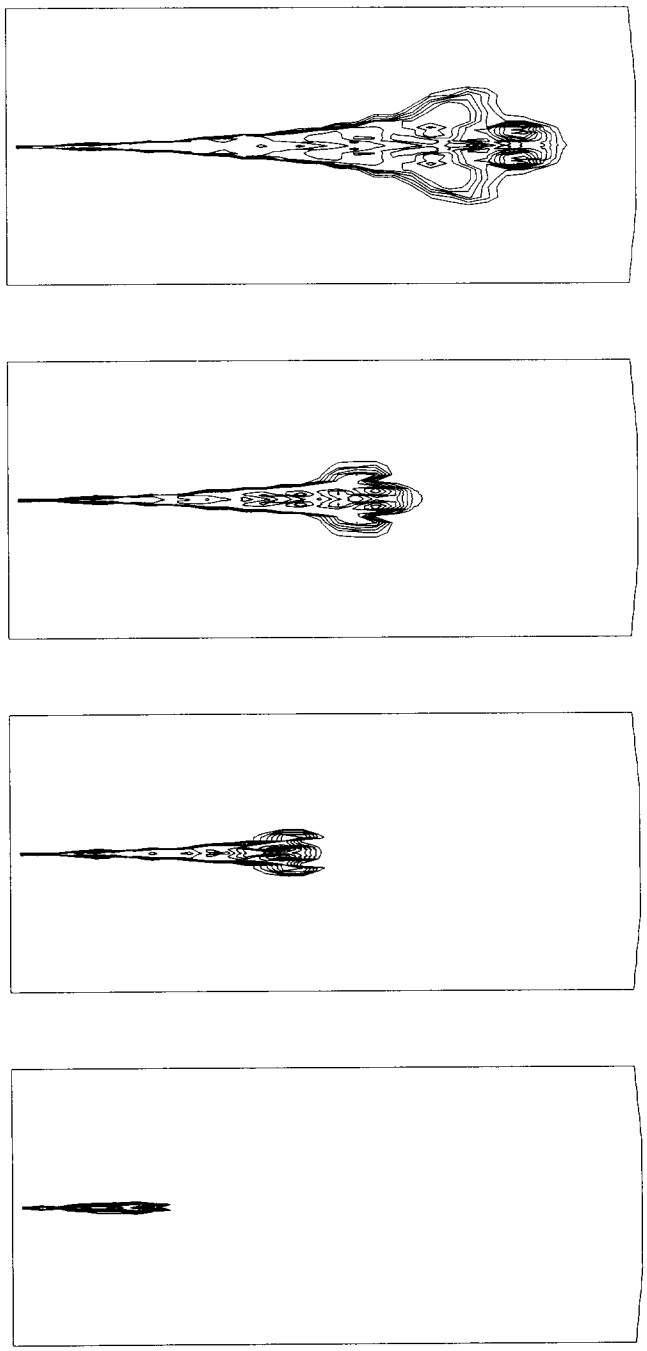

Figure 178. Agent vapor mass fraction contours at 3.5, 8.3, 10.7, 14.3 ms following spray release at 0 ms. Maximum mass fraction=0.209, contour interval=0.0261, spray mean Sauter diameter=200 μm, ambient T=243 K, P=101 kPa, compartment length=1 m.

3.6.3 Establishing Initial/Boundary Conditions from the Vessel Discharge Simulations

3.6.3.1 Overview. A critical element in exercising CONCHAS-SPRAY, KIVA, or any other computational fluid mechanics computer code, for the purpose of providing agent dispersion simulations, is the establishment of a set of initial/boundary conditions. Especially important and problematic is a determination of the characteristics of the agent jet at a location on the jet axis, near the exit section of the discharge vessel, as it enters the protected space. These initial/boundary conditions should be determined from results of a simulation of pressure vessel agent discharge. The purpose of this section is to present a method of estimating the required time-dependent initial/boundary conditions by expanding on the vessel discharge model described in Section 3.2. Although not used in the dispersion computations reported above, this new methodology is expected to be used and evaluated in future CONCHAS-SPRAY and KIVA simulations.

3.6.3.2 Modeling the Early Development of the Jet: From the Exit Section of the Discharge Vessel to a Nearby Section in a State of Thermodynamic Equilibrium and Completed Droplet Formation. It is assumed that within the discharge vessel and upstream of the exit nozzle/orifice the velocity of the liquid agent is so small that its kinetic energy can be neglected in defining its thermodynamic state. Therefore, the thermodynamic state upstream of the nozzle/orifice position can be estimated by the pressure in the discharge vessel, P_{DV}, and the temperature there of the liquid agent, $T_{DV,AL}$. Note that in most applications it is expected that $T_{DV,AL}$ is well approximated by T_{AMB}, the ambient temperature outside the vessel. A point representing the state of the liquid agent in the vessel is indicated in the pressure-enthalpy (P,h) diagram of Figure 179.

Because of the relatively short nozzle/orifice design under consideration, the time interval for the liquid to approach it, pass through it, and enter the outside environment is very small. For conditions of this study this time is of the order of 10^{-3} s. During this time interval the pressure of the traversing liquid is reduced from the high P_{DV} values inside the vessel, of the order of several MPa, to pressures of the order of P_{AMB}, 101 kPa.

As discharging liquid enters and traverses the region of the nozzle/orifice, it will enter and move along superheated metastable thermodynamic states. While dependent on its changing thermodynamic state in the vessel, (P_{DV}, $T_{DV,AL}$), and on its particular thermodynamic properties, as the agent material penetrates the ambient environment it approaches, and likely achieves the P_{AMB} pressure while still in its metastable liquid state. Thus, downstream of a vena contracta the liquid agent develops into a near-uniform-radius liquid jet, r_{LJ}, which can be predicted from traditional incompressible fluid-dynamic considerations. See Figure 180. For the relatively large-vapor-pressure agent materials of interest here, a combination of fluid-dynamic and thermodynamic instabilities will then lead to breakup into small droplets and flashing (*i.e.*, rapid evaporation to a two-phase equilibrium thermodynamic state) of the metastable liquid jet (Lienhard and Day, 1970).

Prior to the onset of breakup and/or flashing the metastable liquid is expected to move through thermodynamic states on near-isentropic paths. However, as discussed in Sections 3.2 and 3.4.3.4, for a given agent and initial-state condition, (P_{DV}, $T_{DV,AL}$), it is possible that the pressure along such a path will not reach P_{AMB} prior to an intersection with the agent's spinoidal curve. Moreover, if such an intersection does occur, then at that instant spontaneous nucleation in the liquid is to be expected (Reid, 1978; Modell and Reid, 1983). It is conjectured that this would lead to near-explosive breakup and flashing of the jet, all of this being initiated within a jet penetration depth (into the outside environment) of the order of a single nozzle/orifice diameter.

Whatever the thermodynamic-state path of the discharging metastable liquid, it is reasonable to assume that a relatively short distance downstream of the nozzle/orifice a thermodynamic equilibrium

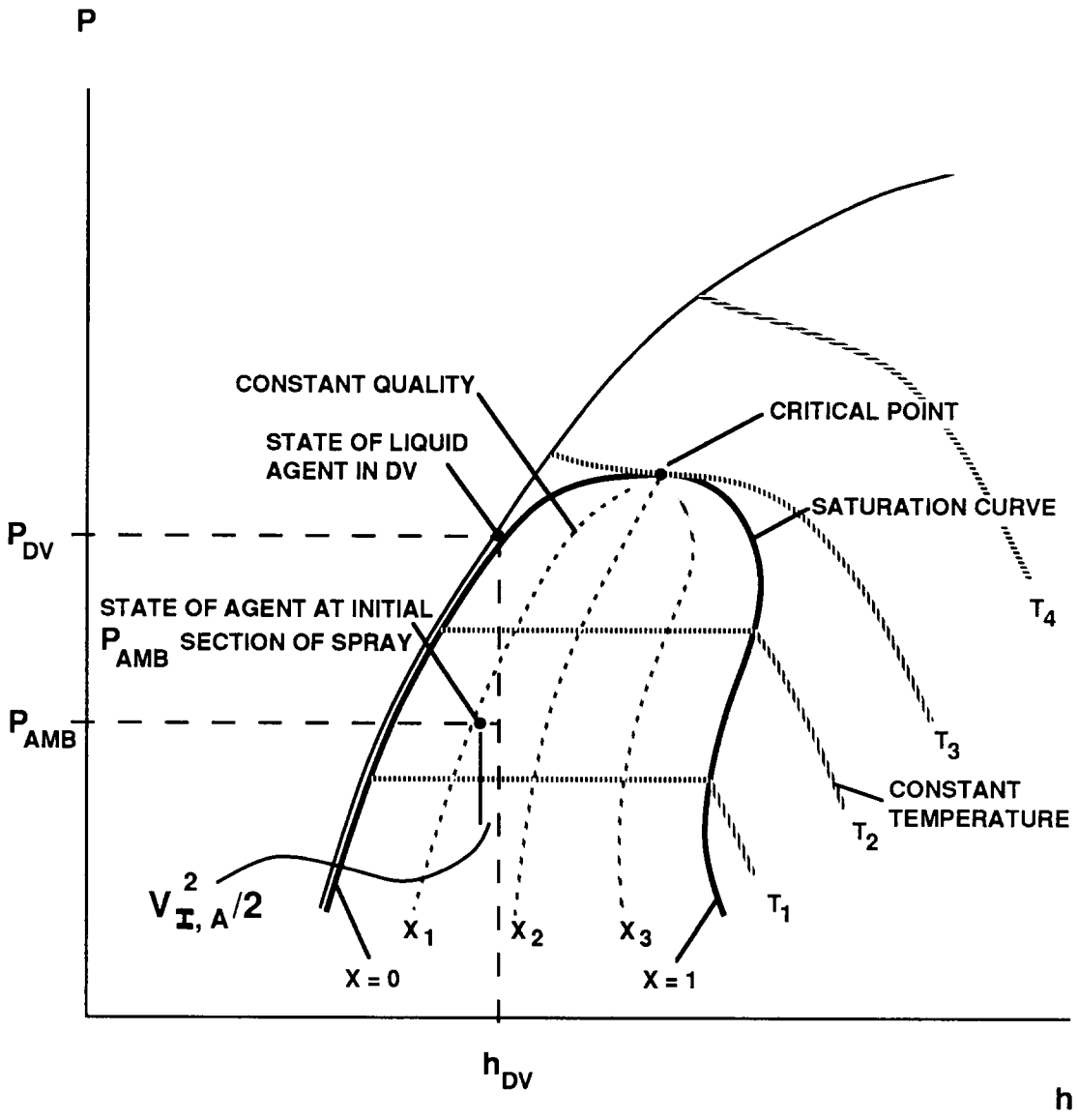

Figure 179. Path in the enthalpy - pressure plane of the thermodynamic state of the initially liquid agent as it flows from inside to outside the pressure vessel and achieves a stable two-phase state at the initial section.

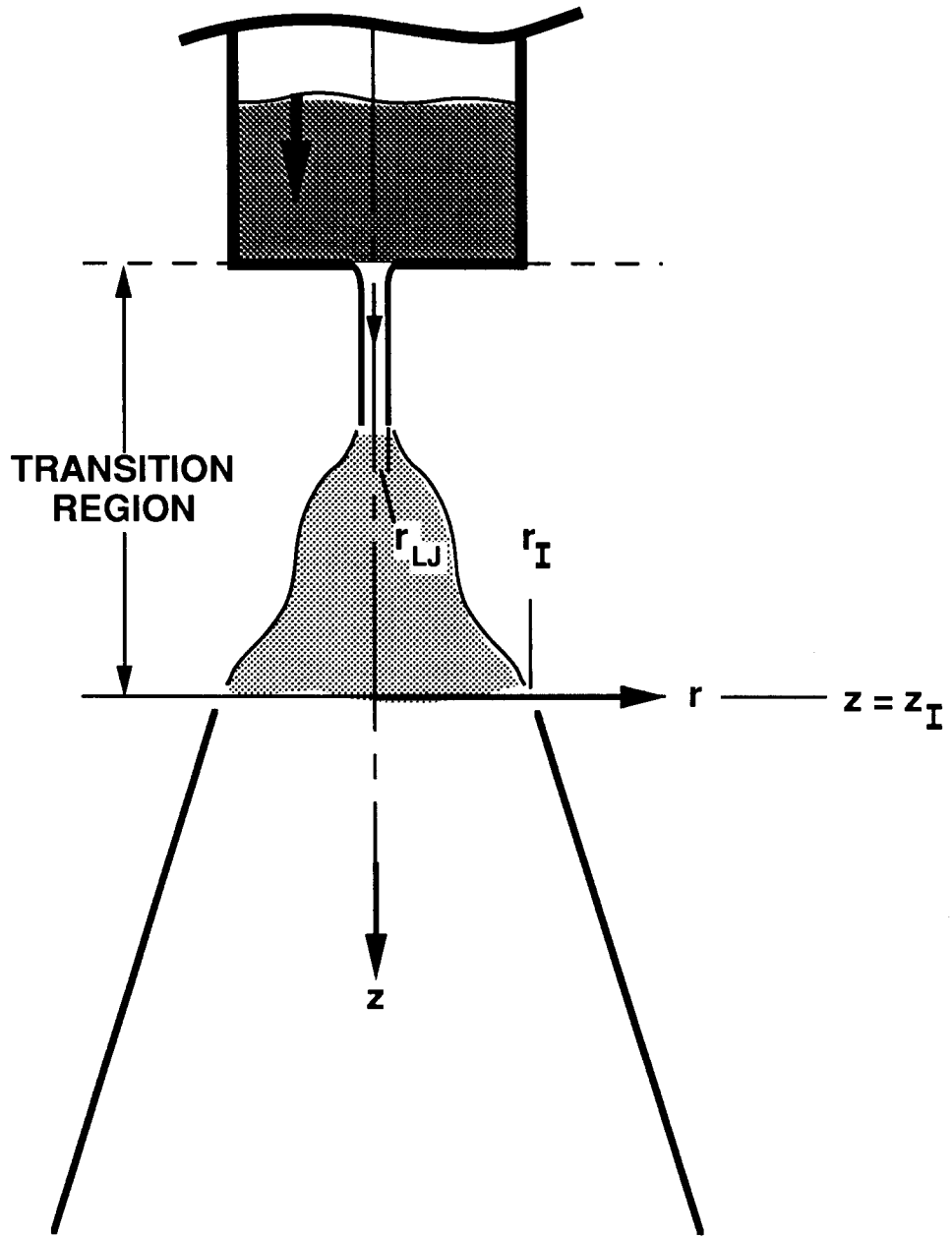

Figure 180. Sketch of the discharging agent, the transition region, and the initial section, $z = z_I$.

state and an end to the droplet-formation phenomenon will be achieved. It is also reasonable to assume that, as the agent flows further downstream, developing as a mixed, two-phase, agent/air jet, thermodynamic equilibrium will be maintained, and droplet collision and agglomeration will not play an important role in jet dynamics. These latter conditions are required if CONCHAS-SPRAY, KIVA, or similar CFD simulations are to be applicable.

The position along the jet axis where both approximate thermodynamic equilibrium and completion of droplet formation is first achieved will be denoted here as the *initial* position of the jet. Associated with this position is the plane section normal to the jet axis, called the *initial* section of the jet. Similarly, the thermodynamic state and properties of the jet at the initial position will be denoted as its *initial* state and *initial* properties. The region of the flow between the nozzle/orifice discharge section and the initial section will be referred to as the transition region of the jet. The *initial* section is a critical portion of the surface that bounds the protected space throughout which the agent is being dispersed.

A detailed description of the initial state and properties of the jet would be extremely complicated. This would include the variation across the initial section of air/gaseous-agent concentrations, temperature, and velocity, and of the size, velocity, and temperature distributions of the liquid agent droplets. Note also that in the present application all of these variables of the initial jet flow field would be time-dependent. In general, an accurate detailed description of the initial state of the jet, whether determined by theoretical or experimental means, is either impractical or beyond the current state of technology.

Although it is not possible to provide a detailed description of the initial state of the jet, it is reasonable to expect that an achievable approximate description, suitable for use in establishing boundary conditions for in the formulation the dispersing-agent-flow-field problem, would lead to good approximations of agent dispersal phenomena. It is the purpose of this work to provide such an approximate description of the initial state.

The dynamic processes that initiate breakup and flashing of the metastable liquid jet and bring it to its initial state are not completely understood. At one extreme, it is possible that the above-mentioned instabilities lead to violent breakup and flashing of the liquid jet immediately upon leaving the exit nozzle/orifice. Such behavior was observed, for example, in some experiments of Brown and York (1962). This was also observed in the current experiments described in Section 3.5 for low-boiling agents.

The metastable state can also persist even as the liquid jet penetrates relatively deeply into the ambient environment. For example, Brown and York (1962) described a liquid water jet of diameter $D = 7.6 \times 10^{-4}$ m, initially at 9.03×10^5 Pa and 415 K, which penetrated up to 0.0254 m, corresponding to $L/D \approx 32$, before initiation of violent breakup/flashing. Similar behaviors were observed for high-boiling agents in the current study. In this regard it is of interest to note that in the literature of the discharge of flashing liquids from high pressure vessels there is a degree of conventional wisdom that analyses of the two-phase flow phenomena, based on thermodynamic equilibrium states, tend to yield good results when the nozzle/piping from the inside to the outside of a high pressure discharge vessel is at least 0.1 m (Lueng and Nazario, 1990).

The initial section will be some incremental distance downstream of the penetration distance of the metastable liquid jet. The studies of Brown and York (1962) and the recent experiments at NIST suggest that this incremental distance will typically not exceed the order of the penetration distance itself. Whatever the distance, it is assumed here that the total length of the transition region is small enough, compared to the characteristic length of the overall agent dispersal problem of interest, that the processes within the transition region can be treated as quasi-steady.

In the transition region it is assumed that momentum transfer and any net work or heat transfer interactions between the penetrating agent jet and the ambient air environment are negligible. Thus,

consistent with the analysis of Epstein *et al.* (1983) for steady, two-phase, air/evaporating-liquid jets, it is assumed that the jet at the initial section can be approximated as consisting only of a two-phase mixture of agent, with no entrained air. Finally, in the transition section it is assumed that increases in the energy of the liquid due to mechanical work by surface tension forces to form the initial-section droplets are negligible compared to the energy transfers involved in phase-change processes.

The above assumptions are used with the following additional considerations to determine the initial state.

The initial section of the jet is defined by a characteristic initial radius r_I. The region $r \leq r_I$ consists of a pure mixture of saturated-agent vapor and liquid (droplets) in thermodynamic equilibrium at ambient pressure, $P_I = P_{AMB}$, and saturation temperature, $T_I = T_{SAT}(P_{AMB})$. The liquid-agent component of the jet consists of droplets of uniform-radius $r_{I,D}$, and these are uniformly dispersed over the region $r \leq r_I$. The agent droplets and gas have the same uniform axial jet velocity, $V_{I,A}$. There is no agent in $r > r_I$, and in the initial section, this outer region is assumed to consist of a uniform ambient-temperature/pressure environment (P_{AMB}, T_{AMB}) of quiescent air.

Conservation of mass and energy is invoked by assuming a quasi-steady state between the initial section and a section in the discharge vessel somewhat upstream of the exit nozzle/orifice. Conservation of mass yields

$$\pi r_I^2 V_{I,A} \rho_{I,A} = \frac{dM_{DV,AL}}{dt}, \tag{43}$$

where

$$\rho_{I,A} = \left[\frac{x_I}{\rho_{I,AG}} + \frac{(1-x_I)}{\rho_{I,AL}} \right]^{-1}. \tag{44}$$

and $\rho_{I,A}$, $\rho_{I,AL}$ and $\rho_{I,AG}$ are the average density of the agent, the density of the liquid agent (droplets), and the density of the agent gas at the initial section, respectively; x_I is the quality of the two-phase flow at the initial section, *i.e.*, the fraction of a mass of agent which is saturated gas; $M_{DV,AL}$ is the instantaneous mass of liquid agent in the discharge vessel; and the right side of Equation (43), determined previously from, *e.g.*, the discharge model of Section 3.2, is assumed to be specified.

When invoking conservation of energy, the kinetic energy at the section in the discharge vessel is assumed negligible compared to that at the initial section. The resulting expressions are

$$h_{DV,AL} = h_{I,AL} + x_I h_{ALG}(T_{sat}) + \frac{V_{I,AG}^2}{2} \tag{45}$$

and

$$h_{ALG}(T_{SAT}) = h_{I,AG} - h_{I,AL}, \tag{46}$$

where $h_{DV,AL}$ and $h_{I,AL}$ are the specific enthalpy of the agent liquid in the discharge vessel and at the initial section, respectively; $h_{I,AG}$ is the specific enthalpy of the agent gas at the initial section; and h_{ALG} is the heat of vaporization of the agent at the temperature T_{SAT}. In Equation (46),

$$h_{ALG} = h_{ALG}(T),\ T \leq T_{CR} \tag{47}$$

is a specified function of temperature, T, where T can not exceed the critical temperature, T_{CR}.

A point representing the state of the agent at the initial section is presented in the (P, h) diagram of Figure 179. Consistent with Equation (45), this reflects the fact that some of the original enthalpy of the liquid agent in its high pressure "near-rest" state, h_{DV}, was exchanged for its now-potentially-significant kinetic energy.

The sketch of the transition region, consistent with the all the above assumptions/ approximations, is presented in Figure 180.

The initial droplet radius is assumed to be specified. According to Brown and York (1962) it is expected that this will be in the range 10 μm - 100 μm. The sensitivity of the downstream agent concentrations to variations of this parameter should be evaluated from future dispersion computations.

The initial jet radius is assumed to be specified. Based on photographic data in Brown and York (1962), r_I/r_{LJ} seems to be of the order of ten to twenty. Thus, in (what is reasonable to construe visually in high speed photographs as) a region of breakup and flashing of the liquid jet to an initial equilibrium state, the radius of the jet increases by a factor between ten and 20. Again, the sensitivity of the downstream agent concentrations to variations of this ratio should be evaluated from future dispersion computations. One would hope that such sensitivity is not great.

In describing the thermodynamic properties of the agent, the liquid state is modeled everywhere as being incompressible, and the gaseous state at the initial section is modeled as a perfect gas. For problems of interest here, agent liquid temperatures are expected to be small enough compared to T_{CR} and vary in a small enough range to permit accurate modeling of the liquid as being incompressible, with density ρ_{AL}, and as having a constant specific heat, C_{AL}. Thus,

$$\rho_{I,AL} = \rho_{AL}. \tag{48}$$

The values of ρ_{AL} and C_{AL} will be taken as

$$\rho = \rho_{AL}(T_{AL});\quad C_{AL} = C_{AL}(T_{AL});\quad T_{AL} = (T_{SAT}+T_{DV,AL})/2, \tag{49}$$

where T_{AL} is taken to be the average temperature of the liquid in the discharge vessel and at the initial state, and where $\rho_{AL}(T)$ and $C_{AL}(T)$ are specified functions of T.
From the assumption of incompressibility it follows that

$$h_{DV,AL}-h_{I,AL} = C_{AL}(T_{DV,AL}-T_{SAT})+\frac{(P_{DV}-P_{AMB})}{\rho_{AL}}. \tag{50}$$

The agent gas is modeled as a perfect gas,

$$\rho_{I,AG} = \frac{P_I}{R_{AG}T_I} = \frac{P_{AMB}}{R_{AG}T_{SAT}}, \tag{51}$$

where R_{AG} is the gas constant.

As discussed above, it is expected that in most instances the liquid jet will achieve P_{AMB} prior to its breakup/flashing. Then, Bernoulli's equation leads to

$$\frac{dM_{DV,AL}}{dt} = \pi r_{LJ}^2 \rho_{AL} \left[\frac{2(P_{DV}-P_{amb})}{\rho_{AL}}\right]^{1/2}, \tag{52}$$

where r_{LJ} is determined from the radius of the exit nozzle/orifice, r_N, and its orifice discharge coefficient, C_D,

$$\left(\frac{r_{LJ}}{r_N}\right)^2 = C_D. \tag{53}$$

Substituting Equations (46) and (50) into Equation (45) leads to

$$\frac{V_{I,A}^2}{2} = C_{AL}(T_{DV,AL}-T_{SAT}) + \frac{(P_{DV}-P_{AMB})}{\rho_{AL}} - x_I h_{ALG}(T_{SAT}). \tag{54}$$

Substituting Equations (44) and (52) into Equation (43) leads to

$$\frac{V_{I,A}^2}{2} = \left(\frac{r_{LJ}}{r_I}\right)^4 \frac{(P_{DV}-P_{AMB})}{\rho_{AL}} \left(\frac{x_I(1-\epsilon)}{\epsilon}\right)^2, \tag{55}$$

where

$$\epsilon = \frac{\rho_{I,AG}}{\rho_{AL}}. \tag{56}$$

Comparing Equations (55) and (54) leads to

$$X^2+\lambda_2 X-(\lambda_1+1) = 0, \tag{57}$$

where

$$X = \frac{x_I}{\epsilon}(1-\epsilon)\left(\frac{r_{LJ}}{r_I}\right)^2; \quad x_I = \frac{X\epsilon}{(1-\epsilon)\left(\frac{r_{LJ}}{r_I}\right)^2}, \tag{58}$$

$$\lambda_1 = \rho_{AL} C_{AL} \frac{T_{DV,AL}-T_{SAT}}{P_{DV}-P_{AMB}}, \tag{59}$$

and

$$\lambda_2 = \frac{\epsilon}{(1-\epsilon)} \frac{\rho_{AL} h_{ALG} T_{SAT}}{\left[P_{DV} - P_{AMB} \left(\frac{r_{LJ}}{r_I} \right)^2 \right]}. \tag{60}$$

The solution to Equation (57) is

$$X = -\frac{\lambda_2}{2} + \left[\left(\frac{\lambda_2}{2} \right)^2 + \lambda_1 + 1 \right]^{1/2}. \tag{61}$$

With Equation (58) and other previous definitions, Equation (61) provides the solution for x_I. This would be used, in turn, to obtain $V_{I,A}$ from Equation (54) or (55), thereby completing the description of the initial state,

$$V_{I,A} = 2X \left(\frac{P_{DV} - P_{AMB}}{\rho_{AL}} \right)^{1/2}. \tag{62}$$

A sketch of the velocity distribution and the mass flux distributions of gaseous and liquid agent at the initial section are presented in Figure 181.

3.6.3.3 Algorithm for Determining the Initial State. The above solution can be implemented with the following algorithm:

1. Specify agent and its thermodynamic properties, including $T_{SAT}(P)$ and $h_{ALG}(T)$, $\rho_{AL}(T)$, and $C_{AL}(T)$.

2. Specify r_I/r_{LJ} (expected range 10 - 20).

3. Specify P_{AMB}, T_{AMB}, and $T_{DV,AL}$. (In most cases expect to specify $T_{DV,AL} = T_{AMB}$.)

4. Specify $T_I = T_{AMB}$ for r > r_I. Compute $T_{SAT}(P_{AMB})$ and then specify $T_I = T_{SAT}$ for $0 \leq r \leq r_I$.

5. Compute $h_{ALG}(T_{SAT})$ from Equation (47).

6. Compute T_{AL} according to Equation (49) and then ρ_{AL} and C_{AL} according to Equation (49) and $\rho_{AL}(T)$ and $C_{AL}(T)$, respectively.

7. Compute $\rho_{I,AG}$ according to Equation (51) and then ε according to Equation (56).

8. Use a component-1 model, *e.g.*, that of Section 3.2, to find the time-dependent values of P_{DV} for a particular Figure 1-configuration of interest.

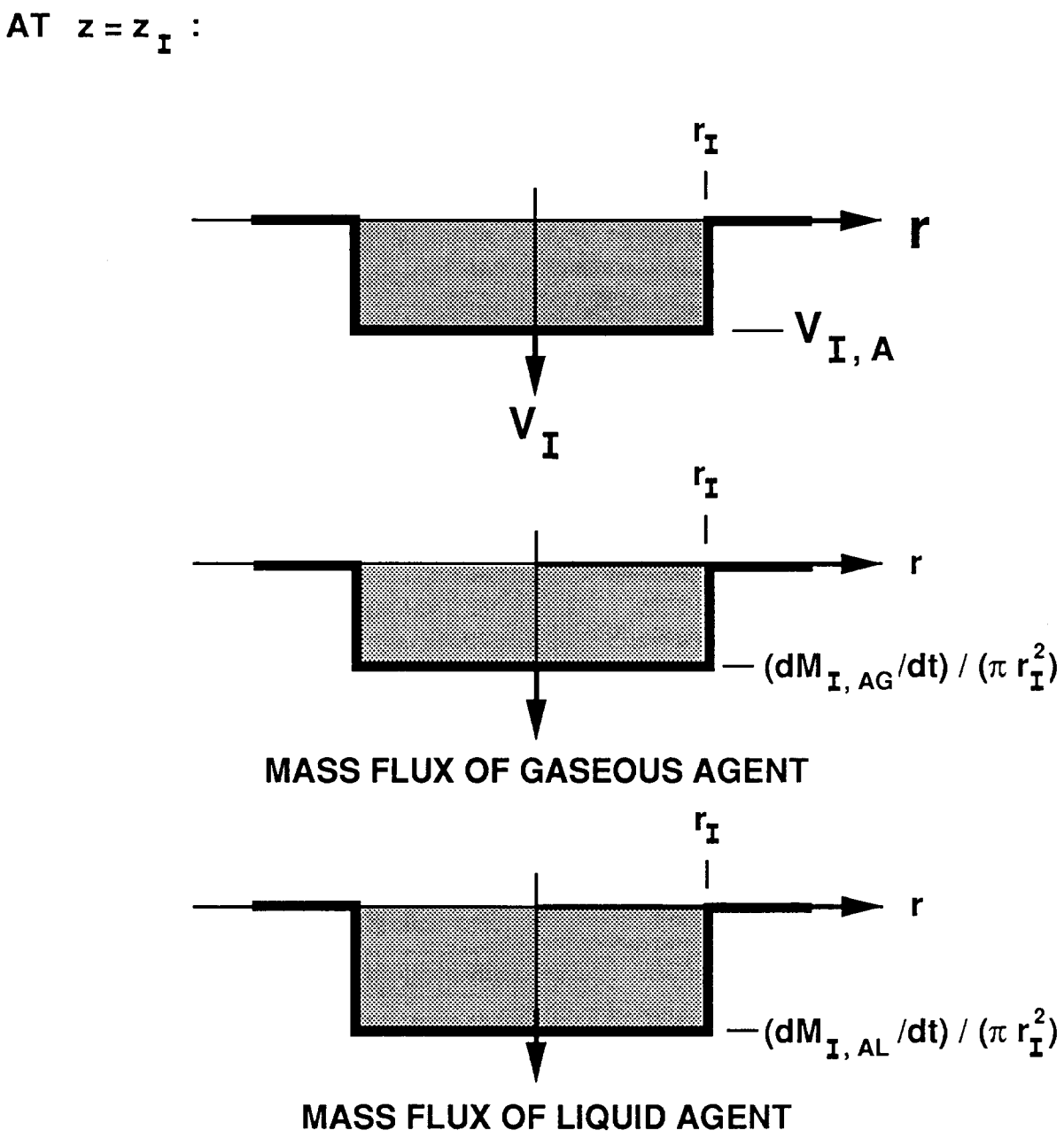

Figure 181. Sketch of the velocity and mass fluxes of agent gas and agent liquid droplets at the initial section, $z = z_I$.

9. For a particular value of P_{DV} compute λ_1 and λ_2 from Equations (59) and (60), and then X from Equation (61).

10. Find x_I from Equation (58) and $V_{I,A}$ from Equation (62).

3.6.3.4 Example Applications of the Initial State Algorithm. The initial-state algorithm was applied in four example simulations. These involve the potential replacement agent HCFC-22 and halon 1301 and two different r_I values, 0.074 m and 0.148 m, corresponding to $r_I = 10r_{LJ}$ and $20r_{LJ}$ and to a value r_{IJ} of 0.0074 m which corresponds, in turn, to a discharge vessel nozzle radius of 0.0095 m and a discharge coefficient of 0.6. The examples involve time-dependent discharges of room-temperature agent from a Figure 1-type configuration with no holding tank. The geometric parameters, orifice coefficient, and initial conditions assumed in the simulated example discharge calculations are presented in Table 11. These are the same parameters used in the example calculations of Section 3.2. During the discharge, the time-dependent value of P_{DV} was computed using the component-1-type model of Section 3.2.

The material property functions for HCFC-22 and halon 1301 which were used in the example calculations are taken from the prescriptions given in Table 12 (Daubert and Danner, 1992).

T_{SAT} was obtained as the root of $P(T_{SAT}) = P_{AMB}$. Then T_{AL} was calculated using Equation (49). Finally, $h_{ALG}(T_{SAT})$, $\rho_{AL}(T_{AL})$, and $C_{AL}(T_{AL})$ were calculated from the property functions of Table 12. Results are presented in Table 13.

The results of the example calculations are tabulated in Table 14 (HCFC-22, $r_I = 10r_{LJ} = 10C_D^{1/2}r_N = 0.0738$ m), Table 15 (halon 1301, $r_I = 10r_{LJ} = 10C_D^{1/2}r_N = 0.0738$ m), Table 16 (HCFC-22, $r_I = 20r_{LJ} = 20C_D^{1/2}r_N = 0.148$ m), and Table 17 (halon 1301, $r_I = 20r_{LJ} = 20C_D^{1/2}r_N = 0.148$ m). Included in the tables are computed values of the variable ζ,

$$\zeta = \frac{M_{DV,AL}}{M_{DV,AL}(t=0)} = \frac{Z}{Z(t=0)} \tag{63}$$

which is the dimensionless mass of liquid agent, $M_{DV,AL}$, or dimensionless elevation of the liquid agent in the discharge vessel, Z.

The tabulated results of Table 14 for the discharge of HCFC-22 ($r_I = 10r_{LJ} = 0.0738$ m) are plotted in Figure 182 through Figure 185. These include plots of the time-dependent values of P_{DV} (Figure 182), $V_{I,A}$ (Figure 183), ζ and x_I (Figure 184), and $dM_{I,AL}/dt$ and $dM_{I,AG}/dt$ (Figure 185).

A study of the results leads to the following observations:

1. For both HCFC-22 and halon 1301, the times to complete the discharge of liquid agent from the pressure vessel are almost identical at 0.024 ± 0.001 s (Table 14 through Table 17).

2. At the initial section, the quality of the two-phase agent flow, x_I, is significantly different for the two agents considered, but for a given agent x_I is relatively independent of t and r_I, for the two initial-section radii values considered ($r_I = 0.0738$ m and 0.148 m). Thus, for the cases considered, $x_I = 0.31 \pm 0.01$ for HCFC-22 (Table 14 and Table 16) and $x_I = 0.54 \pm 0.02$ for halon 1301 (Table 15 and Table 17).

Table 11. Geometric parameters, orifice coefficient, and initial conditions for example discharges from a Figure 1-type configuration with no holding tank

Length of discharge vessel (Z_{DV})	0.255 m
Cross-sectional area of discharge vessel (A_{DV})	0.196×10^{-2} m^2
Volume of discharge vessel (V_{DV})	0.500×10^{-3} m^3
Area of exit nozzle/orifice (A_O)	0.285×10^{-3} m^2
Radius of exit nozzle/orifice (r_O)	0.953×10^{-2} m
Discharge coefficient of exit nozzle/orifice (C_D)	0.6
Initial volume of agent liquid in discharge vessel ($M_{DV,AL,I}$)	0.250×10^{-3} m^3
Initial temperature of gas in the discharge vessel ($T_{DV,I}$)	21 °C
Initial pressure in discharge vessel ($P_{DV,I}$)	41.4×10^5 Pa
Temperature of agent liquid in discharge vessel ($T_{DV,AL}$)	21 °C

3. At the initial section, for a given agent, and for the two initial-section radii values considered, the mass flow rates of liquid or gaseous agent are almost identical at any particular time during the discharge. (For example: for HCFC-22, approximately half-way through the discharge at t = 0.0125 s, values of $dM_{I,AL}/dt$ for r_I = 0.0738 m and r_I = 0.148 m are 8.59 kg/s (Table 14) and 8.49 kg/s (Table 16), respectively; and for halon 1301, approximately half-way through the discharge at t = 0.0122 s, values for $dM_{I,AL}/dt$ for r_I = 0.0738 m and r_I = 0.148 m are 6.95 kg/s (Table 15) and 8.59 kg/s (Table 17), respectively.) However, over the course of the discharge, these mass flow rates are reduced to approximately two thirds of their initial value. (For example: for HCFC-22 and r_I = 0.0738 m, the values of $dM_{I,AL}/dt$ at t = 0 and t = 0.233 s (near the end of the liquid discharge) are 11.78 kg/s and 7.34 kg/s, respectively (Table 14 and Table 16); and for halon 1301, and r_I = 0.0738 m, the values of $dM_{I,AL}/dt$ at t = 0 and t = 0.244 s (near the end of the liquid discharge) are 9.26 kg/s and 5.88 kg/s, respectively (Table 15)).

Table 12. Material Property Functions for HCFC-22 and halon 1301

	HCFC-22	halon 1301
Molecular Weight (kg/mole)	86.47	148.9
$P(T_{SAT})$/Pa = exp[A + $B/(T_{SAT}/R)$ + $C\ln(T_{SAT}/R)$ + $D(T_{SAT}/R)^2$]; $T_1 \le T_{SAT} \le T_2$		
A	9.78×10^{1}	6.28×10^{1}
B	-4.77×10^{-3}	-3.38×10^{3}
C	-1.23×10^{1}	-6.75
D	2.42×10^{-5}	1.44×10^{-5}
T_1	116 K	105 K
T_2	369 K	340 K
$h_{ALG}(T_{SAT})$/(J/kg-mole) = $A(1 - T_{SAT}/T_{CR})^B$; $T_1 \le T_{SAT} \le T_2$		
A	2.96×10^{7}	2.51×10^{7}
B	3.86×10^{-1}	3.57×10^{-1}
T_{CR}	369 K	340 K
T_1	116 K	105 K
T_2	369 K	340 K
$\rho_{AL}(T)$/(kg-mole/m^3) = A/B^F; $F = \{1 + [1 - (T/R)/C]^D\}$; $T_1 \le T \le T_2$		
A	1.60	1.34
B	2.66×10^{-1}	2.70×10^{-1}
C	3.69×10^{2}	3.40×10^{2}
D	2.81×10^{-1}	2.80×10^{-1}
T_1	116 K	105 K
T_2	369 K	340 K
$C_{AL}(T)$/[J/(kg-mole·K)] = A + $B(T/R)$ + $C(T/R)^2$ + $D(T/R)^3$; $T_1 \le T \le T_2$		
A	9.47×10^{4}	1.14×10^{5}
B	3.93×10^{1}	-1.32×10^{2}
C	-8.17×10^{-1}	6.12×10^{-1}
D	2.79×10^{-3}	0
T_1	116 K	193 K
T_2	369 K	298 K

Table 13. Constant properties of the initial state for the example calculations

	HCFC-22	halon 1301
T_{SAT}	-41 °C	-58 °C
T_{AL}	-10 °C	-18.5 °C
$h_{ALG}(T_{SAT})$	0.234×10^6 J/kg	0.118×10^6 J/kg
$\rho_{AL}(T_{AL})$	0.132×10^4 kg/m^3	0.180×10^4 kg/m^3
$C_{AL}(T_{AL})$	0.115×10^4 J/(kg·K)	0.809×10^3 J/(kg·K)

3.6.3.5 Nomenclature

D	diameter of a liquid jet
h	specific enthalpy
h_{DV}	h of agent liquid in the discharge vessel
L	length of liquid jet
P	pressure
P_{AMB}	pressure of the ambient environment
P_{DV}	pressure in the discharge vessel
P_I	pressure at the initial section
R_{AG}	gas constant for the agent gas
r	radius
r_I	radius of two-phase agent jet at the initial section
$r_{I,D}$	radius of agent droplets at initial section
r_{LJ}	radius of the liquid jet outside the discharge vessel
T	absolute temperature
T_{AMB}	temperature of the ambient environment
$T_{DV,AL}$	temperature of liquid agent in the discharge vessel
T_I	temperature at the initial section
T_{SAT}	saturation temperature of the agent
t	time
V_I	velocity at the initial section
$V_{I,A}$	V_I of agent
x_I	quality of the two-phase agent flow at the initial section
z	distance along the jet axis from exit nozzle/orifice
z_I	z at the initial section

3.6.4 Concluding Remarks on Modeling the Discharge Spray. Realistic numerical modeling of the spray discharge process requires an accurate knowledge of the initial conditions surrounding the release of the agent. The conditions prior to bursting the rupture disc in the agent storage vessel are fully established, but a mathematical description of the disintegration of the disc and the motion of the

Table 14. HCFC-22 Jet Behavior for $r_I = 10r_{LJ} = 0.148$ m; $\rho_{AL} = 1320$ kg/m^3; $\rho_{I,AG} = 3.58$ kg/m^3; $T_{I,A} = 232$ K

t (s)	P_{DV} (Pa)	ζ	$V_{I,A}$ (m/s)	x_I	$dM_{I,AG}/dt$ (kg/s)	$dM_{I,AL}/dt$ (kg/s)
0.00000	0.4135×10^7	1.0000	32.21	0.3172	5.36	11.53
0.00179	0.3663×10^7	0.9030	30.13	0.3158	5.01	10.86
0.00358	0.3299×10^7	0.8117	28.45	0.3148	4.73	10.30
0.00537	0.3008×10^7	0.7248	27.05	0.3139	4.50	9.83
0.00716	0.2769×10^7	0.6417	25.86	0.3132	4.30	9.43
0.00895	0.2570×10^7	0.5620	24.83	0.3126	4.13	9.08
0.01073	0.2401×10^7	0.4851	23.92	0.3121	3.98	8.77
0.01252	0.2255×10^7	0.4108	23.12	0.3117	3.85	8.49
0.01431	0.2128×10^7	0.3389	22.40	0.3113	3.73	8.24
0.01610	0.2016×10^7	0.2690	21.75	0.3109	3.62	8.02
0.01789	0.1917×10^7	0.2010	21.16	0.3107	3.52	7.81
0.01968	0.1829×10^7	0.1347	20.62	0.3104	3.43	7.62
0.02147	0.1749×10^7	0.0701	20.12	0.3102	3.35	7.44
0.02326	0.1677×10^7	0.0069	19.67	0.3099	3.27	7.28

liquid agent through the exit plane and for several orifice diameters downstream is far beyond the state of the art for even the simple geometry chosen for the discharge experiments. What is known are the size of the orifice and the emptying rate of the storage vessel, both from the experimental measurements and the model of the emptying process described in Section 3.2. The first-order analysis in the previous section provides a starting point for the droplet enthalpy, but because prediction and/or measurement of droplet size have not yet been developed for these conditions, the droplet size distribution can only be hypothesized.

The general approach for numerically simulating a developing, two-phase, multi-component, compressible, evaporating spray has been presented, and two different Los Alamos computer codes have been described. KIVA-II is the most versatile because it can deal with fully three dimensional flow and boundary conditions, it has a more sophisticated description of the turbulent interactions between the droplets and the gas phase, and it accounts for droplet breakup. There is a severe computational penalty paid for this increased versatility, however. Because the discharge experiments were close to axisymmetric, and because the initial droplet diameter was unknown anyway, the long computational times required for KIVA-II convinced us to chose the more efficient CONCHAS-SPRAY code for our initial parametric study. It was felt that at this stage of our knowledge of the

Table 15. HCFC-22 Jet Behavior for $r_I = 10r_{LJ} = 0.074$ m; $\rho_{AL} = 1320$ kg/m^3; $\rho_{I,AG} = 3.58$ kg/m^3; $T_{I,A} = 232$ K

t (s)	P_{DV} (Pa)	ζ	$V_{I,A}$ (m/s)	x_I	$dM_{I,AG}/dt$ (kg/s)	$dM_{I,AI}/dt$ (kg/s)
0	0.4135×10^7	1.000	122.73	0.3022	5.10	11.78
0.00179	0.3663×10^7	0.9031	115.46	0.3025	4.80	11.07
0.00358	0.3299×10^7	0.8117	109.49	0.3028	4.55	10.48
0.00537	0.3008×10^7	0.7248	104.46	0.3030	4.34	9.99
0.00716	0.2769×10^7	0.6417	100.14	0.3032	4.16	9.57
0.00895	0.2570×10^7	0.5620	96.37	0.3033	4.01	9.20
0.01073	0.2401×10^7	0.4851	93.05	0.3034	3.87	8.88
0.01252	0.2255×10^7	0.4108	90.08	0.3035	3.75	8.59
0.01431	0.2128×10^7	0.3389	87.41	0.3036	3.63	8.33
0.01610	0.2016×10^7	0.2690	84.99	0.3037	3.53	8.10
0.01789	0.1917×10^7	0.2010	82.78	0.3038	3.44	7.89
0.01968	0.1829×10^7	0.1347	80.76	0.3039	3.36	7.69
0.02147	0.1749×10^7	0.0701	78.88	0.3039	3.28	7.51
0.02326	0.1677×10^7	0.0069	77.15	0.3040	3.21	7.34

phenomena, the penalty for using a less sophisticated axisymmetric code would be offset by the increased number of parameters which could be varied.

Sample computations were carried out to evaluate the potential of CONCHAS-SPRAY to provide qualitative understanding of agent spray dispersion. The input data for the calculations were based on the agent discharge experiments described earlier. The geometrical dimensions of the computational domain were smaller than the dimensions of the actual compartment in which the discharges were performed to ensure enough spatial resolution to resolve the controlling parameters.

The calculations have demonstrated that the Los Alamos computer code CONCHAS-SPRAY can be used to analyze the dynamics of halon-alternative agent dispersion and mixing in a space designed for fire protection. Within its physical limitations, it can perform the necessary computations of the discharge process quickly and relatively cheaply, aiding one's understanding and indicating directions for future experiments.

The numerical analysis based on the full fluid dynamics equations as well as a description of the heat and mass transfer leads to the time dependance of the two-dimensional field of all parameters characterizing the agent dispersion phenomena, including velocity, pressure, temperature, density, species mass fraction, mass flux and spray contour. Much of these data are difficult or impossible to measure in experiments.

Table 16. Halon 1301 Jet Behavior for $r_I=10r_{LJ}=0.074$ m; $\rho_{AL}=1800$ kg/m^3; $\rho_{I,AG}=6.17$ kg/m^3; $T_{I,A}=215$ K

t (s)	P_{DV} (Pa)	ζ	$V_{I,A}$ (m/s)	x_I	$dM_{I,AG}/dt$ (kg/s)	$dM_{I,AL}/dt$ (kg/s)
0	0.4135×10^7	1.0000	142.83	0.5181	9.95	9.26
0.00204	0.3687×10^7	0.9030	135.28	0.5205	9.43	8.69
0.00407	0.3338×10^7	0.8111	128.99	0.5224	8.99	8.22
0.00611	0.3057×10^7	0.7236	123.64	0.5239	8.62	7.83
0.00814	0.2826×10^7	0.6397	118.99	0.5252	8.29	7.50
0.01018	0.2631×10^7	0.5590	114.91	0.5263	8.01	7.21
0.01222	0.2465×10^7	0.4812	111.28	0.5273	7.76	6.95
0.01425	0.2322×10^7	0.4058	108.03	0.5281	7.53	6.73
0.01629	0.2197×10^7	0.3327	105.08	0.5289	7.32	6.52
0.01832	0.2086×10^7	0.2616	102.40	0.5295	7.14	6.34
0.02036	0.1988×10^7	0.1924	99.94	0.5301	7.97	6.17
0.02240	0.1899×10^7	0.1248	97.67	0.5307	6.81	6.02
0.02443	0.1820×10^7	0.0588	95.58	0.5311	6.66	5.88

A comparison between KIVA-II and CONCHAS-SPRAY for the same set of conditions is needed to determine the impact of the turbulence and droplet breakup model on the results. If the outcome is independent of the code, additional analyses with CONCHAS-SPRAY could be conducted. If the turbulence and droplet models influence the results, KIVA-II (or better yet, KIVA-III, (Amsden *et al.*, 1993)) should be used for future calculations. KIVA has the additional advantage that fully three dimensional spaces can be handled. Extended resources on the NIST Cray computer would be required for these investigations. The spectrum of parameters influencing the spray dynamics needs to be broadened to include additional compartment geometries, discharge orifice geometry, thermodynamic and gas dynamic parameters of the agent and ambient air, agent injection and atomization parameters as well as consideration of the transition region of the spray.

3.7 Summary and Recommendations

The proposed alternative agents are ranked based on their release, mixing and dispersion, and evaporation behavior. Measurements of the release behaviors for the alternative agents have demonstrated that when the liquid agents are initially at room temperature, all of the agents are released as superheated liquids. Theory predicts that only very small differences in release rates are

Table 17. Halon 1301 Jet Behavior for $r_I=10r_{LJ}=0.148$ m; $\rho_{AL}=1800$ kg/m^3; $\rho_{I,AG}=6.17$ kg/m^3; $T_{I,A}=215$ K

t	P_{DV}	ζ	$V_{I,A}$	x_I	$dM_{I,AG}/dt$	$dM_{I,AL}/dt$
0.00000	0.4135×10^7	1.0000	38.48	0.5583	10.73	8.49
0.00204	0.3687×10^7	0.9030	36.17	0.5566	10.08	8.03
0.00407	0.3338×10^7	0.8111	34.28	0.5552	9.56	7.66
0.00611	0.3057×10^7	0.7236	32.69	0.5541	9.11	7.33
0.00814	0.2826×10^7	0.6397	31.33	0.5532	8.73	7.05
0.01018	0.2631×10^7	0.5590	30.15	0.5524	8.41	6.81
0.01222	0.2465×10^7	0.4812	29.11	0.5518	8.12	6.59
0.01425	0.2322×10^7	0.4058	28.19	0.5512	7.86	6.40
0.01629	0.2197×10^7	0.3327	27.36	0.5507	7.63	6.22
0.01832	0.2086×10^7	0.2616	26.60	0.5503	7.42	6.06
0.02036	0.1988×10^7	0.1924	25.92	0.5499	7.23	5.91
0.02240	0.1899×10^7	0.1248	25.29	0.5496	7.05	5.78
0.02443	0.1820×10^7	0.0588	24.71	0.5492	6.89	5.65

to be expected between agents when this is the case. In fact, experiments indicate that all of the agents have comparable volume release rates. The only indication of a different behavior was observed for halon 1301 for which the liquid apparently flashed just upstream of or in the orifice. As a result of the formation of a two-phase flow, the flow rate of halon 1301 was substantially reduced.

Since the room-temperature release rates are essentially identical for all of the proposed alternative agents, this parameter does not provide a means to differentiate between the agents. As a result the ranking is based solely on their behaviors once released. The results summarized in Section 3.5.5 thus provide the final ranking of the agents based on release behavior, mixing and dispersion, and evaporation rate. The final ratings on these criteria are summarized in Table 10. Note once again that FC-116 has not been included since it is not a liquid at room temperature.

Table 10 presents the result which represent the primary goal of the investigation to rank the alternative agents with regard to release rate, dispersion and mixing, and evaporation rate. However, during the course of the research program a number of observations and secondary conclusions have been obtained which have important implications for the design and engineering of systems for suppression of nacelle and dry bay fires using the proposed alternative agents. During the discussion it should be kept in mind that the experimental system developed for this investigation was designed solely to allow a ranking of the proposed alternative agents. Actual commercial systems designed for suppression of fires on aircraft are likely to be significantly different. On the other hand, many of the findings and conclusions of this work should be applicable to more complicated vessels and flow

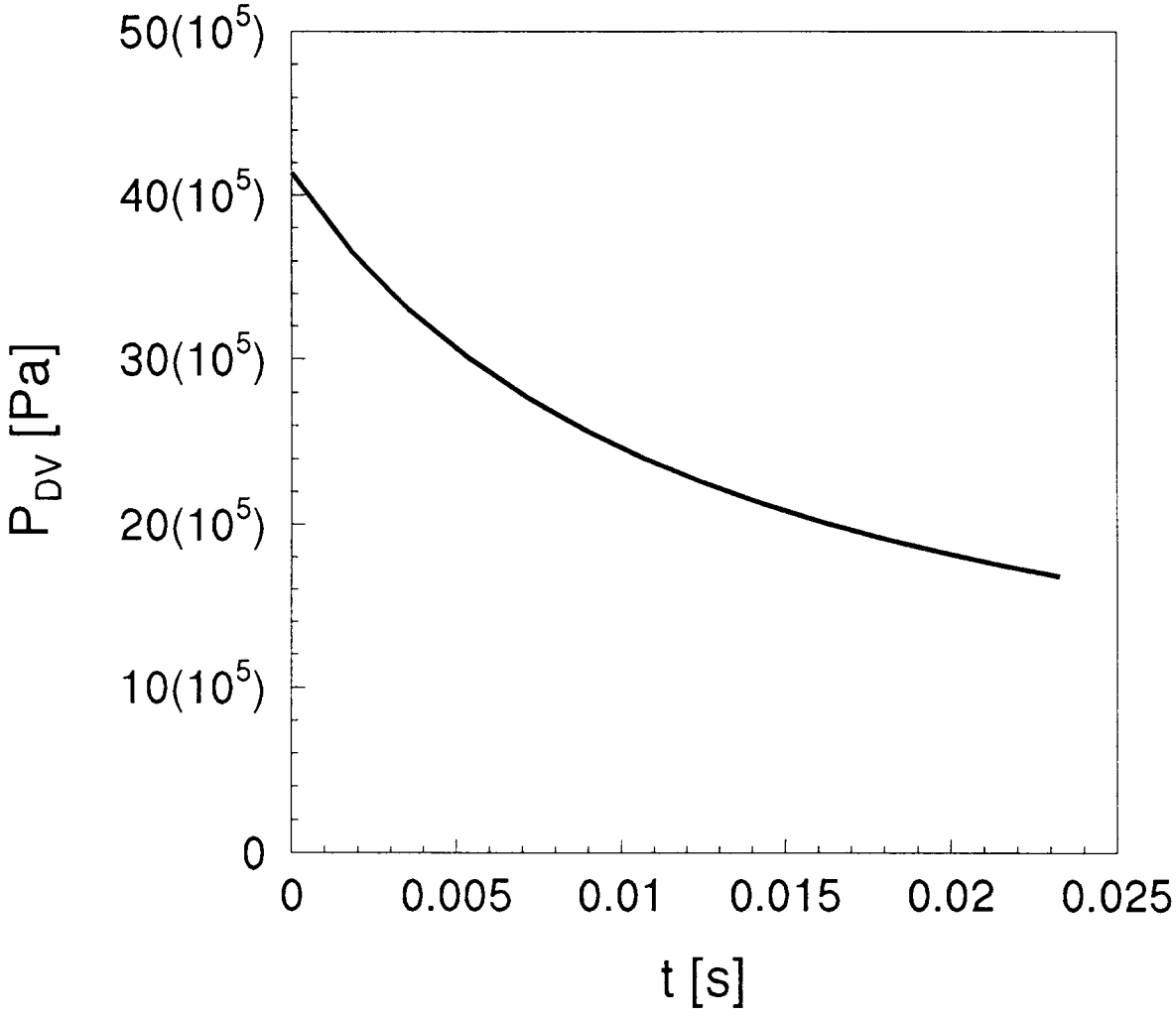

Figure 182. Plot of Table 14 results for P_{DV} as a function of time during vessel discharge of HCFC-22.

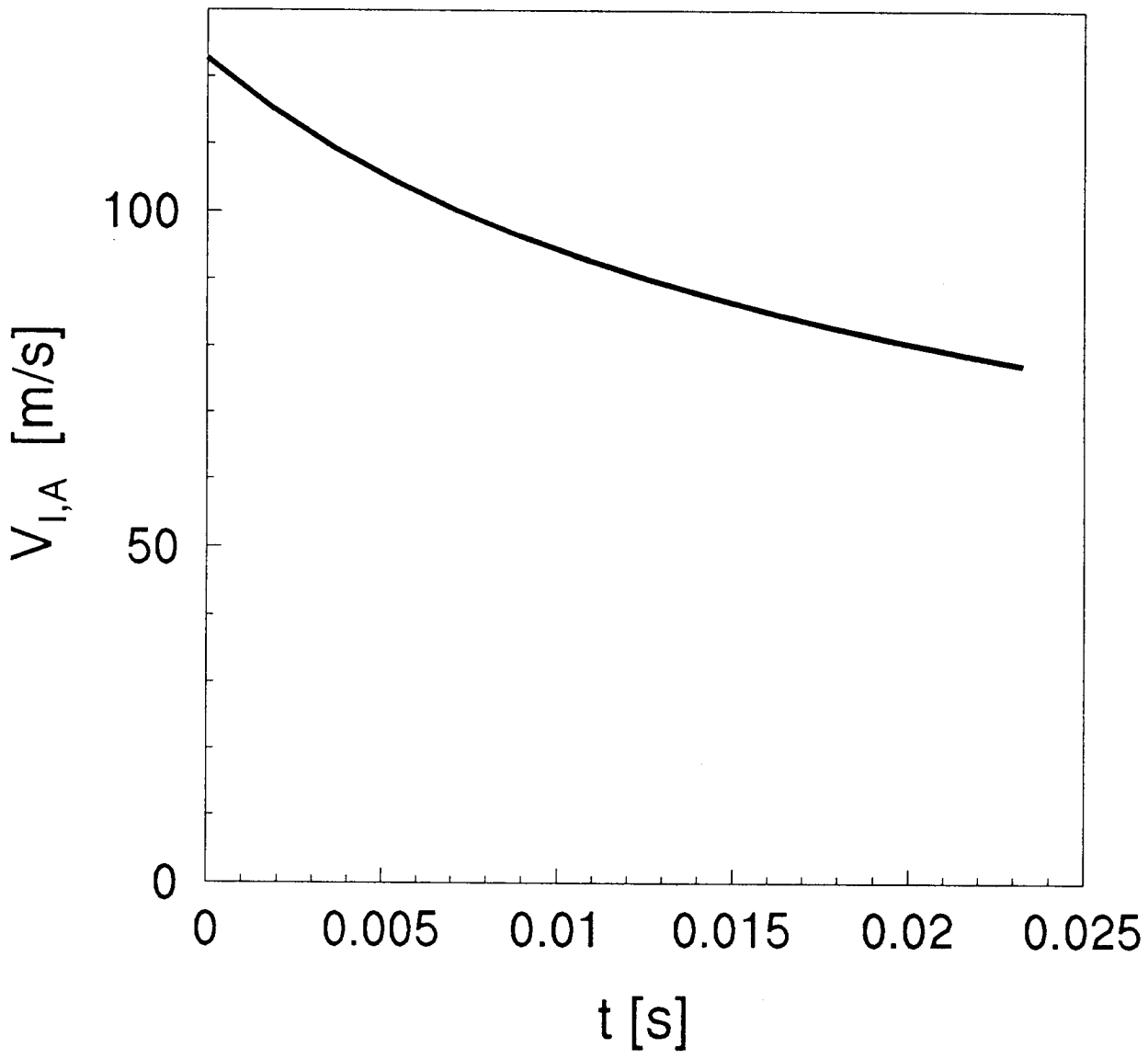

Figure 183. Plot of Table 14 results for $V_{I,A}$ as a function of time during vessel discharge of HCFC-22.

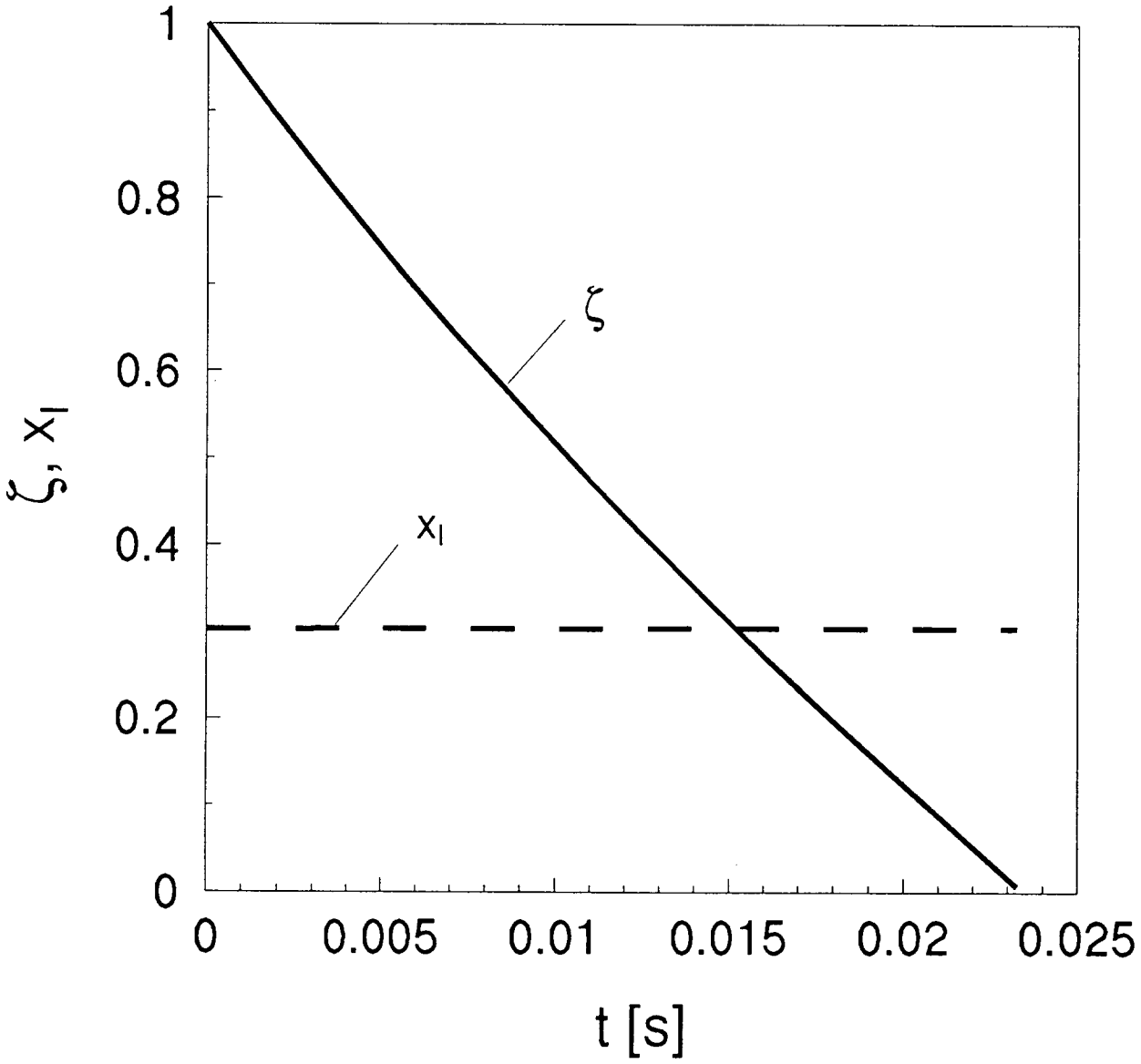

Figure 184. Plots of Table 14 results for ζ and x_I as functions of time during vessel discharge of HCFC-22.

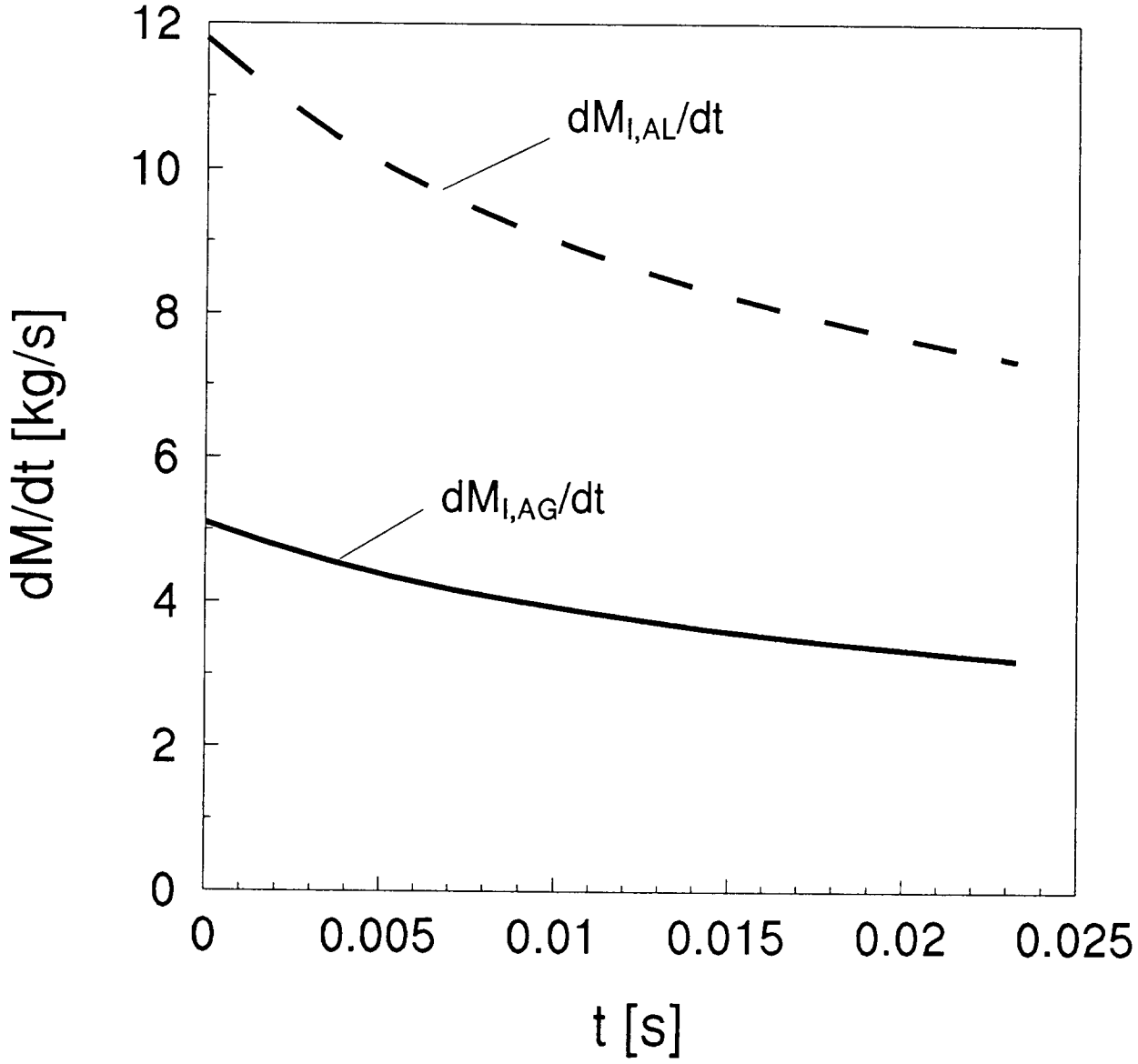

Figure 185. Plots of Table 14 results for $dM_{I,AL}/dt$ and $dM_{I,AG}/dt$ as functions of time during vessel discharge of HCFC-22.

geometries. Where appropriate, suggestions are provided for additional studies which should be considered.

Downward releases of agents will be considered first. Results discussed in Sections 4.2 and 4.4 demonstrate that when agents are released from pressurized vessels as liquids, it is possible to predict release rates and pressure time histories within the vessel quite accurately. The effects of changing a vessel orifice size or degree of pressurization are easily predictable. The only case where premature flashing within the vessel or orifice was found to result in a reduction in release rate was for halon 1301. This agent has the lowest boiling and therefore the highest superheat of the liquids tested. The potential replacement agents may be exposed to ambient temperatures higher than standard room temperature. These higher temperatures result in higher overheats which may ultimately lead to flashing which disrupts the liquid flow. As a result, the release of an agent may require a longer period than predicted based on the assumption of a liquid flow. If this occurs, the agent's fire-fighting effectiveness could be reduced. It would be worthwhile to determine more carefully the conditions for which flashing of a superheated liquid can reduce the release rate. Recall also that it has been hypothesized that a superheated liquid which is rapidly depressurized might reach its spinodial condition and undergo a boiling liquid expanding vapor explosion. Such an event has not been characterized experimentally, but due to the dire consequences which could result, it would be prudent to investigate the possibility further.

The primary effect on the release rate of cooling a vessel containing an agent below room temperature is to reduce the pressure of the driving gas within the vessel. It should be possible to predict these effects using the models developed during the course of this project.

The effects of various system parameters on the dispersion and mixing and evaporation behavior following release of the liquid agents from a pressurized vessel are complex. During the course of this effort several major influencing parameters have been identified. The parameter which has the largest effect on the initial mixing behavior following a room-temperature release of an agent is the degree of superheating. The higher the superheat, the more likely the agent is to flash near the vessel exit. Flashing also appears to occur more rapidly with higher superheats. As a result of flashing the agent is accelerated in multiple directions and is mixed with it surroundings. The velocity measurements also demonstrate that the agent spreading is accelerated by flashing leading to enhanced and more rapid dispersion and better mixing. If the ambient temperature is raised, a liquid will become more superheated and it dispersion and mixing behavior should be enhanced. Cooling of the vessel should have an opposite effect. Measurements with FC-218 demonstrated that the latter was indeed the case.

For the experimental system investigated here only the vessel was cooled. If an agent release occurred into an environment which was also cooled it would be expected that the dispersion and mixing would be hindered even more. It would be useful to investigate release of agents into cooled environments in order to fully characterize these effects. It would also be useful to run flame extinguishment tests such as the Wright-Patterson dry bay test facility under cold conditions to assess the effects on flame-extinguishment effectiveness.

The effects of changes in the degree of vessel pressurization and orifice size on the dispersion and mixing and vaporization behavior are understandable in terms of the flashing and vaporization behavior of the agents once discharged.

Orientation of the release vessel is a parameter which strongly influences the liquid-agent release mechanism and subsequent mixing and agent evaporation. If the bottle is oriented such that the pressurization gas is located next to the release orifice it is released first and release of the liquid agent occurs by boiling and subsequent release of a two-phase flow. Experiments show that not only are the release times for an agent substantially increased, but the dispersion and evaporation behavior are significantly degraded as compared to a downward release. If cooled sufficiently, release of agent

may not occur at all. Designers of extinguisher systems should assess the probability of a pressure vessel being oriented incorrectly as a result of aircraft flight profiles. If such events are probable it may be necessary to design pressure vessels in such a way that nitrogen will always expel liquid from the vessel.

Initial efforts have been described which are aimed at modeling the dispersion and mixing and evaporation of agents following their release as superheated liquids from pressurized bottles. Considerable work remains to be done, but this initial work suggests that simulations sufficiently accurate for engineering design work can be developed. It should be possible to calculate behaviors for releases of agents into complex three-dimensional compartments such as dry bays and engine nacelles. Similar models are widely employed in a wide range of engineering disciplines to reduce design times and limit expensive testing. Efforts to develop effective models for agent releases should be pursued.

The experimental diagnostics which have been used to investigate the release behavior of agents following discharge of the potential fire-fighting agents have provided sufficient characterization to allow a ranking. However, there are a number of characteristics of these releases which have not been addressed. Many of these are expected to be crucial for effective fire fighting. Such properties as the flow fields, the concentration fields, temperature fields, droplet sizes, entrainment rates, and degree of vaporization in the space are required before true models of flame extinction can be developed. Such experimental measurements should be performed to provide a data base for validating models of mixing behavior and flame extinction. Such information would also be very useful for future efforts to develop new and improved flame suppression processes.

3.8 References

Abramowitz, G.N., *The Theory of Turbulent Jets*, MIT Press, Cambridge, MA, 1963.

Allied Signal, Inc., *Genetron® Products Technical Bulletin: R-32/125 Azeotrope*, Allied Signal Inc., Genetron® Products, Morristown, NJ, July, 1991

Amsden, A.A., Ramshaw, J.D., O'Rourke, P.J., and Dukowicz, J.K., *KIVA: A Computer Program for Two- and Three-Dimensional Fluid Flows with Chemical Reactions and Fuel Sprays*, Los Alamos National Laboratory Report No. LA-10245-MS, 1985a.

Amsden, A.A., Butler, T.D., O'Rourke, P.J., and Ramshaw, J.D., *KIVA: A Comprehensive Model for 2D and 3D Engine Simulations*, SAE Technical Paper No. 850554 (1985b).

Amsden, A.A., Ramshaw, J.D., Cloutman, L.D., and O'Rourke, P.J., *Improvements and Extensions to the KIVA Computer Program*, Los Alamos National Laboratory Report No. LA-10534-MS, 1985c.

Amsden, A.A., Butler, T.D., and O'Rourke, P.J., *The KIVA-II Computer Program for Transient Multi-Dimensional Chemically Reactive Flows with Sprays*, SAE Paper 872072; also appears in SAE Transactions (1987).

Amsden, A.A., O'Rourke, P.J., and Butler, T.D., *KIVA-II: A Computer Program for Chemically Reactive Flows with Sprays*, Los Alamos National Laboratory Report No. LA-11560-MS, 1989.

Amsden, A.A., Butler, T.D., O'Rourke, P.J., *KIVA-III: A KIVA Program with Block-Structured Mesh for Complex Geometries*, Los Alamos National Laboratory Report No. LA-12503-MS, 1993.

Avedisian, C.T., "The Homogeneous Nucleation Limits of Liquids," *J. Phys. Chem. Ref. Data 14*, 695 (1985).

Balzhiser, R.E., Samuels, M.R., and Eliassen, J.D., *Chemical Engineering Thermodynamics, The Study of Energy, Entropy, and Equilibrium*, Prentice-Hall, Englewood Cliffs, NJ, 1972.

Bankoff, S.G., "Diffusion-Controlled Bubble Growth," in *Advances in Chemical Engineering, Vol. 6*, Drew, T.B., Hoopes, Jr., J. W., Vermeulen, T., and Cokelet, G. R., Eds., pp. 1-60, Academic Press, New York, 1966.

Beegle, B.L., Modell, M., and Reid, R.C., "Thermodynamic Stability Criterion for Pure Substances and Mixtures," *AIChE Journal 20*, 1200 (1974).

Benjamin, M.W., and Miller, J.G., "The Flow of Saturated Water through Throttling Orifices," *Transactions ASME 63*, 419 (1941).

Bird, R.B., Stewart, W.E., and Lightfoot, E.N., *Transport Phenomena*, John Wiley & Sons, New York, 1960.

Bracco, F.V., *Modeling of Engine Sprays*, SAE Technical Paper No. 850394 (1985).

Bradshaw, P., *An Introduction to Turbulence and Its Measurement*, Pergamon, New York, 1971.

Brown, J.A., and Mears, W.H., "Physical Properties of n-Perfluorobutane," *J. Phys. Chem. 62*, 960 (1958).

Brown, G.L., and Rebollo, M.R., "A Small, Fast-Response Probe to Measure Composition of a Binary Gas Mixture," *AIAA J. 10*, 649 (1972).

Brown, R., and York, J.L., "Sprays Formed by Flashing Liquid Jets," *A.I.Ch.E. Journal 8*, 149 (1962).

Bryner, N.P., personal communication, 1993.

Burnell, J.G., "Flow of Boiling Water through Nozzles, Orifices, and Pipes," *Engineering 164*, 572 (1947).

Butler, T.D., Cloutman L.D., Dukowicz J.K., and Ramshaw J.D., *CONCHAS: An Arbitrary Lagrangian-Eulerian Computer Code for Multicomponent Chemically Reactive Fluid Flow at All Speeds*, Los Alamos Scientific Laboratory Report No. LA-8129-MS, 1979.

Carnahan, B., Luther, H.A., and Wilkes, J.O., *Applied Numerical Methods*, John Wiley & Sons, New York, 1969.

Cattolica, R., and Vosen, S., "Combustion-Torch Ignition: Fluorescence Imaging of OH Concentration," *Combust. Flame 68*, 267 (1987).

Celata, G.P., Cumo, M., Farello, G.E., and Incalcaterra, P.C., "On the Critical Flows of Subcooled Liquids," in *Heat Transfer 1982, Proceedings of the Seventh International Heat Transfer Conference*, Grigull, U., Hahne, E., Stephan, K., and Straub, J., Eds., Hemisphere, New York, 1982.

Celata, G.P., Cumo, M., Farello, G.E., Incalcaterra, P.C., and Naviglio, A., "Thermodynamic Disequilibrium in the Critical Flow of Subcooled Liquids," *Nuclear Technology 60*, 137 (1983).

Chamberlain, G., *Criteria for Aircraft Installation and Utilization of an Extinguishing Agent Concentration Recorder*, Federal Aviation Administration Report NO. FAA-DS-70-3, March, 1970.

Cloutman, L.D., Dukowicz J.K., Ramshaw J.D., and Amsden A.A., *CONCHAS-SPRAY: A Computer Code for Reactive Flows with Fuel Sprays*, Los Alamos National Laboratory Report No. LA-9294-MS, 1982.

Cooper, L.Y., *Discharge of Fire Suppression Agents From a Pressurized Vessel: A Mathematical Model and Its Application to Experimental Design*, National Institute of Standards and Technology Internal Report, NISTIR 5181, 1993a; see also Cooper, L.Y., "Discharge of Fire Suppression Agents From a Pressurized Vessel: A Mathematical Model and Its Application to Experimental Design," *Proceedings of Halon Alternatives Technical Working Conference 1993*, University of New Mexico, New Mexico Engineering Research Center for Global Environmental Technologies, Albuquerque NM, pp. 530-549, 1993a.

Cooper, L.Y., *The Dispersion of Fire Suppression Agents From High Pressure Vessels: Establishing Initial/Boundary Conditions for the Flow Outside the Vessel*, National Institute of Standards and Technology Internal Report, NISTIR 5219, 1993b.

Daubert, T.E., and Danner, R.P., *Physical and Thermodynamic Properties of Pure Chemicals, Data Compilation*, Hemisphere, New York, 1992.

Davis, M.R., "Response of Small Pitot Tubes in Gas-Liquid Flows," *Int. J. Multiphase Flow 6*, 369 (1980).

Day, J.B., *Combined Effects of Superheat and Dynamical Instability on the Breakup of Liquid Jets*, Masters Thesis, University of Kentucky, 1969.

Deardorff, J.W., "On the Magnitude of the Subgrid Scale Eddy Coefficient," *J. Comput. Physics 7*, 120 (1971).

Deragarabedian, P., "The Rate of Growth of Vapor Bubbles in Superheated Water," *J. Applied Mech. 20*, 537 (1953).

Dukowicz, J.K., *Quasi-Steady Droplet Phase Change in the Presence of Convection*, Los Alamos Scientific Laboratory Report No. LA-7997-MS, 1979.

Dukowicz, J.K., "A Particle-Fluid Numerical Model for Liquid Sprays," *J. Comput. Physics 35*, 229 (1980).

Elliot, D.G., Garrison, P.W., Klein, G.A., Moran, K.M., and Zydowicz, M.P., *Flow of Nitrogen-Pressurized Halon 1301 in Fire Extinguishing Systems*, Jet Propulsion Laboratory, JPL Publication 84-62, 1984.

Ely, J., and Huber, M.L., *PROZPER*, Personal Communication with M. L. Huber (1993).

Epstein, M., Henry, R., Midvidy, W., and Pauls, R., "One-Dimensional Modeling of Two-Phase Jet Expansion and Impingement, in *Thermal-Hydraulics of Nuclear Reactors, Vol. II*, 2nd International Topical Meeting on Nuclear Reactor Thermal Hydraulics, Santa Barbara, CA, Jan. 11-14, 1983.

Fletcher, B., "Sudden Discharge of a Superheated Fluid to Atmosphere," *IChemE Symposium Series No. 71*, 25 (1982).

Forest, T.W., and Ward, C.A., "Effect of a Dissolved Gas on the Homogeneous Nucleation Pressure of a Liquid," *J. Chem. Phys. 66*, 2322 (1977).

Forster, H.K, and Zuber, N., "The Growth of a Vapor Bubble in a Superheated Liquid," *J. Appl. Phys. 25*, 474 (1954).

Gmurczyk, G., Lezanski, T., Kesler, M., Chomiak, T., Rychter, T., and Wolanski, P., "Single Compression Machine Study of a Pulsed Jet Combustion (PJC)," *Twenty-Fourth Symposium (International) on Combustion*, pp.1441-1448, Combustion Institute, Pittsburgh, 1992.

Gühler, M., Hannemann, R.J., and Sallet, D.W., "Unsteady Two-Phase Blowdown of a Flashing Liquid from a Finite Reservoir," in *Two-Phase Momentum, Heat and Mass Transfer in Chemical, Process, and Energy Engineering Systems, Vol. 2*, Durst, F., Tsiklauri, G.V., and Afgan, N.H., Eds., pp. 781-795, Hemisphere Publishing Co., Washington, 1979.

Henry, R.E., "The Two-Phase Critical Discharge of Initially Saturated or Subcooled Liquid," *Nuclear Science and Engineering 41*, 336 (1970).

Hesson, J.C., and Peck, R.E., "Flow of Two-Phase Carbon Dioxide through Orifices," *AIChE Journal 4*, 207 (1958).

Johnson, D.W., and Diener, R., "Prediction of Aerosol Formation from the Release of Pressurized, Superheated Liquids to the Atmosphere," *IChemE Symposium Series No. 124*, 87 (1991).

Kim-E, M.E., *The Possible Consequences of Rapidly Depressurizing a Fluid*, M.S. Thesis, Department of Chemical Engineering, Massachusetts Institute of Technology, 1981.

Kim-E, M.E., and Reid, R.C., "The Rapid Depressurization of Hot, High Pressure Liquids or Supercritical Fluids," in *Chemical Engineering at Supercritical Fluid Conditions*, Paulaitia, M.E., Penninger, J.M.L., Gray, Jr., R.D., and Davidson, P., Eds., pp. 81-100, Ann Arbor Science, Ann Arbor, MI, 1983.

Launder, B.E., and Spaulding, D.B., *Mathematical Models of Turbulence*, Academic Press, New York, 1972.

Leung, J.C. and Nazario, F.N., "Two-Phase Flashing Flow Methods and Comparisons," *Journal Loss Prevention Process Industry 3*, 253, (1990).

Lienhard, J.H., "Some Generalizations of the Stability of Liquid-Gas-Vapor Systems," *Int. J. Heat Mass Trans. 7*, 813 (1964).

Lienhard, J.H., "An Influence of Superheat Upon the Spray Configuration of Superheated Liquid Jets," *J. Basic Eng. 88*, 685 (1966).

Lienhard, J.H., and Day, J.B., "The Breakup of Superheated Jets," *J. Basic Eng. 92*, 515 (1970).

Lienhard, J.H., and Stephenson, J.M., "Temperature and Scale Effects Upon Cavitation and Flashing in Free and Submerged Jets," *J. Basic Eng. 88*, 525 (1966).

Military Specification, "Container, Aircraft Fire Extinguishing System, Bromotrifluoromethane, CF_3Br," *Mil-C-22284A(WP)*, September, 1965.

Modell M., and Reid, R.C., *Thermodynamics and Its Applications, 2nd Ed.*, Prentice-Hall, Englewood Cliffs, NJ, 1983.

Moodie, K., and Ewan, B.C.R., "Jets Discharging to Atmosphere," *J. Loss Prev. Process Ind. 3*, 68 (1990).

O'Rourke, P.J., *Collective Drop Effects in Vaporizing Liquid Sprays*, Ph.D. Thesis 1532-T, Princeton University, 1981.

Oran, E.S., "Current Status of Computational Fluid Dynamics in Combustion Modeling," *Eastern States Section Technical Meeting*, Clearwater Beach, FL, December 5-7, 1988.

Pasqua, P.F., "Metastable Flow of Freon-12," *Refrigerating Engineering 61*, 1084A (1953).

Peng, D.-Y., and Robinson, D.B., "A New Two-Constant Equation of State," *Ind. Eng. Chem. Fundam. 15*, 59 (1976).

Perry, Jr., J.A., "Critical Flow Through Sharp-Edged Orifices," *Trans. ASME 71*, 757 (1949).

Perry, R.H., Green, D.W., and Maloney, J.O., *Perry's Chemical Engineers' Handbook*, 6th ed., McGraw-Hill, New York, 1984.

Pitts, W.M., and Kashiwagi, T., "The Application of Laser-Induced Rayleigh Light Scattering to the Study of Turbulent Mixing," *J. Fluid Mech. 141*, 391 (1984).

Pitts, W.M., and McCaffrey, B.J., "Response Behaviour of Hot Wires and Films to Flows of Different Gases," *J. Fluid Mech. 169*, 465 (1986).

Plesset, M.S., and Zwick, S.A., "The Growth of Vapor Bubbles in Superheated Liquids," *J. Appl. Physics 25*, 493 (1954).

Press, W.H., Flannery, B.P., Teukolsky, S.A., and Vetterling, W.T., *Numerical Recipes - The Art of Scientific Computing*, Cambridge University Press, Cambridge, 1986.

Prisco, M.R., Henry, R.E., Hutcherson, M.N., and Linehan, J.L., "Nonequilibrium Critical Discharge of Saturated and Subcooled Liquid Freon-11," *Nuclear Science and Engineering 63*, 365 (1977).

Rayleigh, Lord, "On the Instability of Jets," *Proc. London Math. Soc. 10*, 7 (1878).

Reid, R.C., "Superheated Liquids," *American Scientists 64*, 146 (1976).

Reid, R.C., "Superheated Liquids - A Laboratory Curiosity and, Possibly, an Industrial Curse," *Chemical Engineering Education*, 60 (1978).

Reid, R.C., "Possible Mechanism for Pressurized-Liquid Tank Explosions or BLEVE's," *Science 203*, 1263 (1979).

Reid, R.C., Prausnitz, J.M., and Poling, B.E., *The Properties of Gases and Liquids, 4th Ed.*, McGraw-Hill, New York, 1987.

Richards, C.D., and Pitts, W.M., "Global Density Effects on the Self-Preservation Behaviour of Turbulent Free Jets, *J. Fluid Mech. 254*, 417 (1993).

Roberson, J.A., and Crowe, C.T., *Engineering Fluid Mechanics*, Houghton Mifflin Company, Boston, 1980.

Shapiro, A.H., *The Dynamics and Thermodynamics of Compressible Fluid Flow, Volume 1*, Ronald Press, New York, 1953.

Shirakashi, M., Arakawa, T., and Wakiya, S., "The Turbulent Structure and the Diffusion of the Nozzle Fluid in an Impulsively Started Axisymmetrical Jet," in *Turbulence and Chaotic Phenomena in Fluids*, Tatsumi, T., Ed., pp. 385-390, North-Holland, New York, 1984.

Smith, J.M., and Van Ness, H.C., *Introduction to Chemical Engineering Thermodynamics, 3rd Ed.*, McGraw-Hill, New York, 1975.

Solomon, A.S.P., Chen, L.-D., and Faeth, G.M., *Investigation of Spray Characteristics for Flashing Injection of Fuel Containing Dissolved Air and Superheated Fluids*, NASA Contractor Report 3563, 1982.

Thompson, P.A., *Compressible-Fluid Dynamics*, McGraw-Hill, New York, 1972.

Tong, L.S., *Boiling Heat Transfer and Two-Phase Flow*, John Wiley and Sons, New York, 1965.

Van den Akker, H.E.A., Snoey, H., and Spoelstra, H., "Discharge of Pressurized Liquefied Gases through Apertures and Pipes," *IChemE Symposium Series No. 80*, E23 (1983).

Weber, C., "Zum Zerfall eines Flüssigkeitsstrahles," *Zeit. fur Angew. Math. 11*, 106 (1931).

Williamson, H.V., "Halon 1301 Flow in Pipelines," *Fire Technology 13*, 18 (1976).